Laser Spectroscopy of Alkaline Earth Fluoride Crystals Doped With Trivalent Samarium and Europium Ions

A thesis submitted in partial fulfilment
of the requirements for the Degree
of
Doctor of Philosophy in Physics

by

Jon-Paul Renee Wells

at the

University of Canterbury

1996

Abstract

Alkaline earth fluoride crystals doped with Sm^{3+} and Eu^{3+} ions have been investigated by polarised laser selective excitation, Zeeman infrared and optical absorption. These studies identify four main centres for CaF_2:Sm^{3+} and CaF_2:Eu^{3+} crystals. They are a single RE^{3+}-F^- pair having C_{4v} symmetry, a near-cubic symmetry centre with a non-local charge compensator and two cluster centres. In CaF_2:Sm^{3+} crystals, the cluster centres are entirely non-radiative due to efficient cross-relaxation processes between the constituent Sm^{3+} ions. These centres have been investigated by codoping with additional RE^{3+} ions. Efficient $^4G_{\frac{5}{2}}(Sm^{3+}) \rightarrow {}^5D_0(Eu^{3+})$ energy transfer has been observed for the heterogeneous cluster centres in CaF_2:Sm^{3+}:Eu^{3+}. In SrF_2 crystals doped with Sm^{3+} and Eu^{3+} ions, the dominant centre consists of a single RE^{3+}-F^- pair of C_{4v} symmetry. In SrF_2:Eu^{3+} a weak C_{3v} symmetry centre has been observed which is analogous to the dominant centre in BaF_2:Eu^{3+} crystals.

Upconversion fluorescence has been observed for the dominant spectroscopic centres in CaF_2, SrF_2 and BaF_2 crystals doped with Eu^{3+}. This is assigned as a sequential absorption process with $^5D_0$ as the intermediate state. Enhancement of the upconverted fluorescence is observed for excitation of the $^7F_1 \rightarrow {}^5D_0$ transitions at room temperature.

High-resolution infrared absorption has been employed to study hyperfine structure of sharp absorption lines in CaF_2 and SrF_2 crytsals doped with Pr^{3+}, Tb^{3+} and Ho^{3+}. An interesting hyperfine pattern is observed for CaF_2:Ho^{3+} in which the hyperfine structure of a doublet state has been perturbed by the presence of two nearby singlet states. This pattern has been successfully analysed using the hyperfine interactions between these excited states.

Acknowledgements

Particular thanks to the department for providing funding in the form of a Teaching Assistantship, without which I would not have undertaken studies towards my Ph.D. Thanks also to my supervisor Dr Roger J. Reeves for his advice and guidance and to Dr Glynn D. Jones for his contributions and interest throughout this work.

I should also like acknowledge Wayne Smith and Ron Culley for their technicial assistance particularly with respect to repairs of the R.F. crystal growing furnace, Ross Richie for his assistance with keeping the laser lab operational and Tom Walker and Bob Flygenring for producing liquid helium and nitrogen used in the spectrometers, IR PMT tubes and magnets.

Significant thanks to Drs Mike Staines and Bob Buckley of Industrial Research Limited in Wellington, New Zealand for allowing me access to the Bomem spectrophotometer and for making my I.R.L. visit enjoyable and productive, and to Drs Neil Manson and John Martin of the Laser Physics Centre at the Australian National University in Canberra, Australia for their generousity and interest during a three week visit to their laboratory.

Dr Mike Reid of this Department provided the crystal field fitting programs used in this study and maintained an interest in the work throughout.

Finally I should like to thank my fellow laser spectroscopy students Dr Keith M Murdoch, Dr Nick M Strickland and Steve P Jamison for contributing to stimulating and productive atmosphere of the laser spectroscopy group.

Contents

Figures

Tables

Chapter 1

Introduction

1.1 Motivation

This thesis comprises a study of the fundamental electronic and magnetic properties of rare earth ions in predominantly ionic crystals. It is the existence of permanent (paramagnetic) moments and a shielded valence shell that make such systems interesting (the 4f shell lies within the $5s^2 5p$ shells). As a consequence of the 4f radial wavefunction contraction (see section 1.2), rare earth ions display minimal interaction with their environment leading to extremely sharp spectral lines with excited state lifetimes suitable for applications described below.

The real interest in rare earth doped insulating crystals was sparked off by the prediction of Schawlow and Townes in 1958 [1], of a maser operating in the optical region. In 1960, the laser period was ushered in when Mamian [2] announced the development of a pulsed synthetic ruby laser (Al_2O_3:Cr^{3+}) emitting in the red region of the visible spectrum at 0.6943 μm. Shortly after this, also in 1960, P Sorokin and M Stevenson [3] of the IBM Thomas J Watson Research Center developed a CaF_2:U^{3+} laser at liquid helium temperatures. The same authors reported laser action from CaF_2:Sm^{2+} at 77K thus divalent samarium proved to be the first laser lanthanide ion. The CaF_2:Sm^{2+} system is an example of a four level optically pumped solid state laser. The 708.4 nm lasing transition is a strong 5d$\rightarrow$4f electric dipole transition (oscillator strength f $\sim 10^{-2}$ as compared to f$\rightarrow$f transitions which are characteristed by oscillator strengths f $\sim 10^{-7}$ to 10^{-6}). This arises due to the promotion of a 4f electron out of the 4f shell, a relatively easy accomplishment because of the low binding energy of the 4f electrons.

Since the early days of the 1960's so many rare earth ion activated laser crystals have been developed that it is impossible to list them all. However, one system in particular stands out - YAG:Nd^{3+}. Nd^{3+} is the most widely used laser crystal activator, probably because Nd^{3+} ion lasers tend to have extremely low excitation thresholds. This is attributed to the fact that the terminal level of the induced transition lies about 2000 cm^{-1} above the ground state and is unpopulated at room

temperatures. YAG:Nd^{3+} has been successful in obtaining extremely high power outputs and can now be found in many industries employed in roles such as metal machining.

YAG:Nd^{3+} lasers are generally optically pumped (by flash lamp), however there is the strong desire to replace flash lamp pumping by laser diode pumps with the goal of obtaining highly efficient all solid state compact lasers [4]. A typical laser diode may consist of GaAlAs emitting at 780-870 nm or InGaAs emitting at 900-990 nm, such pump wavelengths are optimal for pumping ions like Nd^{3+}, Tm^{3+} and Er^{3+} providing laser sources at around 1μm, 2μm and 3μm. A 3μm laser source with an extremely short penetration in tissue of around 1μm could be used as a knife in surgery or microsurgery. The strong absorption of 3μm light in tissue leads to immediate partial vapourisation - the most effective cooling process in irradiated tissue. This process reduces the heat flow into the tissue reducing undesired coagulation of the walls of the incision, which in turn leads to faster healing.

Another useful example of rare earth doped crystals is their application as scintillation detectors. In this case, the crystal is irradiated with high energy electromagnetic radiation. This prompts the promotion of an electron from the valence shell to the conduction band with the de-excitation process producing UV light, detectable by photomultipliers. Scintillating crystals are limited by their decay time for fast counting applications. This is determined by the de-excitation process. A simple and efficent de-excitation process would be that where the promoted electron in the conduction band and the hole in the valence band directly recombine. However, this is often not the case and recombination involves intermediate states such as an exciton [5]. Such an example of exciton decay limited scintillation detection is the BaF_2:Ce^{3+} system. In this case, the effective decay time of the Ce^{3+} fluorescence is affected by the 630 ns decay time of the BaF_2 exciton. Thus, it is considerably slower than the instrinsic 27ns decay time of the d$\rightarrow$f transition. CeF_3 and $LuSiO_5$:Ce^{3+} are examples of fast and efficient scintillation detectors.

A further, and perhaps the most promising area of application for RE^{3+} doped compounds is fiber optic communications. Heavy metal fluoride glass fibers have the advantage (over silica glass fibers) that the multiphonon edge is shifted to longer wavelengths as higher energy light oscillates too quickly for the constituent ions (such as Ba^{2+}) to keep up [6]. Since Rayleigh scattering decreases rapidly at longer wavelengths (as $\frac{1}{\lambda^4}$), such glasses may be used as ultra low loss optical fibers. Er^{3+} and Ho^{3+} doped fibers are in particular, relevant, since they operate in the all important 1.55μm telecommunications window. These glasses offer attenuations of the order of 0.01 dB/km at longer wavelengths compared with the 0.12 dB/km obtained for silica. Thus, the opportunity arises for vast economic savings as well as increased efficency and reliability since fewer repeaters or signal regenerators would

be required to amplify the signal.

As noted by Kaminskii [7] it was the work of spectroscopists on the fundamental properties of rare earth doped compounds in the prelaser period which allowed the advance of laser technology to progress so quickly during the sixties and early seventies and it is important that this research is continued using the spectroscopic tools of the nineties and onward such that properties of these compounds (and those still to be developed) which are valuable to industry are exploited to their fullest.

1.2 Rare Earth Ions Doped Into Ionic Crystals

The rare earths are characterised by the progressive filling of their electronic configurations. As such they come in two groups (both of fourteen elements), the lanthanides and the actinides. The interest in this study is in the lanthanides, the common configuration of which is a xenon like rare gas shell of ($1s^2 2s^2 2p^6 3s^2 3p^6 3d^{10} 4s^2 4p^6 4d^{10} 5s^2 5p^6$) with two or three outer electrons ($6s^2$ or $5d6s^2$). The lanthanides commence with the element cerium (Z=58) and end with lutecium (Z=71). They do not include the element lanthanum itself as this has no 4f electrons in its normal configuration.

Table 1.1: Properties of rare earth ions

RE^{3+}	N	Ionic Radius ($\AA$)	Isotope	I_z	Isotopic Abundance (%)
Pr^{3+}	2	1.09	141	$\frac{5}{2}$	100
Sm^{3+}	5	1.04	147	$\frac{7}{2}$	15.0
			149	$\frac{7}{2}$	13.8
Eu^{3+}	6	1.03	151	$\frac{5}{2}$	47.8
			153	$\frac{5}{2}$	52.2
Tb^{3+}	8	1.00	159	$\frac{3}{2}$	100
Ho^{3+}	10	0.97	165	$\frac{7}{2}$	100

Proceeding through the lanthanide series the charge of the nucleus and the number of 4f electrons increases by one at each step. Due to imperfect shielding of 4f electrons by other 4f electrons, with each increase the effective nuclear charge increases causing a reduction in radius of the entire 4f shell. As a result of this contraction, the 4f shell lies inside the $5s^2$ and $5p^6$ shells and behaves as an inner shell. Since the 4f electrons are shielded by the $5s^2 5p^6$ closed shells and the extension of the 4f eigenfunction is minimal any interaction of the 4f electrons with their environment is limited.

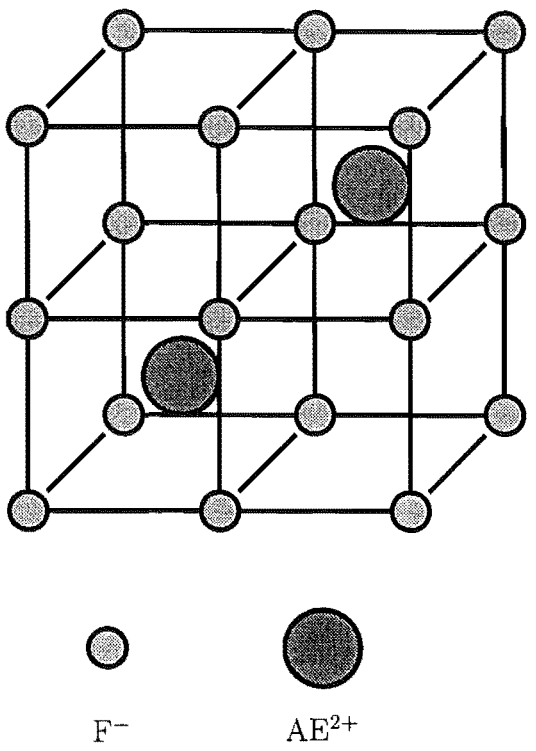

Figure 1.1: Schematic diagram of the alkaline earth fluoride structure

The CaF_2, SrF_2 and BaF_2 crystalline lattice consists of a face centred cubic structure (Figure 1.1). The F^- ions form a cubic lattice cage with a F^- ion at each corner. The alkaline earth then resides at the centre of each alternate cage. Rare earth ions are readily introduced most commonly in the trivalent state. This being so charge compensation is required and can come in many and varied forms. The dominant charge compensation centre in CaF_2 crystals with low concentrations of rare earth dopant (less than 0.1 molar percent) is the now well established C_{4v} symmetry centre [8] where the charge compensating F^- ion occupies a nearest neighbour interstitial position along a $\langle 100 \rangle$ direction[1] (see Figure 1.2). Additionally, there has been observed a secondary centre (of comparable intensity) in which the F^- ion occupies a next nearest neighbour position along a $\langle 111 \rangle$ direction (see Figure 1.3) giving a centre of trigonal C_{3v} symmetry. At higher concentrations the site distribution is dominated by clusters that scavenge fluoride interstitials which result in centres of excess negative charge. It has been suggested that dimers and trimers dominate for rare earths lighter than Gd^{3+} whilst hexamer clusters dominate for the heavier elements [10]. The SrF_2 case is more varied [11], [12], [13], [14], [15] , [16] with C_{4v}

[1]In indexing crystallographic axes and planes the conventions of Kittel [9] pg 12 are adopted. This is as follows: (hkl) denotes a specific plane, {hkl} denotes a general plane, [hkl] denoted a specific axis and ⟨hkl⟩ denotes a general axis

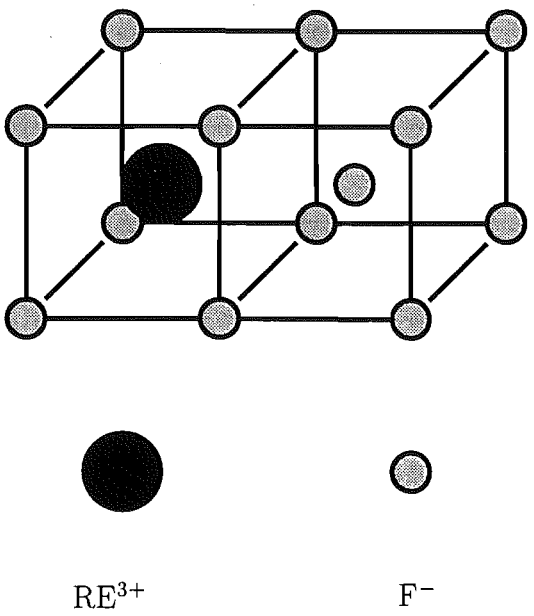

Figure 1.2: Schematic diagram of the C_{4v} centre in alkaline earth fluoride crystals.

centres observed for the first two thirds of the series to Ho^{3+} with a change over between Ho^{3+} and Er^{3+} to C_{3v} trigonal centres observed from Er^{3+} onward [2]. The BaF_2 case is different again with C_{3v} centres observed for most ions of the series with a variety of techniques.

These experimental results essentially confirm the predictions of the simple electrostatic model of Brown et. al. (1969) [20]. This model predicts dominance of the tetragonal C_{4v} centre throughout the entire RE^{3+} series for CaF_2, a change over from tetragonal C_{4v} to trigonal C_{3v} between Dy^{3+} and Ho^{3+} for SrF_2 and a changeover from tetragonal C_{4v} to trigonal C_{3v} for BaF_2 between Pr^{3+} and Nd^{3+}. Corish et. al. (1982) [21] have also simulated the relative stability of the C_{4v} and C_{3v} centres in alkaline earth fluoride crystals, these authors finding that for CaF_2 the C_{4v} centre is dominant throughout the rare earth series, SrF_2 shows intermediate behaviour with a changeover of dominant centre from C_{4v} to C_{3v} between Gd^{3+} and Er^{3+} whilst in the BaF_2 host the C_{3v} is predominant throughout. They comment that the essential factor contributing to the energy of formation appeared to be the relaxations of the lattice ions that surround the dopant. An outward movement which is likely to be most significant in the smallest host for the largest dopant ion, tends to relax the interstitial towards the dopant ion for the C_{4v} centre and thus stabilising it. Conversely, an inward movement of the surrounding lattice ions, favoured by smaller

[2]It should be noted at this point that the optical studies of Mujaji [17] are in disagreement with results obtained from Zeeman infrared absorption [18] and EPR studies [19]. As a consequence the assignment of a dominant centre of tetragonal C_{4v} symmetry in SrF_2:Ho^{3+} can only be considered as tentative

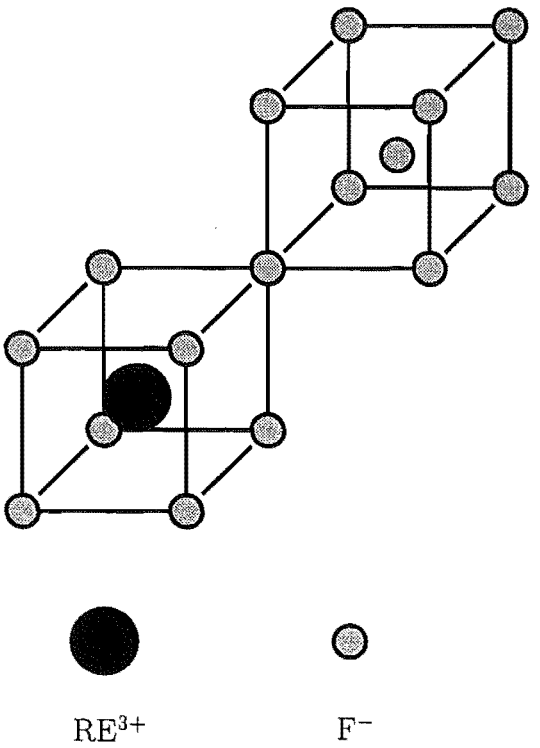

Figure 1.3: Schematic diagram of the C_{3v} centre in alkaline earth fluoride crystals.

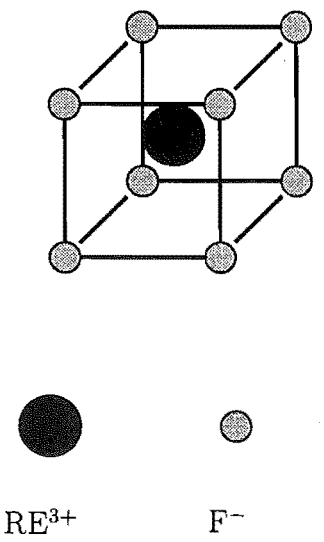

Figure 1.4: Schematic diagram of the O_h centre in alkaline earth fluoride crystals.

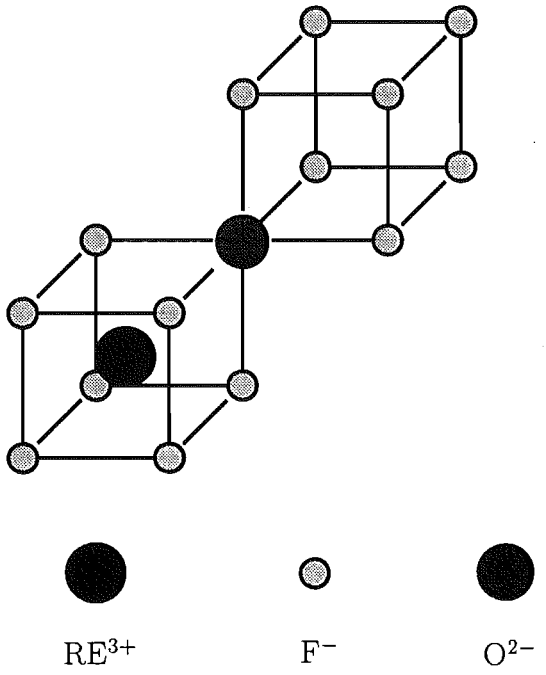

Figure 1.5: Schematic diagram of the G1 centre in alkaline earth fluoride crystals.

dopant ions in larger lattices, assists in the stabilisation of the C_{3v} centre. Cubic centres are also known to exist in alkaline earth fluoride crystals where the charge compensating fluoride ion is non-locally positioned. Such centres cannot always be observed due to the selection rules for centres with inversion symmetry - Figure 1.4.

In addition, if oxygen is present in the crystal it can act as a charge compensator. The predominant oxygen charge compensating center is of C_{3v} symmetry with an O^{2-} ion replacing an F^- ion in a substitutional position along a $\langle 111 \rangle$ direction from the rare earth ion, this centre is commonly denoted as the G_1 centre [14]. This is shown schematically in Figure 1.5. Depending on the severity of the oxidising conditions an additional centre of C_{3v} symmetry is created. This centre has four charge compensating O^{2-} ions producing a very strong trigonal distortion from the parent cubic centre, the so called T_1 centre. The oxygen centres observed in this study have C_{3v} symmetry however we have no information as to the number of O^{2-} ions involved in the centre other than the strength of the axial crystal field splitting due to the trigonal distortion, therefore they are denoted G1 with the most likely probability being that one O^{2-} ion is required for charge compensation due to the low oxygenation periods.

1.3 Laser Selective Excitation

Like all multicentre crystals, RE^{3+} ion doped alkaline earth fluoride crystals can have very complex spectra, particularly at higher concentrations. Conventional (non-selective) optical spectroscopy does not easily yield transition correlation information. It was not until the technique of laser selective excitation (l.s.e.) was first reported in 1975, in a now classic paper by Tallant and Wright [22], that many meaningful analyses of the optical spectra of RE^{3+} doped multicentre crystals were untaken. This technique involves the use of moderately narrowband laser sources (around 0.8 cm^{-1} linewidth is used in this study) to selectively excite individual absorption transitions. Because of the higher resonant intensities associated with laser light sources many ions are excited to the higher state with which the laser is in resonance. Assuming the absorption transition is well resolved from that of other centres only the centre corresponding to the transition in question is excited. Thus complex spectra such as those reported for CaF_2:Er^{3+} by Tallant and Wright (in which 16 centres were present) may be separated and analysed individually. There are many advantages associated with this method, not the least of which is the sensitivity, a consequence of which is that very small samples or even extremely poor optical quality samples can give a wealth of meaningful information about the system under investigation.

A further development of this technique is the laser selected Zeeman fluorescence method developed by Freeth et. al. (1982) [23] where a magnetic field is applied to the crystal (normally parallel or transverse to the principal symmetry axis) and individual Zeeman sublevels are selected out employing the same technique as Tallant and Wright. This yields more information than that obtained by Tallant and Wright since the Zeeman splittings are generally anisotropic with respect to crystallographic axis and obey rigourous selection rules dependent upon the local symmetry experienced by the optically active rare earth ion.

Both of these techniques are now in widespread use in laser spectroscopy laboratories around the world and form the basis of this thesis.

1.4 The Work Outlined

The objectives of this study has been as follows:

- To determine the structure of Eu^{3+} and Sm^{3+} doped defect centres in CaF_2, SrF_2 and BaF_2 crystals using both CW and pulsed laser selective excitation and fluorescence.
- To analyse the observed high symmetry centres via polarisation of the observed fluorescence with the aim of assigning irreducible representations (irreps) to the inferred energy levels.
- To complete Zeeman studies of sharp electronic absorption lines in the 900-10000 cm^{-1} region accessible with the available Digilab FTIR spectrometer and 4T magnet.
- To analyse the crystal and magnetic field data in terms of crystal field calculations from which Zeeman calculations can be performed to check the accuracy of assigned wavefunctions.
- The determination of preferential clustering in CaF_2:RE^{3+} systems using Sm^{3+} as a co-dopant probe
- To record, measure and analyse interesting electron-nuclear interactions in CaF_2 and SrF_2 crystals doped with Ho^{3+}, Tb^{3+} and Pr^{3+}.

In chapter two, a brief survey of crystal and magnetic field theory, hyperfine interactions, transition probabilities and polarisation selection rules are presented. Chapter three discusses experimental procedures such as crystal growth; all crystals used in this study were grown by the author. The remainder of the chapter concentrates on the methods of surveying the prepared samples. As such, this includes the various excitation sources used; two different CW argon ion lasers and a pulsed nitrogen laser have been employed as well as optical and infrared absorption, several different spectrometers, in addition to cryogenic dewars and magnets.

Chapter four presents high resolution infrared absorption for C_{4v} symmetry centres in CaF_2 and SrF_2 crystals doped with Ho^{3+}, Tb^{3+} and Pr^{3+}. All three of these ions have large nuclear magnetic moments and hyperfine structure due to interaction of the magnetic field created by the 4f electrons and the nucleus are observable by conventional spectroscopic means. For Ho^{3+} doped CaF_2, the C_{4v} symmetry centre yields interesting hyperfine transition intensity distributions as the ground state is a pseudo-degenerate state. A particularly interesting hyperfine pattern is present

for absorption to the $^5I_7$ multiplet which is analysed in terms of the superposition of ground state hyperfine structure and that due to interactions between a doublet state and two nearby singlets.

Chapters five and six present the laser spectroscopy of Sm^{3+} doped CaF_2 and SrF_2 crystals and Eu^{3+} doped CaF_2, SrF_2 and BaF_2 crystals respectively. For CaF_2 doped crystals, similar defect distributions are observed for doping of either Sm^{3+} or Eu^{3+} ions. This consists of a dominant centre of C_{4v} symmetry with two preferential cluster centres observed in each case. As both the $^6H_{\frac{5}{2}} \rightarrow ^4G_{\frac{5}{2}}(Sm^{3+})$ and $^7F_0 \rightarrow ^5D_1(Eu^{3+})$ transitions are predominantly magnetic dipole in character, cubic centres are observed. In SrF_2 doped crystals the clustering is not so prominant and thus the C_{4v} centre alone dominates the spectrum. For BaF_2:Eu^{3+} the effects of clustering are still further reduced and the dominant centre has C_{3v} symmetry. This centre is shown to be similar in RE^{3+}-F^- configuration to a minority C_{3v} symmetry centre observed in SrF_2:Eu^{3+}. Crystal field calculations have been performed to give a full analysis of many of these centres with results consistent with that of previous workers.

Chapter seven presents laser selective excitation and fluorescence studies of mixed Sm^{3+}:RE^{3+} doped CaF_2 crystals. This concentrates on preferential cluster centres observed in the parent CaF_2:Sm^{3+} system. This clustering is found to comprise dimers at the early part of the rare earth series with more complex clustering observed for the latter part (e.g CaF_2:Lu^{3+}:Sm^{3+}). The cluster centres observed in CaF_2:Sm^{3+} are shown to be identical to that in CaF_2:Eu^{3+} and virtually one hundred percent efficient energy transfer from $^4G_{\frac{5}{2}}(Sm^{3+})$ to $^5D_0(Eu^{3+})$ is observed.

Chapter eight studies strong infrared absorption transitions of the assigned centres in Sm^{3+} and Eu^{3+} doped CaF_2, SrF_2 and BaF_2 crystals. The effect of a magnetic field on the observed transitions is studied and analysed in order to confirm the centre symmetry assigned from laser selective excitation and to obtain magnetic splitting factors for comparision with those calculated from the crystal field wavefunctions.

Finally, chapter nine summarises the work and discusses the conclusions that can be drawn from these studies. Suggestions for additional experiments are made.

Chapter 2

Theoretical Review

2.1 The Free Ion

The interactions of the $4f^N$ electrons in the free ion may be represented by an interaction Hamiltonian (Weissbluth, 1978) [24]

$$H_{f.i.} = \left[\frac{-\hbar^2}{2m}\Sigma_{i=1}^{N}\nabla_i^2 - \Sigma_{i=1}^{N}\frac{Ze^2}{r_i} + \Sigma_{i<j}^{N}\frac{e^2}{r_{ij}}\right] + \Sigma_{i=1}^{N}\zeta(r_i)l_i \cdot s_i \qquad (2.1)$$

where the first term in Equation 2.1 is the total kinetic energy of all N electrons, the second is their total potential in the electric field of the nucleus whilst the third term is the inter electron (Coulombic) repulsion term. The last term represents the spin orbit interaction of the $4f^N$ electrons. The essential difficulty in solving this equation is that the inter electron repulsion term is too large to be treated as a perturbation. As a consequence, the central field approximation is employed. This entails the construction of a spherically symmetric potential energy function $U(r_i)$ which is a good approximation to the field experienced by a 4f electron due to the nucleus and the other $4f^{N-1}$ electrons. Thus $H_{f.i.}$ may be written

$$H_{f.i.} = H_o + H_{cou} + H_{s.o.}$$

$$= \Sigma_{i=1}^{N}\left[\frac{-\hbar^2}{2m}\nabla_i^2 + U(r_i)\right] + \left[\Sigma_{i=1}^{N}\frac{-Ze^2}{r_i} - \Sigma_{i=1}^{N}U(r_i) + \Sigma_{i<j}^{N}\frac{e^2}{r_{ij}}\right] + \Sigma_{i=1}^{N}\zeta(r_i)l_i \cdot s_i \qquad (2.2)$$

The central field term H_o is now solvable as N single electron equations with solutions of the form

$$\psi_{nlm_lm_s}(r,\theta,\phi) = \frac{R_{nl}(r)}{r}Y_{lm_l}(\theta,\phi)\chi_{m_s} \qquad (2.3)$$

where the radial wavefunctions R_{nl} depend on $U(r_i)$, the Y_{lm_l} are the spherical harmonics and χ_{m_s} are the spin functions. These are then antisymmetrised to satisfy the Pauli exclusion principle.

The remaining terms in Eqn 2.2 can now be treated as perturbations on H_o. Of

these, only

$$\Sigma_{i,j}^{N} \frac{e^2}{r_{ij}} \tag{2.4}$$

and

$$\Sigma_{i=1}^{N} \zeta(r_i) l_i \cdot s_i \tag{2.5}$$

contribute to the splitting of the degenerate configuration. It is sufficient to calculate the matrix elements of these interactions alone. The Coulombic repulsion term splits 4f configuration into terms, each of which is denoted by ^{2S+1}L. The magnitude of this splitting is typically of the order of 10000 cm^{-1}. In heavier elements such as the rare earths, spin orbit coupling is comparable to the Coulomb interaction and splits the ^{2S+1}L terms into $2S+1$ levels, each of $2J+1$ fold degeneracy. Spin orbit coupling may be thought of as the interaction between the spin magnetic moment and the magnetic field produced by the orbital motion of the electron itself. The magnitude of this interaction is around 1000 cm^{-1} and spin orbit levels (or multiplets) are labelled by $^{2S+1}L_J$. Spin orbit coupling will also mix states of the same J (but different L and S).

Additional interactions may be included such as the interaction between different configurations of the same parity (a configuration has odd or even parity depending upon whether the sum of the one electron orbital angular momentum is even or odd) that differ in the coordinates of not more than two electrons. Further refinements can be made with the inclusion of the spin-spin and spin-other-orbit interactions (represented by the Marvin integral, M^k) and finally the electrostatically correlated spin orbit and three body electrostatic interactions with parameters P^k and T^k respectively.

2.2 Crystal Field Theory

The free ion has spherical symmetry with each level being $(2J + 1)$ degenerate. Upon placing the ion in a crystal, the spherical symmetry is lowered to that of the site symmetry in the crystal and the free ion levels split under the influence of the field provided by the neighbouring ions. For the $4f^N$ shell, this splitting is smaller than the spin orbit interaction (weak field coupling scheme) and the crystal field interaction can be treated as a perturbation on the free ion $\mid \alpha LSJ\rangle$ states. This can be represented as

$$H_T = H_{f.i.} + H_{c.f.}$$

As the eigenfunctions of $H_{f.i.}$ have spherical symmetry, we can expand $H_{c.f.}$ in terms of spherical harmonics or operators that transform like spherical harmonics. We can write

$$H_{c.f.} = \Sigma_{k,q,i}^{N} B_q^k (C_q^{(k)})_i \tag{2.6}$$

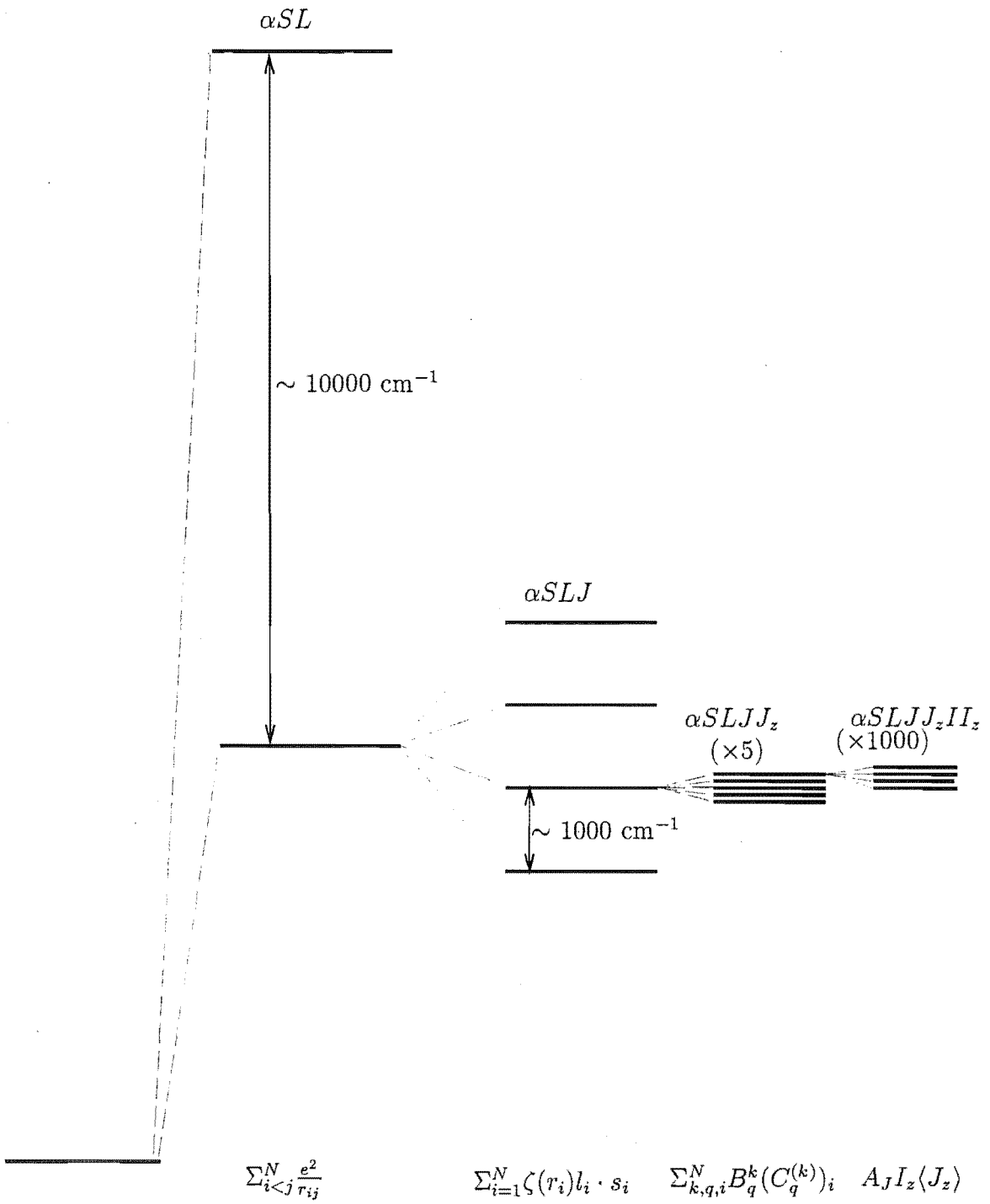

Figure 2.1: Schematic diagram of the successive interactions experienced by rare earth ions in crystalline solids.

where the sum is over the N electrons of the $4f^N$ configuration. The B_q^k are treated as parameters that quantify the strength of the field acting on the rare earth ion. The possible k, q values are governed by triangular rule for the addition of angular momentum which gives non zero matrix elements associated with k even values due to parity. The values of k may be additionally constrained if we assume we are only dealing with states of a single configuration then $2l \geq k \geq 0$. k=0 values will only produce a uniform shift of all levels and hence are neglected. Finally the $C_q^{(k)}$ are the Racah spherical tensor operators, they are related to the spherical harmonics $Y_{k,q}$ by

$$C_q^{(k)} = \sqrt{\frac{4\pi}{2k+1}} Y_{k,q} \tag{2.7}$$

For a given crystal field Hamiltonian, the matrix elements for the interaction term can be calculated as follows

$$\langle f^N \alpha S L J J_z \mid H_{c.f.} \mid f^N \alpha' S L' J' J'_z \rangle = \Sigma_{k,q} B_q^k \langle f^N \alpha S L J J_z \mid U_q^k \mid f^N \alpha' S L J' J'_z \rangle$$

$$\times \langle l \mid\mid C^{(k)} \mid\mid l' \rangle \tag{2.8}$$

where

$$\langle l \mid\mid C^{(k)} \mid\mid l' \rangle = (-1)\sqrt{(2l+1)(2l'+1)} \begin{pmatrix} l & k & l' \\ 0 & 0 & 0 \end{pmatrix} \tag{2.9}$$

and α represents all other quantum numbers necessary to specify the state in question. The U_q^k matrix elements may have their J and J_z dependence removed by application of, first the Wigner Eckart theorem

$$\langle f^N \alpha S L J J_z \mid U_q^k \mid f^N \alpha' S L' J' J'_z \rangle = (-1)^{J-J_z} \sqrt{(2J+1)(2J'+1)} \begin{pmatrix} J & k & J' \\ -J_z & q & J'_z \end{pmatrix}$$

$$\times \langle f^N \alpha S L J \mid\mid U^k \mid\mid f^N \alpha' S L' J' \rangle \tag{2.10}$$

then Egn 2.49 of Wybourne [25]

$$\langle f^N \alpha S L J \mid\mid U^k \mid\mid f^N \alpha' S L' J' \rangle = (-1)^{S+L'+J+k} \sqrt{(2J+1)(2J'+1)} \begin{Bmatrix} J & J' & k \\ L' & L & S \end{Bmatrix}$$

$$\times \langle f^N \alpha S L \mid\mid U^k \mid\mid f^N \alpha' S L' \rangle \tag{2.11}$$

Nielson and Koster [26] tabulate the required reduced matrix elements whilst the values of the 3j and 6j symbols can be found in Rotenburg et. al. [27]. The axial terms U_0^k split the levels of the same J_z, while the U_q^k terms mix the states for which $J_z - J'_z = q$. The consequence of these latter terms, is that J and J_z cease to be good quantum numbers and use of irreps of the point group appropriate to the local symmetry of the ion in the crystal can be used to label electronic states.

For a C_{4v} symmetry centre the crystal field interaction Hamiltonian is given by

$$V_{c.f.} = B_A^2 C_0^{(2)} + B_A^4[C_0^{(4)} - \sqrt{\frac{7}{10}}(C_4^{(4)} + C_{-4}^{(4)})] + B_A^6[C_0^{(6)} + \sqrt{\frac{1}{14}}(C_4^{(6)} + C_{-4}^{(6)})]$$

$$+B_C^4[C_0^{(4)} + \sqrt{\frac{5}{14}}(C_4^{(4)} + C_{-4}^{(4)})] + B_C^6[C_0^{(6)} - \sqrt{\frac{7}{2}}(C_4^{(6)} + C_{-4}^{(6)})] \qquad (2.12)$$

where the B_C^4 and B_C^6 are the parameters of the cubic component of the crystal field and B_A^k are parameters describing the strength of the tetragonal distortion. The relations between this Hamiltonian and that used by Freeth et. al. [11] are given by Mujaji [15].

For a C_{3v} symmetry centre the interaction Hamiltonian is given by

$$V_{c.f.} = B_A^2 + B_A^4[C_0^{(4)} - \frac{1}{2}\sqrt{\frac{7}{10}}(C_3^{(4)} - C_{-3}^{(4)})] + B_A^6[\sqrt{\frac{11}{42}}(C_3^{(6)} - C_{-3}^{(6)}) + \sqrt{\frac{5}{21}}(C_6^{(6)} + C_{-6}^{(6)})]$$

$$+B_{\hat{A}}^6[C_0^{(6)} + \frac{4}{7}\sqrt{\frac{10}{21}}(C_3^{(6)} - C_{-3}^{(6)}) - \frac{4}{7}\sqrt{\frac{11}{21}}(C_6^{(6)} + C_{-6}^{(6)})] + B_C^4[C_0^{(4)} + \sqrt{\frac{10}{7}}(C_3^{(4)} - C_{-3}^{(4)})]$$

$$+B_C^6[C_0^{(6)} - \sqrt{\frac{35}{96}}(C_3^{(6)} - C_{-3}^{(6)}) + \frac{1}{8}\sqrt{77}3(C_6^{(6)} + C_{-6}^{(6)})] \qquad (2.13)$$

where the principal (z) axis is now the $\langle 111 \rangle$ direction. The B_A^k crystal field parameters reflect the strength of the trigonal distortion. It should be noted that the $B_{\hat{A}}^6$ and B_A^6 parameters above (like those of Cockcroft [14]) are oppositely defined to those of Mujaji. The convention of Cockcroft is adopted for simplicity in comparing the trigonal symmetry J centre parameters.

2.3 The Zeeman Effect

The application of a magnetic field lifts any remaining degeneracy of the crystal field levels. The magnetic field is usually applied in a direction either parallel or perpendicular to the principal symmetry axis of the ion in the crystal. The perturbation on the electronic energy levels of the ion provided by the magnets used in this study is small compared to that produced by the crystal field and the Zeeman Hamiltonian may be treated as a perturbation on the crystal field states.

In the theory of the Zeeman effect, the Hamiltonian H_{zmn}, for the interaction between the N electrons and an external magnetic field B, is written as

$$H_{zmn} = \mu_B B \cdot \Sigma_{i=1}^N (l_i + 2s_i) \qquad (2.14)$$

where $\mu_B = \frac{e\hbar}{2m}$ is the Bohr magneton. The parallel and perpendicular Zeeman effects can be calculated from

$$H_{\parallel} = \mu_B B_z (L_z + 2S_z) \tag{2.15}$$

and

$$H_{\perp} = \mu_B B_x (L_x + 2S_x) \tag{2.16}$$

respectively. Within a given J multiplet these interactions give rise to matrix elements of the type

$$\langle f^N \alpha SLJJ_z \mid (L_z + 2S_z) \mid f^N \alpha SLJJ_z \rangle$$
$$= (-1)^{J-J_z} \begin{pmatrix} J & 1 & J \\ -J_z & 0 & J_z \end{pmatrix} \langle f^N \alpha LSJ \mid\mid L + 2S \mid\mid f^N \alpha LSJ \rangle \tag{2.17}$$

At this point it is worth realising that

$$\langle \alpha SLJ \mid\mid L + 2S \mid\mid \alpha SLJ \rangle = (-1)^{S+L+J+1}(2J+1)$$
$$\times \left[\begin{Bmatrix} J & 1 & J \\ L & S & L \end{Bmatrix} \langle \alpha L \mid\mid L \mid\mid \alpha L \rangle + 2 \begin{Bmatrix} J & 1 & J \\ S & L & S \end{Bmatrix} \langle \alpha S \mid\mid S \mid\mid \alpha S \rangle \right]$$

We note from Edmonds pg 76 [28] that

$$\langle \alpha L \mid\mid L \mid\mid \alpha L \rangle = \sqrt{L(L+1)(2L+1)} \tag{2.18}$$

and similarly for S. Further, and also from Edmonds (pg 130), the general expression for the $6j$ is

$$\begin{Bmatrix} a & b & c \\ 1 & c & b \end{Bmatrix} = (-1)^{a+b+c+1} \frac{2[b(b+1) + c(c+1) - a(a+1)]}{\sqrt{2b(2b+1)(2b+2)(2c+1)(2c+2)2c}}. \tag{2.19}$$

Therefore we may write

$$\langle \alpha SLJ \mid\mid L{+}2S \mid\mid \alpha SLJ \rangle = \left[1 + \frac{J(J+1) + S(S+1) - L(L+1)}{2J(J+1)} \right] \sqrt{J(J+1)(2J+1)}$$
$$= g_L \sqrt{J(J+1)(2J+1)} \tag{2.20}$$

In addition we obtain an expression for the $3j$ symbol of Eqn 2.17 as

$$\begin{pmatrix} J & 1 & J \\ -J_z & 0 & J_z \end{pmatrix} = (-1)^{J-J_z} \frac{J_z}{\sqrt{J(J+1)(2J+1)}} \tag{2.21}$$

Substituting both equations 2.20 and 2.21 into 2.17 we obtain the result

$$\langle f^N \alpha SLJJ_z \mid (L_z{+}2S_z) \mid f^N \alpha SLJJ_z \rangle = (-1)^{J-J_z}(-1)^{J-J_z} J_z \frac{(g_L \sqrt{J(J+1)(2J+1)})}{\sqrt{(2J+1)(J+1)J}}$$

$$= g_L J_z \tag{2.22}$$

for the parallel effect. For the perpendicular Zeeman effect we first write the matrix elements of $(L_x + 2S_x)$ in the tensor operator form of Eqn 2.29 of Wybourne [25] and then solve as before yielding

$$\begin{aligned}
&\langle f^N \alpha LSJJ_z + 1 \mid L_{+1} + 2S_{+1} \mid f^N \alpha LSJJ_z \rangle \\
&= (-1)^{J-J_z-1} \begin{pmatrix} J & 1 & J \\ -J_z - 1 & 1 & J_z \end{pmatrix} \langle f^N \alpha LSJ \parallel L + 2S \parallel f^N \alpha LSJ \rangle \\
&= (-1)^{J-J_z-1}(-1)^{J-J_z} \sqrt{\frac{2(J-J_z)(J+J_z+1)}{4J(J+1)(2J+1)}}\, g_L \sqrt{J(J+1)(2J+1)} \\
&= -g_L \sqrt{\frac{1}{2}(J-J_z)(J+J_z+1)}
\end{aligned} \tag{2.23}$$

and

$$\begin{aligned}
&\langle f^N \alpha LSJJ_z - 1 \mid L_{-1} + 2S_{-1} \mid f^N \alpha LSJJ_z \rangle \\
&= (-1)^{J-J_z+1} \begin{pmatrix} J & 1 & J \\ -J_z + 1 & -1 & J_z \end{pmatrix} \langle f^N \alpha LSJ \parallel L + 2S \parallel f^N \alpha LSJ \rangle \\
&= (-1)^{J-J_z-1} \begin{pmatrix} J & 1 & J \\ J_z - 1 & 1 & -J_z \end{pmatrix} (-1)^{2J+1} \langle f^N \alpha LSJ \parallel L + 2S \parallel f^N \alpha LSJ \rangle \\
&(-1)^{J-J_z+1}(-1)^{2J+1}(-1)^{J+J_z} \sqrt{\frac{2(J+J_z)(J-J_z+1)}{4J(J+1)(2J+1)}}\, g_L \sqrt{J(J+1)(2J+1)} \\
&= g_L \sqrt{\frac{1}{2}(J+J_z)(J-J_z+1)}
\end{aligned} \tag{2.24}$$

Finally we obtain

$$\begin{aligned}
&\langle f^N \alpha SLJJ_z \pm 1 \mid (L_x + 2S_x) \mid f^N \alpha SLJJ_z \rangle \\
&= \pm i \langle f^N \alpha SLJJ_z \pm 1 \mid (L_y + 2S_y) \mid f^N \alpha SLJJ_z \rangle \\
&= (\frac{g_L}{2}) \sqrt{(J \mp J_z)(J \pm J_z + 1)}
\end{aligned} \tag{2.25}$$

for the perpendicular effect. The parallel and perpendicular magnetic splitting values, $s_{\parallel}$ and $s_{\perp}$, of the crystal field energy levels can be expressed by the relationship

$$s = \frac{\Delta E}{\mu_B B} \tag{2.26}$$

where ΔE is the energy separation between the components of a doublet in a magnetic field.

2.4 Hyperfine Interactions

The crystal field energy levels can be further split by the interaction between the nuclear magnetic moment and the electron spin and orbital moments. The nuclear magnetic dipole moment μ_I is $g_I \mu_N I$, where g_I is the nuclear g factor and μ_N is the nuclear magneton which is

$$\frac{e\hbar}{2M_p} = \frac{m}{M_p}\mu_B \tag{2.27}$$

with M_p the proton mass. Since $\mu_N = \frac{\mu_B}{1836}$, hyperfine splittings are typically less than 0.1 cm^{-1} and it has not been until the advent of high resolution laser techniques that many examples of well resolved optical hyperfine structure have been observed.

Each 4f electron will produce a magnetic field B^{4f} at the nucleus. The energy of magnetic interaction $H_{h.f.s.}$ between the magnetic field at the nucleus and the nuclear magnetic moment μ_I may be written

$$H_{h.f.s.} = -\Sigma_{i=1}^{N} B^{4f} \cdot \mu_I$$

The main contribution to B^{4f} is that due to the orbital motion of the 4f electrons

$$B^{4f}_{orbital} = -2\mu_B \Sigma_{i=1}^{N} \frac{l_i}{r_i^3} \tag{2.28}$$

where l_i is the orbital angular momentum of the ith 4f electron and r_i is the ith electron nucleus distance. A smaller contribution arises from the intrinsic spin of the 4f electrons s_i

$$B^{4f}_{spin} = 2\mu_B \Sigma_{i=1}^{N} \left(\frac{s_i}{r_i^3} - \frac{3r_i(s_i \cdot r_i)}{r_i^5} \right) \tag{2.29}$$

Thus we may write

$$H_{h.f.s.} = 2\mu_B \mu_N g_I \Sigma_{i=1}^{N} \frac{N_i \cdot I}{r_i^3} \tag{2.30}$$

where $N_i = l_i - s_i + \frac{3r_i(s_i \cdot r_i)}{r_i^2}$. N_i may be put into tensorial form to yield

$$N_i = l_i - (10)^{\frac{1}{2}} (sC^{(2)})_i^{(1)} \tag{2.31}$$

then

$$H_{h.f.s.} = a_l \Sigma_{i=1}^{N} [l_i - (10)^{\frac{1}{2}} (sC^{(2)})_i^{(1)}] \cdot I \tag{2.32}$$

where $a_l = 2\mu_B \mu_N g_I \langle r^{-3} \rangle$, $\langle r^{-3} \rangle$ being the expectation value of the inverse cube radius of the electron orbital.

In the absence of external fields (such as in the free ion), the matrix elements of

$H_{h.f.s.}$ are evaluated in the $JIFM$ coupling scheme. J and I are regarded as coupling together to form a resultant total angular momentum F. Employing Eqn 2.47 of Wybourne in the $JIFM$ coupling scheme we may obtain the matrix elements of $H_{h.f.s.}$ as

$$\langle \alpha JIFM \mid H_{h.f.s.} \mid \alpha JIFM \rangle = (-1)^{J+I+F} a_l \left\{ \begin{array}{ccc} J & J & 1 \\ I & I & F \end{array} \right\} \langle I \mid\mid I^{(1)} \mid\mid I \rangle$$

$$\times \langle \alpha J \mid\mid \Sigma_{i=1}^{N} N_i \mid\mid \alpha' J \rangle \tag{2.33}$$

The components of this matrix may be solved in a similar manner to that of the Zeeman matrices. This yields

$$\langle \alpha JIFM \mid H_{h.f.s.} \mid \alpha JIFM \rangle = (-1)^{J+I+F} a_l (-1)^{J+I+F+1}$$

$$\times \frac{2[J(J+1)+I(I+1)-F(F+1)]}{\sqrt{2J(2J+1)(2J+2)(2I+1)(2I+2)2I}} \sqrt{I(I+1)(2I+1)} \langle \alpha J \mid\mid \Sigma_{i=1}^{N} N_i \mid\mid \alpha' J \rangle$$

$$= \frac{a_l}{2} \left(\frac{F(F+1)-J(J+1)-I(I+1)}{\sqrt{J(J+1)(2J+1)}} \right) \langle \alpha J \mid\mid \Sigma_{i=1}^{N} \mid\mid \alpha' J \rangle \tag{2.34}$$

Let

$$A_J = \frac{a_l (\alpha J \mid\mid \Sigma_{i=1}^{N} N_i \mid\mid \alpha' J)}{[J(J+1)(2J+1)]^{\frac{1}{2}}} \tag{2.35}$$

where A_J is known as the magnetic hyperfine structure constant. We can evaluate for A_J starting with the angular component. We note that

$$\frac{(\alpha SLJ \mid\mid L \mid\mid \alpha SLJ)}{[J(J+1)(2J+1)]^{\frac{1}{2}}} = 2 - g \tag{2.36}$$

whilst the spin part (the matrix element in $(sC^{(2)})_i^{(1)}$) may be evaluated (Wybourne) [29] to give

$$\langle f^N \alpha SLJ \mid\mid (10)^{\frac{1}{2}} \Sigma_{i=1}^{N} (sC^{(2)})_i^{(1)} \mid\mid f^N \alpha' S'L'J \rangle = (30)^{\frac{1}{2}} (2J+1) \left\{ \begin{array}{ccc} S & S' & 1 \\ L & L' & 2 \\ J & J & 1 \end{array} \right\}$$

$$\times \langle f \mid\mid C^{(2)} \mid\mid f \rangle \langle f^N \alpha SL \mid\mid V^{(12)} \mid\mid f^N \alpha' S'L' \rangle \tag{2.37}$$

Therefore the final expression is

$$A_J = a_l \left[2 - g + 2 \left(\frac{14(2J+1)}{J(J+1)} \right)^{\frac{1}{2}} \langle f^N \alpha SL \mid\mid V^{(12)} \mid\mid f^N \alpha' S'L' \rangle \left\{ \begin{array}{ccc} S & S' & 1 \\ L & L' & 2 \\ J & J & 1 \end{array} \right\} \right] \tag{2.38}$$

In crystalline solids, the splittings produced by the crystal field are usually much larger than those produced by any hyperfine interactions (that is the interaction between I and J), thus it is physically realistic to work in an JJ_zII_z coupling scheme. In this scheme, the diagonal matrix elements of the $AI \cdot J$ effective Hamiltonian are

$$\langle \alpha SLJJ_zII_z \mid AI \cdot J \mid \alpha' SL'JJ_zII_z \rangle = AI_zJ_z \tag{2.39}$$

and the off diagonal elements $\langle \alpha SLJJ_zII_z \mid AI \cdot J \mid \alpha' SL'JJ_z \pm 1II_z \pm 1 \rangle$ are

$$\frac{1}{2}[J(J+1) - J_z(J_z \pm 1)][I(I+1) - I_z(I_z \mp 1)]^{\frac{1}{2}} \tag{2.40}$$

Further splittings may occur due to the interaction between, firstly the rare earth ion electronic moment and the nuclear quadrupole moment and secondly the interaction of the nuclear quadrupole moment with the electric field gradient at the nucleus. There is an electrostatic energy that varies with nuclear orientation and therefore only nuclei with $I \geq 1$ can possess a nuclear quadrupole moment since turning the nucleus end for end does not change the electrostatic energy, Slichter[30] (1978).

2.5 Intensities in Rare Earth Spectra

Rare earth ions may interact with the electromagnetic field of an exciting light source via several mechanisms, of which the most commonly observed is through the possession of an electric dipole moment. However, intraconfigurational transitions are forbidden for the odd parity electric dipole operator and we require admixtures of odd parity wavefunctions from higher configurations into at least one of the "pure" $4f^N$ wavefunctions involved in the transition to observe electric dipole transitions. A non spherically symmetric crystal field can produce the required mixing through odd terms in the crystal field expansion.

Following Wybourne [25] we denote two mixed parity states $|A\rangle$ and $|B\rangle$ such that

$$\langle A \mid = \langle JJ_z \mid -\Sigma_\kappa \frac{\langle JJ_z \mid V \mid \kappa \rangle \langle \kappa \mid}{E_{JJ_z} - E_\kappa} \tag{2.41}$$

and

$$\mid B \rangle = \mid J'J'_z \rangle - \Sigma_\kappa \frac{\mid \kappa \rangle \langle \kappa \mid V \mid J'J'_z \rangle}{E_{J'J'_z} - E_\kappa} \tag{2.42}$$

where $\langle JJ_z \mid$ and $\mid J'J'_z \rangle$ are two states of a configuration nl^N which have become admixed by the crystal field with states κ of $nl^{N-1}nl'$. The electric dipole operator

$$P = -e\Sigma_i r_i \tag{2.43}$$

can be written in tensorial form as

$$P_\rho^{(1)} = -e\Sigma_{\rho,i} r_i (C_\rho^{(1)})_i \tag{2.44}$$

and is a rank 1 tensor with ρ=0 corresponding to the z component and ρ=$\pm$1 the x$\pm$iy components for π and σ polarised transitions respectively. This yields non zero matrix elements in $P_\rho^{(1)}$ between the mixed parity states as

$$\langle A \mid P_\rho^{(1)} \mid B \rangle = -\Sigma_\kappa \frac{\langle JJ_z \mid V \mid \kappa \rangle \langle \kappa \mid P_\rho^{(1)} \mid J'J'_z \rangle}{E_{JJ_z} - E_\kappa} - \Sigma_\kappa \frac{\langle JJ_z \mid V \mid \kappa \rangle \langle \kappa \mid V \mid J'J'_z \rangle}{E_{J'J'_z} - E_\kappa} \tag{2.45}$$

where the summation in κ is over all the perturbing states. The solution to this expression is problematical since the odd terms in the crystal field expansion and the energies of the perturbing states are unknown. The Judd-Ofelt [31] [32] closure approximation replaces the energy denominators with a single average value E_{av} and uses $\Sigma_\kappa \mid \kappa \rangle \langle \kappa \mid$=1. It is pointed put by Ofelt [32] that this not to be taken to mean that the entire width of the $4f^{N-1}$nl configuration is small compared to the distance between the pertinant configurations but rather that the connected states of the $4f^{N-1}$nl configuration are considered degenerate. Obviously the strength of intermediate coupling in the $4f^{N-1}$nl configuration must be taken into account to the extent that if it is large the entire $4f^{N-1}$nl configuration must be considered degenerate. Then

$$\langle A \mid P_\rho^{(1)} \mid B \rangle = \Sigma_{\lambda,q} Y(\lambda, q, \rho) \langle f^N \alpha S L J J_z \mid U_{\rho+q}^{(\lambda)} \mid f^N \alpha' S' L' J' J'_z \rangle \tag{2.46}$$

where

$$Y(\lambda, q, \rho) = -\frac{2}{E_{av}} \Sigma_k (-1)^{q+\rho} (2\lambda + 1) \begin{pmatrix} 1 & \lambda & k \\ \rho & -(q+\rho) & q \end{pmatrix} \begin{pmatrix} l & l & \lambda \\ 1 & k & l' \end{pmatrix}$$

$$\times \langle l \mid\mid C^{(1)} \mid\mid l' \rangle \langle l' \mid\mid C^{(k)} \mid\mid l \rangle B_q^k e \int R_{nl}(r) r R_{n'l'}(l) dr \tag{2.47}$$

The application of the triangular rules for the addition of angular momentum on the 3j and 6j symbols above yields the following selection rules for electric dipole transitions:

$$\Delta l = \pm 1$$

$$\Delta S = 0$$

$$\mid \Delta L \mid, \mid \Delta J \mid \leq 2l$$

An additional selection rule applies for transitions involving states of J=0 which forbids transitions to or from states other than those of J=2,4 or 6. A quite rigorous example of this can be found for transitions between levels of the Eu^{3+} ground term. However in most cases, J mixing (by the crystal field) will lead to a break down of these selection rules and this has been formalised by Lowther [33].

Magnetic dipole transitions will also be allowed within states of the $4f^N$ configuration since the magnetic dipole operator $(L + 2S)$ has even symmetry under parity operations. This involves matrix elements of the type

$$\langle f^N \alpha SLJJ_z \mid L + 2S \mid f^N \alpha SLJJ_z \rangle = (-1)^{J-J_z} \begin{pmatrix} J & 1 & J' \\ -J_z & \rho & J'_z \end{pmatrix}$$

$$\times \langle f^N \alpha SLJ \mid\mid L + 2S \mid\mid f^N \alpha SLJ' \rangle \tag{2.48}$$

where ρ=0 corresponds to the z component of the magnetic moment and ρ=$\pm$1 the x$\pm$iy components. The appropriate selection rules are

$$\Delta l = 0$$

$$\Delta S = 0$$

$$\Delta L = 0$$

$$\Delta J = 0, \pm 1 (\text{not} 0 \leftrightarrow 0)$$

It is noted that as with electric dipole selection rules, the breakdown of LS coupling will lead to a relaxation of these selection rules a notable example being the $^7F_0 \rightarrow {}^5D_1$ transitions of Eu^{3+}. This is the result of spin orbit coupling mixing into each level small admixtures of states with the appropriate spin quantum number.

2.6 Polarisation and Selection Rules

The crystal field wavefunctions may be labelled by the irreducible representations of the symmetry group appropriate for the environment experienced by the RE^{3+} ion. For Kramers ions, the appropriate double group representation must be used as the character (or trace of the representation matrix) is not single valued under a rotation of 2π as they are for non-Kramers ions.

In order to determine whether a transition between two states $\mid \Phi_i\rangle$ and $\mid \Phi_f\rangle$ is allowed, we need to determine the non-zero matrix elements

$$\int \Phi_f^{\dagger} H_{op} \Phi_i d\tau$$

where H_{op} is the electric or magnetic dipole operator in our case. The matrix element $\langle \Phi_f \mid H_{op} \mid \Phi_f \rangle$ will be zero unless

$$\Gamma_{op} \times \Gamma_i \supset \Gamma_f$$

where the operator in question transforms, or has the same symmetry under the group operations, as the Γ_{op} irrep of the relevant group and connects the two crystal field states $\mid \Phi_i\rangle$ and $\mid \Phi_f\rangle$ represented by Γ_i and Γ_f respectively.

The majority of transitions observed as intra 4f configurational transitions will be of electric dipole character. Under C_{4v} symmetry the electric dipole operator transforms as the $\gamma_1(z)$ and $\gamma_5(x,y)$ irreps of this group. Similarly, transitions of magnetic dipole character may be present, the magnetic dipole operator transforms as the $\gamma_2(S_z)$ and $\gamma_5(S_x,S_y)$ irreps. From the group multiplication tables given by Koster et. al. [34] we can construct the electric dipole and magnetic dipole selection rules as shown in Tables 2.1 and 2.2. There the π and σ notation indicates electric dipole transitions polarised parallel and perpendicular to the four fold symmetry z axis of the C_{4v} centre. In a similar fashion the π' and σ' notation indicates magnetic dipole transitions polarised parallel and perpendicular to the four fold axis of the C_{4v} centre. We can also use the C_{3v} multiplication table from Koster et. al. to obtain the C_{3v} selection rules shown in Tables 2.3 and 2.4 apply.

There are also symmetry restrictions for ions in centres of cubic symmetry. For Kramers ions (of interest to us in this work) transitions between states of $\Gamma_6^{(2)}$ and $\Gamma_7^{(2)}$ symmetry are forbidden. It should be kept in mind that only magnetic dipole transitions are allowed between the crystal field states of cubic centres as the odd parity terms in the crystal field expansion, responsible for the admixture higher configurations into the $4f^N$ wavefunctions, vanish for centres with inversion symmetry.

Table 2.1: Electric and magnetic dipole polarisation selection rules for non-Kramers ions in centres of C_{4v} symmetry

C_{4v}	γ_1	γ_2	γ_3	γ_4	γ_5
γ_1	π	(π')			$\sigma(\sigma')$
γ_2	(π')	π			$\sigma(\sigma')$
γ_3			π	(π')	$\sigma(\sigma')$
γ_4			(π')	π	$\sigma(\sigma')$
γ_5	$\sigma(\sigma')$	$\sigma(\sigma')$	$\sigma(\sigma')$	$\sigma(\sigma')$	$\pi(\pi')$

Table 2.2: Electric and magnetic dipole polarisation selection rules for Kramers ions in centres of C_{4v} symmetry

C_{4v}	γ_6	γ_7
γ_6	$\pi\sigma(\pi'\sigma')$	$\sigma(\sigma')$
γ_7	$\sigma(\sigma')$	$\pi\sigma(\pi'\sigma')$

Table 2.3: Electric and magnetic dipole polarisation selection rules for non-Kramers ions in centres of C_{3v} symmetry

C_{3v}	γ_1	γ_2	γ_3
γ_1	π	(π')	$\sigma(\sigma')$
γ_2	(π')	π	$\sigma(\sigma')$
γ_3	$\sigma(\sigma')$	$\sigma(\sigma')$	$\pi\sigma(\pi\sigma')$

Table 2.4: Electric and magnetic dipole polarisation selection rules for Kramers ions in centres of C_{3v} symmetry

C_{3v}	γ_4	$\gamma_{5,6}$
γ_4	$\pi\sigma(\pi'\sigma')$	$\sigma(\sigma')$
$\gamma_{5,6}$	$\sigma(\sigma')$	$\pi\sigma(\pi'\sigma')$

2.6.1 Polarisation Behaviour of Rare Earth Centres

The polarisation behaviour of rare earth ions in cubic alkaline earth fluoride crystals, arises from the fundamental nature of the interaction of electromagnetic radiation with the permanent electric or magnetic dipole moments of the RE^{3+} ion in question. As the differing orientations of the rare earth ion centres in alkaline earth fluoride crystals are equivalent in the absence of a significant external magnetic field we may not expect any distinct polarisation dependence to be obtained. However, Feofilov [35] showed, as early as 1959, that polarisation effects could be obtained. More recently it has been demonstrated by Reeves (1987) [12] and Cockcroft (1987) [14] that the polarisation behaviour of these centres can aid in the assignment of level symmetries.

Following Reeves (1987), we introduce a notation for the polarisation geometry so as to appropriately describe the effects. This author denotes the experimental geometry as X(AB)Z, where X is the direction of the exciting laser radiation, Z is the direction of propagation of the observed fluorescence and A and B are the planes of polarisation of the exciting laser light and resultant fluorescence, as appropriate. This is shown schematically in Figure 2.2.

We consider the polarisation dependence of a non-Kramers ion in a C_{4v} symmetry centre first (and most fully as this dependence is used for the Eu^{3+} ion with the most success). The highest symmetry four fold axis can be oriented along either the [100], [010] or [001] crystallographic axes. For a transition between the $^7F_0$ and $^5D_0$ states, the selection rules of Table 2.1 show that this transition can only be excited in π polarisation. If the incoming laser light is polarised along the Y direction of our laboratory coordinate frame then only the centre with its four fold symmetry axis along Y (say [010]) will be excited. Thus if the fluorescence is polarised along, first the X [100] direction then along the Y [010] direction, a net polarisation effect will be observed. Consider emission to a state of γ_1 symmetry allowed by π emission. If only the [010] centre is excited then polarisation of the emission along X gives no emitted radiation, whilst for polarising the emission along Y emission is obtained. Therefore a ratio of 0:1 is achieved. If the emitted radiation is σ allowed then the converse is true. Polarising along X gives emission whilst polarising along Y does not and a ratio of 1:0 is achieved. In this way, we can build up the ratios given in Table 2.5. One should note that for magnetic dipole transitions the transverse oscillations of the magnetic field vector of the light with respect to that of the electric field vector give rise to inverted polarisation ratios. For Kramers ions in centres of C_{4v} symmetry the polarisation effects are not as clear as a consequence of the less well defined selection rules. A further complication arises in that whenever the absorption or emission is between levels of the same irrep symmetry no inherent

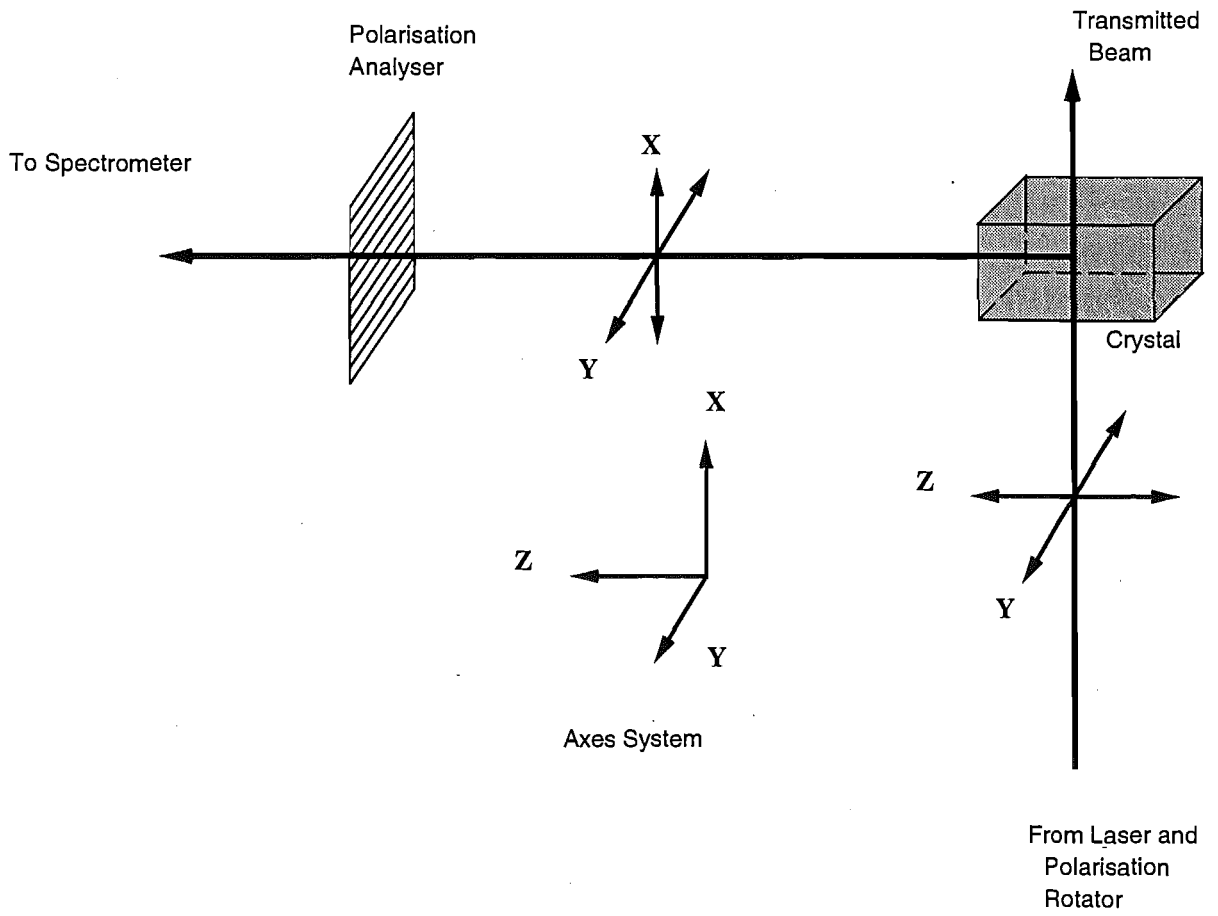

Figure 2.2: Schematic of the experimental geometry for the polarisation experiments

Table 2.5: Predicted polarisation ratios for non-Kramers ions in centres of C_{4v} symmetry in ⟨100⟩ oriented alkaline earth fluoride crystals

Transition Polarisation		Experimental Geometry			
Excitation	Decay	YX	YY	ZX	ZY
σ	π	1	0	1	1
	σ	1	2	1	1
	π'	0	1	1	1
	σ'	2	1	1	1
π	π	0	1	0	0
	σ	1	0	1	1
	π'	1	0	0	0
	σ'	0	1	1	1
σ'	π	0	0	0	1
	σ	1	1	1	0
	π'	0	0	1	0
	σ'	1	1	0	1
π'	π	1	1	1	0
	σ	1	1	1	2
	π'	1	1	0	1
	σ'	1	1	2	1

polarisation is expected (these transitions being allowed in both σ and π). Table 2.6 gives the pertinent σ polarisation ratios.

Table 2.6: Predicted polarisation ratios for Kramers ions in centres of C_{4v} symmetry in ⟨100⟩ oriented alkaline earth fluoride crystals

Transition Polarisation		Experimental Geometry			
Excitation	Decay	YX	YY	ZX	ZY
σ	σ	1	2	1	1
	σ'	2	1	1	1
σ'	σ	1	1	1	2
	σ'	1	1	2	1

For non-Kramers and Kramers ions in centres of C_{3v} symmetry no polarisation dependence will be observed for ⟨100⟩ oriented crystals, as all possible orientations of the three fold axis will be equally oriented to the field. However, for ⟨111⟩ oriented samples a polarisation dependence is expected. As the four three fold axes are not orthogonal, the σ and π polarised components of the transition moment will not be clearly separated and the analysis is far more complicated. Cockcroft [14] deals with

this in some detail and no further discussion is necessary here. Table 2.7 presented the expected ratios for both non-Kramers and Kramers ions. It should be noted that for trigonal centres the polarisation ratios do not depend on the direction of the exciting laser beam. Therefore, samples may be prepared by simply cleaving two flat {111} planes and grinding entrance and exit faces anywhere perpendicular to the {111} planes. It should be noted that if either transition is a $\gamma_3 \rightarrow \gamma_3$ transition for

Table 2.7: Predicted polarisation ratios for non-Kramers and Kramers ions in centrs of C_{3v} symmetry in (111) oriented alkaline earth fluoride crystals

Transition Polarisation		Experimental Geometry			
Excitation	Decay	YX	YY	ZX	ZY
σ	π	7	3	8	8
	σ	11	15	10	10
	π'	3	7	8	8
	σ'	15	11	10	10
π	π	2	6	1	1
	σ	7	3	8	8
	π'	6	2	1	1
	σ'	3	7	8	8
σ'	π	8	8	7	3
	σ	10	10	11	15
	π'	8	8	3	7
	σ'	10	10	15	11
π'	π	1	1	2	6
	σ	8	8	7	3
	π'	1	1	6	2
	σ'	8	8	3	7

non-Kramers ions and $\gamma_4 \rightarrow \gamma_4$ for Kramers ions in C_{3v} centres then the transition is allowed to occur in both the π and σ polarisations with resulting polarisation ratios that are essentially arbitrary.

This polarisation behaviour is temperature dependent. As the crystal is warmed from 10K through to 200K the observed ratios decay from the approximately 0:1 values observed for non-Kramers ions in tetragonal C_{4v} centres (at 10K) to 1:1. This arises because the charge compensating F^- ions gain sufficient thermal energy at higher temperatures such that ionic movement is no longer electrostatically inhibited. Therefore, interstitial F^- ions in, for example, the C_{4v} centre in CaF_2:RE^{3+} systems would be able to jump between the various possible orthogonal orientations leading to a blurring of the desired polarisation effects which increases with temperature. Voron'ko et. al. (1994) [36] and Jamison and Reeves (1995) [37] have

measured such effects for tetragonal C_{4v} centres in CaF_2 and SrF_2 crystals doped with Pr^{3+} and Eu^{3+} ions obtaining barrier heights and depolarisation temperatures.

Chapter 3

Experimental Considerations

3.1 Crystal Preparation

3.1.1 Alkaline Earth Fluorides

The rare earth doped alkaline earth fluoride samples used in this work were grown by the author from offcuts of the relevant alkaline earth fluoride crystals purchased from Optovac Inc. (U.S.A.). The crushed offcuts were then mixed with the appropriate rare earth trifluoride at the pertinent concentrations. In all cases, at least one molar percent of PbF_2 was added to scavenge for oxygen. Two percent by mass of PbF_2 was added to encourage the stability of the trivalent state for samarium doped samples which are prone to reduction to Sm^{2+} in the reducing atmosphere provided by the graphite crucibles.

The crystals were grown in graphite crucibles over a period of 18 hours using an Arthur D. Little 38kW radio frequency furnace. The temperature gradient (Bridgman-Stockbarger) method was employed in the crystal growth process which entailed lowering the crucible through a temperature gradient in a vacuum of around 10^{-5} Torr. Annealing is achieved via an automatic cooling cycle which leads to improved quality crystals. The crystals grown in this study were generally coloured to some extent due to the presence of the divalent species. This colouration (green in the case of CaF_2:Sm^{3+} samples and violet for CaF_2:Eu^{3+}) arises from strong (electric dipole allowed) interconfigurational $4f^N \rightarrow 4f^{N-1}5d$ transitions.

Oriented boules were generally required and these were obtained either by cleaving the crystal boule along its (111) cleavage planes or by cleaving two (111) planes intersecting at an angle of 109.7 degrees which could then be glued in an angled holder for $\langle 100 \rangle$ orientation. In the latter case, or if an unoriented sample was used, the boules were cut with a diamond saw and then polished using successive grades of emery paper followed with a final polish using a water/tin-oxide paste on photographic paper to give a smooth finish. The tin-oxide powder was supplied by Micro Abrasives Corporation of Westfield (U.S.A.).

3.1.2 The Oxygenation Process

The method of oxygenating the crystals used in this study was essentially a variant of the method of Hall and Schumacher (1962) [38] for hydrogenation of alkaline earth fluoride crystals. This process involves wrapping coils of aluminium wire onto the faces of the crystal and heating in two thirds of an atmosphere of O_2 gas at 850-900 °C.

Prior to oxygenation, the sample and aluminium should be cleaned in acetone to minimise possible surface contaminants. In addition, the crystal faces should be handled as little as possible to avoid such contaminants as finger grease being deposited on the surface of the crystal. The crystal plus aluminium can then be placed inside an alumina crucible (which itself should have been cleaned in acetone) and placed in quartz tube. This is then placed centrally inside an electric furnace and evacuated using a mercury diffusion pump. The furnace is set to a temperature setting of 150 °C to dry any moisture from the system.

After 4-5 hours dry oxygen gas is flushed through the system several times before finally introducing the required two thirds of an atmosphere of gas and sealing the sample off from the diffusion pump. The furnace temperature should then be raised to 850 °C over two hours and left at that temperature for the desired period of time. The crystals used in this study were left for around 30 minutes before switching off the furnace.

Finally the crystals may be etched in dilute hydrochloric acid to remove any aluminium left on the surfaces of the crystal and then polished to obtain the best optical quality.

3.2 Infrared Absorption Spectroscopy

Infrared spectra were taken with the Physics and Astronomy departments Digilab FTS-40 Infrared Fourier Transform spectrometer. The FTS-40 is a single beam spectrometer which employs a He-Ne 3121 H-P model laser to determine the interference fringe spacings. It has two compartments. One uses a deuterated triglylcline sulphate detector to cover the 400-4500 cm^{-1} spectral range at room temperature. The other compartment uses either a mercury cadmium telluride (M.C.T.) detector which is fifteen times more sensitive than the D.TG.S. detector coupled with a KBr beamsplitter and globar source for response in the 400-4000 cm^{-1} region or for experiments in the 4000-10000 cm^{-1} region, an indium antimonide detector, quartz

beamsplitter and quartz-halogen source. The interferometer of this system comes as a 'lift-out' unit which could be changed with comparative ease. The spectrometer has a resolving power down to 0.1 cm^{-1}. The entire beam path is flushed with dry N_2 gas to minimise the effects of strong atmospheric absorption in the regions of interest in this study.

Zeeman infrared spectroscopy was undertaken using an Oxford Instruments 4 Tesla superconducting magnet. The magnet which operates in persistent mode, was energised by a British Oxygen Company PS60/72A power supply which provides the magnet with a 51.55 ampere operating current. The magnet is built into the bottom of a 5 litre stainless steel dewar. An 8 litre liquid nitrogen jacket surrounds the upper portion of the helium can, whilst the tail (which has a bore down the centre for optical access is thermally protected by a copper radiation shield. A copper sample holder screw fits into a copper ring which is brazed into the center of the bore to act as a sampleholder mount and cooling is via thermal contact. The experimental configuration is such that the infrared radiation propagates parallel to the magnetic field, consequently of the σ and π transitions which might be seen in a $\mathbf{B} \perp k$ configuration, only the σ transitions are observed here.

Once the sample is in place the tail of the magnet is lowered into the external ESC compartment of the spectrometer and alignment of the optics may take place.

A visit to Industrial Research Limited (I.R.L.) in Lower Hutt, Wellington provided the opportunity to use a Bomem DA3.02 interferometric spectrophotometer system on which the high resolution infrared absorption spectra presented in Chapter 4 were obtained. This system employs a CTI-Cryogenics Model 22C Cryodyne Cryocooler to cool samples, mounted on copper sampleholders, to better than 10K. The primary advantage of the Bomem DA3.02 spectrophotometer over the Digilab FTS-40 spectrometer is the enhanced resolution (variable from 64 cm^{-1} to a maximum apodised resolution of 0.04 cm^{-1}). A liquid nitrogen cooled Infrared Associates InSb detector is employed to detect the transmitted beam. The entire beam path is held under a vacuum of 0.5 Torr thus eliminating the need for flushing with dry N_2 gas.

The spectrophotometer system is controlled by a PDP-11 computer with a RT-11 operating system connected to a DEC VT125 terminal. A Bomem High Speed Vector Processor (HSVPS) preforms the Fourier transforms and other spectral compilation related tasks.

3.3 Optical Spectroscopy

3.3.1 Absorption

Absorption spectra in the optical region of the electromagnetic spectrum were recorded on a SPEX 1700 series 0.75m single monochromator which has a Czerny-Turner configuration. This spectrometer has a single grating with 1180 lines per mm. The radiation source used was a 100W tungsten halogen lamp with power supplied from a 12V regulated power supply. An EMI 9659 QA photomultiplier with standard S-20 response was employed to detect the transmitted signal. The photomultiplier tube was cooled to -25 °C by a Products for Research refrigerated chamber. The output signal could then be processed by a Keithley Instruments Model 610 electrometer and displayed on a chart recorder or, for digitised data, recorded via a custom made current to frequency converter connected to an Apple IIe personal computer which then stored the data on floppy disk. This data could then be transferred to the University of Canterbury Computer Services Centre Unix based Sun network for the presentation of figures.

3.3.2 CW Laser Selective Excitation and Fluorescence

A Spectra Physics Model 2045E argon ion laser, fitted with 23-30W tubes, employed to pump a Spectra Physics Model 375 dye laser was used to obtain the LSE spectra presented in this work. A Spectra Physics Model 573 three plate birefringent tuning element provided the capability to continuously vary the output laser frequency via the rotation of a micrometer screw. The dye laser output had a linewidth of 0.8 cm^{-1} and was linearly polarised. For polarised fluorescence measurements this could be rotated with a Spectra Physics Model 310 polarisation rotator. During several periods of this work the Spectra Physics 2045E argon laser failed and required service. During these periods a Coherent INNOVA 90 series argon laser was subsituted for the larger Spectra Physics argon laser. The Coherent argon laser provided 5 Watts of all lines (visible) power and thus enabled the majority of the routine experiments to continue.

A Spectra Physics Model 376B and two model 376 dye circulators were assigned to the dye laser, primarily to reduce the risk of contamination of the higher energy coumarin dyes with rhodamine dye solutions. Three dyes were used for CW spectroscopy. Coumarin 540, in a solution of 75% ethylene glycol and 25% benzyl alcohol, was used to excite the $^4F_{\frac{3}{2}}$ multiplet of Sm^{3+}, the $^5D_1$ multiplet of Eu^{3+} and the $^5F_4$ and $^5S_2$ multiplets of Ho^{3+}. These experiments required the 488 nm argon laser ouput and the addition of cyclo-octatetraene (C.O.T.) to the dye as it aged.

Both the C.O.T. and the dyes used in this study were supplied by Exciton Chemical Company Ltd. For the excitation of the $^4G_{\frac{5}{2}}$ multiplet of Sm^{3+} Rhodamine 560, in a 100% ethylene glycol solution, was used since this dye had extended range into the red thereby allowing the excitation of the trigonal oxygen centres at 17500 cm^{-1}. Rhodamine 560 was excited using the multiline output of the argon laser. Finally for excitation of the $^5D_0$ multiplet of Eu^{3+} Rhodamine 590 perchlorate, in a 100% ethylene glycol solution, was used. This was appropriate, even though R560 reached $^5D_0$ comparatively easily, because of the higher output powers attainable with R590 which prove valuable when studying the Eu^{3+} upconversion process.

Broadband excitation spectra shown in this thesis were obtained using a 0.25m Bausch and Lomb single monochromator with a 1350 lines per mm grating. This was coupled to an EMI 9659 QA photomultiplier tube connected to a photon counting system. This comprised a Princeton Applied Research Corp Model 1121 discriminator unit with a Princeton Applied Research Corp Model 1112 Photon Counter. Often, due to high signal intensities, Optics Technology Inc neutral density filters were used to attenuate the signal. In addition to this, Corning glass filters were used to eliminate any scattered laser light.

A SPEX series 1403 0.85m double monochrometer was used to record fluorescence and centre selective excitation spectra when monitoring in the 11000-31000 cm^{-1} region. This spectrometer has a Czerny-Turner configuration with twin 1800 line per mm holographic gratings. Slitwidths were typically in the range 10-150μm. A SPEX model CD2A Compudrive was used to scan the spectrometer with the option of manual or computer control. An RCA C31034 photomultiplier with extended S20 response cooled to -25 °C was used to detect fluorescence in the 11000-31000 cm^{-1} region. For monitoring fluorescence at longer wavelengths an RCA 7102 photomultiplier cooled to -100 °C in a Princeton Applied Research Model TE-176-RF liquid nitrogen refrigeration chamber on the SPEX 1700 single monochromator. Both spectrometers were fitted with Hanle quartz wedges to equalise the grating response to differing polarisation direction.

3.3.3 Pulsed Laser Experiments

Excited state lifetimes were determined using a Photochemical Research Associates (PRA) model LN1000 nitrogen laser to excite a PRA model LN107 dye laser. The nitrogen laser has a wavelength of 337.1 nm and provides a 1 mJ laser pulse of width 600 ps with a maximum repetition rate of 20 Hz. The dye laser employs a 40/60 beamsplitter in which 40% of the UV output of the nitrogen laser is focussed into a line image on the dye cell by a cylindrical quartz lens. The dye laser includes an amplifying stage to increase its output up to 110 μJ. R560 and C500 dyes were

used to excite the $^5D_0$ and $^5D_1$ multiplets of Eu^{3+} whilst C540A or C500 could be used to excite either the $^4G_{\frac{5}{2}}$ or $^4F_{\frac{3}{2}}$ multiplets of Sm^{3+}. The SPEX 1700 series single monochromator and EMI 9659 QA photomultiplier were used to record the fluorescence of a given centre. The output of the photomultiplier tube stored by a Hitachi model VC 6275 digital storage oscilloscope which was triggered by the nitrogen laser pulse (as monitored by an RCA 931A S11 photomultiplier tube).

As with all laser selective excitation and fluorescence measurements a CTI-Cryogenics model 21C Cryodyne Cryocooler was employed to cool the samples to a base temperature of 12-16K. A custom made heating unit with resistors attached to the base of the cold head provided continuous temperature variability in the 16-300K region.

Chapter 4

High Resolution Infrared Absorption Studies of CaF_2 and SrF_2 Crystals doped with Pr^{3+}, Tb^{3+} and Ho^{3+}

4.1 Introduction

One of the earliest and clearest examples of magnetic hyperfine structure, and the Zeeman effect on these, was given by Dieke at the 1967 Zeeman centennial conference in Amsterdam for the $LaCl_3$:Ho^{3+} system [39]. This paper, now something of a classic, shows fully resolved eight-line hyperfine patterns and Zeeman hyperfine patterns which are analysed in terms of the nuclear magnetic and Zeeman interactions between the electron-nuclear and electronic states involved. Various spectroscopic studies of Ho^{3+} hyperfine structure have followed with a strikingly clear example given by Agladze et. al. [40] who showed the isotope shift of Li^7 and Li^6 in the hyperfine structure of monoisotopic Ho^{3+} doped into $LiYF_4$ crystals.

Mujaji et. al. [17] reported an extensive polarisation study of the crystal field levels of CaF_2:Ho^{3+} using site-selective laser spectroscopy for both the dominant tetragonal C_{4v} symmetry A centre and a minority trigonal centre labelled B. Following this, Boonyarith et. al. [41] observed and analysed hyperfine structure for transitions from the $Z_1\gamma_3$ ground state to levels of the $^5F_5$ multiplet of the B centre, using optically detected nuclear magnetic resonance (ODNMR) and two-laser hole burning. These authors demonstrated the mixing of excited-state wavefunctions by the off-diagonal hyperfine interaction between nearby singlet and doublet levels, leading to the appearance of otherwise unobserved hyperfine transitions in the optical spectrum. Martin et. al. [42] considered the enhanced nuclear magnetism in the pseudo-degenerate ground state of the A centre in CaF_2:Ho^{3+}. They later extended this work to include determination of the nuclear magnetic and pseudoquadrupole parameters for the transitions involved [43]. Heron [18] observed hyperfine structure in the infrared-absorption spectrum of the A centre in CaF_2:Ho^{3+}, for transitions from the $Z_{1,2}\gamma_{1,2}$ ground states to levels of the $^5I_7$ multiplet around 5300 cm^{-1}. However, the spectra were at a resolution of 0.1 cm^{-1} and the observed hyperfine structure only partially resolved. In addition, the globar source and KBr beamsplit-

ter in the FTIR spectrometer used in that study do not have optimal performance in the 5300 cm^{-1} region of the infrared spectrum making observation of the weaker hyperfine transitions difficult.

Macfarlane et. al. [44] studied hyperfine structure of the $Z_1\gamma_5$ ground state in the C_{4v} symmetry centre of CaF_2:Pr^{3+} for the strong $^3H_4 \rightarrow {}^1D_2$ absorption transitions. These studies display impressive 18 line [100] and 12 line [111] Zeeman hyperfine patterns for low magnetic fields. Reeves et. al. [45] extended hyperfine studies of the ground state for the C_{4v} symmetry centres of Pr^{3+} in alkaline-earth fluoride crystals. Both the $C_{4v}(F^-)$ and $C_{4v}(D^-)$ centres were studied for the CaF_2 and SrF_2 hosts, however in neither case was any interpretation given.

Polarised laser-selective excitation and fluorescence studies of the dominant centres in CaF_2 and SrF_2 crystals doped with Tb^{3+} ions have been studied by Jones and Murdoch [46] who assign both systems to have dominant centres of C_{4v} symmetry. An earlier study by Falin et. al. [47] using the ENDOR technique, reached the conclusion that the dominant Tb^{3+} ion centre was of C_{4v} symmetry as did Jones and Murdoch, however Falin's study had the advantage that the exact charge compensation configuration was assigned. The infrared-absorption studies presented in section 4.4 are based on the assignments of Murdoch [16], though Zeeman spectra have been taken and analysed for appropriately sharp and intense infrared absorption transitions.

4.2 Spectroscopy of the C_{4v} Symmetry A Centre in CaF_2:Ho^{3+}

The f^{10} configuration is appropriate for Ho^{3+} and has two multiplets ($^5I_7$ and $^5I_6$) easily accessible to the FTIR spectrometers used in this study. The ground multiplet is $^5I_8$. Throughout this chapter, and those to come, the energy levels of RE^{3+} ions will be denoted with the Dieke's alphabetical label for the multiplet and level. Where appropriate, this will be followed by the irrep symmetry label of the state wavefunction.

4.2.1 Laser Spectroscopy for Transitions to the $^5I_6$ Multiplet

An extensive polarisation study of fluorescence transitions of the CaF_2:Ho^{3+} A centre enabled Mujaji to construct an energy-level scheme with irrep assignments. However that study [15] did not include transitions to the $^5I_6$ multiplet. In order to classify and analyse the hyperfine structure observed in infrared absorption to the $^5I_6$ multiplet it was necessary to selectively excite the A centre and analyse the fluorescence

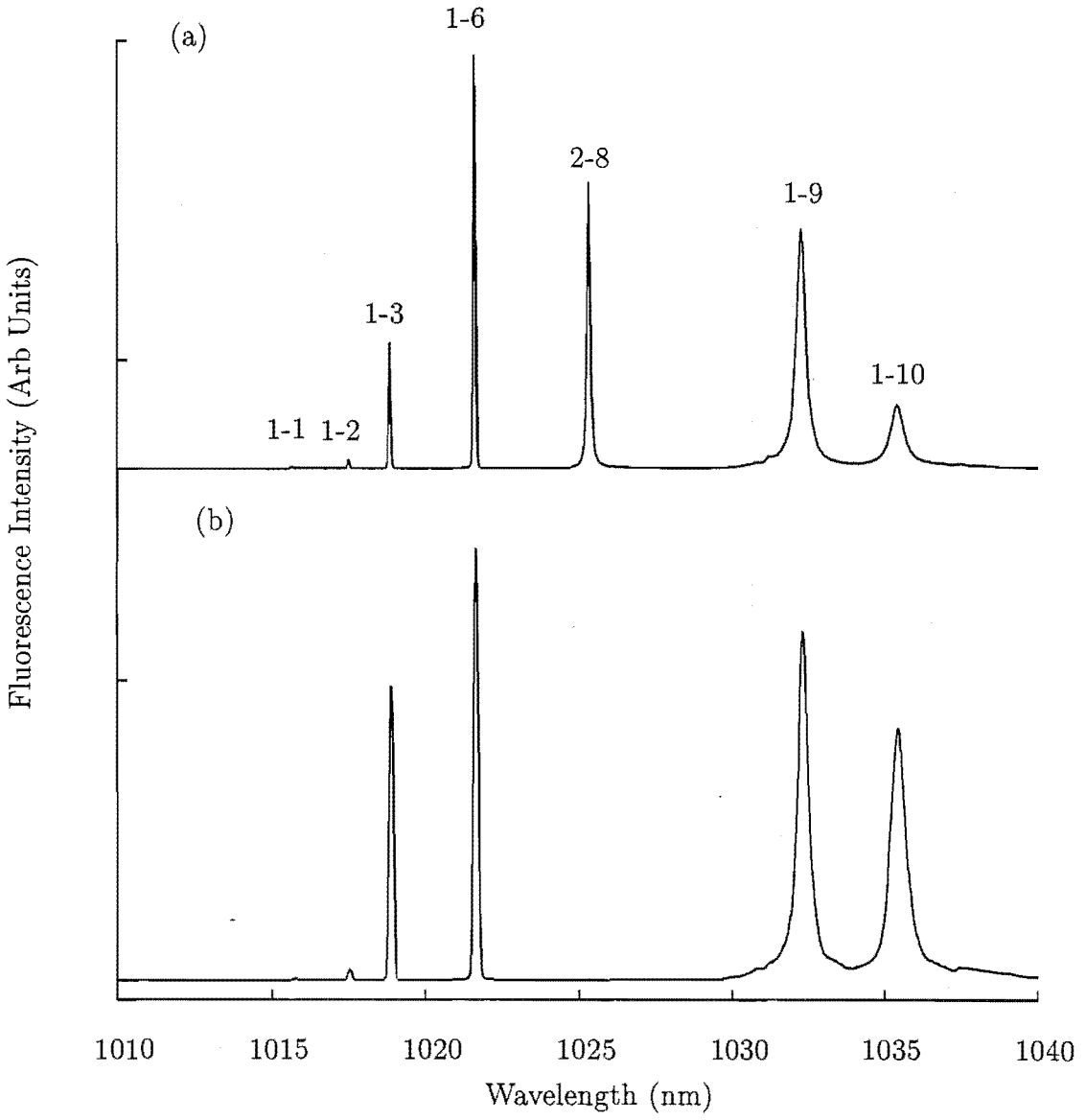

Figure 4.1: Unpolarised fluorescence for the $^5F_4$ and $^5S_2$ to $^5I_6$ transitions of the A centre in CaF_2:0.005%Ho^{3+} at (a) 16K and (b) 2K. Excitation is at the 18613 cm^{-1} $Z_{1,2}\gamma_{1,2} \rightarrow E_2\gamma_1$ transition.

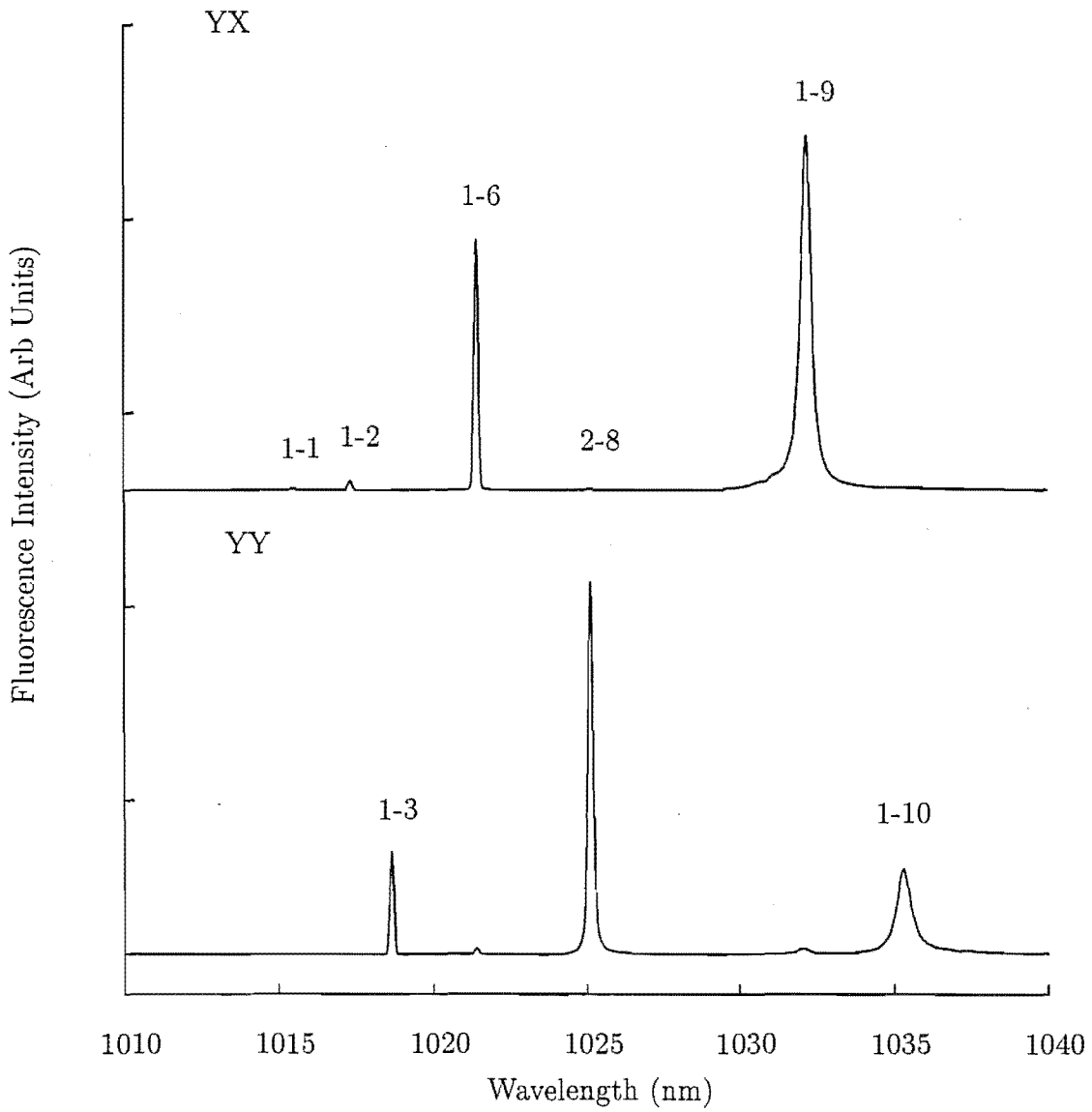

Figure 4.2: Polarised fluorescence for the $^5F_4$ and $^5S_2$ to $^5I_6$ transitions of the A centre in CaF_2:0.005%Ho^{3+}. Excitation is at the 18613 cm^{-1} $Z_{1,2}\gamma_{1,2} \rightarrow E_2\gamma_1$ transition.

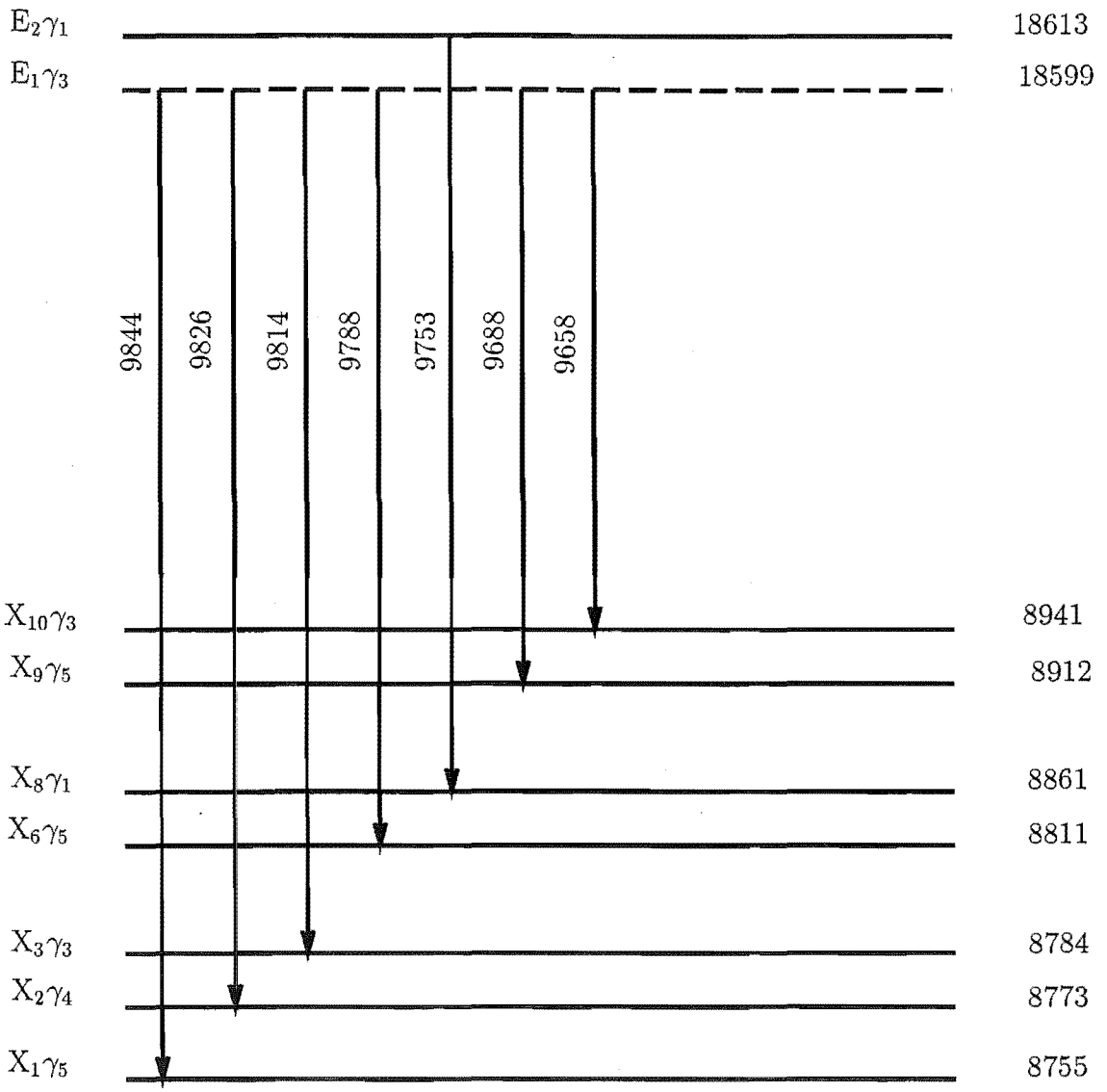

Figure 4.3: Schematic diagram of fluorescence transitions from the $^5S_2$ multiplet to the $^5I_6$ multiplet energy levels of the A centre in CaF_2:Ho^{3+}.

Table 4.1: Polarised fluorescence transitions (in air cm^{-1}, ± 1 cm^{-1}) between the $^5S_2$ and $^5I_6$ multiplets for the A centre in CaF_2:0.005%Ho^{3+}.

Transition	Frequency	Polarisation
$E_1\gamma_3 \rightarrow X_{10}\gamma_3$	9658	π
$E_1\gamma_3 \rightarrow X_9\gamma_5$	9688	σ
$E_2\gamma_1 \rightarrow X_8\gamma_1$	9753	π
$E_1\gamma_3 \rightarrow X_6\gamma_5$	9788	σ
$E_1\gamma_3 \rightarrow X_4\gamma_3$	9814	π
$E_1\gamma_3 \rightarrow X_3\gamma_4$	9826	π'
$E_1\gamma_3 \rightarrow X_1\gamma_5$	9844	σ

transitions to this multiplet.

A $\langle 100 \rangle$ oriented CaF_2 crystal with a nominal dopant concentration of 0.005 % of Ho^{3+} was excited at the 18613 cm^{-1} resonant $Z_{1,2}\gamma_{1,2} \rightarrow E_2\gamma_1$ transition of the A centre. This was chosen since it is conveniently pumped with available C540 dye and produces emission from the $^5S_2$ multiplet levels $E_1\gamma_3$ and $E_2\gamma_1$ at 18599 cm^{-1} and 18613 cm^{-1} respectively. This is appropriate since transitions from either of these two levels are, electric or magnetic dipole allowed to all levels of the $^5I_6$ multiplet. All transitions to levels of the $^5I_6$ multiplet are allowed from either of the $^5S_2$ levels by radiation of electric or magnetic dipole character. Mujaji has presented the broadband and site selective excitation spectra for the coincident $^5S_2$ and $^5F_4$ multiplets documenting the A centre transitions. This work contributes nothing further to the spectroscopy of these multiplets already presented in [15].

Strong fluorescence is observed to the $^5I_6$ multiplet and Figure 4.1 (a) and (b) shows unpolarised emission at 2K and 16K to the crystal field levels of $^5I_6$ from the $^5S_2$ multiplet. The fluorescence is centred around 9770 cm^{-1} (1024 nm) and seven transitions are observed. Emission from either singlet state of the $^5S_2$ multiplet (that is either the $E_1\gamma_3$ or $E_2\gamma_1$ state) is allowed by both the electric and magnetic dipole selection rules to γ_5 doublet states of the $^5I_6$ multiplet in σ (ed) or σ' (md) polarisation.

From Figure 4.2 we observe three transitions to be σ polarised at wavelengths of 1015.85, 1021.66 and 1032.20 nm. Of these the weak transition at 1015.85 nm is assigned as a transition from the $E_1\gamma_3$ state to the $X_1\gamma_5$ state at an energy of 8755 cm^{-1}. This is because the intensity of the transition does not vanish as the sample is cooled to 2K. Its presence in the 2K spectrum shows that it does not originate from the higher $E_2\gamma_1$ level due being thermally populated at 16K. The 1021.66 and 1032.20 nm transitions are of comparable intensity and are assigned as originating from the

$E_1\gamma_3$ state at 18599 cm^{-1}, just as with the $E_1\gamma_3 \rightarrow X_1\gamma_5$ 1015.85 nm transition. The respective terminating states are the $X_6\gamma_5$ and $X_9\gamma_5$ states at 8811 and 8912 cm^{-1}.

Three transitions are observed to be π (ed) polarised as given in Table 4.1. These transitions correspond to emission from either singlet state ($E_1\gamma_3$ or $E_2\gamma_1$) to $^5I_6$ singlet states in accordance with the appropriate selection rules (see chapter 2). The 1018.95 and 1035.41 nm features are assigned as the $E_1\gamma_3 \rightarrow X_3\gamma_3$ and $X_{10}\gamma_3$ transitions placing the $^5I_6$ states at energies of 8785 and 8941 cm^{-1} respectively. Only the 1025.33 nm feature is attributed to a transition from the $E_2\gamma_1$ state as it is absent from the 2K spectrum. We assign this as the $E_2\gamma_1 \rightarrow X_8\gamma_1$ transition in accordance with its observed polarisation behaviour. The 1017.71 nm feature is assigned as a magnetic-dipole transition of π' polarisation and is quite weak, as can be observed in Figure 4.2. The strength of this transition is consistent with its assignment as magnetic dipole in origin, and the transition is specifically assigned as $E_1\gamma_3 \rightarrow X_2\gamma_4$, with the $X_2\gamma_4$ state at 8773 cm^{-1}. Figure 4.3 shows a schematic of the observed fluorecence transitions.

4.2.2 Extension of Mujaji's Crystal Field Analysis to Include the $^5I_6$ Multiplet

To ensure an accurate analysis of $^5I_6$ multiplet hyperfine structure, the crystal field calculation and fit of Mujaji must be extended specifically to include this multiplet. Having obtained seven experimental levels for the $^5I_6$ multiplet, these were included with the levels previously determined by Mujaji, in a crystal field fit to a Hamiltonian incorporating the interactions described in chapter two, for the f^4 configuration appropriate for Ho^{3+}. The program used was Dr Mike Reid's F-Shell Empirical Program. In total, forty-five experimental levels were fitted using nine adjustable parameters, comprising the five crystal field parameters appropriate for C_{4v} symmetry, the spin orbit parameter, ζ, and the three Slater parameters, F^2, F^4 and F^6. The fits were to the $^5I_8$, $^5I_7$, $^5I_6$, $^5S_2$, $^5F_4$ and $^5F_3$ multiplets of Ho^{3+}. The three lowest ^5I term multiplets are essentially pure LS coupled (Russell-Saunders) multiplets, which simplifies the calculations of the magnetic-hyperfine parameter, A_J, presented in Appendix A. The observed and calculated energies are presented in Table 4.2, whilst the best fit parameters are given in Table 4.3 together with those obtained by Mujaji.

To test the crystal field analysis, the magnetic splitting factors of the ground state wavefunctions with those derived from the EPR data of Kornienko and Rybaltovskii [48]. Ho^{3+} is a non-Kramers ion having an even number of 4f electrons. For the CaF_2:Ho^{3+} C_{4v} symmetry centre there are no matrix elements for the perpendicular Zeeman effect since the operator $J_\pm$ cannot connect the $|\ J_z\rangle$ states of the ground

Table 4.2: C_{4v} symmetry crystal field fits to the $^5I_8$, $^5I_7$, $^5I_6$, $^5F_5$, $^5S_2$, $^5F_4$ and $^5F_3$ multiplets of the A centre in CaF_2:Ho^{3+}. All energies are measured in air cm^{-1}. Those additional energy levels measured in this study are denoted by † and have an uncertainty of ± 1 cm^{-1}, whilst the remainder of the experimental levels are reproduced from Mujaji [17]

State & Symmetry		Calc Energy	Exptl Energy	State & Symmetry		Calc Energy	Exptl Energy
	$Z_1\gamma_1$	-2.3	0		$X_6\gamma_5$	8817.8	8811†
	$Z_2\gamma_2$	-1.5	1.7		$X_7\gamma_4$	8838.4	-
	$Z_3\gamma_5$	84.2	83.0		$X_8\gamma_1$	8869.2	8861†
	$Z_4\gamma_3$	117.4	115.5		$X_9\gamma_5$	8919.9	8912†
	$Z_5\gamma_5$	134.3	128.0		$X_{10}\gamma_3$	8953.5	8941†
	$Z_6\gamma_4$	163.5	158.0		$D_1\gamma_3$	15606.8	15605.0
$^5I_8$	$Z_7\gamma_1$	288.9	284.5		$D_2\gamma_5$	15609.7	15619.5
	$Z_8\gamma_2$	292.8	292.5		$D_3\gamma_2$	15623.7	15623.0
	$Z_9\gamma_3$	449.1	455.0	$^5F_5$	$D_4\gamma_1$	15672.4	15682.0
	$Z_{10}\gamma_5$	471.5	475.0		$D_5\gamma_5$	15755.7	15752.2
	$Z_{11}\gamma_1$	494.0	492.0		$D_6\gamma_2$	15758.4	15756.1
	$Z_{12}\gamma_5$	512.3	513.0		$D_7\gamma_4$	15770.2	-
	$Z_{13}\gamma_4$	513.2	-		$D_8\gamma_5$	15821.6	15823.5
	$Y_1\gamma_5$	5255.1	5257.0		$E_1\gamma_3$	18606.4	18599.0
	$Y_2\gamma_3$	5271.7	5273.0		$E_2\gamma_1$	18615.0	18613.2
	$Y_3\gamma_5$	5269.4	5274.0		$E_3\gamma_5$	18656.8	18655.1
	$Y_4\gamma_2$	5273.4	-		$E_4\gamma_4$	18660.6	18666.5
	$Y_5\gamma_4$	5280.3	-	$^5S_2$	$E_5\gamma_3$	18673.8	18681.5
	$Y_6\gamma_1$	5304.2	5308.5	$^5F_4$	$E_6\gamma_5$	18730.8	18726.8
$^6I_7$	$Y_7\gamma_5$	5332.1	5332.0		$E_7\gamma_1$	18748.3	-
	$Y_8\gamma_3$	5356.0	5355.0		$E_8\gamma_4$	18789.8	-
	$Y_9\gamma_4$	5404.1	-		$E_9\gamma_2$	18832.1	18834.9
	$Y_{10}\gamma_5$	5414.2	5413.0		$E_{10}\gamma_5$	18858.9	18861.5
	$Y_{11}\gamma_2$	5422.0	-		$E_{11}\gamma_1$	18889.7	18888.3
	$X_1\gamma_5$	8750.3	8755†		$F_1\gamma_2$	20742.6	20741.6
	$X_2\gamma_4$	8774.2	8773†		$F_2\gamma_5$	20782.5	20781.6
	$X_3\gamma_3$	8785.2	8785†	$^5F_3$	$F_3\gamma_4$	20848.4	-
	$X_4\gamma_1$	8788.5	-		$F_4\gamma_3$	20862.6	-
$^5I_6$	$X_5\gamma_2$	8809.7	-		$F_5\gamma_5$	20926.2	20924.5

Table 4.3: C_{4v} symmetry crystal field parameters for the A centre in CaF_2:Ho^{3+}. All parameters are in cm^{-1} with those in square brackets not being varied.

Parameter	This Study	Mujaji
F^2	95803	95960
F^4	66899	66876
F^6	46741	47097
α	[17.3]	17.3
β	[-624.0]	-624.0
γ	[2084.0]	2084.0
T^2	[287.0]	287.0
T^3	[37.0]	37.0
T^4	[98.0]	98.0
T^6	[-313.0]	-313.0
T^7	[421.0]	421.0
T^8	[359.0]	359.0
M^{TOT}	[3.04]	3.04
P^{TOT}	[528.0]	528.0
ζ	2137	2139
B_A^2	678	685
B_A^4	345	356
B_A^6	420	419
B_C^4	-1075	-1085
B_C^6	559	557

state whose composition is given as

$$\begin{array}{ll} Z_1\gamma_1 & \text{-0.4900}|8\rangle\text{+0.5077}|4\rangle\ \text{-0.0576}|0\rangle\text{+0.5077}|\text{-}4\rangle\text{-0.4900}|\text{-}8\rangle \\ Z_2\gamma_2 & \text{-0.4927}|8\rangle\text{+0.5067}|4\rangle\ \text{-0.5067}|\text{-}4\rangle\text{+0.4927}|\text{-}8\rangle \end{array}$$

Between these states one has an effective $\langle\gamma_1 \mid J_z \mid \gamma_2\rangle = \langle J_z\rangle_{1,2}$ of 5.92. The matrix elements of the parallel Zeeman effect are of the form

$$\mu_B g_L B_z \langle\gamma_1 \mid J_z \mid \gamma_2\rangle$$

where μ_B is the Bohr magneton (with $\mu_B B$=1 cm^{-1} for B=2.142 Tesla) and g_L, the Lande g factor corrected for intermediate coupling (as derived in Appendix A with g_L=1.24 for the $^5I_8$ multiplet). For the CaF_2:Ho^{3+} A centre, the ground state is a pseudo-degenerate $\gamma_{1,2}$ doublet with an energy separation of 2Δ=1.7 cm^{-1} giving rise to a second-order Zeeman effect between them:

	γ_1	γ_2
γ_1	$-\Delta$	$\mu_B g_L B\langle J_z\rangle_{1,2}$
γ_2	$\mu_B g_L B\langle J_z\rangle_{1,2}$	Δ

This has the energy eigenvalues $E_\pm = \Delta \pm \sqrt{\Delta^2 + (J_z g_L \mu_B B)^2}$. For a 2 Tesla field, we obtain a value of $g_\parallel$=14.79 in excellent agreement with the EPR value of $g_\parallel = \frac{\delta E}{\mu B}$=14.8.

4.2.3 0.25 cm^{-1} Infrared Absorption Studies of CaF_2:Ho^{3+}

Infrared-absorption spectra (recorded at 0.25 cm^{-1} resolution) of a 27mm thick CaF_2:0.02%Ho^{3+} crystal were measured with the Digilab FTIR spectrometer, employing the optional wide range quartz-beamsplitter and a quartz-halogen source. For these experiments, the crystal was cooled to 10K. For detection a liquid nitrogen cooled indium antimonide infrared detector provided good signal response over the 2800-11000 cm^{-1} region. The $^5I_7$ and $^5I_6$ multiplets could then be studied with a significantly improved signal-to-noise ratio over that obtained by Heron [18] in earlier studies. For absorption to the $^5I_7$ multiplet, eight and five transitions could be identified for the A and B centres respectively, by comparison with the laser excited fluorescence results of Mujaji [15] - see Figure 4.4(a). The absorption features of the A centre all have the 1.7 cm^{-1} ground-state splitting which is modified by any hyperfine structure for the upper state. These modifications are particularly obvious for the $Z_{1,2}\gamma_{1,2} \rightarrow Y_3\gamma_5$ transition, which is affected by the presence of two nearby singlet states, as shown in section 4.2.4. Absorption measurements in this region of the infrared spectrum are made more difficult by the simultaneous occurrence of strong atmospheric absorption. In order to minimise these features, the entire beam path

of the Digilab FTIR was flushed with dry nitrogen gas for prolonged periods prior to scanning the spectrum. Despite these efforts, small, regularly spaced absorption features still remain, particularly around the $Z_{1,2}\gamma_{1,2} \rightarrow Y_{10}\gamma_5$ transitions at 5417.86 and 5413.88 cm^{-1}.

Several features observed in this spectrum remain unassigned. Attempts to correlate these features with the CS1,2 and CB1,2 centres of Mujaji, from the presence of small quantities of Sr^{2+} and Ba^{2+} impurities into the crystal were unsuccessful. Stronger unassigned features of the spectrum are unlabelled.

Transitions to the $^5I_6$ multiplet are less well documented since Mujaji did not study fluorescence to this multiplet and only the A centre has been studied here. Of the four A centre transitions shown in Figure 4.4(b), the feature assigned as the $Z_{1,2}\gamma_{1,2} \rightarrow X_8\gamma_1$ transition is anomalous because we observe only one transition, where we expect two, separated by the ground state 1.7 cm^{-1} splitting. The explanation for this is that the transitions to the $^5I_6$ multiplet have virtually no magnetic dipole moment, unlike transitions to the $^5I_7$ multiplet. Thus, only the $Z_1\gamma_1 \rightarrow X_8\gamma_1$ transition is observed, a transition from the $Z_2\gamma_2$ level requiring absorption of magnetic dipole character. A significant number of absorption features observed to the $^5I_6$ multiplet remain unassigned. More work is required to unravel these spectra of the higher $^5I_6$ and $^5I_5$ multiplets of Ho^{3+} in CaF_2. Many of the $^5I_8 \rightarrow {}^5I_6$ transitions observed lower in energy than the main $Z_{1,2}\gamma_{1,2} \rightarrow X_1\gamma_5$ transition at 8755 cm^{-1} would be associated with the trigonal symmetry B centre.

Table 4.4: Energy levels (in vacuum cm^{-1}, ± 0.02), intensities (relative to the strongest line in the spectrum (=100)) and linewidths (in vacuum cm^{-1}, ± 0.1) as observed for the A and B centres of CaF_2:0.02%Ho^{3+}.

Center	Multiplet	Transition	Energy	Intensity	Linewidth
A	$^5I_7$	$Z_2\gamma_2 \rightarrow Y_1\gamma_5$	5256.38	51	0.7
		$Z_1\gamma_1 \rightarrow Y_1\gamma_5$	5257.81	100	0.9
		$Z_2\gamma_2 \rightarrow Y_3\gamma_5$	5272.87	36	0.9
		$Z_1\gamma_1 \rightarrow Y_3\gamma_5$	5274.7±0.3	15	0.9
		$Z_2\gamma_2 \rightarrow Y_6\gamma_1$	5307.26	10	0.5
		$Z_1\gamma_1 \rightarrow Y_6\gamma_1$	5309.18	12	0.4
		$Z_2\gamma_2 \rightarrow Y_{10}\gamma_5$	5413.88	14	1.4
		$Z_1\gamma_1 \rightarrow Y_{10}\gamma_5$	5417.86	18	1.5
	$^5I_6$	$Z_2\gamma_2 \rightarrow X_1\gamma_5$	8754.64	22	0.8
		$Z_1\gamma_1 \rightarrow X_1\gamma_5$	8756.06	24	0.7
		$Z_2\gamma_2 \rightarrow X_6\gamma_5$	8811.42	5	0.6
		$Z_1\gamma_1 \rightarrow X_6\gamma_5$	8812.05	3	0.5
		$Z_{1,2}\gamma_{1,2} \rightarrow X_8\gamma_1$	8862.41	3	0.8
		$Z_{1,2}\gamma_{1,2} \rightarrow X_9\gamma_5$	8913.77	5	2.5
B	$^5I_7$	$Z_1\gamma_3 \rightarrow Y_1\gamma_3$	5203.42	100	0.5
		$\rightarrow Y_2\gamma_1$	5214.65	33	1.3
		$\rightarrow Y_4\gamma_2$	5223.10	86	0.6
		$\rightarrow Y_5\gamma_3$	5236.23	42	0.6
		$\rightarrow Y_6\gamma_1$	5238.26	52	1.5

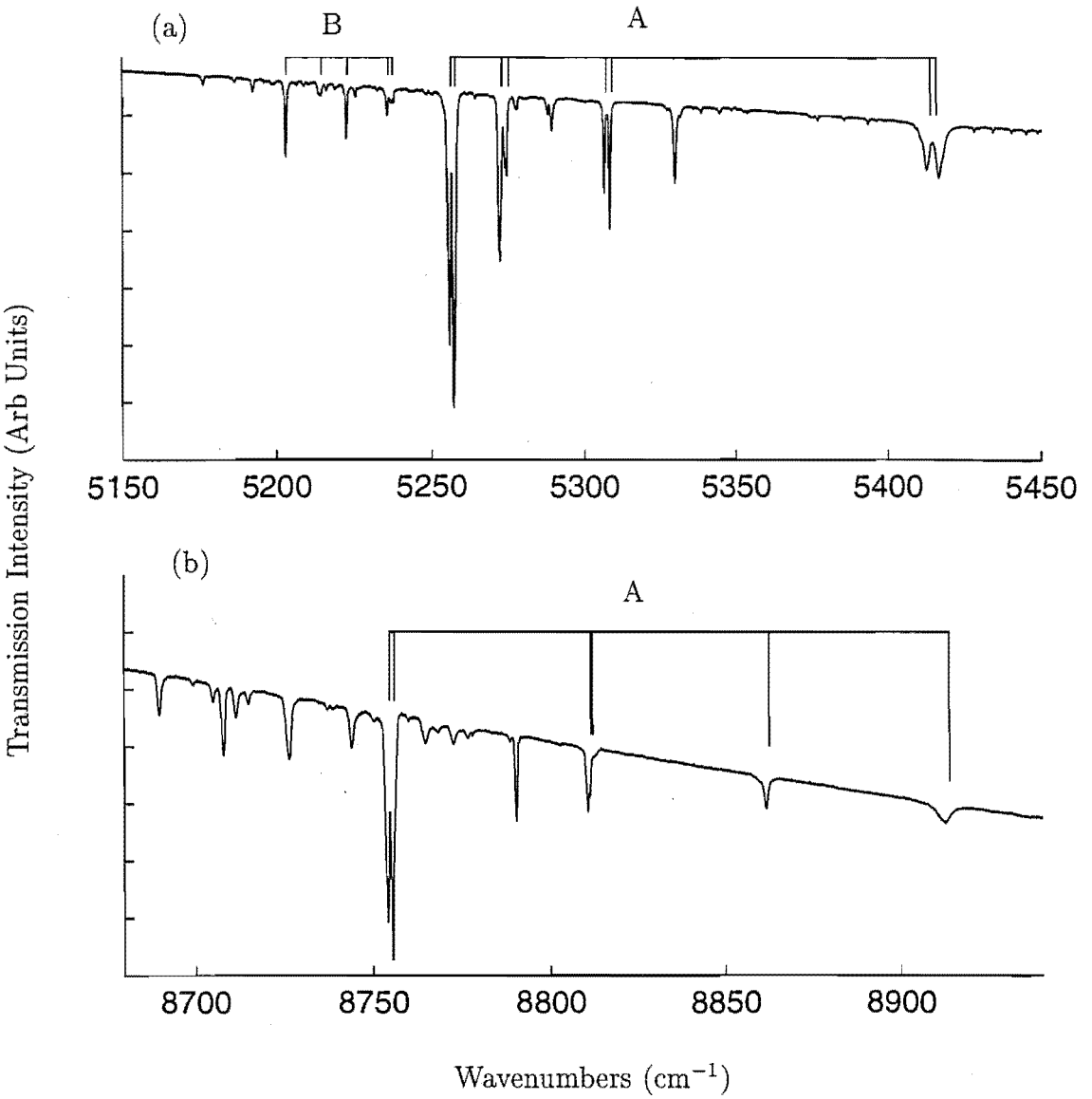

Figure 4.4: Infrared absorption spectra of the (a) $^5I_7$ and (b) $^5I_6$ multiplets for CaF_2:0.02%Ho^{3+}. The spectra were recorded at 10K.

4.2.4 High-Resolution Infrared Absorption for the A Centre in CaF_2:Ho^{3+}

The infrared-absorption spectrum of a 23.8 mm thick CaF_2:0.003%Ho^{3+} crystal was measured to investigate transitions from the pseudo-degenerate $Z_{1,2}\gamma_{1,2}$ ground state of the A centre to the higher $^5I_7$ multiplet centred near 5300 cm^{-1}. From the polarised fluorescence measurements of Mujaji, four transitions could be assigned to this A centre. Heron has presented infrared absorption spectra for these transitions, with partially resolved hyperfine structure present for the 5256 cm^{-1} and 5273 cm^{-1} transition groups. Those spectra are, however, resolution limited to 0.1 cm^{-1}. In addition Heron's spectra have atmospheric absorption lines in the region of interest, tending to obscure the weaker hyperfine transitions, particularly the $Z_{1,2}\gamma_{1,2}\rightarrow Y_1\gamma_5$ crystal field transition at 5256 cm^{-1}. The spectra presented here were recorded on the Bomem DA3 0.02 spectrometer at New Zealand Industrial Research Limited in Lower Hutt, employing the highest resolution available of 0.04 cm^{-1}. Furthermore, the entire beam path of the Bomem spectrometer is evacuated to around 0.5 Torr to minimise (if not entirely eliminate) the effects of atmospheric absorption. An overview of the hyperfine patterns obtained is given in Figure 4.5.

(a) Pseudo-Quadrupole Hyperfine Splittings in the Ground State of the A Centre

For axial symmetry, the hyperfine interaction $H_{h.f.s}$ takes the form

$$H_{h.f.s.} = A_{\parallel} J_z I_z + \frac{1}{2} A_{\perp} (J_+ I_- + J_- I_+)$$

where the much smaller electric quadrupole interaction has been neglected. Within the $^5I_8$ multiplet we have the electronic ground state of the Ho^{3+} ion in the A centre which comprises two close-lying singlet levels, transforming as the γ_1 and γ_2 irreps of the C_{4v} group and separated by an energy spacing of around 1.7 cm^{-1} (=2Δ). These singlet states independently have a zero expectation value of J_z. However given their proximity the mixing of their wavefunctions through the parallel hyperfine interaction gives an enhanced magnetic moment with a $\langle \gamma_1 \mid J_z \mid \gamma_2 \rangle$ of 5.92. There is no perpendicular hyperfine interaction as $\langle \gamma_1 \mid J_\pm \mid \gamma_2 \rangle = 0$. The wavefunctions of the γ_1 and γ_2 both states that comprise the ground state are derived from the crystal field calculations (section 4.2.2) to be:

$$\begin{array}{ll} Z_1\gamma_1 & -0.4900|8\rangle+0.5077|4\rangle\ -0.0576|0\rangle+0.5077|-4\rangle-0.4900|-8\rangle \\ Z_2\gamma_2 & -0.4927|8\rangle+0.5067|4\rangle\ -0.5067|-4\rangle+0.4927|-8\rangle \end{array}$$

The hyperfine splitting of these ground states from the pseudo-quadrupole (second

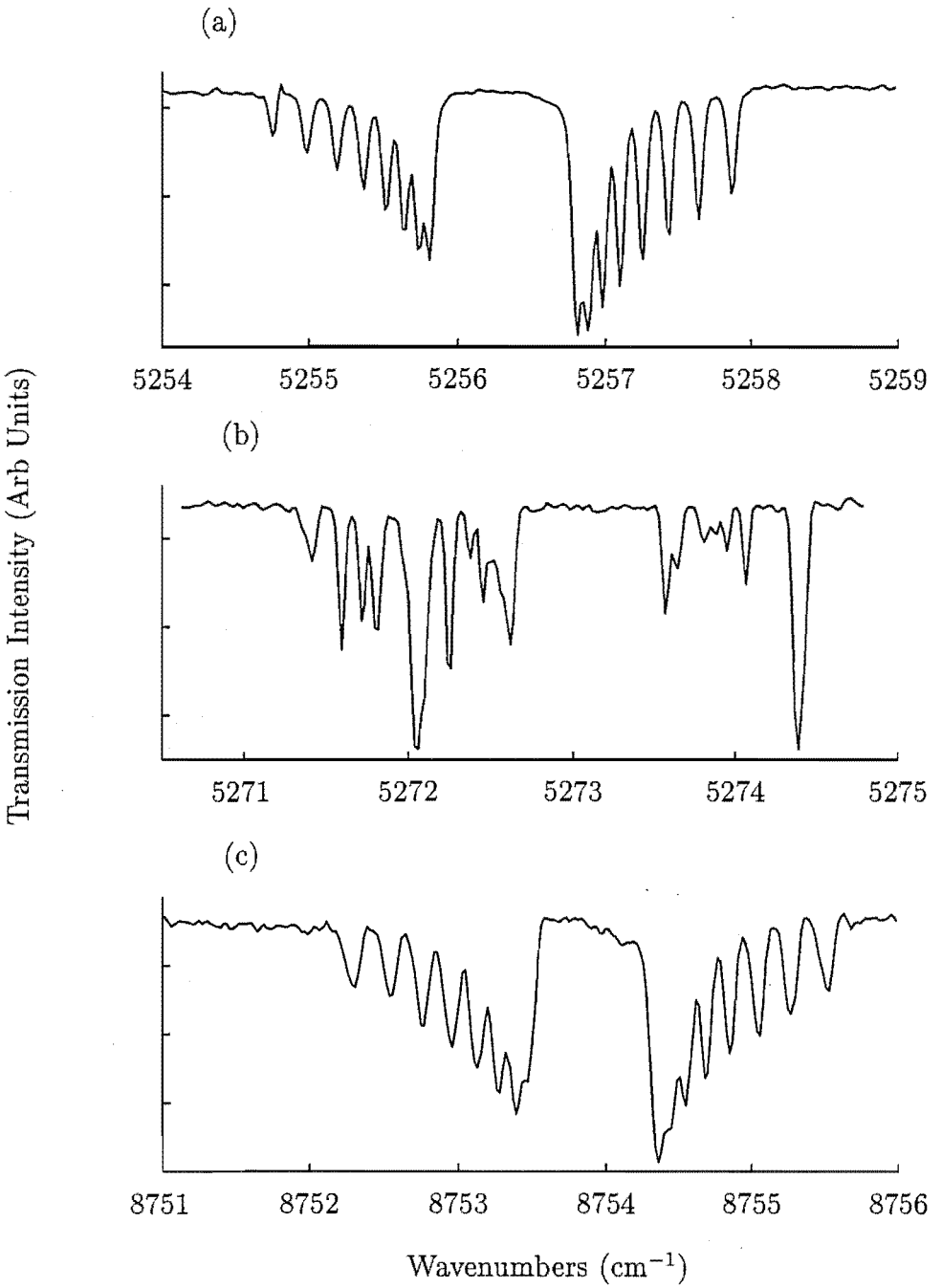

Figure 4.5: Hyperfine structure observed in the $Z_{1,2}\gamma_{1,2}\rightarrow$ (a) $Y_1\gamma_5$, (b) $Y_2\gamma_3$, $Y_3\gamma_5$, $Y_4\gamma_2$ and (c) $X_1\gamma_5$ transitions. The spectra were recorded at 10K.

order magnetic) hyperfine interaction is given by the interaction matrix:

	γ_1	γ_2
γ_1	$-\Delta$	$A_8 I_z \langle J_z \rangle$
γ_2	$A_8 I_z \langle J_z \rangle$	Δ

Solving for the eigenvalues gives the energies (or energy spectrum in GHz) as:

$$E(I_z) = \pm\sqrt{\Delta^2 + (A_J \langle J_z \rangle I_z)^2}$$

Therefore with A_8, the magnetic hyperfine constant of the $^5I_8$ multiplet, as 812MHz, 2Δ=1.7 cm^{-1}=51 GHz, $I = \frac{7}{2}$ and $\langle \gamma_1 \mid J_z \mid \gamma_2 \rangle$=5.92, the calculated magnetic hyperfine splittings are as shown in Figure 4.6. This pseudo-quadrupole splitting gives four doubly degenerate levels with separations in the ratio 3:2:1. It can be noted from Figure 4.6 that the calculated I_z splittings are 0.88 GHz ($\pm\frac{1}{2} - \pm\frac{3}{2}$), 1.69 GHz ($\pm\frac{3}{2} - \pm\frac{5}{2}$) and 2.36 GHz ($\pm\frac{5}{2} - \pm\frac{7}{2}$). These splittings are too small to be resolved, even with the Bomem spectrometer at 0.04 cm^{-1} (1.2 GHz) resolution. Hence these calculated splittings cannot be directly checked through infrared absorption to, say the $^5I_7Y_6\gamma_1$ singlet state at 5307.5 cm^{-1} which shows virtually no structure from this ground state hyperfine interaction (see Figure 4.7).

(b) Superimposed Ground State and $^5I_7$ and $^5I_6$ Multiplet Doublet State Hyperfine Structure

The infrared spectrum of the $Z_{1,2}\gamma_{1,2} \rightarrow Y_1\gamma_5$ transition group near 5256 cm^{-1} reveals two sets of fully resolved eight line hyperfine patterns separated by slightly more than 1.7 cm^{-1} (see Figure 4.8). As the γ_5 upper state doublet has non-zero $\langle J_z \rangle$ of 5.26 the nuclear states of this level are split by the hyperfine term $A_7 I_z \langle J_z \rangle$ into $(2I + 1)$ levels with equal spacing $A_7 \langle J_z \rangle$ (where the magnetic hyperfine constant for the $^5I_7$ multiplet is denoted A_7). The electronic wavefunction for this $Y_1\gamma_5$ state is

$$Y_1\gamma_5^{\pm} \quad \pm 0.8578 \mid \pm 7\rangle \mp 0.4057 \mid \pm 3\rangle \mp 0.1571 \mid \mp 1\rangle \mp 0.2682 \mid \mp 5\rangle$$

The hyperfine interaction matrix for this $Y_1\gamma_5$ state is

	γ_5^+	γ_5^-
γ_5^+	$A_7 I_z \langle J_z \rangle$	
γ_5^-		$-A_7 I_z \langle J_z \rangle$

The observed splittings of Figure 4.8 represent the superposition of the hyperfine structure of the ground state with that of this upper $Y_1\gamma_5$ doublet. Transitions are observed only between electron-nuclear states of the same I_z value. In Table

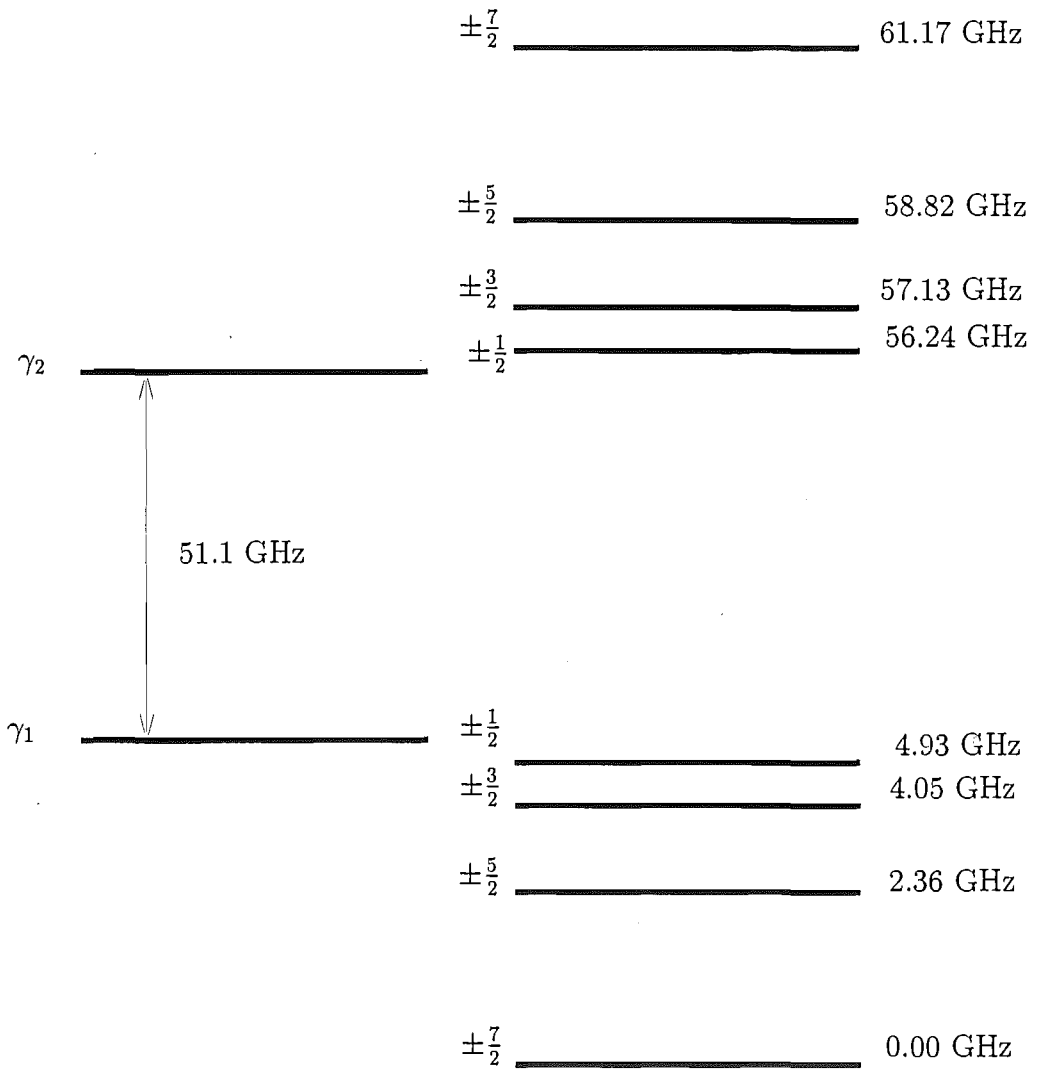

Figure 4.6: Calculated pseudo-quadrupole hyperfine pattern for the ground state of the A centre in CaF_2:Ho^{3+}

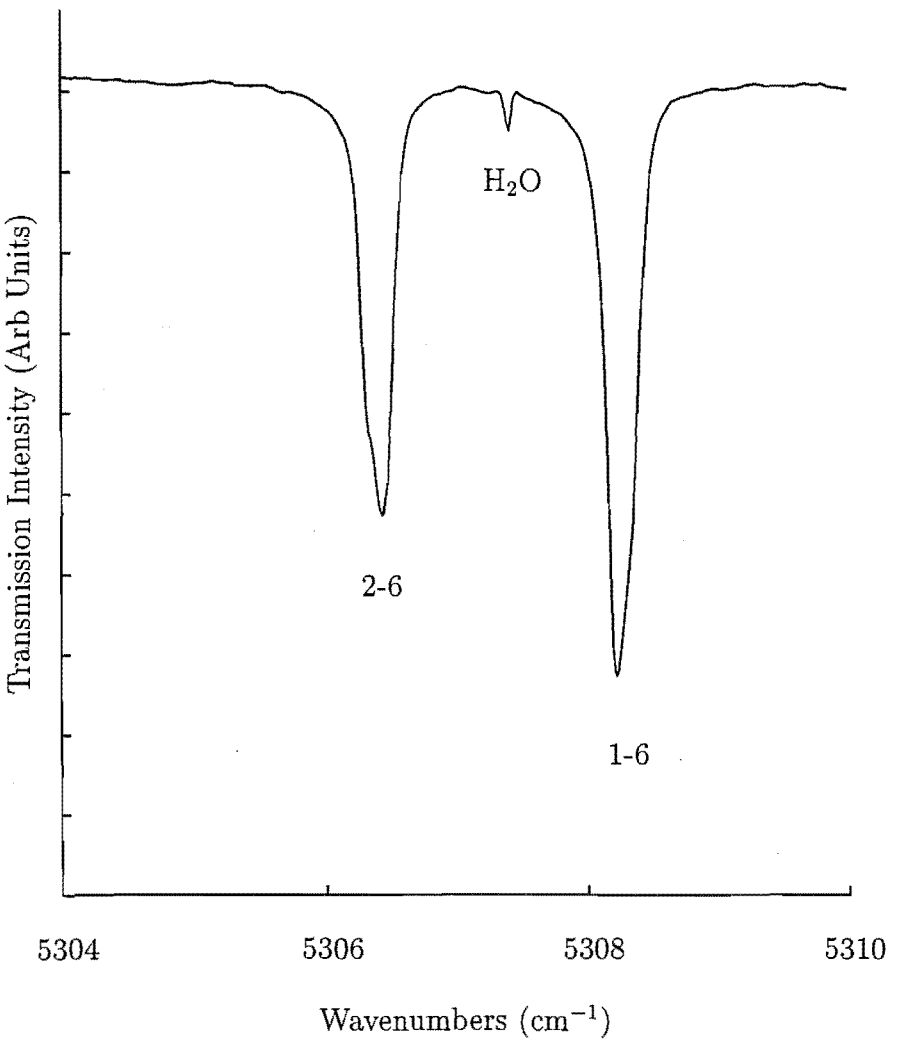

Figure 4.7: Unresolved hyperfine structure in the $Z_{1,2}\gamma_{1,2} \rightarrow Y_6\gamma_1$ transition of the A centre in CaF_2:0.003%Ho^{3+}. The spectrum was recorded at 10K.

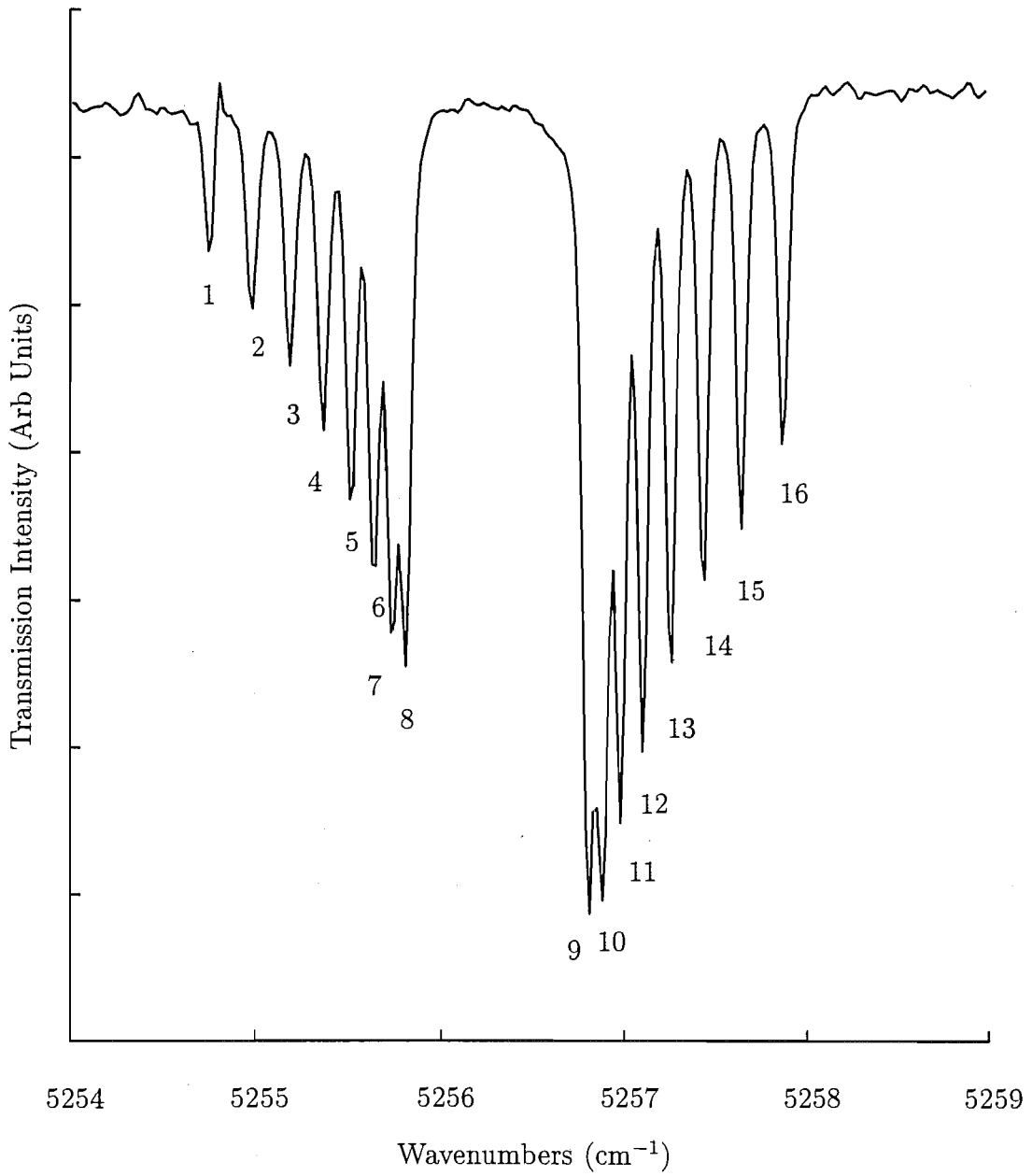

Figure 4.8: Hyperfine structure for the $Z_{1,2}\gamma_{1,2} \rightarrow Y_1\gamma_5$ absorption transition of the A centre in CaF_2:0.003%Ho^{3+}. The spectrum was recorded at 10K.

Table 4.5: Calculated and experimental hyperfine splittings (in GHz ±0.6) in the $Z_{1,2}\gamma_{1,2} \rightarrow Y_1\gamma_5$ absorption transition near 5250.5 cm^{-1}. An A_7 value of 0.883 GHz has used to calculate these splittings.

		Hyperfine Splittings	
Line	$\mathbf{I_z}$	**Calc**	**Expt**
1-8	$\pm\frac{7}{2}$	32.5	30.3
2-7	$\pm\frac{5}{2}$	23.2	21.7
3-6	$\pm\frac{3}{2}$	13.9	13.2
4-5	$\pm\frac{1}{2}$	4.6	4.3
9-16	$\pm\frac{7}{2}$	32.5	30.0
10-15	$\pm\frac{5}{2}$	23.2	21.4
11-14	$\pm\frac{3}{2}$	13.9	12.8
12-13	$\pm\frac{1}{2}$	4.6	4.3

4.5 we compare the calculated hyperfine transition I_z splittings with those observed experimentally and good agreement is obtained.

For transitions to the $^5I_6$ multiplet, a 27mm thick CaF_2:0.02%Ho^{3+} crystal was required for these weaker absorption transitions. It is observed that the $Z_{1,2}\gamma_{1,2} \rightarrow X_1\gamma_5$ transition group near 8755 cm^{-1} also has two sets of eight-line hyperfine patterns very similar to the $Z_{1,2}\gamma_{1,2} \rightarrow Y_1\gamma_5$ transitions already shown in Figure 4.8. We interpret this structure similarly. The crystal-field wavefunction for the $X_1\gamma_5$ state is:

$$X_1\gamma_5^{\pm} \quad -0.0840 \mid \pm 1\rangle - 0.9936 \mid \pm 5\rangle$$

with a $\langle J_z \rangle$ value of 4.94. For the $^5I_6$ multiplet, the magnetic hyperfine constant A_6, has a value 0.969 GHz - see Appendix A. Therefore employing the same interaction matrix as for the $Z_{1,2}\gamma_{1,2} \rightarrow Y_1\gamma_5$ case we obtain hyperfine splittings for the $Z_{1,2}\gamma_{1,2} \rightarrow X_1\gamma_5$ transitions, which are in excellent agreement with the experimental values in Table 4.6.

(c) Least Squares Fitting to the Hyperfine Constants

An alternative approach to the direct calculation is to fit the A_8, A_7 and A_6 magnetic

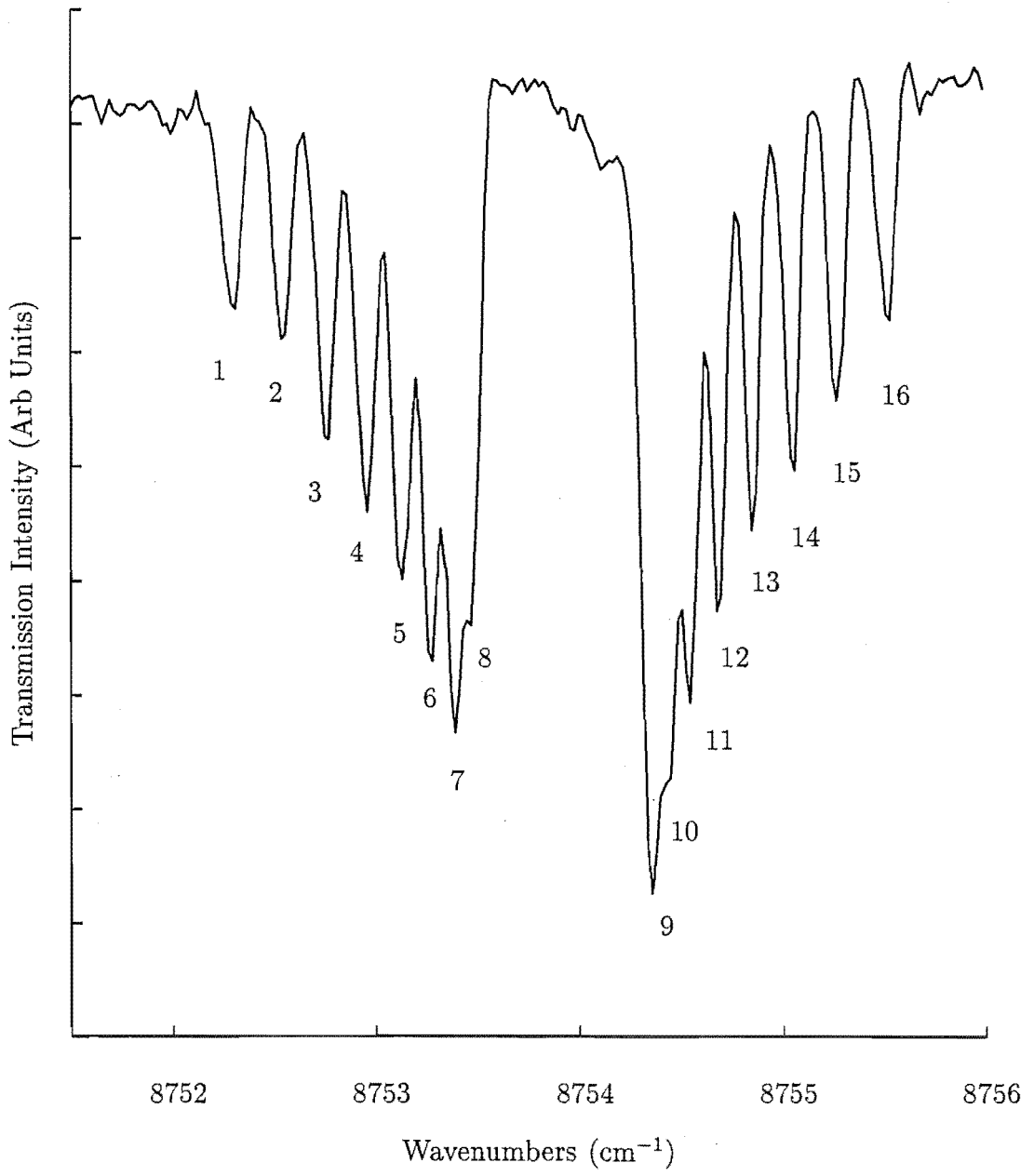

Figure 4.9: Hyperfine structure in the $Z_{1,2}\gamma_{1,2} \rightarrow X_1\gamma_5$ absorption transition of the A centre in CaF_2:0.02%Ho^{3+}. The spectrum was recorded at 10K.

Table 4.6: Calculated and experimental hyperfine splittings (in GHz ±0.6) in the $Z_{1,2}\gamma_{1,2} \rightarrow X_1\gamma_5$ transition near 8755 cm^{-1}. The value of A_6, the magnetic hyperfine constant for the $^5I_6$ multiplet, used for this calculation was 0.969 GHz.

		Hyperfine Splittings	
Line	$\mathbf{I_z}$	**Calc**	**Expt**
1-8	$\pm\frac{7}{2}$	33.5	35.0
2-7	$\pm\frac{5}{2}$	24.0	28.1
3-6	$\pm\frac{3}{2}$	14.4	15.3
4-5	$\pm\frac{1}{2}$	4.8	4.9
9-16	$\pm\frac{7}{2}$	33.5	34.8
10-15	$\pm\frac{5}{2}$	24.0	25.1
11-14	$\pm\frac{3}{2}$	14.4	15.3
12-13	$\pm\frac{1}{2}$	4.8	5.1

hyperfine constants from the experimental data. We do this using the MATLAB 'fmins' least squares fitting routine. Fitting the $Z_{1,2}\gamma_{1,2} \rightarrow Y_1\gamma_5$ hyperfine transitions, with the A_8 and A_7 hyperfine constants treated as adjustable parameters we obtain A_8=0.782 GHz and A_7=0.884 GHz. The A_7 value is in excellent agreement with the calculated value whilst the A_8 value is lower than the free ion value of 0.812 GHz. Boonyarith et. al. [43] also found this obtaining a value of 0.795 GHz from analysis of $^5I_8 \rightarrow {}^5F_5$ absorption transitions, in good agreement with both the free ion value and that obtained here. Fitting the A_8 and A_6 hyperfine constants to the $Z_{1,2}\gamma_{1,2} \rightarrow X_1\gamma_5$ transitions we obtain A_8=0.832 GHz and A_6=1.012 GHz, both values once again in good agreement with the calculated and the free ion values. However the discrepancy between the two best fit values of A_8 indicates the limits of using data that is both instrument and inhomogeneous linewidth limited.

(d) Intensity Calculations

A stringent check on the validity of the energy level calculations is to simulate the systematically increasing then decreasing intensity patterns of the observed $\gamma_{1,2} \rightarrow \gamma_5$ transitions. The intensity of a hyperfine transition from an initial state $\mid i\rangle$ to a final state $\mid f\rangle$ is proportional to their population difference and the square of the transition matrix element between them:

$$I \propto (n_i - n_f) \mid \langle i \mid H_{\text{at-rad}} \mid f\rangle \mid^2$$

which is an application of Fermi's Golden Rule [55]. Here $\langle i \mid H_{\text{at-rad}} \mid f\rangle$ is the relevant atom-radiation interaction and n_i and n_f are the initial and final state populations. Following Boonyarith [49] we note the population of the excited states will be essentially zero at 10K. With the nuclear spin projection being conserved during the transition (ΔI_z =0), it is convenient to write the transition intensities as:

State	Intensity
$\mid \gamma_1 I_z\rangle \rightarrow \mid \gamma_5^+ I_z\rangle$	$\mid a_1(I_z)M + a_2(I_z)N \mid^2 exp(\frac{-\Delta E(I_z)}{k_B T})$
$\mid \gamma_1 I_z\rangle \rightarrow \mid \gamma_5^- I_z\rangle$	$\mid a_1(I_z)M - a_2(I_z)N \mid^2 exp(\frac{-\Delta E(I_z)}{k_B T})$
$\mid \gamma_2 I_z\rangle \rightarrow \mid \gamma_5^+ I_z\rangle$	$\mid a_3(I_z)M + a_4(I_z)N \mid^2 exp(\frac{-\Delta E(I_z)}{k_B T})$
$\mid \gamma_2 I_z\rangle \rightarrow \mid \gamma_5^- I_z\rangle$	$\mid a_3(I_z)M - a_4(I_z)N \mid^2 exp(\frac{-\Delta E(I_z)}{k_B T})$

where the factors $a_1(I_z)$, $a_2(I_z)$, $a_3(I_z)$ and $a_4(I_z)$ are the admixture coefficients for the two ground state wavefunctions expressed in the form

$$\begin{array}{ll} Z_1\gamma_1 I_z & a_1 \mid \gamma_1 I_z\rangle + a_2 \mid \gamma_2 I_z\rangle \\ Z_2\gamma_2 I_z & a_3 \mid \gamma_1 I_z\rangle + a_4 \mid \gamma_2 I_z\rangle \end{array}$$

$\Delta E(I_z)$ is the energy above the ground state of the I_z level in question and M and N are the matrix elements $\langle \gamma_1 \mid H_{\text{at-rad}} \mid \gamma_5^{\pm}\rangle$ and $\langle \gamma_2 \mid H_{\text{at-rad}} \mid \gamma_5^{\pm}\rangle$ respectively. The $Z_{1,2}\gamma_{1,2} \rightarrow \gamma_5$ transitions are electric dipole allowed in σ polarisation with matrix elements:

$$\langle \gamma_1 \mid D^+ \mid \gamma_5^+\rangle = \langle \gamma_1 \mid D^- \mid \gamma_5^-\rangle = M$$
$$\langle \gamma_2 \mid D^+ \mid \gamma_5^+\rangle = -\langle \gamma_2 \mid D^- \mid \gamma_5^-\rangle = N$$

where D^+ and D^- are the left and right circularly-polarized electric dipole operators with the appropriate phase relations included [43]. Hence the matrix elements for

Table 4.7: Ground state nuclear wavefunction composition for the A centre in CaF_2:0.003%Ho^{3+}

State	Wavefunction
$Z_1\gamma_1 \pm \frac{7}{2}$	$-0.9579 \mid \gamma_1 \pm \frac{7}{2}\rangle \pm 0.2870 \mid \gamma_2 \pm \frac{7}{2}\rangle$
$Z_1\gamma_1 \pm \frac{5}{2}$	$-0.9759 \mid \gamma_1 \pm \frac{5}{2}\rangle \pm 0.2181 \mid \gamma_2 \pm \frac{5}{2}\rangle$
$Z_1\gamma_1 \pm \frac{3}{2}$	$-0.9906 \mid \gamma_1 \pm \frac{3}{2}\rangle \pm 0.1371 \mid \gamma_2 \pm \frac{3}{2}\rangle$
$Z_1\gamma_1 \pm \frac{1}{2}$	$-0.9989 \mid \gamma_1 \pm \frac{1}{2}\rangle \pm 0.0468 \mid \gamma_2 \pm \frac{1}{2}\rangle$
$Z_2\gamma_2 \pm \frac{7}{2}$	$0.9579 \mid \gamma_2 \pm \frac{7}{2}\rangle \pm 0.2870 \mid \gamma_1 \pm \frac{7}{2}\rangle$
$Z_2\gamma_2 \pm \frac{5}{2}$	$0.9759 \mid \gamma_2 \pm \frac{5}{2}\rangle \pm 0.2181 \mid \gamma_1 \pm \frac{5}{2}\rangle$
$Z_2\gamma_2 \pm \frac{3}{2}$	$0.9906 \mid \gamma_2 \pm \frac{3}{2}\rangle \pm 0.1371 \mid \gamma_1 \pm \frac{3}{2}\rangle$
$Z_2\gamma_2 \pm \frac{1}{2}$	$0.9989 \mid \gamma_2 \pm \frac{1}{2}\rangle \pm 0.0468 \mid \gamma_1 \pm \frac{1}{2}\rangle$

the $\mid \gamma_2 I_z\rangle \rightarrow \mid \gamma_5^+ I_z\rangle$ and $\mid \gamma_2 I_z\rangle \rightarrow \mid \gamma_5^- I_z\rangle$ transitions are equal. The ground-state nuclear-wavefunction composition can be taken from the earlier ground-state hyperfine-energy level calculations (presented in Table 4.7).

A choice is needed for the lineshape function. The transitions observed here are to the lowest levels of the $^5I_7$ and $^5I_8$ multiplets and are sharp, inhomogeneously-broadened lines with minimal probability for spontaneous phonon emission [50]. It is usual to take the inhomogeneous lineshape as Gaussian [51]. However as is pointed out by Macfarlane [52], [53], many different lineshapes have been observed for inhomogeneously broadened lines at different concentrations. Here a Lorentzian-lineshape-function is employed as this seems the most representative for the line-shapes observed:

$$F_L(\nu) = \frac{\Delta\nu}{(\nu_0 - \nu)^2 + (\Delta\nu)^2}.$$

A simulated spectrum for the $Z_{1,2}\gamma_{1,2} \rightarrow Y_1\gamma_5$ transitions near 5256.5 cm^{-1} is shown in Figure 4.10. The linewidth parameter, $\Delta\nu$ is chosen as 0.04 cm^{-1}, the temperature is 10K and the optical transition parameters M and N are assumed equal. For these good agreement between the experimental and calculated spectra are obtained given the assumptions made. No attempt was made to simulate the similar $Z_{1,2}\gamma_{1,2} \rightarrow X_1\gamma_5$ spectrum near 8755 cm^{-1} since the intensity variation is again determined by the off-diagonal mixing occuring in the ground state, thus any simulation would give the same spectral fit as that in Figure 4.10 except for a different linewidth parameter $\Delta\nu$.

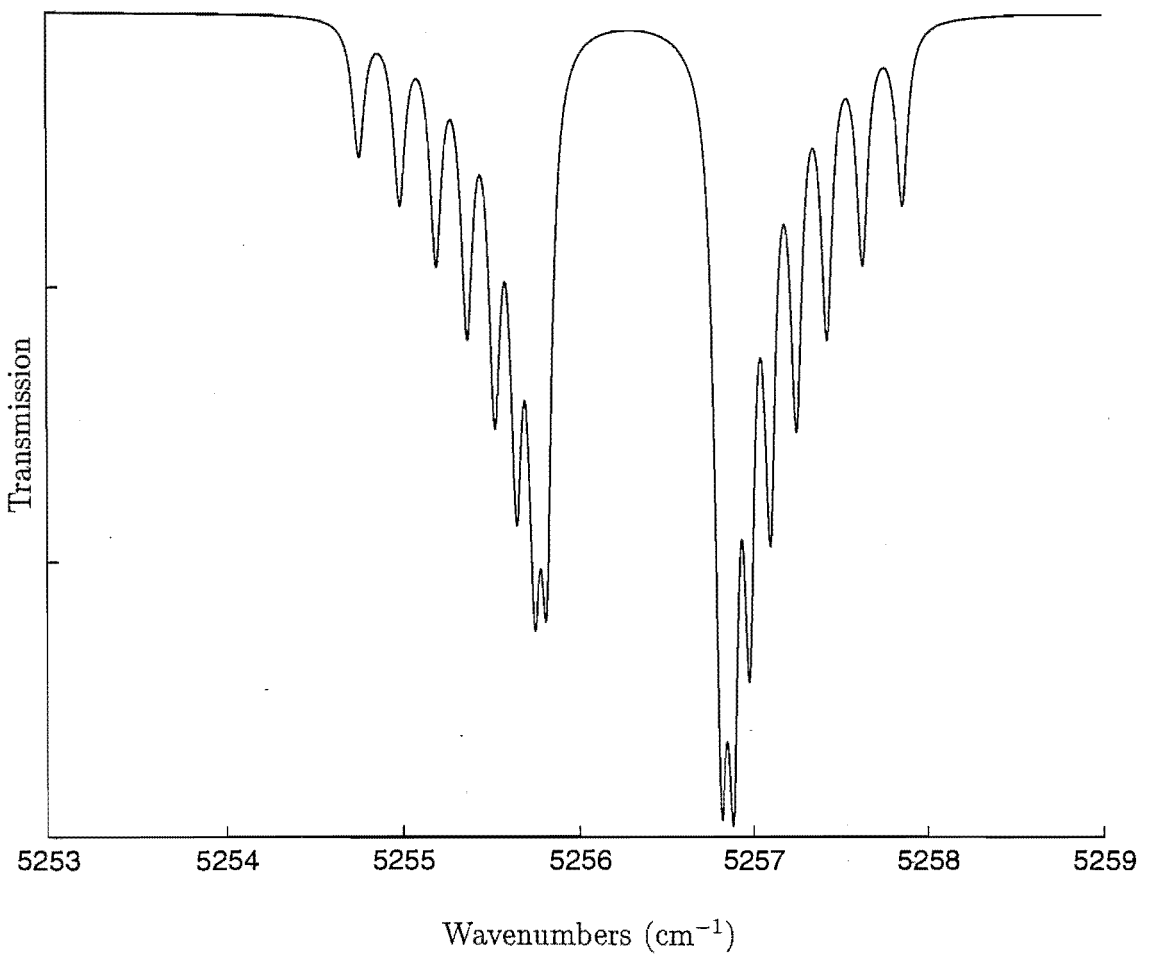

Figure 4.10: Simulated absorption spectrum for the $Z_{1,2}\gamma_{1,2} \rightarrow Y_1\gamma_5$ transition of the A centre. A crystal temperature of 10K was used in the simulation.

(e) Perturbed Hyperfine Patterns: The Effect of Two Nearby Singlets on the Hyperfine Structure in a $^5I_7$ Multiplet Doublet

The transition group centred around 5274 cm^{-1} has a hyperfine pattern corresponding to the resolved hyperfine pattern of the $Y_3\gamma_5$ doublet superimposed upon the ground state pseudo-quadrupole hyperfine structure. However the observed pattern is not as simple as the previously discussed $Z_{1,2}\gamma_{1,2} \rightarrow Y_1\gamma_5$ and $X_1\gamma_5$ patterns and we believe that nearby singlet states perturb the pattern. The spectral analysis of Mujaji [17] puts a $Y_2\gamma_3$ singlet state just 1 cm^{-1} away from the $Y_3\gamma_5$ doublet state. In addition the crystal-field analysis suggests a second γ_2 singlet state further perturbs the hyperfine pattern of the doublet state. Thus the complexity of this pattern is derived from the perturbation of the $Z_{1,2}\gamma_{1,2} \rightarrow Y_3\gamma_5$ hyperfine structure due to the presence of two nearby singlet states. For absorption from the $Z_{1,2}\gamma_{1,2}$ ground state, only transitions to the $Y_3\gamma_5$ and $Y_4\gamma_2$ states will be observed. The γ_3 state could only appear if there were strong mixing with the γ_5 state via the perpendicular hyperfine interaction. The hyperfine Hamiltionian is:

$$H_{h.f.s.} = A_{\parallel} J_z I_z + \frac{1}{2} A_{\perp} (J_+ I_- + J_- I_+)$$

and the wavefunctions of the three states are:

$$\begin{array}{ll} \gamma_3 & 0.6095 \mid 6\rangle - 0.3528 \mid 2\rangle + 0.3528 \mid -2\rangle - 0.6095 \mid -6\rangle \\ \gamma_5^{\pm} & \mp 0.3528 \mid \pm 7\rangle \mp 0.0465 \mid \pm 3\rangle \pm 0.3014 \mid \mp 1\rangle \mp 0.8823 \mid \mp 5\rangle \\ \gamma_2 & 0.6563 \mid 4\rangle - 0.3691 \mid 0\rangle + 0.6563 \mid -4\rangle \end{array}$$

These wavefunctions are mixed by both the perpendicular hyperfine interaction, $J_{\pm}$, and the parallel hyperfine interaction J_z. The appropriate recursion relations are given by Schiff [54] as:

$$\langle J_z + 1 \mid J_+ \mid J_z \rangle = \sqrt{J(J+1) - J_z(J_z+1)}$$

$$\langle J_z - 1 \mid J_- \mid J_z \rangle = \sqrt{J(J+1) - J_z(J_z-1)}$$

$$\langle J_z \mid J_z \mid J_z \rangle = J_z$$

yielding

$$\langle \gamma_2 \mid J_+ \mid \gamma_5^+ \rangle = \langle \gamma_2 \mid J_- \mid \gamma_5^- \rangle = 4.51$$

$$\langle \gamma_3 \mid J_+ \mid \gamma_5^+ \rangle = \langle \gamma_3 \mid J_- \mid \gamma_5^- \rangle = 2.83$$

$$\langle \gamma_5^+ \mid J_z \mid \gamma_5^+ \rangle = 3.11 = -\langle \gamma_5^- \mid J_z \mid \gamma_5^- \rangle$$

The hyperfine interaction matrix for the two singlet states, $Y_2\gamma_3$ and $Y_4\gamma_2$, and the $Y_3\gamma_5$ doublet state involves energy separations δ and Δ between the γ_3-$\gamma_5^{\pm}$ and $\gamma_5^{\pm}$-γ_2

states respectively. The γ_5 doublet itself is split by the parallel hyperfine interaction whilst the two singlets are mixed with the doublet via the perpendicular hyperfine interaction $\frac{1}{2}A_\perp(J_+I_- + J_-I_+)$. There is no direct coupling between the two singlet states as neither the J_z nor $J_\pm$ operators of the parallel and perpendicular hyperfine interactions can connect the J_z kets of these states. The interactions of either of the singlets with the doublet will be such that for a given value I_z of the singlet state, the mixed doublet-state components are necessarily either $I_z + 1$ or $I_z - 1$. These doublet $I_z \pm 1$ states will be split by the parallel hyperfine interaction $A_\parallel\langle J_z\rangle I_z \pm 1$ (where once again I_z is of the singlets). The hyperfine interactions for one I_z of the singlets can be represented as:

I_z	γ_3	γ_5^+	γ_5^-	γ_2
γ_3	δ	$\frac{1}{2}A_\perp\langle\gamma_3 \mid J_- \mid \gamma_5^+\rangle I_+$	$\frac{1}{2}A_\perp\langle\gamma_3 \mid J_+ \mid \gamma_5^-\rangle I_-$	0
γ_5^+	$\frac{1}{2}A_\perp\langle\gamma_5^+ \mid J_- \mid \gamma_3\rangle I_+$	$A_\parallel\langle J_z\rangle(I_z - 1)$	0	$\frac{1}{2}A_\perp\langle\gamma_5^+ \mid J_+ \mid \gamma_2\rangle I_-$
γ_5^-	$\frac{1}{2}A_\perp\langle\gamma_5^- \mid J_+ \mid \gamma_3\rangle I_-$	0	$-A_\parallel\langle J_z\rangle(I_z + 1)$	$\frac{1}{2}A_\perp\langle\gamma_5^- \mid J_- \mid \gamma_2\rangle I_+$
γ_2	0	$\frac{1}{2}A_\perp\langle\gamma_2 \mid J_+ \mid \gamma_5^+\rangle I_-$	$\frac{1}{2}A_\perp\langle\gamma_2 \mid J_- \mid \gamma_5^-\rangle I_+$	Δ

The analytical form of the energy spectrum from this matrix is too complex to be given here and numerical solutions were used.

The problem is rendered more difficult because the exact energies of the $Y_2\gamma_3$ and $Y_4\gamma_2$ singlet states relative to the doublet are not known. Since the energy positions of the hyperfine levels and their relative intensities will be critically sensitive to the mixing between these states, an unambiguous energy level fit cannot be realised. Instead we fit the relative intensities of the transition group as a whole. The approach taken here is to alter the relative energy-level spacings of the $Y_2\gamma_3$, $Y_3\gamma_5$ and $Y_4\gamma_2$ crystal field states ($\mid JJ_z\rangle$) in steps until the calculated intensity pattern resembles the experimentally measured pattern. The calculations were performed in a similar manner to the intensity calculations for the $Z_{1,2}\gamma_{1,2} \rightarrow Y_1\gamma_5$ and $X_1\gamma_5$ patterns. Electric and magnetic dipole transition matrix elements will only be non zero between the $Y_3\gamma_5$ and $Y_4\gamma_2$ states with wavefunctions expressed in general form as:

$$\begin{array}{ll} Y_2\gamma_3 I_z & b_1 \mid \gamma_3 I_z\rangle + b_2 \mid \gamma_5^\pm I_z \pm 1\rangle \\ Y_3\gamma_5^\pm I_z & b_3 \mid \gamma_5^\pm I_z\rangle + b_4 \mid \gamma_2 I_z \pm 1\rangle + b_5 \mid \gamma_3 I_z \pm 1\rangle \\ Y_4\gamma_2 I_z & b_6 \mid \gamma_2 I_z\rangle + b_7 \mid \gamma_5^\pm I_z \pm 1\rangle \end{array}$$

From this we obtain transition intensity matrix elements of the form:

State	Intensity
$\mid \gamma_1 I_z\rangle \rightarrow \mid \gamma_5^+ I_z\rangle$	$\mid a_1(I_z)b_3(I_z)H + a_2(I_z)b_3(I_z)J \mid^2 exp(\frac{-\Delta E(I_z)}{k_B T})$
$\mid \gamma_1 I_z\rangle \rightarrow \mid \gamma_5^- I_z\rangle$	$\mid a_1(I_z)b_3(I_z)H - a_2(I_z)b_3(I_z)J \mid^2 exp(\frac{-\Delta E(I_z)}{k_B T})$
$\mid \gamma_2 I_z\rangle \rightarrow \mid \gamma_5^+ I_z\rangle$	$\mid a_3(I_z)b_3(I_z)H + a_4(I_z)b_3(I_z)J \mid^2 exp(\frac{-\Delta E(I_z)}{k_B T})$
$\mid \gamma_2 I_z\rangle \rightarrow \mid \gamma_5^- I_z\rangle$	$\mid a_3(I_z)b_3(I_z)H - a_4(I_z)b_3(I_z)J \mid^2 exp(\frac{-\Delta E(I_z)}{k_B T})$
$\mid \gamma_1 I_z\rangle \rightarrow \mid \gamma_2 I_z\rangle$	$\mid a_1(I_z)b_6(I_z)G + a_2(I_z)b_6(I_z)K \mid^2 exp(\frac{-\Delta E(I_z)}{k_B T})$
$\mid \gamma_2 I_z\rangle \rightarrow \mid \gamma_2 I_z\rangle$	$\mid a_3(I_z)b_6(I_z)G + a_4(I_z)b_6(I_z)K \mid^2 exp(\frac{-\Delta E(I_z)}{k_B T})$

Where $b_1(I_z)$, $b_2(I_z)$, $b_3(I_z)$, $b_4(I_z)$, $b_5(I_z)$, $b_6(I_z)$ and $b_7(I_z)$ are the admixture coefficients of the four excited state wavefunctions and H, J, G and K are the $Z_1\gamma_1 \rightarrow Y_3\gamma_5$, $Z_2\gamma_2 \rightarrow Y_3\gamma_5$, $Z_1\gamma_1 \rightarrow Y_4\gamma_2$ and $Z_2\gamma_2 \rightarrow Y_4\gamma_2$ optical transition parameters. All other terms are as explained earlier. The admixture of electron-nuclear states via the perpendicular hyperfine interaction introduces additional matrix elements of the form:

$$\mid \gamma_1 I_z \pm 1\rangle \rightarrow \mid \gamma_5^+ I_z \pm 1\rangle \quad \mid a_1(I_z \pm 1)b_{2,7}(I_z \pm 1)H + a_2(I_z \pm 1)b_{2,7}(I_z \pm 1)J \mid^2 \times exp(\frac{-\Delta E(I_z \pm 1)}{k_B T})$$

$$\mid \gamma_1 I_z \pm 1\rangle \rightarrow \mid \gamma_5^- I_z \pm 1\rangle \quad \mid a_1(I_z \pm 1)b_{2,7}(I_z \pm 1)H - a_2(I_z \pm 1)b_{2,7}(I_z \pm 1)J \mid^2 \times exp(\frac{-\Delta E(I_z \pm 1)}{k_B T})$$

$$\mid \gamma_2 I_z \pm 1\rangle \rightarrow \mid \gamma_5^+ I_z \pm 1\rangle \quad \mid a_3(I_z \pm 1)b_{2,7}(I_z \pm 1)H + a_4(I_z \pm 1)b_{2,7}(I_z \pm 1)J \mid^2 \times exp(\frac{-\Delta E(I_z \pm 1)}{k_B T})$$

$$\mid \gamma_2 I_z \pm 1\rangle \rightarrow \mid \gamma_5^- I_z \pm 1\rangle \quad \mid a_3(I_z \pm 1)b_{2,7}(I_z \pm 1)H - a_4(I_z \pm 1)b_{2,7}(I_z \pm 1)J \mid^2 \times exp(\frac{-\Delta E(I_z \pm 1)}{k_B T})$$

for either of the two singlets $Y_2\gamma_3$ and $Y_4\gamma_2$ as appropriate. The I_z above is of the singlets. For the $Y_3\gamma_5^{\pm}$ doublet states there are additional matrix elements:

$$\mid \gamma_1 I_z \pm 1\rangle \rightarrow \mid \gamma_2 I_z \pm 1\rangle \quad \mid a_1(I_z \pm 1)b_4(I_z \pm 1)G + a_2(I_z \pm 1)b_4(I_z \pm 1)K \mid^2 \times exp(\frac{-\Delta E(I_z \pm 1)}{k_B T})$$

$$\mid \gamma_2 I_z \pm 1\rangle \rightarrow \mid \gamma_2 I_z \pm 1\rangle \quad \mid a_3(I_z \pm 1)b_4(I_z \pm 1)G + a_4(I_z \pm 1)b_4(I_z \pm 1)K \mid^2 \times exp(\frac{-\Delta E(I_z \pm 1)}{k_B T})$$

where, here the I_z is of the doublet.

The best fit was obtained for a crystal field energy level scheme for the three levels

with the $Y_2\gamma_3$ state 0.7 cm^{-1} below the $Y_2\gamma_5^{\pm}$ state and the $Y_4\gamma_2$ state 0.3 cm^{-1} above the $Y_2\gamma_5^{\pm}$ state. This gives the energy level scheme for the hyperfine structure of the excited Y_2, Y_3 and Y_4 states as given in Figure 4.11. An energy level and intensity pattern which accounts for the main experimental features can be constructed from this crystal field energy scheme, first ignoring the mixing of states of different I_z and with the optical transition parameters all set to unity (including magnetic dipole). It is far more satisfactory, however, to include the I_z mixing in the intensity calculation despite the fact that this greatly increases the calculational tedium. In order to limit the extent of, and because of approximations inherent in the calculation, only components 1% or greater were considered.

Figure 4.12 gives the crystal-field assignments for the various components of the spectrum and gives a schematic representation of the calculated hyperfine splitting obscured by the inhomogeneous linewidth. The simulated spectrum is compared with the experimental spectrum in Figure 4.13 where, on the whole, good agreement is obtained. We consider the transition groups in turn from higher to lower energy. The strong absorption peak at 5274.384 cm^{-1} is assigned as the $Z_1\gamma_1 \rightarrow Y_4\gamma_2$ transition. No resolved hyperfine structure is observed here because the $Y_4\gamma_2$ I_z spectrum is inverted with respect to that in the ground state $Z_1\gamma_1$ level and therefore all of the transitions between the hyperfine levels of these two crystal field states will be superimposed to give the single feature observed. As can be seen in Figure 4.13 the simulated spectrum well accounts for this. One should also note that these transitions are magnetic dipole in origin and the strength of this feature vindicates the comparable weighting given to both magnetic dipole and electric dipole transition strengths.

The transition group between 5273.5 and 5274.3 cm^{-1} is not so well accounted for theoretically. These features are assigned as the $Z_1\gamma_1 \rightarrow Y_3\gamma_5^{\pm}$ transitions. Only six transitions are present in the experimental spectrum, a problem only partially explained by the merging of the $Z_1\gamma_1 \pm \frac{7}{2} \rightarrow Y_3\gamma_5^{\pm}\frac{7}{2}$ transition with the $Z_1\gamma_1 \rightarrow Y_4\gamma_2$ transitions. The additional transition appears to be hidden within the 5273.643 and 5273.567 cm^{-1} structure. The dissimilarity of the theoretical with the experimental spectrum has to be attributed to the simplicity of the model. The three crystal field levels are considered in total isolation when it is known from Mujaji's analysis [17] and that undertaken here, that the $Y_1\gamma_5$ state is 17 cm^{-1} (510 GHz) lower in energy. However we have considered the smaller contributions made by the $Y_1\gamma_5$ state and this is not appreciable with the largest shifts for the $\pm\frac{7}{2}$ states of around 0.006 cm^{-1} (close to 0.18 GHz). Thus the source of the disparity between the experimental and calculated intensities must be the optical transition parameters.

The next set of features, present some 1 cm^{-1} lower in energy, are assigned as the $Z_2\gamma_2 \rightarrow Y_4\gamma_2$ transition group. In this case the hyperfine splittings of the $Z_2\gamma_2$ state

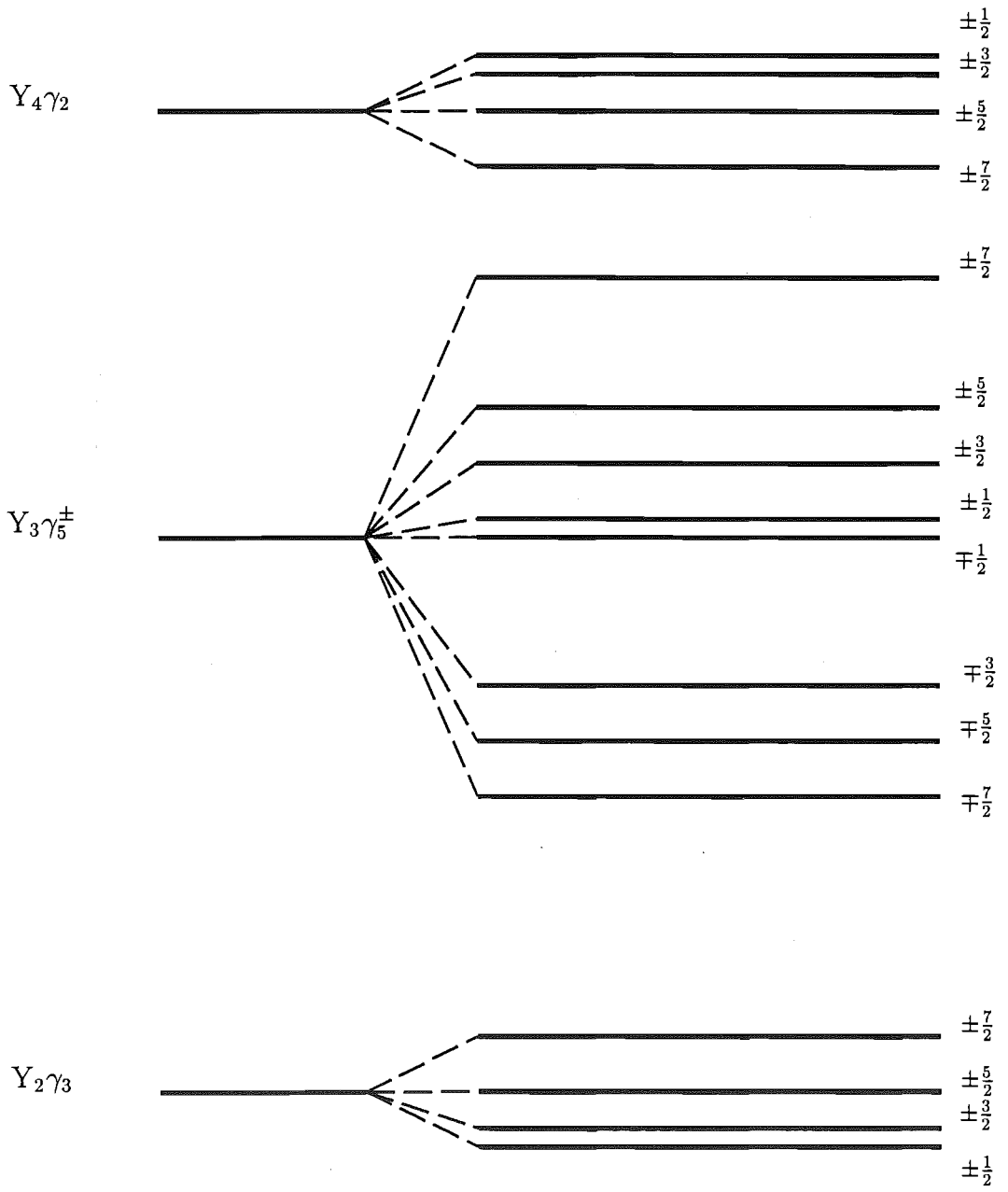

Figure 4.11: Schematic diagram of the hyperfine structure for the $Y_2\gamma_3$, $Y_4\gamma_5^{\pm}$ and $Y_4\gamma_2$ states of the A centre in CaF_2:0.003%Ho^{3+}

Table 4.8: Calculated and experimental magnetic hyperfine energy levels for the $Z_{1,2}\gamma_{1,2} \rightarrow Y_2\gamma_3$, $Y_3\gamma_5^{\pm}$ and $Y_4\gamma_2$ states of the A centre in CaF_2:0.003%Ho^{3+}. Experimental uncertainties are ± 0.020 cm^{-1} unless otherwise stated and energies are as measured in vacuum. The $Z_2\gamma_2 \pm \frac{1}{2} \rightarrow Y_4\gamma_2 \pm \frac{1}{2}$ transition is used as an arbitrarily chosen reference point. * indicates a tentative assignment.

Line	Transition Assignment	Calc Energy (GHz)	Expt Energy (GHz)	Expt Energy (Absolute) (cm^{-1})
17	$Z_1\gamma_1 \pm \frac{7}{2} \rightarrow Y_4\gamma_2 \pm \frac{7}{2}$	53.88	52.74	5274.384
17	$Z_1\gamma_1 \pm \frac{5}{2} \rightarrow Y_4\gamma_2 \pm \frac{5}{2}$	52.81	52.74	5274.384
17	$Z_1\gamma_1 \pm \frac{3}{2} \rightarrow Y_4\gamma_2 \pm \frac{3}{2}$	51.91	52.74	5274.384
17	$Z_1\gamma_1 \pm \frac{1}{2} \rightarrow Y_4\gamma_2 \pm \frac{1}{2}$	51.31	52.74	5274.384
17	$Z_1\gamma_1 \pm \frac{7}{2} \rightarrow Y_3\gamma_5^{\pm} \pm \frac{7}{2}$	50.31	52.74	5274.384
16	$Z_1\gamma_1 \pm \frac{5}{2} \rightarrow Y_3\gamma_5^{\pm} \pm \frac{5}{2}$	41.06	43.26*	5274.068
15	$Z_1\gamma_1 \pm \frac{3}{2} \rightarrow Y_3\gamma_5^{\pm} \pm \frac{3}{2}$	37.40	39.66*	5273.948
14	$Z_1\gamma_1 \pm \frac{1}{2} \rightarrow Y_3\gamma_5^{\pm} \pm \frac{1}{2}$	34.39	37.71*	5273.883
13	$Z_1\gamma_1 \pm \frac{1}{2} \rightarrow Y_3\gamma_5^{\mp} \pm \frac{1}{2}$	33.79	35.46*	5273.808
12	$Z_1\gamma_1 \pm \frac{7}{2} \rightarrow Y_3\gamma_5^{\mp} \pm \frac{7}{2}$	29.16	30.51*	5273.643
12	$Z_1\gamma_1 \pm \frac{5}{2} \rightarrow Y_3\gamma_5^{\mp} \pm \frac{5}{2}$	28.61	30.51*	5273.643
11	$Z_1\gamma_1 \pm \frac{3}{2} \rightarrow Y_3\gamma_5^{\mp} \pm \frac{3}{2}$	27.83	28.23*	5273.567
10	$Z_2\gamma_2 \pm \frac{1}{2} \rightarrow Y_4\gamma_2 \pm \frac{1}{2}$	0.00	0.00	5272.626
9	$Z_2\gamma_2 \pm \frac{3}{2} \rightarrow Y_4\gamma_2 \pm \frac{3}{2}$	-1.17	-1.50	5272.576
8	$Z_2\gamma_2 \pm \frac{5}{2} \rightarrow Y_4\gamma_2 \pm \frac{5}{2}$	-3.64	-4.98	5272.460
7	$Z_2\gamma_2 \pm \frac{7}{2} \rightarrow Y_4\gamma_2 \pm \frac{7}{2}$	-7.29	-7.38	5272.380
6	$Z_2\gamma_2 \pm \frac{7}{2} \rightarrow Y_3\gamma_5^{\pm} \pm \frac{7}{2}$	-10.86	-11.13	5272.255
5	$Z_2\gamma_2 \pm \frac{5}{2} \rightarrow Y_3\gamma_5^{\pm} \pm \frac{5}{2}$	-15.40	-16.1±3.0	5272.09±0.10
5	$Z_2\gamma_2 \pm \frac{3}{2} \rightarrow Y_3\gamma_5^{\pm} \pm \frac{3}{2}$	-15.69	-16.1±3.0	5272.09±0.10
5	$Z_2\gamma_2 \pm \frac{1}{2} \rightarrow Y_3\gamma_5^{\pm} \pm \frac{1}{2}$	-16.92	-16.1±3.0	5272.09±0.10
5	$Z_2\gamma_2 \pm \frac{1}{2} \rightarrow Y_3\gamma_5^{\mp} \pm \frac{1}{2}$	-17.52	-16.1±3.0	5272.09±0.10
4	$Z_2\gamma_2 \pm \frac{3}{2} \rightarrow Y_3\gamma_5^{\mp} \pm \frac{3}{2}$	-25.25	-17.13	5271.814
3	$Z_2\gamma_2 \pm \frac{5}{2} \rightarrow Y_3\gamma_5^{\mp} \pm \frac{5}{2}$	-27.85	-24.36	5271.734
2	$Z_2\gamma_2 \pm \frac{7}{2} \rightarrow Y_3\gamma_5^{\mp} \pm \frac{7}{2}$	-32.01	-30.66	5271.604
1	$Z_2\gamma_2 \pm \frac{1}{2} \rightarrow Y_2\gamma_3 \pm \frac{3}{2}$	-38.79	-36.09	5271.423
1	$Z_2\gamma_2 \pm \frac{1}{2} \rightarrow Y_2\gamma_3 \pm \frac{1}{2}$	-38.93	-36.09	5271.423
1	$Z_2\gamma_2 \pm \frac{3}{2} \rightarrow Y_2\gamma_3 \pm \frac{1}{2}$	-39.82	-36.09	5271.423
1	$Z_2\gamma_2 \pm \frac{5}{2} \rightarrow Y_2\gamma_3 \pm \frac{7}{2}$	-40.27	-36.09	5271.423
1	$Z_2\gamma_2 \pm \frac{3}{2} \rightarrow Y_2\gamma_3 \pm \frac{5}{2}$	-40.92	-36.09	5271.423
1	$Z_2\gamma_2 \pm \frac{5}{2} \rightarrow Y_2\gamma_3 \pm \frac{3}{2}$	-41.36	-36.09	5271.423

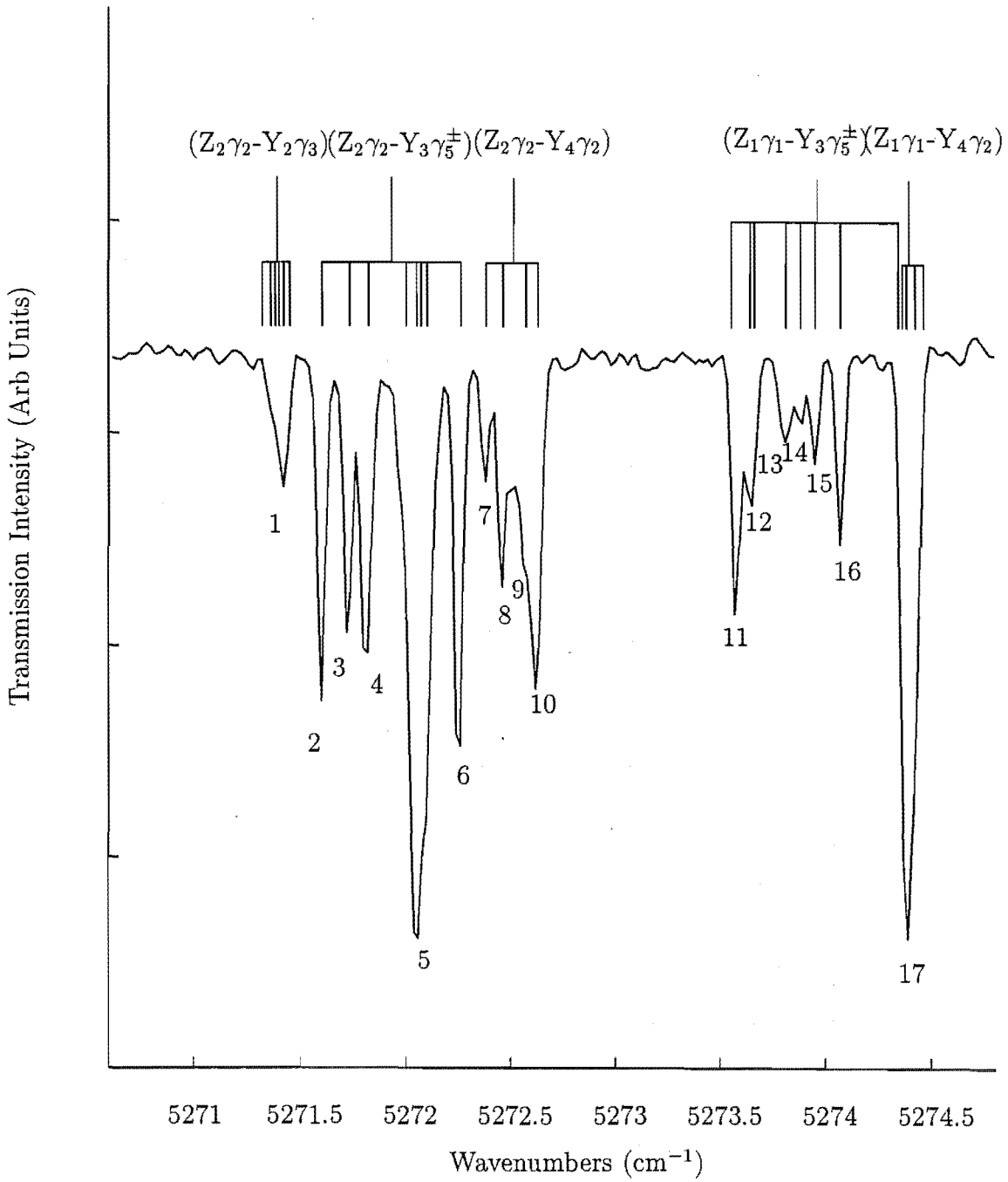

Figure 4.12: Experimental $Y_2\gamma_3$-$Y_3\gamma_5^{\pm}$-$Y_4\gamma_2$ hyperfine spectra for the A centre in CaF_2:0.003%Ho^{3+}

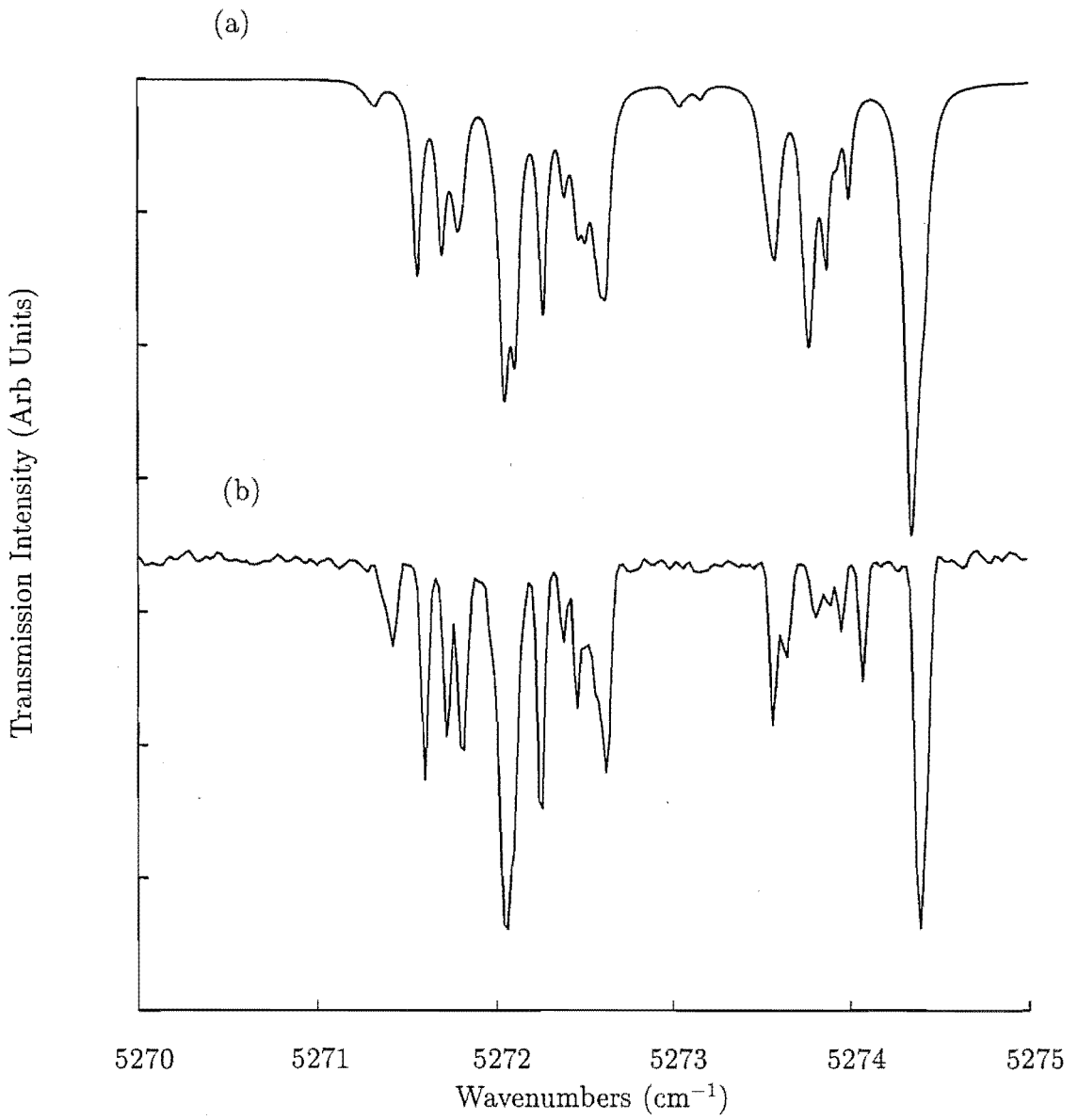

Figure 4.13: The (a) simulated and (b) experimental $Y_2\gamma_3$-$Y_3\gamma_5^{\pm}$-$Y_4\gamma_2$ hyperfine spectra for the A centre in CaF_2:0.003%Ho^{3+}. The experimental spectrum was recorded at 10K.

Table 4.9: Nuclear wavefunction composition for the $Y_2\gamma_3$, $Y_3\gamma_5^{\pm}$ and $Y_4\gamma_2$ states of the A centre in CaF_2:0.003%Ho^{3+}. The wavefunctions are truncated to components 1% or larger.

Irrep	I_z	Wavefunction
$Y_4\gamma_2$	$(\pm\frac{7}{2})$	$\mp 0.6478 \mid \gamma_5^{\pm} \pm \frac{5}{2}\rangle \mp 0.7542 \mid \gamma_2 \pm \frac{7}{2}\rangle$
	$(\pm\frac{5}{2})$	$\mp 0.2037 \mid \gamma_2 \mp \frac{3}{2}\rangle \pm 0.5360 \mid \gamma_5^{\pm} \pm \frac{3}{2}\rangle - 0.7902 \mid \gamma_2 \pm \frac{5}{2}\rangle \pm 0.1706 \mid \gamma_5^{\mp} \pm \frac{7}{2}\rangle$
	$(\pm\frac{3}{2})$	$0.1765 \mid \gamma_2 \mp \frac{5}{2}\rangle + 0.1407 \mid \gamma_5^{\mp} \mp \frac{3}{2}\rangle + 0.4678 \mid \gamma_5^{\pm} \pm \frac{1}{2}\rangle + 0.8098 \mid \gamma_2 \pm \frac{3}{2}\rangle$ $+0.2521 \mid \gamma_5^{\mp} \pm \frac{5}{2}\rangle$
	$(\pm\frac{1}{2})$	$\mp 0.4063 \mid \gamma_5^{\pm} \mp \frac{1}{2}\rangle \mp 0.8445 \mid \gamma_2 \pm \frac{1}{2}\rangle \mp 0.3345 \mid \gamma_5^{\mp} \pm \frac{3}{2}\rangle$
$Y_3\gamma_5^{\pm}$	$(\pm\frac{7}{2})$	$\pm 0.1087 \mid \gamma_3 \pm \frac{5}{2}\rangle \pm 0.9933 \mid \gamma_5^{\pm} \pm \frac{7}{2}\rangle$
	$(\pm\frac{5}{2})$	$0.1492 \mid \gamma_3 \pm \frac{3}{2}\rangle + 0.7352 \mid \gamma_5^{\pm} \pm \frac{5}{2}\rangle - 0.6522 \mid \gamma_3 \pm \frac{7}{2}\rangle$
	$(\pm\frac{3}{2})$	$\mp 0.1401 \mid \gamma_5^{\pm} \mp \frac{5}{2}\rangle - 0.1308 \mid \gamma_2 \mp \frac{5}{2}\rangle + 0.1994 \mid \gamma_5^{\mp} \mp \frac{3}{2}\rangle \mp 0.1513 \mid \gamma_2 \mp \frac{3}{2}\rangle$ $\pm 0.2806 \mid \gamma_5^{\mp} \mp \frac{1}{2}\rangle \pm 0.2173 \mid \gamma_3 \pm \frac{1}{2}\rangle \pm 0.7020 \mid \gamma_5^{\pm} \pm \frac{3}{2}\rangle \mp 0.4605 \mid \gamma_2 \pm \frac{5}{2}\rangle$ $\mp 0.2272 \mid \gamma_5^{\mp} \pm \frac{7}{2}\rangle$
	$(\pm\frac{1}{2})$	$\pm 0.1043 \mid \gamma_5^{\pm} \mp \frac{7}{2}\rangle \pm 0.1696 \mid \gamma_2 \mp \frac{5}{2}\rangle \mp 0.3264 \mid \gamma_5^{\mp} \mp \frac{3}{2}\rangle \pm 0.1055 \mid \gamma_3 \pm \frac{1}{2}\rangle$ $+0.1759 \mid \gamma_5^{\mp} \mp \frac{1}{2}\rangle \pm 0.7372 \mid \gamma_5^{\pm} \pm \frac{1}{2}\rangle \mp 0.2983 \mid \gamma_2 \pm \frac{3}{2}\rangle \mp 0.3902 \mid \gamma_5^{\mp} \pm \frac{5}{2}\rangle$
	$(\mp\frac{1}{2})$	$0.1286 \mid \gamma_3 \pm \frac{5}{2}\rangle + 0.6040 \mid \gamma_5^{\mp} \pm \frac{3}{2}\rangle + 0.1221 \mid \gamma_2 \pm \frac{1}{2}\rangle - 0.7478 \mid \gamma_5^{\pm} \mp \frac{1}{2}\rangle$ $-0.1640 \mid \gamma_3 \mp \frac{3}{2}\rangle + 0.1182 \mid \gamma_5^{\mp} \pm \frac{5}{2}\rangle$
	$(\mp\frac{3}{2})$	$0.1598 \mid \gamma_3 \pm \frac{3}{2}\rangle + 0.4585 \mid \gamma_5^{\mp} \pm \frac{1}{2}\rangle - 0.5062 \mid \gamma_2 \mp \frac{1}{2}\rangle + 0.6739 \mid \gamma_5^{\pm} \mp \frac{3}{2}\rangle$ $+0.2223 \mid \gamma_3 \mp \frac{5}{2}\rangle$
	$(\mp\frac{5}{2})$	$\mp 0.1726 \mid \gamma_5^{\mp} \pm \frac{5}{2}\rangle + 0.2503 \mid \gamma_5^{\mp} \mp \frac{1}{2}\rangle - 0.4099 \mid \gamma_2 \mp \frac{3}{2}\rangle + 0.8130 \mid \gamma_5^{\pm} \mp \frac{5}{2}\rangle$ $+0.2318 \mid \gamma_3 \mp \frac{7}{2}\rangle$
	$(\mp\frac{7}{2})$	$\pm 0.1160 \mid \gamma_5^{\mp} \mp \frac{5}{2}\rangle \mp 0.2872 \mid \gamma_2 \mp \frac{5}{2}\rangle \pm 0.9486 \mid \gamma_5^{\pm} \mp \frac{7}{2}\rangle$
$Y_2\gamma_3$	$(\pm\frac{7}{2})$	$0.2993 \mid \gamma_3 \mp \frac{7}{2}\rangle \pm 0.2270 \mid \gamma_5^{\mp} \pm \frac{5}{2}\rangle \mp 0.9192 \mid \gamma_3 \pm \frac{7}{2}\rangle$
	$(\pm\frac{5}{2})$	$0.2730 \mid \gamma_3 \mp \frac{3}{2}\rangle + 0.2378 \mid \gamma_5^{\mp} \pm \frac{3}{2}\rangle - 0.9240 \mid \gamma_3 \pm \frac{5}{2}\rangle$
	$(\pm\frac{3}{2})$	$\mp 0.2585 \mid \gamma_3 \mp \frac{5}{2}\rangle \pm 0.2365 \mid \gamma_5^{\mp} \pm \frac{1}{2}\rangle \mp 0.9176 \mid \gamma_3 \pm \frac{3}{2}\rangle \pm 0.1376 \mid \gamma_5^{\pm} \pm \frac{5}{2}\rangle$
	$(\pm\frac{1}{2})$	$-0.1137 \mid \gamma_3 \mp \frac{1}{2}\rangle \pm 0.2128 \mid \gamma_5^{\mp} \mp \frac{1}{2}\rangle \mp 0.9474 \mid \gamma_3 \pm \frac{1}{2}\rangle \pm 0.1794 \mid \gamma_5^{\pm} \pm \frac{3}{2}\rangle$

are not inverted with respect to those of the $Y_4\gamma_2$ state and four hyperfine transitions are apparent as given in Table 4.8.

The $Z_2\gamma_2 \rightarrow Y_3\gamma_5^{\pm}$ transitions are observed in 5271.6-5272.2 cm^{-1} region. It can be observed from Figure 4.13 that this portion of the experimental spectrum is particularly well accounted for by the theoretical spectrum. The dominant feature is the 5272.090 cm^{-1} transition which is assigned as the superposition of the $\gamma_2 \pm \frac{5}{2} \rightarrow \gamma_5^{\pm} \pm \frac{5}{2}$, $\gamma_2 \pm \frac{3}{2} \rightarrow \gamma_5^{\pm} \pm \frac{3}{2}$, $\gamma_2 \pm \frac{1}{2} \rightarrow \gamma_5^{\pm} \pm \frac{1}{2}$ and $\gamma_2 \pm \frac{1}{2} \rightarrow \gamma_5^{\mp} \pm \frac{1}{2}$ transitions. The final feature observed in the experimental spectrum at 5271.143 cm^{-1} is assigned as the $Z_2\gamma_2 \rightarrow Y_2\gamma_3$ transition. In the absence of any hyperfine interactions this is forbidden by symmetry considerations, however the γ_3 state can gain intensity due to mixing between itself and the $\gamma_5^{\pm}$ state via the perpendicular hyperfine interaction. From Table 4.9 we see that the $Y_2\gamma_3$ nuclear wavefunctions are typically comprised of 5% $\gamma_5^{\pm}$. Thus it is not unexpected that this transition is observed however it is troublesome because no $Z_1\gamma_1 \rightarrow Y_2\gamma_3$ transitions are observed. The explanation is that the $Z_2\gamma_2 \rightarrow Y_2\gamma_3$ transition group at 5271.423 cm^{-1} is the superposition of all the hyperfine transitions to the $Y_2\gamma_3$ state (as outlined in Table 4.8). For transitions from $Z_1\gamma_1$ to this level there would be no superposition of hyperfine transitions and thus it is possible that the individual transitions would not be observed above the noise.

4.3 High Resolution Infrared Absorption of the $^3H_4$ and $^3H_5$ Multiplets of the C_{4v} Centres in CaF_2:Pr^{3+} and SrF_2:Pr^{3+}

Naturally-occuring Pr contains 100% of the Pr^{141} isotope with a nuclear spin of $I=\frac{5}{2}$. Macfarlane et. al. [56] have determined the Pr^{141} nuclear magnetic moment to be $4.2754\mu_N$, which is comparable to that of Ho^{165}, making Pr^{3+} another suitable candidate for high resolution studies of nuclear hyperfine interactions. Whilst the hyperfine structure of the $^3H_4 \rightarrow {}^1D_2$ absorption transitions have been extensively studied [44], [56], [45], [57], [58], [59], [60], [61] hyperfine structure for the $^3H_4 \rightarrow {}^3H_5$ and $^3H_6$ absorption transitions in the infrared have not yet been reported and these form the basis of this study. Here, the dominant C_{4v} symmetry centres in CaF_2:Pr^{3+} and SrF_2:Pr^{3+} are labelled as A and C, following Tissue and Wright [62] (1987) and Cleven, Lee and Wright [63] (1991).

4.3.1 Hyperfine Patterns for the C_{4v} Symmetry Centre of CaF_2

(a) Hyperfine Patterns for Transitions to the $^3H_5$ Multiplet

Infrared absorption spectra of a 15.3 mm thick CaF_2:0.003%Pr^{3+} crystal were recorded for transitions to the $^3H_5$ and $^3H_6$ multiplets. Wells [64], [65] presented 0.1 cm^{-1} resolution spectra for these multiplets and identified the two sharp transitions at 2189.11 and 2211.11 cm^{-1} as transitions to the $Y_1\gamma_2$ and $Y_2\gamma_1$ states assigned by Reeves et. al. [45]. Their measured linewidths of 0.4 cm^{-1} are narrow enough to reveal the magnetic hyperfine structure of the $Z_1\gamma_5$ ground state. The two upper states, Y_1 and Y_2, are both singlets and thus are independently non-magnetic. However there can be a pseudo-quadrupole splitting between them. The crystal-field wavefunctions for these two Y_1 and Y_2 states (Wells [65]) are:

$$\begin{array}{ll} Y_1\gamma_2 & 0.6975 \mid 4\rangle - 0.1141 \mid 0\rangle + 0.6975 \mid -4\rangle \\ Y_2\gamma_1 & 0.6935 \mid 4\rangle - 0.1288 \mid 0\rangle - 0.6935 \mid -4\rangle \end{array}$$

yielding a value of 3.870 for $\langle\gamma_2 \mid J_z \mid \gamma_1\rangle$. The hyperfine interaction $A_5I_zJ_z$ (where A_5 is the magnetic hyperfine constant for the $^3H_5$ multiplet) shifts the $\gamma_{2,1}$ hyperfine levels by

$$E(I_z) = \frac{I_z^2 A_5^2 \mid \langle\gamma_2 \mid J_z \mid \gamma_1\rangle \mid^2}{\Delta}$$

Using a value of 0.802 GHz for A_5 (see Appendix A) and a separation Δ of 660 GHz (22 cm^{-1}) the calculated shift is 0.09 GHz. As this shift is unresolvable by the Bomem spectrometer used in this study, we neglect this interaction.

Figures 4.14 and 4.15 show the recorded $Z_1\gamma_5 \rightarrow Y_1\gamma_2$ and $Y_2\gamma_1$ absorption transition. Clearly apparant are the six-line hyperfine patterns consistent with I=$\frac{5}{2}$ for Pr^{3+} and these patterns are the ground state hyperfine structure. There is a deeper central dip in the six-line pattern which originates from a distribution of non-axial distortions arising from internal strain within the crystal [66]. From the crystal field analysis of Wells and Jones [65] the ground state crystal field wavefunction is:

$$Z_1\gamma_5^{\pm} \quad \mp 0.9415 \mid \pm 3\rangle \pm 0.3299 \mid \mp 1\rangle$$

which yields a $\langle J_z\rangle$ value of 2.54. Abragham and Bleaney [67] give the value of the magnetic hyperfine constant A_4 for the $^3H_4$ multiplet to be 1.093 GHz. The hyperfine interaction for the ground state $\gamma_5^{\pm}$ can be accounted for with an interaction matrix of the form:

	γ_5^+	γ_5^-
γ_5^+	$A_4I_z\langle J_z\rangle$	D_4
γ_5^-	D_4	$-A_4I_z\langle J_z\rangle$

Where D_4 is a parameter representing a random distribution of non-axial distortions. The energy of each I_z component is therefore

$$E(I_z) = \sqrt{(A_4\langle J_z\rangle I_z)^2 + D_4^2}$$

Fitting the experimental data to the energies of each I_z component with the magnetic hyperfine constant A_4, and strain distortion parameter D_4 treated as a free parameters and using the MATLAB 'fmins' least squares fitting routine yields values for A_4 of 1.0926 GHz and D_4 of 0.6106 GHz. There is an almost exact agreement of this A_4 value with that given by Abragham and Bleaney whilst the value of the strain distortion parameter, D_4 is attributed to the introduction of the Pr^{3+} dopant itself into the host lattice. Table 4.10 compares the experimental splittings observed in the $Z_1\gamma_5 \rightarrow Y_1\gamma_2$ and $Z_1\gamma_5 \rightarrow Y_2\gamma_1$ transitions with those calculated with excellent agreement between the experimental and calculated values. Good agreement is also obtained with the high resolution (2 MHz) laser data of Burum et. al. [60]. These authors observe hyperfine splittings of 2.77 GHz for measurement of the $Z_1\gamma_5 \rightarrow D_1\gamma_2$ transition at 594.1 nm.

Table 4.10: Calculated and experimental A centre $Z_1\gamma_5$ ground-state magnetic hyperfine splittings (in GHz, ± 0.6) as observed for the $Z_1\gamma_5 \rightarrow Y_1\gamma_2$ and $Z_1\gamma_5 \rightarrow Y_2\gamma_1$ transitions

Line		Experimental		Calculated	
Separation	I_z	Y_1	Y_2	D_4=0.6106	D_4=0
3-4	$\pm\frac{1}{2}$	3.1	3.0	3.033	2.775
2-5	$\pm\frac{3}{2}$	8.4	8.4	8.418	8.325
1-6	$\pm\frac{5}{2}$	13.8	13.9	13.935	13.876

(b) Hyperfine Patterns for Transitions to the $^3H_6$ Multiplet

Only a few weak absorption transitions are observable to the $^3H_6$ multiplet. Consequently a higher concentration was necessary to observe hyperfine structure in the electronic transitions to this multiplet and a 40.5 mm thick CaF_2:0.03%Pr^{3+} sample was chosen for measurement. Wells [64] has identified the 4204.21 cm^{-1} absorption transition as terminating on the $X_1\gamma_5$ state assigned by Reeves [45]. This transition was noted to show an asymmetrical splitting indicative of possible resolvable hyperfine structure. In Figure 4.16 we see a six-line hyperfine pattern in the

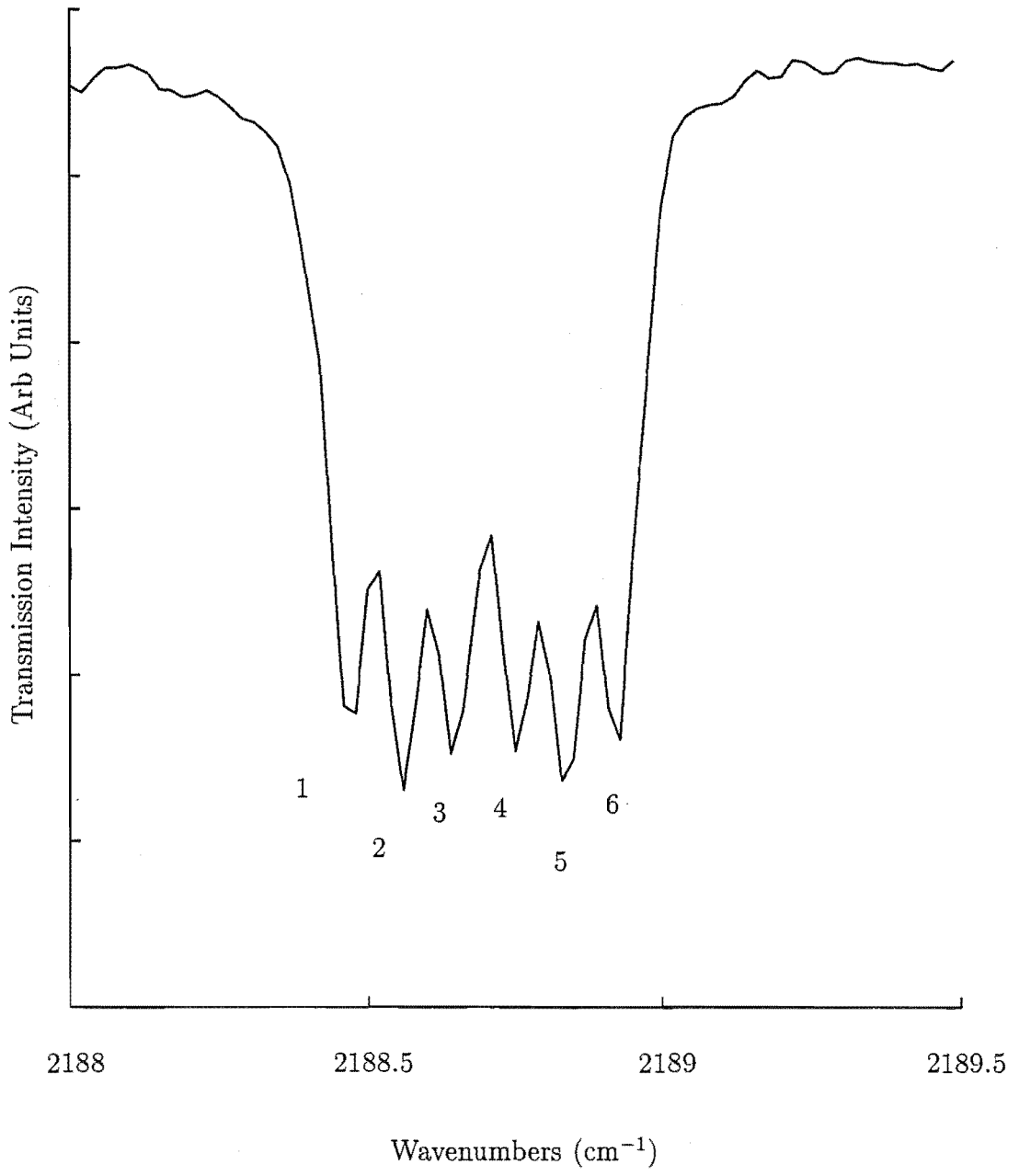

Figure 4.14: Magnetic hyperfine structure for the $Z_1\gamma_5 \rightarrow Y_1\gamma_2$ absorption transition of the A centre in CaF_2:0.003%Pr^{3+}. The spectrum was recorded at 10K.

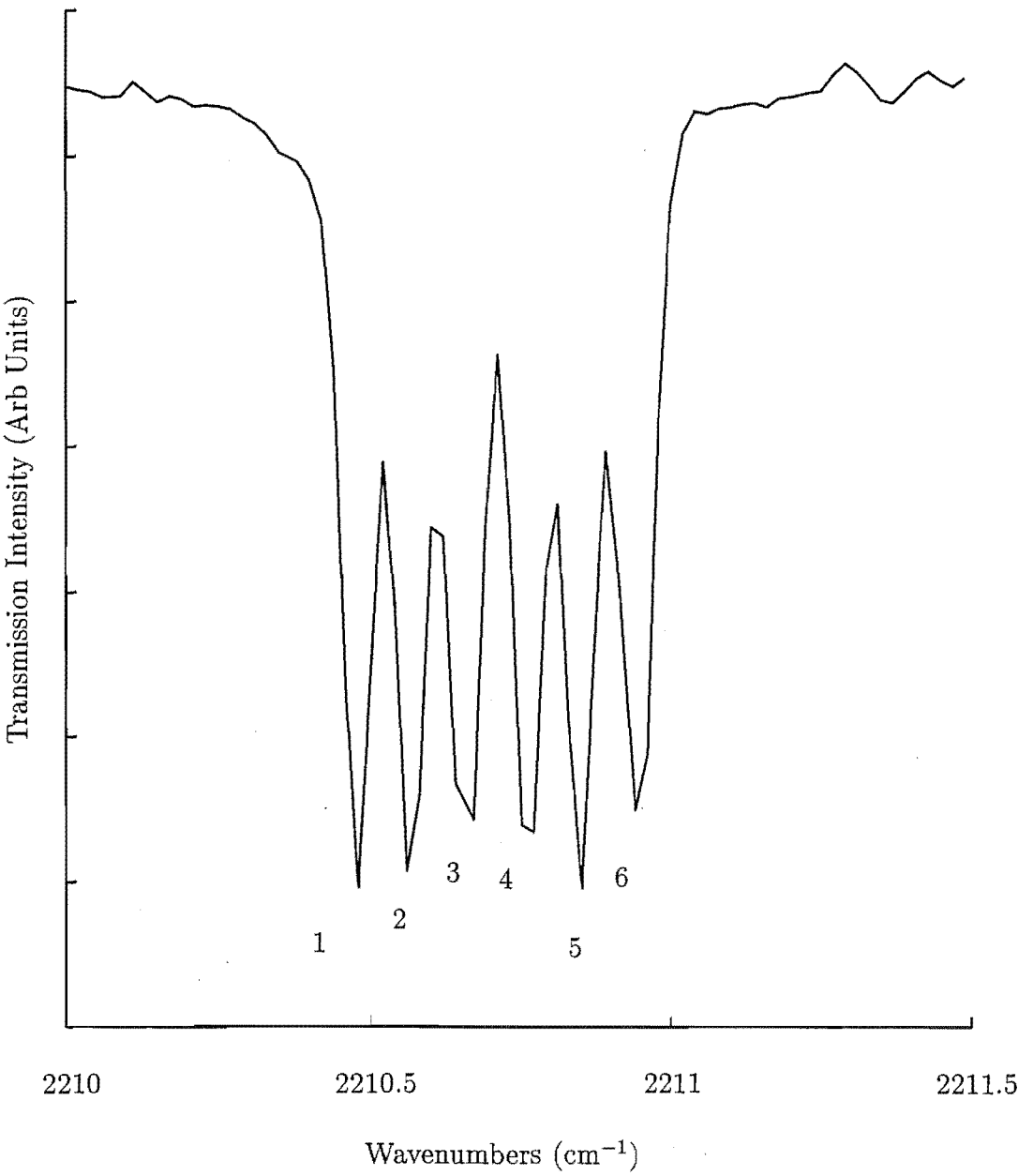

Figure 4.15: Magnetic hyperfine structure for the $Z_1\gamma_5 \rightarrow Y_2\gamma_1$ absorption transition of the A centre in CaF_2:0.003%Pr^{3+}. The spectrum was recorded at 10K.

Table 4.11: Ground-state $Z_1\gamma_5$ nuclear-wavefunction composition for the A centre of CaF_2:0.003%Pr^{3+}

State	I_z	Wavefunction
	$\pm\frac{5}{2}$	$0.9990 \mid Z_1\gamma_5^{\pm} \pm \frac{5}{2}\rangle + 0.0439 \mid Z_1\gamma_5^{\mp} \pm \frac{5}{2}\rangle$
	$\pm\frac{3}{2}$	$0.9974 \mid Z_1\gamma_5^{\pm} \pm \frac{3}{2}\rangle + 0.0727 Z_1 \mid \gamma_5^{\mp} \pm \frac{3}{2}\rangle$
	$\pm\frac{1}{2}$	$0.9786 \mid Z_1\gamma_5^{\pm} \pm \frac{1}{2}\rangle + 0.2057 \mid Z_1\gamma_5^{\mp} \pm \frac{1}{2}\rangle$
$\gamma_5^{\pm}$	$\mp\frac{1}{2}$	$-0.9786 \mid Z_1\gamma_5^{\pm} \mp \frac{1}{2}\rangle + 0.2057 \mid Z_1\gamma_5^{\mp} \mp \frac{1}{2}\rangle$
	$\mp\frac{3}{2}$	$-0.9974 \mid Z_1\gamma_5^{\pm} \mp \frac{3}{2}\rangle + 0.0727 \mid Z_1\gamma_5^{\mp} \mp \frac{3}{2}\rangle$
	$\mp\frac{5}{2}$	$-0.9990 \mid Z_1\gamma_5^{\pm} \mp \frac{5}{2}\rangle + 0.0439 \mid Z_1\gamma_5^{\mp} \mp \frac{5}{2}\rangle$

$Z_1\gamma_5 \rightarrow X_1\gamma_5$ transition. The splitting pattern observed is larger than those observed for the $Z_1\gamma_5 \rightarrow Y_1\gamma_2$ and $Y_2\gamma_1$ transitions.

This is because the pattern observed is the superposition of hyperfine pattern of the ground state and of the $X_1\gamma_5$ state, which is inverted with respect to that in the ground state. These combine to give the larger splitting observed in Figure 4.16. From the crystal-field analysis of Wells and Jones [65] the crystal-field wavefunction of the $X_1\gamma_5$ state is:

$$X_1\gamma_5^{\pm} \quad 0.1069 \mid ^3H_6 \mp 3\rangle + 0.1658 \mid ^3F_2 \pm 1\rangle - 0.9649 \mid ^3H_6 \pm 5\rangle - 0.1523 \mid ^3H_6 \pm 1\rangle$$

with $\langle J_z\rangle$=4.67. A value of A_6=0.633 GHz has been calculated for the $^3H_6$ multiplet (see Appendix A). However since the intermediate coupled wavefunctions used in these calculations were those calculated for LaF_3:Pr^{3+} [68] we consider them as an initial set only for fitting the superimposed hyperfine structure observed experimentally. Both the $Z_1\gamma_5^{\pm}$ ground state and $X_1\gamma_5^{\pm}$ excited state hyperfine structure must be considered.

The interaction matrix for the $X_1\gamma_5$ excited state is identical to that used for the ground state, with the hyperfine interaction now $A_6I_zJ_z$ and the strain distortion parameter for the $^3H_6$ multiplet D_6. Treating the A_6 and D_6 variables as adjustable parameters, we obtain values for A_6 of 0.585 GHz and D_6 of 0.1169 GHz. The A_6 value is close to the starting value of 0.633 GHz whilst the value of D_6 is small because the central dip in the pattern is not as pronouced as for the $^3H_5$ transitions. Tables 4.12 and 4.13 give the calculated and experimental energy separations and nuclear-wavefunction compositions respectively. There are several additional weak 'forbidden' transitions observed in the hyperfine transitions to the $X_1\gamma_5$ state, namely the $|Z_1\gamma_5^{\pm} \pm \frac{1}{2}\rangle \rightarrow |X_1\gamma_5^{\pm} \mp \frac{1}{2}\rangle$ transitions. These transitions are induced by

the strain distortion in the ground state which more strongly couples the states of lower I_z. The result is that the wavefunctions of these states become mixed (4.2% in the case of the $Z_1\gamma_5^{\pm} \pm \frac{1}{2}$ states) and therefore weak 'forbidden' transitions will be observed as in Figure 4.16. A schematic of all hyperfine transitions observed to $X_1\gamma_5$ is given in Figure 4.17.

Table 4.12: Transition assignments and experimental and calculated energies (in vacuum GHz, ± 0.6) for the $Z_1\gamma_5 \rightarrow X_1\gamma_5$ transition of the A center in CaF_2:Pr^{3+}. a denotes an arbitrarily chosen reference value.

Line	Transition Assignment	Hyperfine Energy Experimental	Calculated
6	$\mid Z_1\gamma_5^{\pm} \pm \frac{5}{2}\rangle \rightarrow \mid X_1\gamma_5^{\pm} \pm \frac{5}{2}\rangle$	E_0+10.8	E_0+10.9
5	$\mid Z_1\gamma_5^{\pm} \pm \frac{3}{2}\rangle \rightarrow \mid X_1\gamma_5^{\pm} \pm \frac{3}{2}\rangle$	E_0+5.4	E_0+5.4
4	$\mid Z_1\gamma_5^{\pm} \pm \frac{1}{2}\rangle \rightarrow \mid X_1\gamma_5^{\pm} \pm \frac{1}{2}\rangle$	E_0^a	E_0^a
7,8	$\mid Z_1\gamma_5^{\pm} \pm \frac{1}{2}\rangle \rightarrow \mid X_1\gamma_5^{\pm} \mp \frac{1}{2}\rangle$	E_0−2.9	E_0−3.0
3	$\mid Z_1\gamma_5^{\pm} \mp \frac{1}{2}\rangle \rightarrow \mid X_1\gamma_5^{\pm} \mp \frac{1}{2}\rangle$	E_0−5.8	E_0−5.8
2	$\mid Z_1\gamma_5^{\pm} \mp \frac{3}{2}\rangle \rightarrow \mid X_1\gamma_5^{\pm} \mp \frac{3}{2}\rangle$	E_0−11.3	E_0−11.2
1	$\mid Z_1\gamma_5^{\pm} \mp \frac{5}{2}\rangle \rightarrow \mid X_1\gamma_5^{\pm} \mp \frac{5}{2}\rangle$	E_0−16.8	E_0−16.7

Table 4.13: $X_1\gamma_5$ nuclear-wavefunctions for the A centre in CaF_2:0.003%Pr^{3+}

State	I_z	Wavefunction
	$\pm\frac{5}{2}$	$1.000 \mid X_1\gamma_5^{\pm} \pm \frac{5}{2}\rangle + 0.0086 \mid X_1\gamma_5^{\mp} \pm \frac{5}{2}\rangle$
	$\pm\frac{3}{2}$	$0.9999 \mid X_1\gamma_5^{\pm} \pm \frac{3}{2}\rangle + 0.0142 \mid X_1\gamma_5^{\mp} \pm \frac{3}{2}\rangle$
$\gamma_5^{\pm}$	$\pm\frac{1}{2}$	$0.9991 \mid X_1\gamma_5^{\pm} \pm \frac{1}{2}\rangle + 0.0426 \mid X_1\gamma_5^{\mp} \pm \frac{1}{2}\rangle$
	$\mp\frac{1}{2}$	$-0.9991 \mid X_1\gamma_5^{\pm} \mp \frac{1}{2}\rangle + 0.0426 \mid X_1\gamma_5^{\mp} \mp \frac{1}{2}\rangle$
	$\mp\frac{3}{2}$	$-0.9999 \mid X_1\gamma_5^{\pm} \mp \frac{3}{2}\rangle + 0.0142 \mid X_1\gamma_5^{\mp} \mp \frac{3}{2}\rangle$
	$\mp\frac{5}{2}$	$-1.000 \mid X_1\gamma_5^{\pm} \mp \frac{5}{2}\rangle + 0.0086 \mid X_1\gamma_5^{\mp} \mp \frac{5}{2}\rangle$

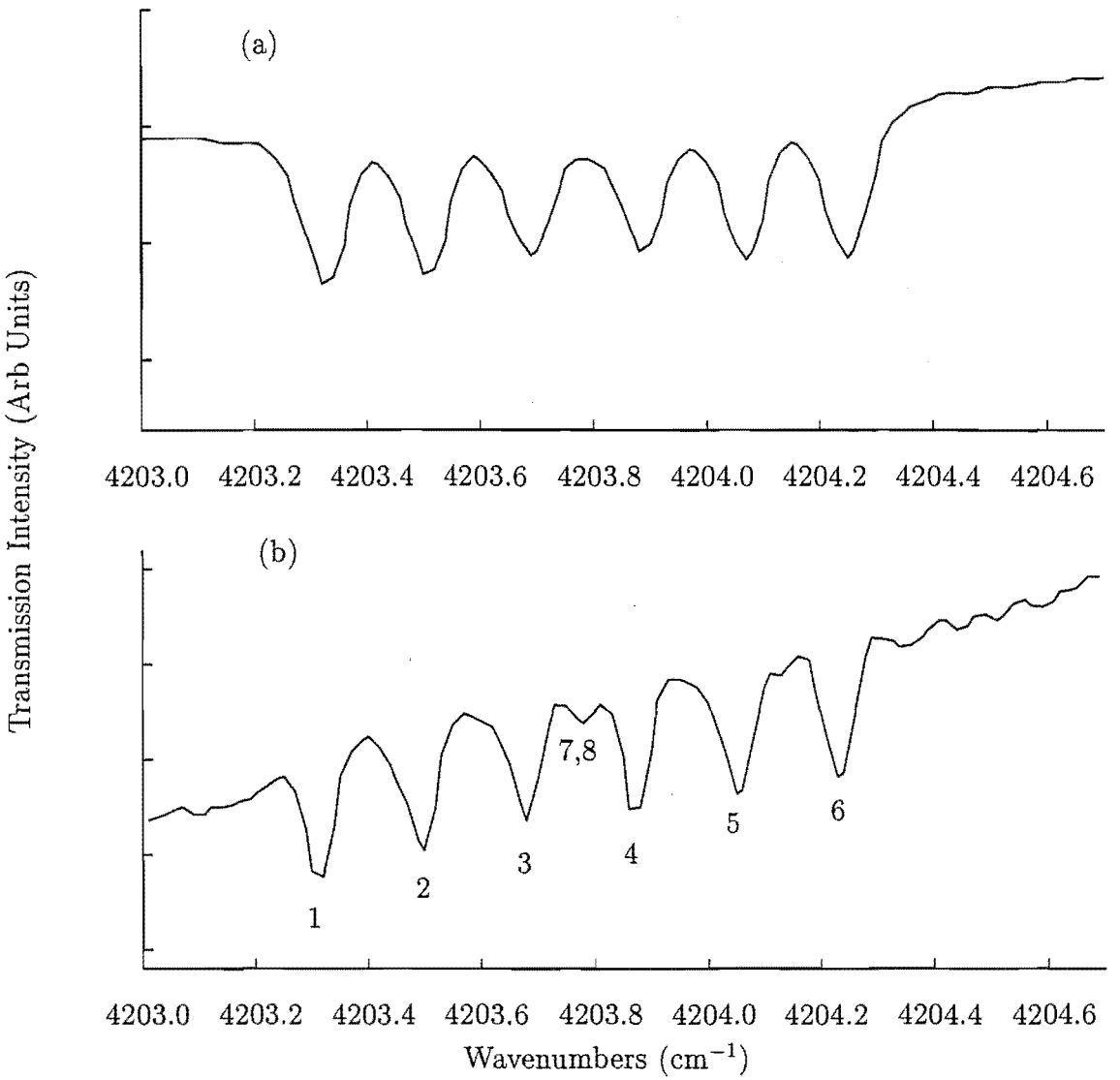

Figure 4.16: Superimposed magnetic hyperfine structure of the $Z_1\gamma_5 \rightarrow X_1\gamma_5$ absorption transition for the A centre in (a) CaF_2:0.03%Pr^{3+} and (b) CaF_2:0.003%Pr^{3+}. The spectra were recorded at 10K.

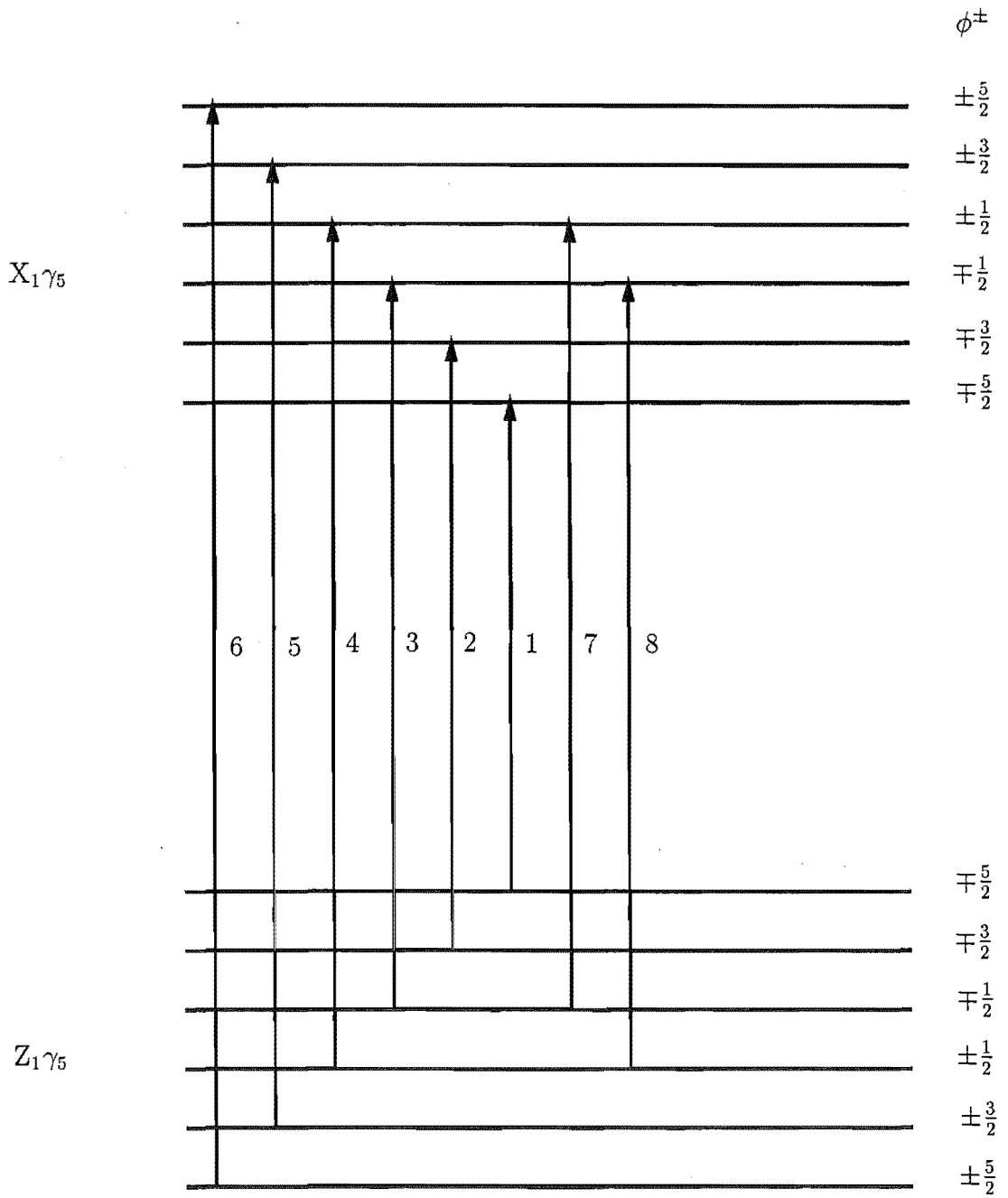

Figure 4.17: Schematic diagram of $Z_1\gamma_5 \rightarrow X_1\gamma_5$ hyperfine transitions for the A and C centres in CaF_2:Pr^{3+} and SrF_2:Pr^{3+}

4.3.2 Hyperfine Patterns for the C_{4v} Symmetry Centre of SrF_2

(a) Hyperfine Patterns for Transitions to the $^3H_5$ Multiplet

The infrared spectrum of the C_{4v} symmetry C centre for SrF_2:Pr^{3+} reported by Wells [64], is similar to that in CaF_2:Pr^{3+}. Therefore, we may expect hyperfine structure for this system too. The infrared spectrum of the $^3H_5$ and $^3H_6$ multiplets was recorded with a 28mm thick SrF_2:0.03%Pr^{3+} crystal. As the $Z_1\gamma_5 \rightarrow X_1\gamma_5$ transition is weak, a higher concentration of the dopant ion was used with the result that the $Z_1\gamma_5 \rightarrow Y_1\gamma_2$ and $Y_2\gamma_1$ transitions are too strongly absorbing to reveal well resolved hyperfine structure. Figures 4.18 and 4.19 show the $Z_1\gamma_5 \rightarrow Y_1\gamma_2$ and $Y_2\gamma_1$ transitions at 2194.20 and 2220.40 cm^{-1} respectively.

The C centre $Z_1\gamma_5$ ground state magnetic hyperfine structure is most clearly observed in the $Z_1\gamma_5 \rightarrow Y_2\gamma_1$ transition (Figure 4.19) and it is this data we use to fit the magnetic hyperfine constant A_4 and the strain distortion parameter D_4 for this transition. The required hyperfine interaction matrix is the same as that used to analyse the CaF_2:Pr^{3+} $Z_1\gamma_5$ ground-state magnetic hyperfine structure. In this case we also neglect any pseudo quadrupole interaction between the $Y_1\gamma_2$ and $Y_2\gamma_1$ states which are 26.2 cm^{-1} apart. The wavefunction of the $Z_1\gamma_5$ state is:

$$Z_1\gamma_5^{\pm} \quad \pm 0.3634 \mid \mp 1\rangle \mp 0.9298 \mid \pm 3\rangle$$

with $\langle J_z \rangle$=2.46.

Use of the MATLAB 'fmins' routine to fit the measured hyperfine transition frequencies (with A_4 and D_4 treated as free parameters) yields A_4=1.0189 GHz and D_4=1.0438 GHz. The A_4 value is in good agreement with the free ion value of Abragham and Bleaney [67]. It is noted that the central dip in the hyperfine patterns of Figs 4.18 and 4.20 is significantly deeper than for the corresponding patterns in CaF_2 This is reflected in the strain distortion parameter D_4, which is nearly twice as large as that for CaF_2:Pr^{3+}. This is partially attributed to the higher concentrations of Pr^{3+} dopant used here. Table 4.14 compares the calculated and experimental I_z splittings for the $Z_1\gamma_5$ ground state. It is difficult to compare these results with those obtained optically [45], as no well resolved splitting were observed for SrF_2:Pr^{3+} crystals for transitions to the $^1D_2$ multiplet.

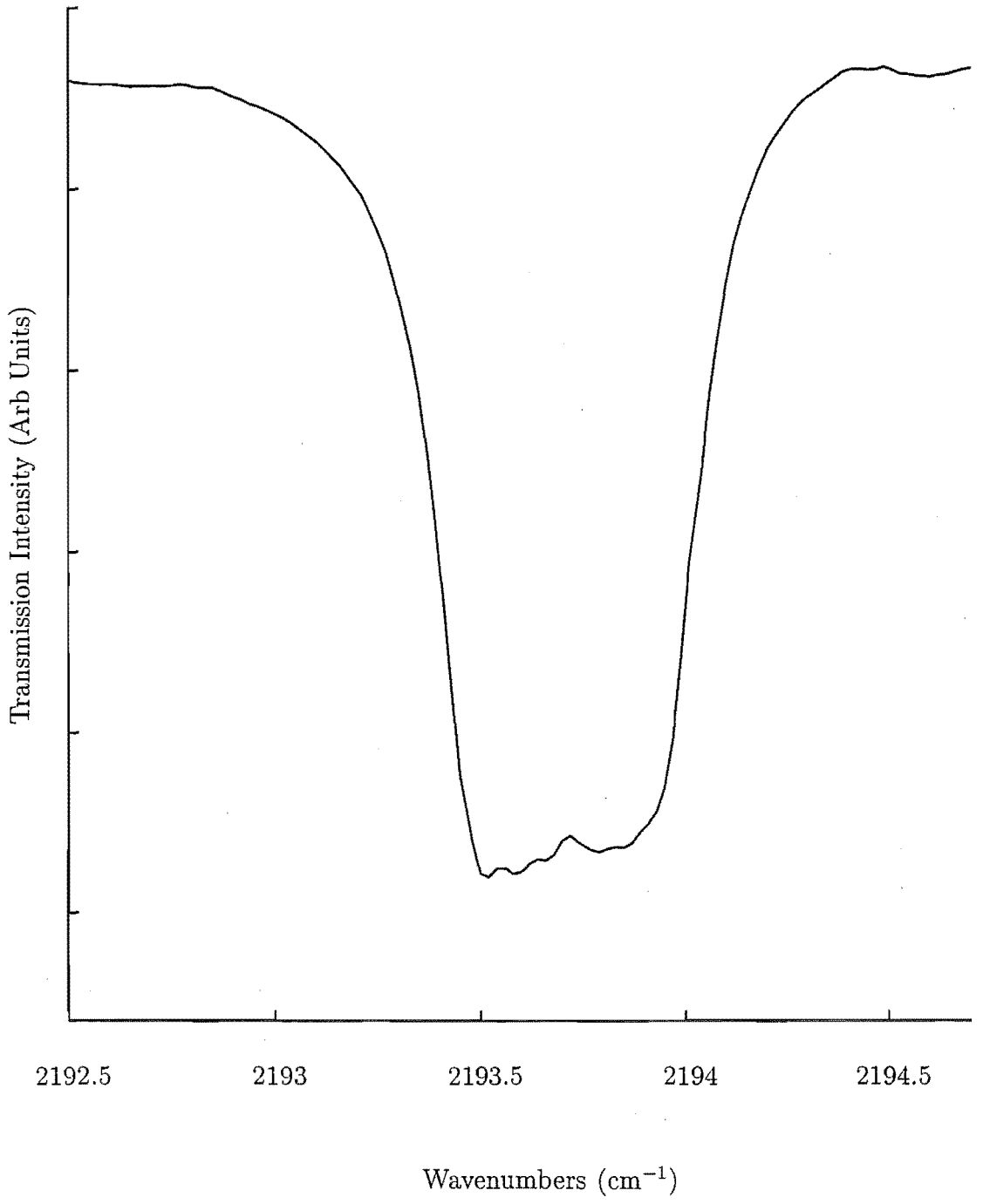

Figure 4.18: Magnetic hyperfine structure in the $Z_1\gamma_5 \rightarrow Y_2\gamma_1$ absorption transition of the C centre in SrF_2:0.03%Pr^{3+} for a strongly absorbing crystal. The spectrum was recorded at 10K.

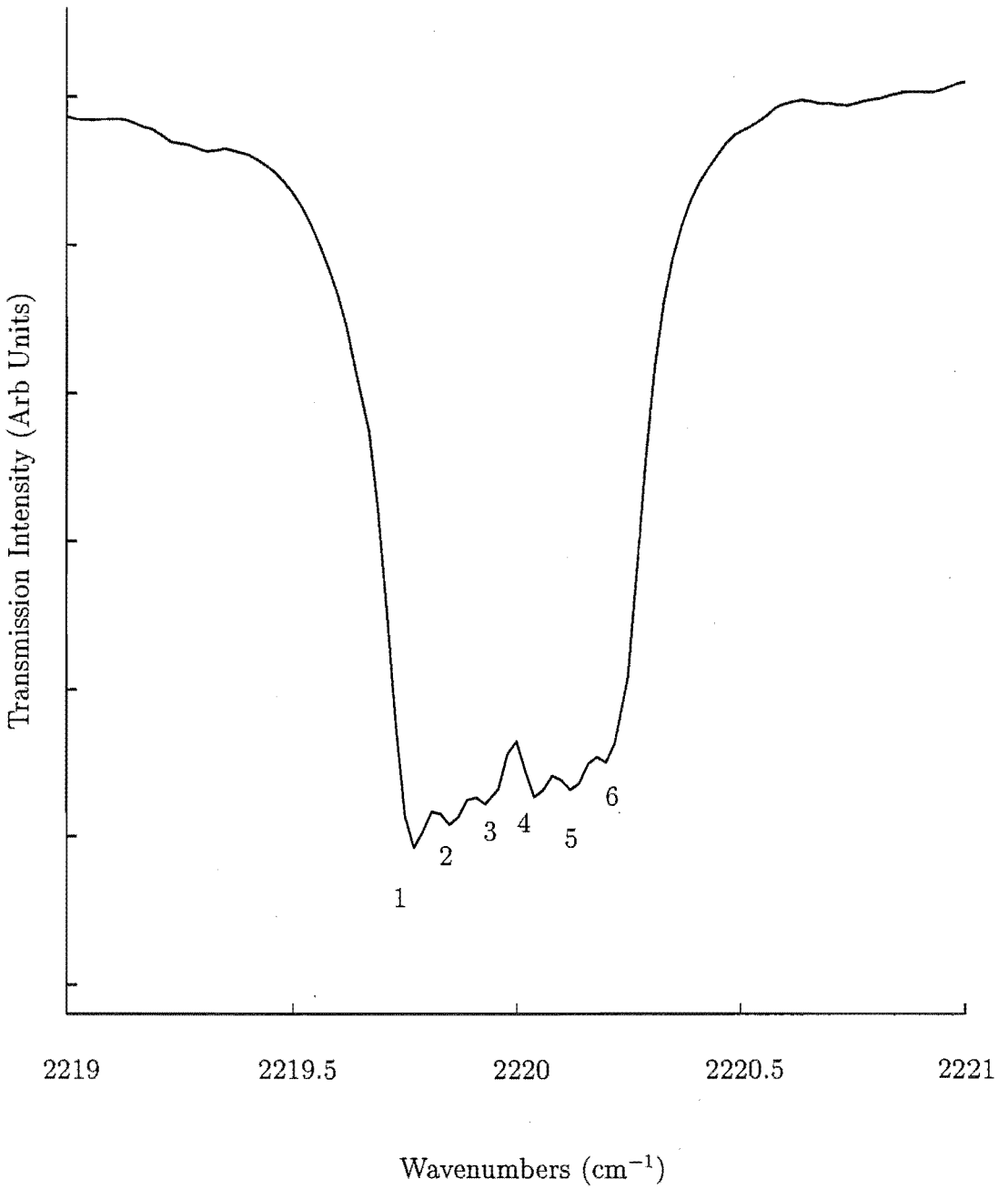

Figure 4.19: Magnetic hyperfine structure in the $Z_1\gamma_5 \rightarrow Y_2\gamma_1$ absorption transition of the C centre in SrF_2:0.03%Pr^{3+} in a strongly absorbing crystal. The spectrum was recorded at 10K.

Table 4.14: Calculated and experimental C centre $Z_1\gamma_5$ ground-state magnetic hyperfine splittings (in GHz, ± 0.6) as observed in the $Z_1\gamma_5 \rightarrow Y_2\gamma_1$ transition in SrF_2:0.03%Pr^{3+}

Line Separations	I_z	Calculated D_4=1.0438	Calculated D_4=0	Experimental
3-4	$\pm\frac{1}{2}$	3.262	2.506	3.3
2-5	$\pm\frac{3}{2}$	7.804	7.519	8.0
1-6	$\pm\frac{5}{2}$	12.705	12.532	13.0

Table 4.15: $Z_1\gamma_5$ nuclear-wavefunctions for the C centre in SrF_2:0.03%Pr^{3+}

State	I_z	Wavefunction
$\gamma_5^{\pm}$	$\pm\frac{5}{2}$	$0.9966 \mid Z_1\gamma_5^{\pm} \pm \frac{5}{2}\rangle + 0.0824 \mid Z_1\gamma_5^{\mp} \pm \frac{5}{2}\rangle$
	$\pm\frac{3}{2}$	$0.9909 \mid Z_1\gamma_5^{\pm} \pm \frac{3}{2}\rangle + 0.1349 \mid Z_1\gamma_5^{\mp} \pm \frac{3}{2}\rangle$
	$\pm\frac{1}{2}$	$0.9404 \mid Z_1\gamma_5^{\pm} \pm \frac{1}{2}\rangle + 0.3401 \mid Z_1\gamma_5^{\mp} \pm \frac{1}{2}\rangle$
	$\mp\frac{1}{2}$	$-0.9404 \mid Z_1\gamma_5^{\pm} \mp \frac{1}{2}\rangle + 0.3401 \mid Z_1\gamma_5^{\mp} \mp \frac{1}{2}\rangle$
	$\mp\frac{3}{2}$	$-0.9909 \mid Z_1\gamma_5^{\pm} \mp \frac{3}{2}\rangle + 0.1349 \mid Z_1\gamma_5^{\mp} \mp \frac{3}{2}\rangle$
	$\mp\frac{5}{2}$	$-0.9966 \mid Z_1\gamma_5^{\pm} \mp \frac{5}{2}\rangle + 0.0824 \mid Z_1\gamma_5^{\mp} \mp \frac{5}{2}\rangle$

(b) Hyperfine Patterns for Transitions to the $^3H_6$ Multiplet

The $Z_1\gamma_5 \rightarrow X_1\gamma_5$ transition is observed by Wells [64] to be centred at 4250.42 cm^{-1}. The evenly-spaced six-line hyperfine structure observed in Figure 4.20 is, as with CaF_2:Pr^{3+} $Z_1\gamma_5 \rightarrow X_1\gamma_5$ hyperfine structure, a superposition of the ground state magnetic hyperfine structure and that of the $X_1\gamma_5$ state. The wavefunction of the $X_1\gamma_5$ state is:

$$X_1\gamma_5^{\pm} \quad \mp 0.1105\,|^3\,H_6 \pm 1\rangle \pm 0.1477\,|^3\,F_2 \pm 1\rangle \pm 0.0812\,|^3\,H_6 \mp 3\rangle \mp 0.9758\,|^3\,H_6 \pm 5\rangle$$

which yields $\langle J_z\rangle$=4.78. We calculate the initial value of the magnetic hyperfine constant for the $^3H_6$ multiplet as A_6=0.633 GHz for fitting the six line pattern. Using the same interaction matrix as for the CaF_2:Pr^{3+} $Z_1\gamma_5 \rightarrow X_1\gamma_5$ hyperfine transitions we obtain values of A_6=0.6102 GHz and D_6=0.625 GHz for the adjustable parameters. The value of the strain distortion parameter is smaller than that for the $Z_1\gamma_5$ ground state transition, yet larger than those for CaF_2. Again, an additional feature of the spectrum is the observation of the forbidden $|\,\gamma_5^{\pm} \mp \frac{1}{2}\rangle \rightarrow |\,\gamma_5^{\pm} \pm \frac{1}{2}\rangle$ transitions, which occur through the off diagonal mixing of the hyperfine wavefunctions induced by the strain distortion. Table 4.16 gives the nuclear wavefunctions for the $X_1\gamma_5$ state whilst Table 4.17 compares the fitted and experimental hyperfine transition energies, with good agreement obtained.

Table 4.16: $X_1\gamma_5$ nuclear wavefunctions for the C centre in SrF_2:0.03%Pr^{3+}

State	I_z	Wavefunction
	$\pm\frac{5}{2}$	$0.9992\,\|\,X_1\gamma_5^{\pm} \pm \frac{5}{2}\rangle + 0.0408\,\|\,X_1\gamma_5^{\mp} \pm \frac{5}{2}\rangle$
	$\pm\frac{3}{2}$	$0.9977\,\|\,X_1\gamma_5^{\pm} \pm \frac{3}{2}\rangle + 0.0677\,\|\,X_1\gamma_5^{\mp} \pm \frac{3}{2}\rangle$
$\gamma_5^{\pm}$	$\pm\frac{1}{2}$	$0.9812\,\|\,X_1\gamma_5^{\pm} \pm \frac{1}{2}\rangle + 0.1929\,\|\,X_1\gamma_5^{\mp} \pm \frac{1}{2}\rangle$
	$\mp\frac{1}{2}$	$-0.9812\,\|\,X_1\gamma_5^{\pm} \mp \frac{1}{2}\rangle + 0.1929\,\|\,X_1\gamma_5^{\mp} \mp \frac{1}{2}\rangle$
	$\mp\frac{3}{2}$	$-0.9977\,\|\,X_1\gamma_5^{\pm} \mp \frac{3}{2}\rangle + 0.0677\,\|\,X_1\gamma_5^{\mp} \mp \frac{3}{2}\rangle$
	$\mp\frac{5}{2}$	$-0.9992\,\|\,X_1\gamma_5^{\pm} \mp \frac{5}{2}\rangle + 0.0408\,\|\,X_1\gamma_5^{\mp} \mp \frac{5}{2}\rangle$

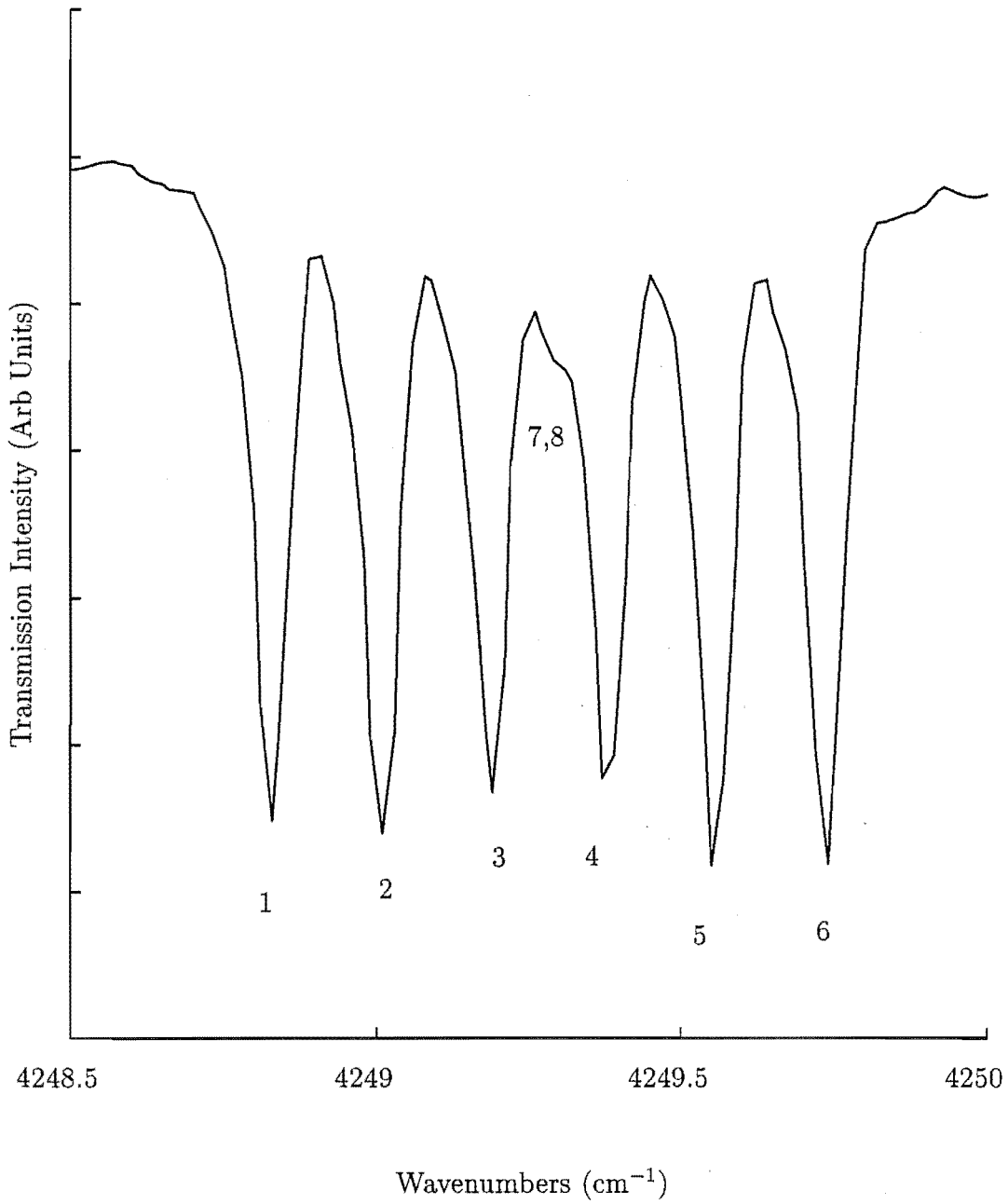

Figure 4.20: Superimposed magnetic hyperfine structure of the $Z_1\gamma_5 \rightarrow X_1\gamma_5$ transition for the C centre in SrF_2:0.03%Pr^{3+}. The spectrum was recorded at 10K.

Table 4.17: Transition assignments and experimental and calculated energies (in vacuum GHz, ±0.6) for the $Z_1\gamma_5 \rightarrow X_1\gamma_5$ transition of the C center in SrF_2:Pr^{3+}. a denotes an arbitrarily chosen reference value.

Line	Transition Assignment	Energy Experimental	Energy Calculated
6	$\mid Z_1\gamma_5^{\pm} \pm \frac{5}{2}\rangle \rightarrow \mid X_1\gamma_5^{\pm} \pm \frac{5}{2}\rangle$	E_0+10.6	E_0+10.7
5	$\mid Z_1\gamma_5^{\pm} \pm \frac{3}{2}\rangle \rightarrow \mid X_1\gamma_5^{\pm} \pm \frac{3}{2}\rangle$	E_0+5.2	E_0+5.4
4	$\mid Z_1\gamma_5^{\pm} \pm \frac{1}{2}\rangle \rightarrow \mid X_1\gamma_5^{\pm} \pm \frac{1}{2}\rangle$	E_0^a	E_0^a
7,8	$\mid Z_1\gamma_5^{\pm} \pm \frac{1}{2}\rangle \rightarrow \mid X_1\gamma_5^{\pm} \mp \frac{1}{2}\rangle$	E_0−3.3	E_0−2.2
3	$\mid Z_1\gamma_5^{\pm} \mp \frac{1}{2}\rangle \rightarrow \mid X_1\gamma_5^{\pm} \mp \frac{1}{2}\rangle$	E_0−6.5	E_0−5.7
2	$\mid Z_1\gamma_5^{\pm} \mp \frac{3}{2}\rangle \rightarrow \mid X_1\gamma_5^{\pm} \mp \frac{3}{2}\rangle$	E_0−11.7	E_0−11.0
1	$\mid Z_1\gamma_5^{\pm} \mp \frac{5}{2}\rangle \rightarrow \mid X_1\gamma_5^{\pm} \mp \frac{5}{2}\rangle$	E_0−17.1	E_0−16.4

4.4 Spectroscopy of the C_{4v} Centres in CaF_2:Tb^{3+} and SrF_2:Tb^{3+}

4.4.1 Zeeman Studies of Infrared Absorption Transitions

A 23.4 mm thick CaF_2 crystal containing 0.07 molar % of Tb^{3+} and a 25.6 mm thick SrF_2 crystal containing 0.09 molar % of Tb^{3+} have been measured in infrared absorption using the Digilab FTIR FTS 40 spectrometer. Murdoch [16] [46] has previously studied both CaF_2:Tb^{3+} and SrF_2:Tb^{3+} crystals using polarised laser-selective excitation. From the inferred energy levels and their assigned irrep symmetries, crystal field analyses were completed. However as only 22 levels were fitted, it is important to add Zeeman data to check whether the crystal-field parameters of Murdoch yield physically reasonable $\langle J_z \rangle$ values. Like the A centre in CaF_2:Ho^{3+}, the C_{4v} symmetry centres in CaF_2:Tb^{3+} and SrF_2:Tb^{3+} are unusual in having a pseudo-degenerate ground-state. Seven infrared transitions are observed to levels of the $^7F_5$, $^7F_4$ and $^7F_3$ multiplets from these pseudo-degenerate $Z_{1,2}$ ground states for both CaF_2:Tb^{3+} and SrF_2:Tb^{3+}. The ground state consists of γ_3 and γ_4 singlet (with the γ_3 lowest in energy) separated by 0.18 cm^{-1} and 0.48 cm^{-1} in CaF_2:Tb^{3+} and SrF_2:Tb^{3+} respectively. This is henceforth denoted as $\gamma_{3,4}$ in an analogous to the ground state of the C_{4v} symmetry centre of CaF_2:Ho^{3+}. As for Ho^{3+} these states have an effective magnetic moment between them through the parallel hyperfine interaction.

The infrared spectrum of CaF_2:0.07%Tb^{3+} is rendered more complex by the presence of many additional centres than the C_{4v} symmetry centre (see Figure 4.21). Three

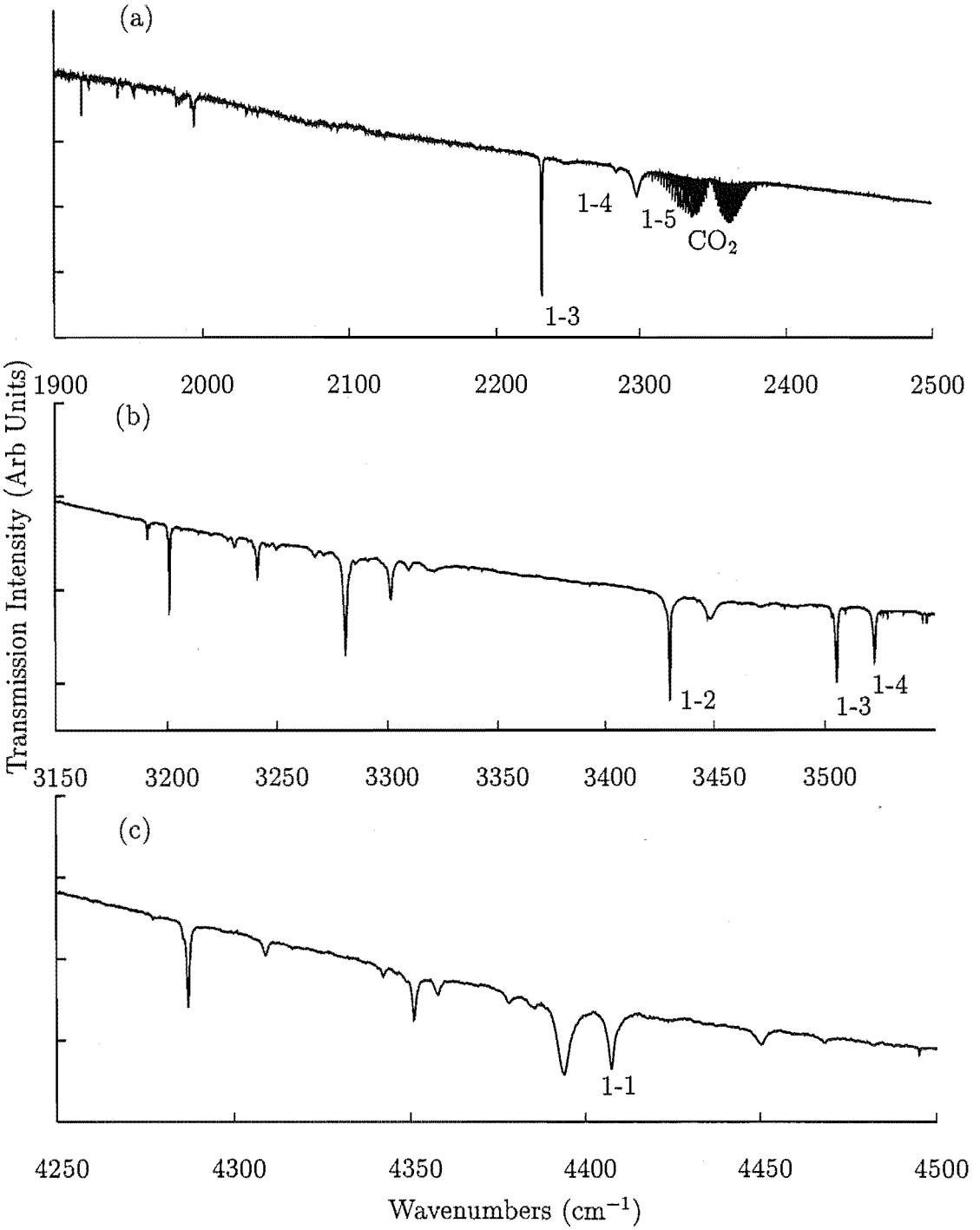

Figure 4.21: Infrared absorption spectra for transitions from the $^7F_6$ ground multiplet to levels of (a) the $^7F_5$ multiplet, (b) the $^7F_4$ multiplet and (c) the $^7F_3$ multiplet of CaF_2:0.07%Tb^{3+}. The labelled transitions are those to of the C_{4v} symmetry centre. The spectra were recorded at 16K.

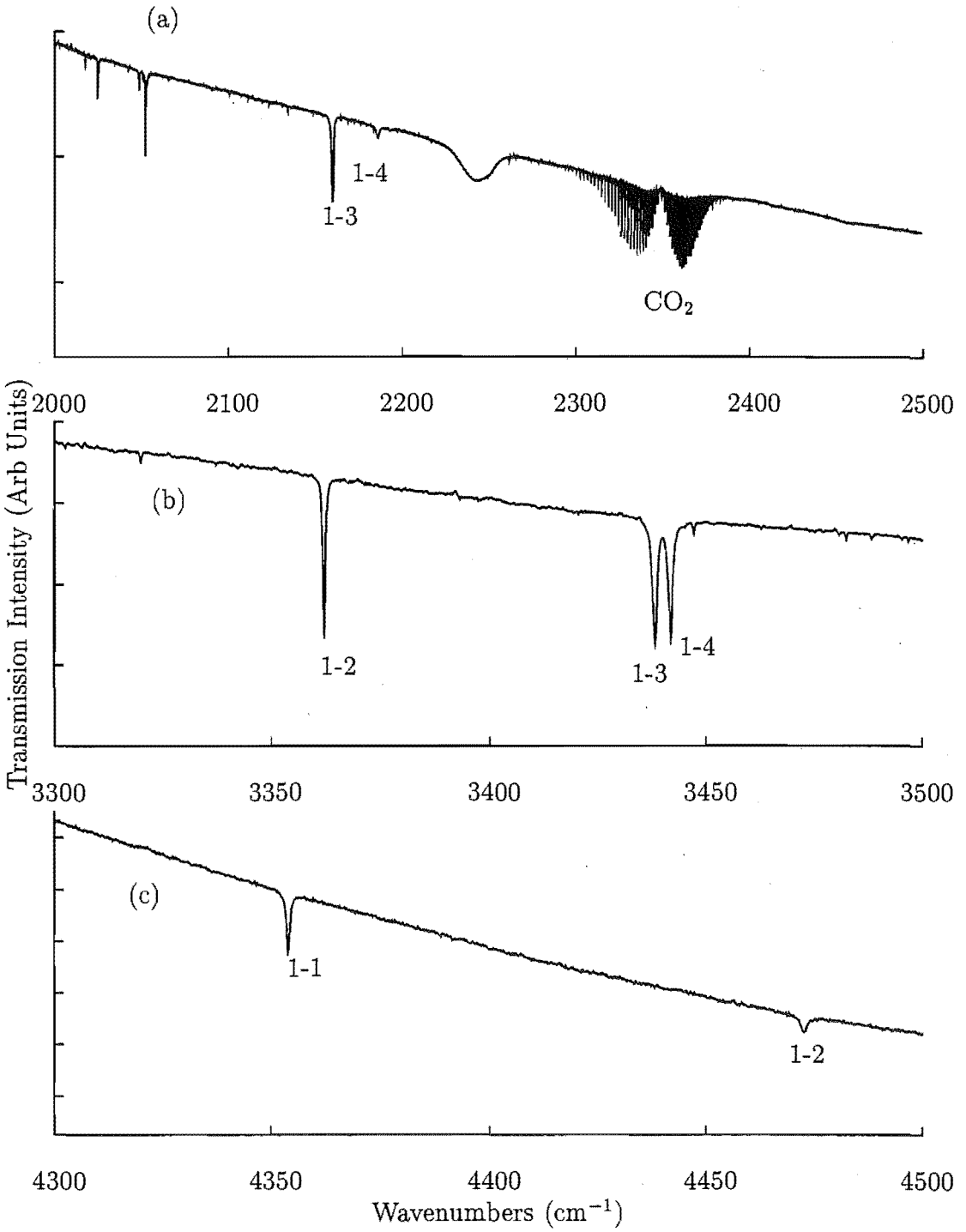

Figure 4.22: Infrared absorption spectra for transitions from the $^7F_6$ ground multiplet to levels of (a) the $^7F_5$ multiplet, (b) the $^7F_4$ multiplet and (c) the $^7F_3$ multiplet of SrF_2:0.09%Tb^{3+}. The labelled transitions are those of the C_{4v} symmetry centre. The spectra were recorded at 10K.

C_{4v} absorption transitions to the $^7F_5$ multiplet are observed, with their energies given in Table 1.18. Of these three, the $Z_{1,2}\gamma_{3,4} \rightarrow Y_3\gamma_5$ transition is strong and sharp and a good candidate for Zeeman spectroscopy and high resolution studies. Transitions to the $^7F_4$ multiplet are more complex because of the overlap of lines of that multiplet with an atmospheric absorption band centred around 3700 cm^{-1} and small features which correspond to absorption by water vapour can be observed in Figure 4.21 near 3600 cm^{-1}. Three transitions of the C_{4v} centre to the $^7F_4$ multiplet are observed in the 3400-3550 cm^{-1} region. A transition at 3448.97 cm^{-1} and the absorption features in the 3150-3350 cm^{-1} and 4250-4500 cm^{-1} regions are not associated with the C_{4v} centre. Only one electronic transition assigned by Murdoch to the C_{4v} centre is observed to the $^7F_3$ multiplet. The energy of this crystal field level is measured to be 4409.05 cm^{-1} and was assigned by Murdoch as a transition from the $^7F_6$ ground state to the lowest crystal field level of the $^7F_3$ multiplet.

The additional centres include the C_{3v}, modified Sr^{2+} and Ba^{2+} centres (whose presence were noted by Murdoch) and clusters centres. The broad feature centred at 2249 cm^{-1} is not associated with the C_{4v} centre and may be associated with the absorption features noted around 1950 cm^{-1}. A more thorough assessment of the defect centre distribution in CaF_2:Tb^{3+} than that completed by Murdoch is required to confirm the assignment of this feature and to study the origin of the additional centres observed in the infrared absorption spectra. In this study we consider only the regular C_{4v} centre and transition assignments are made with reference to the state assignments made by Murdoch on the basis of polarised laser selective excitation.

Table 4.18: 10K energy levels (in vacuum cm^{-1}, ± 0.02), intensities (relative to the strongest line in the spectrum (=100)) and linewidths (in vacuum cm^{-1}, ± 0.1) as observed for the C_{4v} centre in CaF_2:0.07%Tb^{3+}.

Multiplet	Transition	Energy	Intensity	Linewidth
	$Z_{1,2}\gamma_{3,4} \rightarrow Y_3\gamma_5$	2231.83	60	0.7
$^7F_5$	$\rightarrow Y_4\gamma_3$	2283.83	8	1.7
	$\rightarrow Y_5\gamma_5$	2298.51	29	3.8
	$\rightarrow X_2\gamma_4$	3430.44	32	0.7
$^7F_4$	$\rightarrow X_3\gamma_3$	3506.04	67	0.9
	$\rightarrow X_4\gamma_5$	3523.44	16	0.9
$^7F_3$	$\rightarrow W_1\gamma_3$	4409.05	100	1.4

The infrared spectrum of SrF_2:0.09%Tb^{3+} is relatively simple. Two transitions of the C_{4v} centre to the $^7F_5$ multplet are observed at 2160.65 cm^{-1} and 2186.08 cm^{-1}. An assymetrical absorption band around 20 cm^{-1} in width is observed centred at 2243

Table 4.19: Energy levels (in vacuum cm^{-1}, ± 0.02), intensities (relative to the strongest line in the spectrum (=100)) and linewidths (in vacuum cm^{-1}, ± 0.1) as observed for the C_{4v} centre in SrF_2:0.09%Tb^{3+}.

Multiplet	Transition	Energy	Intensity	Linewidth
	$Z_{1,2}\gamma_{3,4} \rightarrow Y_3\gamma_5$	2160.65	82	1.1
$^7F_5$	$\rightarrow Y_4\gamma_3$	2186.08	16	1.6
	$\rightarrow X_2\gamma_4$	3362.54	69	0.5
$^7F_4$	$\rightarrow X_3\gamma_3$	3439.72	93	0.8
	$\rightarrow X_4\gamma_5$	3442.34	84	0.8
$^7F_3$	$\rightarrow W_1\gamma_3$	4354.54	54	0.6
	$\rightarrow W_2\gamma_5$	4473.52	100	1.1

cm^{-1}. The origin of this feature is unknown but it would not appear to be related to the electronic structure of the C_{4v} centre. Transitions in the 2000-2080 cm^{-1} region are also unrelated. As with the C_{4v} centre in CaF_2:Tb^{3+}, three transitions are observed to the $^7F_4$ multiplet. Because of the lower energy of these levels they do not overlap the atmospheric absorption around 3700 cm^{-1}. The $^7F_3$ multiplet spectrum is simplier than that of the CaF_2:Tb^{3+} with only two lines present which are transitions associated with the C_{4v} centre as given in Table 4.19.

For the sharper transitions observed, the linewidths of analogous transitions in the two isomorphic hosts are larger for the SrF_2:Tb^{3+} system. Apart from the effects of concentration differences these linewidth differences are attributed to the larger ground state separation of 0.48 cm^{-1} for SrF_2:Tb^{3+}.

The Zeeman infrared spectra of the Tb^{3+} electronic energy levels for the C_{4v} centre were measured. The splitting of the ground state, evident in all transitions, has been measured to have a spectroscopic splitting factor of 9.87 ± 10 and 10.18 ± 0.10 for CaF_2:Tb^{3+} and SrF_2:Tb^{3+} respectively. For non-Kramers ions in centres of C_{4v} symmetry, the magnetic moments along the x and y axes is essentially zero therefore the measured $\langle 111 \rangle$ splitting factors are essentially an average of the parallel Zeeman effect for the three alternate orientations of the C_{4v} centre. As a consequence the parallel spectroscopic splitting factor of the pseudo-degenerate ground-state is inferred to be 17.10 for CaF_2:Tb^{3+} and 17.63 for SrF_2:Tb^{3+} in agreement with the E.P.R. data of Forrester and Hempstead [69] of 17.77 ± 0.02 and Antipin et. al. [70] of 17.95 ± 0.05.

Apart from this ground-state splitting several γ_5 excited state doublets were observed to split for CaF_2:Tb^{3+} and SrF_2:Tb^{3+}. For the CaF_2:Tb^{3+} system the $Y_3\gamma_5$ state at 2231.83 cm^{-1} and the $X_4\gamma_5$ state at 3523.44 cm^{-1} were observed to split into two

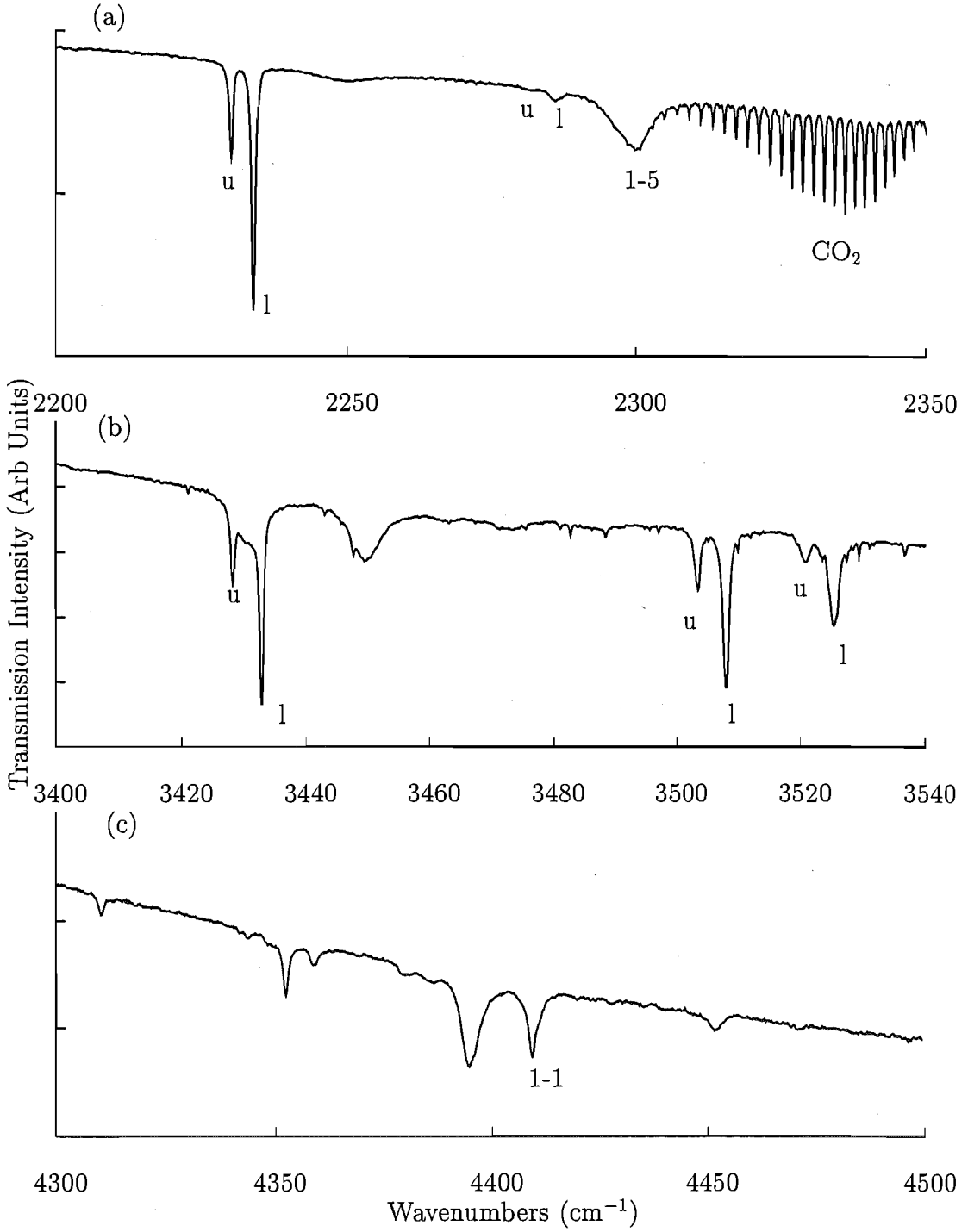

Figure 4.23: 4.2K, 1 Tesla Zeeman infrared absorption spectra for transitions from the $^7F_6$ ground multiplet to levels of (a) the $^7F_5$ multiplet, (b) the $^7F_4$ multiplet and (c) the $^7F_3$ multiplet of a $\langle 111 \rangle$ oriented CaF_2:0.07%Tb^{3+} crystal. The u and l notation denotes transitions from the upper and lower components of the magnetically split ground state of the C_{4v} centre.

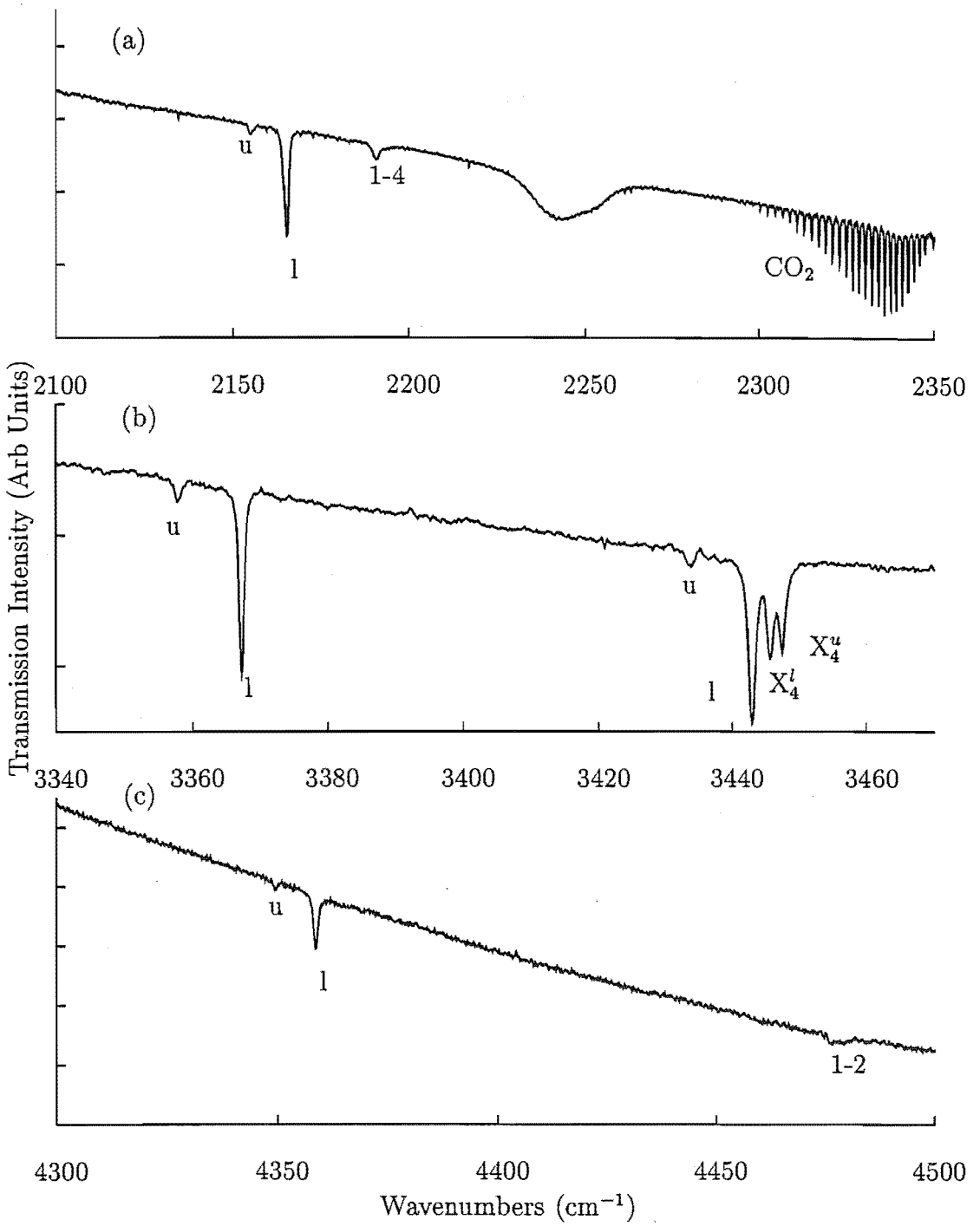

Figure 4.24: 4.2K, 2 Tesla Zeeman infrared absorption spectra for transitions from the $^7F_6$ ground multiplet to levels of (a) the $^7F_5$ multiplet, (b) the $^7F_4$ multiplet and (c) the $^7F_3$ multiplet of a ⟨111⟩ oriented SrF_2:0.09%Tb^{3+} crystal. The u and l notation denotes transitions from the upper and lower components of the magnetically split ground state of the C_{4v} centre as previously. The split upper state doublet $X_4\gamma_5$ components are denoted X_4^l and X_4^u as appropriate.

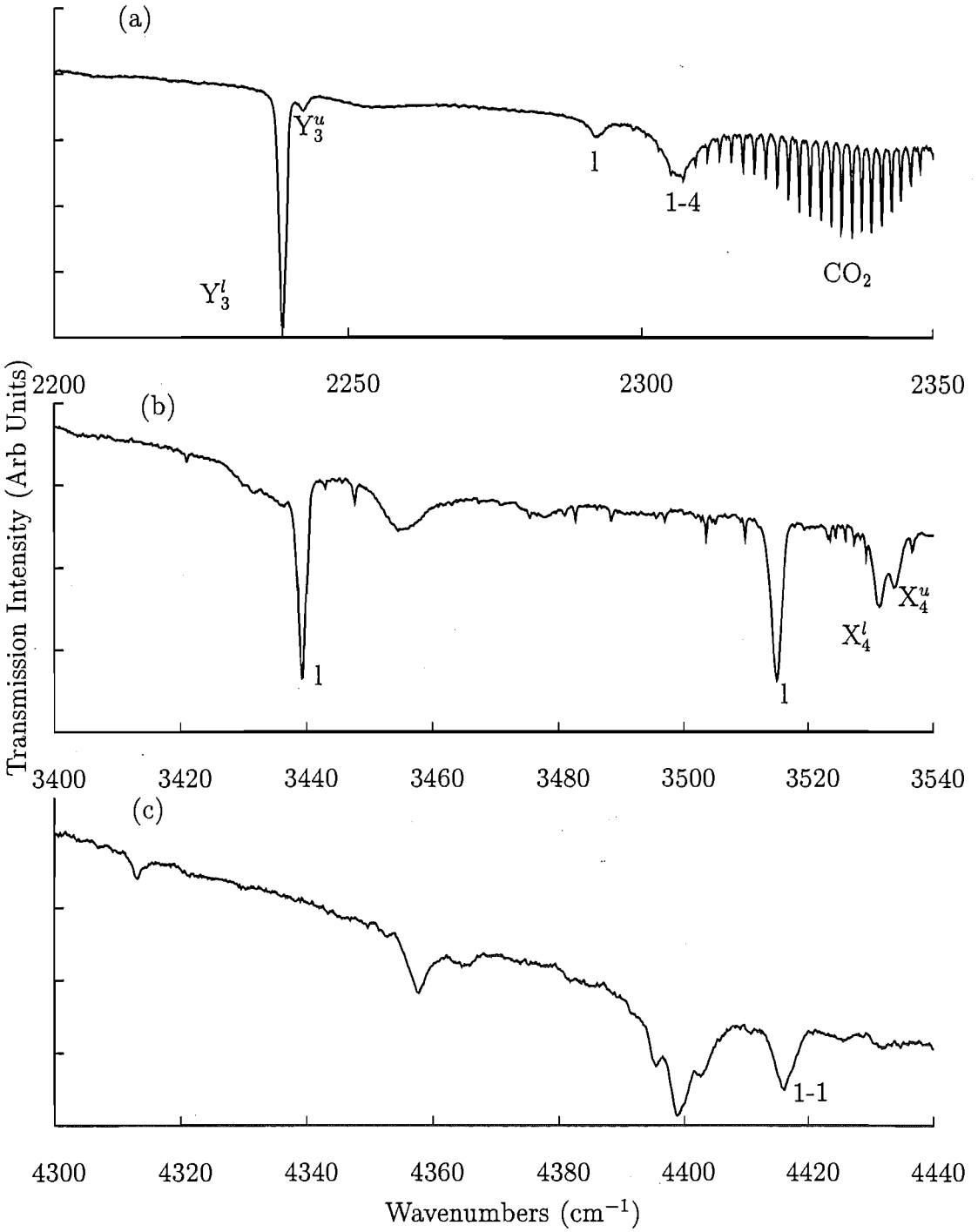

Figure 4.25: 4.2K, 4 Tesla Zeeman infrared absorption spectra for transitions from the $^7F_6$ ground multiplet to levels of (a) the $^7F_5$ multiplet, (b) the $^7F_4$ multiplet and (c) the $^7F_3$ multiplet of a (111) oriented CaF_2:0.07%Tb^{3+} crystal.

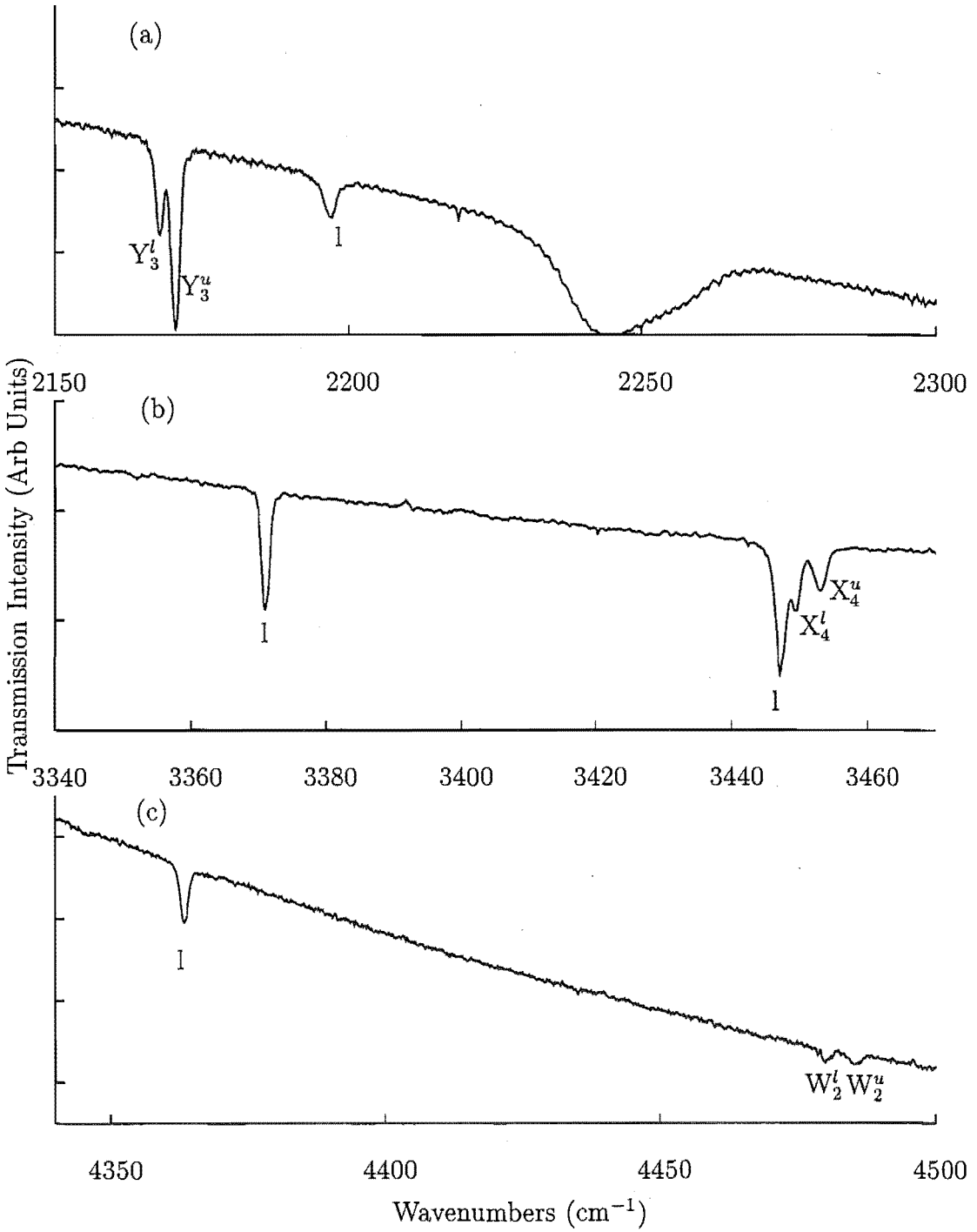

Figure 4.26: 4.2K, 4 Tesla Zeeman infrared absorption spectra for transitions from the $^7F_6$ ground multiplet to levels of (a) the $^7F_5$ multiplet, (b) the $^7F_4$ multiplet and (c) the $^7F_3$ multiplet of a (111) oriented SrF_2:0.09%Tb^{3+} crystal.

Zeeman sub-transitions from the lower Zeeman sub-transition of the ground-state. Their splitting factors are as given in Table 4.20 where reasonable agreement with the values calculated from the parameters of Murdoch and experiment is obtained. The transition from the ground state to the $Y_5\gamma_5$ state was not observed to split because this transition is too broad to reveal the Zeeman subcomponents. For the SrF_2:Tb^{3+} system the $Y_3\gamma_5$ at 2160.65 cm^{-1}, the $X_4\gamma_5$ state at 3442.34 cm^{-1} and the $W_2\gamma_5$ state at 4473.52 cm^{-1} all showed Zeeman splittings. All data is presented in Table 4.20, where experimental splitting factors agree with the calculated values giving confidence in wavefunctions calculated using Murdoch's parameters. Zeeman infrared spectra are given in Figures 4.23 through to 4.26.

Table 4.20: Calculated and measured magnetic splitting factors as observed for the C_{4v} centres in CaF_2:0.07%Tb^{3+} and SrF_2:0.09%Tb^{3+}.

Crystal	State	Field	Magnetic Splitting Factors s_{111}	
		Tesla	Calculated	Experimental
CaF_2:Tb^{3+}	$Z_1\gamma_{3,4}$	1	10.34	9.87±0.10
	$Y_3\gamma_5$	4	2.33	1.84±0.10
	$X_4\gamma_5$	4	1.36	1.30±0.10
SrF_2:Tb^{3+}	$Z_1\gamma_{3,4}$	2	10.32	10.18±0.10
	$Y_3\gamma_5$	4	1.31	1.42±0.10
	$X_4\gamma_5$	4	1.82	1.88±0.10
	$W_2\gamma_5$	4	2.6	2.8±0.2

4.4.2 0.04 cm^{-1} Infrared Absorption Studies

(a) Hyperfine Patterns for the C_{4v} Centre in CaF_2

100% abundant Tb isotope Tb^{159} ion has a nuclear spin I= $\frac{3}{2}$ and a nuclear magnetic moment only half the size of those of Pr^{3+} and Ho^{3+}. Hyperfine structure will be difficult to observe by conventional spectroscopic means. For the cases of Tb^{3+} doped CaF_2 and SrF_2, the terbium ion resides in a C_{4v} symmetry centre with some doublet levels and a twin singlet ground state that has an enhanced magnetic moment. Therefore these systems have advantages for studying Tb^{3+} hyperfine coupling. The first examples of CaF_2:Tb^{3+} hyperfine structure observed in the optical region are presented below.

0.04 cm^{-1} resolution infrared absorption spectra of a 26.5 mm thick CaF_2 crystal doped with 0.005 molar % of Tb^{3+} have been obtained using the Bomem DA3.02 spectrometer. The ground-state of the C_{4v} centre in CaF_2:Tb^{3+} is a pseudo-degenerate

doublet comprising γ_3 and γ_4 states with wavefunctions:

$$\begin{array}{ll} Z_1\gamma_3 & (0.7062)|\ 6\ \rangle + (0.7062)|\ -6\ \rangle \\ Z_2\gamma_4 & (0.7068)|\ 6\ \rangle - (0.7068)\ |\ -6\ \rangle \end{array}$$

These are derived from crystal field calculations employing the parameters of Murdoch. As for Ho^{3+} the mixing of two singlet ground-state wavefunctions via the parallel hyperfine interaction yields an effective $\langle\gamma_3 \mid J_z \mid \gamma_4\rangle$ of 5.98 between them. With A_6=530 MHz, 2Δ=0.18 cm^{-1}=5.4 GHz, $I = \frac{3}{2}$ and this $\langle\gamma_3 \mid J_z \mid \gamma_4\rangle$, the ground state pseudo-quadrupole splittings can be calculated from the hyperfine interaction matrix

	γ_3	γ_4
γ_3	-Δ	$A_6 I_z \langle J_z\rangle$
γ_4	$A_6 I_z \langle J_z\rangle$	Δ

This yields the predicted pseudo-quadrupole splitting for the $Z_{1,2}\gamma_{3,4}$ ground state in Figure 4.28. The predicted 0.078 cm^{-1} splitting in each component of the ground state should just be observable with the 0.04 cm^{-1} resolution of the Bomem DA3.02 spectrometer. However, due to the selection rules for non-Kramers ions in centres of C_{4v} symmetry few transitions are observed to the lowest crystal field levels of each multiplet; the higher energy levels observed are generally homogeneously broadened via spontaneous phonon emission. The observed $Z_{1,2}\gamma_{3,4} \rightarrow X_2\gamma_4$ transition at 3430.44 cm^{-1} is only 22.4 cm^{-1} above the $X_1\gamma_1$ level and is sharp enough to show hyperfine structure. In Figure 4.27 we observe barely resolved two-line hyperfine patterns from the pseudo-quadrupole ground state hyperfine splittings superposed on both transitions from the 0.18 cm^{-1} split ground state. Table 4.22 compares the calculated and experimental hyperfine structure.

Table 4.21: Nuclear-wavefunction composition for the $Z_{1,2}\gamma_{3,4}$ ground state of the C_{4v} centre in CaF_2:0.005%Tb^{3+}

State	Wavefunction
$Z_1\gamma_3 \pm \frac{3}{2}$	$-0.8641\lvert\ \gamma_3 \pm \frac{3}{2}\rangle \pm 0.5033\ \lvert\ \gamma_4 \pm \frac{3}{2}\rangle$
$Z_1\gamma_3 \pm \frac{1}{2}$	$-0.9649\lvert\ \gamma_3 \pm \frac{1}{2}\rangle \pm 0.2625\ \lvert\ \gamma_4 \pm \frac{1}{2}\rangle$
$Z_2\gamma_4 \pm \frac{1}{2}$	$0.9649\lvert\ \gamma_4 \pm \frac{1}{2}\rangle \pm 0.2625\ \lvert\ \gamma_3 \pm \frac{1}{2}\rangle$
$Z_2\gamma_4 \pm \frac{3}{2}$	$0.8641\lvert\ \gamma_4 \pm \frac{3}{2}\rangle \pm 0.5033\ \lvert\ \gamma_3 \pm \frac{3}{2}\rangle$

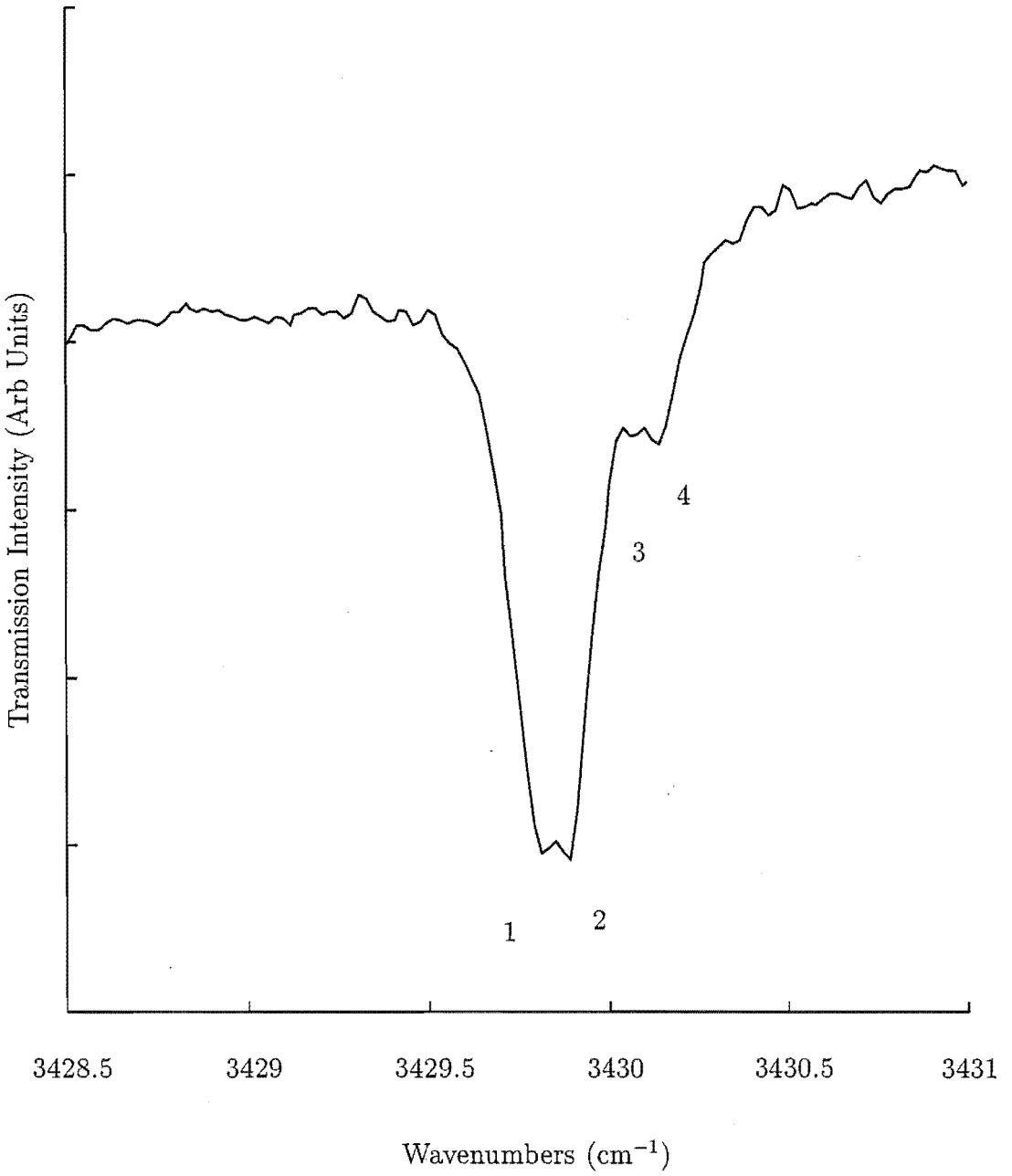

Figure 4.27: Hyperfine structure in the $Z_{1,2}\gamma_{3,4} \rightarrow X_2\gamma_4$ transitions of the C_{4v} centre for CaF_2:0.005%Tb^{3+}. The spectrum was recorded at 10K.

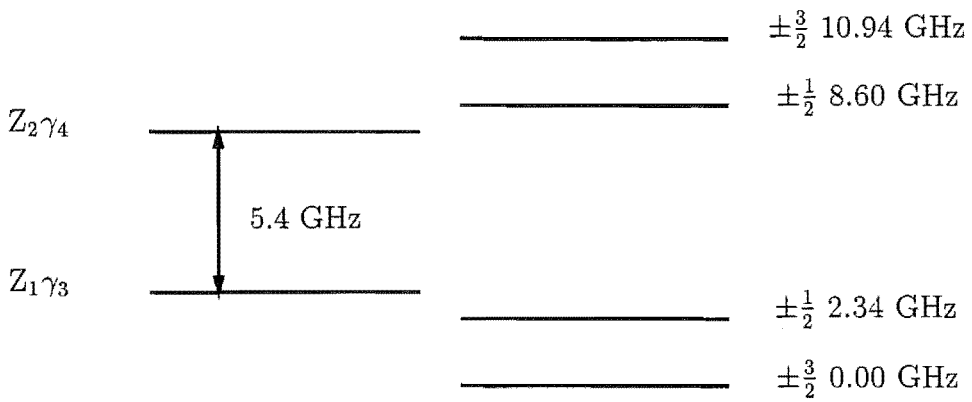

Figure 4.28: Calculated pseudo-quadrupole hyperfine structure in the ground state of the C_{4v} centre for CaF_2:Tb^{3+}.

Table 4.22: Transition assignments and experimental and calculated energies (in vacuum GHz, ±0.6) for the $Z_{1,2}\gamma_{3,4} \rightarrow X_2\gamma_4$ transitions of the C_{4v} centre for CaF_2:Tb^{3+}. a denotes an arbitrarily chosen reference value.

Line	Transition Assignment	Energy Experimental	Energy Calculated
4	$\mid Z_1\gamma_3 \pm \frac{3}{2}\rangle \rightarrow \mid X_2\gamma_4\rangle$	E_0+2.34	E_0+2.16
3	$\mid Z_1\gamma_3 \pm \frac{1}{2}\rangle \rightarrow \mid X_2\gamma_4\rangle$	E_0^a	E_0^a
2	$\mid Z_2\gamma_4 \pm \frac{1}{2}\rangle \rightarrow \mid X_2\gamma_4\rangle$	E_0−6.26	E_0−5.52
1	$\mid Z_2\gamma_4 \pm \frac{3}{2}\rangle \rightarrow \mid X_2\gamma_4\rangle$	E_0−8.6	E_0−7.56

The $Z_{1,2}\gamma_{3,4} \rightarrow Y_3\gamma_5$ transition is expected to have an additional four line hyperfine pattern from the $Y_3\gamma_5$ doublet level which will be superimposed on the ground state pseudo-quadrupole splitting. The wavefunction of the $Y_3\gamma_5$ state is:

$$Y_3\gamma_5^{\pm} \quad 0.6692 \mid \pm 5\rangle + 0.5156 \mid \pm 1\rangle - 0.5153 \mid \mp 3\rangle$$

with $\langle J_z\rangle$=1.71. For A_5=0.468 GHz and $E(I_z)=A_5\langle J_z\rangle I_z$, the total spread of the hyperfine pattern for this $Y_3\gamma_5^{\pm}$ state is just 0.08 cm^{-1} and is unresolved - see Figure 4.29. Figure 4.29 also shows the $Z_{1,2}\gamma_{3,4} \rightarrow X_3\gamma_3$ transitions whose intensity patterns are inverted to what is observed for the $Z_{1,2} \rightarrow X_2\gamma_4$ transitions. This occurs because $\gamma_3 \rightarrow \gamma_4$ and $\gamma_4 \rightarrow \gamma_3$ transitions are electric dipole allowed only through the admixture of the ground state wavefunctions by the parallel hyperfine interaction $A_J J_z I_z$. The intensity inversion confirms the γ_3 and γ_4 irrep assignments for these levels.

(b) Hyperfine Patterns for the C_{4v} Centre in SrF_2

A 29 mm thick SrF_2 crystal doped with 0.01 molar % of Tb^{3+} was studied for related examples of hyperfine structure. In this case the C_{4v} centre has the two ground state singlets split by 0.48 cm^{-1} (14.4 GHz=2Δ). From this separation the ground state pseudo-quadrupole hyperfine energies $E(I_z)$ are $\sqrt{\Delta^2 + (A_6 I_z\langle J_z\rangle)^2}$. From the ground state wavefunctions of:

$$\begin{array}{ll} Z_1\gamma_3 & 0.7041 \mid 6\rangle + 0.7041 \mid -6\rangle \\ Z_2\gamma_4 & 0.7065 \mid 6\rangle - 0.7065 \mid -6\rangle \end{array}$$

With the value of Δ of 7.2 GHz, A_6=0.530 GHz and the $\langle J_z\rangle$ value of 5.70 we obtain the ground state hyperfine splitting as shown in Figure 4.30. This hyperfine separation of 0.04 cm^{-1} at the limit of the available resolution used here and no hyperfine structure is observed for the transitions shown in Figure 4.31.

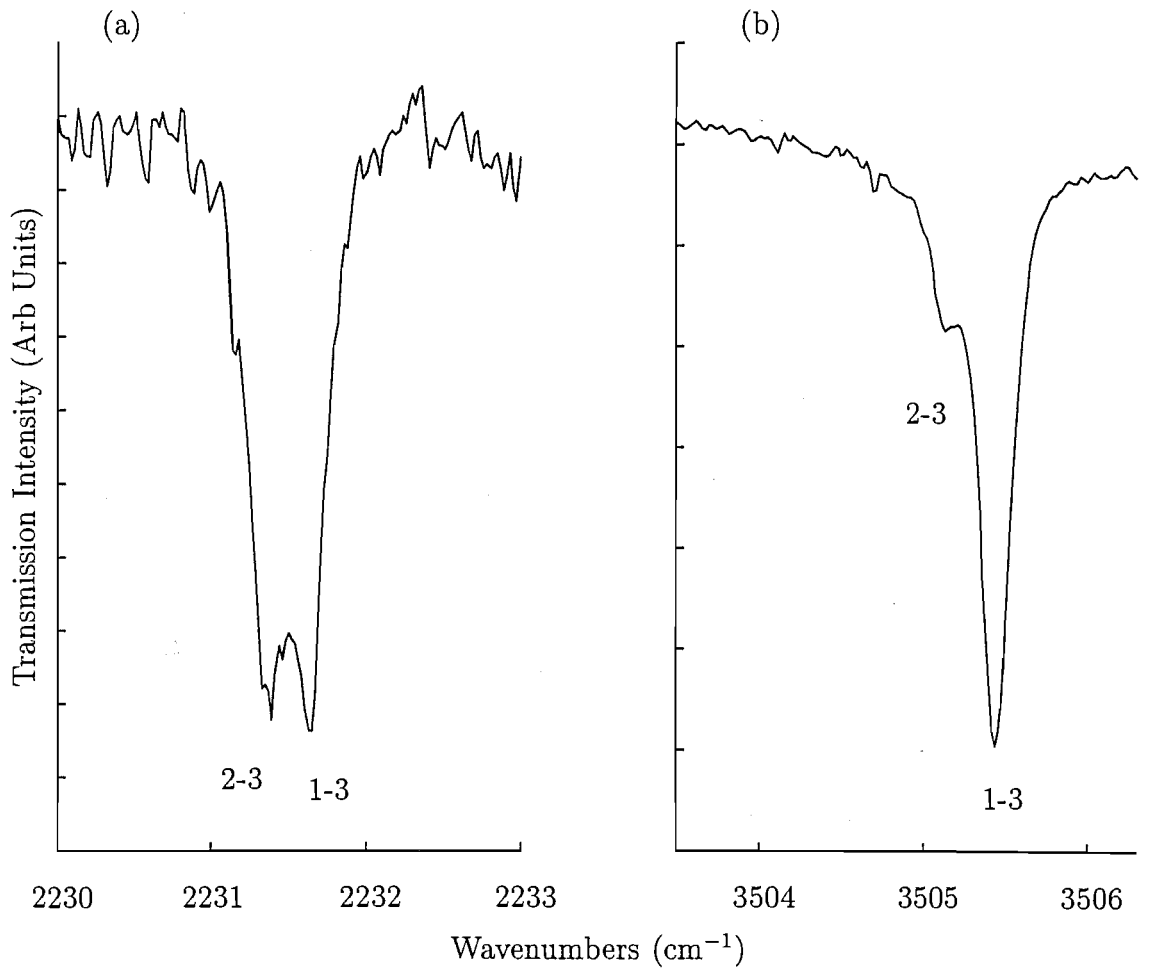

Figure 4.29: Transitions from the $Z_{1,2}\gamma_{3,4}$ ground state to the (a) $Y_3\gamma_5$ state and (b) the $X_3\gamma_3$ state of the C_{4v} centre in CaF_2:0.005%Tb^{3+}. The i-j labelling denotes a transition from the Z_i level to the appropriate j-th upper level. The spectra were recorded at 10K.

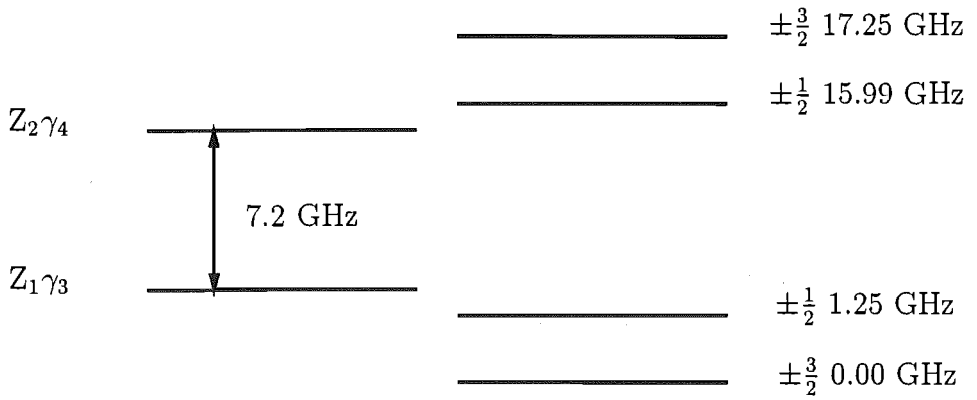

Figure 4.30: Calculated pseudo-quadrupole hyperfine structure of the ground state of the C_{4v} centre for SrF_2:Tb^{3+}.

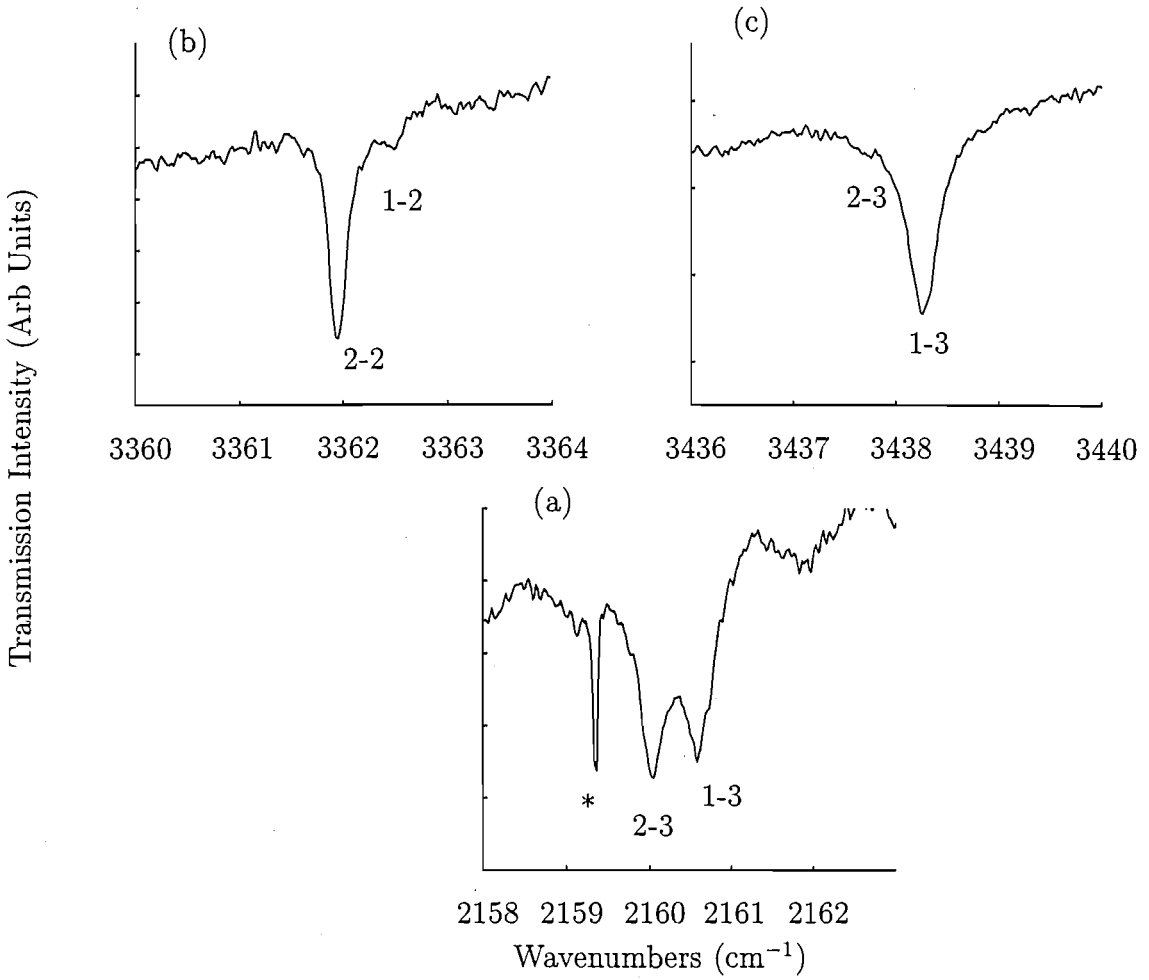

Figure 4.31: Transitions from the $Z_{1,2}\gamma_{3,4}$ ground state to the (a) $Y_3\gamma_5$ state, (b) the $X_2\gamma_4$ state and (c) the $X_3\gamma_3$ state of the C_{4v} centre in SrF_2:0.01%Tb^{3+}. * indicates an unassigned Tb^{3+} feature. The spectra were recorded at 10K.

Table 4.23: Nuclear wavefunction composition for the $Z_{1,2}\gamma_{3,4}$ ground state of the C_{4v} centre in SrF_2:0.01%Tb^{3+}

State	Wavefunction
$Z_1\gamma_3 \pm \frac{3}{2}$	$-0.9579\vert\ \gamma_3 \pm \frac{3}{2}\rangle \pm 0.2873\ \vert\ \gamma_4 \pm \frac{3}{2}\rangle$
$Z_1\gamma_3 \pm \frac{1}{2}$	$-0.9942\vert\ \gamma_3 \pm \frac{1}{2}\rangle \pm 0.1079\ \vert\ \gamma_4 \pm \frac{1}{2}\rangle$
$Z_2\gamma_4 \pm \frac{1}{2}$	$0.9942\vert\ \gamma_4 \pm \frac{1}{2}\rangle \pm 0.1079\ \vert\ \gamma_3 \pm \frac{1}{2}\rangle$
$Z_2\gamma_4 \pm \frac{3}{2}$	$0.9579\vert\ \gamma_4 \pm \frac{3}{2}\rangle \pm 0.2873\ \vert\ \gamma_3 \pm \frac{3}{2}\rangle$

Chapter 5

Spectroscopy of Sm^{3+} Ions in CaF_2 and SrF_2 Crystals

5.1 Introduction

Trivalent samarium doped fluorite crystals have generated much interest over the years, largely as a spin off from the very early successes in obtaining stimulated emission from the divalent species (Kaminskii) [7], Kaiser et. al. (1961) [71] and Wood and Kaiser (1962) [72].

This work, reports the first laser selective excitation study of Sm^{3+} ions in CaF_2 and SrF_2 crystals known to the author. Early optical spectroscopy concentrated on the CaF_2 host, Rabbiner [73] (1963) and Ewansizky et. al. [74] (1965). Two distinct types of spectra were obtained, which were labelled type I and II. Spectra of type I were assigned to be due to O^{2-} charge compensation. The type II spectra were associated with Sm^{3+}-F^- pairs in C_{4v} symmetry centres. Later, the type II spectra were analysed in terms of a C_{4v} symmetry crystal field, Rabbiner [75] (1967). However, the measured fluorescence data was not entirely due to the tetragonal centre and this distorted the analysis. Further measurements on this system [Nara and Schlesinger [76] (1971)] attempted to unravel the low lying (6000-10700 cm^{-1}) energy level structure. These authors were thwarted by low resolution and the usual problems associated with non selective measurements for multicentre crystals.

A more consistent set of results might have been expected from electron paramagnetic resonance measurements, however this did not prove to be the case. Almost simultaneously, Low (1964) [77] and independently Weber and Bierig (1964) [8] performed measurements on the CaF_2:Sm^{3+} system with the same result. Both obtained a dominant centre of C_{4v} symmetry and g values for the ground state of $g_{\|}$=0.907±0.01 and $g_{\perp}$=0.544±0.015 and $g_{\|}$=0.93±0.04 and $g_{\perp}$=0.57±0.05 respectively.

A later study by Antipin et. al. [78] (1965) reported a dominant C_{4v} symme-

try centre. This centre was quite different spectroscopically, to that reported in the earlier studies. The g values reported for this centre were $g_{\|}$=0.00±0.06 and $g_{\perp}$=0.823±0.003. This result was later confirmed by Evans and McLaughlan [79] (1966) . They obtained g values of $g_{\|} \leq 0.1$ and $g_{\perp}$=0.822±0.001. Interestingly, the ground state wavefunctions calculated by Rabbiner [Rabbiner (1967) [75]] are consistent with the g values obtained by both Antipin et. al. and Evans and McLaughlan for the tetragonal C_{4v} symmetry centre.

Evans and McLaughlan, also made measurements on a trigonal site. This was assumed to be associated with oxygen charge compensation which gave g values of $g_{\|}$=0.415±0.001 and $g_{\perp}$=0.934±0.001.

Newman and Woodward [80] (1974), studied SrF_2:Sm^{3+} by E.P.R. methods. They obtained g values for the dominant tetragonal centre of $g_{\|}$=0.00±0.006 and $g_{\perp}$=0.823±0.003. They also saw resonances associated with hydrogenic (tetragonal) centres and a trigonal oxygen centre. Thus, EPR studies yielded dominant centres of C_{4v} symmetry for both CaF_2:Sm^{3+} and SrF_2:Sm^{3+}. The two different C_{4v} symmetry centres were observed in CaF_2:Sm^{3+}. In addition, C_{3v} symmetry centres associated with oxygen charge compensation of the rare earth ion, were observed.

Wells [64] has studied CaF_2 and SrF_2 crystals doped with trivalent samarium. Zeeman infrared absorption spectroscopy for transitions to the ${}^6H_{\frac{7}{2}}$, ${}^6H_{\frac{9}{2}}$ and ${}^6H_{\frac{11}{2}}$ multiplets was employed. This study confirmed the presence of a dominant centre of tetragonal symmetry. Zeeman subtransitions that were electric dipole forbidden were observed. It was concluded that a significant magnetic dipole component was present for some infrared transitions.

5.2 Spectroscopy of CaF_2:Sm^{3+}

The trivalent samarium ion has an f^5 configuration with $\frac{14!}{5!(14-5)!} = 2002$ electronic states. This corresponds to the number of different ways of putting 5 electrons into 14 possible states. However, since Sm^{3+} is a Kramers ion, the crystalline field will not lift the two fold residual time reversal (Kramers) degeneracy and a maximum of 1001 electronic states will be observable (unless a magnetic field is applied). Crystal field levels will be labelled according to the usual conventions of an arbitrary alphabetical label (following Dieke [81] (1968)), a numerical subscript and, as appropriate, the irrep symmetry of the point group in question. Table 5.1 gives the decomposition of the relevant ${}^{(2S+1)}L_J$ multiplets under the point group symmetries studied in this work. Figure 5.1 gives the Sm^{3+} free-ion (multiplet) level structure below 20000 cm^{-1}, which we study in this thesis.

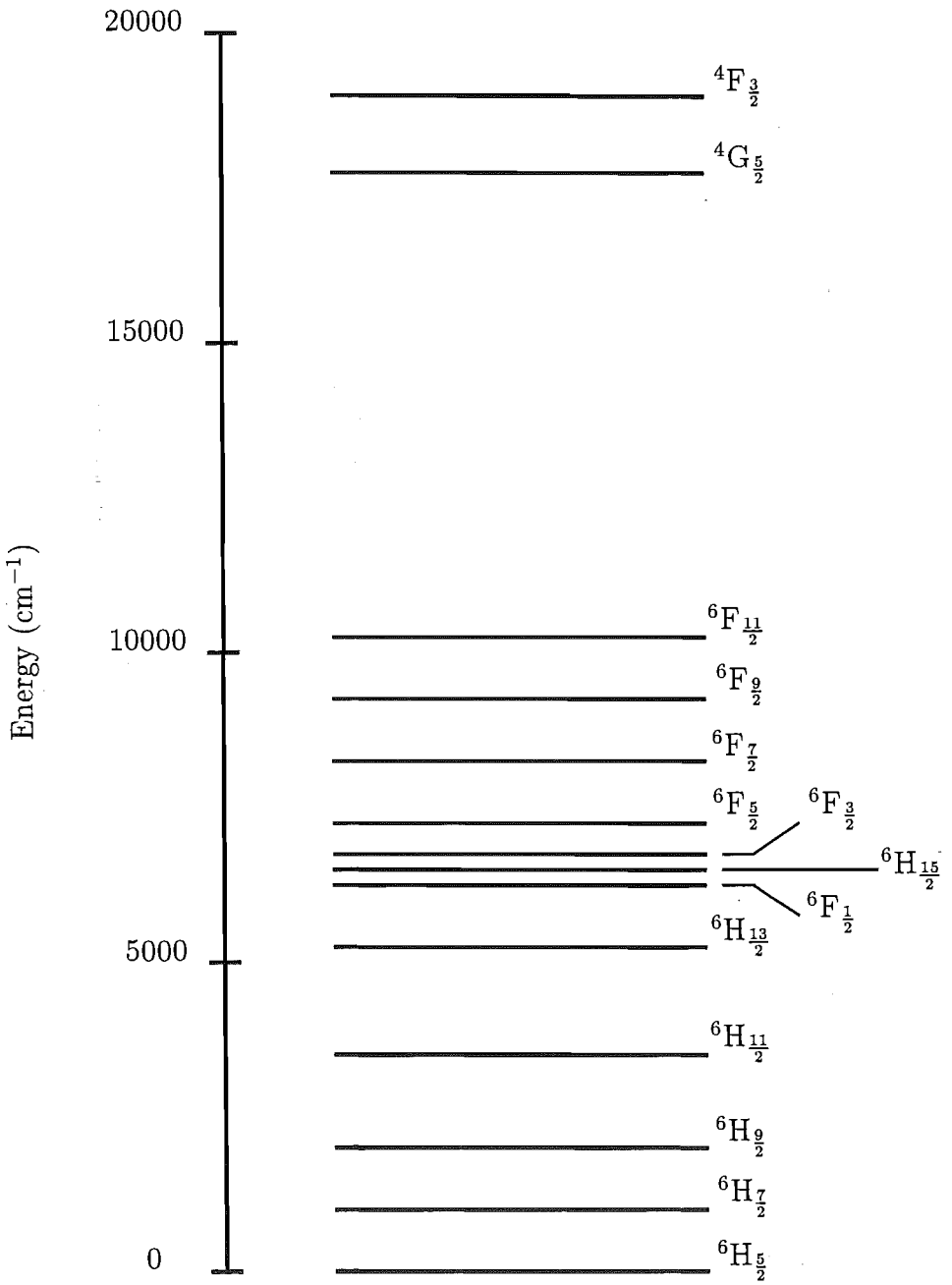

Figure 5.1: Sm^{3+} multiplet level structure below 20000 cm^{-1}.

Table 5.1: Decompositon of the free ion (spin-orbit | LSJ)) states into irreps of the cubic O_h, tetragonal C_{4v} and trigonal C_{3v} point groups for selected multiplets of the f^5 configuration.

$^{(2S+1)}L_J$	O_h	C_{4v}	C_{3v}
$^6H_{\frac{5}{2}}$	$\Gamma_7+\Gamma_8$	$\gamma_6+2\gamma_7$	$\gamma_4+\gamma_{5,6}$
$^6H_{\frac{7}{2}}$	$\Gamma_6+\Gamma_7+\Gamma_8$	$2\gamma_6+2\gamma_7$	$3\gamma_4+\gamma_{3,4}$
$^6H_{\frac{9}{2}}$	$\Gamma_6+2\Gamma_8$	$3\gamma_6+2\gamma_7$	$3\gamma_4+2\gamma_{5,6}$
$^6H_{\frac{11}{2}}$	$\Gamma_6+\Gamma_7+\Gamma_8$	$3\gamma_6+3\gamma_7$	$4\gamma_4+2\gamma_{5,6}$
$^6H_{\frac{13}{2}}$	$\Gamma_6+2\Gamma_7+4\Gamma_8$	$3\gamma_6+4\gamma_7$	$5\gamma_4+2\gamma_{5,6}$
$^6H_{\frac{15}{2}}$	$\Gamma_6+\Gamma_7+3\Gamma_8$	$4\gamma_6+4\gamma_7$	$5\gamma_4+3\gamma_{5,6}$
$^6F_{\frac{1}{2}}$	Γ_6	γ_6	γ_4
$^6F_{\frac{3}{2}}$	Γ_8	$\gamma_6+\gamma_7$	$\gamma_4+\gamma_{5,6}$
$^6F_{\frac{5}{2}}$	$\Gamma_7+\Gamma_8$	$\gamma_6+2\gamma_7$	$2\gamma_4+\gamma_{5,6}$
$^6F_{\frac{7}{2}}$	$\Gamma_6+\Gamma_7+\Gamma_8$	$2\gamma_6+2\gamma_7$	$3\gamma_4+\gamma_{5,6}$
$^4G_{\frac{5}{2}}$	$\Gamma_7+\Gamma_8$	$\gamma_6+2\gamma_7$	$2\gamma_4+\gamma_{5,6}$
$^4F_{\frac{3}{2}}$	Γ_8	$\gamma_6+\gamma_7$	$\gamma_4+\gamma_{5,6}$

5.2.1 Optical Absorption Spectra

The absorption spectrum of the $^4G_{\frac{5}{2}}$ multiplet has been recorded for CaF_2:Sm^{3+}. The 20 mm thick crystals were cooled to a temperature of 16K. Concentrations of 0.01%, 0.05% and 0.2% of SmF_3 were used. The spectra are shown in Figure 5.2. Absorption transitions to the $^4G_{\frac{5}{2}}$ multiplet are typically quite weak, at less than 5% of the total transmission, for this length of crystal and concentrations of 0.05 molar % of the dopant. This is to be expected, as the $^6H_{\frac{5}{2}} \rightarrow ^4G_{\frac{5}{2}}$ transitions are nominally spin forbidden. For CaF_2:0.01%Sm^{3+} crystals, three sharp features are readily apparant at 558.3, 560.5 and 560.9 nm. The absorption peaks at 558.3 and 560.5 nm are correlated and dominate the absorption spectrum for concentrations of Sm^{3+} lower than 0.2 mol %. In Figure 5.2, these absorption transitions are denoted as A and it is not unreasonable to assume that these transitions are associated with the tetragonal C_{4v} centre observed in EPR experiments.

For CaF_2:0.05%Sm^{3+}, the spectrum is dominated by two absorption features at 560.9 and 561.5 nm labelled R and Q. These features increase dramatically with concentration and can be tentatively assigned as associated with rare earth ion clusters from their concentration dependence. The 566.4 nm absorption feature, labelled O, is also observed to increase in intensity as the R and Q absorptions increase. At these higher concentrations, many weak additional lines are observed. It is assumed they are associated with multi-ion centres. It has been suggested that

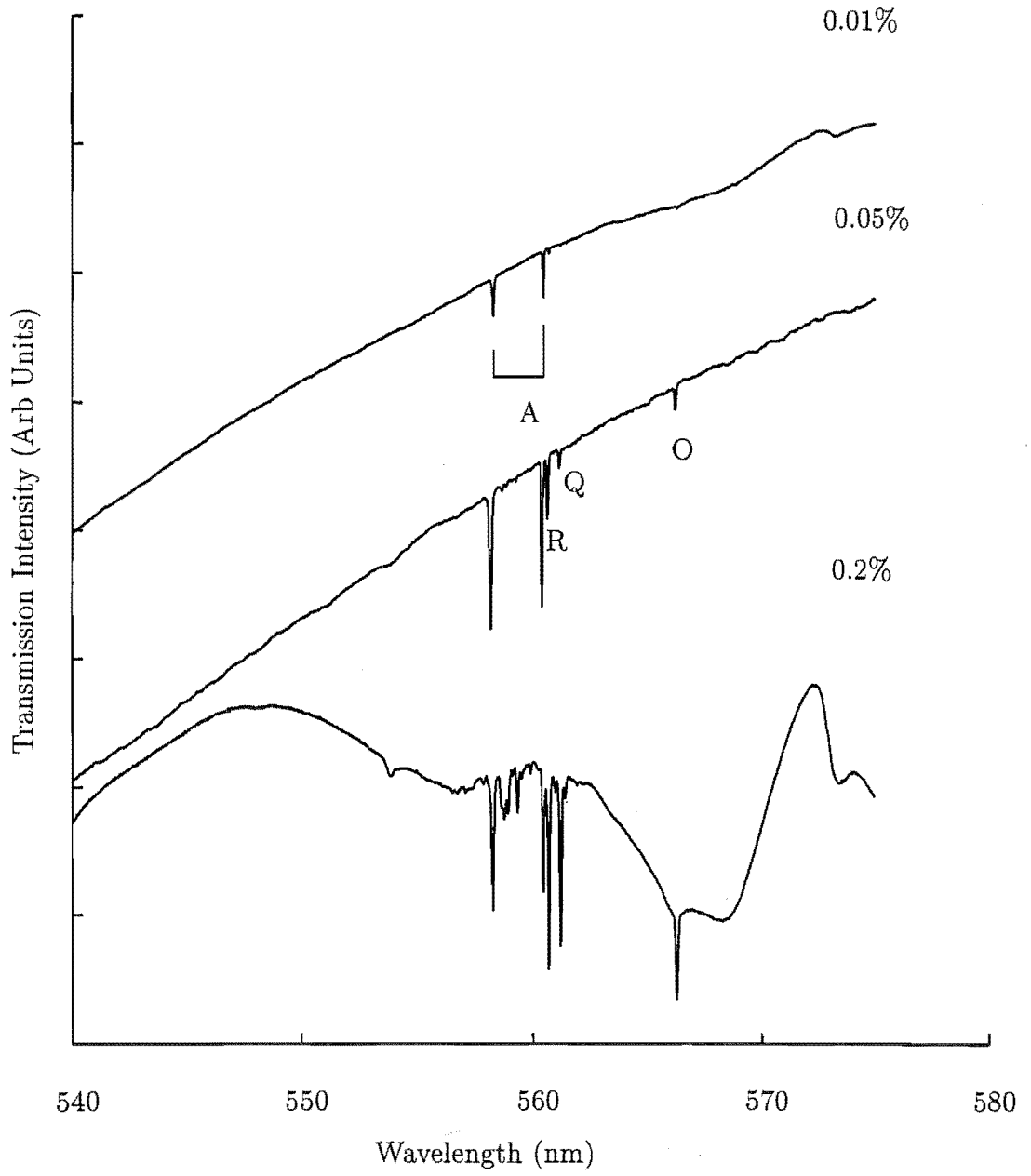

Figure 5.2: Absorption spectrum of the $^4G_{\frac{5}{2}}$ multiplet in CaF_2:x%Sm^{3+} where x=0.01, 0.05 and 0.2. All spectra were recorded at 16K.

such clusters are efficient scavengers of interstitial fluorines [82].

An additional feature of the spectra, is the broad absorption bands at the long wavelength end. These are particularly noticeable in the CaF_2:0.2%Sm^{3+} sample. Their appearance is correlated with a green colouration of the crystal. This identifies these bands as Sm^{2+} $4f \rightarrow 4f^{N-1}5d$ absorption structure [83].

5.2.2 Excitation Spectra

Excitation spectra were recorded using the CW dye laser discussed in chapter three. The appropriate laser dye for excitation of the $^4G_{\frac{5}{2}}$ multiplet was Rhodamine 560. All excitation features measured in this study, were recorded using the SPEX 1700 series single monochromator in zero order or, on occasions, the Bausch and Lomb 0.25m monochromator monitoring at 600 nm (all transitions $^4G_{\frac{5}{2}} \rightarrow {}^6H_{\frac{9}{2}}$). An EMI 9659 QA photoelectrically cooled photomultiplier tube was employed to detect the emitted radiation in either case. A Corning 2-62-1 glass filter was used to eliminate unwanted laser scatter. All spectra were recorded at 16K.

Figure 5.3 shows the $^4G_{\frac{5}{2}}$ excitation spectrum of a 2mm slice of CaF_2:0.05%Sm^{3+}. Fluorescence was monitored in zero order on the SPEX 1700 single monochromator. Narrow-band excitation spectra, where fluorescence from only one centre is monitored, is presented in Figure 5.4.

The dominant transitions observed in excitation correspond to A centre transitions. Three excitation features are observed at 17837, 17908 and 18240 cm^{-1}. These are shown for the narrowband excitation spectrum in Figure 5.4(a). The highest frequency transition was not observed in the absorption measurements, most likely because the feature is weak and broad.

The second most strongly fluorescing centre has excitation features at 17653 and 18053 cm^{-1}. This centre was labelled O in section 5.2.1. The observed fluorescence from this centre is 100 times reduced in intensity from that of the A centre. Only two absorption transitions to the $^4G_{\frac{5}{2}}$ multiplet were identified. From this, and the manifold degeneracy of ^6H_J and ^6F_J (presented below), we assign this centre as having cubic O_h symmetry.

It is noticeable that the two absorption features present at 560.9 and 561.5 nm in the optical absorption spectra of section 5.2.1 are not observed in the excitation spectra. Broadband monitoring of fluorescence to different multiplets using the Bausch and

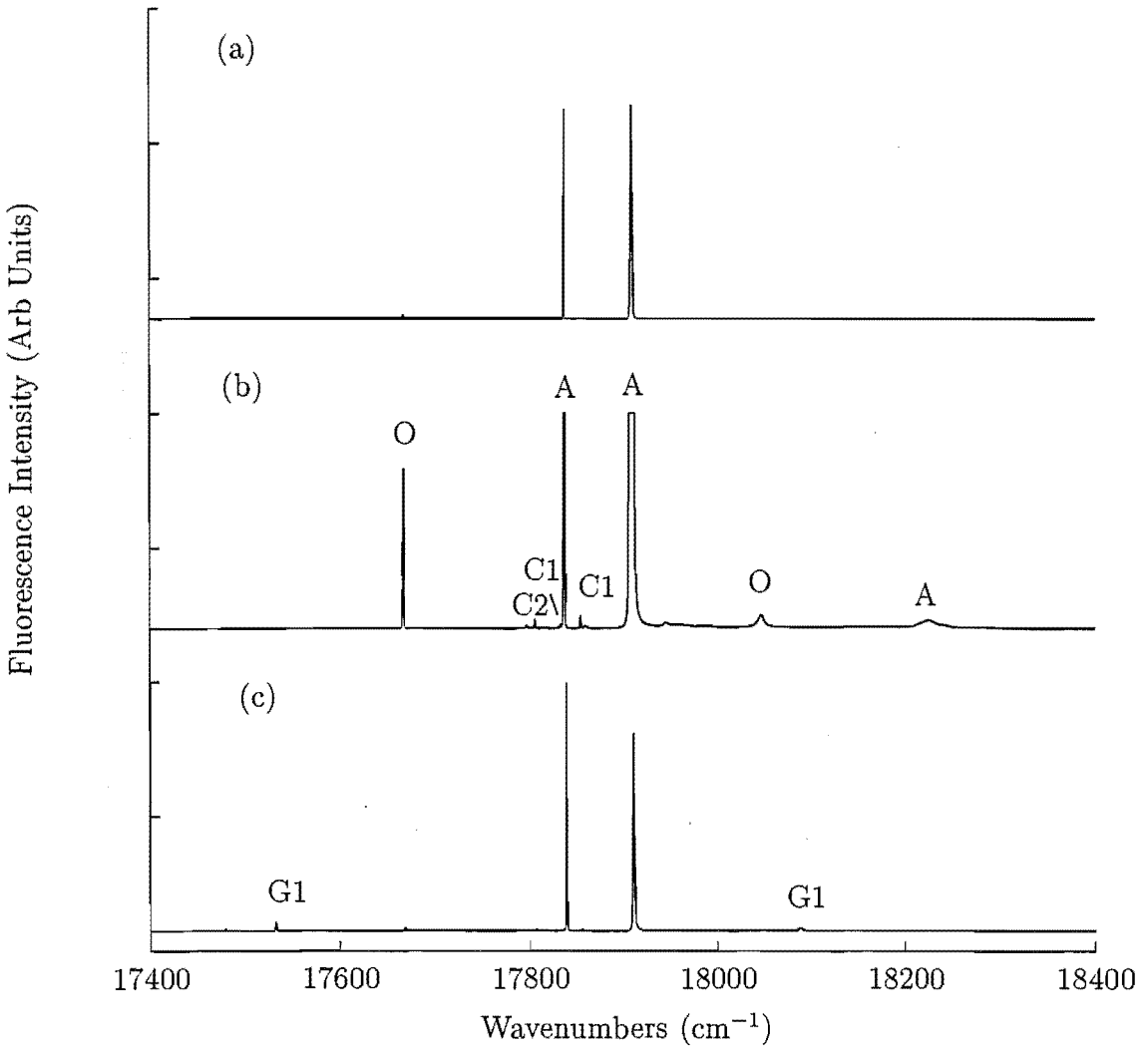

Figure 5.3: Excitation spectra of the $^4G_{\frac{5}{2}}$ multiplet in CaF_2:0.05%Sm^{3+} for broadband detection monitoring all fluorescence in zero order on the SPEX 1700 (a) As grown crystals (×1 amplification) (b) As grown crystals (×100 amplification (c) After 30 minutes oxygenation (×1 amplification). All spectra were recorded at 16K.

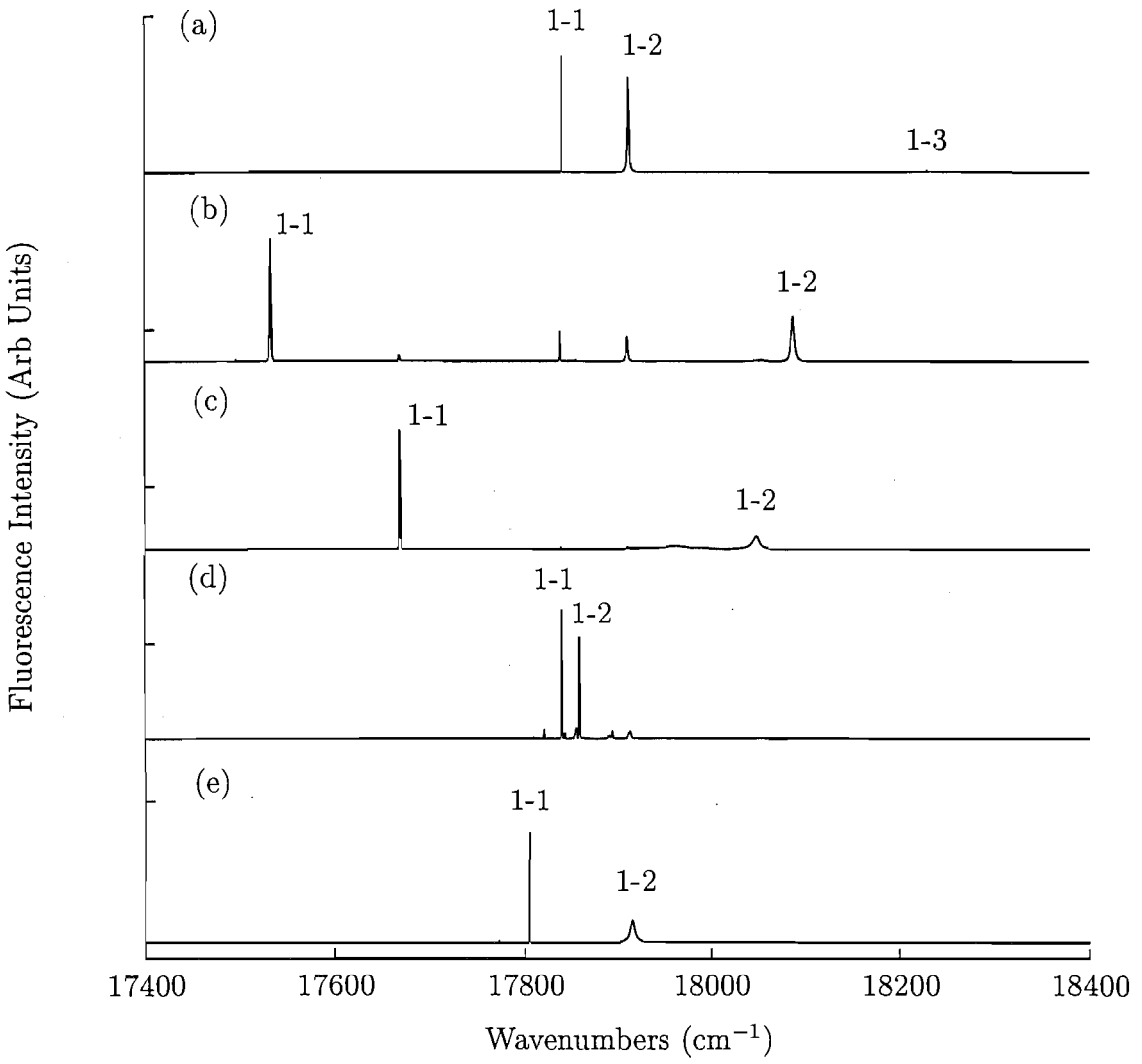

Figure 5.4: Narrowband excitation spectra of the $^4G_{\frac{5}{2}}$ multiplet in CaF_2:0.05%Sm^{3+} for (a) the A centre 14333 cm^{-1}, (b) the G1 centre at 13900 cm^{-1}, (c) the O centre at 12804 cm^{-1}, (d) the C1 centre at 15590 cm^{-1} and (e) the C2 centre at 16839 cm^{-1}. All spectra were recorded at 16K.

Lomb 0.25m spectrometer did not detect any fluorescence for excitation at 560.9 or 561.5 nm nor did monitoring in zero order on the SPEX 1700 single monochromator. From the concentration dependence of the absorption peaks, these centres would appear to be clusters. No fluorescence from these centres can be detected to the limits of the detection sensitivities available. It is concluded that extremely efficient cross-relaxation processes must dominate the relaxation mechanisms in these centres. A more extensive study of these centres is given in chapter 7.

Two additional centres observed in excitation, arbitrarily labelled C1 and C2, have excitation features at 17834 and 17855 cm^{-1} and 17799 and 17913 cm^{-1}, respectively. These transitions are one tenth the intensity of the O centre transitions. The spectra for these centres are shown in Figures 5.4(d) and (e). Excitation of the $Z_1 \rightarrow A_2$ transition of the C2 centre is particularly difficult since this transition is substantially overlapped by the A centre $Z_1 \rightarrow A_2$ transition at 17908 cm^{-1}.

After 30 minutes oxygenation treatment (as described in chapter three), the crystals were still perfectly clear and without any damage from the penetration of the oxygen ions. Two strong excitation features associated with an oxygen charge compensated Sm^{3+} ion, are observed at 17511 and 18095 cm^{-} (Figure 5.4(b)). The common form of charge compensation involving an O^{2-} ion is that where an oxygen ion resides in a nearest neighbour position along a $\langle 111 \rangle$ direction. It has been labelled the G1 centre. It is noted that as the severity of the oxygenation increases, an additional centre associated with oxygen charge compensation grows in intensity. A transition associated with this centre is present in the $^6H_{\frac{5}{2}} \rightarrow ^4G_{\frac{5}{2}}$ excitation spectrum of Figure 5.3 that has a measured excitation frequency of 17456 cm^{-1}. The fluorescence spectra of this centre have not been studied here.

Figures 5.5 and 5.8 show excitation to the $^4F_{\frac{3}{2}}$ multiplet at around 18970 cm^{-1}. Coumarin 540 was the appropriate dye to excite these transitions. This dye can also reach the $^4G_{\frac{5}{2}}$ multiplet at 17850 cm^{-1}. However, it fails to completely cover the range of excitation features observed, particularly after the crystals are oxygenated. The excitation transitions observed to $^4F_{\frac{3}{2}}$ mimic the site distribution observed for excitation of $^4G_{\frac{5}{2}}$. The A centre $Z_1 \rightarrow B_1$ transition at 18950 cm^{-1} dominates all other excitation features. Excitation transitions of the G1 oxygen centre are identifiable using a 1000 fold magnification of the detection sensitivity. The excitation frequencies of these centres, as well as the O, C_1 and C_2 centres are given in Table 5.2.

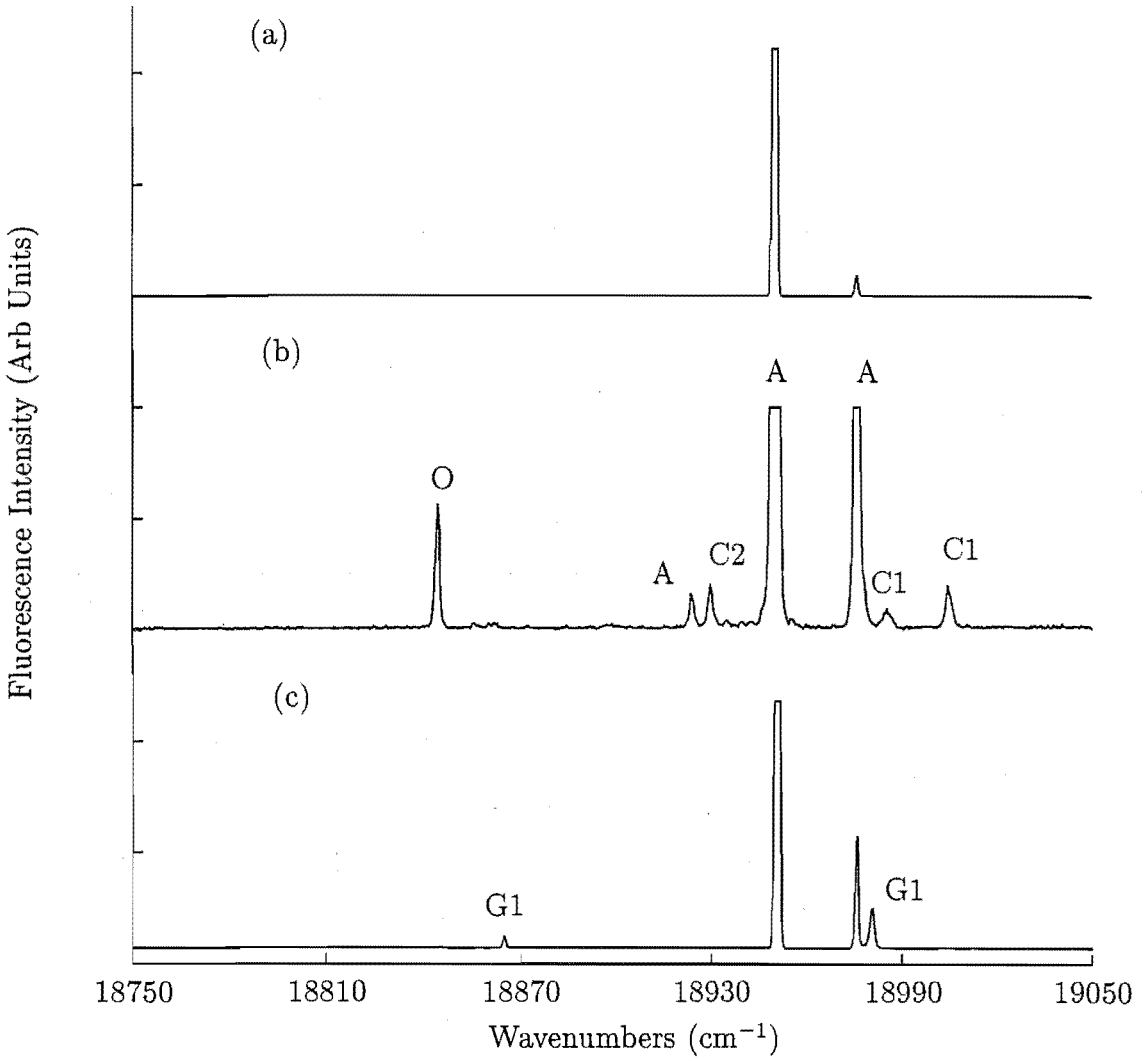

Figure 5.5: Excitation spectra of the $^4F_{\frac{3}{2}}$ multiplet in CaF_2:0.05%Sm^{3+} for broadband detection monitoring all fluorescence in zero order on the SPEX 1700 (a) As grown crystals, (b) × 100 and (c) After 30 minutes oxygenation. All spectra were recorded at 16K. The low frequency A centre transition in (b) is a transition from Z_2 at 47 cm^{-1}.

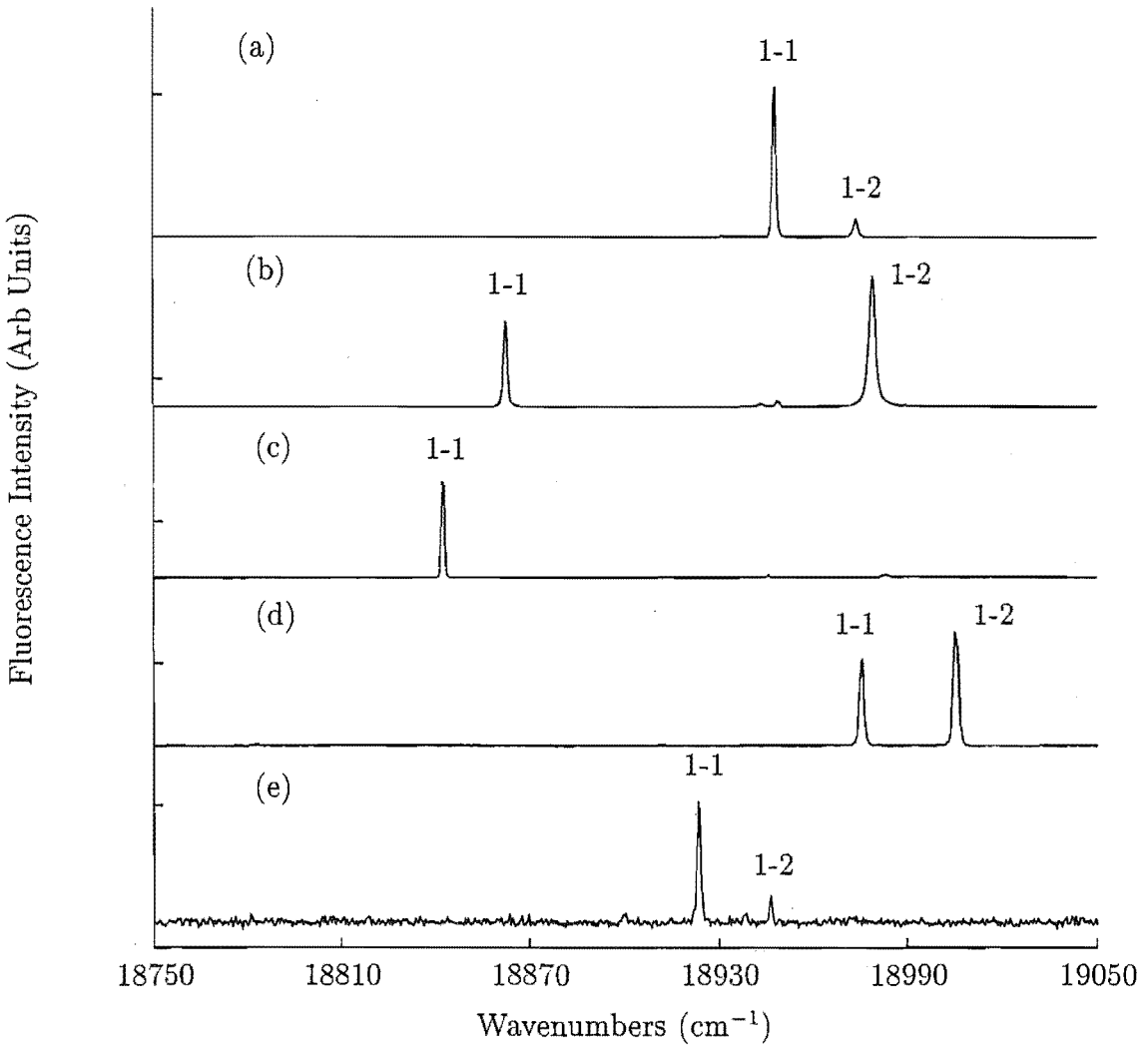

Figure 5.6: Narrowband excitation spectra of the (a) A centre monitoring at 17837 cm^{-1}, (b) the G1 centre monitoring at 17511 cm^{-1}, (c) the O centre monitoring at 17654 cm^{-1}, (d) the C1 centre monitoring at 17854 cm^{-1} and (e) the C2 centre monitoring at 17799 cm^{-1} for the $^4F_{\frac{3}{2}}$ multiplet in CaF_2:0.05%Sm^{3+}. All spectra were recorded at 16K.

Table 5.2: Excitation frequencies of the A, G1, O, C1, C2 centres for the $^4G_{\frac{5}{2}}$ and $^4F_{\frac{3}{2}}$ multiplets in CaF_2:0.05%Sm^{3+}. All energies are as measured in air and have an uncertainty of ± 1 cm^{-1}.

Multiplet	Level	A	G1	O	C1	C2
	A_1	17837	17511	17653	17834	17799
$^4G_{\frac{5}{2}}$	A_2	17908	18095	18053	17855	17913
	A_3	18240	-	-	-	-
$^4F_{\frac{3}{2}}$	B_1	18950	18867	18842	18975	18939
	B_2	18976	18981	-	18996	18954

5.2.3 A Centre Fluorescence

A centre emission, from the $^4G_{\frac{5}{2}}$ multiplet to the crystal field levels of the ^6H_J and ^6F_J multiplets was recorded. The crystal temperature was 16K for all spectra. A standard concentration of 0.05% of the Sm^{3+} ions was used. In most cases, centre selective spectra were recorded pumping the $^6H_{\frac{5}{2}}Z_1 \rightarrow {}^4G_{\frac{5}{2}}A_1$ transition at 17837 cm^{-1}. For fluorescence to the $^6H_{\frac{5}{2}}$ multiplet, the $^6H_{\frac{5}{2}}Z_1 \rightarrow {}^4G_{\frac{5}{2}}A_3$ transition, at 18240 cm^{-1}, was pumped.

Figure 5.7(a) shows the fluorescence spectrum to the $^6H_{\frac{5}{2}}$ multiplet. The dominant features of the spectrum are the $A_1 \rightarrow Z_1$ and $A_1 \rightarrow Z_2$ transitions at 17837 and 17790 cm^{-1}, respectively. Group theory predicts three levels for a $J=\frac{5}{2}$ multiplet in a tetragonal C_{4v} symmetry crystal field. We have observed the two levels of the split cubic ground state Γ_8 energy level, however the $\Gamma_7\gamma_7$ will be much harder to observe. This is because it lies amongst phonon sidebands coupled to the $A_1 \rightarrow Z_1$ and Z_2 electronic transitions. These transitions are shown in Figure 5.8. This structure extends to a displacement of close to 400 cm^{-1} from the 'zero phonon' electronic transitions. We can identify many intensity maxima as corresponding to peaks in the CaF_2 host lattice phonon spectrum [84], [85], [86], [87], [88], [90], [89]. The corresponding phonon energies are presented in Table 5.3.

An additional feature at 17653 cm^{-1} is assigned as the O centre $A_1 \rightarrow Z_1$ transition. This is excited because the A centre $Z_1 \rightarrow A_3$ transition, overlaps vibronic bands associated with the O centre.

The $^4G_{\frac{5}{2}} \rightarrow {}^6H_{\frac{7}{2}}$ fluorescence spectrum is given in Figure 5.7(b). In this case, the $Z_1 \rightarrow A_1$ absorption transition at 17837 cm^{-1} is excited. Four electronic transitions are observed in the 16900-16300 cm^{-1} region, all emanating from the A_1 level. The spectrum is dominated by an asymmetrical feature, at a frequency of 16677 cm^{-1}.

Table 5.3: Energies of the vibronic sideband peaks (in air (± 1 cm^{-1})) observed coupled to the 17837 cm^{-1} $A_1 \rightarrow Z_1$ transition. The notations TA, TO and LO indicate the transverse acoustic, transverse optical and longitudinal optical phonon modes respectively whilst X and L are the $\langle 100 \rangle$ and $\langle 111 \rangle$ directions.

Transition Energy	Shift From 17837 cm^{-1}	Assignment
17737	151	TA(X)
17611±5	226	-
17568	269	TO(L)
17540±10	297	LO(L)
17492	345	TO(X)
17467	370	LO(L)
17442	395	LO(X)

This corresponds to the $A_1 \rightarrow Y_2$ transition and places the Y_2 level at 1160 cm^{-1}. The asymmetry is undoubtedly associated with the A centre as the relative intensity of all features does not change, upon tuning through the $Z_1 \rightarrow A_1$ electronic resonance or even for pumping the $Z_1 \rightarrow A_2$ transition at 17908 cm^{-1}. The shoulder is at 16703 cm^{-1}, a shift of 148 cm^{-1} from the $A_1 \rightarrow Y_1$ transition. From this, we assign the origin of the shoulder as a transition terminating on the TA(X) vibronic of the host lattice. The $A_1 \rightarrow Y_1$ transition at 16851 cm^{-1}, is twenty seven times weaker but well isolated and clear. The energies of these $^6H_{\frac{7}{2}}$ states are given in Table 5.4 which also presents the measured polarisation data. From theory, four electronic energy levels are expected for a J=$\frac{7}{2}$ multiplet under C_{4v} symmetry ($2\gamma_6+2\gamma_7$). The remaining two transitions are found at 16524 and 16419 cm^{-1} respectively. The stronger feature at 16485 cm^{-1} is assigned as vibronic in origin. This transition is 366 cm^{-1} from the transition to the Y_1 state and 192 cm^{-1} from the transition to the Y_2 state. Thus, assignment to a specific phonon peak is difficult.

Transitions to the $^6H_{\frac{9}{2}}$ multiplet occur in the 15700-15200 cm^{-1} region. All five expected transitions are observed. The spectrum is given in Figure 5.7(c).

Fluorescence to the $^6H_{\frac{11}{2}}$ multiplet has been recorded. The four fluorescence transitions detected to this multiplet, occur in the 14400-13900 cm^{-1} region. This is shown in Figure 5.9(a). Only the $A_1 \rightarrow W_1$, W_2 and W_5 transitions are observed. The remaining transition, at 14180 cm^{-1}, terminates on a lattice vibronic level.

Fluorescence to the $^6H_{\frac{13}{2}}$ multiplet is observed in the 13000-12400 cm^{-1} region. Six transitions are observed. Only the $A_1 \rightarrow V_4$ is not apparant. The spectra are shown in Figure 5.9(b).

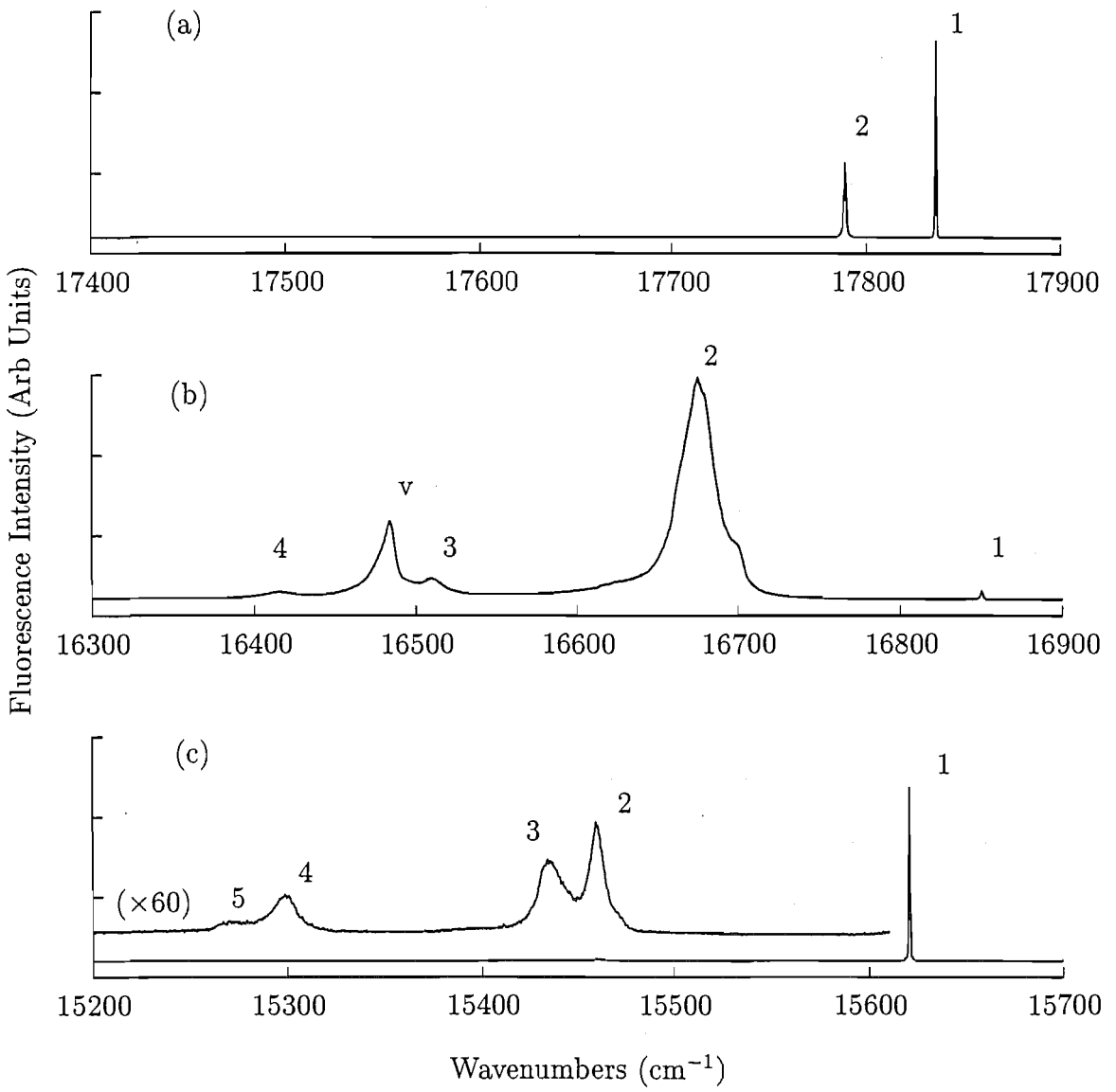

Figure 5.7: Fluorescence spectrum of the A centre for transitions from $^4G_{\frac{5}{2}}$ to (a) the $^6H_{\frac{5}{2}}$ multiplet, (b) the $^6H_{\frac{7}{2}}$ multiplet and (c) the $^6H_{\frac{9}{2}}$ multiplet in CaF_2:0.05%Sm^{3+}. For measurement of the $^4G_{\frac{5}{2}} \rightarrow {}^4F_{\frac{5}{2}}$ spectrum the 18240 cm^{-1} $Z_1 \rightarrow A_3$ absorption transition was excited, while for all others the 17837 cm^{-1} transition was excited. The spectra were recorded at 16K.

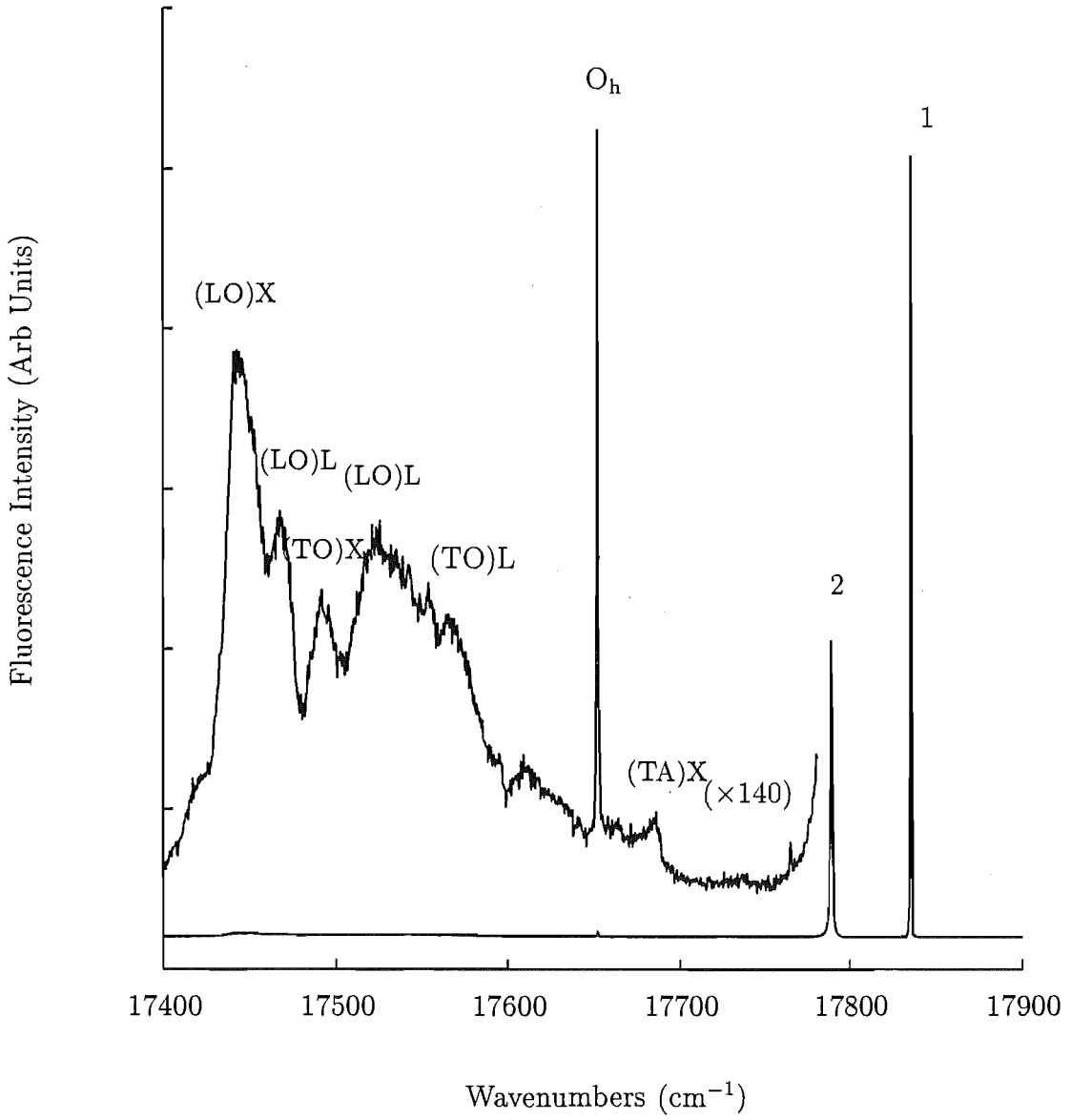

Figure 5.8: 16K vibronic sideband coupling to the $A_1 \rightarrow Z_1$ transition of the A centre in CaF_2:0.05%Sm^{3+}

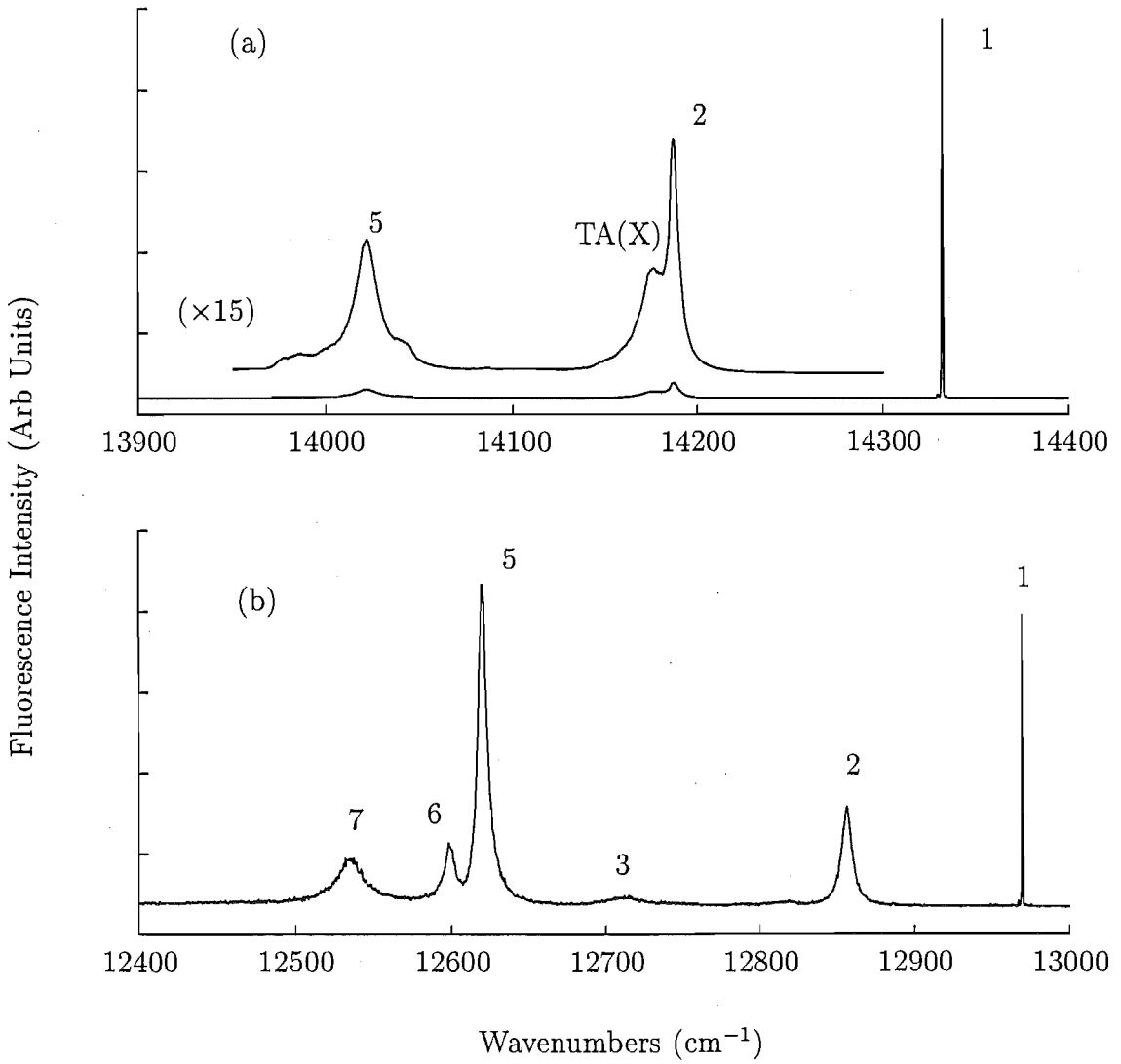

Figure 5.9: Fluorescence spectrum for the A centre for transitions from $^4G_{\frac{5}{2}}$ to (a) the $^6H_{\frac{11}{2}}$ multiplet and (b) the $^6H_{\frac{13}{2}}$ multiplet in CaF_2:0.05%Sm^{3+}. Excitation is at the 17837 cm^{-1} $Z_1 \rightarrow A_1$ absorption transition. The spectra were recorded at 16K.

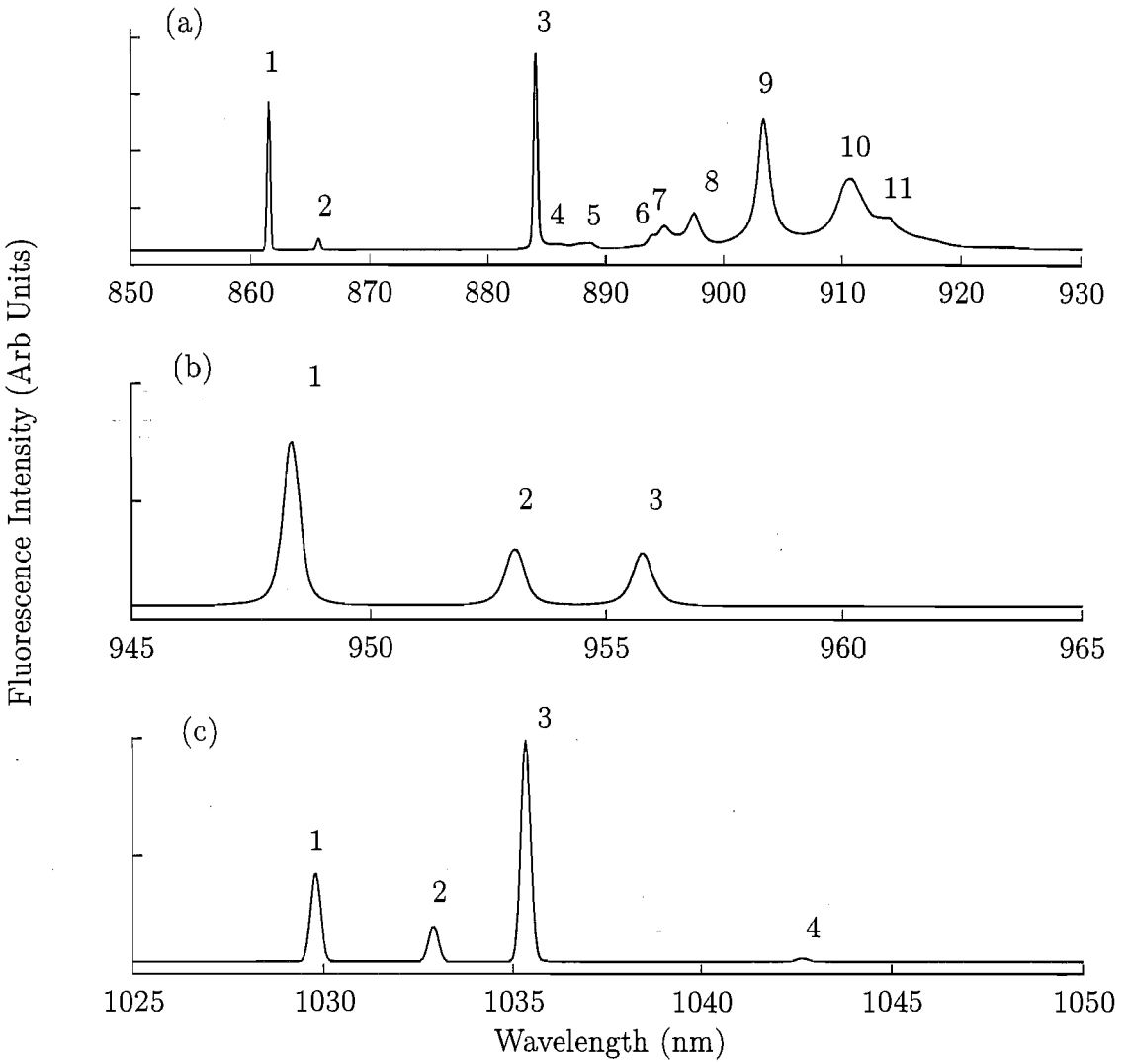

Figure 5.10: Fluorescence spectra for the A centre for transitions $^4G_{\frac{5}{2}}$ to (a) the $^6H_{\frac{15}{2}}$, $^6F_{\frac{1}{2}}$ and $^6F_{\frac{3}{2}}$ multiplets, (b) the $^6F_{\frac{5}{2}}$ multiplet and (c) the $^6F_{\frac{7}{2}}$ multiplet in CaF_2:0.05%Sm^{3+}. Excitation is at the 17837 cm^{-1} $Z_1 \rightarrow A_1$ absorption transition. The spectra were recorded at 16K.

Table 5.4: Transition frequencies (air cm^{-1} ± 1 unless otherwise stated), measured polarisation ratios and terminating states for emission from the $^4G_{\frac{5}{2}}$ to the $^6H_{\frac{5}{2},\frac{7}{2},\frac{9}{2},\frac{11}{2},\frac{13}{2},\frac{15}{2}}$ and $^6F_{\frac{1}{2},\frac{3}{2},\frac{5}{2},\frac{7}{2}}$ multiplets of the A centre in CaF_2:0.05%Sm^{3+}.

Multiplet	Terminating State		Transition	Polarisation Ratio	
	Label	Energy	Frequency	ZX	ZY
$^6H_{\frac{5}{2}}$	Z_1	0	17837	1.8	1.0
	Z_2	47	17790	1.0	1.1
$^6H_{\frac{7}{2}}$	Y_1	985	16851	1.7	1.0
	Y_2	1160	16677	2.4	1.0
	Y_3	1313	16524	1.8	1.0
	Y_4	1418	16419	1.7	1.0
$^6H_{\frac{9}{2}}$	X_1	2215	15622	1.0	1.7
	X_2	2377	15460	1.0	1.7
	X_3	2404	15433	1.0	1.6
	X_4	2537	15300	1.5	1.0
	X_5	2568	15269±5	1.0	1.6
$^6H_{\frac{11}{2}}$	W_1	3504	14333	1.0	1.9
	W_2	3649	14188	1.9	1.0
	W_5	3815	14022	1.0	1.6
$^6H_{\frac{13}{2}}$	V_1	4867	12970	1.0	1.1
	V_2	4982	12855	1.0	1.7
	V_3	5126	12711±5	1.3	1.0
	V_5	5217	12620	2.1	1.0
	V_6	5239	12598	1.0	1.5
	V_7	5301	12536	2.6	1.0
$^6H_{\frac{15}{2}}$, $^6F_{\frac{1}{2}}$ and $^6F_{\frac{3}{2}}$	S_1	6232	11605	1.6	1.0
	S_2	6286	11551	1.0	1.0
	S_3	6525	11312	1.2	1.0
	S_4	6557	11280	1.1	1.0
	S_5	6585	11252±5	1.1	1.0
	S_6	6649	11188	1.1	1.0
	S_7	6667	11170	1.3	1.0
	S_8	6692	11145	1.3	1.0
	S_9	6766	11071	1.0	1.3
	S_{10}	6852	10985±5	1.3	1.0
	S_{11}	6885	10952	-	-
$^6F_{\frac{5}{2}}$	R_1	7291	10546	1.7	1.0
	R_2	7343	10494	1.0	1.0
	R_3	7372	10465	1.0	1.3
$^6F_{\frac{7}{2}}$	Q_1	8125	9712	1.2	1.0
	Q_2	8155	9682	1.4	1.0
	Q_3	8175	9662	1.9	1.0
	Q_4	8247	9590	1.1	1.0

Figure 5.10(a) shows a more complex spectrum for the close lying $^6H_{\frac{15}{2}}$, $^6F_{\frac{1}{2}}$ and $^6F_{\frac{3}{2}}$ multiplets. The fluorescence transitions for these multiplets were detected on a SPEX 1700 single monochromator with an RCA 7102 photomultiplier tube, liquid nitrogen cooled to -100 °C. This tube has a spectral response between 800 and 1050 nm in the near infrared. As the crystal field levels of the $^6H_{\frac{15}{2}}$, $^6F_{\frac{1}{2}}$ and $^6F_{\frac{3}{2}}$ multiplets will be heavily mixed by the crystal field, to label them independently would be misleading. Therefore, a single alphabetical label of S_a (where a=1,2,3...,12) has been adopted for the crystal field levels of these three multiplets. The transition frequencies are given in Table 5.4.

Figures 5.10(b) and (c) show the $^4G_{\frac{5}{2}}$ to $^6F_{\frac{5}{2}}$ and $^6F_{\frac{7}{2}}$ fluorescence spectra, respectively. Both spectra are very clear with the site-selective fluorescence being well discriminated. Three transitions are observed to the $^6F_{\frac{5}{2}}$ multiplet and four transitions are observed to the $^6F_{\frac{7}{2}}$ multiplet.

Polarisation studies have been completed for the A centre that yield some information about the nature of the transitions observed. For excitation of the $Z_1 \rightarrow A_1$ transition at 17837 cm^{-1}, the observed fluorescence is known to polarise in the X(ZX)Z:X(ZY)Z geometry (from here on denoted ZX:ZY) for ⟨100⟩ oriented crystals. This yields 2:1 type polarisation ratios, confirming the centre is of C_{4v} symmetry (Table 5.4). To get meaningful polarisation ratios for excitation of Kramers ions in centres of C_{4v} symmetry, it is necessary to pump transitions between levels that transforms as dissimilar C_{4v} irreps. This aviods exciting different centres contributing to the absorption intensity in different polarisations - see chapter three. The calculations of Reid and Butler [91] (1982) for the A centre in CaF_2:Sm^{3+}, have placed the $^6H_{\frac{5}{2}}\Gamma_8\gamma_6$ state lowest in energy. This assignment yields g values consistent with Antipin et. al. [78] (1965).

The reduction of symmetry for the RE^{3+} from cubic to tetragonal will split the $^4G_{\frac{5}{2}}$ multiplet into $2\gamma_7 + \gamma_6$ C_{4v} irreps. The A_1 and A_3 states are assigned as having γ_7 symmetry. This is because excitation of these transitions give the most distinct polarisation ratios. Thus, for excitation of the $A_3\gamma_7$ state in the ZX:ZY geometry, the observed ratio of 1.8:1 is entirely consistent with a σ' (md) $A_1\gamma_7 \rightarrow Z_1\gamma_6$ transition. The remaining $^4G_{\frac{5}{2}}$ state must transform as a γ_6 irrep.

Since it is the ZX:ZY polarisation geometry which gives the strongest polarisation effects, we can infer that the $^6H_{\frac{5}{2}}$ to $^4G_{\frac{5}{2}}$ transitions are of predominately magnetic dipole character. This is something that might be expected since magnetic dipole transitions will be strongest for $\Delta J=0,\pm1$ transitions. Magnetic dipole transitions will also be present for transitions which do not obey this selection rule because the

crystal field will induce admixtures of states of different J into levels of nominally single J. This effect is particularly prominent amongst the crystal field levels of the ^6H_J and ^6F_J multiplets. A consequence of this is that the measured polarisation ratios are not well defined for Sm^{3+} ions as the emission is of comparable electric and magnetic dipole character. This tends to force the ratio towards 1:1. Thus, minimal information is obtained on the irrep symmetry labels of the electronic levels by polarisation studies.

5.2.4 O Centre Fluorescence

Emission from the $^4G_{\frac{5}{2}}$ multiplet to levels of the ^6H_J and ^6F_J multiplets have been recorded for excitation of the O centre $^4G_{\frac{5}{2}}$ absorption transitions. Concentrations of 0.05 molar % of Sm^{3+} was used as for the A centre. Polarisation measurements were made with both $\langle 111 \rangle$ and $\langle 100 \rangle$ oriented samples with no polarisation dependence apparant for either crystal orientation. This corroborates the assignment of this centre as an isolated rare earth ion with non-local charge compensation. As with the cubic 'O' centre in CaF_2:0.05%Eu^{3+} [92] and the cubic centre in CaF_2:Er^{3+} [90], [93], [94], the cubic centre observed in CaF_2:0.05%Sm^{3+} is present in significant concentrations. Particularly, at rare earth dopant concentrations greater than 0.05%. This is a consequence of fluorine gettering by cluster centres leaving isolated Sm^{3+} ions in the lattice. Hydrogenation and oxygenation is also known to promote the cubic centre populations. Cockcroft et. al. [95] (1990) speculate that as H^- ions substitute for lattice F^- ions in the vicinity of the 'cubic' (or more appropriately, remotely compensated) centres, the inversion symmetry is lowered therefore relaxing the selection rules for electric dipole transitions. However, the pump transitions in Sm^{3+} doped CaF_2 and SrF_2 crystals ($^6H_{\frac{5}{2}} \rightarrow ^4G_{\frac{5}{2}}$) are magnetic dipole transitions and therefore, a relaxation of the selection rules is not required.

Figures 5.11 to 5.13 show the fluorescence spectra obtained. Strong coupling to the lattice is evident in the $^6H_{\frac{7}{2}}$, $^6H_{\frac{9}{2}}$, $^6H_{\frac{11}{2}}$ and $^6H_{\frac{13}{2}}$ spectra by the presence vibronic sidebands. These vibronic peaks are denoted as v or, where possible, by the appropriately assigned phonon mode in the presented spectra. Often, it is comparatively easy to identify such phonon sidebands by their frequency displacement from the electronic transitions or the width and symmetry of the lineshapes. The peculiar phonon sideband lineshapes arise as the transitions reflect the broad and asymmetric distribution of phonon energies.

The cubic crystal field experienced by the Sm^{3+} ion in the O centre, can be approximated by the cubic component of the A centre crystal field. Therefore, cubic crystal field parameters of magnitude B_C^4=-1200 cm^{-1} and B_C^6=650 cm^{-1} should adequately

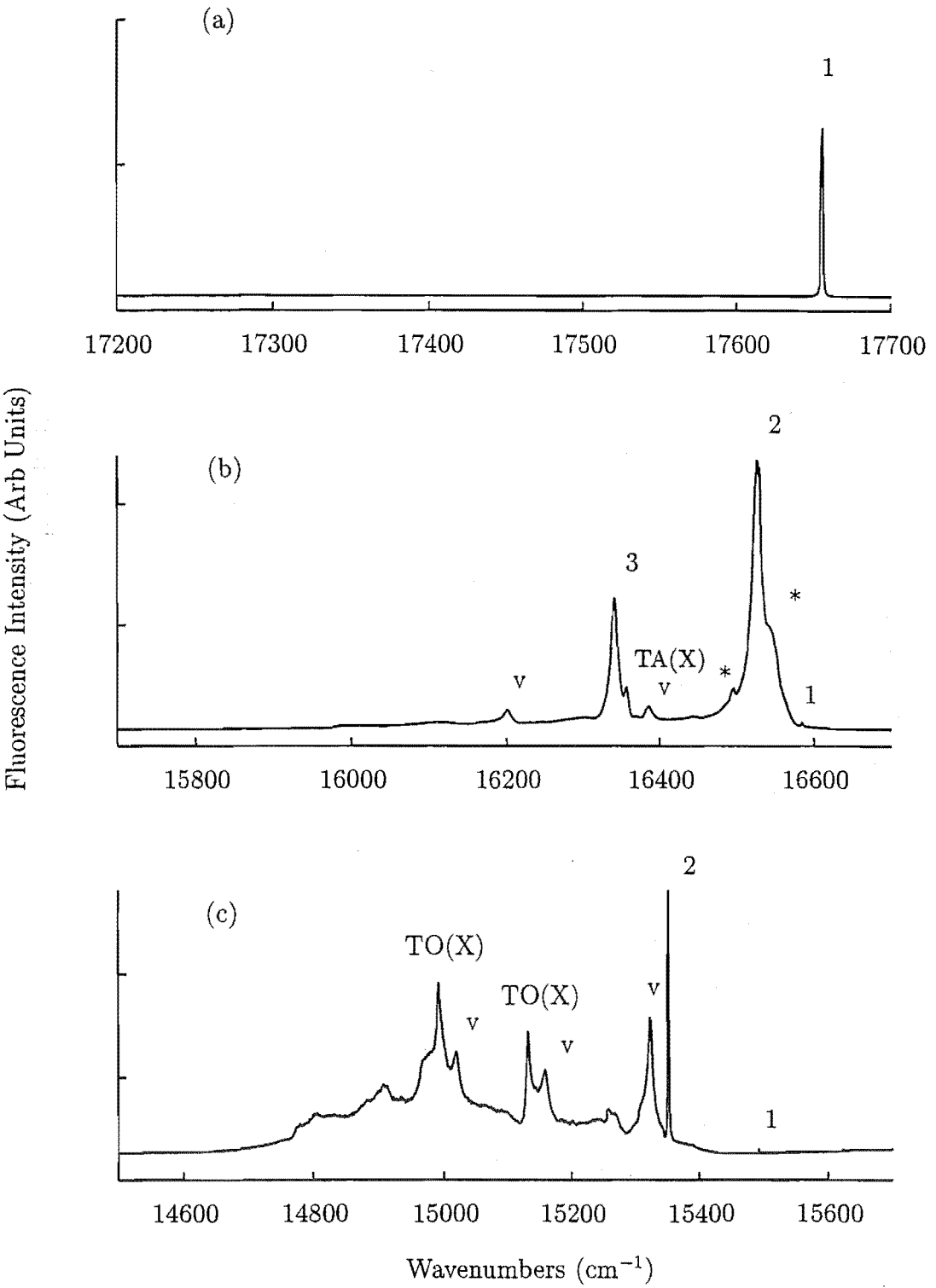

Figure 5.11: 16K fluorescence spectrum of the O centre for transitions $^4G_{\frac{5}{2}}$ to (a) $^6H_{\frac{5}{2}}$, (b) $^6H_{\frac{7}{2}}$ and (c) $^6H_{\frac{9}{2}}$ in CaF_2:0.05%Sm^{3+}. Excitation is at the 18053 cm^{-1} $Z_1 \rightarrow A_2$ absorption transition for (a) and the $Z_1 \rightarrow A_1$ transition at 17511 cm^{-1} for (b) and (c). * indicates an unassigned feature. The spectra were recorded at 16K.

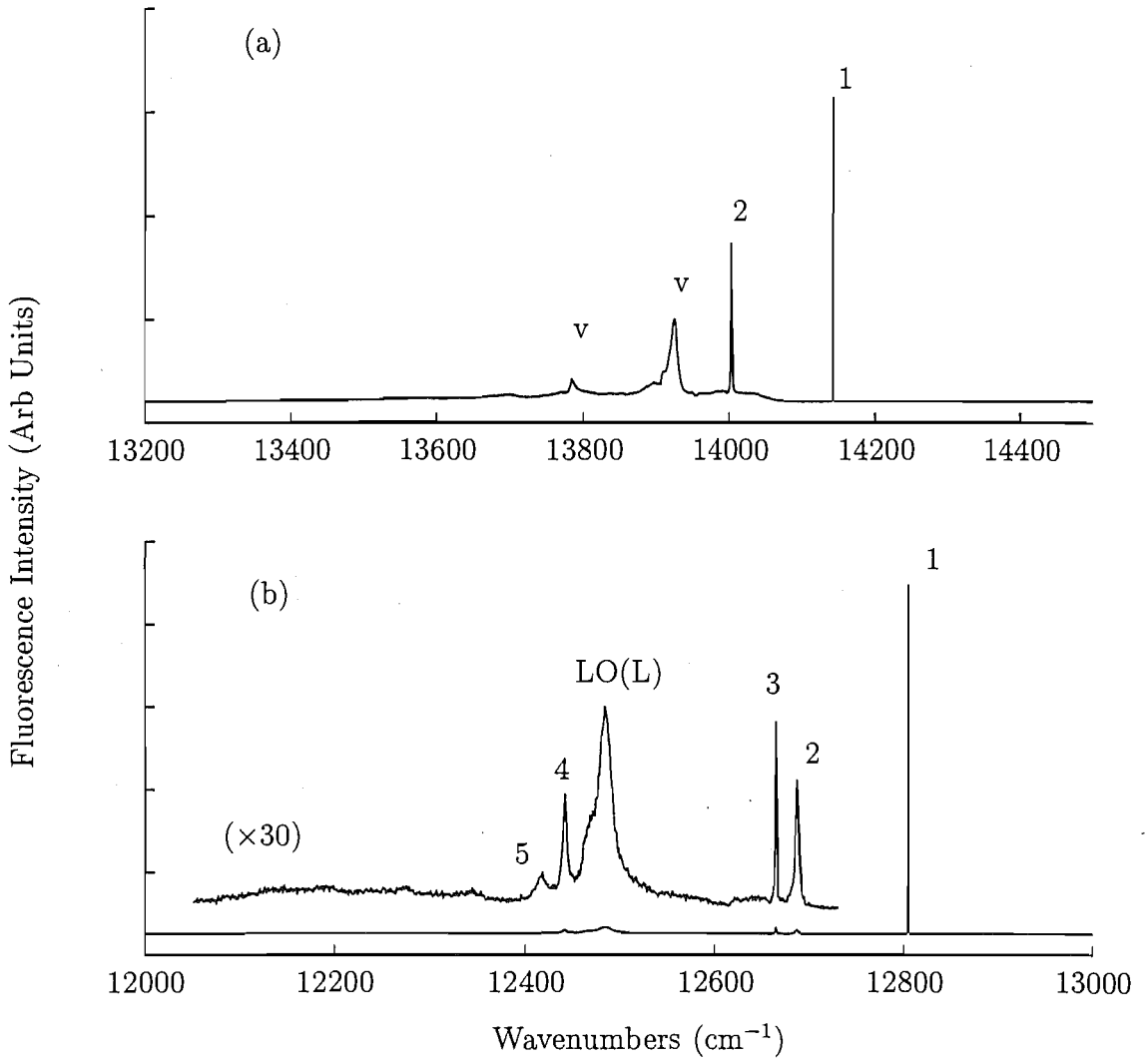

Figure 5.12: Fluorescence spectrum of the O centre for transitions $^4G_{\frac{5}{2}}$ to the (a) $^6H_{\frac{11}{2}}$ and (b) $^6H_{\frac{13}{2}}$ multiplets in CaF_2:0.05%Sm^{3+}. Excitation is at the 17653 cm^{-1} $Z_1 \rightarrow A_1$ absorption transition. The spectre were recorded at 16K.

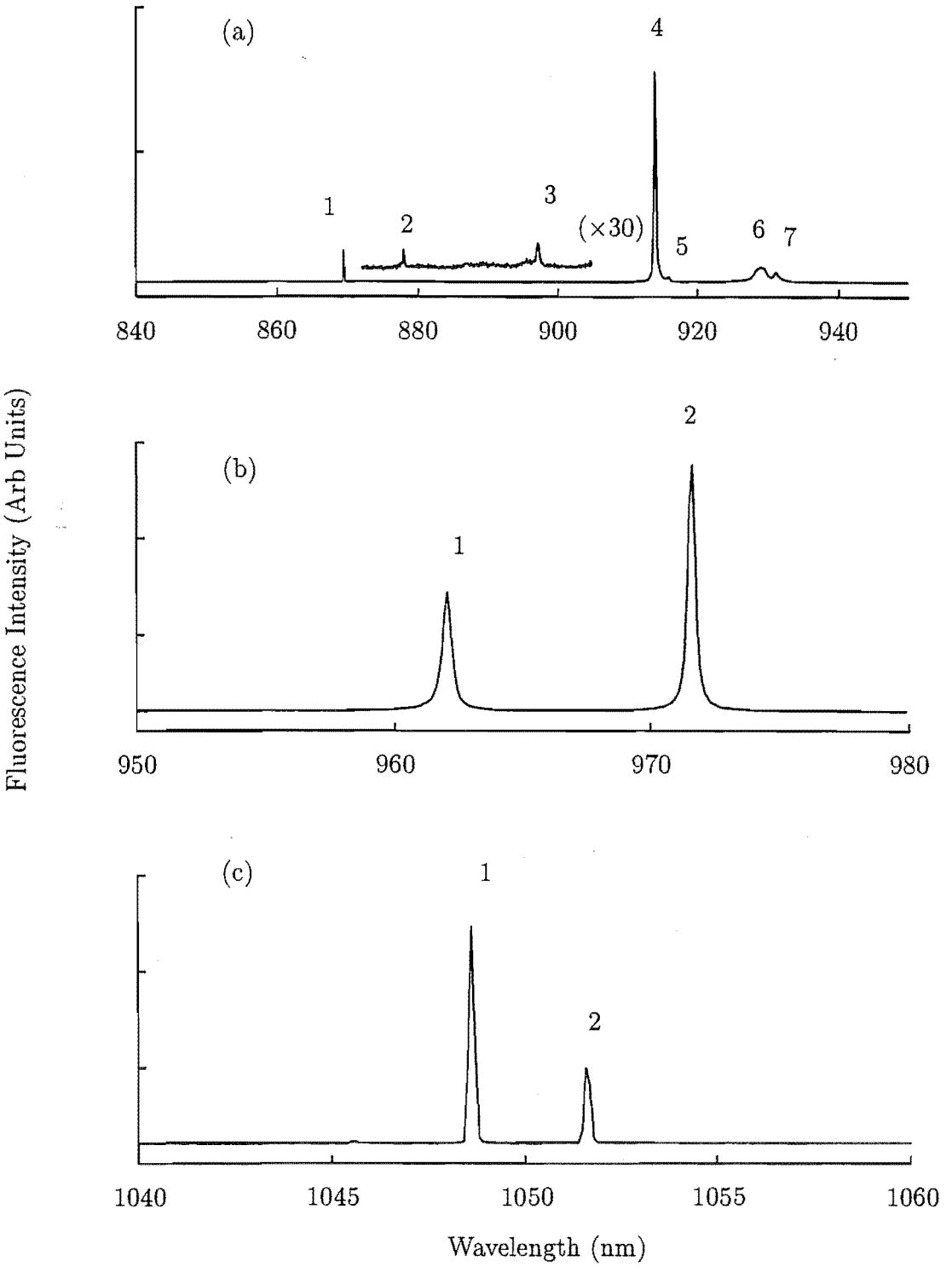

Figure 5.13: Fluorescence spectrum of the O centre for transitions $^4G_{\frac{5}{2}}$ to the (a) $^6H_{\frac{15}{2}}$, $^6F_{\frac{1}{2}}$, $^6F_{\frac{3}{2}}$, (b) $^6F_{\frac{5}{2}}$ and (c) $^6F_{\frac{7}{2}}$ multiplets in CaF_2:0.05%Sm^{3+}. Excitation is at the 17653 cm^{-1} $Z_1 \rightarrow A_1$ absorption transition. The spectra were recorded at 16K.

Table 5.5: Transition frequencies (air $cm^{-1}\pm1$ unless otherwise stated) and assignments for electronic transitions of the O centre in CaF_2:0.05%Sm^{3+}

Multiplet	Transition Frequency	State Energy	Transition Assignment
$^6H_{\frac{5}{2}}$	17653	0	$A_1\Gamma_7 \rightarrow Z_1\Gamma_8$
$^6H_{\frac{7}{2}}$	16583	1070	$A_1\Gamma_7 \rightarrow Y_1\Gamma_6$
	16523	1130	$A_1\Gamma_7 \rightarrow Y_2\Gamma_7$
	16339	1314	$A_1\Gamma_7 \rightarrow Y_3\Gamma_8$
$^6H_{\frac{9}{2}}$	15490	2163	$A_1\Gamma_7 \rightarrow X_1\Gamma_6$
	15351	2302	$A_1\Gamma_7 \rightarrow X_2\Gamma_8$
$^6H_{\frac{11}{2}}$	14142	3511	$A_1\Gamma_7 \rightarrow W_1\Gamma_8$
	14002	3651	$A_1\Gamma_7 \rightarrow W_3\Gamma_8$
$^6H_{\frac{13}{2}}$	12804	4849	$A_1\Gamma_7 \rightarrow V_1\Gamma_8$
	12686	4967	$A_1\Gamma_7 \rightarrow V_2\Gamma_7$
	12664	4989	$A_1\Gamma_7 \rightarrow V_3\Gamma_8$
	12440	5213	$A_1\Gamma_7 \rightarrow V_4\Gamma_7$
	12418±2	5235	$A_1\Gamma_7 \rightarrow V_5\Gamma_6$
$^6H_{\frac{15}{2}}$, $^6F_{\frac{1}{2}}$ and $^6F_{\frac{3}{2}}$	11499	6154	$A_1\Gamma_7 \rightarrow S_1\Gamma_8$
	11394	6259	$A_1\Gamma_7 \rightarrow S_2\Gamma_6$
	11153	6500	$A_1\Gamma_7 \rightarrow S_3\Gamma_6$
	10939	6714	$A_1\Gamma_7 \rightarrow S_4\Gamma_8$
	10917	6736	$A_1\Gamma_7 \rightarrow S_5\Gamma_8$
	10759	6894	$A_1\Gamma_7 \rightarrow S_6\Gamma_7$
	10739	6914	$A_1\Gamma_7 \rightarrow S_7\Gamma_8$
$^6F_{\frac{5}{2}}$	10393	7260	$A_1\Gamma_7 \rightarrow R_1\Gamma_7$
	10291	7362	$A_1\Gamma_7 \rightarrow R_2\Gamma_8$
$^6F_{\frac{7}{2}}$	9536	8117	$A_1\Gamma_7 \rightarrow Q_1\Gamma_7$
	9509	8144	$A_1\Gamma_7 \rightarrow Q_2\Gamma_8$

account for the gross features of the manifold splittings. Such a calculation predicts that the $^4G_{\frac{5}{2}}$ multiplet splits into two cubic levels of Γ_8 and Γ_7 symmetry, with the Γ_7 level lowest. From this, we assign the 17654 cm^{-1} state as $A_1\Gamma_7$ and the 18053 cm^{-1} state as $A_2\Gamma_8$. This assignment is interesting as emission to crystal field levels transforming as a Γ_6 irrep of the cubic group should not be allowed from the $A_1\Gamma_7$ state.

The number of transitions observed exceeds the maximum number allowed, if this strict cubic symmetry selection rule is obeyed. Therefore, the centre cannot be of exact cubic symmetry. Table 5.5 summarises the observed electronic transitions. This table also gives a set of tentative transition assignments based on a cubic crystal field calculation that employs the parameters given above.

The observation that the centre is not of exact cubic symmetry is not unexpected as the centre still requires charge compensation. This is provided non-locally. However, the charge compensating fluorine ion may be in sufficiently close spatial proximity, to provide a weak axial distortion. Then the crystal field wavefunctions would no longer be pure cubic field wavefunctions.

5.2.5 G1 Centre Fluorescence

Many EPR experiments have reported the presence of trigonal oxygen centres in CaF_2:Sm^{3+} crystals. The oxygen has been generally introduced as an unintentional impurity during crystal growth [8], [79]. The O^{2-} ions, can then charge compensate the Sm^{3+} ions taking the position of a substitutional F^- ion, in a nearest neighbour position along a $\langle 111 \rangle$ direction. This creates a centre of C_{3v} symmetry. In this study, oxygen ions have been introduced into CaF_2:Sm^{3+} crystals deliberately. This was done using the method described in chapter three. Several previous optical studies of the CaF_2:Sm^{3+}:O^{2-} system [96], [97] have been completed. However, this is the first laser selective excitation study known to the author. The fluorescence spectra obtained are shown in Figures 7.14 throught to 7.16.

Muto and Awazu [96] have observed a similar emission spectrum to that observed here after the deliberate addition of oxygen ions into CaF_2:Sm^{3+} crystals. However, in their case additional emission lines are observed. This is probably due to the creation of more complex oxygen compensated centres, such as those observed by Newman and Woodward [80] for SrF_2:Sm^{3+}. Muto and Awazu state that their samples were opaque in colour, tending to support this assertion. These authors also claim that oxygen was easily diffused into the crystals in a moist atmosphere but that difficulty was had in obtaining good oxygen penetration in an O_2 atmosphere.

This has not been found to be the case in this study, where oxygenation periods of as little as 15 minutes were adequate to obtain significant quantities of oxygen into the crystals. This was judged by the comparative strengths of the A and G1 centre $^4G_{\frac{5}{2}}$ excitation strengths. In fact, oxygen was found to enter the CaF_2 lattice (and charge compensate the rare earth ions) so readily that precautions had to be taken during crystal growth to avoid contaminating crystals with (generally) unwanted oxygen. The oxygenated crystals used in this study were clear, with minimal damage created by the oxygenation process. It has been noted that for more heavily oxygenated samples, an excitation feature belonging to an additional, distinct oxygen centre is observed at 17456 cm^{-1}. This centre has not been studied in this work.

For excitation of the $^4G_{\frac{5}{2}}A_2$ state at 18095 cm^{-1}, three emission peaks are observed to the $^6H_{\frac{5}{2}}$ ground multiplet in the 17550-17000 cm^{-1} region (see Figure 5.14(a)). Two features of comparable intensities are observed at 17511 and 17476 cm^{-1}. These correspond to the $A_1 \rightarrow Z_1$ and Z_2 transitions. This places the Z_2 state, 35 cm^{-1} above the ground state. A broad, weaker feature at 17090 cm^{-1} is the $A_1 \rightarrow Z_3$ transition. The Z_3 state is therefore determined to be 421 cm^{-1} higher in energy than the ground state. Polarisation studies of the exciting beam and emitted fluorescence reveals a weak polarisation dependence for $\langle 111 \rangle$ oriented crystals in the ZX:ZY polarisation geometry (Table 5.6). For $\langle 100 \rangle$ oriented crystals, the G1 centre fluorescence transitions display no polarisation effects. This confirms the symmetry of the centre as C_{3v} and indicates that as with the O and A centres, the absorption transition is of magnetic dipole character. No attempt is made to assign irrep symmetry labels or to analyse the spectra in terms of a crystal field model as the polarisation effects are weak.

An interesting feature is observed at 1013.56 nm. This is amongst fluorescence to the overlapping $^6H_{\frac{15}{2}}$, $^6F_{\frac{1}{2}}$, $^6F_{\frac{3}{2}}$ and $^6F_{\frac{5}{2}}$ multiplets. The feature is extremely sharp. Its occurence is somewhat anomalous since if it is a G1 centre transition it should be broad, given the numerous relaxation pathways available to it. An alternative explanation is that we are observing emission from the $^6F_{\frac{11}{2}}$ multiplet at 10600 cm^{-1}. However, we would then expect to see a transition to the first excited state of the $^6H_{\frac{5}{2}}$ multiplet. This is not observed. To further investigate this emission, the 17511 cm^{-1} $^4G_{\frac{5}{2}}$ absorption transition was excited with the pulsed laser, whilst the 1013.56 nm transition was monitored. The purpose of this investigation was to observe a difference in the decay transient for this transition. This would indicate that either an additional centre was being excited, or in the case of a build up time, infer $^6F_{\frac{11}{2}}$ emission. Regettably, no emission signal could be detected on the storage oscilloscope. We assign this emission peak as the $A_1 \rightarrow S_{11}$ transition however this should be regarded as extremely tentative.

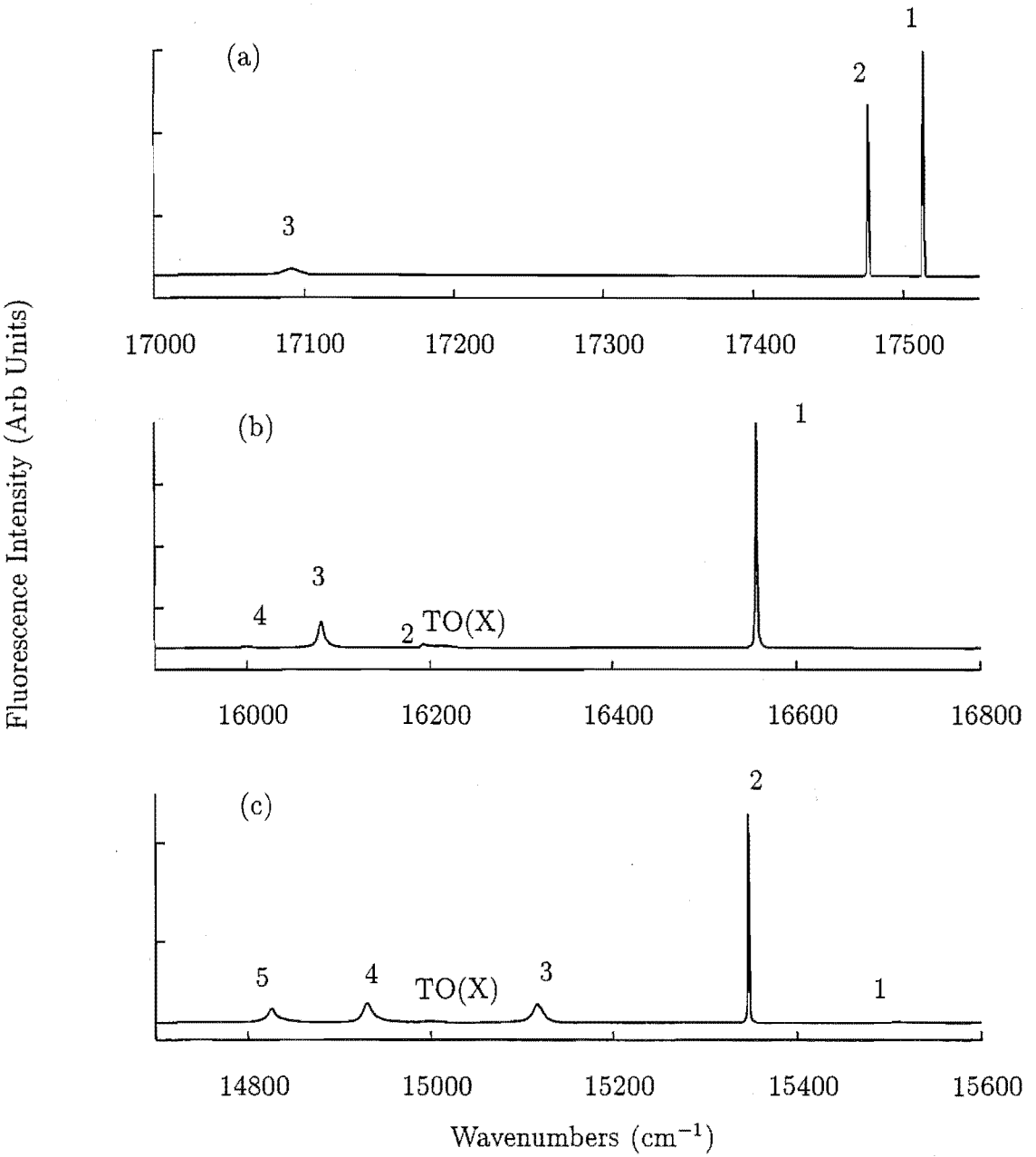

Figure 5.14: Fluorescence spectrum of the G1 centre for transitions $^4G_{\frac{5}{2}}$ to the (a) $^6H_{\frac{5}{2}}$, (b) $^6H_{\frac{7}{2}}$ and (c) $^6H_{\frac{9}{2}}$ multiplets in CaF_2:0.05%Sm^{3+}. Excitation is at the 18095 cm^{-1} $Z_1 \rightarrow A_2$ absorption transition for the $^6H_{\frac{5}{2}}$ fluorescence while for all others the $Z_1 \rightarrow A_1$ transition at 17511 cm^{-1} was excited. The spectra were recorded at 16K.

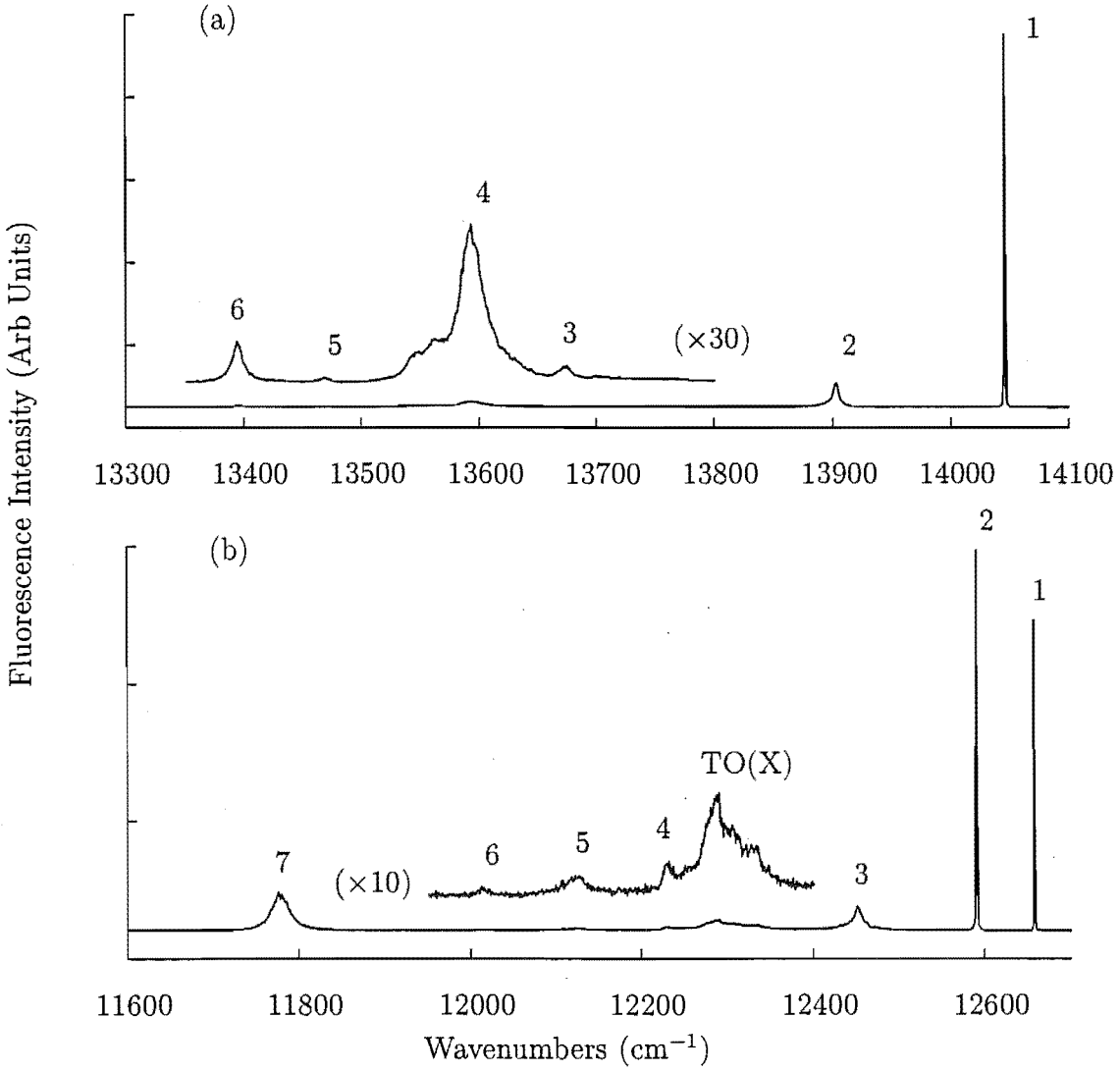

Figure 5.15: Fluorescence spectrum of the G1 centre for transitions $^4G_{\frac{5}{2}}$ to the (a) $^6H_{\frac{11}{2}}$ and (b) $^6H_{\frac{13}{2}}$ multiplets in CaF_2:0.05%Sm^{3+}. Excitation is at the 17511 cm^{-1} $Z_1 \rightarrow A_1$ absorption transition. The spectra were recorded at 16K.

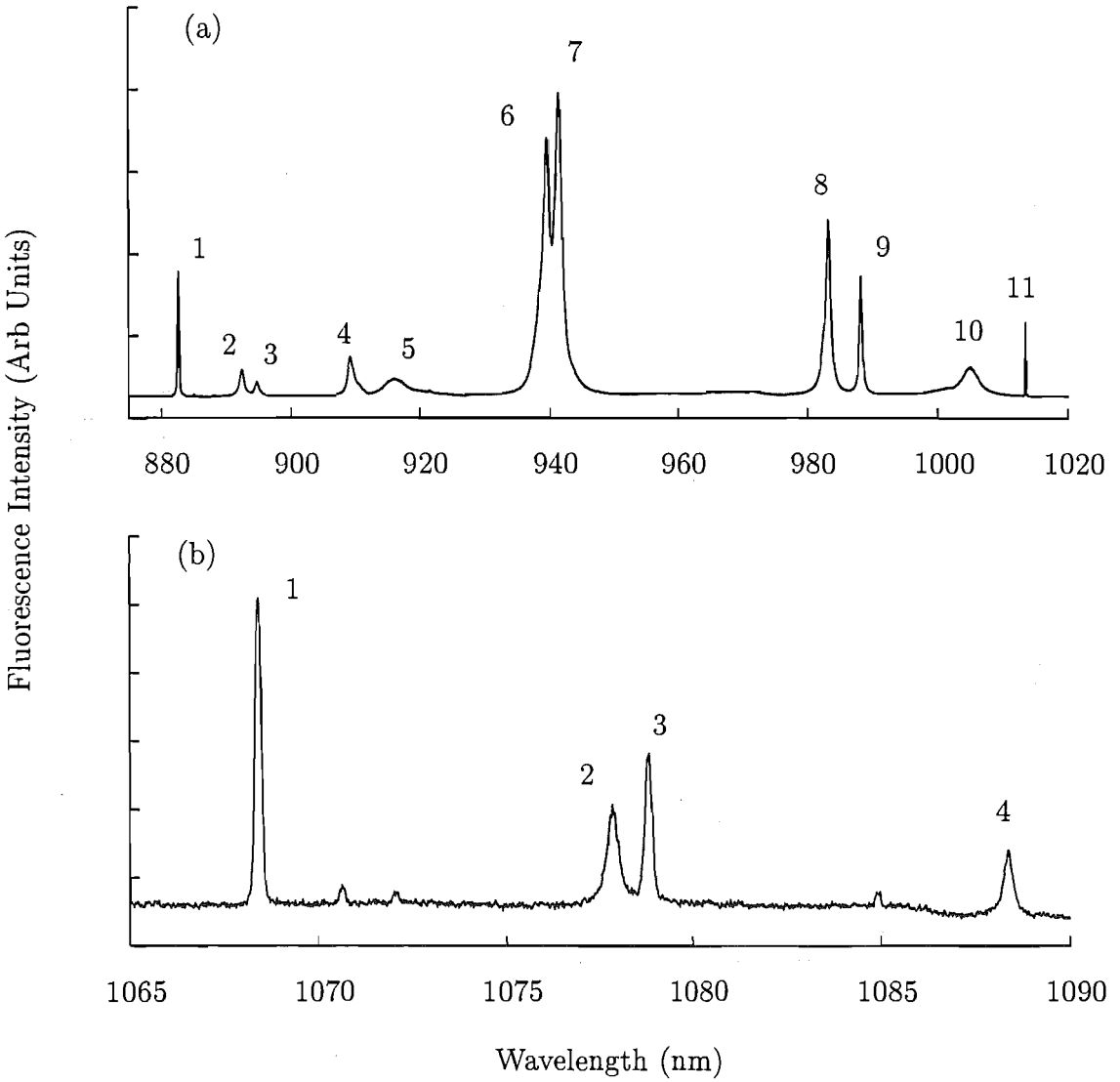

Figure 5.16: Fluorescence spectrum of the G1 centre for transitions $^4G_{\frac{5}{2}}$ to the (a) $^6H_{15/2}$, $^6F_{\frac{1}{2}}$, $^6F_{\frac{3}{2}}$ and $^6F_{\frac{5}{2}}$ multiplets and the (b) $^6F_{\frac{7}{2}}$ multiplet in CaF_2:0.05%Sm^{3+}. Excitation is at the 17511 cm^{-1} $Z_1 \rightarrow A_1$ absorption transition. The spectra were recorded at 16K.

Table 5.6: Transition frequencies (air cm^{-1} ± 1 unless otherwise stated), measured polarisation ratios and terminating states for emission from the $^4G_{\frac{5}{2}}$ to the $^6H_{\frac{5}{2},\frac{7}{2},\frac{9}{2},\frac{11}{2},\frac{13}{2},\frac{15}{2}}$ and $^6F_{\frac{1}{2},\frac{3}{2},\frac{5}{2},\frac{7}{2}}$ multiplets of the G1 centre in CaF_2:0.05%Sm^{3+}.

Multiplet	Terminating State Label	Terminating State Energy	Transition Frequency	Polarisation Ratio ZX	Polarisation Ratio ZY
$^6H_{\frac{5}{2}}$	Z_1	0	17511	1.3	1.0
	Z_2	35	17476	1.1	1.0
	Z_3	421	17090	1.3	1.0
$^6H_{\frac{7}{2}}$	Y_1	957	16554	1.1	1.0
	Y_2	1322	16189	1.0	1.1
	Y_3	1432	16079	1.4	1.0
	Y_4	1515	15996	1.3	1.0
$^6H_{\frac{9}{2}}$	X_1	2001	15510	1.2	1.0
	X_2	2166	15345	1.0	1.0
	X_3	2401	15110	1.0	1.5
	X_4	2587	14924	1.5	1.0
	X_5	2689	14822	1.0	1.5
$^6H_{\frac{11}{2}}$	W_1	3467	14044	1.0	1.1
	W_2	3611	13900	1.0	1.4
	W_3	3840	13671	1.1	1.0
	W_4	3921	13590	1.2	1.0
	W_5	4043	13468	-	-
	W_6	4117	13394	1.4	1.1
$^6H_{\frac{13}{2}}$	V_1	4854	12657	1.0	1.0
	V_2	4916	12595	1.0	1.0
	V_3	5063	12447	1.3	1.0
	V_4	5274	12237	-	-
	V_5	5380	12131	-	-
	V_6	5490	12021	-	-
	V_7	5734	11777	1.3	1.0
$^6H_{\frac{15}{2}}$, $^6F_{\frac{1}{2}}$, $^6F_{\frac{3}{2}}$ and $^6F_{\frac{5}{2}}$	S_1	6184	11327	1.0	1.0
	S_2	6304	11203	1.0	1.3
	S_3	6338	11173	1.0	1.1
	S_4	6515	10996	1.0	1.4
	S_5	6601	10910	1.1	1.0
	S_6	6869	10642	1.0	1.0
	S_7	6890	10621	1.0	1.0
	S_8	7342	10169	1.0	1.1
	S_9	7394	10117	1.4	1.0
	S_{10}	7562	9949	1.0	1.4
	S_{11}	7645	9866	1.3	1.0
$^6F_{\frac{7}{2}}$	Q_1	8151	9360	1.6	1.0
	Q_2	8233	9278	1.0	1.0
	Q_3	8242	9269	1.0	1.1
	Q_4	8323	9188	1.0	1.0

5.2.6 C1, C2 and C3 Centre Fluorescence

For excitation to the $^4G_{\frac{5}{2}}$ multiplet, two weak centres were observed in Section 5.2.2. Initially, it was hoped that these centres may be associated with the R and Q absorption features observed in Section 5.2.1. This proved not to be the case. The centres are discussed in turn, the C2 centre first, being the clearest spectroscopically.

The excitation and fluorescence spectra of the arbitrarily labelled C2 centre resemble that of the tetragonal symmetry A centre. In addition, it is the only other rare earth centre observed in CaF_2:Sm^{3+} that has 2:1 type polarisation ratios (given in Table 5.7). This suggests a high symmetry. The possibility arises that this centre is associated with Sr^{2+} or Ba^{2+} impurity in the stock CaF_2, used to grow the crystal. Both Khong [98] and Mujaji [15] report the presence of such modified centres for both unintentional and intentional doping of Sr^{2+} into the CaF_2 lattice. In these cases, Pr^{3+} and Ho^{3+} respectively were the rare earth (probe) dopant ions and a modified centre retaining the C_{4v} symmetry of the parent centre has been observed. In this case, the Sr^{2+} ion substitutes for the host alkaline earth ion, next to the interstitial F^- ion along the RE^{3+} - F^- axis opposite to the RE^{3+} ion. This yields a centre which preserves the C_{4v} symmetry of the parent A centre.

For emission to the $^6H_{\frac{5}{2}}$ multiplet, the $Z_1 \rightarrow A_2$ transition at 17913 cm^{-1} has been excited. Due to the significant overlap of this transition, with the $Z_1 \rightarrow A_2$ transition of the A centre, the emission spectra of both centres is observed. To further complicate matters, vibronic sidebands associated with the cubic O centre overlap the $Z_1 \rightarrow A_2$ absorption transition C2 centre. Thus, the $A_1 \rightarrow Z_1$ electronic transition of the O centre is also observed in the emission spectrum. This is shown in Figure 5.17. The two transitions associated with the C2 centre are observed. These are at frequencies of 17799 and 17764 cm^{-1}. From this, the Z_2 state is placed 35 cm^{-1} above the ground state. This is a 12 cm^{-1} smaller splitting of the cubic Γ_8 irrep, than measured for the A centre. This is consistent with smaller axial crystal field parameters (compared with the CaF_2:Ho^{3+} A centre) obtained by Mujaji [15] in her crystal field analysis of the modified Ho^{3+} C_{4v} symmetry centres. The remaining CaF_2:Sm^{3+} C2 centre spectra are shown in Figures 5.18 and 5.19.

For excitation of the $Z_1 \rightarrow A_2$ transition of the C1 centre at 17855 cm^{-1}, a complex emission spectrum to the $^6H_{\frac{5}{2}}$ multiplet is observed. The 21 cm^{-1} splitting of the A_1 and A_2 $^4G_{\frac{5}{2}}$ states of the C1 centre should help identify the transitions of this centre. However, this is confused by a comparable 21 cm^{-1} Z_1-Z_2 splitting in the $^6H_{\frac{5}{2}}$ ground state. The $A_1 \rightarrow Z_1$ and Z_2 transitions of the A centre and the $A_1 \rightarrow Z_1$ transition of the near cubic O centre are also observed. In addition to the $A_1 \rightarrow Z_1$

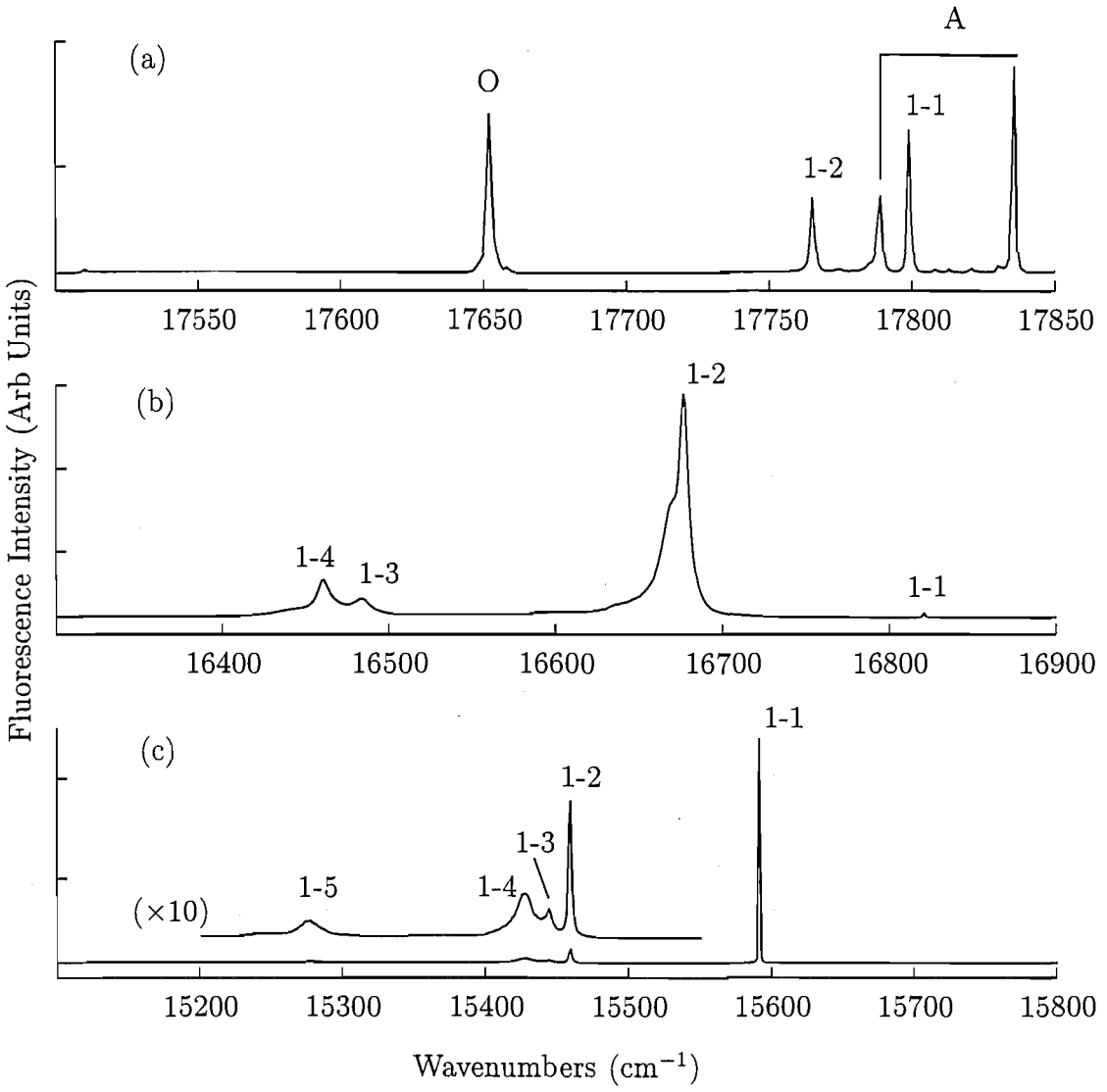

Figure 5.17: Fluorescence spectrum of the C2 centre for transitions $^4G_{\frac{5}{2}}$ to (a) the $^6H_{\frac{5}{2}}$ multiplet (b) the $^6H_{\frac{7}{2}}$ multiplet and (c) the $^6H_{\frac{9}{2}}$ multiplet in CaF_2:0.05%Sm^{3+}. The spectra were recorded at 16K.

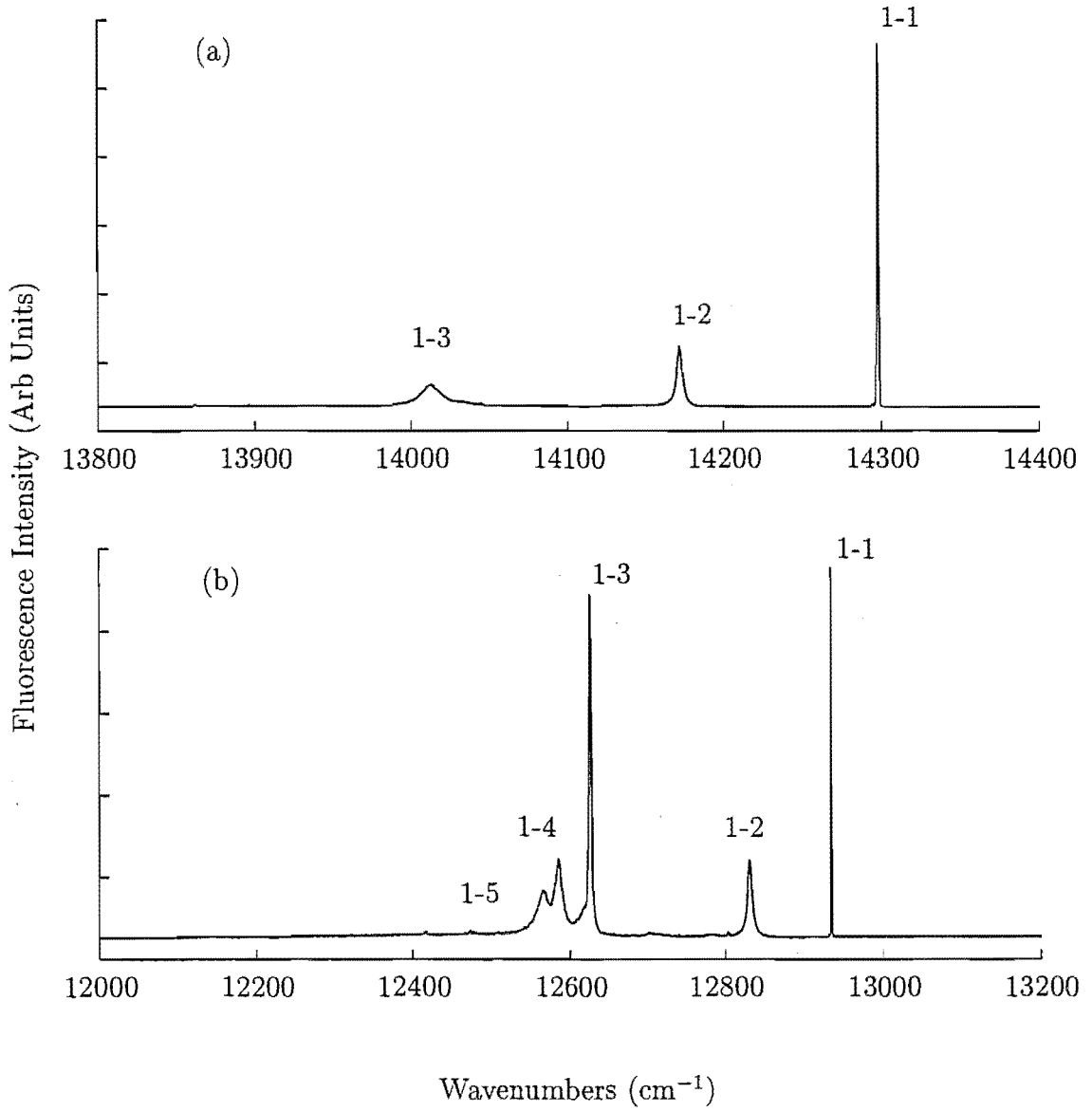

Figure 5.18: Fluorescence spectrum of the C2 centre for transitions $^4G_{\frac{5}{2}}$ to (a) the $^6H_{\frac{11}{2}}$ multiplet and (b) the $^6H_{\frac{13}{2}}$ multpiplet in CaF_2:0.05%Sm^{3+}. The spectra were recorded at 16K

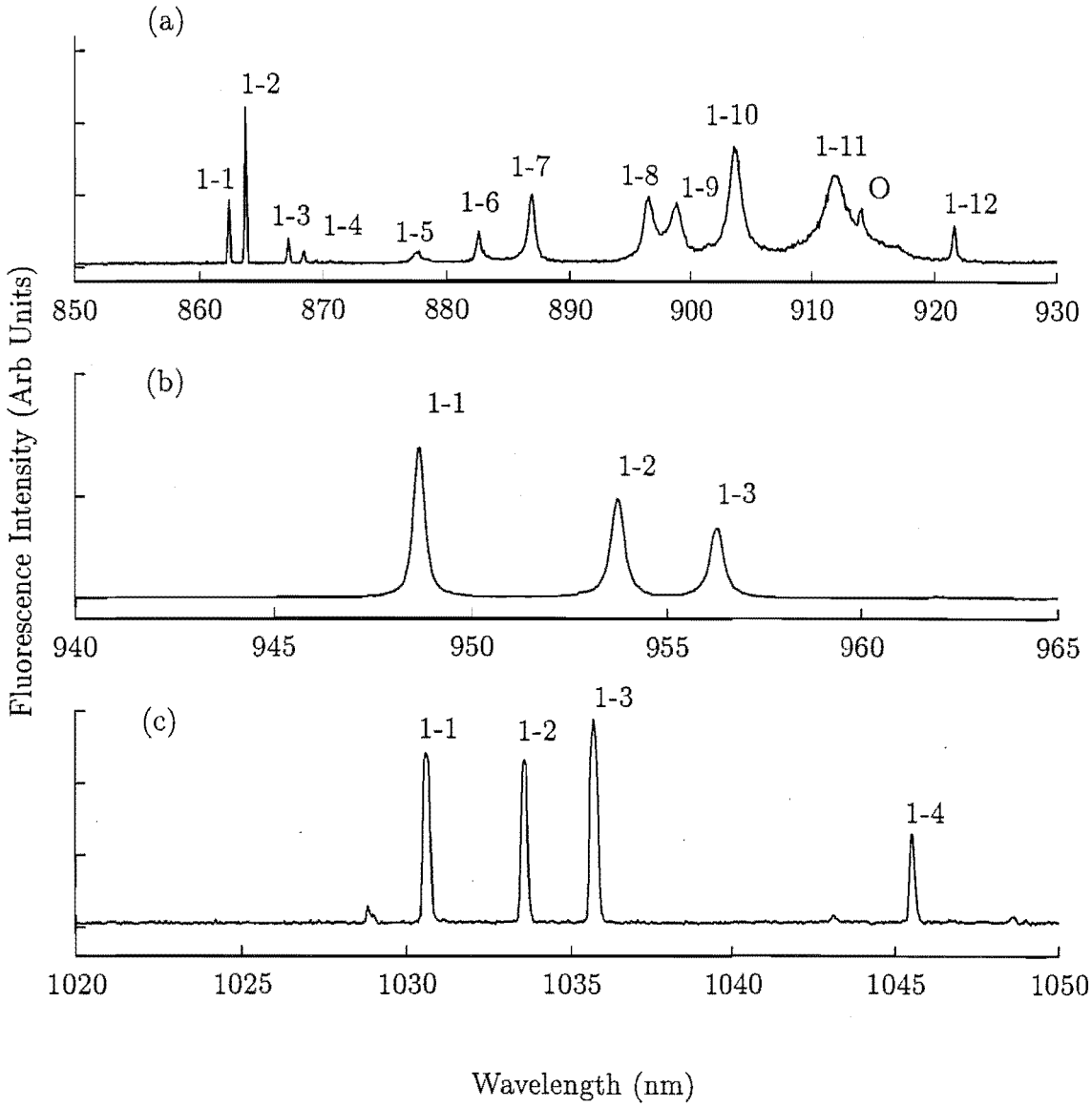

Figure 5.19: Fluorescence spectrum of the C2 centre for transitions $^4G_{\frac{5}{2}}$ to (a) the $^6H_{\frac{15}{2}}$, $^6F_{\frac{1}{2}}$ and $^6F_{\frac{3}{2}}$ multiplets, (b) the $^6F_{\frac{5}{2}}$ multiplet and (c) the $^6F_{\frac{5}{2}}$ multiplet in CaF_2:0.05%Sm^{3+}. Excitation is at the 17799 cm^{-1} $Z_1 \rightarrow A_1$ absorption transition.

Table 5.7: Transition frequencies (air cm^{-1} ± 1 unless otherwise stated), measured polarisation ratios and terminating states for emission from the $^4G_{\frac{5}{2}}$ to the $^6H_{\frac{5}{2},\frac{7}{2},\frac{9}{2},\frac{11}{2},\frac{13}{2},\frac{15}{2}}$ and $^6F_{\frac{1}{2},\frac{3}{2},\frac{5}{2},\frac{7}{2}}$ multiplets of the C2 centre in CaF_2:0.05%Sm^{3+}.

Multiplet	Terminating State		Transition	Polarisation Ratio	
	Label	Energy	Frequency	ZX	ZY
$^6H_{\frac{5}{2}}$	Z_1	0	17799	1.9	1.0
	Z_2	35	17764	1.0	1.1
$^6H_{\frac{7}{2}}$	Y_1	981	16818	1.1	1.0
	Y_2	1125	16674	2.5	1.0
	Y_3	1318	16481	2.7	1.0
	Y_4	1342	16457	2.8	1.0
$^6H_{\frac{9}{2}}$	X_1	2209	15590	1.0	1.1
	X_2	2341	15458	1.0	1.3
	X_3	2455	15444	1.0	1.1
	X_4	2371	15428	1.0	1.1
	X_5	2524	15275	2.2	1.0
$^6H_{\frac{11}{2}}$	W_1	3501	14298	1.0	1.2
	W_2	3627	14172	1.9	1.0
	W_3	3788	14011	1.0	1.0
$^6H_{\frac{13}{2}}$	V_1	4865	12934	1.0	1.0
	V_2	4969	12830	1.0	1.6
	V_3	5173	12626	2.0	1.0
	V_4	5209	12590	1.2	1.0
	V_5	5230	12569	2.0	1.0
$^6H_{\frac{15}{2}}$, $^6F_{\frac{1}{2}}$ and $^6F_{\frac{3}{2}}$	S_1	6206	11593	1.0	1.1
	S_2	6224	11575	2.8	1.0
	S_3	6272	11527	1.2	1.0
	S_4	6287	11512	1.1	1.0
	S_5	6405	11394	1.0	1.1
	S_6	6472	11327	1.0	1.1
	S_7	6526	11273	1.1	1.0
	S_8	6646	11153	1.6	1.0
	S_9	6674	11125	1.9	1.0
	S_{10}	6735	11064	1.0	1.6
	S_{11}	6834	10965	1.3	1.0
	S_{12}	6950	10849	1.0	1.0
$^6F_{\frac{5}{2}}$	R_1	7261	10538	1.9	1.0
	R_2	7316	10483	1.0	1.1
	R_3	7344	10455	1.0	2.0
$^6F_{\frac{7}{2}}$	Q_1	8097	9702	1.2	1.0
	Q_2	8124	9675	2.0	1.0
	Q_3	8144	9655	3.6	1.0
	Q_4	8235	9564	1.0	1.2

and Z_2 transitions of the C1 centre at 17834 and 17813 cm^{-1} respectively, a stronger, broader feature at 17735 cm^{-1} is also observed. This does not appear to be correlated with the C1 centre as there is no 'hot' transition from the A_2 state 21 cm^{-1} higher in frequency. Such a transition would be clearly observable for the 17735 cm^{-1} transition unless restricted by symmetry considerations. This is a possibility we do not exclude, but regard as unlikely in the expectation that the weak centres observed in excitation are low symmetry cluster centres less tightly coupled than the arbitrarily labelled R and Q features observed in absorption.

Similar spectra are observed to the excited multiplets of the ^6H and ^6F terms with many levels assigned to the C1 centre via their common A_1-A_2 splitting of 21 cm^{-1}. The spectra are given in Figures 7.20 to 7.22. Extra transitions are also observed, without such a splitting. These are generally stronger in intensity. Therefore, it is concluded that for excitation of the C1 centre at 17855 cm^{-1}, an additional centre, arbitrarily labelled C3, is also excited. Neither centre has a marked polarisation dependence for $\langle 100 \rangle$ or $\langle 111 \rangle$ oriented crystals. It is possible that they correspond to a loosely coupled pair such as that observed by Cockcroft [14] for CaF_2:Er^{3+}. However, in that case entirely distinct excitation and emission spectra were obtained whereas the C1 and C3 centres do not appear as distinct features in excitation. Transition frequencies and terminating state energies for the C1 centre are given in Table 5.8. However, for the C3 centre the $^4G_{\frac{5}{2}}$ states are unknown and only the transition energies are listed in Table 5.9.

Table 5.8: Transition frequencies (air cm^{-1} ± 1 unless otherwise stated), terminating state energies and transition assignments for emission from the $^4G_{\frac{5}{2}}$ to the $^6H_{\frac{5}{2},\frac{7}{2},\frac{9}{2},\frac{11}{2},\frac{13}{2}}$ and $^6F_{\frac{5}{2}}$ multiplets of the C1 centre in CaF_2:0.05%Sm^{3+}.

Transition Frequency	State Energy	Transition Assignment	Transition Frequency	State Energy	Transition Assignment
17834	0	$A_1 \rightarrow Z_1$	14414	3420	$A_1 \rightarrow W_1$
17813	21	$A_1 \rightarrow Z_2$	12945	4910	$A_2 \rightarrow V_1$
16891	964	$A_2 \rightarrow Y_1$	12924	4910	$A_1 \rightarrow V_1$
16871	963	$A_1 \rightarrow Y_1$	12912	4943	$A_2 \rightarrow V_2$
16839	1016	$A_2 \rightarrow Y_2$	12892	4942	$A_1 \rightarrow V_2$
16819	1015	$A_1 \rightarrow Y_2$	12882	4973	$A_2 \rightarrow V_3$
16774	1081	$A_2 \rightarrow Y_3$	12861	4973	$A_1 \rightarrow V_3$
16753	1081	$A_1 \rightarrow Y_3$	10721	7134	$A_2 \rightarrow R_1$
15702	2153	$A_2 \rightarrow X_1$	10710	7145	$A_2 \rightarrow R_2$
15680	2154	$A_1 \rightarrow X_1$	10700	7134	$A_1 \rightarrow R_1$
15671	2184	$A_2 \rightarrow X_2$	10690	7144	$A_1 \rightarrow R_2$
15652	2182	$A_1 \rightarrow X_2$	10680	7154	$A_1 \rightarrow R_3$
14434	3421	$A_2 \rightarrow W_1$			

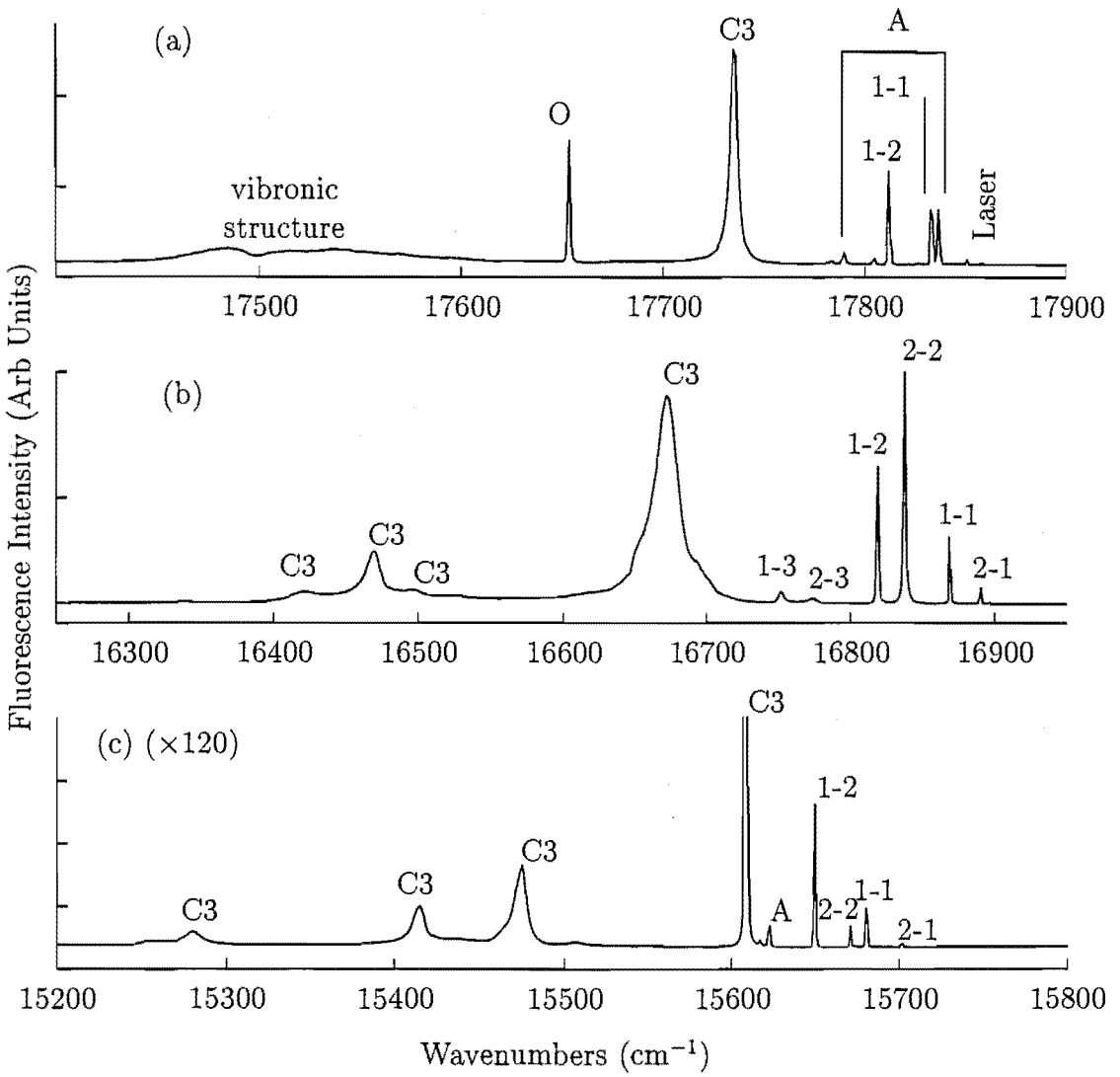

Figure 5.20: Fluorescence spectrum of the C1 and C3 centres for transitions $^4G_{\frac{5}{2}}$ to (a) the $^6H_{\frac{5}{2}}$ multiplet, (b) the $^6H_{\frac{7}{2}}$ multiplet and (c) the $^6H_{\frac{11}{2}}$ multiplet in CaF_2:0.05%Sm^{3+}. The spectra were recorded at 16K.

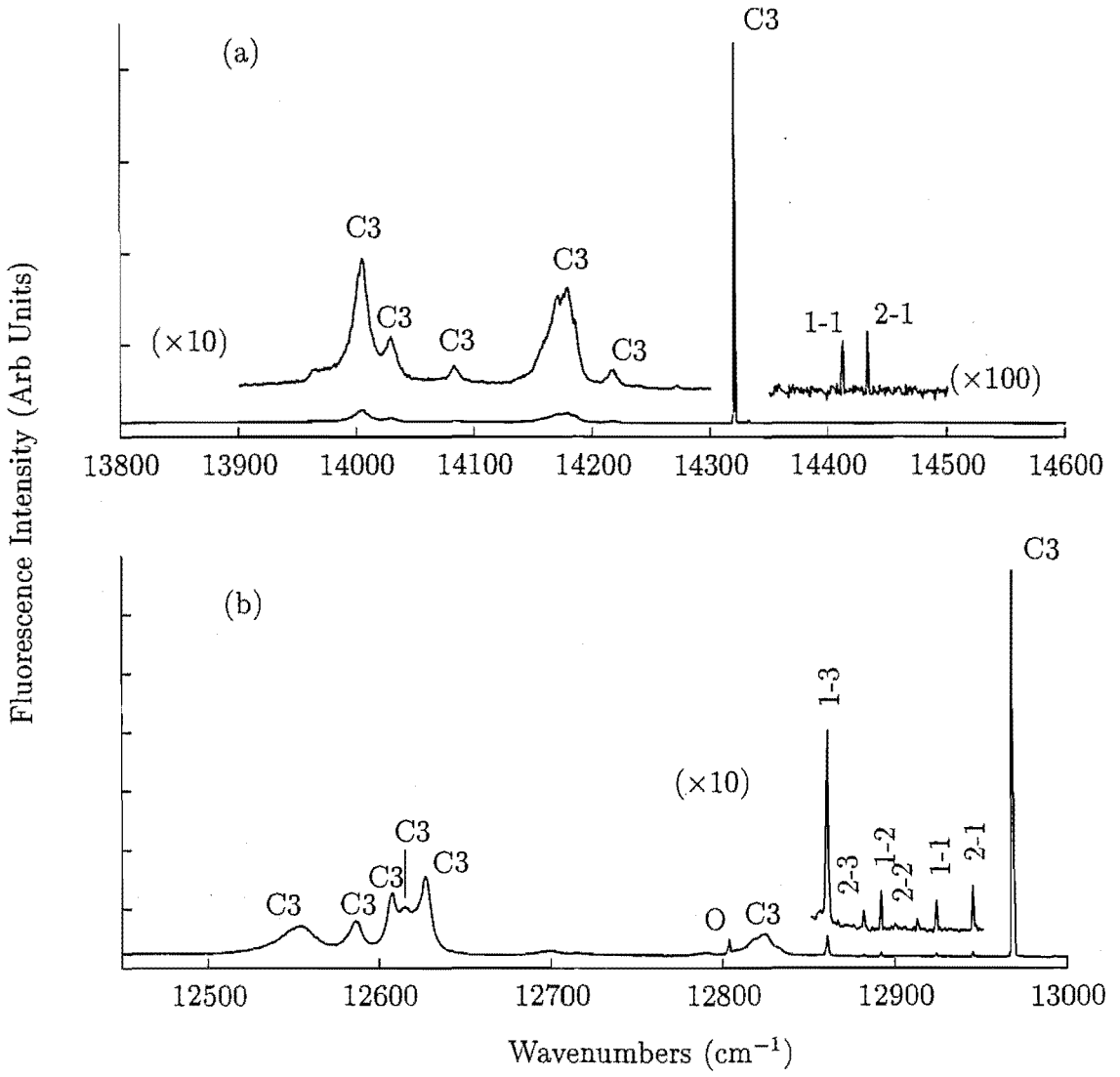

Figure 5.21: Fluorescence spectra of the C1 and C3 centres for transitions $^4G_{\frac{5}{2}}$ to (a) the $^6H_{\frac{11}{2}}$ multiplet and (b) the $^6H_{\frac{13}{2}}$ multiplet in CaF_2:0.05%Sm^{3+}. The spectra were recorded at 16K.

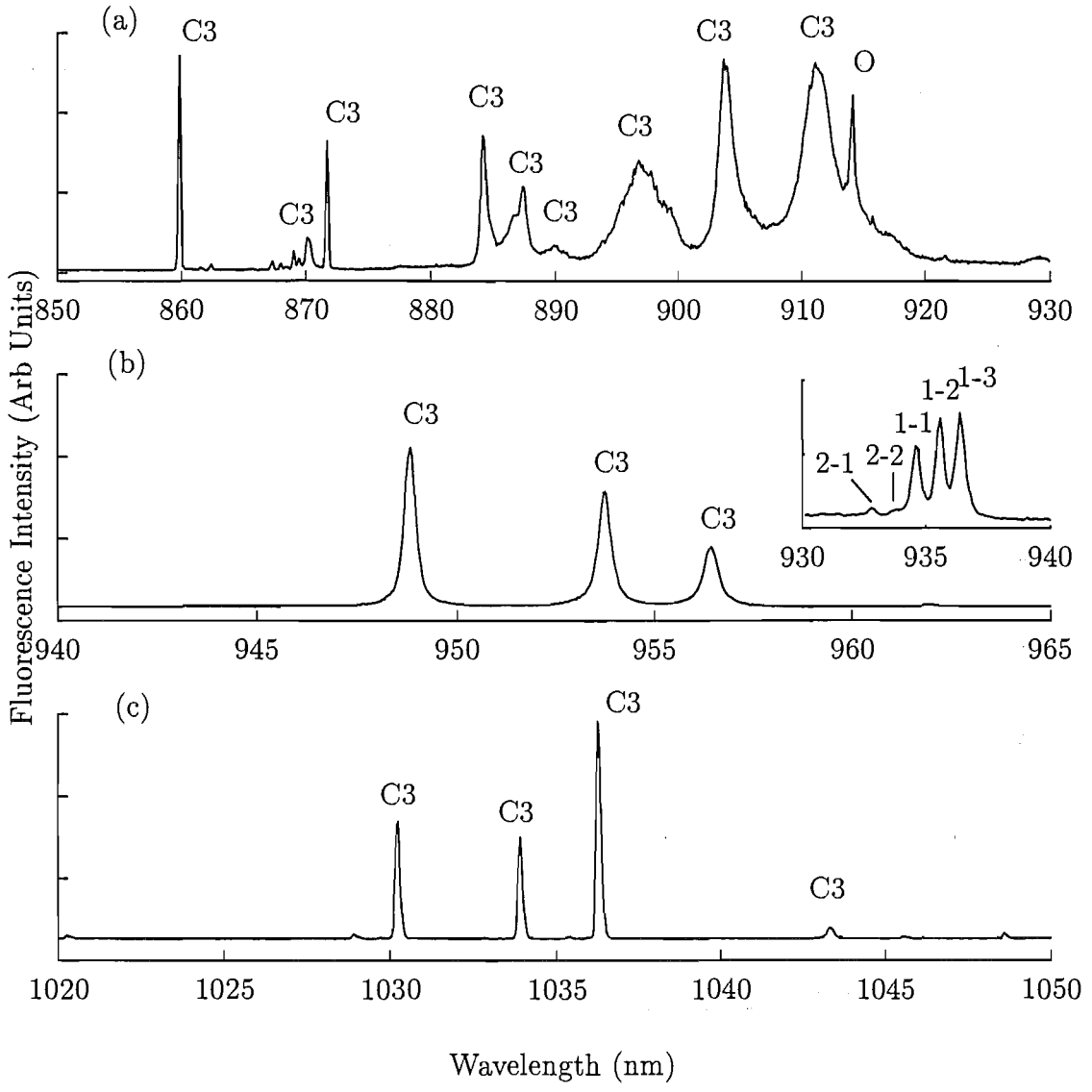

Figure 5.22: Fluorescence spectrum of the C3 centres for transitions from $^4G_{\frac{5}{2}}$ to (a) the $^6H_{\frac{15}{2}}$, $^6F_{\frac{1}{2}}$ and $^6F_{\frac{3}{2}}$ multiplets, (b) the $^6F_{\frac{5}{2}}$ multiplet (inset is the spectrum to the $^6F_{\frac{5}{2}}$ multiplet for the C1 centre) and (c) the $^6F_{\frac{7}{2}}$ multiplet in CaF_2:0.05%Sm^{3+}. The spectra were recorded at 16K.

Table 5.9: Transition frequencies (air cm^{-1} ± 1 unless otherwise stated) of the C3 centre in CaF_2:0.05%Sm^{3+}

Multiplet	Transition Frequency	Multiplet	Transition Frequency
$^6H_{\frac{5}{2}}$	17735	$^6H_{\frac{13}{2}}$	12608
	16897		12585
$^6H_{\frac{7}{2}}$	16674		12552
	16474		11627
	16419		11490
	15609		11469
	15475	$^6H_{\frac{15}{2}}$, $^6F_{\frac{1}{2}}$	11308
$^6H_{\frac{9}{2}}$	15415	and $^6F_{\frac{3}{2}}$	11267
	15281		11242
	14322		11149
	14217		11061
	14175±2		10975
$^6H_{\frac{11}{2}}$	14083		10537
	14030	$^6H_{\frac{5}{2}}$	10483
	14005		10453
	12968		9706
	12825	$^6F_{\frac{7}{2}}$	9672
	12630		9650
	12615		9585

5.3 Spectroscopy of $SrF_2:Sm^{3+}$

5.3.1 Optical Absorption Spectra

The absorption to the $^4G_{\frac{5}{2}}$ multiplet, of a 3 cm boule of SrF_2:0.05%Sm^{3+} is presented in Figure 5.23. The crystal was cooled to 16K for this experiment. As with $CaF_2:Sm^{3+}$, absorption to this multiplet is weak, as it is nominally spin forbidden. The even transmission background in this figure indicates an absence of Sm^{2+} in the crystal. The recorded spectrum is seen to be significantly simpler than the $^6H_{\frac{5}{2}} \rightarrow ^4G_{\frac{5}{2}}$ absorption spectrum in CaF_2:0.05%Sm^{3+}. Only two absorption features at 560.5 and 557.6 nm are observed. Given the similarity of these two transitions to the $Z_1 \rightarrow A_1$ and A_2 transitions of the A centre in $CaF_2:Sm^{3+}$, it is not unreasonable to assign these transitions to the A centre in $SrF_2:Sm^{3+}$. Thus, the broadening observed for the shorter wavelength transition is ascribed to relaxation of the A_2 level to the A_1.

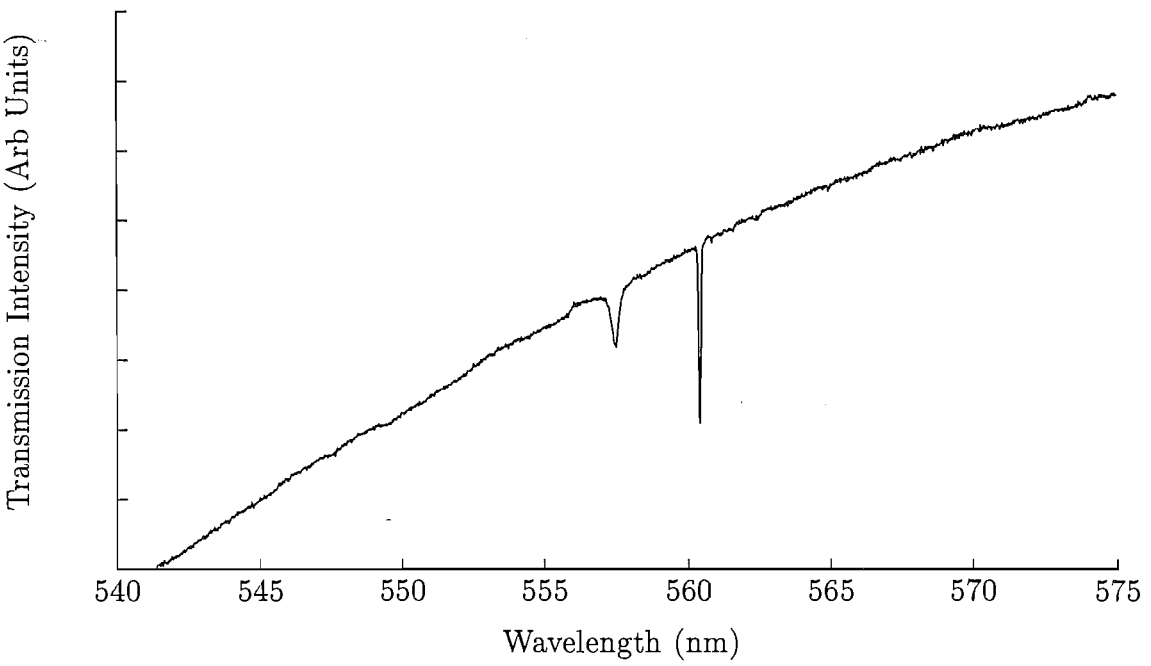

Figure 5.23: Absorption spectrum for the $^4G_{\frac{5}{2}}$ multiplet in SrF_2:0.05%Sm^{3+}. The spectrum was recorded at 16K.

5.3.2 Excitation Spectra

Laser excitation spectra for the $^4G_{\frac{5}{2}}$ and $^4F_{\frac{3}{2}}$ multiplets of a SrF_2:0.05%Sm^{3+} sample were recorded using the SPEX 1700 series single monochromator. The spectrum was scanned with the spectrometer set to the zero order of diffraction. The fluorescence was detected with an EMI 9659 QA photomultiplier. Figure 5.24(a) shows the recorded spectrum. This is dominated by two transitions which, as shown in Figure 5.25(a), belong to the same centre with an additional weaker transition at a higher frequency as given in Table 5.10. The structure of this centre matches the dominant features observed in absorption to this multiplet and is identical to that observed for the CaF_2:Sm^{3+} A centre.

In Figure 5.24(b) the zero order excitation spectrum for the $^4G_{\frac{5}{2}}$ multiplet is amplified 15 times. A weak transition is observed at 17699 cm^{-1}. In Figure 5.25(c) the spectrum for the centre corresponding to this transition is monitored selectively at 16575 cm^{-1}. Two transitions are observed for the centre of interest which we label O due to the similarity between this centre and the CaF_2:Sm^{3+} near cubic centre. This spectrum is not entirely centre selective as we can observe the two A centre transitions at 17839 and 17934 cm^{-1}.

Oxygen was found to enter the SrF_2 crystals very easily. Oxygenation periods of up to 30 minutes were used for the spectroscopic studies completed here. In Figure 5.24(c) the zero order excitation spectrum of the $^4G_{\frac{5}{2}}$ multiplet after 30 minutes exposure to dry oxygen at 900 °C is shown. The spectrum is amplified 5 times and features of a new centre due to oxygen charge compensation are observable. This centre is very like that observed for CaF_2:Sm^{3+}:O^{2-}. The narrowband spectrum for this centre is presented in Figure 7.25(b).

The $^4F_{\frac{3}{2}}$ multiplet is roughly 1000 cm^{-1} higher in energy. In Figure 5.26(a) a single transition is seen to dominate the spectrum. For monitoring the A centre transition frequency of 17839 cm^{-1}, this line plus two additional lines are observed to relate to the A centre. The lowest frequency transition appears to originate from a thermally populated ground multiplet level 35 cm^{-1} above the ground state. This is shown in Figure 5.27(a).

Selectively monitoring at 17699 cm^{-1} whilst scanning the $^4F_{\frac{3}{2}}$ transitions yields Figure 5.27(c). A transition at 18871 cm^{-1} is assigned to this centre labelled O. From the transitions observed, it is clear that this is a centre of cubic symmetry from the $^4G_{\frac{5}{2}}$ and $^4F_{\frac{3}{2}}$ manifold degeneracies. If the 17544 cm^{-1} transition of the oxygen related centre is monitored we observe two transitions to the $^4F_{\frac{3}{2}}$ multiplet.

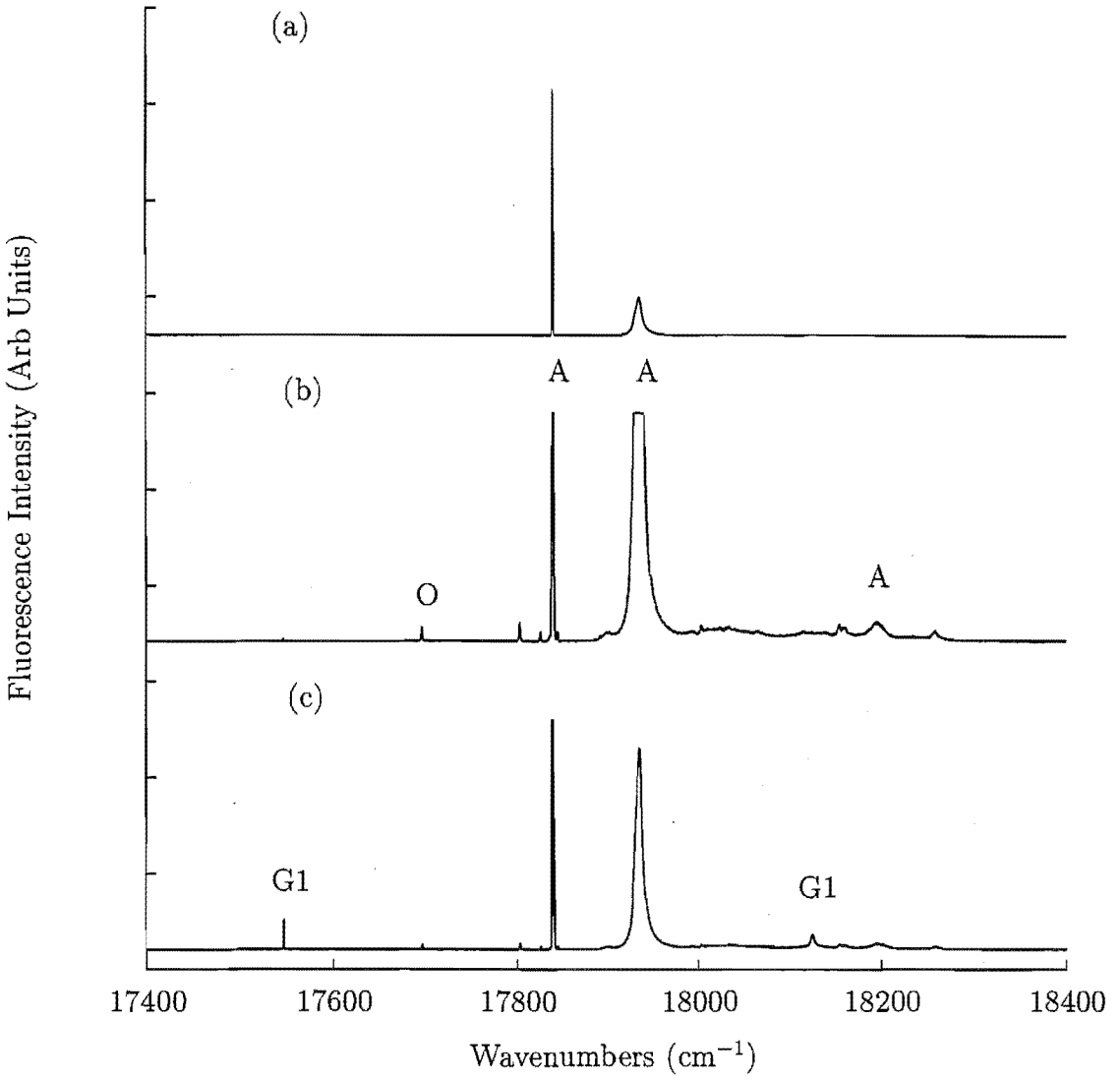

Figure 5.24: Broadband excitation spectra of the $^4G_{\frac{5}{2}}$ multiplet in SrF_2:0.05%Sm^{3+} for (a) as grown crystal (amplification ×1) (b) as grown crystals (×15) and (c) 30 minutes oxygenation (×5). The spectra were recorded at 16K.

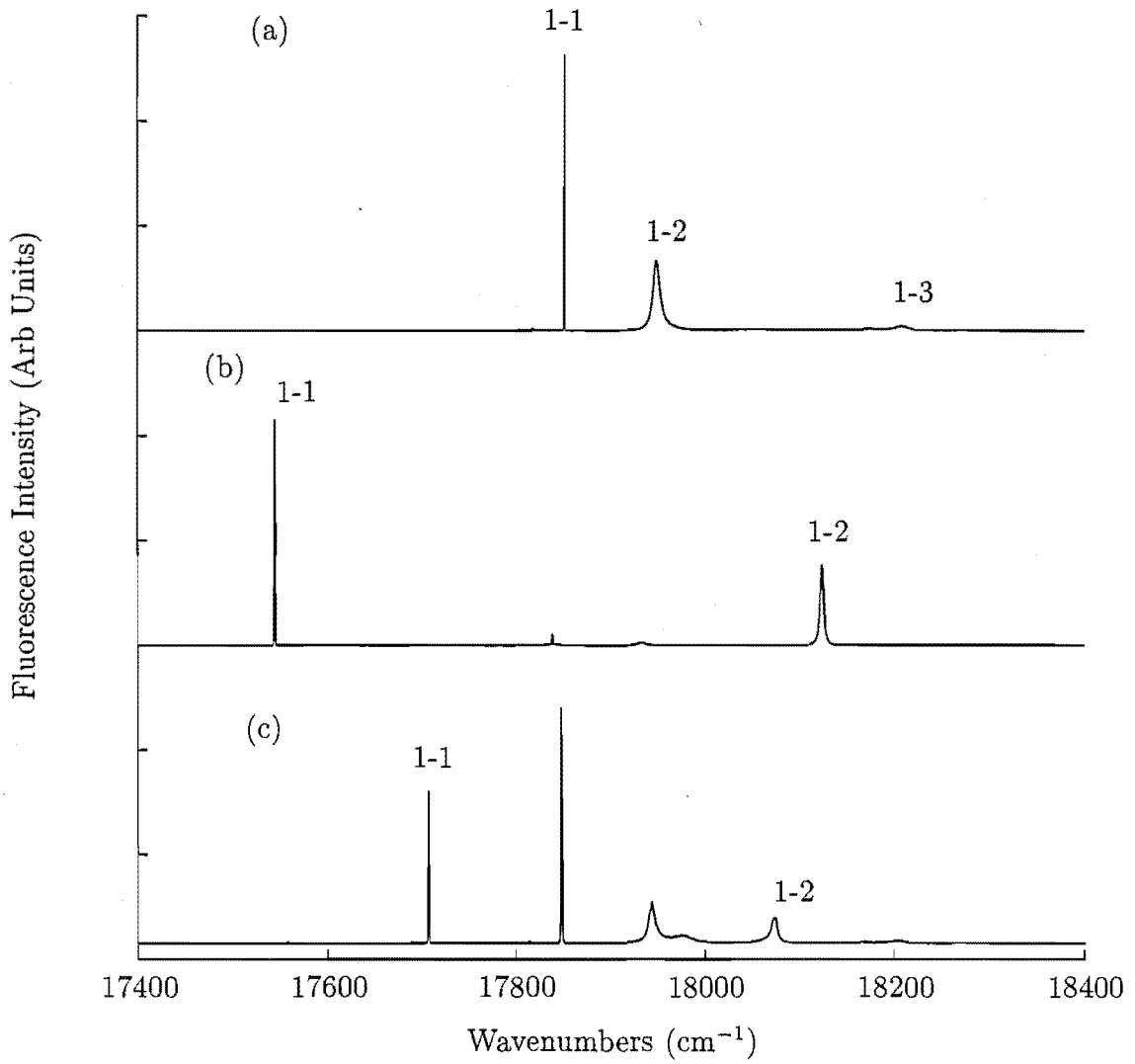

Figure 5.25: Narrowband excitation spectra of the $^4G_{\frac{5}{2}}$ multiplet in SrF_2:0.05%Sm^{3+} for (a) the A centre monitoring at 16731 cm^{-1}, (b) the G1 centre monitoring at 16575 cm^{-1} and (c) the O centre monitoring at 16606 cm^{-1}. The spectra were recorded at 16K.

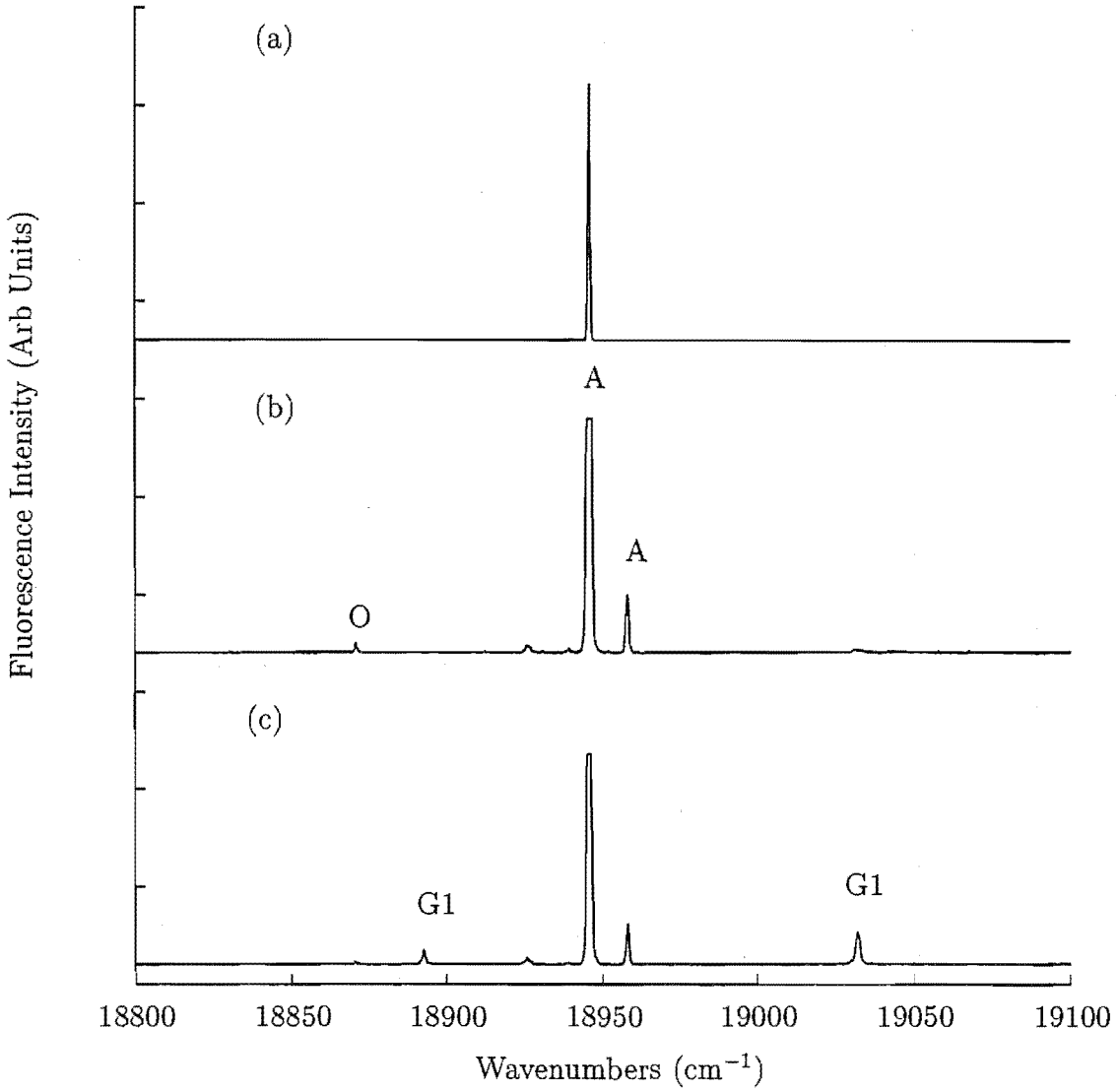

Figure 5.26: Broadband excitation spectra of the $^4F_{\frac{3}{2}}$ multiplet in SrF_2:0.05%Sm^{3+} for (a) as grown crystals (×1 amplification), (b) as grown crystals (×100) and (c) after 30 minutes oxygenation (×100). The spectra were recorded at 16K.

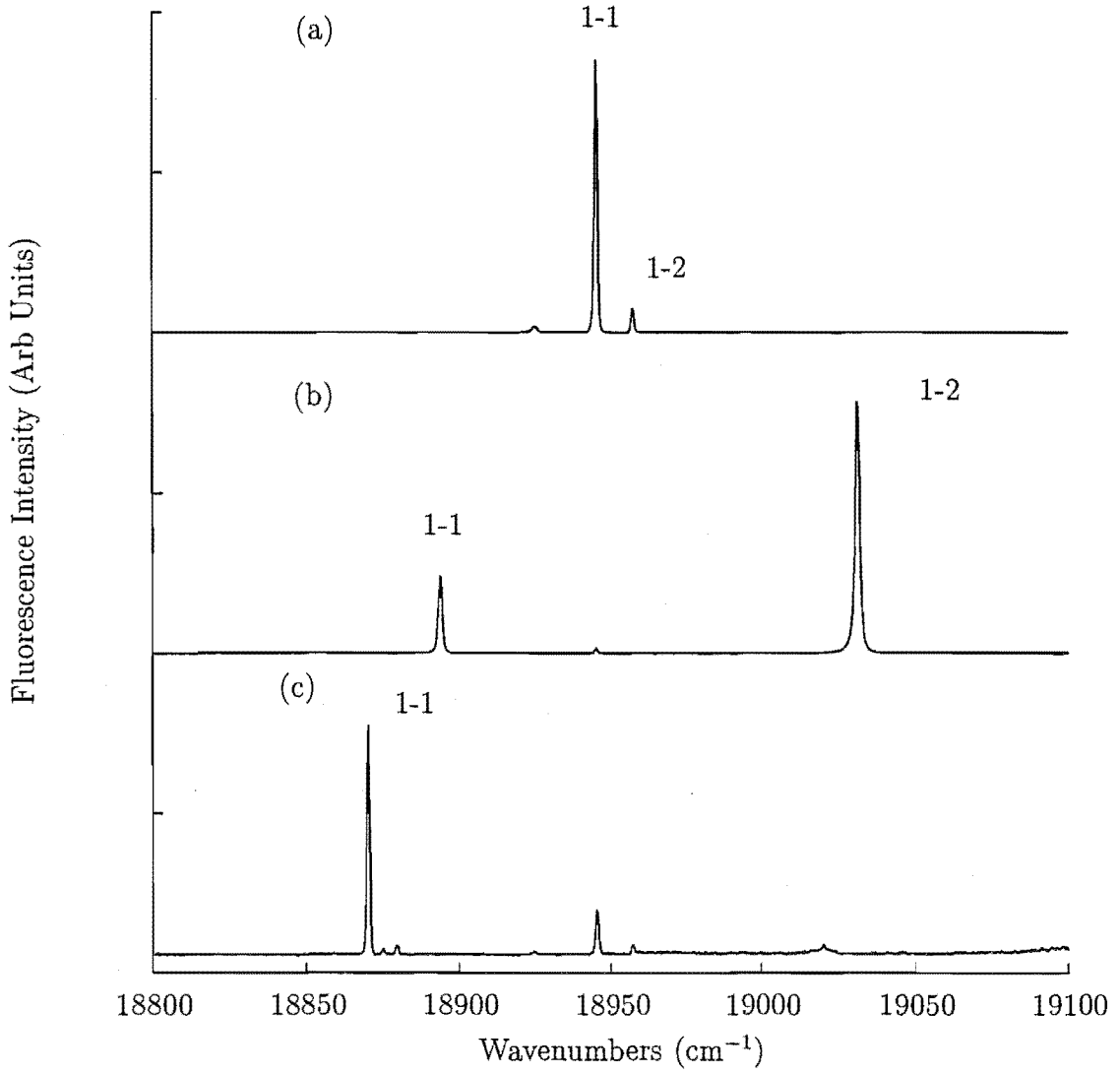

Figure 5.27: Narrowband excitation spectra of the (a) A monitoring at 17839 cm^{-1}, (b) the G1 monitoring at 17544 cm^{-1} and (c) the O centre monitoring at 17699 cm^{-1} for the $^4F_{\frac{3}{2}}$ multiplet in SrF_2:0.05%Sm^{3+}. The spectra were recorded at 16K.

The recorded spectrum is given in Figure 5.27(b). From the magnitude of the $^4F_{\frac{3}{2}}$ splitting we label this centre G1 because it is similar to the dominant oxygen charge compensated centre detected in CaF_2:Sm^{3+} crystals. The excitation frequencies for all centres observed are given in Table 5.10.

Table 5.10: $^4G_{\frac{5}{2}}$ and $^4F_{\frac{3}{2}}$ excitation frequencies (in air ± 1 cm^{-1}) for the A, G1 and O centers in SrF_2:0.05%Sm^{3+}

Multiplet	State	A	G1	O
$^4G_{\frac{5}{2}}$	A_1	17839	17544	17699
	A_2	17934	18126	18070
	A_3	18195	-	-
$^4F_{\frac{3}{2}}$	B_1	18949	18899	18871
	B_2	18963	19032	-

5.3.3 A Centre Fluorescence

Fluorescence spectra from the $^4G_{\frac{5}{2}}$ multiplet to crystal field levels of the ^6H_J and ^6F_J multiplets of the A centre were recorded. The crystal was cooled to 16K. The spectra are presented in Figures 5.28-5.30. Most spectra were recorded pumping the $^6H_{\frac{5}{2}}Z_1 \rightarrow {}^4G_{\frac{5}{2}}A_1$ transition at 17839 cm^{-1}. For fluorescence to the $^6H_{\frac{5}{2}}$ ground multiplet the $Z_1 \rightarrow A_3$ transition was excited. The fluorescence transitions of this centre show 2:1 type polarisation ratios for $\langle 100 \rangle$ oriented crystals. From this, and the spectroscopic similarity of this centre with the A centre in CaF_2:Sm^{3+}, we assign this centre as having C_{4v} symmetry. Charge compensation is provided by an F^- ion in the nearest neighbour interstitial position along a $\langle 100 \rangle$ direction. The measured transition frequencies are given in Table 5.12.

For excitation of the $Z_1 \rightarrow A_3$ transition at 18195 cm^{-1}, two strong emission peaks are observed at frequencies of 17839 and 17804 cm^{-1} (Figure 5.28(a)). These transitions terminate on the ground multiplet ($^6H_{\frac{5}{2}}$) of the Sm^{3+} ion. From the frequency difference of these two transitions we infer that the ground - first excited crystal field state splitting is 35 cm^{-1}.

For transitions to the $^6H_{\frac{7}{2}}$ multiplet, the $Z_1 \rightarrow A_1$ transition at 17839 cm^{-1} is excited. Two distinct electronic transitions are observed at 16849 and 16731 cm^{-1} as can be observed in Figure 5.28(b). These transitions correspond to $A_1 \rightarrow Y_1$ and Y_2. The positions of the $^6H_{\frac{7}{2}}$ levels are determined to be at 990 and 1108 cm^{-1}, respectively. The remainder of the spectrum is quite complex (Figure 5.28(b) and 5.31(a)). The

features in the 16700-16640 cm^{-1} region are assigned as transitions to vibrational levels of the lattice. The fluorescence energies for these transitions are given in Table 5.11. Broad agreement is obtained between the vibronic intervals observed here, and those observed by Wood and Kaiser [72], Richman [99], and Aizenberg et. al. [90].

The second group of transitions in the 16600-16500 cm^{-1} region, are a combination of the remaining two electronic transitions expected for a J=$\frac{7}{2}$ multiplet and vibronic sidebands. The $A_1 \rightarrow Y_3$ and Y_4 transitions are observed at 16556 and 16530 cm^{-1}. This puts the Y_3 and Y_4 states at 1283 and 1309 cm^{-1}, respectively.

Table 5.11: Zero phonon electronic lines and vibrational sidebands observed for the $^6H_{\frac{7}{2}}$ and $^6H_{\frac{11}{2}}$ multiplets of the A centre in SrF_2:0.05%Sm^{3+}.

$^6H_{\frac{7}{2}}$				$^6H_{\frac{11}{2}}$		
Transition Assignment	**Energy**	**Shift From Y_1**	**Shift From Y_2**	**Transition Assignment**	**Energy**	**Shift From W_1**
Y_1	16849	0	-118	W_1	14326	0
Y_2	16731	118	0	W_2	14220	106
a	16699	150	32	a	14175	151
b	16687	162	44	b	14164	162
c	16674	175	57	c	14155±5	171
d	16666	183	65	d	14143	183
e	16657	192	74	e	14134	192
f	16649	200	82	f	14122	204
Y_3	16556	293	175	W_4	14094±3	232
e	16540	309	191	W_5	14083	243
Y_4	16530	319	201	W_6	14015	311
f	16522±5	327	209	LO	13966±10	360

Fluorescence to the $^6H_{\frac{9}{2}}$, $^6H_{\frac{11}{2}}$ and $^6H_{\frac{13}{2}}$ multiplets are very simple to interpret. This is because the transitions are generally isolated and the spectra are not complicated by phonon sidebands. The recorded spectra are shown in Figure 5.28(c) for the $^6H_{\frac{9}{2}}$ multiplet and Figure 5.29(a) and (b) for the $^6H_{\frac{11}{2}}$ and $^6H_{\frac{13}{2}}$ multiplets, respectively.

Transitions to the overlapping $^6H_{\frac{15}{2}}$, $^6F_{\frac{1}{2}}$ and $^6F_{\frac{3}{2}}$ multiplets are observed in the 11700-11000 cm^{-1} (855-910 nm) region. These spectra were recorded using the SPEX 1700 single monochromator and RCA 7102 PMT. Despite the higher wavelength transitions overlapping, the spectrum is clear as the transitions are intense and observed as distinct peaks. A transition observed at 896.70 nm is assigned as terminating on the transverse optical phonon mode of the lattice at 221 cm^{-1}. The spectrum is shown in Figure 5.30(a).

The transitions to the $^6F_{\frac{5}{2}}$ and $^6F_{\frac{7}{2}}$ multiplets are observed in the 10650-10500

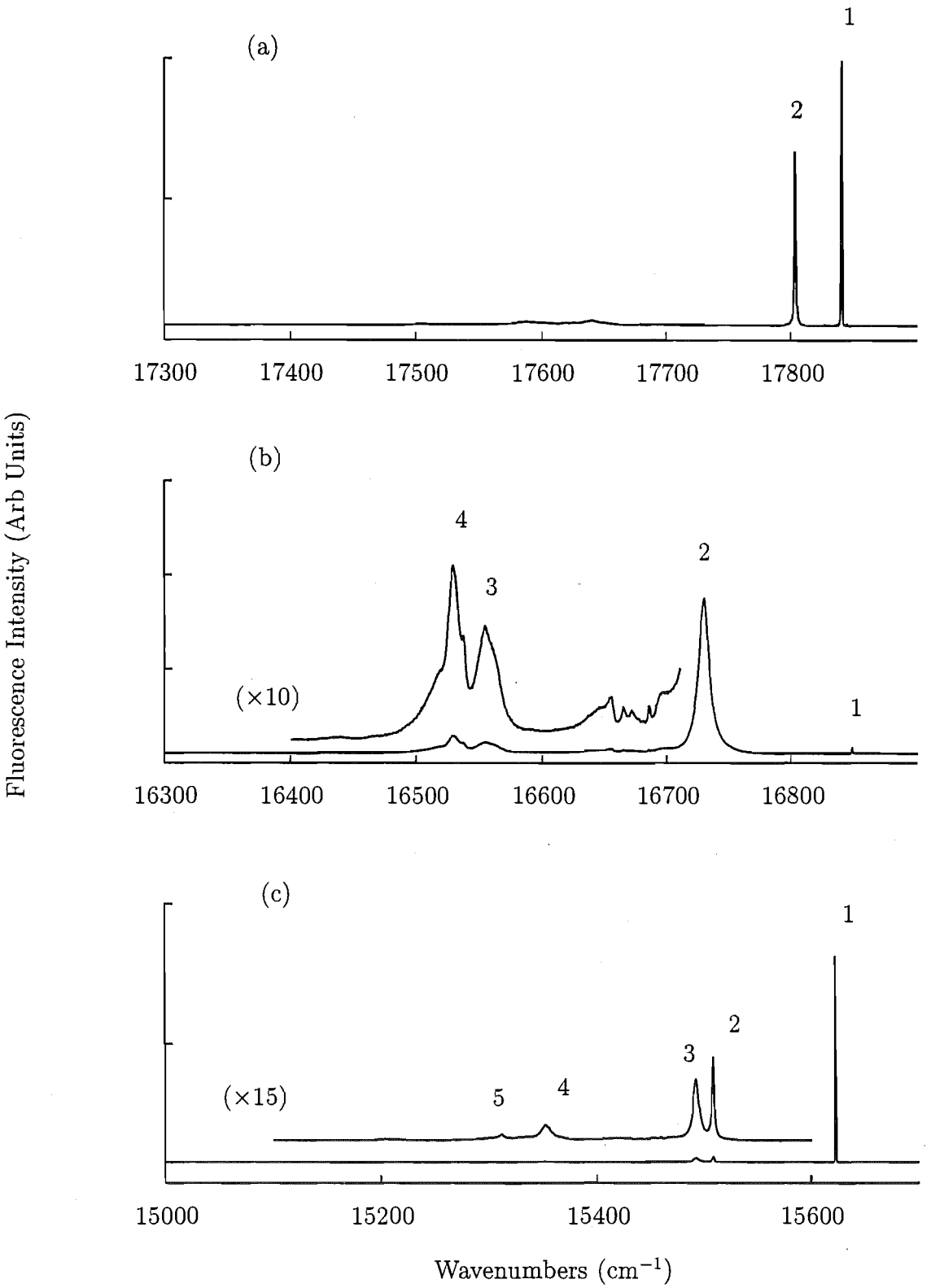

Figure 5.28: Fluorescence spectrum of the A centre for transitions $^4G_{\frac{5}{2}}$ to the (a) $^6H_{\frac{5}{2}}$ (b) $^6H_{\frac{7}{2}}$ and (c) $^6H_{\frac{9}{2}}$ multiplets in SrF_2:0.05%Sm^{3+}. For (a) excitation is at the 18195 cm^{-1} $Z_1 \rightarrow A_3$ transition, for (b) and (c) it is at the 17839 cm^{-1} $Z_1 \rightarrow A_1$ transition. The spectra were recorded at 16K.

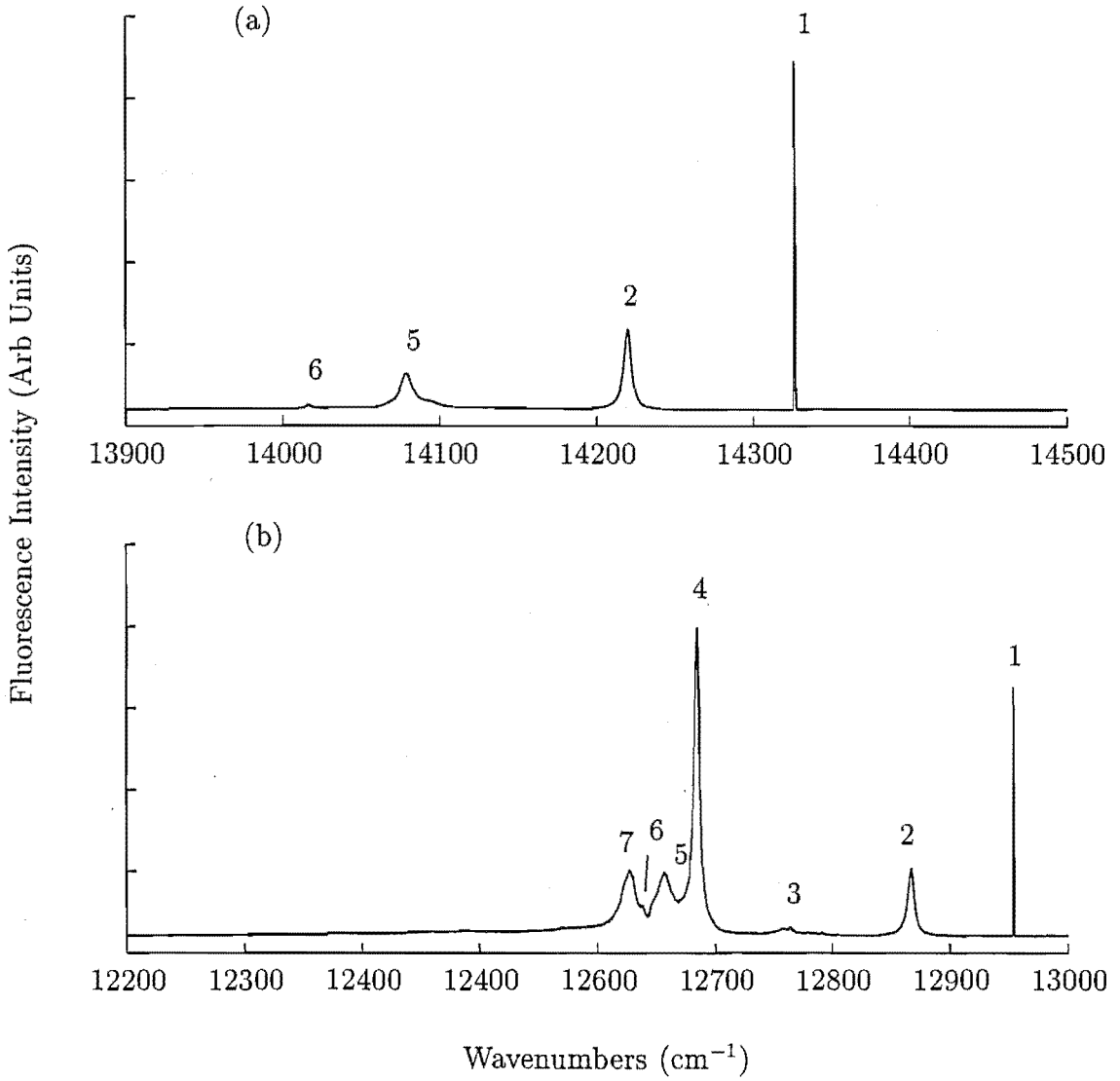

Figure 5.29: Fluorescence spectrum of the A centre for transitions from $^4G_{\frac{5}{2}}$ to the (a) $^6H_{\frac{11}{2}}$ and (b) $^6H_{\frac{13}{2}}$ multiplets in SrF_2:0.05%Sm^{3+}. Excitation is at the 17839 cm^{-1} $Z_1 \rightarrow A_1$ transition. The spectra were recorded at 16K.

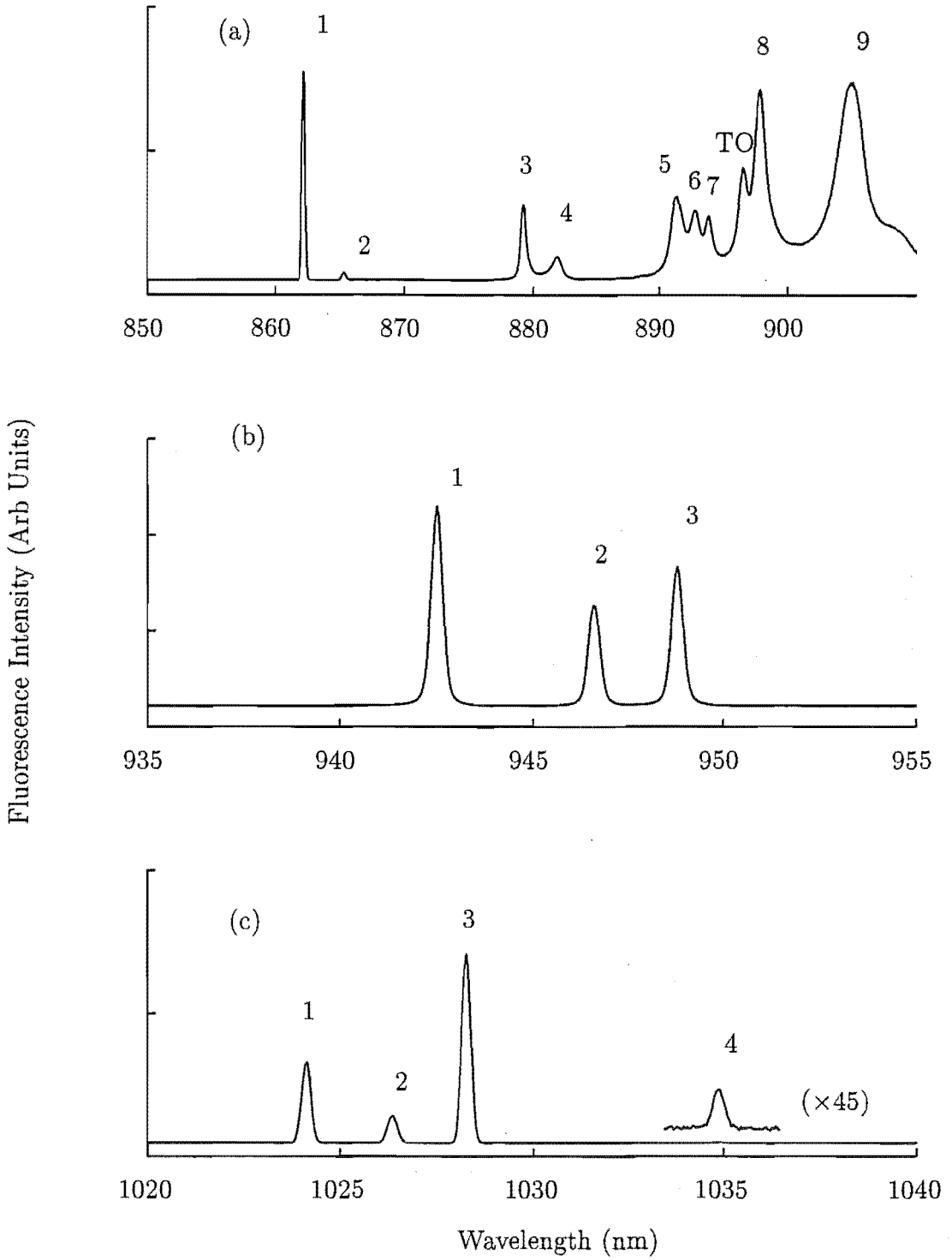

Figure 5.30: Fluorescence spectrum of the A centre for transitions $^4G_{\frac{5}{2}}$ to the (a) $^6H_{\frac{15}{2}}$, $^6F_{\frac{1}{2}}$, $^6F_{\frac{3}{2}}$, (b) $^6F_{\frac{5}{2}}$ and (c) $^6F_{\frac{7}{2}}$ multiplets in SrF_2:0.05%Sm^{3+}. Excitation is at the 17839 cm^{-1} $Z_1 \rightarrow A_1$ transition. The spectra were recorded at 16K.

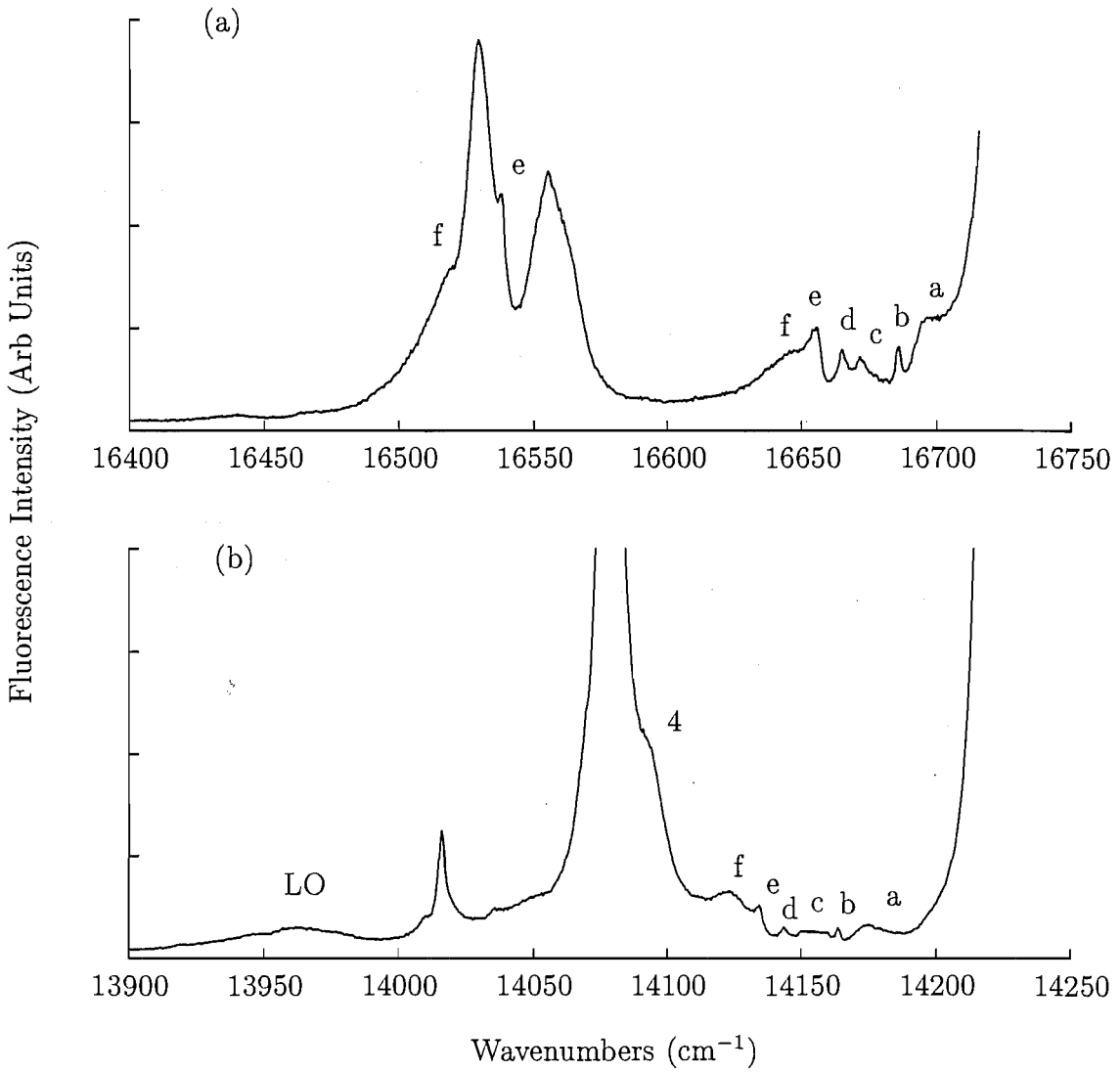

Figure 5.31: Vibronic sidebands of fluorescence to the (a) $^6H_{\frac{7}{2}}$ and (b) $^6H_{\frac{11}{2}}$ multiplets for the A centre in SrF_2:0.05%Sm^{3+}. The spectra were recorded at 16K.

Table 5.12: Fluorescent energies (air cm^{-1} ± 1 unless otherwise stated), measured polarisation ratios and terminating states for emission from the $^4G_{\frac{5}{2}}$ multiplet to the $^6H_{\frac{5}{2},\frac{7}{2},\frac{9}{2},\frac{11}{2},\frac{13}{2},\frac{15}{2}}$, $^6F_{\frac{1}{2},\frac{3}{2},\frac{5}{2},\frac{7}{2}}$ multiplets of the A centre in SrF_2:0.05%Sm^{3+}.

Multiplet	Terminating State Label	Terminating State Energy	Transition Frequency	Polarisation Ratio ZX	Polarisation Ratio ZY
$^6H_{\frac{5}{2}}$	Z_1	0	17839	1.9	1.0
	Z_2	35	17804	1.0	2.2
$^6H_{\frac{7}{2}}$	Y_1	990	16849	1.1	1.0
	Y_2	1108	16731	2.9	1.0
	Y_3	1283	16556	2.6	1.0
	Y_4	1309	16530	2.3	1.0
$^6H_{\frac{9}{2}}$	X_1	2216	15623	1.0	1.8
	X_2	2330	15509	1.0	1.8
	X_3	2345	15494	1.0	1.7
	X_4	2486	15353	3.3	1.0
	X_5	2527	15312	2.0	1.0
$^6H_{\frac{11}{2}}$	W_1	3513	14326	1.0	1.8
	W_2	3619	14220	2.0	1.0
	W_4	3745	14094	-	-
	W_5	3760	14083	1.1	1.0
	W_6	3824	14015	1.0	1.7
$^6H_{\frac{13}{2}}$	V_1	4885	12954	1.0	1.5
	V_2	4971	12868	1.0	2.1
	V_3	5078	12761±5	1.6	1.0
	V_4	5154	12685	2.1	1.0
	V_5	5181	12658	1.0	1.2
	V_6	5198	12641	2.0	1.0
	V_7	5210	12629	3.3	1.0
$^6H_{\frac{15}{2}}$, $^6F_{\frac{1}{2}}$ and $^6F_{\frac{3}{2}}$	S_1	6241	11598	2.1	1.0
	S_2	6282	11557	1.1	1.0
	S_3	6466	11373	1.1	1.0
	S_4	6500	11339	1.1	1.0
	S_5	6619	11220	1.3	1.0
	S_6	6636	11203	1.4	1.0
	S_7	6650	11189	1.2	1.0
	S_8	6702	11137	1.0	1.2
	S_9	6787	11052±5	1.4	1.0
$^6F_{\frac{5}{2}}$	R_1	7228	10611	1.6	1.0
	R_2	7274	10565	1.2	1.0
	R_3	7299	10540	1.0	1.2
$^6F_{\frac{7}{2}}$	Q_1	8075	9764	2.1	1.0
	Q_2	8096	9743	1.1	1.0
	Q_3	8112	9727	1.3	1.0
	Q_4	8173	9666	1.4	1.0

cm^{-1} (940-950 nm) and 9800-9600 cm^{-1} (1020-1040 nm) regions, respectively. All expected transitions are observed for both multiplets.

5.3.4 O Centre Fluorescence

For excitation of the 18070 cm^{-1} transition of the O centre in SrF_2:0.05%Sm^{3+}, emission is observed to the ^6H_J and ^6F_J multiplets as shown in Figures 5.32 through 5.34. The observed fluorescence displays no polarisation dependence for either ⟨100⟩ or ⟨111⟩ oriented crystals. On the basis of this measurement, and the observed transition multiplicity, the centre is assigned as a near cubic symmetry centre.

Transitions to the $^6H_{\frac{7}{2}}$, $^6H_{\frac{9}{2}}$ and $^6H_{\frac{11}{2}}$ show vibronic sidebands. The sidebands associated with the $^6H_{\frac{7}{2}}$ and $^6H_{\frac{11}{2}}$ multiplets are readily analysed in terms of peaks in the SrF_2 host lattice, density of states given by Bilz and Kress [85] and those vibronic intervals already observed for the A centre in SrF_2:0.05%Sm^{3+} crystals. Those associated with the $^6H_{\frac{7}{2}}$ multiplet are given in Table 5.14. The 17699 cm^{-1} transition being excited here, overlaps an absorption transition of an unrelated centre whose emission cannot be discriminated against. Transitions associated with this centre are denoted by * in the spectra presented.

A tentative energy level scheme can be obtained through analogy with that obtained for the CaF_2:Sm^{3+} near-cubic centre. The resultant transition assignments are given in Table 5.13. From this it is apparant that transitions to crystal field levels transforming as cubic Γ_6 irreps, which should be forbidden from the $A_1\Gamma_7$ emitting level in strict cubic symmetry, are of greater intensity than analogous transitions for the CaF_2:Sm^{3+} near-cubic centre. This indicates that the non-cubic distortion is greater for the SrF_2:Sm^{3+} near-cubic centre. This may be because the charge compensating fluorine ion is closer in the SrF_2 host.

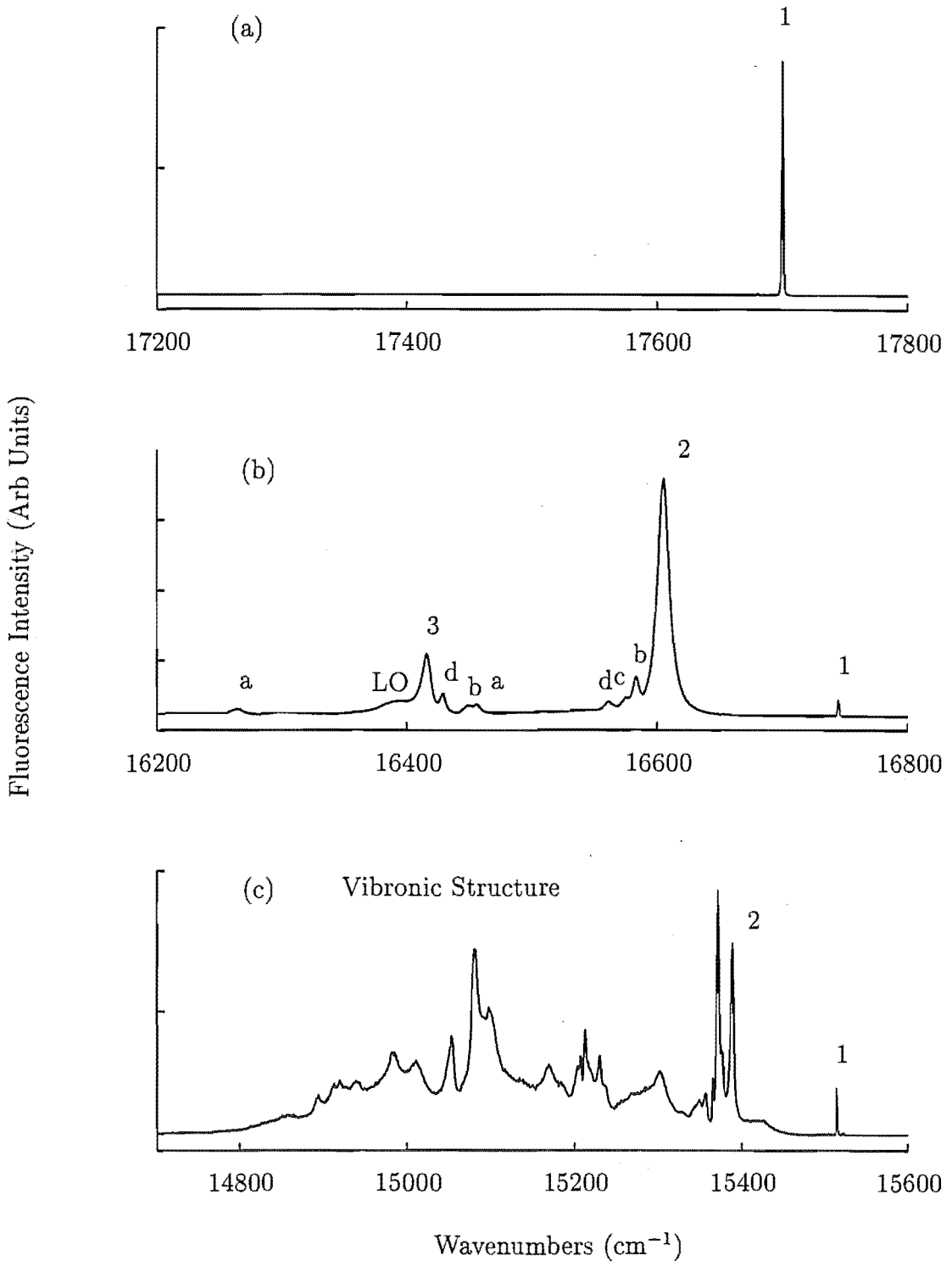

Figure 5.32: Fluorescence spectrum of the O centre for transitions from $^4G_{\frac{5}{2}}$ to the (a) $^6H_{\frac{5}{2}}$, (b) $^6H_{\frac{7}{2}}$ and (c) $^6H_{\frac{9}{2}}$ multiplets in SrF_2:0.05%Sm^{3+}. Excitation is at the 17699 cm^{-1} $Z_1 \rightarrow A_1$ transition. The spectra were recorded at 16K.

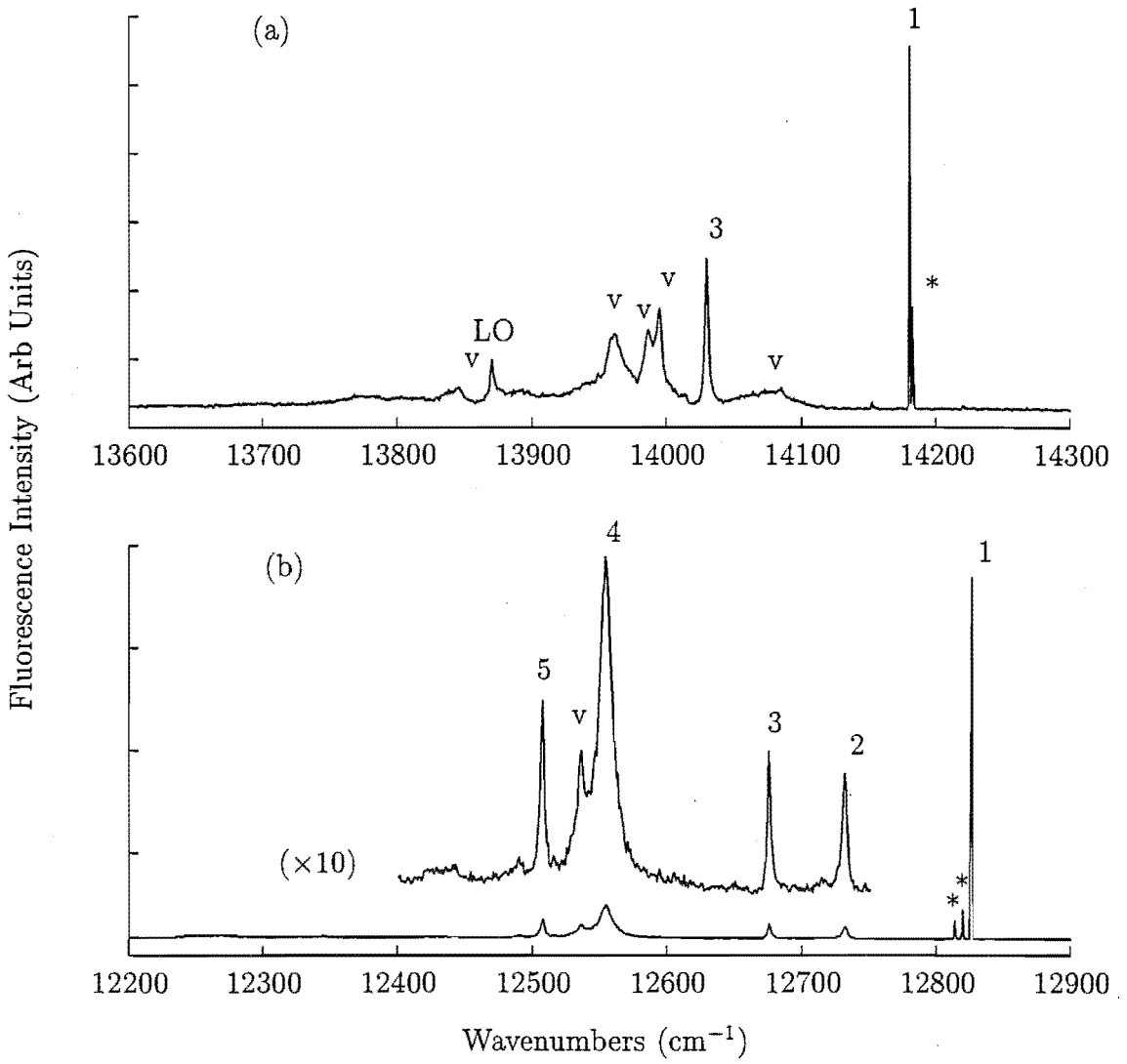

Figure 5.33: Fluorescence spectrum of the O centre for transitions from $^4G_{\frac{5}{2}}$ to the (a) $^6H_{\frac{11}{2}}$ and (b) $^6H_{\frac{13}{2}}$ multiplets in SrF_2:0.05%Sm^{3+}. Excitation is at the 17699 cm^{-1} $Z_1 \rightarrow A_1$ transition. Those features labelled * are not related to the O centre. The spectra were recorded at 16K.

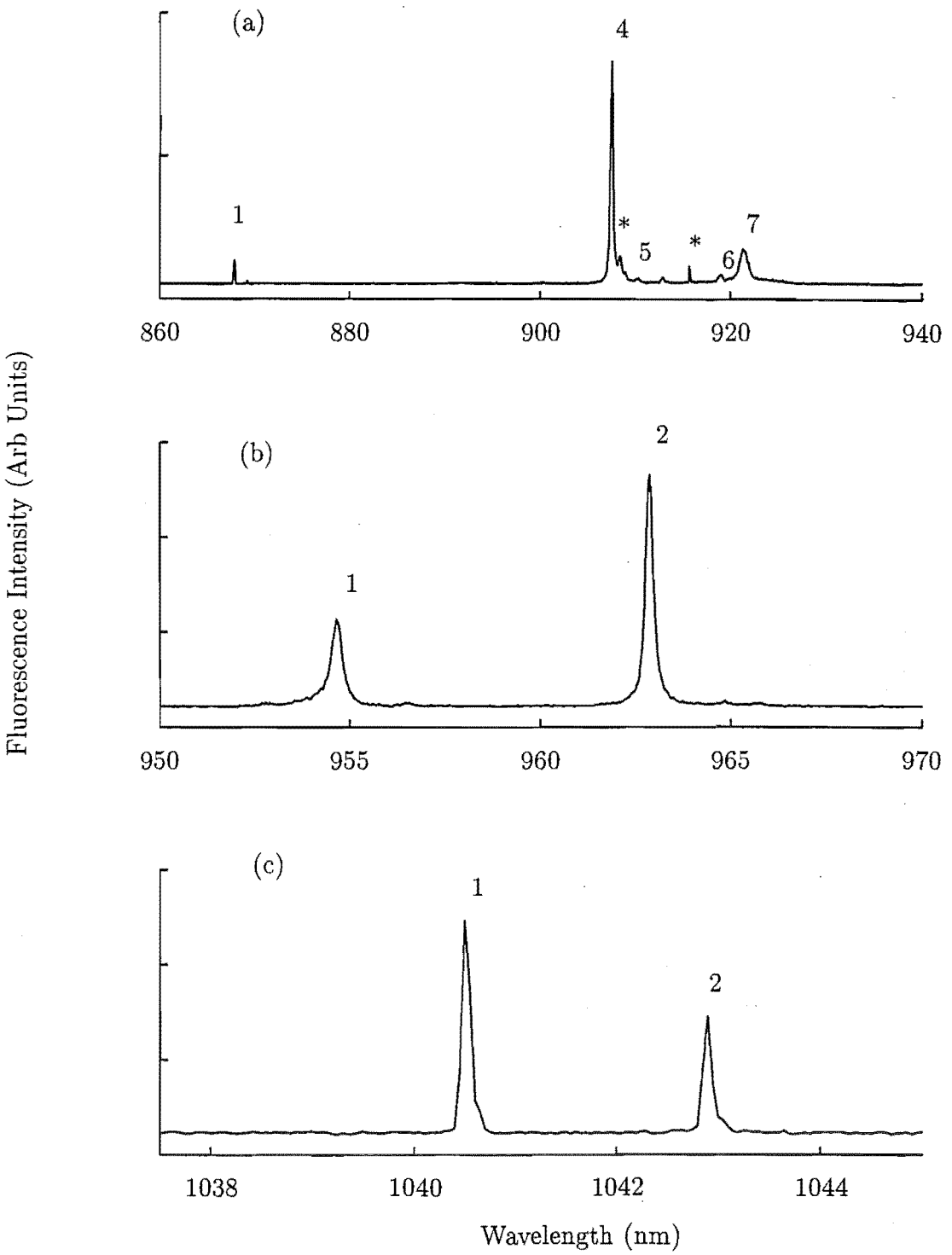

Figure 5.34: Fluorescence spectrum of the O centre for transitions from $^4G_{\frac{5}{2}}$ to the (a) $^6H_{\frac{15}{2}}$, $^6F_{\frac{1}{2}}$, $^6F_{\frac{3}{2}}$, (b) $^6F_{\frac{5}{2}}$ and (c) $^6F_{\frac{7}{2}}$ multiplets in SrF_2:0.05%Sm^{3+}. Excitation is at the 17699 cm^{-1} $Z_1 \rightarrow A_1$ transition. Those features labelled * are not related to the O centre. The spectra were recorded at 16K.

Table 5.13: Transition frequencies (air $cm^{-1}\pm1$ unless otherwise stated) and assignments for electronic transitions of the O centre in SrF_2:0.05%Sm^{3+}

Multiplet	Transition Frequency	State Energy	Transition Assignment
$^6H_{\frac{5}{2}}$	17699	0	$A_1\Gamma_7 \rightarrow Z_1\Gamma_8$
$^6H_{\frac{7}{2}}$	16744	955	$A_1\Gamma_7 \rightarrow Y_1\Gamma_6$
	16606	1093	$A_1\Gamma_7 \rightarrow Y_2\Gamma_7$
	16415	1284	$A_1\Gamma_7 \rightarrow Y_3\Gamma_8$
$^6H_{\frac{9}{2}}$	15514	2185	$A_1\Gamma_7 \rightarrow X_1\Gamma_6$
	15366	2333	$A_1\Gamma_7 \rightarrow X_2\Gamma_8$
$^6H_{\frac{11}{2}}$	14179	3520	$A_1\Gamma_7 \rightarrow W_1\Gamma_8$
	14029	3670	$A_1\Gamma_7 \rightarrow W_3\Gamma_8$
$^6H_{\frac{13}{2}}$	12827	4872	$A_1\Gamma_7 \rightarrow V_1\Gamma_8$
	12732	4967	$A_1\Gamma_7 \rightarrow V_2\Gamma_7$
	12676	5023	$A_1\Gamma_7 \rightarrow V_3\Gamma_8$
	12553	5146	$A_1\Gamma_7 \rightarrow V_4\Gamma_7$
	12507	5192	$A_1\Gamma_7 \rightarrow V_5\Gamma_6$
$^6H_{\frac{15}{2}}$, $^6F_{\frac{1}{2}}$ and $^6F_{\frac{3}{2}}$	11523	6176	$A_1\Gamma_7 \rightarrow S_1\Gamma_8$
	11016	6682	$A_1\Gamma_7 \rightarrow S_4\Gamma_8$
	10981	6718	$A_1\Gamma_7 \rightarrow S_5\Gamma_8$
	10882	6817	$A_1\Gamma_7 \rightarrow S_6\Gamma_7$
	10852	6848	$A_1\Gamma_7 \rightarrow S_7\Gamma_8$
$^6F_{\frac{5}{2}}$	10472	7227	$A_1\Gamma_7 \rightarrow R_1\Gamma_7$
	10383	7316	$A_1\Gamma_7 \rightarrow R_2\Gamma_8$
$^6F_{\frac{7}{2}}$	9612	8087	$A_1\Gamma_7 \rightarrow Q_1\Gamma_7$
	9590	8109	$A_1\Gamma_7 \rightarrow Q_2\Gamma_8$

Table 5.14: Fluorescence energies (±1 cm^{-1}) of vibronic sidebands observed for the $^6H_{\frac{7}{2}}$ multiplet of the cubic centre in SrF_2:Sm^{3+}

Transition Frequency	Shift From Y_1	Y_2	Y_3	Assignment
16582	162	-	-	b
16575	169	-	-	c
16561	183	-	-	d
16455	-	151	-	a
16446	-	160	-	b
16427	-	179	-	d
16335	389			LO
16264	-	-	151	a

5.3.5 G1 Centre Fluorescence

Light oxygenation of Sm^{3+} doped alkaline earth fluoride crystals produces new centres where the Sm^{3+} ion is charge compensated by an O^{2-} ion. In this study, crystals were treated in a dry oxygen atmosphere at 900 °C. The oxygenation period ranged between 30 minutes to an hour in length. Only one new centre is created for this period of treatment. This centre has $^4G_{\frac{5}{2}}$ excitation features at 17544 and 18126 cm^{-1}. Exciting either of these transitions, yields a system of 43 fluorescence transitions shown in Figures 5.35, 5.36 and 5.37. The polarisation dependence of these transitions has been measured in both ⟨111⟩ and ⟨100⟩ oriented crystals. For ⟨100⟩ crystals, no discernable dependence is observed. Crystals oriented along their ⟨111⟩ cleavage planes yield a weak dependence upon the polarisation of the exciting laser radiation and resultant fluorescence (as shown in Table 5.15). This is consistent with a trigonal symmetry centre. This is not an unexpected discovery as it has previously been observed for the CaF_2 host crystal that the O^{2-} and Sm^{3+} ions reside as simple pairs of trigonal symmetry. In that case, the specific form of charge compensation is that of a ⟨111⟩ oriented O^{2-} ion, in the nearest neighbour substitutional position. It is proposed that this is also the centre configuration for $SrF_2:Sm^{3+}:O^{2-}$ crystals. The large magnitude of the crystal field splittings and the observed polarisation dependence support this assertion. This centre has been observed using the EPR technique by Newman and Woodward [80].

The similarity of the recorded spectra with that of the G1 centre in $CaF_2:Sm^{3+}$ provides further confirmation that the charge compensation configuration for the two centres is the same. As with all Sm^{3+} centres studied previously, vibronic sidebands are observed at varying energy separations from the electronic emission lines. These energy separations are consistent with vibronic sidebands observed by Aizenberg et. al. [90] and are assigned as such on the spectra.

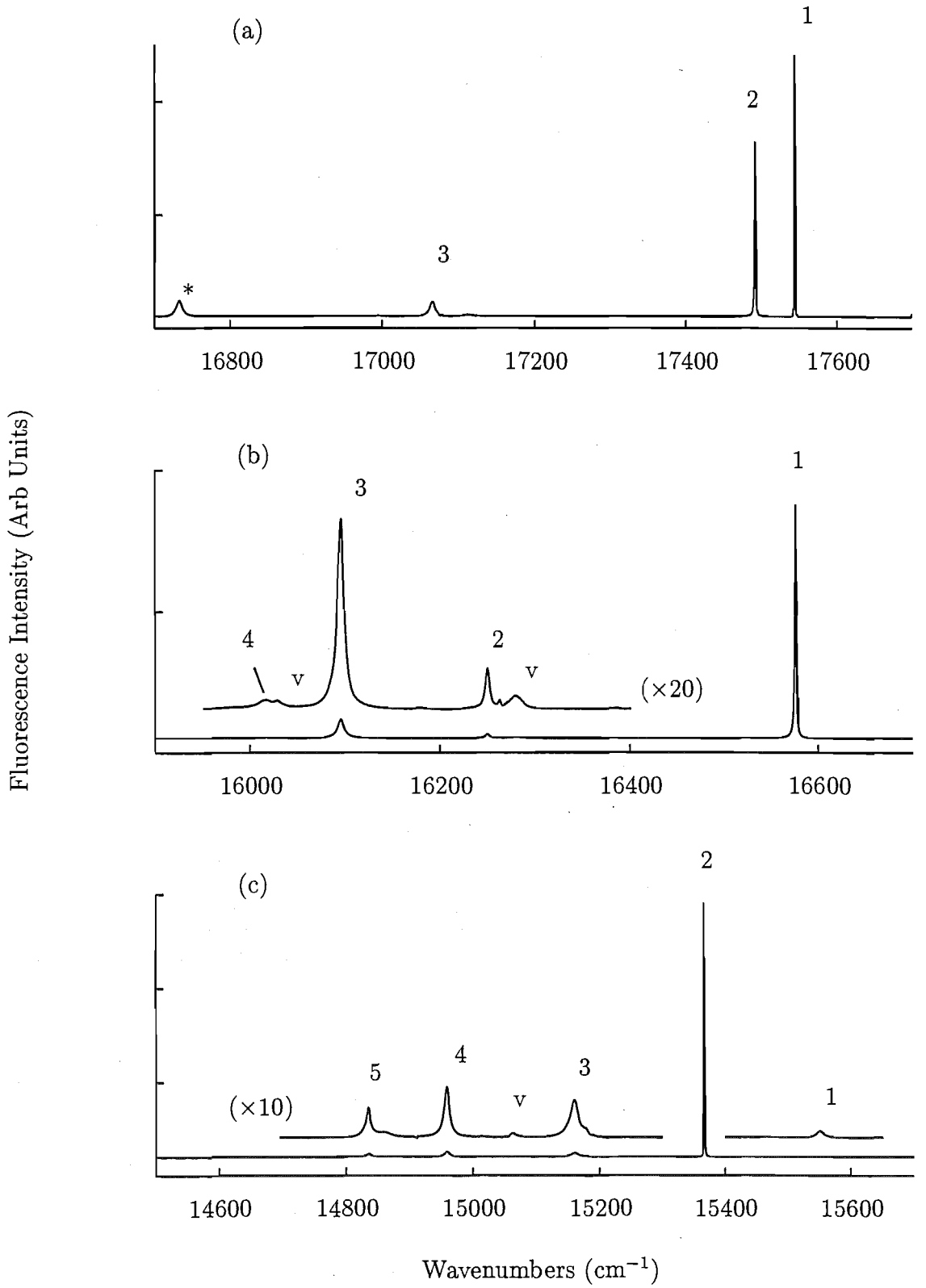

Figure 5.35: Fluorescence spectrum of the G1 centre for transitions from $^4G_{\frac{5}{2}}$ to the (a) $^6H_{\frac{5}{2}}$, (b) $^6H_{\frac{7}{2}}$ and (c) $^6H_{\frac{9}{2}}$ multiplets in SrF_2:0.05%Sm^{3+}. Excitation is at the 18126 cm^{-1} $Z_1 \rightarrow A_1$ transition. The spectra were recorded at 16K.

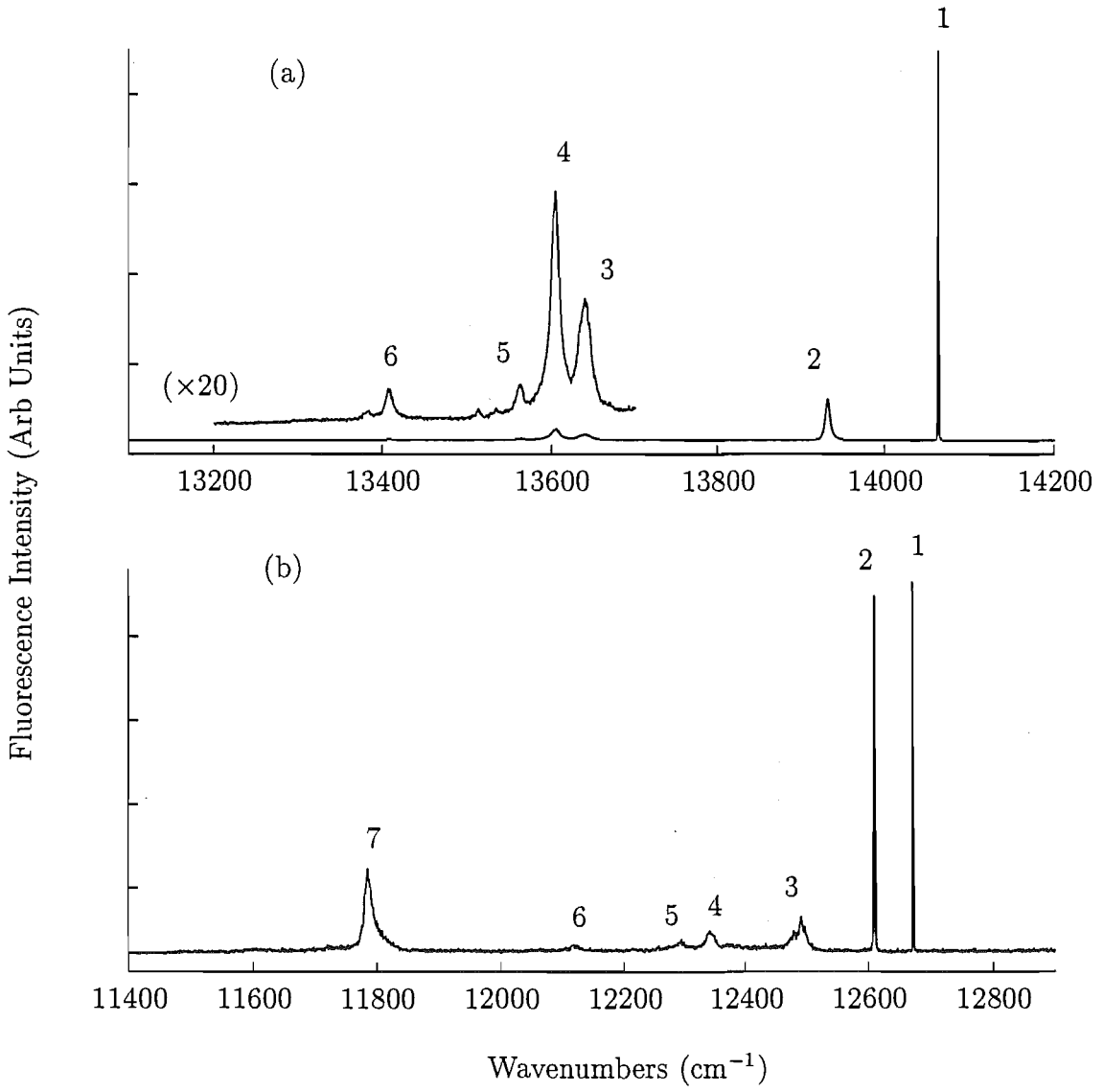

Figure 5.36: Fluorescence spectrum of the G1 centre for transitions from $^4G_{\frac{5}{2}}$ to the (a) $^6H_{\frac{11}{2}}$ and (b) $^6H_{\frac{13}{2}}$ multiplets in SrF_2:0.05%Sm^{3+}. Excitation is at the 17544 cm^{-1} $Z_1 \rightarrow A_1$ transition. The spectra were recorded at 16K.

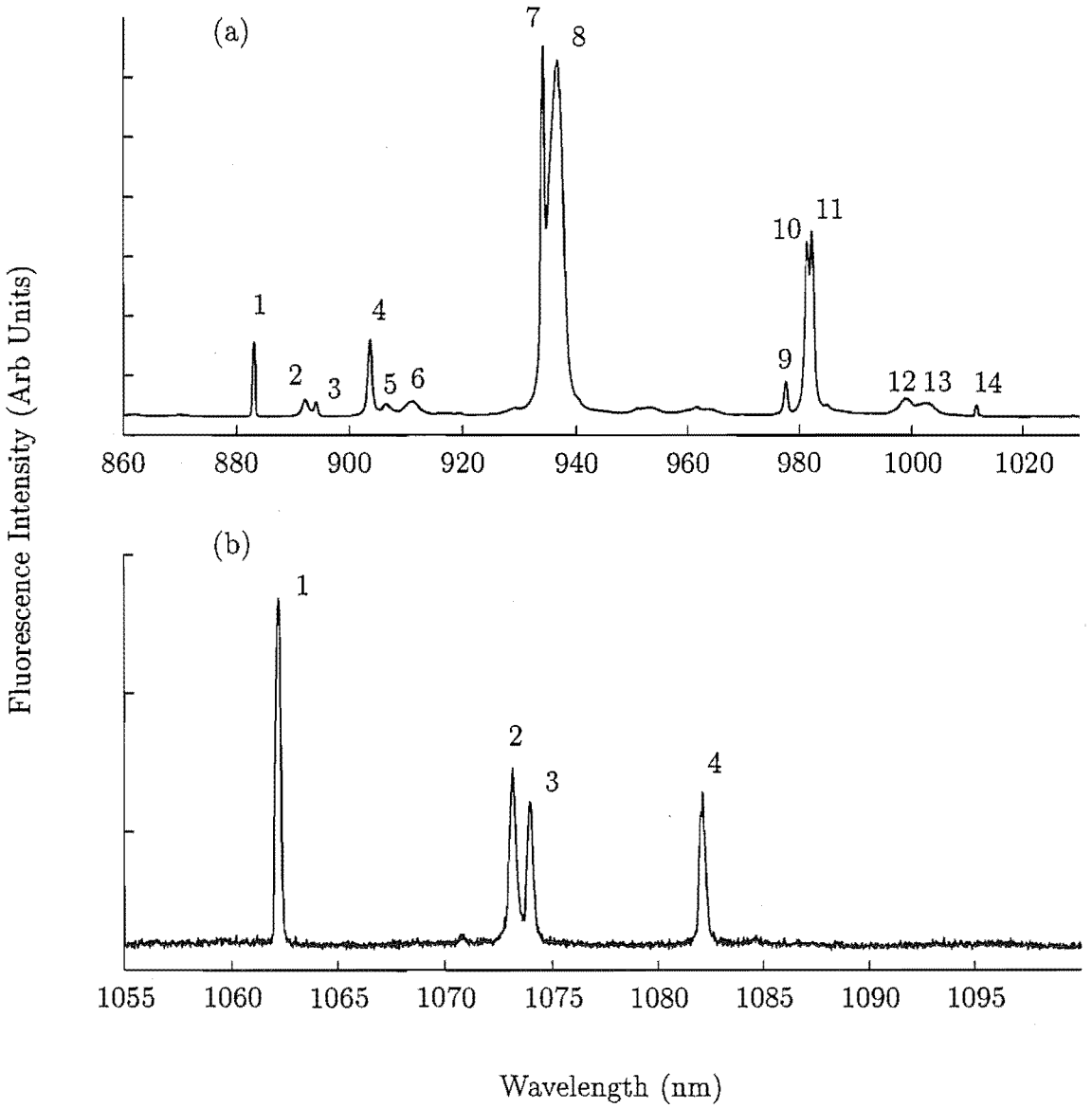

Figure 5.37: Fluorescence spectrum of the G1 centre for transitions $^4G_{\frac{5}{2}}$ to the (a) $^6H_{\frac{15}{2}}$, $^6F_{\frac{1}{2}}$, $^6F_{\frac{3}{2}}$, $^6F_{\frac{5}{2}}$ and (b) $^6F_{\frac{7}{2}}$ multiplets in SrF_2:0.05%Sm^{3+}. Excitation is at the 17544 cm^{-1} $Z_1 \rightarrow A_1$ transition. The spectra were recorded at 16K.

Table 5.15: Transition frquencies (air cm^{-1} ± 1 unless otherwise stated), measured polarisation ratios and terminating states for emission from the $^4G_{\frac{5}{2}}$ to the $^6H_{\frac{5}{2},\frac{7}{2},\frac{9}{2},\frac{11}{2},\frac{13}{2},\frac{15}{2}}$ and $^6F_{\frac{1}{2},\frac{3}{2},\frac{5}{2},\frac{7}{2}}$ multiplets of the G1 centre in SrF_2:0.05%Sm^{3+}.

Multiplet	Terminating State		Fluorescence	Polarisation Ratio	
	Label	Energy	Frequency	ZX	ZY
$^6H_{\frac{5}{2}}$	Z_1	0	17544	1.1	1.0
	Z_2	45	17472	1.0	1.5
	Z_3	477	17067	1.0	1.3
$^6H_{\frac{7}{2}}$	Y_1	969	16575	1.0	1.1
	Y_2	1294	16250	1.0	1.1
	Y_3	1449	16095	1.0	1.1
	Y_4	1527	16017	1.1	1.0
$^6H_{\frac{9}{2}}$	X_1	1989	15555	1.2	1.0
	X_2	2176	15368	1.1	1.0
	X_3	2380	15164	1.1	1.0
	X_4	2582	14962	1.1	1.0
	X_5	2710	14834	1.1	1.0
$^6H_{\frac{11}{2}}$	W_1	3481	14063	1.2	1.0
	W_2	3612	13932	1.2	1.0
	W_3	3906	13638	1.3	1.0
	W_4	3941	13603	1.2	1.0
	W_5	3980	13564	1.1	1.0
	W_6	4135	13409	1.0	1.3
$^6H_{\frac{13}{2}}$	V_1	4872	12672	1.1	1.0
	V_2	4934	12610	1.1	1.0
	V_3	5049	12495	-	-
	V_4	5199	12345	-	-
	V_5	5247	12297	-	-
	V_6	5420	12124	-	-
	V_7	5758	11786	1.3	1.0
$^6H_{\frac{15}{2}}$, $^6F_{\frac{1}{2}}$, $^6F_{\frac{3}{2}}$ and $^6F_{\frac{5}{2}}$	S_1	6222	11322	1.0	1.5
	S_2	6337	11207	1.0	1.1
	S_3	6363	11181	1.0	1.1
	S_4	6479	11065	1.0	1.8
	S_5	6514	11030	1.0	1.7
	S_6	6575	10969	1.0	1.3
	S_7	6840	10704	1.0	1.1
	S_8	6869	10675	1.0	1.0
	S_9	7316	10228	1.0	1.3
	S_{10}	7356	10188	1.0	1.0
	S_{11}	7365	10179	1.1	1.0
	S_{12}	7533	10011	1.0	1.4
	S_{13}	7569	9975	1.0	1.2
	S_{14}	7664	9880	1.0	1.0
$^6F_{\frac{7}{2}}$	Q_1	8130	9414	1.0	1.1
	Q_2	8226	9318	1.0	1.4
	Q_3	8232	9312	1.0	1.4
	Q_4	8303	9241	1.0	1.8

5.4 Crystal Field Analysis for the C_{4v} Symmetry Centres

Single electron crystal field analyses for the dominant C_{4v} symmetry centres in both CaF_2 and SrF_2 crystals doped with Sm^{3+} ions were completed. This was done with the crystal field (F-Shell Empirical) fitting programs of Dr M F Reid of this department. For CaF_2:Sm^{3+} and SrF_2:Sm^{3+}, 48 and 52 experimental levels were least squares fitted to the interactions described in chapter two for the f^5 configuration appropriate for Sm^{3+}. The lowest 250 electronic states of the f^5 configuration were fitted, with 9 free parameters, to the Hamiltonian of Eqn 2.12 that is appropriate for a centre with C_{4v} symmetry. It is important to include a significant portion of the configuration to properly account for the effects of intermediate coupling within the states of the $4f^5$ configuration.

It can be seen in Tables 5.16 and 5.17, that levels of the $^6F_{\frac{9}{2}}$ and $^6F_{\frac{11}{2}}$ multiplets are also included in the crystal-field fits performed in this section. The experimental data for these levels, was obtained from infrared absorption as is given in chapter eight. The levels were assigned on the basis of crystal field fits to all other multiplets and from the similarity between the CaF_2:Sm^{3+} and SrF_2:Sm^{3+} absorption spectra. This is simplest in the SrF_2:Sm^{3+} case since clustering is less important at the concentrations studied here and the absorption spectra is predominantly due to the C_{4v} centre alone. The 2567 cm^{-1} level assigned to the C_{4v} symmetry A centre in CaF_2:Sm^{3+} was not fitted as this appears to be anomalous and cannot be accounted for at all accurately by the crystal field calculation. The inclusion of this level distorts the parameters to such an extent that the measured Zeeman splitting factors in chapter eight are no longer well accounted for.

It should be kept in mind, that the crystal field fits presented in Tables 5.16 and 5.17 were constructed with minimal experimental irrep symmetry assignments for the crystal field energy levels. The irrep assignments have been made through comparision with calculations which use interpolated parameters. These parameters were obtained from crystal field analyses to levels of the C_{4v} symmetry centres in CaF_2:Nd^{3+} (Han [100] 1993) and CaF_2:Eu^{3+} (this study, chapter six) and SrF_2:Nd^{3+} (Han [100] 1993) and SrF_2:Eu^{3+} (this study, chapter six). Despite this, the fits seem reasonable. Good agreement is obtained with the previously optimised parameters for C_{4v} symmetry centres in CaF_2 and SrF_2 host crystals. These are compared in chapter nine. The standard deviations of the fits obtained (denoted σ in Table 5.18) are acceptable, remaining under 15 cm^{-1} for both centres.

Table 5.19 gives the Sm^{3+} free ion wavefunctions and calculated barycentre energies for those multiplets of interest in this study. These have been calculated with the

Table 5.16: Crystal field fits to the $^6H_{\frac{5}{2},\frac{7}{2},\frac{9}{2},\frac{11}{2},\frac{13}{2},\frac{15}{2}}$, $^6F_{\frac{1}{2},\frac{3}{2},\frac{5}{2},\frac{7}{2}}$, $^4G_{\frac{5}{2}}$ and $^4F_{\frac{3}{2}}$ multiplets for the C_{4v} symmetry A centre in CaF_2:Sm^{3+}. The level in brackets has not been fitted to the crystal field Hamiltonian.

State & Symmetry	Calc Energy	Exptl Energy	State & Symmetry	Calc Energy	Exptl Energy
$Z_1\gamma_6$	10	0	$S_6\gamma_6$	6667	6660
$Z_2\gamma_7$	47	47	$S_7\gamma_6$	6692	6693
$Z_3\gamma_7$	367	-	$S_8\gamma_7$	6766	6768
$Y_1\gamma_6$	984	985	$S_9\gamma_6$	6859	6852
$Y_2\gamma_7$	1169	1160	$S_{10}\gamma_7$	6878	6885
$Y_3\gamma_7$	1334	1323	$S_{11}\gamma_7$	6916	-
$Y_4\gamma_6$	1402	1418	$R_1\gamma_7$	7282	7293
$X_1\gamma_6$	2209	2215	$R_2\gamma_6$	7338	7345
$X_2\gamma_6$	2378	2376	$R_3\gamma_7$	7381	7375
$X_3\gamma_7$	2394	2403	$Q_1\gamma_7$	8130	8126
$X_4\gamma_7$	2533	2537	$Q_2\gamma_6$	8148	8156
$X_5\gamma_6$	2629	(2567)	$Q_3\gamma_7$	8156	8178
$W_1\gamma_6$	3494	3504	$Q_4\gamma_6$	8247	8246
$W_2\gamma_7$	3651	3648	$P_1\gamma_6$	9287	9270
$W_3\gamma_6$	3740	-	$P_2\gamma_6$	9290	9288
$W_4\gamma_6$	3791	-	$P_3\gamma_7$	9342	9356
$W_5\gamma_7$	3809	3814	$P_4\gamma_6$	9363	9372
$W_6\gamma_7$	3975	-	$P_5\gamma_7$	9414	-
$V_1\gamma_6$	4859	4866	$O_1\gamma_7$	10582	-
$V_2\gamma_7$	4976	4981	$O_2\gamma_6$	10698	10697
$V_3\gamma_7$	5131	5125	$O_3\gamma_7$	10711	-
$V_4\gamma_6$	5215	-	$O_4\gamma_6$	10727	10734
$V_5\gamma_7$	5216	5217	$O_5\gamma_6$	10785	10767
$V_6\gamma_6$	5240	5238	$O_6\gamma_7$	10794	-
$V_7\gamma_7$	5323	5300	$A_1\gamma_7$	17836	17837
$S_1\gamma_7$	6231	6230	$A_2\gamma_6$	17932	17908
$S_2\gamma_6$	6281	6286	$A_3\gamma_7$	18217	18240
$S_3\gamma_6$	6554	6527	$B_1\gamma_6$	18943	18950
$S_4\gamma_6$	6583	6580	$B_2\gamma_7$	18985	18976
$S_5\gamma_7$	6647	6651			

Table 5.17: Crystal field fits to the $^6H_{\frac{5}{2},\frac{7}{2},\frac{9}{2},\frac{11}{2},\frac{13}{2},\frac{15}{2}}$, $^6F_{\frac{1}{2},\frac{3}{2},\frac{5}{2},\frac{7}{2}}$, $^4G_{\frac{5}{2}}$ and $^4F_{\frac{3}{2}}$ multiplets for the C_{4v} symmetry A centre in SrF_2:Sm^{3+}

State & Symmetry	Calc Energy	Exptl Energy	State & Symmetry	Calc Energy	Exptl Energy
$Z_1\gamma_6$	7	0	$S_6\gamma_7$	6640	6636
$Z_2\gamma_7$	33	35	$S_7\gamma_7$	6655	6650
$Z_3\gamma_7$	259	-	$S_8\gamma_7$	6701	6702
$Y_1\gamma_6$	992	990	$S_9\gamma_6$	6787	6787
$Y_2\gamma_7$	1113	1108	$S_{10}\gamma_6$	6796	-
$Y_3\gamma_7$	1276	1283	$S_{11}\gamma_7$	6812	-
$Y_4\gamma_6$	1300	1309	$R_1\gamma_7$	7220	7228
$X_1\gamma_6$	2212	2216	$R_2\gamma_6$	7274	7274
$X_2\gamma_6$	2324	2330	$R_3\gamma_7$	7311	7299
$X_3\gamma_7$	2342	2345	$Q_1\gamma_7$	8076	8075
$X_4\gamma_7$	2477	2486	$Q_2\gamma_6$	8094	8096
$X_5\gamma_6$	2519	2527	$Q_3\gamma_7$	8103	8112
$W_1\gamma_6$	3510	3513	$Q_4\gamma_6$	8185	8173
$W_2\gamma_7$	3621	3619	$P_1\gamma_6$	9240	9244
$W_3\gamma_6$	3688	-	$P_2\gamma_6$	9250	9258
$W_4\gamma_6$	3740	-	$P_3\gamma_7$	9277	9295
$W_5\gamma_7$	3756	3760	$P_4\gamma_6$	9299	9310
$W_6\gamma_7$	3863	3824	$P_5\gamma_7$	9346	9346
$V_1\gamma_6$	4881	4885	$O_1\gamma_7$	10577	-
$V_2\gamma_7$	4969	4971	$O_2\gamma_6$	10647	10653
$V_3\gamma_7$	5092	5078	$O_3\gamma_7$	10650	10669
$V_4\gamma_7$	5157	5154	$O_4\gamma_6$	10683	10673
$V_5\gamma_6$	5167	5181	$O_5\gamma_6$	10730	10705
$V_6\gamma_6$	5189	5198	$O_6\gamma_7$	10735	-
$V_7\gamma_7$	5208	5210	$A_1\gamma_7$	17831	17839
$S_1\gamma_7$	6246	6241	$A_2\gamma_6$	17962	17934
$S_2\gamma_6$	6281	6282	$A_3\gamma_7$	18175	18195
$S_3\gamma_6$	6487	6466	$B_1\gamma_6$	18943	18949
$S_4\gamma_6$	6521	6500	$B_2\gamma_7$	18969	18963
$S_5\gamma_6$	6596	6619			

Table 5.18: C_{4v} symmetry crystal field parameters for the A centres in CaF_2:Sm^{3+} and SrF_2:Sm^{3+}. All quantities are in wavenumbers. Those parameters that are in square brackets were not varied, but are fixed at the values for $LaCl_3$:Sm^{3+}. [68].

Parameter	CaF_2:Sm^{3+}	SrF_2:Sm^{3+}
F^2	77869	79062
F^4	57491	56870
F^6	38548	40077
α	[21.6]	[21.6]
β	[-724]	[-724]
γ	[1700]	[1700]
T^2	[291]	[291]
T^3	[13]	[13]
T^4	[34]	[34]
T^6	[-193]	[-193]
T^7	[288]	[288]
T^8	[330]	[330]
M^{TOT}	[2.4]	[2.4]
P^{TOT}	[341]	[341]
ζ	1165	1168
B_A^2	749	472
B_A^4	616	545
B_A^6	617	489
B_C^4	-1208	-1204
B_C^6	669	562
σ	12	13
n	48	52

Table 5.19: Intermediate coupled free-ion wavefunctions for Sm^{3+}

SLJ State	Calculated Energy	Wavefunction
$^6H_{\frac{5}{2}}$	0	$0.9782\|^6H_{\frac{5}{2}}\rangle$ -0.1268$\|^4G^1_{\frac{5}{2}}\rangle$ -0.1540$\|^4G^4_{\frac{5}{2}}\rangle$
$^6H_{\frac{7}{2}}$	1000	-0.9852$\|^6H_{\frac{7}{2}}\rangle$ +0.1020$\|^4G^1_{\frac{7}{2}}\rangle$ +0.1251$\|^4G^4_{\frac{7}{2}}\rangle$
$^6H_{\frac{9}{2}}$	2200	$0.9898\|^6H_{\frac{9}{2}}\rangle$
$^6H_{\frac{11}{2}}$	3600	$0.9906\|^6H_{\frac{11}{2}}\rangle$
$^6H_{\frac{13}{2}}$	5000	$0.9869\|^6H_{\frac{13}{2}}\rangle$ +0.1301$\|^4I^3_{\frac{13}{2}}\rangle$
$^6F_{\frac{1}{2}}$	6300	-0.9848$\|^6F_{\frac{1}{2}}\rangle$ -0.1089$\|^4D^2_{\frac{1}{2}}\rangle$ -0.1061$\|^4D^3_{\frac{1}{2}}\rangle$
$^6H_{\frac{15}{2}}$	6400	-0.9783$\|^6H_{\frac{15}{2}}\rangle$ -0.1838$\|^4I^3_{\frac{15}{2}}\rangle$
$^6F_{\frac{3}{2}}$	6500	-0.9783$\|^6F_{\frac{3}{2}}\rangle$ -0.1017$\|^4D^2_{\frac{3}{2}}\rangle$ -0.1083$\|^4F^3_{\frac{3}{2}}\rangle$
$^6F_{\frac{5}{2}}$	7000	-0.9722$\|^6F_{\frac{5}{2}}\rangle$ -0.1483$\|^4F^3_{\frac{5}{2}}\rangle$
$^6F_{\frac{7}{2}}$	7900	-0.9754$\|^6F_{\frac{7}{2}}\rangle$ -0.1521$\|^4F^3_{\frac{7}{2}}\rangle$
$^6F_{\frac{9}{2}}$	9000	$0.9823\|^6F_{\frac{9}{2}}\rangle$ -0.1229$\|^4F^3_{\frac{9}{2}}\rangle$
$^6F_{\frac{11}{2}}$	10400	-0.9872$\|^6F_{\frac{11}{2}}\rangle$ -0.1071$\|^4G^3_{\frac{11}{2}}\rangle$
$^4G_{\frac{5}{2}}$	17800	-0.5379$\|^4G^4_{\frac{5}{2}}\rangle$ -0.4520$\|^4F^3_{\frac{5}{2}}\rangle$ -0.1683$\|^6H_{\frac{5}{2}}\rangle$
		-0.2180$\|^4F^1_{\frac{5}{2}}\rangle$ -0.1919$\|^4F^4_{\frac{5}{2}}\rangle$ -0.4003$\|^4G^1_{\frac{5}{2}}\rangle$
		+0.2548$\|^4G^2_{\frac{5}{2}}\rangle$ -0.1825$\|^4G^3_{\frac{5}{2}}\rangle$ -0.1342$\|^2F^2_{\frac{5}{2}}\rangle$
		-0.1178$\|^2F^5_{\frac{5}{2}}\rangle$ -0.1258$\|^2F^6_{\frac{5}{2}}\rangle$ -0.1338$\|^2F^7_{\frac{5}{2}}\rangle$
$^4G_{\frac{3}{2}}$	18900	0.1433$\|^6F_{\frac{3}{2}}\rangle$ -0.3986$\|^4F^1_{\frac{3}{2}}\rangle$ +0.8210$\|^4F^3_{\frac{3}{2}}\rangle$
		+0.3469$\|^4F^4_{\frac{3}{2}}\rangle$

free ion parameters obtained for CaF_2:Sm^{3+}. We observe that the multiplets of the ^6H and ^6F terms are only weakly mixed by intermediate coupling being $\geq$95% pure LS (Russell-Saunders) states. By contrast, the multiplets from $^4G_{\frac{5}{2}}$ and beyond are heavily mixed by intermediate coupling. One result is that the $^6H_{\frac{5}{2}} \rightarrow ^4G_{\frac{5}{2}}$ optical transitions are no longer spin forbidden.

5.5 Fluorescence Lifetimes

The $^4G_{\frac{5}{2}}$ fluorescence lifetimes of the A, G1 and near cubic O centres have been measured in CaF_2:Sm^{3+} and SrF_2:Sm^{3+} crystals. For these experiments, the PRA pulsed nitrogen laser was used to pump a tunable dye laser which was then tuned into resonance with the required electronic transition(s). This is described fully in chapter three. The resulting fluorescence was recorded on the SPEX 1700 series single monochromator with the EMI 9659 QA photomultiplier used to detect the emitted radiation. The PMT was then connected to a Hitachi model VC 6275 digital storage oscilloscope with the capability to average 256 individual transients.

Table 5.20: 16K $^4G_{\frac{5}{2}}$ fluorescent lifetimes (in msecs±0.1) for the A, G1 and O centres in CaF_2:Sm^{3+} and SrF_2:Sm^{3+}.

Crystal	Centre	Lifetime
CaF_2:0.05%Sm^{3+}	A	10.4
	G1	6.3
CaF_2:0.2%Sm^{3+}	O	26.3
SrF_2:0.05%Sm^{3+}	A	10.5
	G1	5.3
SrF_2:0.2%Sm^{3+}	O	22.5

The measured 16K $^4G_{\frac{5}{2}}$ lifetimes are given in Table 5.20 with the individual transients for each centre presented in Figures 5.38 through to 5.43. In all cases, the $^4F_{\frac{3}{2}}$ multiplet (which has no measureable lifetime) was excited using Coumarin 500 dye. Single exponential functions of the form shown below have been used to fit this data.

$$y = A + Bexp(-\lambda t)$$

where A is the baseline, or y axis displacement and B is a scaling factor.

As the $^4G_{\frac{5}{2}}$ lifetimes for the C_{4v} symmetry centres are of the order of tens of milliseconds, it is possible upconversion processes are occurring. In order to determine

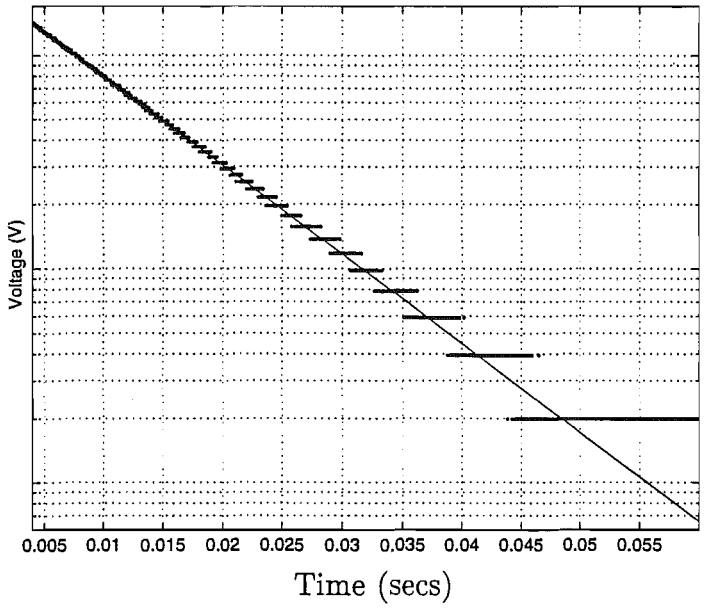

Figure 5.38: 16K fluorescence transient for the A centre CaF_2:0.05%Sm^{3+} $^4G_{\frac{5}{2}}A_1 \rightarrow {}^6H_{\frac{5}{2}}Z_1$ transition at 17837 cm^{-1}.

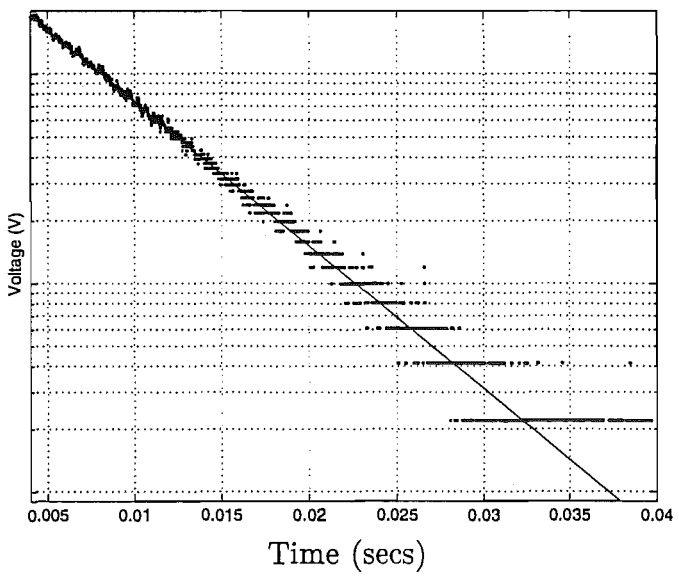

Figure 5.39: 16K fluorescence transient for the G1 centre CaF_2:0.05%Sm^{3+} $^4G_{\frac{5}{2}}A_1 \rightarrow {}^6H_{\frac{5}{2}}Z_1$ transition at 17511 cm^{-1}.

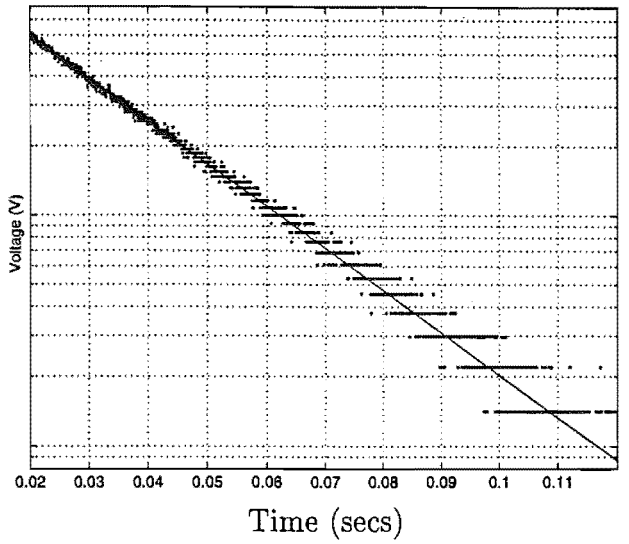

Figure 5.40: 16K fluorescence transient for the O centre CaF_2:0.05%Sm^{3+} $^4G_{\frac{5}{2}}A_1 \rightarrow {}^6H_{\frac{5}{2}}Z_1$ transition at 17653 cm^{-1}.

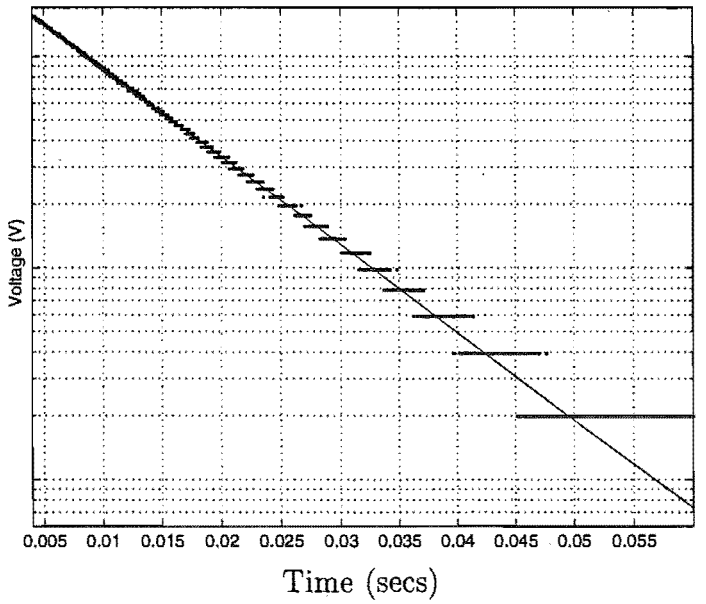

Figure 5.41: 16K fluorescence transient for the A center SrF_2:0.05%Sm^{3+} $^4G_{\frac{5}{2}}A_1 \rightarrow {}^6H_{\frac{5}{2}}Z_1$ transition at 17839 cm^{-1}.

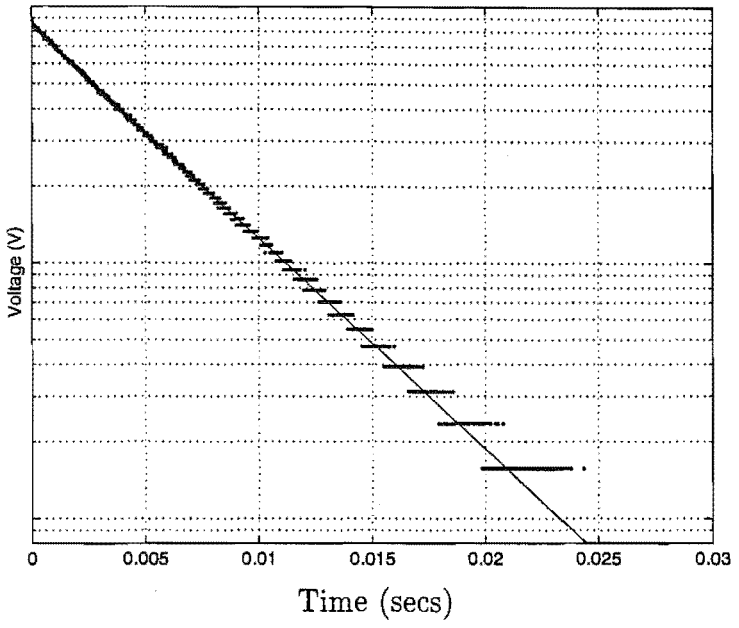

Figure 5.42: 16K fluorescence transient for the G1 centre SrF_2:0.05%Sm^{3+} $^4G_{\frac{5}{2}}A_1 \rightarrow {}^6H_{\frac{5}{2}}Z_1$ transition at 17544 cm^{-1}.

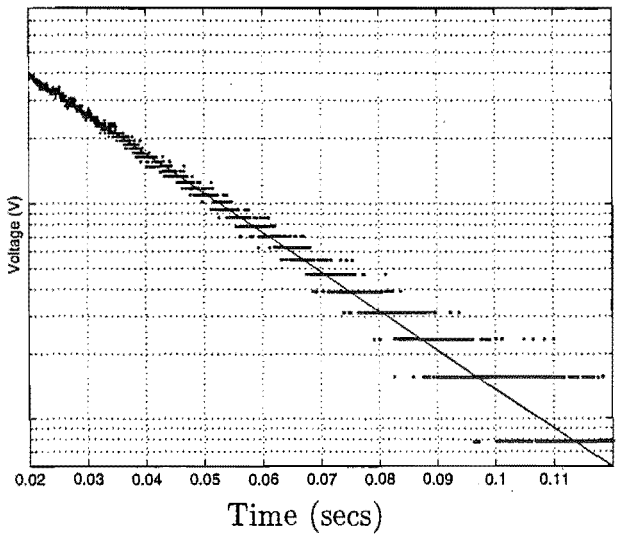

Figure 5.43: 16K fluorescence transient for the O centre SrF_2:0.2%Sm^{3+} $^4G_{\frac{5}{2}}A_1 \rightarrow {}^6H_{\frac{5}{2}}Z_1$ transition at 17699 cm^{-1}.

whether such processes were occurring the 17837 cm^{-1} transition of the CaF_2:Sm^{3+} A centre was pumped with CW laser excitation powers of 400 mW. To the limits of the detection sensitivity available, no upconverted fluorescence could be detected. Due to the high density of electronic states at energies higher than the $^4G_{\frac{5}{2}}$ multiplet it is most likely that any upconverted fluorescence is non-radiatively quenched and all emission is thus observed from $^4G_{\frac{5}{2}}$.

In the SrF_2 host, the high frequency phonon cutoff is approximately eighty wavenumbers lower than in CaF_2 and therefore, the probability that upconverted emission will be observed is also higher. Despite this, an extensive search for fluorescence lines at higher frequencies than that of the laser revealed no additional Sm^{3+} fluorescence. Given that the $^4G_{\frac{5}{2}}$ lifetime is so long, it is improbable that excited state absorption processes are not occurring. To test this, the fluorescence intensity as a function of the intensity of excitation was measured and this plotted in Figures 5.44 and 5.45. These plots show distinct non-linearities which may be indicative of two effects:

- Saturation of the absorption transition will occur at higher excitation densities, that is to say the efficiency of the absortion process is not linear as a function of the input power.
- Higher order absorption processes such as sequential absorption upconversion may also be responsible. In this case, for every two (or more) photons absorbed only one will be emitted from the $^4G_{\frac{5}{2}}$ multiplet as the photon energy above one quanta is released by the ion as lattice vibrations (phonons).

Although this does not unambigously prove that sequential absorption is occurring in the A centres studied here, it does seem a reasonable proposal. Certainly for Sm^{3+} systems with a lower energy phonon cutoff, the conversion of yellow-green light to blue (via emission from $^4F_{\frac{7}{2}}$ at 20000 cm^{-1}) seems a near certainty.

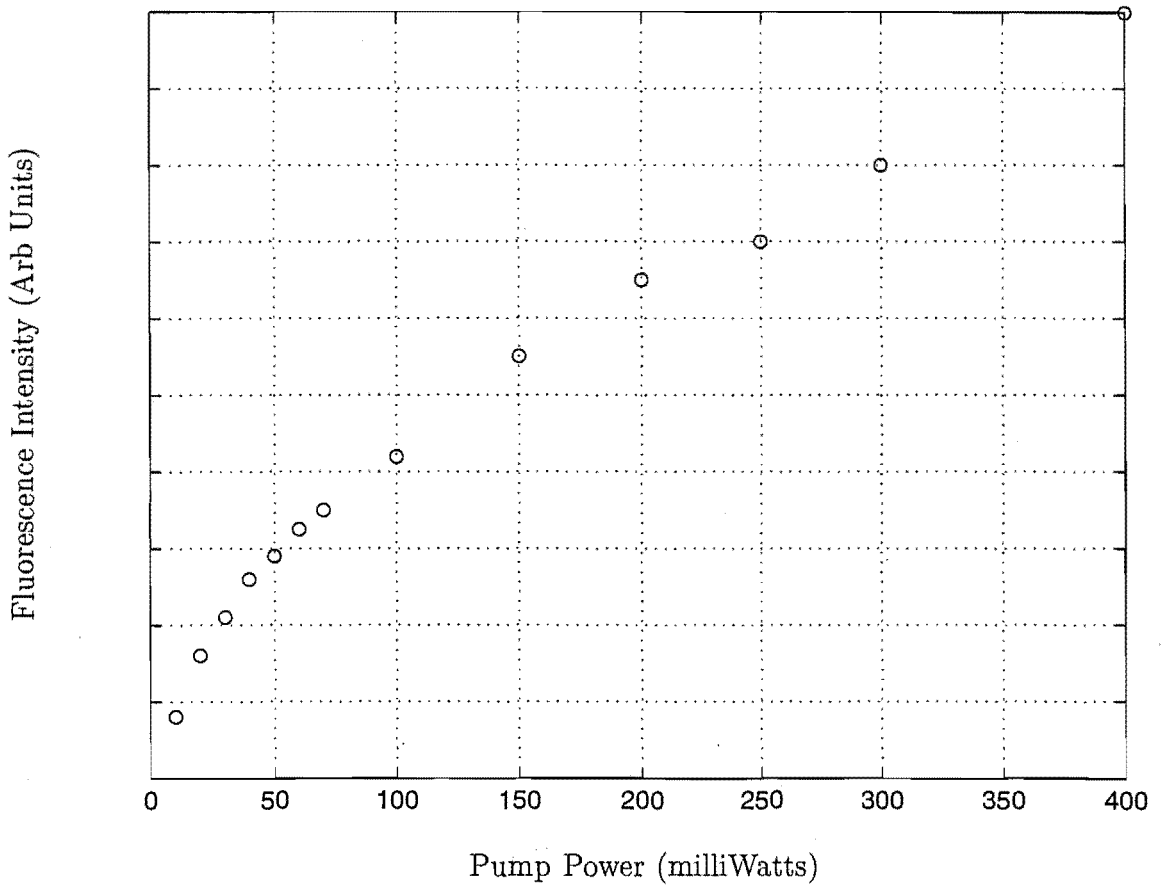

Figure 5.44: $^4G_{\frac{5}{2}}$ fluorescence intensity as a function of pump power for the A centre in CaF_2:0.05%Sm^{3+}. Fluorescence was monitored at 16851 cm^{-1}.

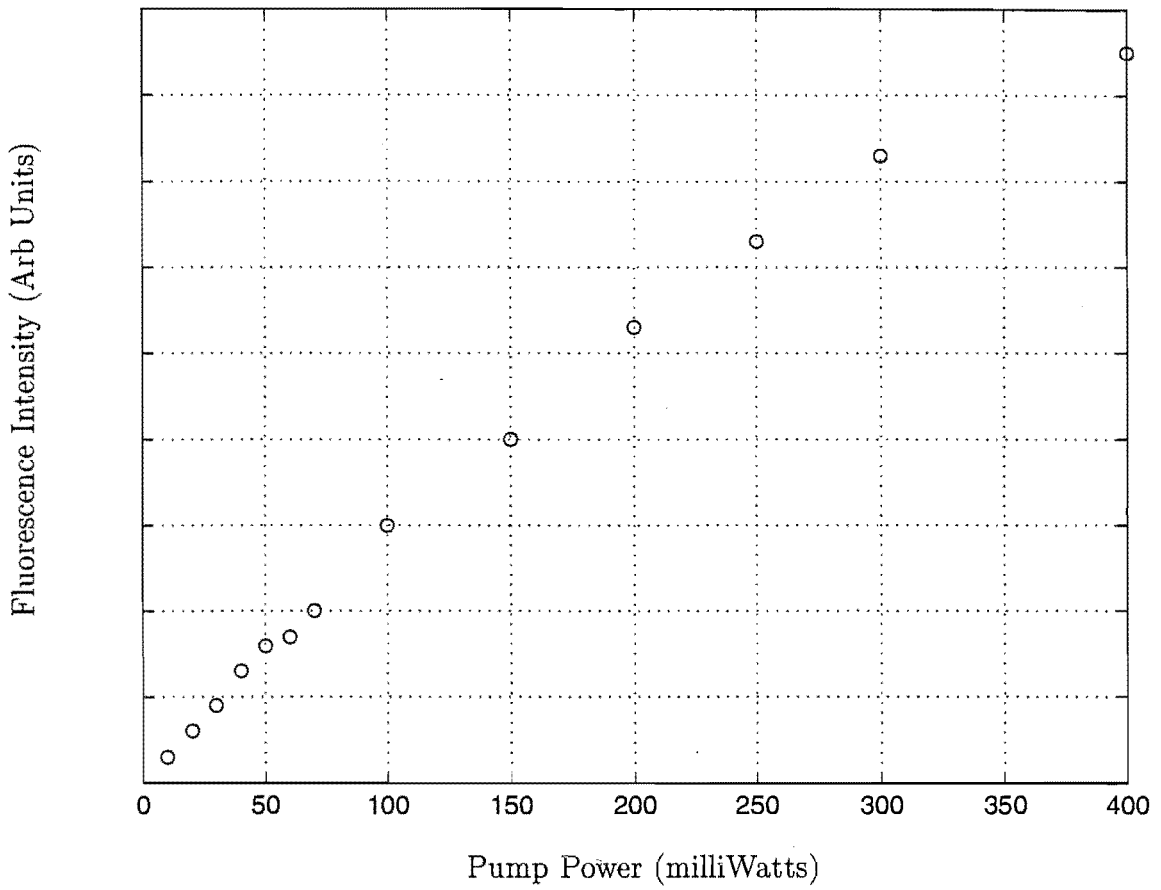

Figure 5.45: $^4G_{\frac{5}{2}}$ fluorescence intensity as a function of pump power for the A centre in SrF_2:0.05%Sm^{3+}. Fluorescence was monitored at 16849 cm^{-1}.

Chapter 6

Spectroscopy of Eu^{3+} Ions in CaF_2, SrF_2 and BaF_2 Crystals

6.1 Introduction

The spectra of trivalent europium has received much attention in the literature. This is, in part, due to the extreme sharpness of the $^7F_0 \rightarrow ^5D_0$ transition in some crystalline hosts at low temperatures [101]. The width of this transition (and the implicit slow optical dephasing of the excited $^5D_0$ state) can be used as an effective and sensitive probe of disorder due to the introduction of defects and strains during the crystal preparation and growth.

The earliest work on Eu^{3+} doped alkaline earth fluoride crystals known to the author concentrated on the CaF_2 host crystal. Voronko et. al. [102] used the concentration series method to elucidate information on the defect distribution, inferring the presence of at least three distinct centres. Following this Zarkharchenya and Rusanov [103] carried out optical Zeeman spectroscopy which identified a cubic symmetry centre for the magnetic dipole transitions $^7F_0 \rightarrow ^5D_1$.

With the advent of laser spectroscopic techniques more thorough studies were completed. Hamers et. al. [104] comprehensively studied the defect equilibria using laser selective measurements for CaF_2:0.1%Eu^{3+}. Five major centres were found and fluorescent transitions assigned to them. The observed centres were a cubic O centre, tetragonal A centre, an unassigned single ion centre (labelled P) and two cluster centres (labelled Q and R) which were assigned as dimers. The Q centre was proposed to comprise a pair of equivalent Eu^{3+} ions whilst the R centre of two inequivalent Eu^{3+} ions. In more recent work, Cirillo-Penn and Wright [10] have examined the Q and R centres more closely through the addition of LaF_3, GdF_3 and LuF_3 observing the $^7F_0 \rightarrow ^5D_1$ transitions of the respective centres shift in frequency as the local crystal field about the Eu^{3+} ion is altered through the addition of ions of different ionic radius.

The SrF_2:Eu^{3+} and BaF_2:Eu^{3+} systems have been less thoroughly studied, however laser selective excitation measurements have been performed at 77K to identify the dominant centres in both cases. Jouart et. al. [105] measured the fluorescence spectrum of SrF_2:Eu^{3+} using excitation from the 457.9 nm argon laser line and relying on vibronic sideband absorption to populate the appropriate electronic states. As a consequence, these measurements are largely non-selective. Site selective measurements were performed for the $^5D_0$ multiplet only, using R6G dye laser excitation. Three major centres were studied; a cubic O_h centre, a tetragonal C_{4v} symmetry centre and a trigonal C_{3v} symmetry centre. Some energy levels and their appropriate irrep labels were given, however the method of assignment is not clear.

Analogous studies were carried out by the same authors [106] for BaF_2:Eu^{3+}. In this case, a dominant centre of trigonal C_{3v} symmetry was found. Jouart, Bouffard, Klein and Mary [92] (1991) concentrated on the cubic centres observed for Eu^{3+} doped CaF_2, SrF_2, BaF_2, CdF_2 and PbF_2, observable via the strong $^7F_0 \rightarrow ^5D_1$ magnetic dipole transitions. That work established energy level schemes for these centres and gave irrep labels for the inferred energy levels as appropriate.

The studies presented here, intend to provide indepth analysis of individual centres through polarised laser selective excitation and fluorescence, optical absorption and Zeeman infrared spectroscopy culminating in comprehensive crystal field analyses for the high symmetry centres. Zeeman energy calculations are performed which compare well with the Zeeman results obtained for the energy levels of the ^7F_J multiplets. Upconversion fluorescence is reported for Eu^{3+} doped alkaline earth fluorides and this aides the assignment of energy level designations and irrep labels.

6.2 Spectroscopy of CaF_2:Eu^{3+}

The f^6 configuration, appropriate for trivalent europium, consists of $\frac{14!}{6!(14-6)!}$=3003 electronic states. In this study, tunable organic dye lasers are used as excitation sources. Therefore, only the ^7F_J and $^5D_0$, $^5D_1$, $^5D_2$ and $^5D_3$ multiplets of the Eu^{3+} ion are accessible. As a consequence only 65 electronic states of this configuration are considered (2.2%). Table 6.1 gives the manifold degeneracies for the variety of centres considered here.

6.2.1 Optical Absorption and Excitation Spectra

The absorption spectra of a 19.8 mm thick CaF_2:0.15%Eu^{3+} crystal have been recorded for optical transitions to the $^5D_0$, $^5D_1$, $^5D_2$ and $^5D_3$ multiplets. The crystal

Table 6.1: Decomposition of the free ion (spin-orbit | SLJ)) states into irreps of the cubic O_h, tetragonal C_{4v} and trigonal C_{3v} point groups for the f^6 configuration

$^{(2S+1)}L_J$	O_h	C_{4v}	C_{3v}
$^7F_0$	Γ_1	γ_1	γ_1
$^7F_1$	Γ_4	$\gamma_2+\gamma_5$	$\gamma_2+\gamma_3$
$^7F_2$	$\Gamma_3+\Gamma_4$	$\gamma_1+\gamma_3+\gamma_4+\gamma_5$	$\gamma_1+2\gamma_3$
$^7F_3$	$\Gamma_2+\Gamma_4+\Gamma_5$	$\gamma_2+\gamma_3+\gamma_4+\gamma_5$	$\gamma_1+2\gamma_2+2\gamma_3$
$^7F_4$	$\Gamma_1+\Gamma_3+\Gamma_4+\Gamma_5$	$2\gamma_1+\gamma_2+\gamma_3+\gamma_4+2\gamma_5$	$2\gamma_1+\gamma_2+3\gamma_3$
$^7F_5$	$\Gamma_3+2\Gamma_4+\Gamma_5$	$\gamma_1+2\gamma_2+\gamma_3+\gamma_4+3\gamma_5$	$\gamma_1+2\gamma_2+4\gamma_3$
$^7F_6$	$\Gamma_1+\Gamma_2+\Gamma_3+\Gamma_4+2\Gamma_5$	$2\gamma_1+\gamma_2+2\gamma_3+2\gamma_4+3\gamma_5$	$3\gamma_1+2\gamma_2+4\gamma_3$
$^5D_0$	Γ_1	γ_1	γ_1
$^5D_1$	Γ_4	$\gamma_2+\gamma_5$	$\gamma_2+\gamma_3$
$^5D_2$	$\Gamma_3+\Gamma_4$	$\gamma_1+\gamma_3+\gamma_4+\gamma_5$	$\gamma_1+2\gamma_3$
$^5D_3$	$\Gamma_2+\Gamma_4+\Gamma_5$	$\gamma_2+\gamma_3+\gamma_4+\gamma_5$	$\gamma_1+2\gamma_2+2\gamma_3$

was cooled to 16K for these experiments. The recorded spectra are shown in Figure 6.1. Only transitions to the $^5D_1$ and $^5D_2$ multiplets are observed. This is not unexpected as strict LS coupling forbids J=0→0, 1, 3 and 5 transitions for electric dipole radiation. The observed transitions to the $^5D_1$ multiplet are well known to be magnetic dipole in character.

In Figure 6.1(a) transitions to the $^5D_1$ multiplet are shown. All transitions are of comparable intensity, however the features assigned by Hamers et. al. [104] to a tetragonal symmetry centre dominate (labelled A). A strong transition, labelled O, is due to a cubic centre, observable here because of the magnetic dipole character of the $^7F_0 \rightarrow ^5D_1$ transitions. Five additional transitions are observed, labelled Q and R as appropriate. These are due to preferential cluster centre formation.

Transitions to the $^5D_2$ multiplet shown in Figure 6.1(b), display a similar defect centre distribution with the exception of the absence of cubic centre transitions due to the restrictive selection rules for these ions in centres with inversion symmetry. A centre transitions are observed at 464.31 and 465.23 nm whilst transitions to the R and Q centres are observed at 464.98 and 465.46 nm and 464.81, 464.87 and 465.52 nm respectively.

Laser excitation has been employed to study transitions to the $^5D_0$ and $^5D_1$ multiplets. In these experiments, the more standard concentration of 0.05 molar % of Eu^{3+} has been used. For the $^5D_0$ multiplet, the higher excitation intensities of laser pumping is particularly advantageous as no absorption transitions can be observed

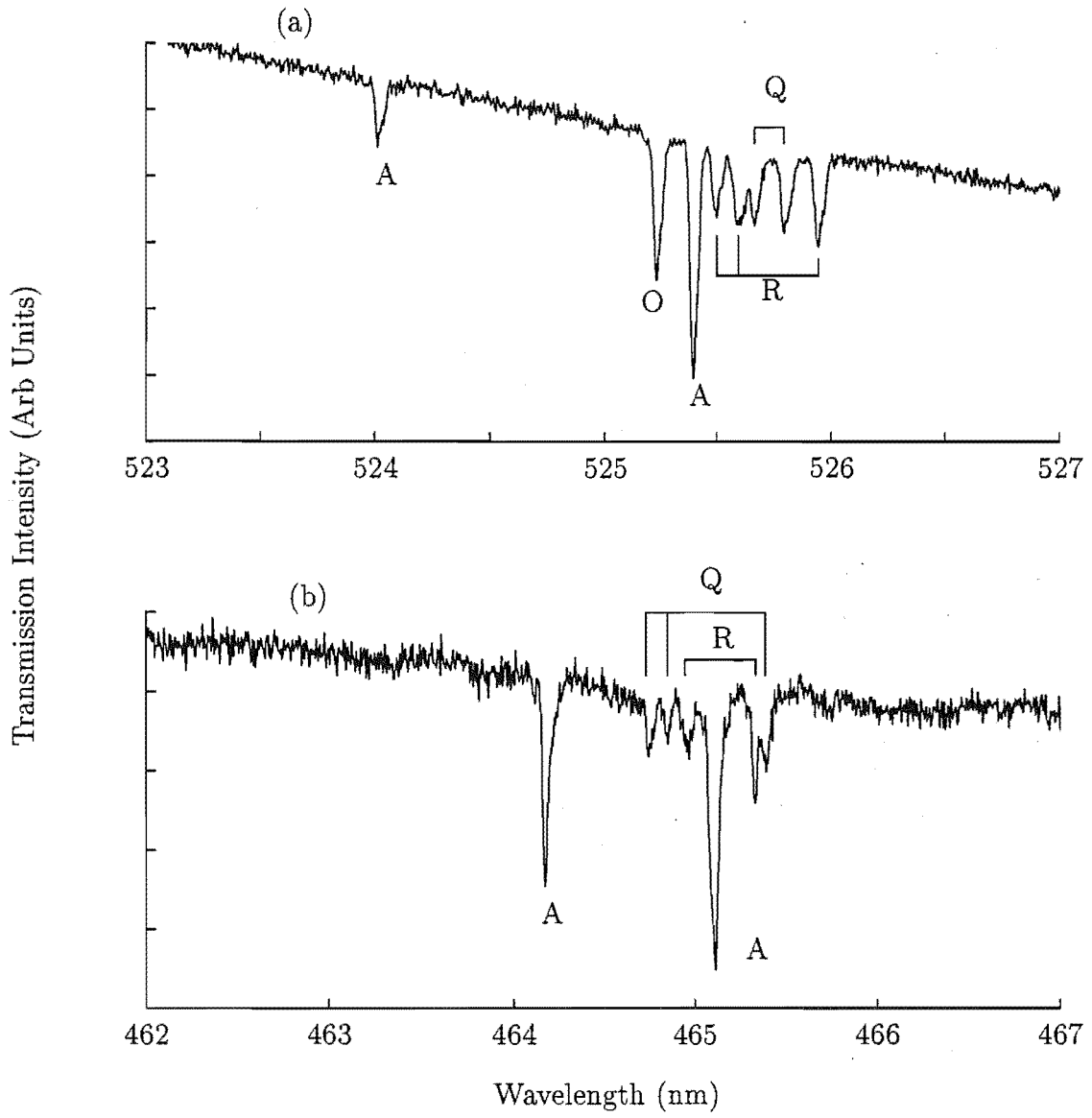

Figure 6.1: Absorption spectra for the (a) $^5D_1$ and (b) $^5D_2$ multiplets in CaF_2:0.15%Eu^{3+}. The spectra were recorded at 16K.

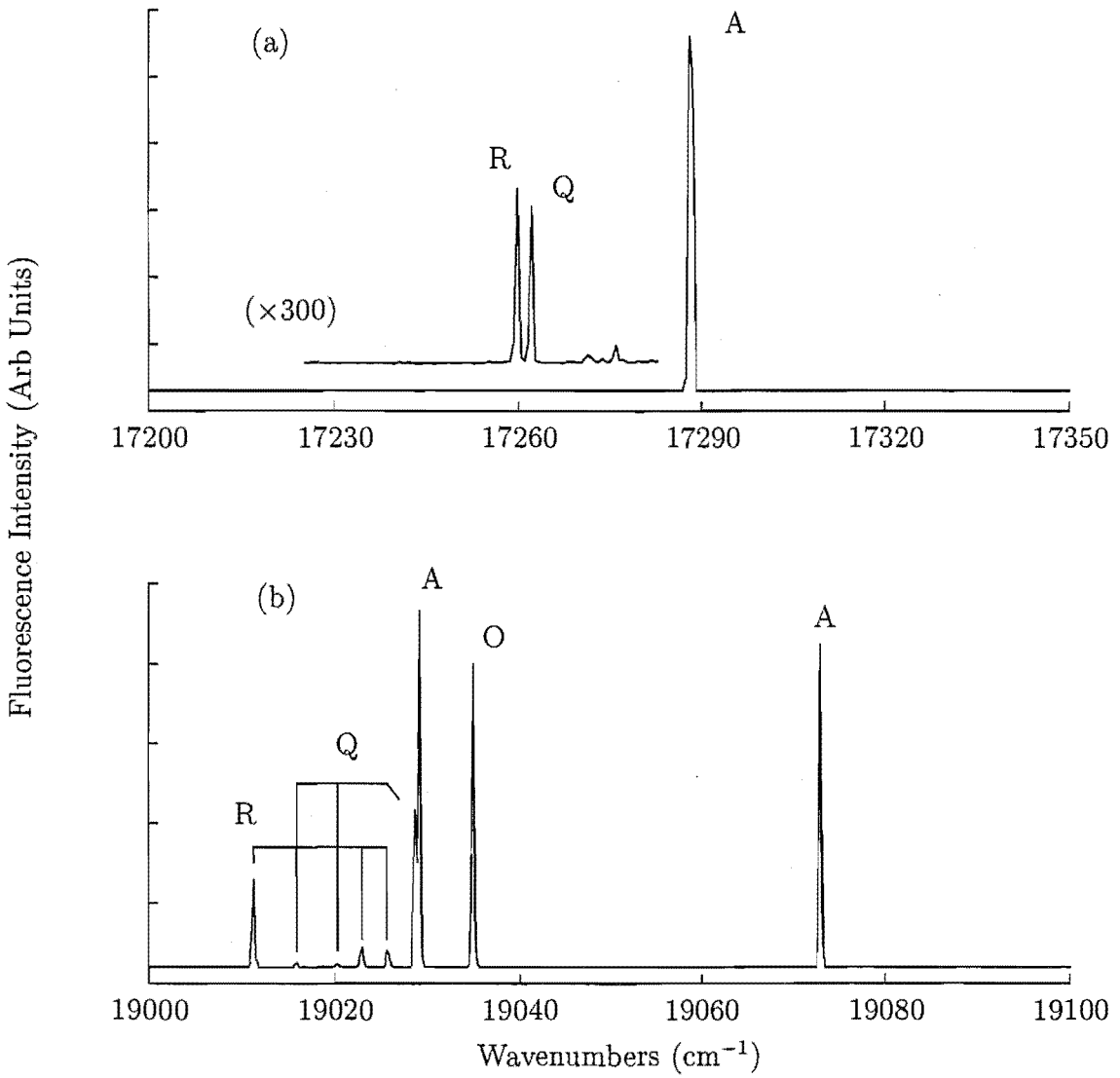

Figure 6.2: Excitation spectra for the (a) $^5D_0$ multiplet and (b) $^5D_1$ multiplet CaF_2:0.05%Eu^{3+}. The spectra were recorded at 16K.

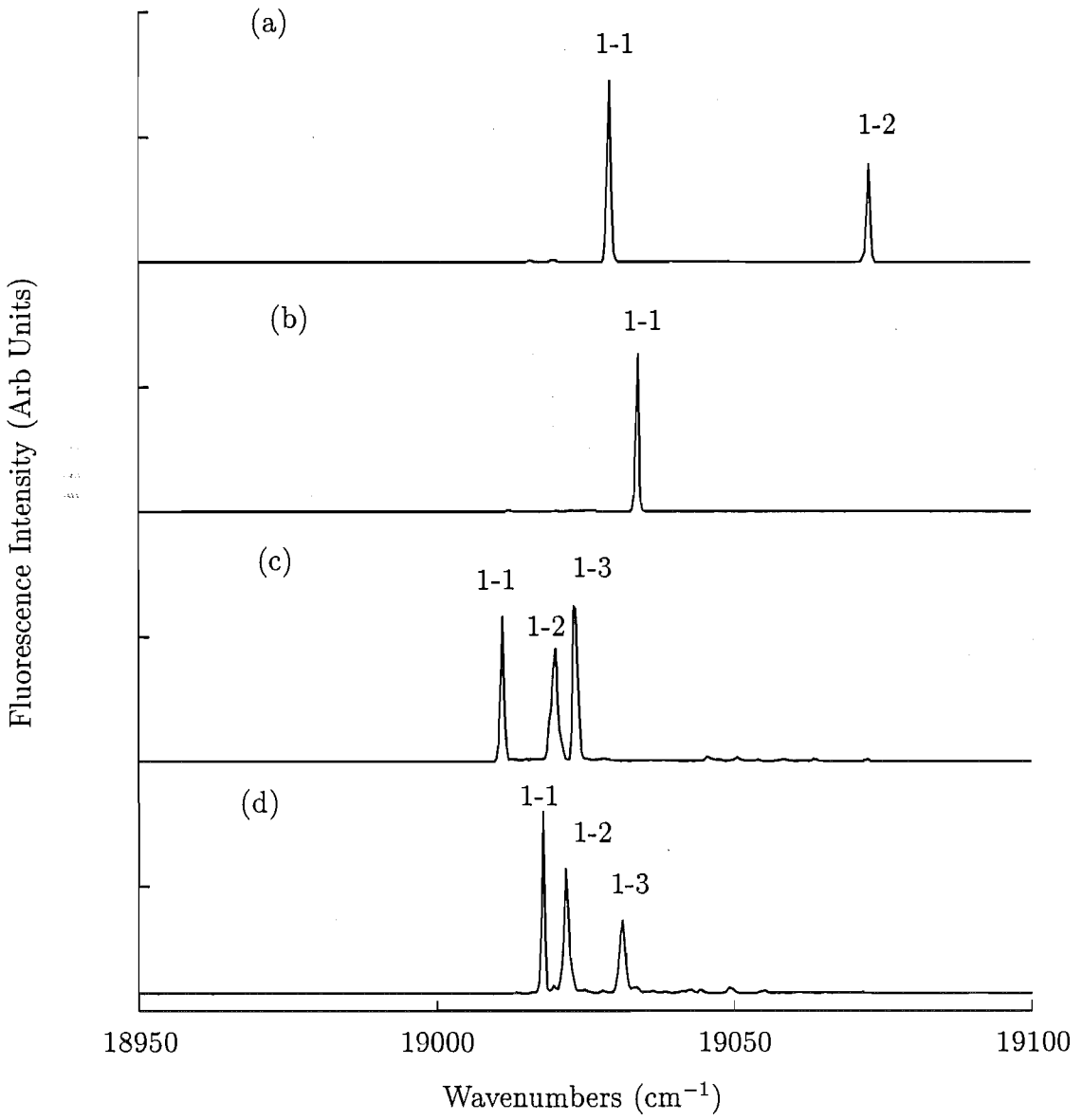

Figure 6.3: Narrowband excitation spectra of the $^5D_1$ multiplet for the (a) A centre monitoring at 16981 cm^{-1}, (b) the O centre monitoring at 16937 cm^{-1}, (c) the R centre monitoring at 16878 cm^{-1} and (d) the Q centre, monitoring at 16935 cm^{-1}, in CaF_2:0.05%Eu^{3+}. The spectra were recorded at 16K.

to the limits of the detection sensitivities available. The recorded excitation spectra for monitoring all emission transitions around 625 nm are given in Figures 6.2(a) and (b). The $^5D_0$ spectrum consists of essentially one transition, that of the A centre at 17288 cm^{-1}. At intensities more than 100 times weaker than this excitation features due to R and Q centre absorption transitions, are present. The $^5D_1$ excitation spectrum shown in Figure 6.2(b) is very similar to the absorption spectrum for this multiplet with the exception that an additional Q centre transition can be resolved partially overlapping the 19023 cm $^{-1}$ A centre peak. Selective excitation spectra for the $^5D_1$ multiplet, monitoring indiviual centre emission transitions are given in Figure 6.3. In Table 6.2 transition frequencies are given as measured from the excitation and absorption spectra.

Table 6.2: A, O, R and Q centre excitation frequencies (in air $cm^{-1}\pm1$) and absorption wavelengths (in air nm±0.05) for the $^5D_0$ and $^5D_1$ multiplets in CaF_2:0.05%Eu^{3+}

Centre & Symmetry	Multiplet	Transition Assignment	Excitation Frequency	Absorption Wavelength
A (C_{4v})	$^5D_0$	$Z_1 \rightarrow A_1$	17288	-
	$^5D_1$	$Z_1 \rightarrow B_1$	19029	525.54
		$Z_1 \rightarrow B_2$	19073	524.31
O (O_h)	$^5D_1$	$Z_1 \rightarrow B_1$	19029	525.35
R	$^5D_0$	$Z_1 \rightarrow A_1$	17259	-
	$^5D_1$	$Z_1 \rightarrow B_1$	19004	526.25
		$Z_1 \rightarrow B_2$	19016	525.90
		$Z_1 \rightarrow B_3$	19020	525.73
Q	$^5D_0$	$Z_1 \rightarrow A_1$	17262	-
	$^5D_1$	$Z_1 \rightarrow B_1$	19009	526.04
		$Z_1 \rightarrow B_2$	19014	525.94
		$Z_1 \rightarrow B_3$	19024	-

6.2.2 A Centre Fluorescence

The CaF_2:Eu^{3+} system has been studied previously with the laser selective excitation technique by Hamers et. al. [104]. Although fluorescence spectra were recorded, and then measured for the emission frequencies, the study concentrated on the defect chemistry of the system. This work builds upon the study of Hamers. Again laser selective excitation and emission is used, although in this case it is coupled with polarisation measurements which provide information on the irrep symmetry labels for the inferred energy levels. A significantly greater number of fluorescence transitions are observed in this work (compared to Hamers study). This leads to a definitive understanding of the low lying energy level structure of the high symmetry centres.

The polarisation selection rules and consequent ratios are outlined in chapter 2. It is useful to discuss how these selection rules apply to Eu^{3+} ions in a C_{4v} symmetry centre, for emission emanating from $^5D_0$ and $^5D_1$. We consider $^5D_0$ emission first. States of J=0 are not degenerate and consist of a single state transforming as a γ_1 C_{4v} irrep under C_{4v} symmetry. As such, $^7F_0 \rightarrow ^5D_0$ absorption transitions are allowed in π polarisation from the C_{4v} selection rules, which are given in chapter two. Emission from $^5D_0\gamma_1$ is allowed to states transforming as the following C_{4v} irreps:

- γ_1 - in this case, only radiation of electric dipole character will connect $^5D_0$ and the terminating state in question. The fluorescence will be π polarised and a polarisation ratio of 0:1 is expected in the YX:YY polarisation geometry.
- γ_2 - the fluorescence will be magnetic dipole π' polarised and a ratio of 1:0 is expected for the YX:YY geometry.
- γ_5 - in this case, the fluorescence may be electric dipole σ (1:0) and/or magnetic dipole σ' (0:1) polarised. The most common observation for fluorescence terminating on states of γ_5 irrep symmetry is a degraded polarisation effect. This arises because there are comparable contributions from both the electric and magnetic dipole mechanisms to the observed emission linestrength.

The polarised fluorescence spectra, for exciting the 17288 cm^{-1} $^5D_0$ absorption transition, are given in Figures 6.4 through to 6.9. Table 6.3 gives the measured polarised behaviour of the individual transitions and the level assignments based upon this. From the experimental data presented, it is observed that the $^7F_0 \rightarrow ^5D_0$ transitions are of magnetic dipole character. This is a general observation for Eu^{3+} doped compounds (eg Görller-Walrand et. al. [107] (1985) and Fluyt [108](1995) or Pellé et. al. [109] (1995)).

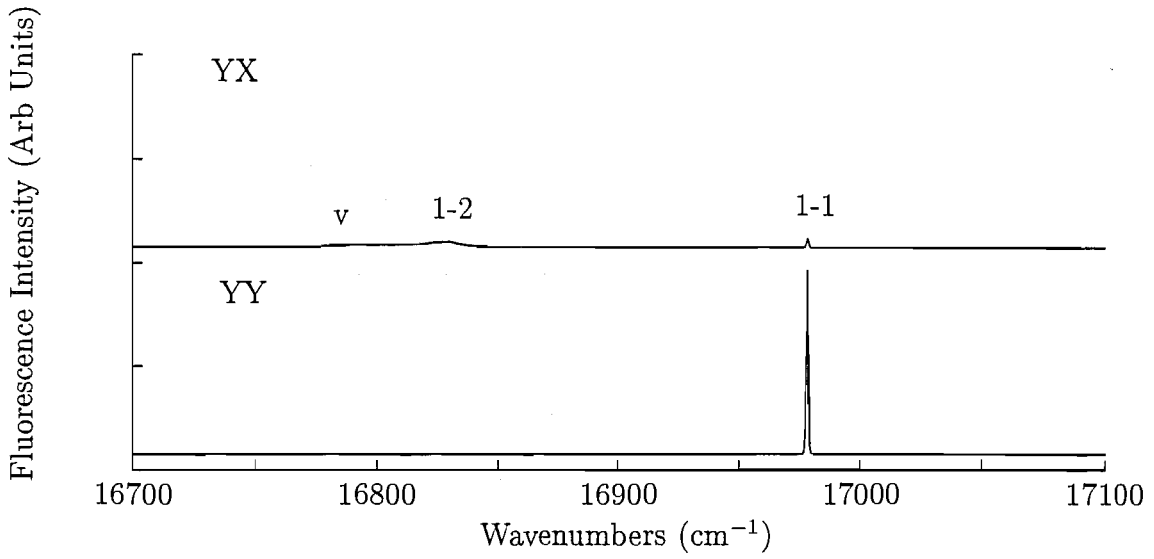

Figure 6.4: Polarised fluorescence spectrum for transitions $^5D_0 \rightarrow {}^7F_1$ of the A centre in CaF_2:0.05%Eu^{3+}. The spectra were recorded at 16K.

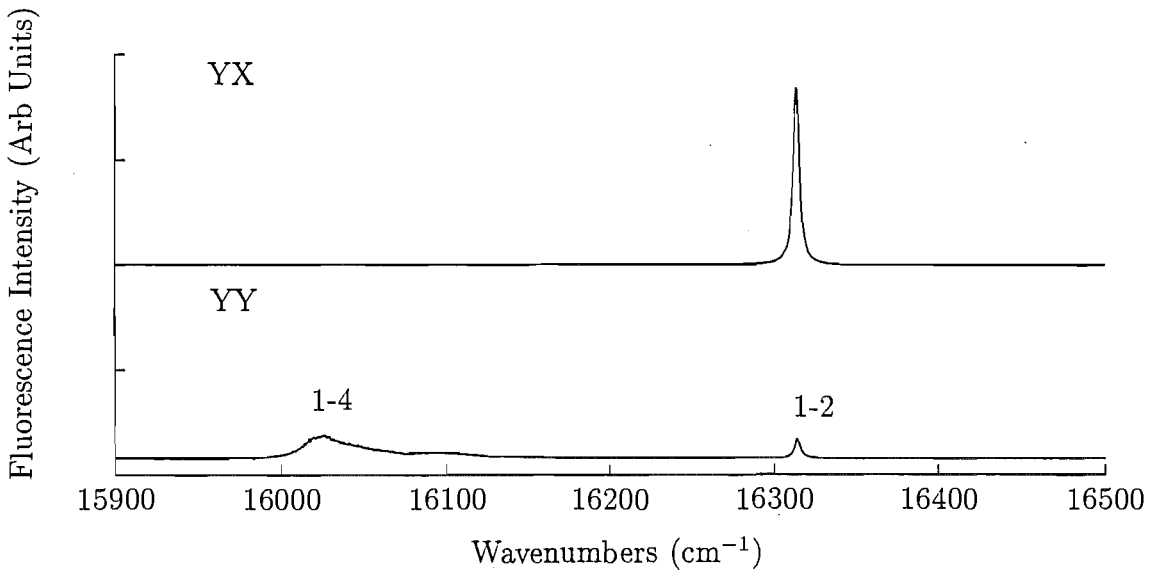

Figure 6.5: Polarised fluorescence spectrum for transitions $^5D_0 \rightarrow {}^7F_2$ of the A centre in CaF_2:0.05%Eu^{3+}. The spectra were recorded at 16K.

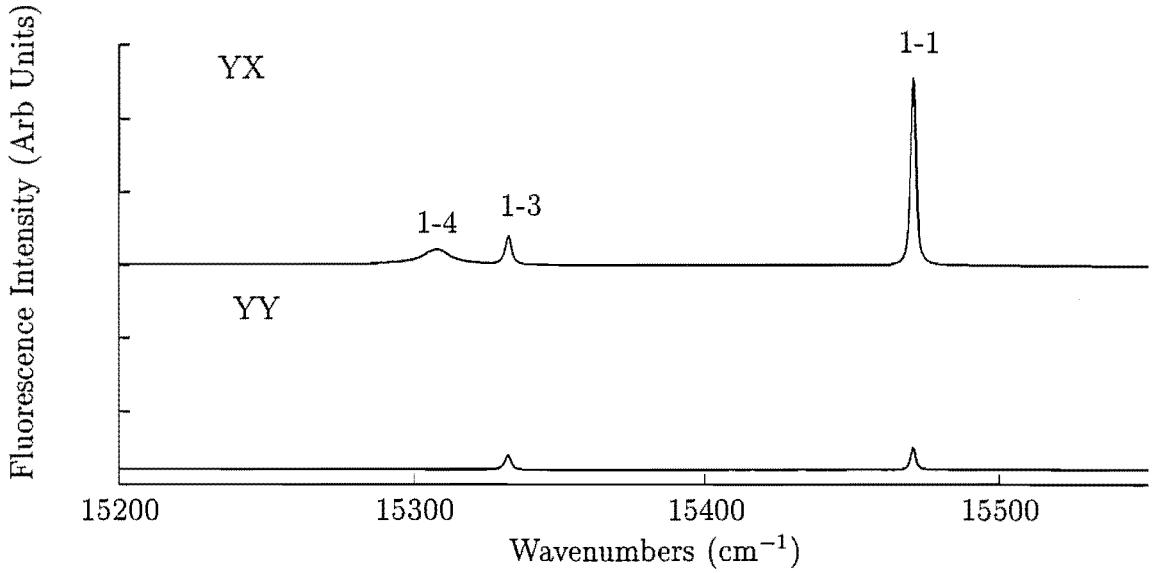

Figure 6.6: Polarised fluorescence spectrum for transitions $^5D_0 \rightarrow ^7F_3$ of the A centre in CaF_2:0.05%Eu^{3+}. The spectra were recorded at 16K.

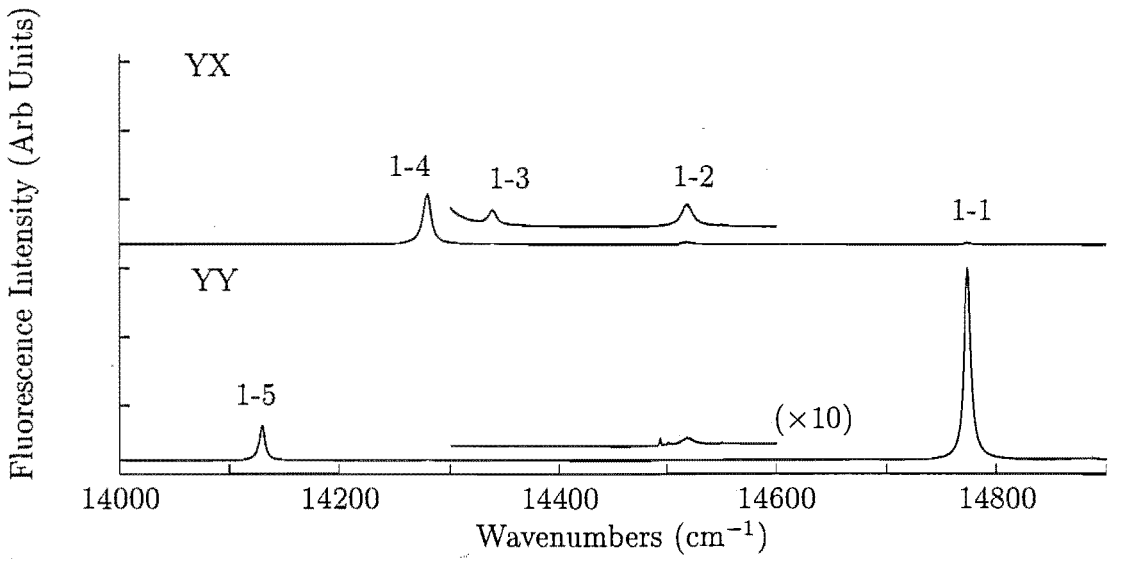

Figure 6.7: Polarised fluorescence spectrum for transitions $^5D_0 \rightarrow ^7F_4$ of the A centre in CaF_2:0.05%Eu^{3+}. The spectra were recorded at 16K.

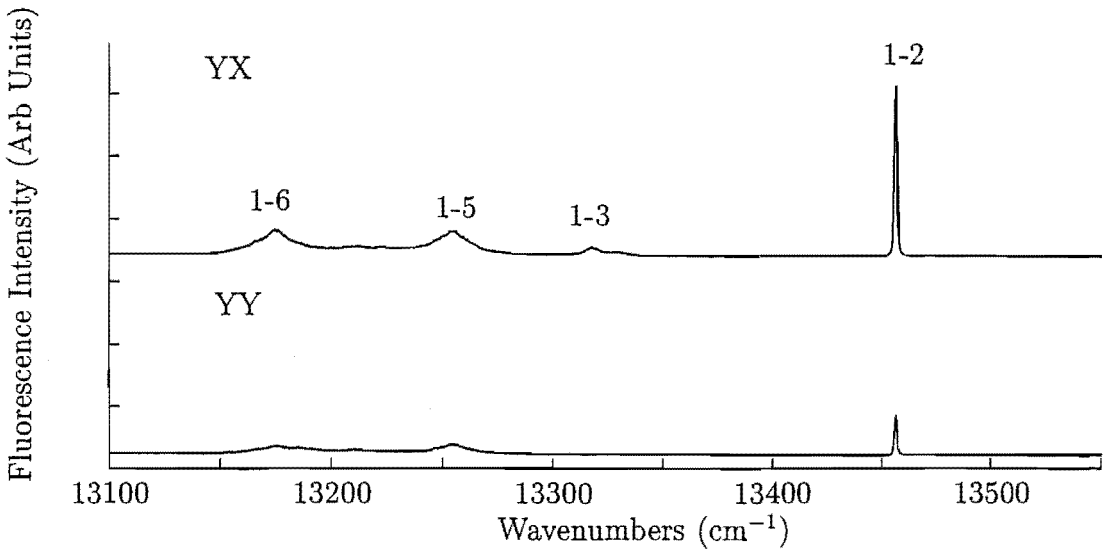

Figure 6.8: Polarised fluorescence spectrum for transitions $^5D_0 \rightarrow ^7F_5$ of the A centre in CaF_2:0.05%Eu^{3+}. The spectra were recorded at 16K.

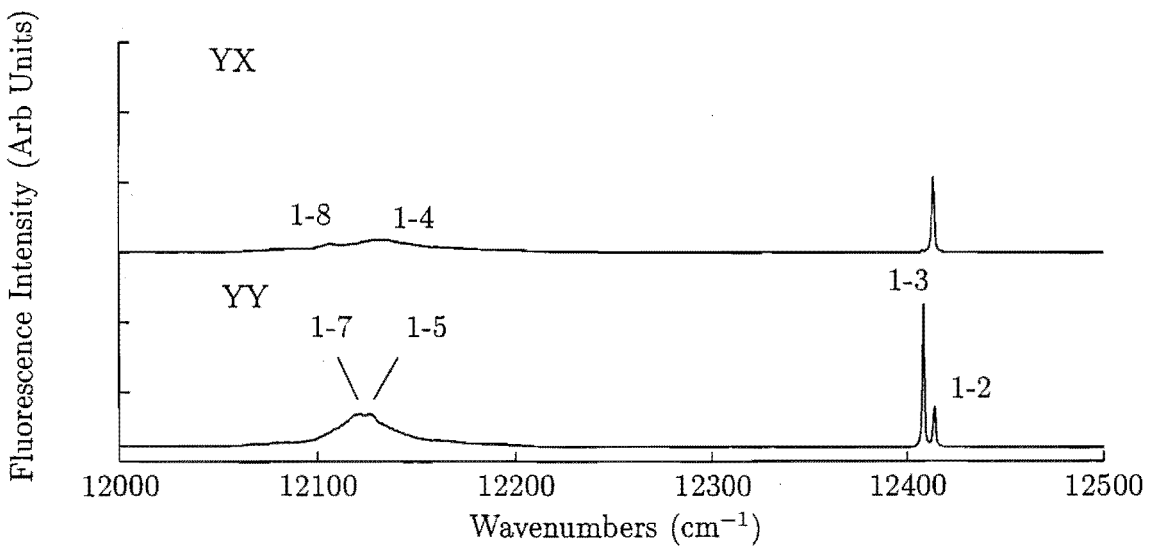

Figure 6.9: Polarised fluorescence spectrum for transitions $^5D_0 \rightarrow ^7F_6$ of the A centre in CaF_2:0.05%Eu^{3+}. The spectra were recorded at 16K.

Table 6.3: Polarisation data, level assignments and energies for the A centre in CaF_2:0.05%Eu^{3+} obtained in emission from $^5D_0\gamma_1$ at 17288 cm^{-1}. Energies are measured in air cm^{-1} and have an uncertainty of ± 1 cm^{-1} unless otherwise stated.

Terminating Multiplet	Transition Frequency	State Energy	State & Symmetry	Polarisation Assignment
$^5F_1$	16981	307	$Y_1\gamma_5$	σ'
	16832	456	$Y_2\gamma_2$	π'
$^5F_2$	16317	971	$X_2\gamma_5$	σ
	16026±5	1261	$X_4\gamma_1$	π
$^5F_3$	15473	1814	$W_1\gamma_5$	σ
	15335	1953	$W_3\gamma_5$	σ (mixed)
	15310	1977	$W_4\gamma_2$	σ'
$^5F_4$	14777	2510	$V_1\gamma_1$	π
	14488	2800	$V_2\gamma_5$	σ (mixed)
	14341	2947	$V_3\gamma_2$	π'
	14281	3006	$V_4\gamma_5$	σ
	14132	3156	$V_7\gamma_1$	π
$^5F_5$	13458	3829	$U_2\gamma_5$	σ (mixed)
	13317	3970	$U_3\gamma_2$	π'
	13253	4035	$U_5\gamma_5$	σ
	13173	4115	$U_6\gamma_5$	σ
$^5F_6$	12415	4873	$T_2\gamma_5$	σ
	12409	4879	$T_3\gamma_1$	π
	12138	5150	$T_4\gamma_2$	π'
	12130	5158	$T_5\gamma_5$	σ'(mixed)
	12121	5167	$T_7\gamma_1$	π
	12104	5184	$T_8\gamma_5$	σ

Under C_{4v} symmetry, states of J=1 split into two crystal field levels transforming as the γ_5 and γ_2 irreps as appropriate. Figures 6.10 through to 6.15 present the fluorescence spectra obtained for excitation of the 19029 cm^{-1} $^7F_0 \rightarrow ^5D_1$ transition. The measured transition frequencies are given in Table 6.4. From the number of fluorescence transitions observed, it is apparant that the lowest $^5D_1$ state is the γ_5 doublet. The 19073 cm^{-1} state must therefore transform as a γ_2 irrep.

Excitation of the 19029 cm^{-1} transition is allowed by either electric dipole σ or magnetic dipole σ' polarisation. Polarisation effects are observed in the ZX:ZY experimental geometry indicating the $^5D_0$ transitions are predominantly magnetic dipole in character. All emission is observed from either the $^5D_1$ doublet state or, because $^5D_1$ can readily decay to $^5D_0$ by non-radiative processes, $^5D_0$. For $^5D_1$ emission, transitions to all possible terminating states will be allowed as prescribed by the C_{4v} selection rules. The polarisation behaviour of the transitions can be placed into two categories:

- Singlet states - transitions to states transforming as the γ_1, γ_2, γ_3 and γ_4 C_{4v} irreps are allowed in either σ' or σ polarisation. This leads to either 2:1 or 1:2 ratios in the ZX:ZY geometries respectively. Obviously, states observed at energies differing from those observed in the $^5D_0$ emission are likely to be of either γ_3 or γ_4 symmetry.
- Transitions to states transforming with γ_5 irrep symmetry (doublets) - in this case, the observed fluorescence can be π or π' polarised giving 1:0 or 0:1 ratios. Thus, the clearest ratios may be obtained in this case, as long as the character of the fluorescence is not mixed.

Table 6.4 gives the polarisation behaviour and level assignments of the observed transitions. From this, it is observed that the $^5D_1 \rightarrow ^7F_2$ transitions are also predominantly magnetic dipole in character as might be expected from the $\Delta J=\pm 1$ selection rule imposed on these transitions. It is also noted that the $^5D_1$ emission is significantly weaker than that from $^5D_0$. This is because $^5D_1$ can decay non-radiatively to $^5D_0$. In fact, this is a far more efficient manner in which to populate the $^5D_0$ level than direct optical excitation.

Several transitions in the 16950 - 16850 cm^{-1} and 16300 - 16150 cm^{-1} regions (Figures 6.12 and 6.13) are assigned as emanating from a slightly less numerous cluster centre arbitrarily labelled Q. This emission arises because the A centre, 19029 cm^{-1} transition, is strongly overlapped by the Q centre 19028 cm^{-1} transition. Therefore, the A centre spectra are not entirely centre selective.

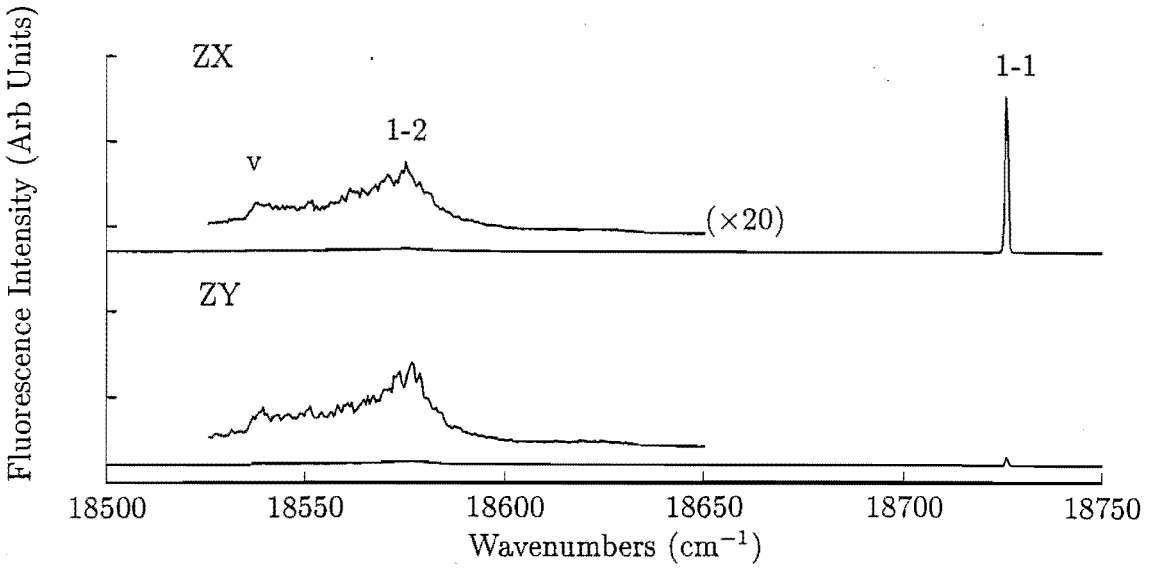

Figure 6.10: Polarised fluorescence spectrum for transitions $^5D_1 \rightarrow ^7F_1$ of the A centre in CaF_2:0.05%Eu^{3+}. The spectra were recorded at 16K.

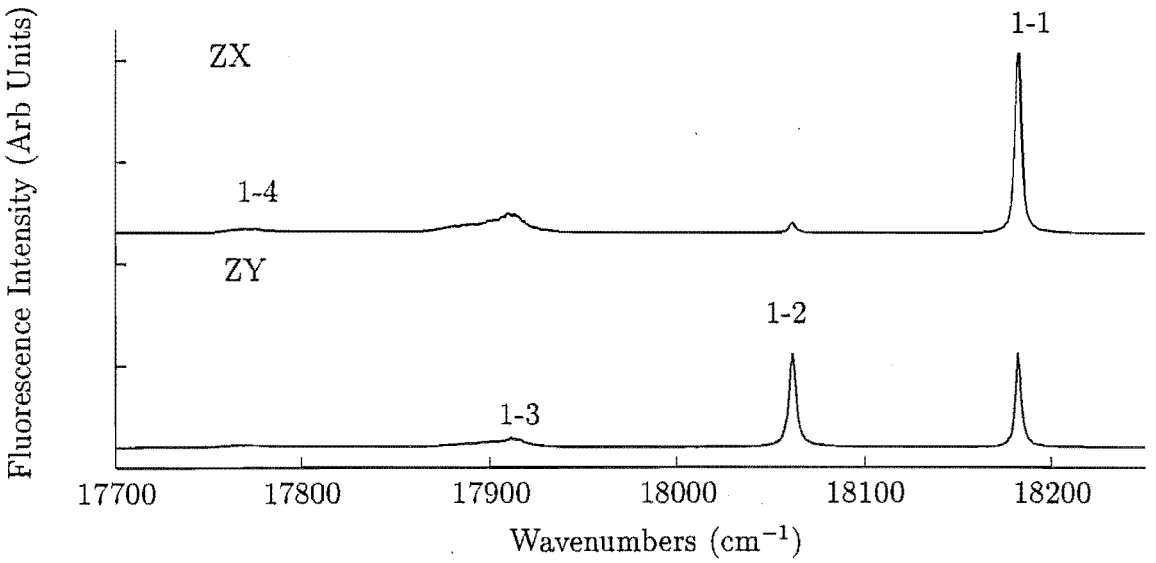

Figure 6.11: Polarised fluorescence spectrum for transitions $^5D_1 \rightarrow ^7F_2$ of the A centre in CaF_2:0.05%Eu^{3+}. The spectra were recorded at 16K.

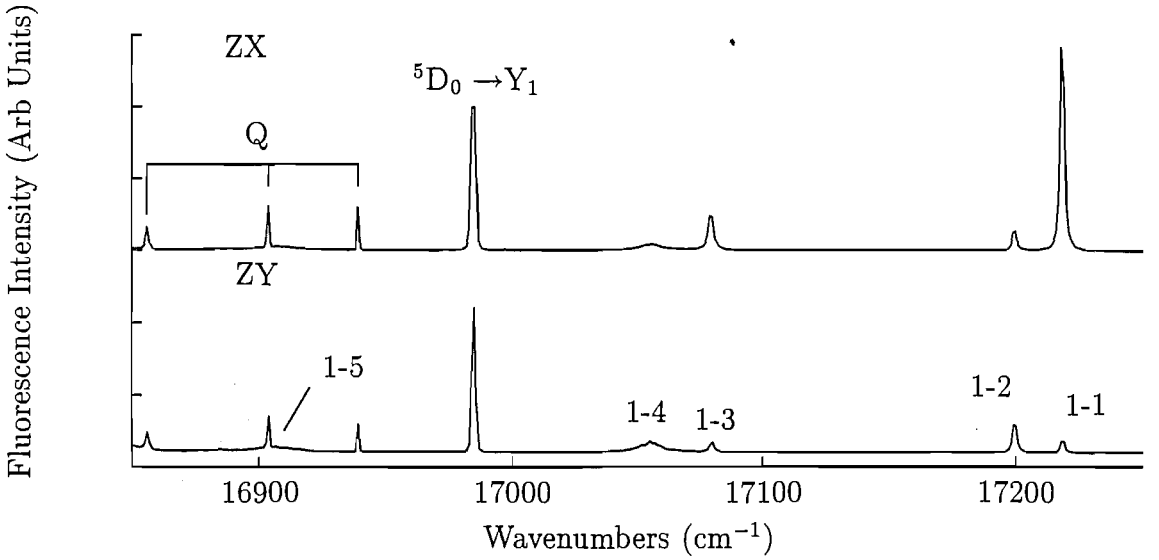

Figure 6.12: Polarised fluorescence spectrum for transitions $^5D_1 \rightarrow ^7F_3$ of the A centre in CaF_2:0.05%Eu^{3+}. The transitions labelled Q are Q centre emission features. The spectra were recorded at 16K.

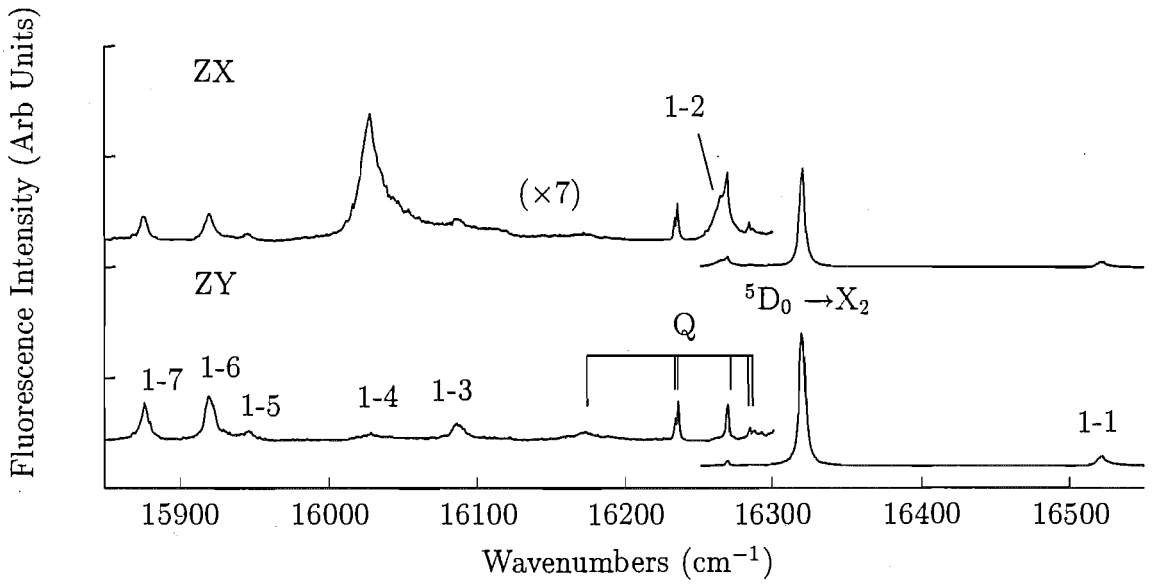

Figure 6.13: 16K polarised fluorescence spectrum for transitions $^5D_1 \rightarrow ^7F_4$ of the A centre in CaF_2:0.05%Eu^{3+}.The transitions labelled Q are Q centre emission features. The spectra were recorded at 16K.

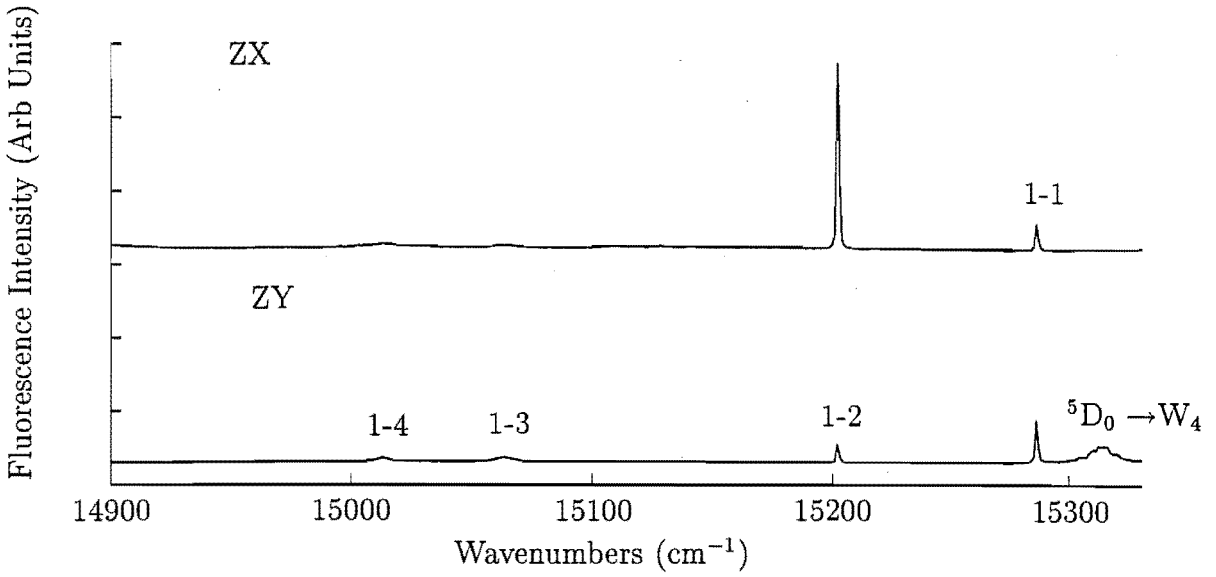

Figure 6.14: Polarised fluorescence spectrum for transitions $^5D_1 \rightarrow ^7F_5$ of the A centre in CaF_2:0.05%Eu^{3+}. The spectra were reocrded at 16K.

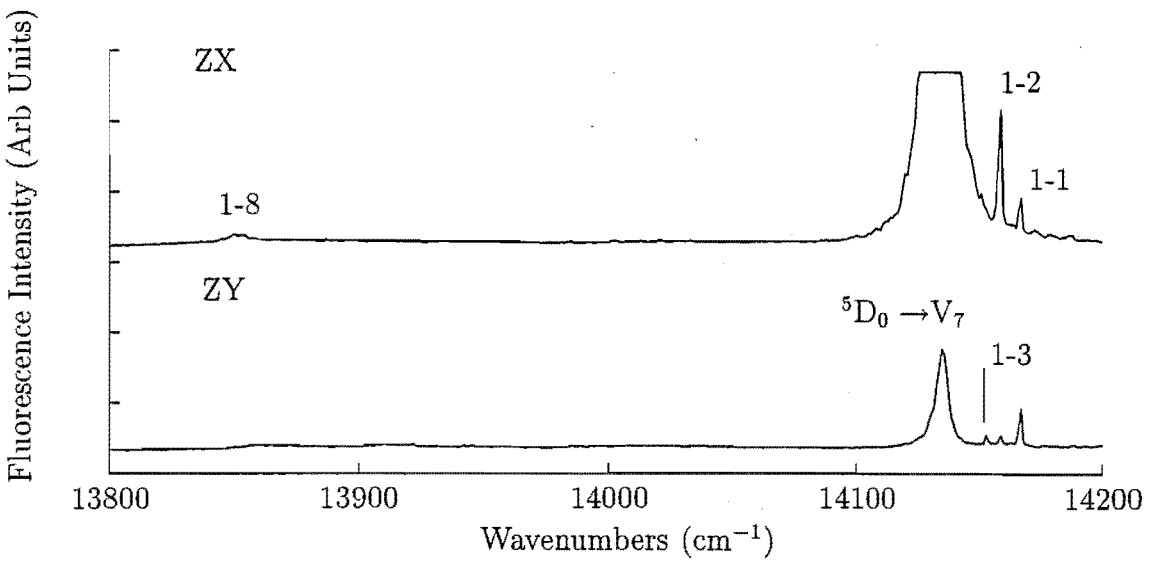

Figure 6.15: Polarised fluorescence spectrum for transitions $^5D_1 \rightarrow ^7F_6$ of the A centre in CaF_2:0.05%Eu^{3+}. The spectra were recorded at 16K.

Table 6.4: Polarisation data, level assignments and energies for the A centre in CaF_2:0.05%Eu^{3+} obtained in emission from $^5D_1\gamma_1$ at 19029 cm^{-1}. Frequencies are as measured in air cm^{-1} and have an uncertainty of ± 1 cm^{-1} unless otherwise stated.

Terminating Multiplet	Transition Frequency	State Energy	State & Symmetry	Polarisation Assignment
$^5F_1$	18721	309	$Y_1\gamma_5$	π
	18572	457	$Y_2\gamma_2$	σ
$^5F_2$	18177	852	$X_1\gamma_4$	σ'
	18056	973	$X_2\gamma_5$	π'
	17906	1123	$X_3\gamma_3$	σ'
	17766	1263	$X_4\gamma_1$	σ'
$^5F_3$	17214	1815	$W_1\gamma_5$	π
	17195	1835	$W_2\gamma_4$	σ
	17075	1955	$W_3\gamma_5$	π
	17053	1976	$W_4\gamma_2$	σ
	16899	2130	$W_5\gamma_3$	(mixed)
$^5F_4$	16517	2512	$V_1\gamma_1$	σ
	16230	2799	$V_2\gamma_5$	π
	16084	2945	$V_3\gamma_2$	(mixed)
	16023	3006	$V_4\gamma_5$	π
	15940	3089	$V_5\gamma_3$	(mixed)
	15915	3114	$V_6\gamma_4$	σ
	15873	3156	$V_7\gamma_1$	σ
$^5F_5$	15283	3747	$U_1\gamma_4$	σ
	15199	3831	$U_2\gamma_5$	π
	15059	3970	$U_3\gamma_2$	σ (mixed)
	15009	4020	$U_4\gamma_1$	(mixed)
$^5F_6$	14163	4866	$T_1\gamma_4$	(mixed)
	14155	4874	$T_2\gamma_5$	π
	14150	4879	$T_3\gamma_1$	
	13846±2	5183	$T_8\gamma_5$	π

6.2.3 Q Centre Fluorescence

Q centre fluorescence was excited at the 17262 cm^{-1} $Z_1 \rightarrow A_1$ transition. A CaF_2:0.05%Sm^{3+} crystal was cooled to 16K for these experiments. Figures 6.16 and 6.17 show fluorescence from $^5D_0$ to the ^7F_J multiplets. The fluorescence observed is consistent with a low symmetry centre in that all $^7F_1$ multiplet degeneracy is removed. This has been noted by Hamers et. al. [104] who concluded that the centre comprised two equivalent coupled rare earth ions. No emission from $^5D_1$ was studied as this is weak due to cross relaxation processes between the Eu^{3+} ions that make up the centre. As the centre is of low symmetry no symmetry restrictions are likely to be acting on the $^5D_0 \rightarrow ^7F_J$ transitions and all observable states should be detectable.

The fluorescence observed by Hamers, is on the whole identical to that observed here. However there are some exceptions. Transitions in the 13850 - 13700 and 12000 - 11750 cm^{-1} regions observed by Hamers could not be detected by this author. It is possible that at the higher Eu^{3+} concentrations used by Hamers (0.1 molar %) additional weaker cluster lines overlap the Q center absorption transitions and thus additional transitions are observed which do not belong to the centre in question and these transitions appear to have been misassigned by Hamers. The transitions detected in this work are given in Table 6.5.

More recent work, Cirillo-Penn and Wright (1990, 1991) [110] [10], has reassigned the Q centre as an anion-excess trimer centre. This assignment was based on analysis of the centre concentrations as a function of annealing time. For this, the only reasonable fit to the experimental data was for a centre including three rare earth ions and four fluorine ions. From the excitation experiments presented in section 6.2.1, our results appear consistent with the conclusions of Cirillo-Penn and Wright. Further studies of this centre are undertaken in chapter seven.

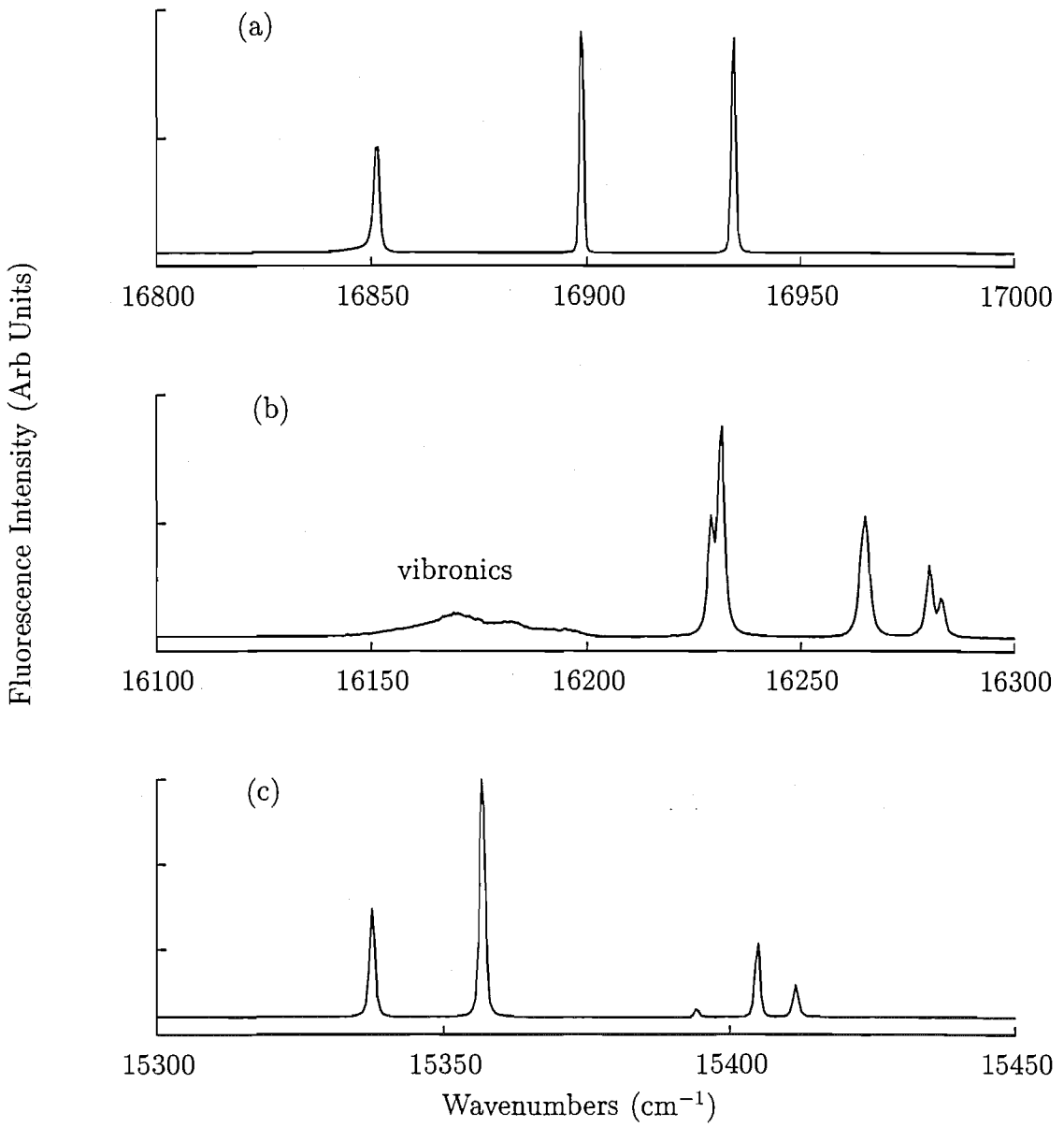

Figure 6.16: Fluorescence spectra for the (a) $^7F_1$ and (b) $^7F_2$ and (c) $^7F_3$ multiplets of the Q centre in CaF_2:0.05%Eu^{3+}. All fluorescence emanates from $^5D_0$. The spectra were recorded at 16K.

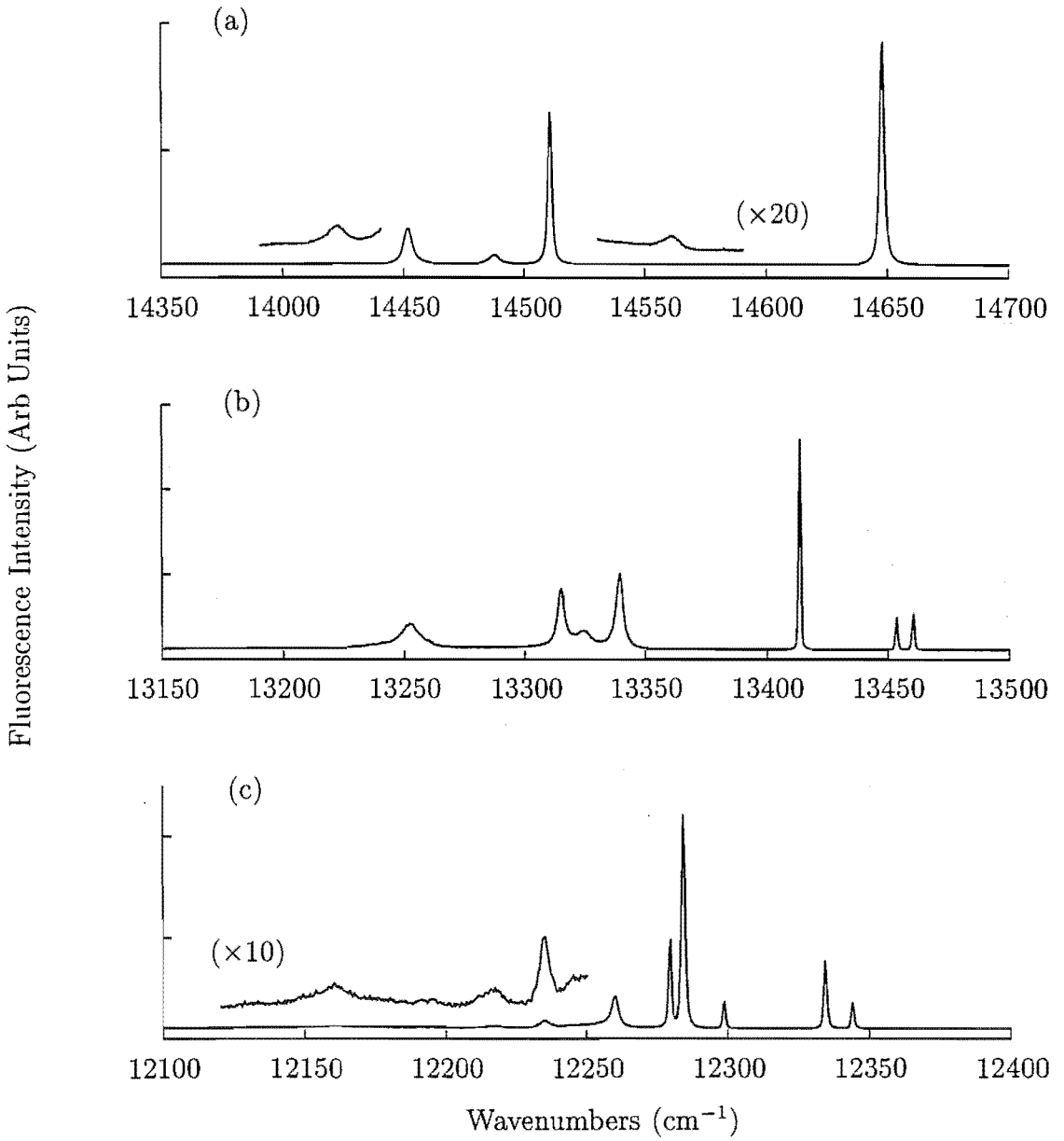

Figure 6.17: Fluorescence spectra for the (a) $^7F_4$, (b) $^7F_5$ and (c) $^7F_6$ multiplets of the Q centre in CaF_2:0.05%Eu^{3+}. All fluorescence emanates from $^5D_0$. The spectra were recorded at 16K.

Table 6.5: Transition frequencies (in air $cm^{-1} \pm 1$) for the Q centre in CaF_2:0.05%Eu^{3+}

Multiplet	Transition Frequency	State Energy
	16935	327
$^7F_1$	16900	362
	16852	410
	16284	978
	16281	981
$^7F_2$	16266	996
	16232	1030
	15230	1032
	15413	1849
	15406	1856
$^7F_3$	15395	1866
	15358	1904
	15339	1923
	14648	2613
	14562	2700
	14512	2750
$^7F_4$	14488	2773
	14452	2809
	14423	2839
	13461	3801
	13454	3807
	13414	3847
$^7F_5$	13340	3922
	13325	3936
	13315	3946
	13254	4008
	12345	4917
	12335	4926
	12300	4962
	12285	4976
$^7F_6$	12281	4981
	12261	5001
	12238	5024
	12220	5042
	12163	5099

6.2.4 R Centre Fluorescence

The fluorescence spectrum of the R centre was measured for excitation of the 17259 cm^{-1} $^7F_0$ $\rightarrow ^5D_0$ transition. For emission to the $^7F_1$ multiplet, four transitions are observed as shown in Figure 6.18(a). On the whole more than (2J+1) crystal field levels are observed to the ^7F_J multiplets (Figures 6.18 and 6.19). This is not consistent with the spectra of a single ion centre. We conclude that the R centre comprises at least two inequivalent Eu^{3+} ions, that is two Eu^{3+} ions experiencing different crystal fields. This is consistent with the conclusions of Hamers et. al. [104]. As with the Q centre, emission emanating from the $^5D_1$ multiplet has not been studied. The observed $^5D_0$ transition frequencies are given in Table 6.6.

Hamers et. al. [104] observed fluorescence transitions to the $^7F_6$ multiplet that they assign as R centre fluorescence (observed in the 11750 - 12000 cm^{-1} region). These transitions could not be observed in the CaF_2:Eu^{3+} crystals studied in this work. It is expected that these transitions are due to centre overlap thereby yielding non-selective excitation of the R centre absorption transition. A broad transition to the $^7F_1$ multiplet centred at 16843 cm^{-1} is assigned by Hamers to be a local mode phonon. The measured vibronic interval is 96 cm^{-1}, this energy is consistent with the observation of previous workers [89]. With an energy of 96 cm^{-1} this is a pseudo-localised mode of vibration of the Eu^{3+} ions. That is to say the phonon is spatial localised to the rare earth ion centre as the perfect lattice does not have many phonons propagating at 96 cm^{-1}.

Cirillo-Penn and Wright have studied the R centre in CaF_2:Eu^{3+} [10] [110]. The centre concentrations as a function of annealing time are shown to be consistent with the assignment of Hamers et. al that this centre contains only two rare earth ions. The R centre is proposed to be anion excess with an additional F^- ion scavenged from single Eu^{3+}-F^- pair sites. In this case, it is possible that the additional F^- ion is the source of the assymetry.

As multi-rare-earth ion centres, both the R and Q centres are particularly interesting as they form as preferential cluster centres as opposed to ions in close proximity for statistical reasons. By co-doping with additional rare earth ions, for example Sm^{3+}, ion-ion interactions such as energy transfer should be more readily observable and this is explored in chapter seven. Further to this, it is possible that these cluster centres observed in Eu^{3+} doped CaF_2 are related to those observed in CaF_2:Sm^{3+} which also form preferentially.

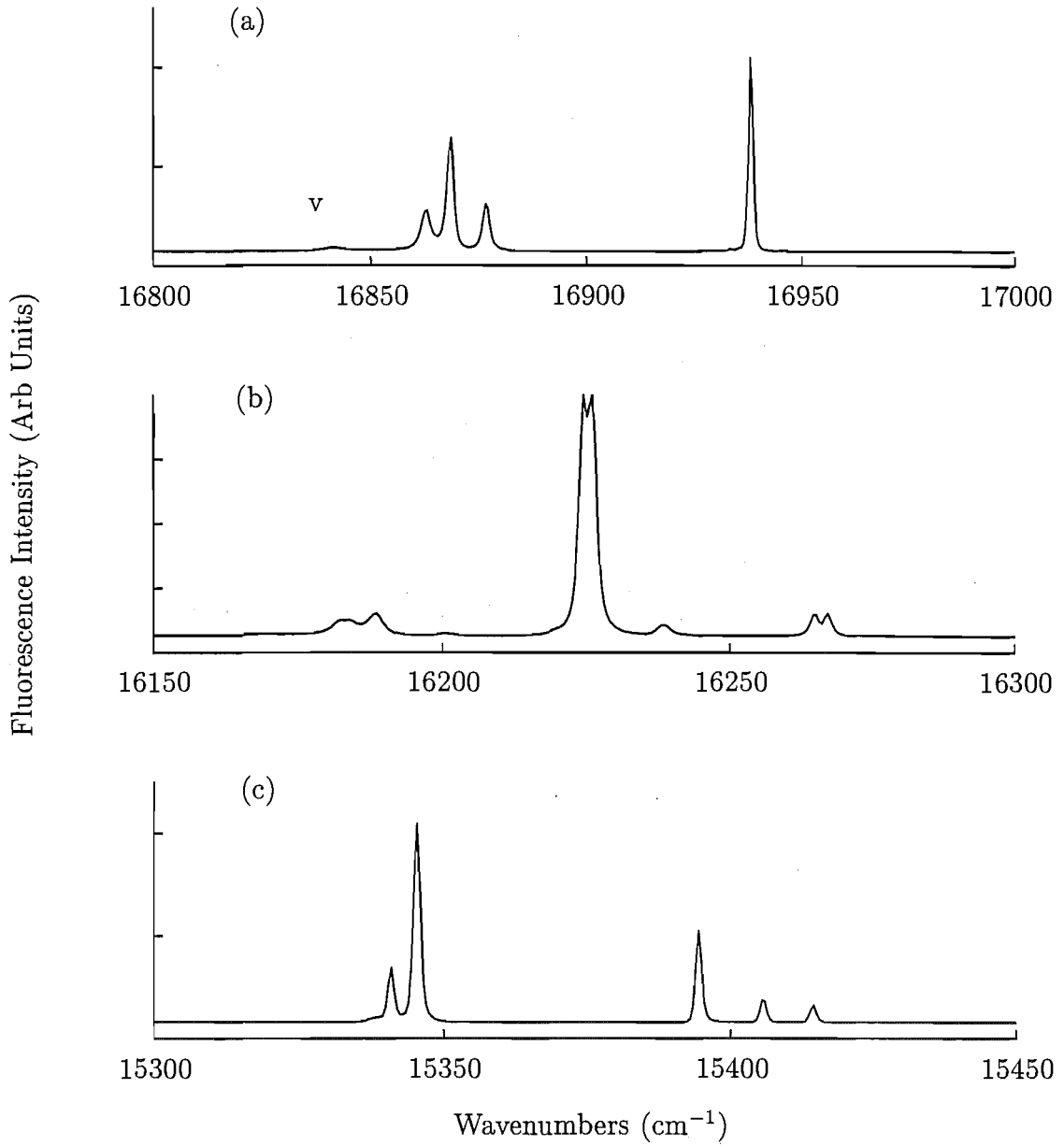

Figure 6.18: 16K fluorescence spectra for the (a) $^7F_1$, (b) $^7F_2$ and $^7F_3$ multiplets of the R centre in CaF_2:0.05%Eu^{3+}. All fluorescence emanates from $^5D_0$. The spectra were recorded at 16K.

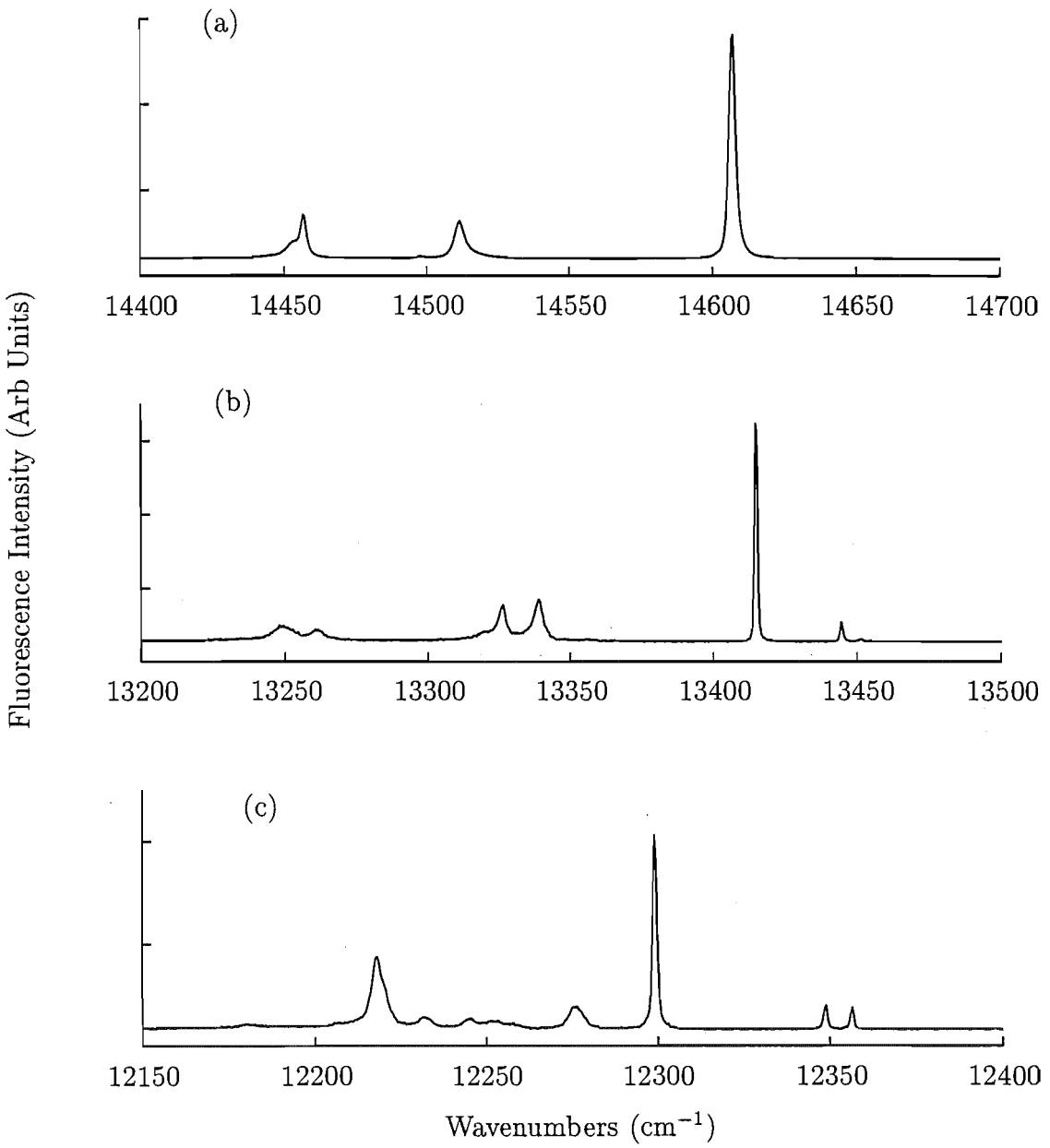

Figure 6.19: Fluorescence spectra for the (a) $^7F_4$, (b) $^7F_5$ and $^7F_6$ multiplets of the R centre in CaF_2:0.05%Eu^{3+}. All fluorescence emanates from $^5D_0$. The spectra were recorded at 16K.

Table 6.6: Transition frequencies (in air $cm^{-1}\pm1$) for the R centre in CaF_2:0.05%Eu^{3+}. Excitation is at 17259 cm^{-1}.

Multiplet	Transition Frequency	State Energy
	16939	320
	16878	381
$^7F_1$	16870	390
	16864	395
	16268	991
	16266	993
	16239	1020
	16227	1032
$^7F_2$	16226	1034
	16202	1057
	16189	1070
	16185	1074
	15416	1843
	15407	1852
$^7F_3$	15396	1864
	15347	1913
	15342	1917
	14608	2652
	14512	2747
$^7F_4$	14498	2761
	14457	2802
	14454	2805
	13452	3808
	13445	3814
	13415	3844
$^7F_5$	13339	3920
	13327	3933
	13262	3998
	13251	4009
	12356	4903
	12349	4911
	12299	4960
	12278	4982
$^7F_6$	12254±4	5005
	12247	5013
	12234	5026
	12220	5040
	12181	5079

6.3 Spectroscopy of $SrF_2:Eu^{3+}$

6.3.1 Absorption and Excitation Spectra

The optical absorption spectra of a 22.2 mm thick SrF_2:0.2%Eu^{3+} crystal was measured for absorption to the $^5D_1$, $^5D_2$ and $^5D_3$ multiplets. These spectra are shown in Figure 6.20. Only transitions assigned to be due to the C_{4v} symmetry centre by Jouart et. al. [105], have been observed. We denote this centre as the A centre from its similarity with the tetragonal A centre in CaF_2 crystals. Absorption transitions to the $^5D_0$ multiplet were searched for, however none could be observed.

Transitions to $^5D_0$ can be detected with the more sensitive laser selective excitation technique as shown in Figure 6.21. The dominant feature of this spectrum is the A centre transition at 17298 cm^{-1}. At an intensity over 1000 times less than that of the A centre, is a transition assigned by Jouart to be due to a C_{3v} symmetry centre (which we label J). It is possible, that the intensity of this transition indicates a low electric dipole transition moment arising from weak interconfigurational mixing due to a reduced axial distortion. Measurement of the $^5D_1$ excitation spectrum seems to confirm this, as the J centre transition intensities increase by a factor of ten relative to the A centre transitions (see Figures 6.22 and 6.23). The $^5D_0$ and $^5D_1$

Table 6.7: A and J centre excitation frequencies (in air $cm^{-1}\pm1$) for the $^5D_0$ and $^5D_1$ multiplets in SrF_2:0.05%Eu^{3+}

Centre	Multiplet	Transition	Frequency
A (C_{4v})	$^5D_0$	$Z_1 \rightarrow A_1$	17298
	$^5D_1$	$Z_1 \rightarrow B_1$	19049
		$Z_1 \rightarrow B_2$	19082
J (C_{3v})	$^5D_0$	$Z_1 \rightarrow A_1$	17295
	$^5D_1$	$Z_1 \rightarrow B_1$	19046
		$Z_1 \rightarrow B_2$	19061

transition frequencies are given in Table 6.7 as measured from the laser selective excitation spectra. The $^5D_2$ absorption spectrum transitions cannot be assigned from this measurement alone, however Jouart et. al. [105] have measured the $^5D_2$ spectrum by argon laser excitation at 77K. From the two observed transitions in Figure 6.20(b) are assigned as the A centre $Z_1 \rightarrow C_2$ and C_3 transitions at 464.88 nm (21511 cm^{-1}) and 463.95 nm (21554 cm^{-1}). The remaining two transitions to this multiplet are symmetry forbidden from the ground state. The transition at 409.17 nm is unassigned from this data but is shown from upconversion fluorescence to terminate on the upper most $^5D_3$ crystal field level.

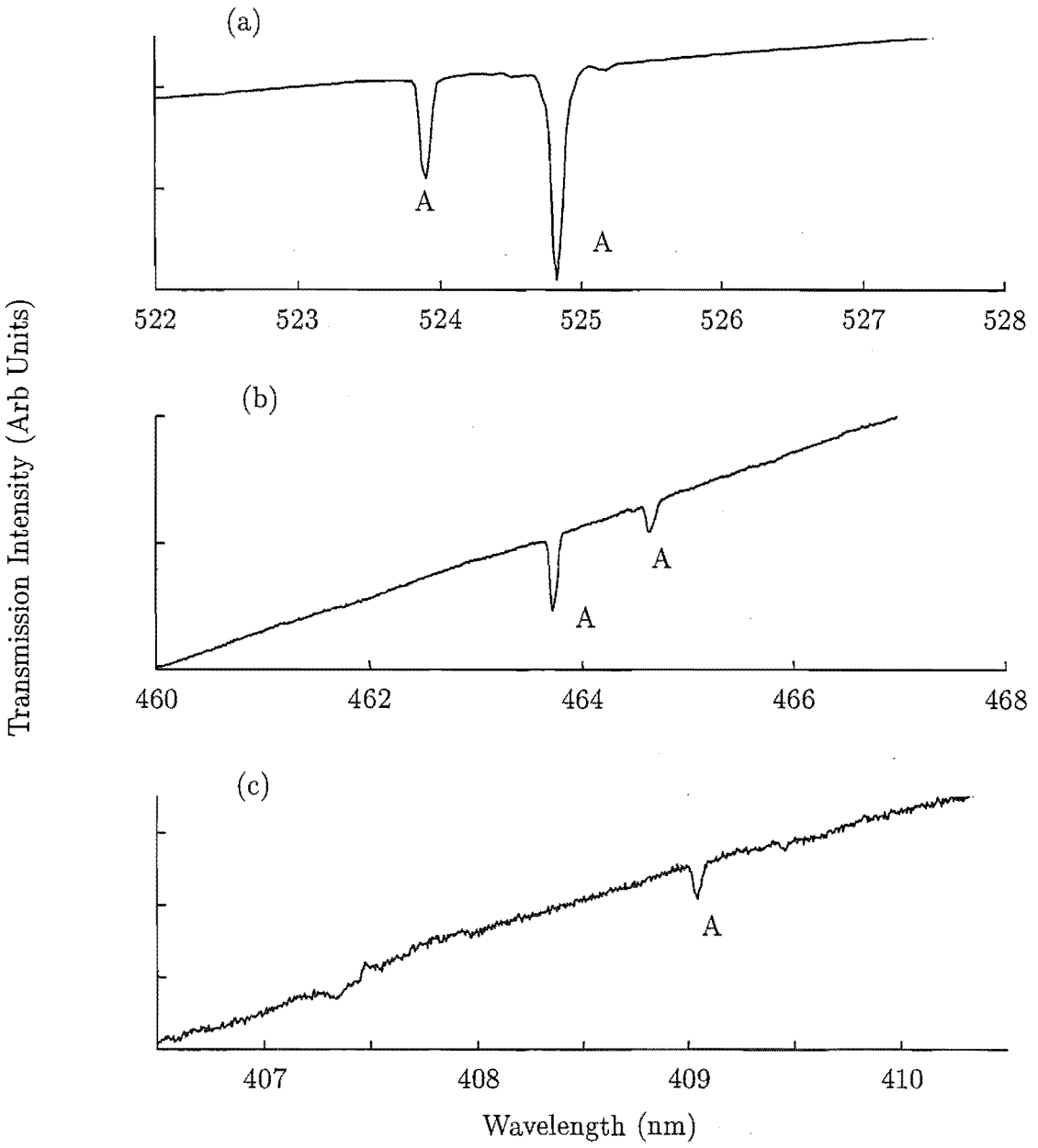

Figure 6.20: 16K optical absorption spectra of the (a) $^5D_1$ multiplet, (b) the $^5D_2$ multiplet and (c) the $^5D_3$ multiplet for SrF_2:0.2%Eu^{3+}. The spectra were recorded at 16K.

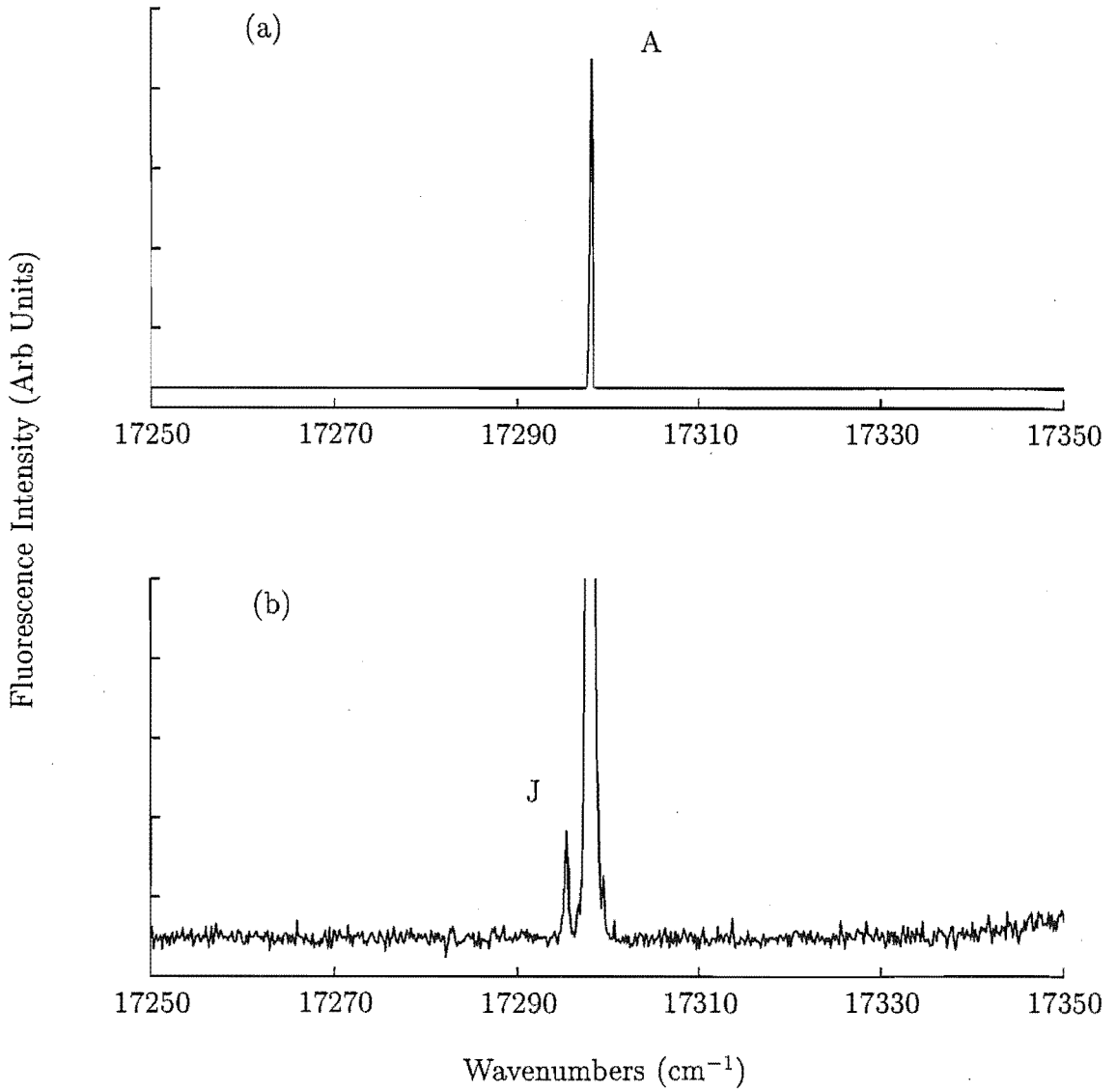

Figure 6.21: 16K excitation spectrum of the $^5D_0$ multiplet in SrF_2:0.05%Eu^{3+} monitoring all transitions at 625 nm. (a) ×1 amplification and (b) ×1000 amplification. The spectra were recorded at 16K.

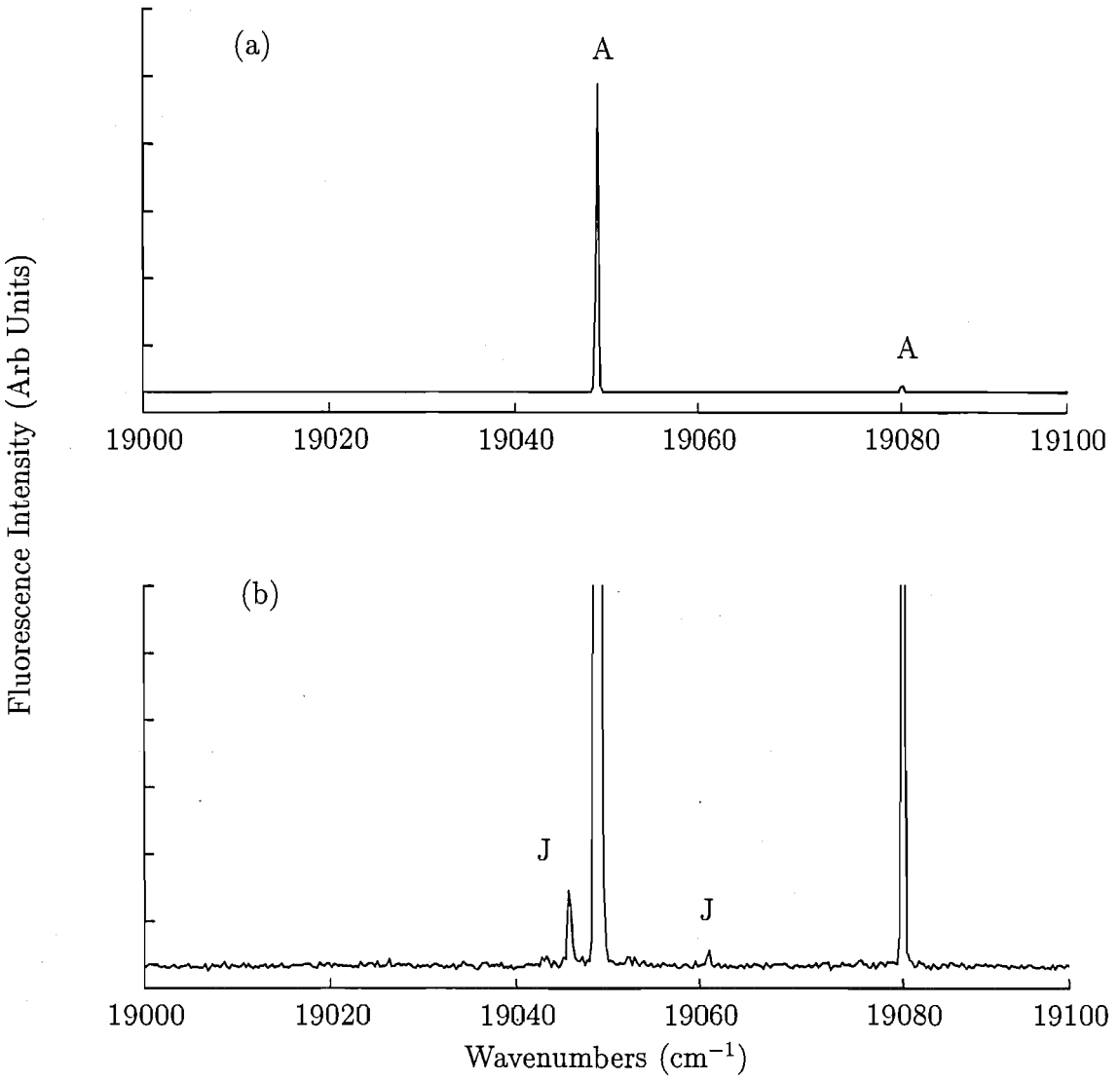

Figure 6.22: Excitation spectrum of the $^5D_1$ multiplet in SrF_2:0.05%Eu^{3+} monitoring all transitions at 625 nm. (a) ×1 amplification and (b) ×100 amplification. The spectra were recorded at 16K.

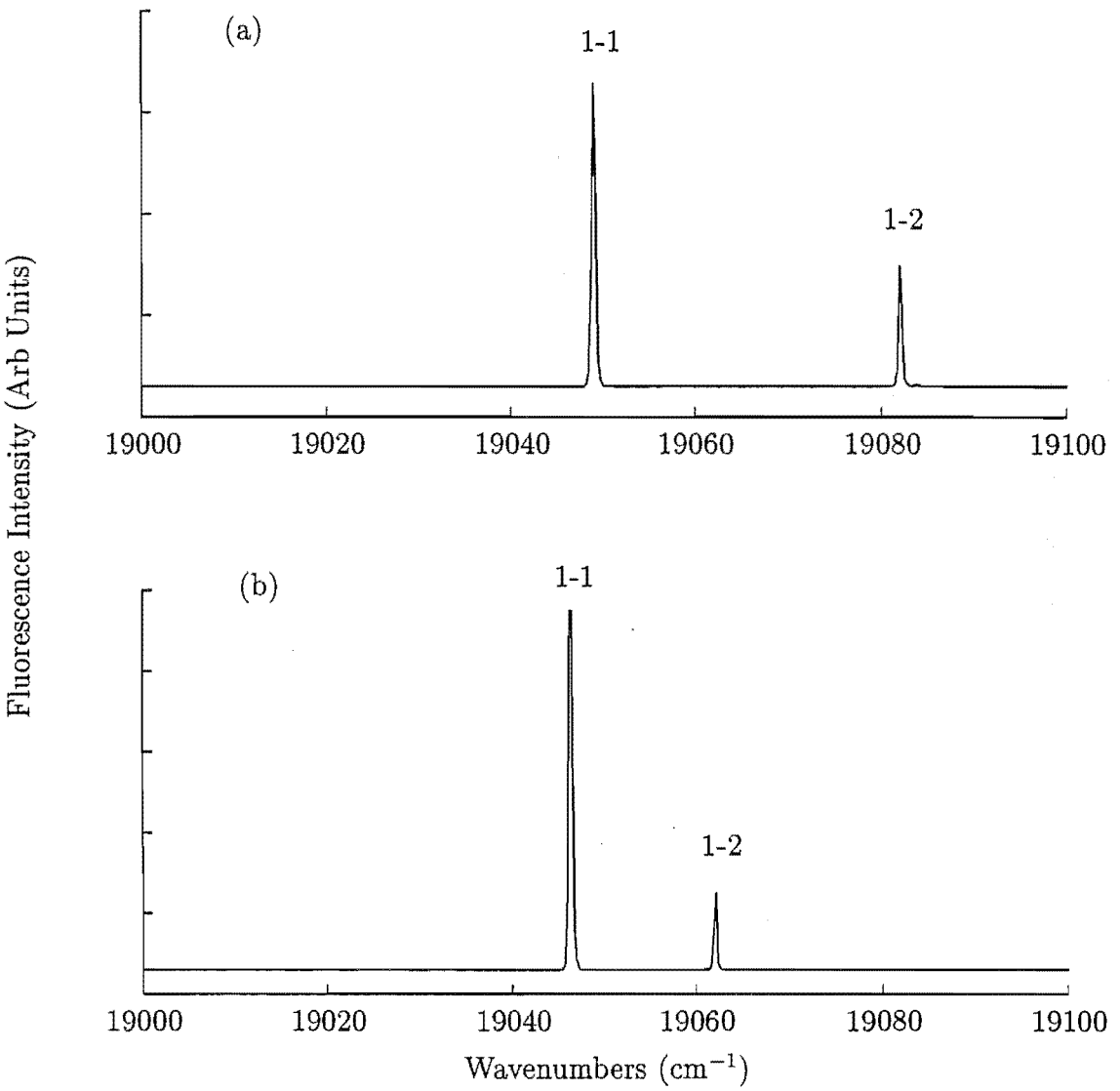

Figure 6.23: Excitation spectrum of the $^5D_1$ multiplet in SrF_2:0.05%Eu^{3+}. (a) the A centre monitoring at 16974 cm^{-1} and (b) the J centre monitoring at 16442 cm^{-1}. The spectra were recorded at 16K.

6.3.2 A Centre Fluorescence

Early ionic thermocurrent experiments (den Hartog and Nakata [111] 1983) determined the dominant trivalent europium ion centre in SrF_2:Eu^{3+} crystals. This was ascribed to a Eu^{3+} - F^- dipole with tetragonal symmetry. In that work, electron paramagnetic resonance was also employed to detect Eu^{2+} ions present in the lattice. It was concluded that even at high concentrations of Eu dopant, the divalent ions do not participate in clustering with the trivalent ions. A later study of the SrF_2:Eu^{3+} system used the laser selective excitation technique (Jouart et. al. [105] 1985). Three Eu^{3+} centres were found to dominate at low concentrations, C_{4v} and C_{3v} symmetry Eu^{3+} - F^- pairs and a non-locally compensated Eu^{3+} ion (near cubic symmetry). Irreducible representations were assigned to some levels, although the method of assignment is not clear and does not seem to be based on experiment data.

The fluorescence spectra of the dominant A centre in SrF_2:Eu^{3+} crystals was measured for concentrations of 0.01 and 0.05 mol % of the rare-earth dopant ion. In neither case were the spectra of additional centres apparant for excitation of the $^7F_0 \rightarrow {}^5D_0$ transition at 17298 cm^{-1} or the $^7F_0 \rightarrow {}^5D_1B_1\gamma_5$ transition at 19048 cm^{-1}. As a consequence, the higher concentration was chosen for presentation because higher signal intensities were obtained. Down-converted selective fluorescence was obtained from the $^5D_0$ and $^5D_1$ multiplets only, emission from the $^5D_2$ and $^5D_3$ multiplets was obtained from the upconversion process to be discussed in a following section of this chapter.

Polarised fluorescence spectra to the ^7F_J multiplets are shown in Figures 6.24 through to 6.35 with the measured transition frequencies and polarisation assignments given in Tables 6.8 and 6.9 for $^5D_0$ and $^5D_1$ emission, as is appropriate. As with the C_{4v} symmetry A centre in CaF_2:Eu^{3+}, some transitions are observed to have significantly degraded polarisation ratios. This is because the emissive linestrengths have comparable electric and magnetic dipole character.

Three-fold structure is apparant on the 16064 cm^{-1} fluorescence peak. The transition is assigned as $B_1\gamma_5 \rightarrow V_4\gamma_5$. As the transition is between two doublet states, it is possible that the observed structure is associated with superimposed hyperfine patterns. As magnetic hyperfine constants are not known for the trivalent europium ion, it is not possible to verify this by a calculation of the expected hyperfine patterns.

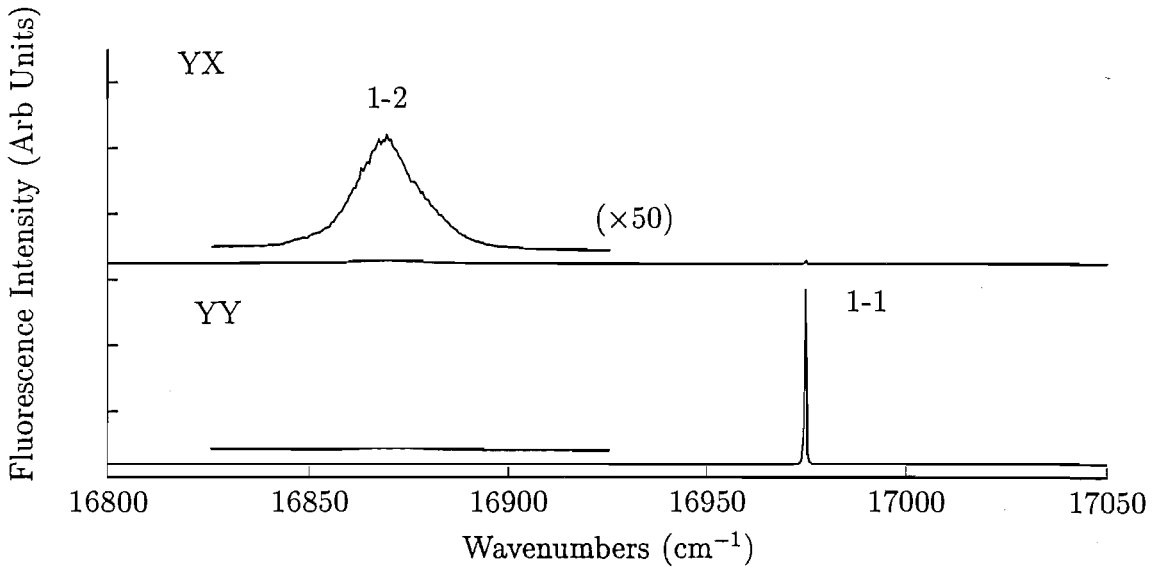

Figure 6.24: $^5D_0$ to $^7F_1$ polarised emission for the A centre in SrF_2:0.05%Eu^{3+}. The excitation frequency is 17298 cm^{-1}. The spectra were recorded at 16K.

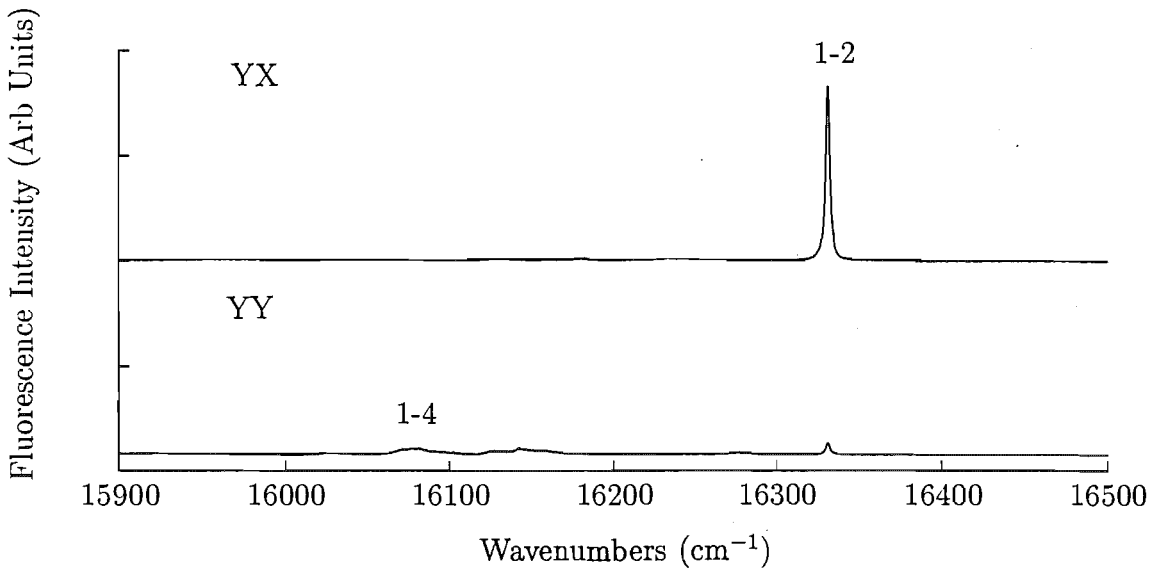

Figure 6.25: $^5D_0$ to $^7F_2$ polarised emission for the A centre in SrF_2:0.05%Eu^{3+}. The excitation frequency is 17298 cm^{-1}. The spectra were recorded at 16K.

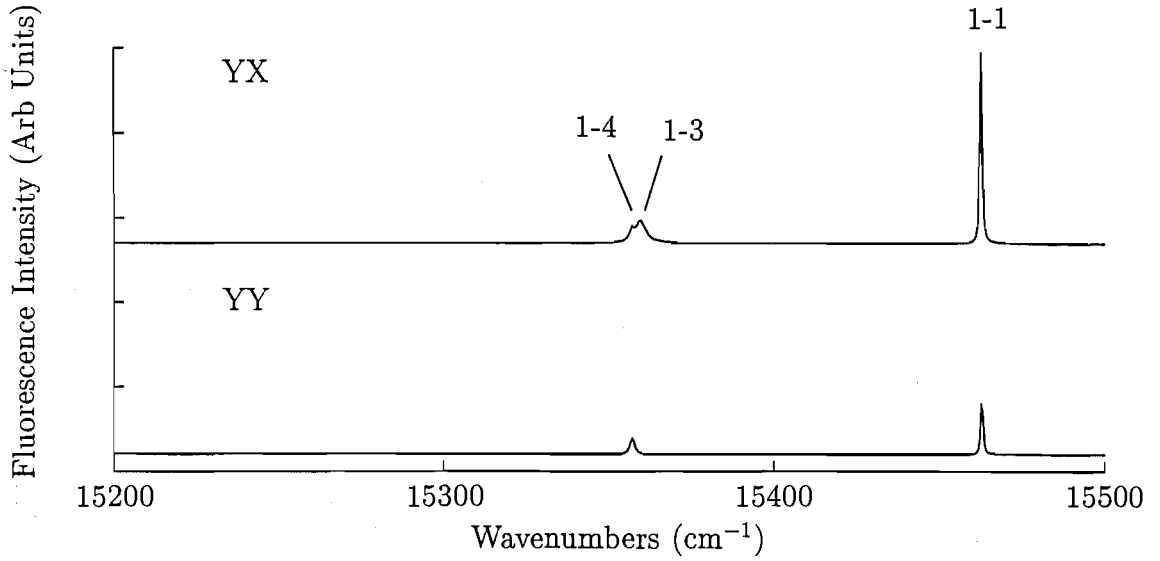

Figure 6.26: $^5D_0$ to $^7F_3$ polarised emission for the A centre in SrF_2:0.05%Eu^{3+}. The spectra were recorded at 16K.

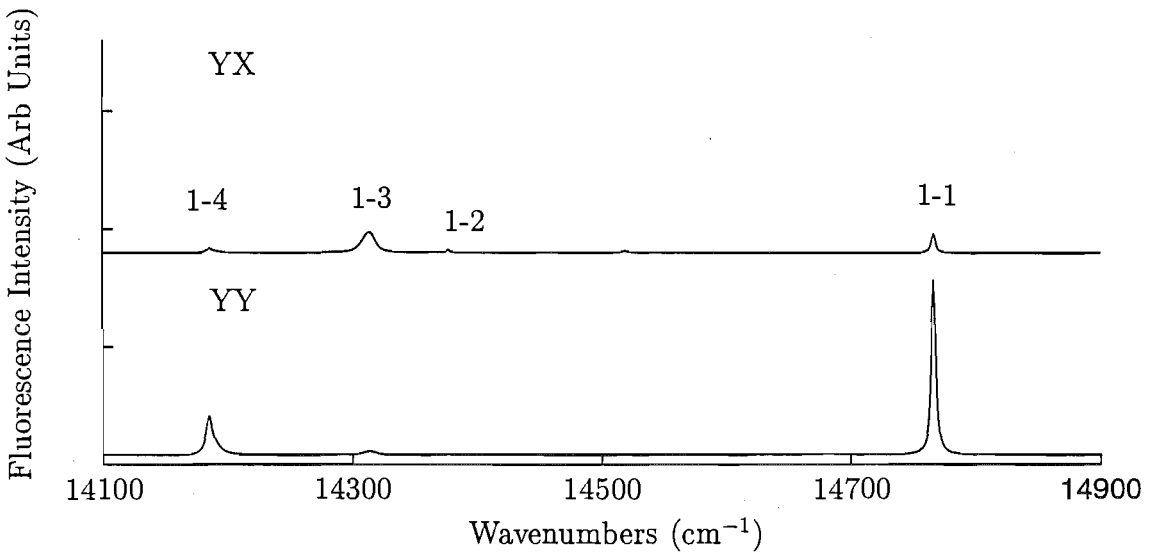

Figure 6.27: $^5D_0$ to $^7F_4$ polarised emission for the A centre in SrF_2:0.05%Eu^{3+}. The excitation frequency is 17298 cm^{-1}. The spectra were recorded at 16K.

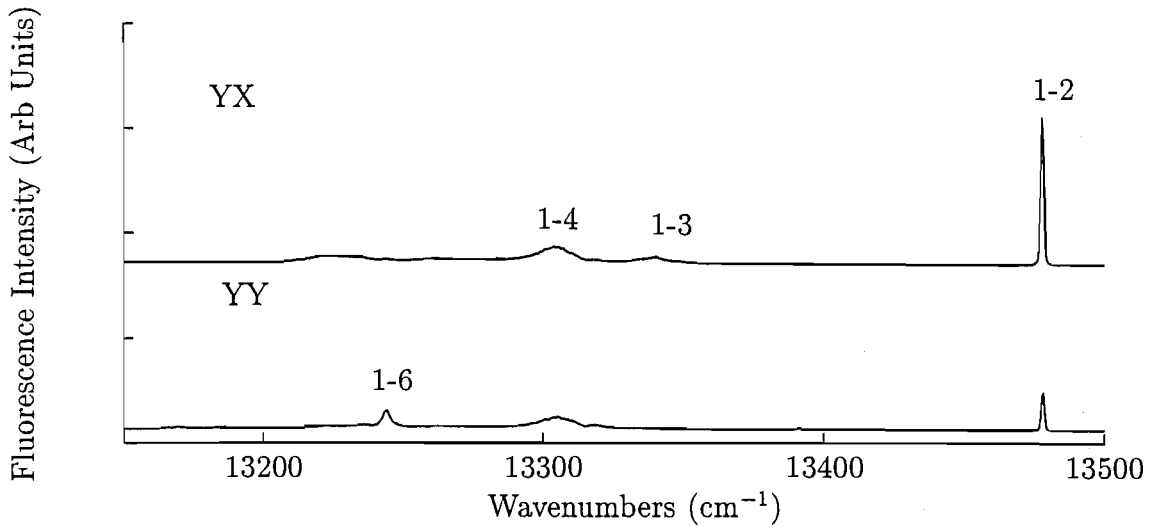

Figure 6.28: $^5D_0$ to $^7F_5$ polarised emission for the A centre in SrF_2:0.05%Eu^{3+}. The spectra were recorded at 16K.

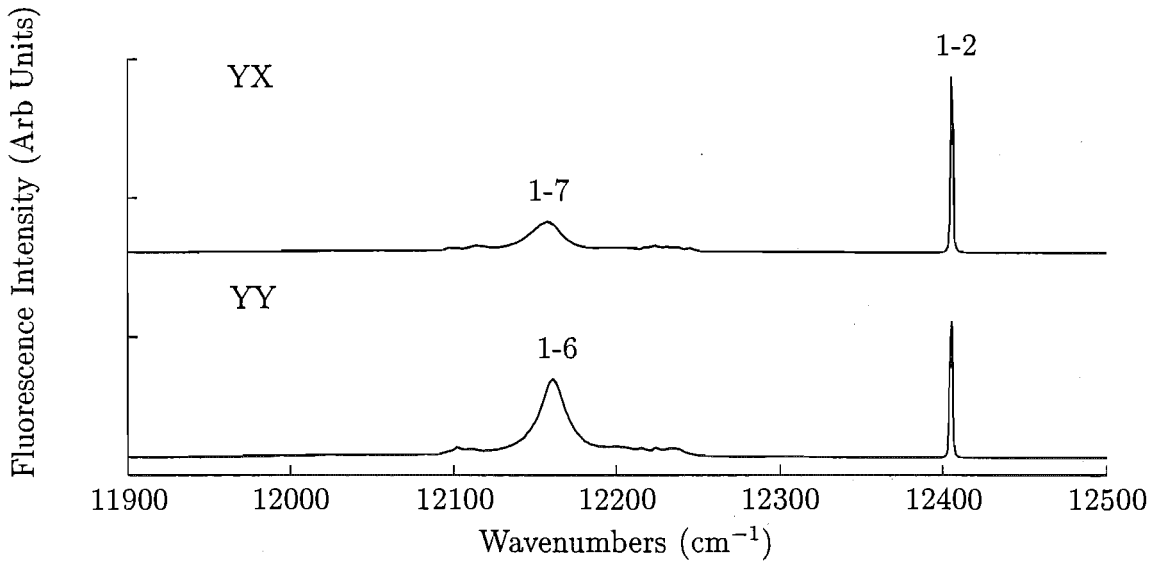

Figure 6.29: $^5D_0$ to $^7F_6$ polarised emission for the A centre in SrF_2:0.05%Eu^{3+}. The excitation frequency is 17298 cm^{-1}. The spectra were recorded at 16K.

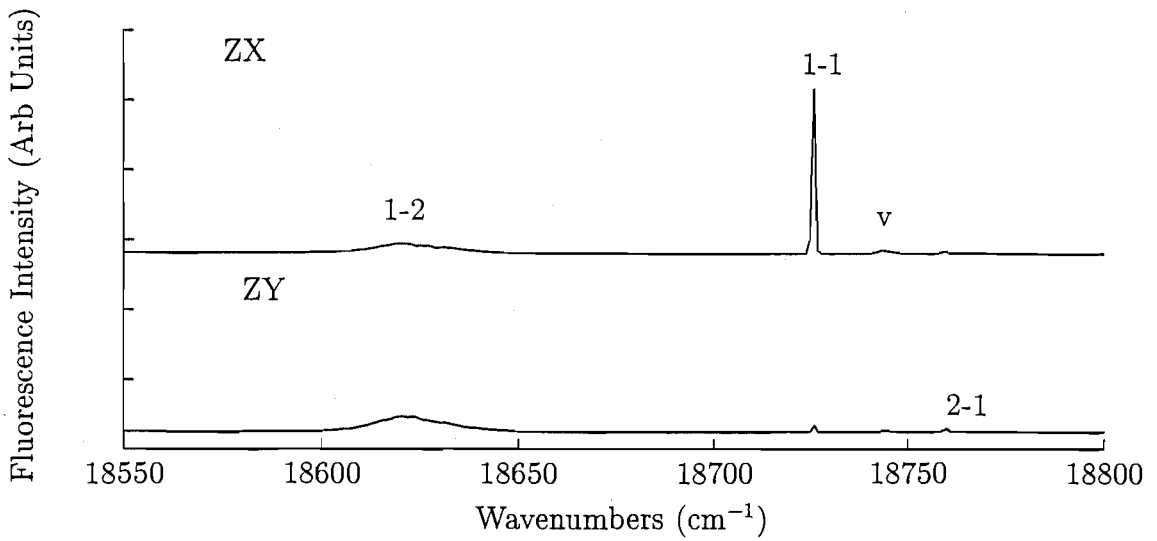

Figure 6.30: $^5D_1$ to $^7F_1$ polarised emission for the A centre in SrF_2:0.05%Eu^{3+}. The excitation frequency is 19048 cm^{-1}. The spectra were recorded at 16K.

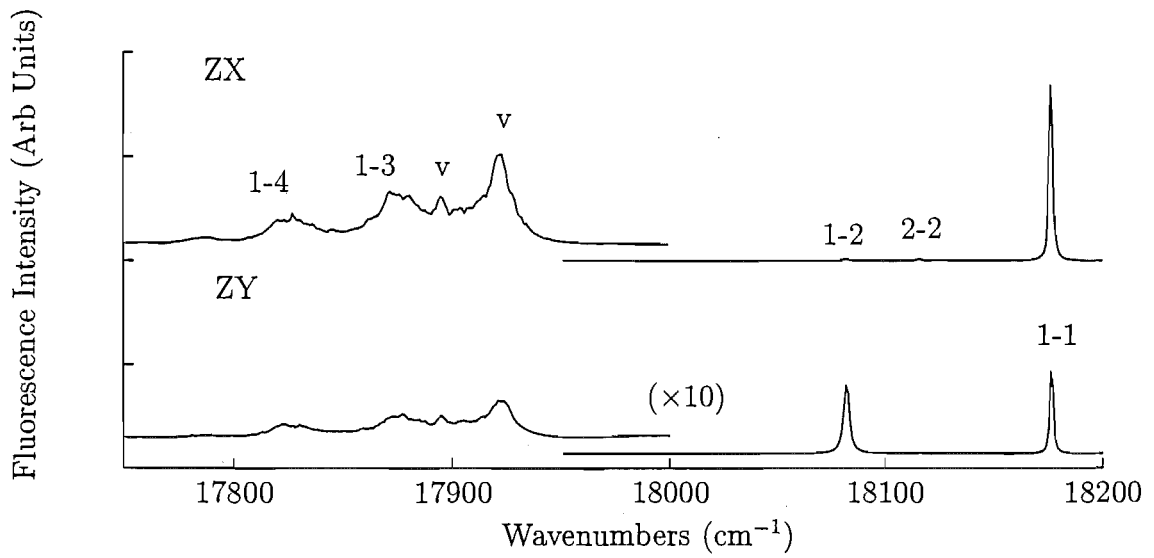

Figure 6.31: $^5D_1$ to $^7F_2$ polarised emission for the A centre in SrF_2:0.05%Eu^{3+}. The excitation frequency is 19048 cm^{-1}. The spectra were recorded at 16K.

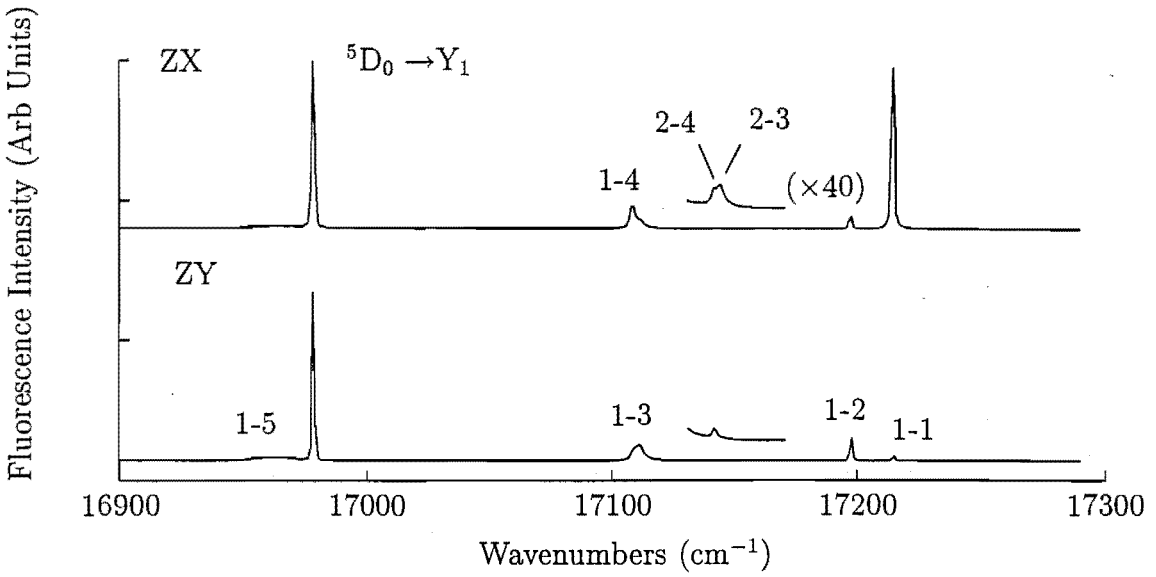

Figure 6.32: $^5D_1$ to $^7F_3$ polarised emission for the A centre in SrF_2:0.05%Eu^{3+}. The excitation frequency is 19048 cm^{-1}. The spectra were recorded at 16K.

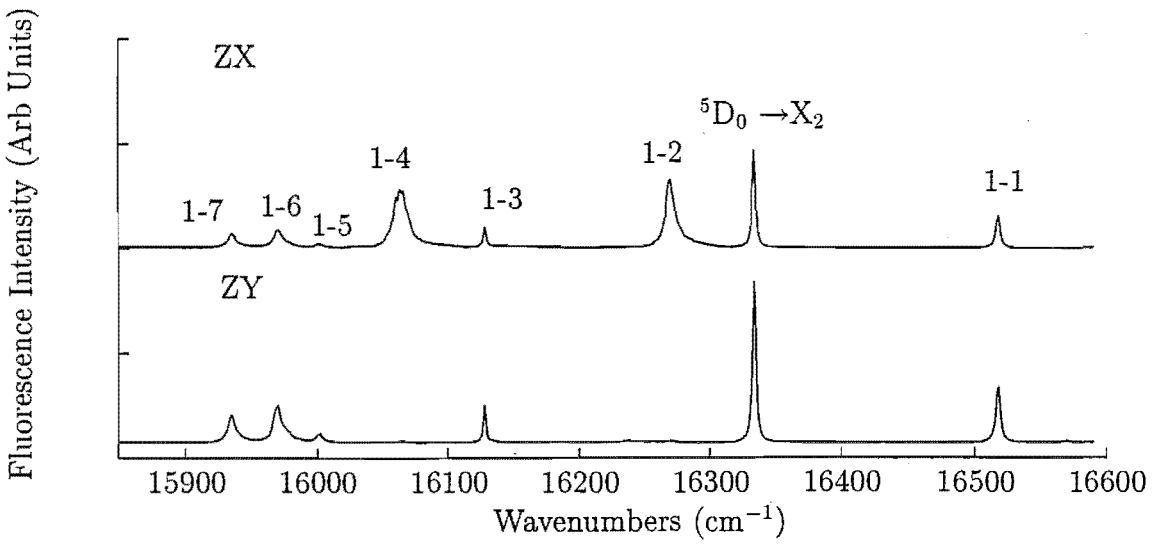

Figure 6.33: $^5D_1$ to $^7F_4$ polarised emission for the A centre in SrF_2:0.05%Eu^{3+}. The excitation frequency is 19048 cm^{-1}. The spectra were recorded at 16K.

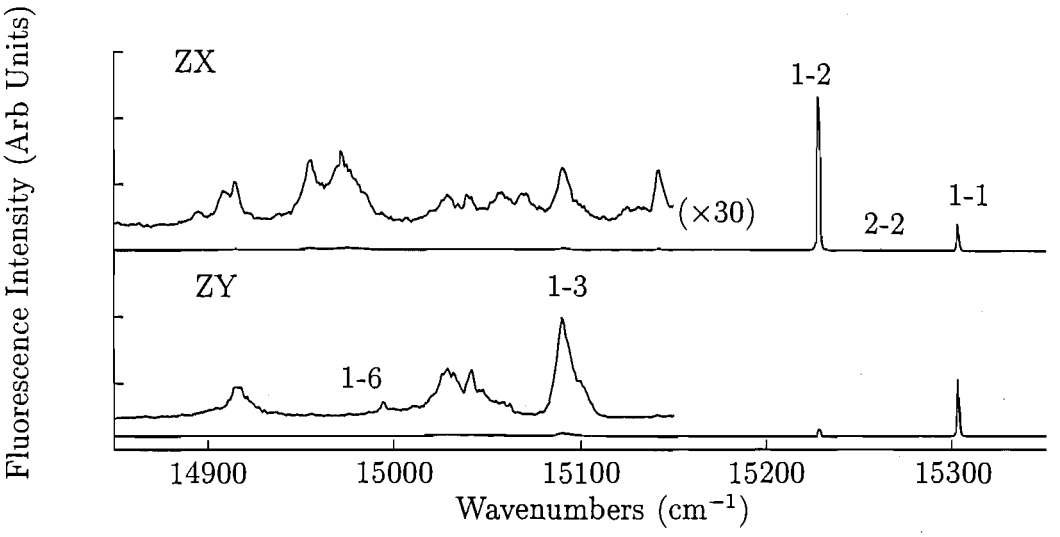

Figure 6.34: $^5D_1$ to $^7F_5$ polarised emission for the A centre in SrF_2:0.05%Eu^{3+}. The excitation frequency is 19048 cm^{-1}. The spectra were recorded at 16K.

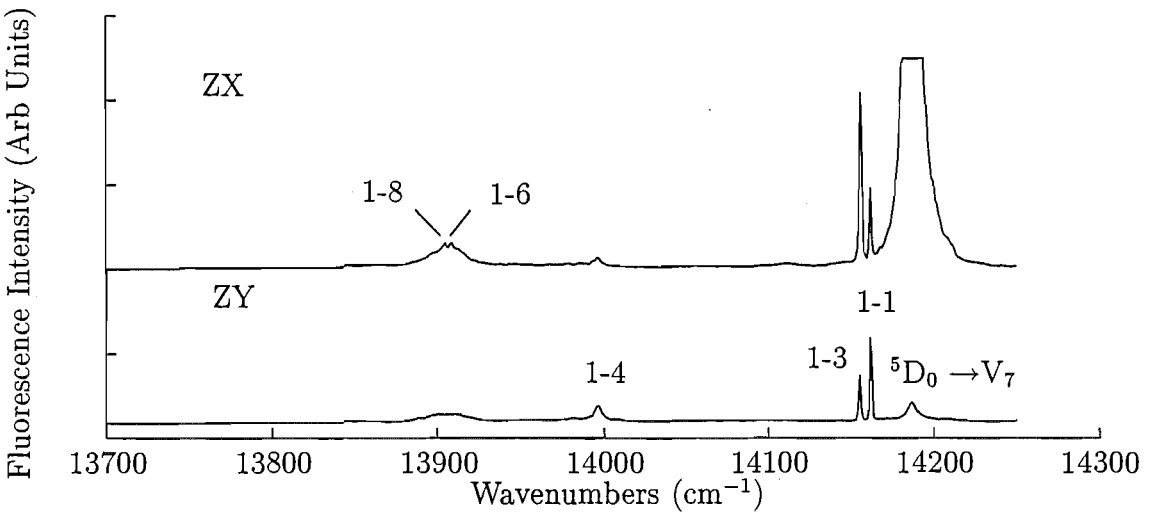

Figure 6.35: $^5D_1$ to $^7F_6$ polarised emission for the A centre in SrF_2:0.05%Eu^{3+}. The excitation frequency is 19048 cm^{-1}. The spectra were recorded at 16K.

Table 6.8: Polarisation data, level assignments and energies for the A centre in SrF_2:0.05%Eu^{3+} obtained in emission from $^5D_0\gamma_1$ at 17298 cm^{-1}. Energies are measured in air cm^{-1} and have an uncertainty of ± 1 cm^{-1} unless otherwise stated.

Terminating Multiplet	Transition Energy	State Energy	State & Symmetry	Polarisation Assignment
$^7F_1$	16974	324	$Y_1\gamma_5$	σ'
	16870±5	427	$Y_2\gamma_2$	π'
$^7F_2$	16330	968	$X_2\gamma_5$	σ
	16077	1221	$X_4\gamma_1$	π
$^7F_3$	15463	1835	$W_1\gamma_5$	σ
	15361	1936	$W_3\gamma_2$	π'
	15359	1939	$W_4\gamma_5$	(mixed) σ
$^7F_4$	14767	2531	$V_1\gamma_1$	π
	14518	2779	$V_2\gamma_5$	σ
	14376	2921	$V_3\gamma_2$	π'
	14311	2986	$V_4\gamma_5$	σ
	14184	3114	$V_7\gamma_1$	π
$^7F_5$	13478	3820	$U_2\gamma_5$	σ
	13337	3960	$U_3\gamma_2$	π'
	13304±2	3994	$U_4\gamma_5$	σ
	13243	4054	$U_6\gamma_5$	σ'
$^7F_6$	12405	4892	$T_2\gamma_5$	(mixed)σ
	12159	5139	$T_6\gamma_1$	π
	12158	5140	$T_7\gamma_5$	σ

Table 6.9: Polarisation data, level assignments and energies for the A centre in SrF_2:0.05%Eu^{3+} obtained in emissionfrom $^5D_1\gamma_1$ at 19048 cm^{-1}. ‡ is used to indicate where emission is observed from $^5D_1\gamma_2$ at 19082 cm^{-1}. Energies are measured in air cm^{-1} and have an uncertainty of ±1 cm^{-1} unless otherwise stated.

Terminating Multiplet	Transition Energy	State Energy	State & Symmetry	Polarisation Assignment
	18758‡	324	$Y_1\gamma_5$	(mixed)
$^7F_1$	18724	325	$Y_1\gamma_5$	π
	18620±5	429	$Y_2\gamma_2$	σ
$^7F_2$	18175	874	$X_1\gamma_4$	σ'
	18114‡	969	$X_2\gamma_5$	σ'
	18081	969	$X_2\gamma_5$	π'
	17880±2	1169	$X_3\gamma_3$	σ'
	17823±5	1226	$X_4\gamma_1$	σ'
$^7F_3$	17213	1836	$W_1\gamma_5$	π
	17196	1853	$W_2\gamma_4$	σ
	17147‡	1935	$W_3\gamma_2$	π
	17113	1936	$W_3\gamma_2$	σ
	17144‡	1939	$W_4\gamma_5$	σ'
	17110	1940	$W_4\gamma_5$	π
	16966±2	2084	$W_5\gamma_3$	σ
$^7F_4$	16516	2534	$V_1\gamma_1$	σ
	16268	2782	$V_2\gamma_5$	π
	16126	2923	$V_3\gamma_2$	σ
	16064	2985	$V_4\gamma_5$	π
	15999	3051	$V_5\gamma_3$	σ
	15969	3081	$V_6\gamma_4$	σ
	15933	3116	$V_7\gamma_1$	σ
$^7F_5$	15302	3748	$U_1\gamma_4$	(σ)
	15261‡	3822	$U_2\gamma_5$	(mixed)
	15227	3823	$U_2\gamma_5$	π
	15090	3959	$U_3\gamma_2$	σ
	14993	4057	$U_6\gamma_5$	(mixed)
$^7F_6$	14160	4889	$T_1\gamma_4$	(mixed)
	14155	4895	$T_3\gamma_1$	σ'
	13995	5055	$T_4\gamma_2$	σ
	13904±1	5142	$T_6\gamma_1$	σ'
	13900±1	5145	$T_8\gamma_3$	σ'

6.3.3 J Centre Fluorescence

A minority centre with a $^5D_0$ excitation frequency of 17295 cm^{-1}, has been labelled here as the J centre. This centre has been observed previously by Jouart et. al. [105]. They have noted that the crystal field splittings due to the axial distortion are weaker and conclude that the most suitable model for this centre is that of a rare earth ion charge compensated by a nearest neighbour interstitial F^- ion along the $\langle 111 \rangle$ direction. This gives a centre of trigonal C_{3v} symmetry.

In this work, both $\langle 111 \rangle$ and $\langle 100 \rangle$ oriented crystals have been studied from their respective transition polarisation dependence. A weak $\langle 111 \rangle$ orientational dependence is observed, however there is no polarisation dependence for $\langle 100 \rangle$ oriented crystals. This is consistent with the behaviour expected for a trigonal C_{3v} symmetry centre.

The 17295 cm^{-1}, $^7F_0 \rightarrow ^5D_0$ transition of this centre is particularly weak. This makes fluorescence measurements difficult. Despite this, a system of 18 electronic fluorescence transitions has been determined. The spectra are shown in Figures 6.36 to 6.41. Fluorescence to the $^7F_1$ multiplet is observed in the 17000 - 16850 cm^{-1} region and three transitions are observed. This is because the A centre is also excited, leading to the observation of the $A_1\gamma_1 \rightarrow Y_1\gamma_5$ transition of that centre, as shown in Figure 6.36(a). Transitions at 16977 and 16898 cm^{-1} are J centre transitions and give σ' and π' polarisation dependences. Both these transitions are magnetic dipole transitions as expected and are assigned as the $A_1\gamma_1 \rightarrow Y_1\gamma_3$ and $Y_2\gamma_2$ transitions. The smaller $^7F_1$ multiplet splitting (compared to that of the A centre) is indicative of a weaker axial distortion consistent with a charge compensation model of a next nearest neighbour F^- ion along the $\langle 111 \rangle$ direction. Figure 6.36(b) shows fluorescence transitions to the $^7F_1$ multiplet in the 18800 - 18600 cm^{-1} region for excitation of the $^5D_1$ multiplet 19046 cm^{-1} transition. In this case, four transitions are observed as the $^5D_1$ B_2 state is only 15 cm^{-1} higher in energy than the 19046 cm^{-1} state. Thus, the B_2 state has a significant thermal population and emission is observed from that state. Polarisation ratios for emission from the 19046 cm^{-1} state are particularly poor and it is concluded that the doublet state is lowest for the $^5D_1$ multiplet, consistent with the assignment of Jouart et. al. Thus, we neglect polarisation studies for emission from this multiplet as minimal information will be obtained. The 19061 cm^{-1} transition is assigned as the $Z_1\gamma_1 \rightarrow Y_2\gamma_2$ transition as under C_{3v} symmetry the $^5D_1$ multiplet consists only of two states with γ_3 and γ_2 symmetries respectively.

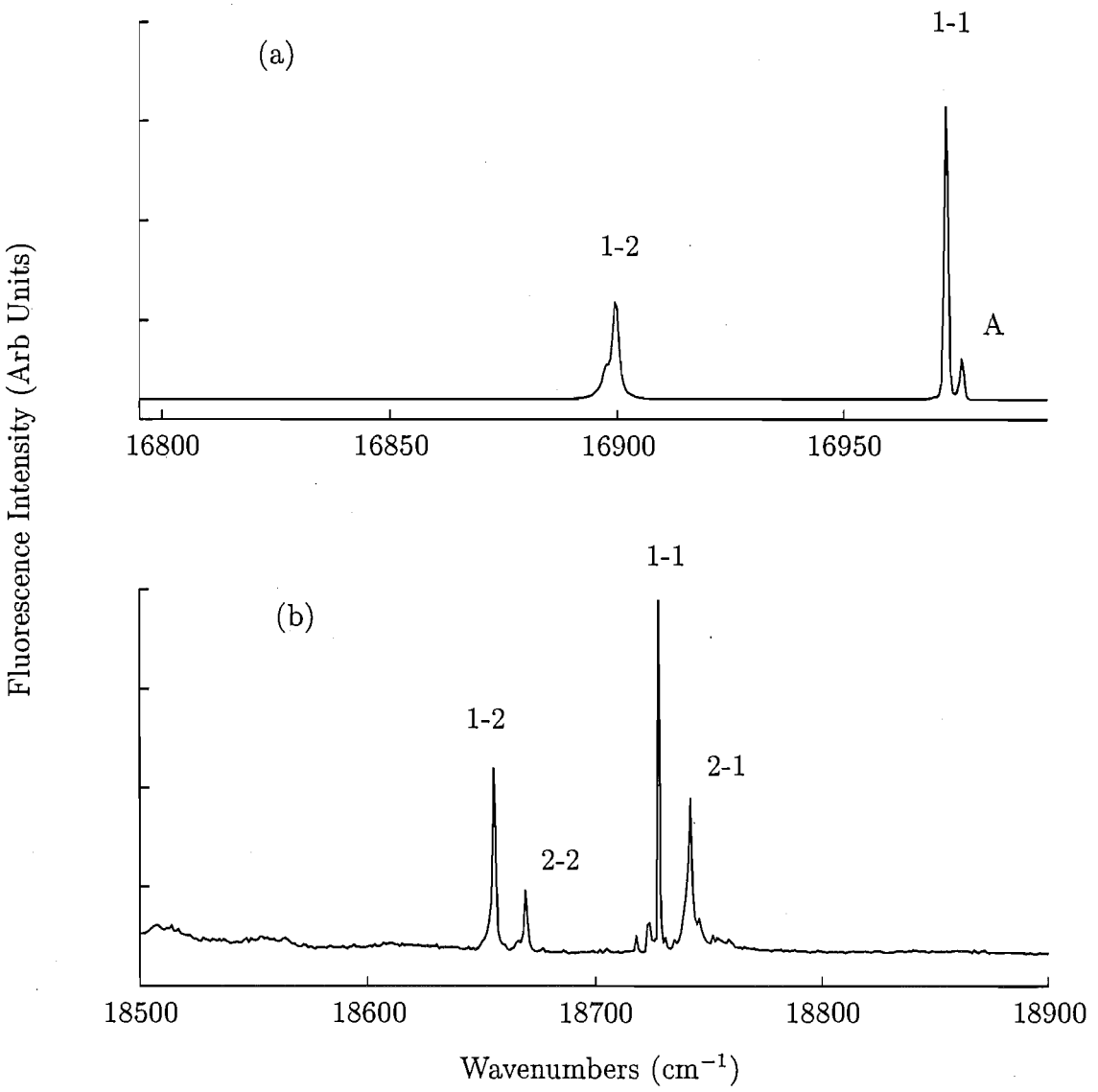

Figure 6.36: Unpolarised fluorescence from the (a) $^5D_0$ and (b) $^5D_1$ multiplets to the $^7F_1$ multiplet for the J centre in SrF_2:0.05%Eu^{3+}. The transition labelled A is the $A_1 \rightarrow Y_1$ transition of the A centre. The spectra were recorded at 16K.

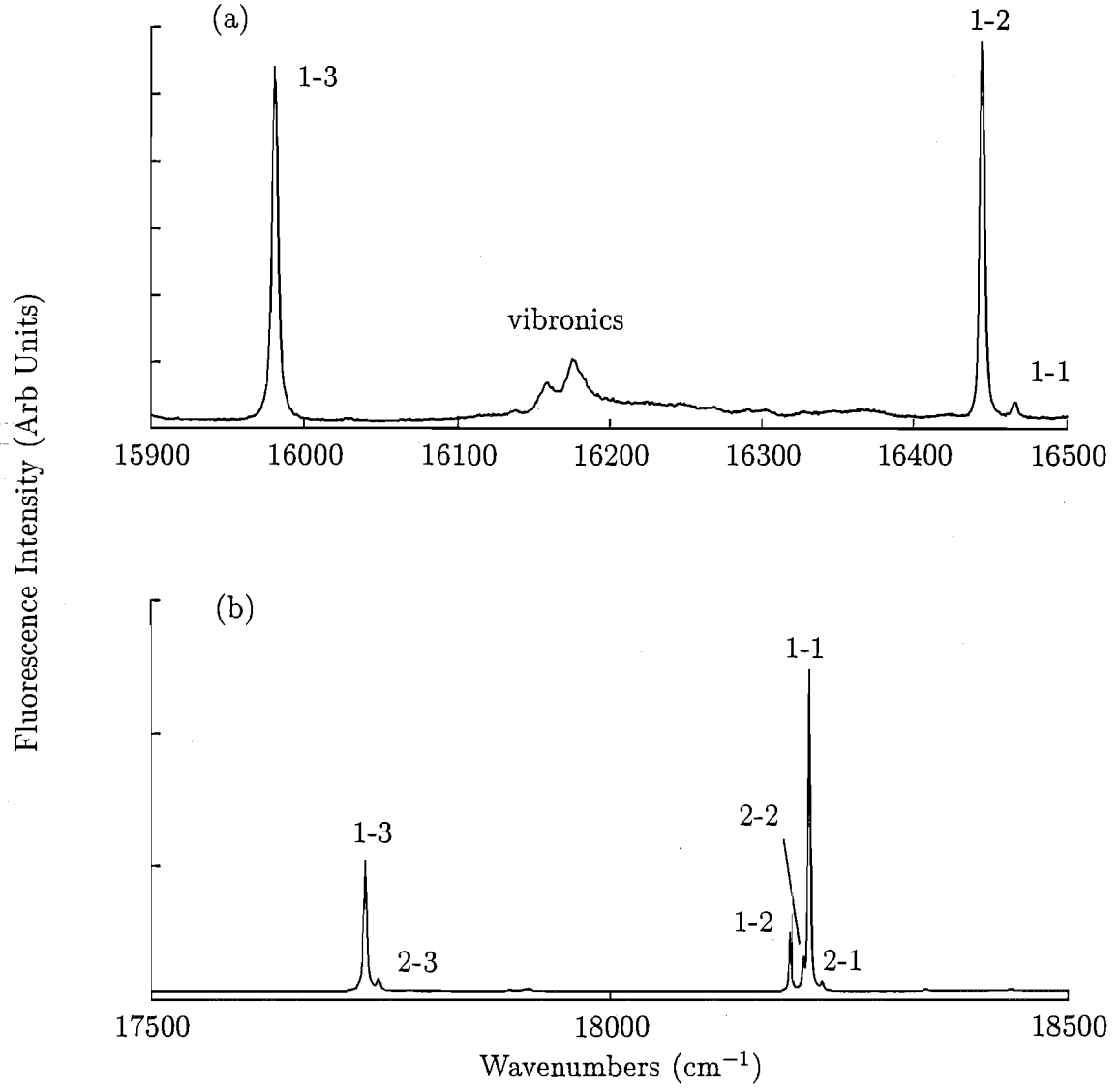

Figure 6.37: Unpolarised fluorescence from the (a) $^5D_0$ and (b) $^5D_1$ multiplets to the $^7F_2$ multiplet for the J centre in SrF_2:0.05%Eu^{3+}. The spectra were recorded at 16K.

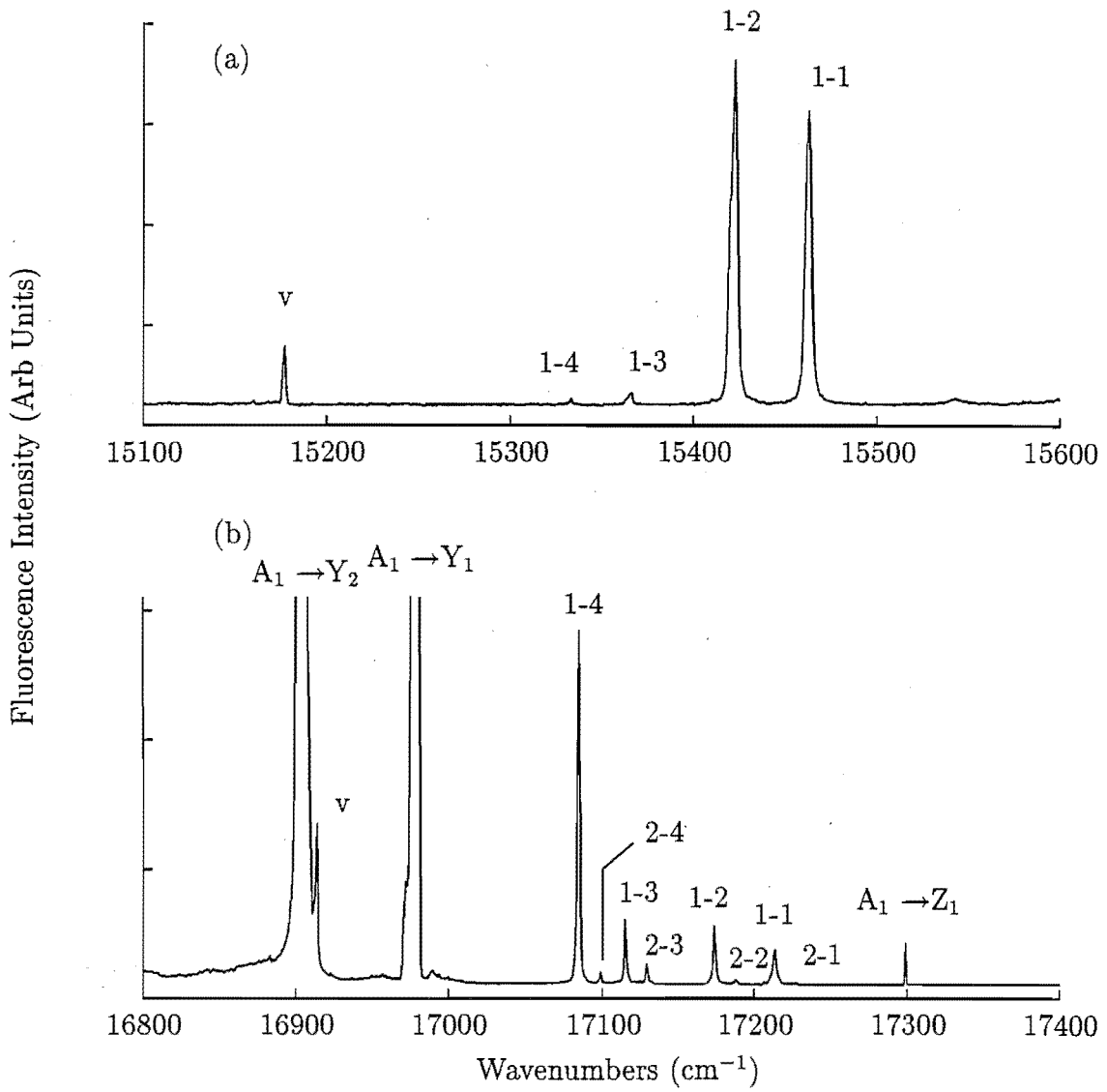

Figure 6.38: Unpolarised fluorescence from the (a) $^5D_0$ and (b) $^5D_1$ multiplets to the $^7F_3$ multiplet for the J centre in SrF_2:0.05%Eu^{3+}. The spectra were recorded at 16K.

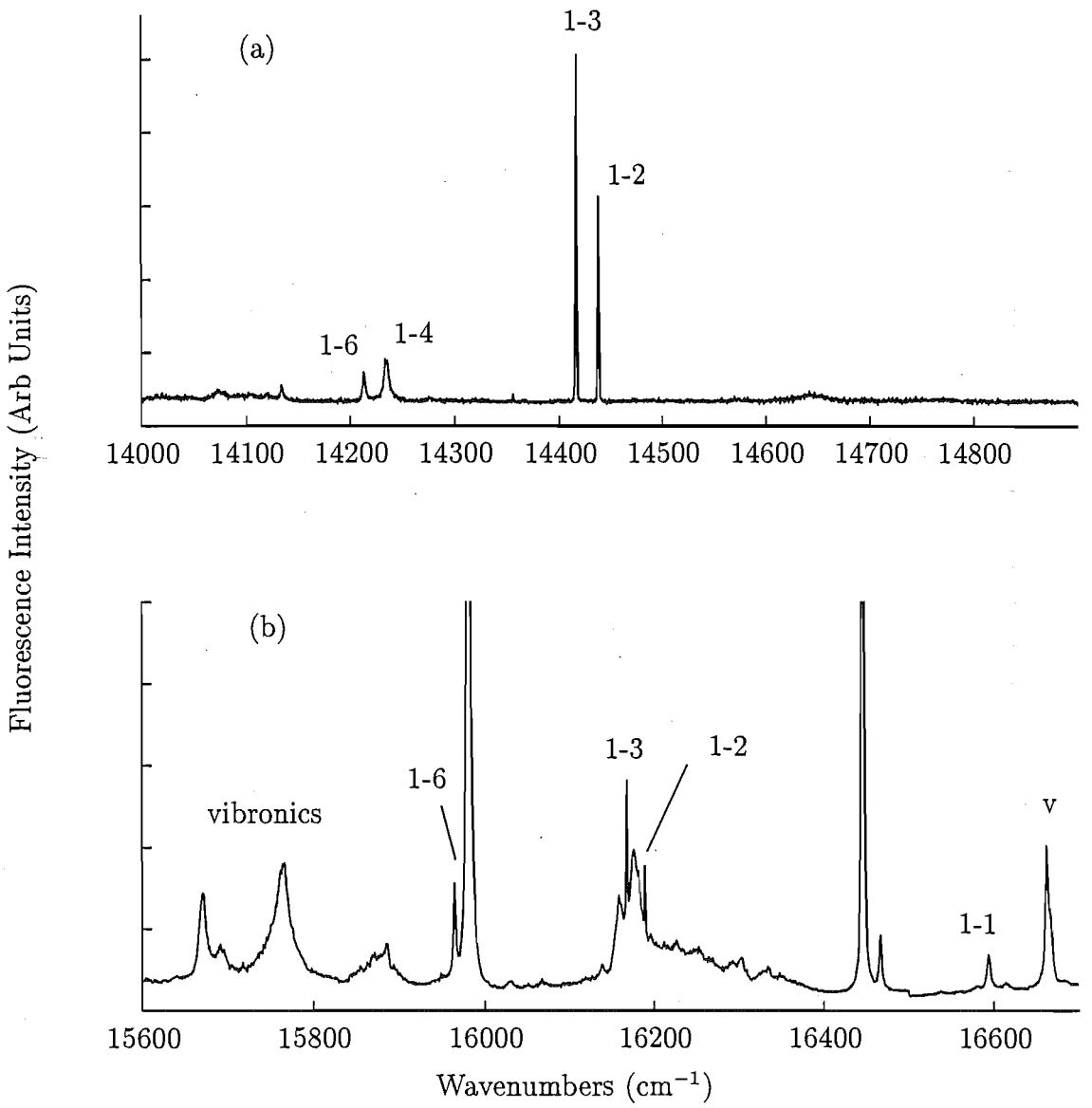

Figure 6.39: Unpolarised fluorescence from the (a) $^5D_0$ and (b) $^5D_1$ multiplets to the $^7F_4$ multiplet for the J centre in SrF_2:0.05%Eu^{3+}. The unlabelled structure originates from $^5D_0$ and the notation v indicates a vibronic level.

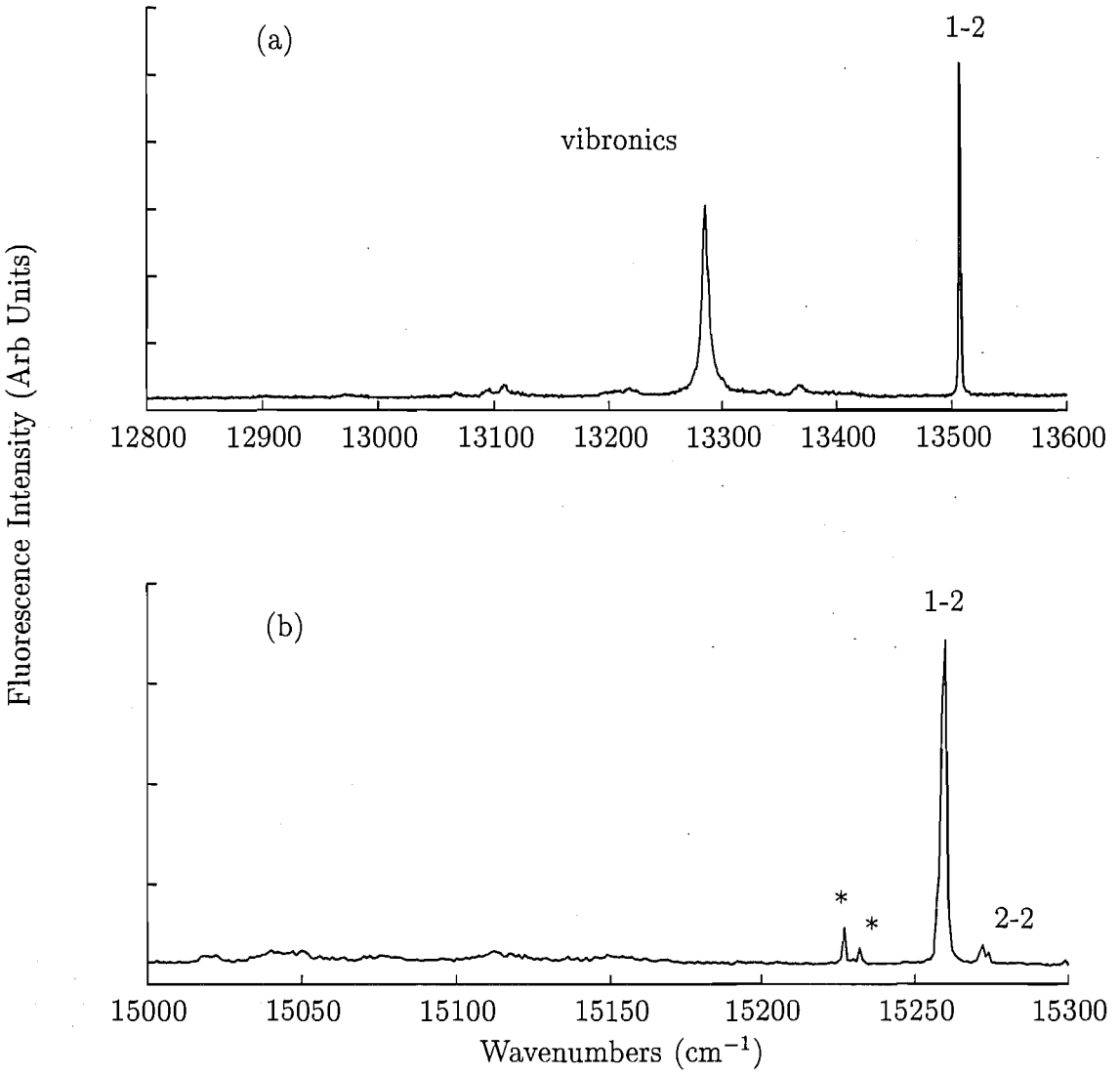

Figure 6.40: Unpolarised fluorescence from the (a) $^5D_0$ and (b) $^5D_1$ multiplets to the $^7F_5$ multiplet for the J centre in SrF_2:0.05%Eu^{3+}. The * notation indicates an unassigned feature. The spectra were recorded at 16K.

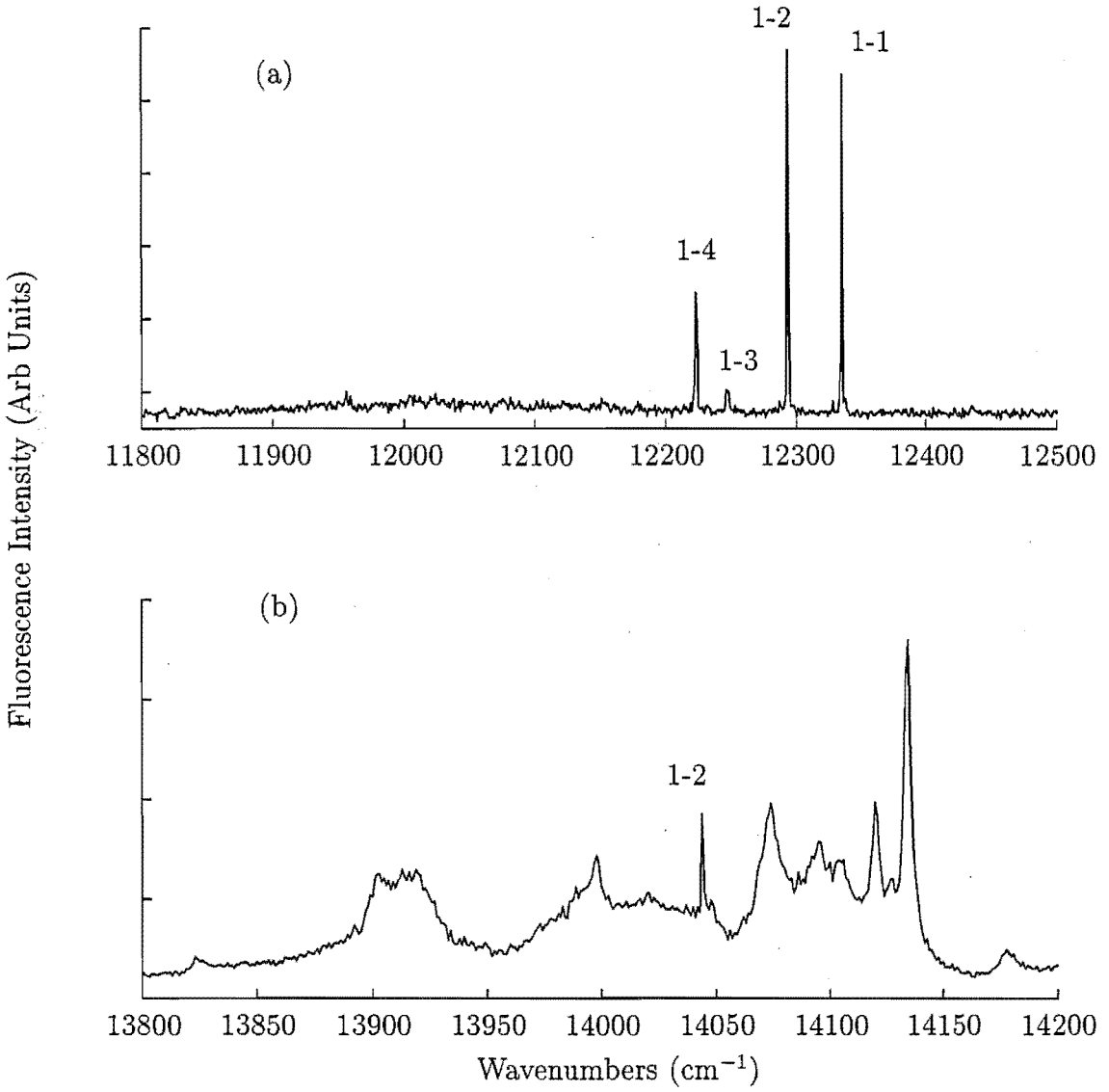

Figure 6.41: Unpolarised fluorescence from the (a) $^5D_0$ and (b) $^5D_1$ multiplets to the $^7F_6$ multiplet for the J centre in SrF_2:0.05%Eu^{3+}. The spectra were recorded at 16K.

Table 6.10: Polarisation data, level assignments and energies for the J centre in SrF_2:0.05%Eu^{3+} obtained in emission from $^5D_0\gamma_1$ at 17295 cm^{-1}. Energies are measured in air cm^{-1} and have an uncertainty of ± 1 cm^{-1} unless otherwise stated.

Terminating Multiplet	State & Symmetry	Transition Frequency	State Energy	Polarisation (YY:YX)	Polarisation Assignment
$^5F_1$	$Y_1\gamma_3$	16977	318	2.24:1	σ'
	$Y_2\gamma_2$	16898	397	1:2.65	π'
$^5F_2$	$X_1\gamma_3$	16464	831	-	-
	$X_2\gamma_1$	16442	853	2.66:1	π
	$X_3\gamma_3$	15979	1316	1:1.7	σ(mixed)
$^5F_3$	$W_1\gamma_2$	15459	1836	1:2.62	π'
	$W_2\gamma_3$	15420	1875	2.1:1	σ'
	$W_3\gamma_1$	15361	1934	1.54:1	π
	$W_4\gamma_3$	15328	1967	-	-
$^5F_4$	$V_2\gamma_2$	14435	2860	1:2.43	π'
	$V_3\gamma_3$	14414	2881	2.1:1	σ'
	$V_4\gamma_3$	14232	3063	1.47:1	σ'(mixed)
	$V_6\gamma_3$	14211	3084	1:1.54	π'(mixed)
$^5F_5$	$U_2\gamma_1$	13504	3791	2.6:1	π
$^5F_6$	$T_1\gamma_1$	12333	4962	1.8:1	π
	$T_2\gamma_3$	12292	5003	2.3:1	σ'
	$T_3\gamma_3$	12246	5049	-	-
	$T_4\gamma_2$	12222	5073	1:2.4	π'

Table 6.11: Fluorescence transitions from $^5D_1$ to the ^7F_J multiplets of the SrF_2:Eu^{3+} J Centre. Emission originates from the $B_1\gamma_3$ state at 19046 cm^{-1} and the $B_2\gamma_2$ state at 19061 cm^{-1}. All transition frequencies are as measured in air (cm^{-1},±1)

Multiplet	Transition		State
	Frequency	Assignment	Energy
$^7F_1$	18739	$B_2\gamma_2 \rightarrow Y_1\gamma_3$	322
	18725	$B_1\gamma_3 \rightarrow Y_1\gamma_3$	321
	18666	$B_2\gamma_2 \rightarrow Y_2\gamma_2$	395
	18652	$B_1\gamma_3 \rightarrow Y_2\gamma_2$	396
$^7F_2$	18229	$B_2\gamma_2 \rightarrow X_1\gamma_3$	832
	18215	$B_1\gamma_3 \rightarrow X_1\gamma_3$	831
	18207	$B_2\gamma_2 \rightarrow X_2\gamma_1$	854
	18193	$B_1\gamma_3 \rightarrow X_2\gamma_1$	853
	17744	$B_2\gamma_2 \rightarrow X_3\gamma_3$	1317
	17730	$B_1\gamma_3 \rightarrow X_3\gamma_3$	1316
$^7F_3$	17224	$B_2\gamma_2 \rightarrow W_1\gamma_2$	1837
	17208	$B_1\gamma_3 \rightarrow W_1\gamma_2$	1838
	17185	$B_2\gamma_2 \rightarrow W_2\gamma_3$	1876
	17171	$B_1\gamma_3 \rightarrow W_2\gamma_3$	1875
	17127	$B_2\gamma_2 \rightarrow W_3\gamma_1$	1934
	17112	$B_1\gamma_3 \rightarrow W_3\gamma_1$	1934
	17096	$B_2\gamma_2 \rightarrow W_4\gamma_3$	1965
	17082	$B_1\gamma_3 \rightarrow W_4\gamma_3$	1964
$^7F_4$	16592	$B_1\gamma_3 \rightarrow V_1\gamma_1$	2454
	16187	$B_1\gamma_3 \rightarrow V_2\gamma_2$	2859
	16167	$B_1\gamma_3 \rightarrow V_3\gamma_3$	2879
	15962	$B_1\gamma_3 \rightarrow V_6\gamma_3$	3084
$^7F_5$	15271	$B_2\gamma_2 \rightarrow U_2\gamma_1$	3790
	15257	$B_1\gamma_3 \rightarrow U_2\gamma_1$	3789
$^7F_6$	14043	$B_1\gamma_3 \rightarrow T_2\gamma_3$	5003

Transitions from $^5D_0$ to the $^7F_2$ multiplet are observed in the 16500-15900 cm^{-1} region. Three electronic transitions are observed as shown in Figure 6.37(a). A strong transition at 16442 displays a π polarisation dependence and we therefore assign this transition as terminating on a singlet state of γ_1 symmetry at 853 cm^{-1}. This means the remaining two transitions must be doublets as J=2 multiplets decompose into two doublets and a γ_1 singlet under C_{3v} symmetry. The 16464 cm^{-1} transition is too weak to obtain a meaningful polarisation ratio. The 15979 cm^{-1} transition displays a degraded σ polarisation dependence (as shown in Table 6.10) and we assign the X_1 and X_3 states at 831 and 1316 cm^{-1}, γ_3 symmetry. Broad peaks at 16170 and 16161 cm^{-1} correspond to energy shifts of 294 and 281 cm^{-1} from the 16464 and

16442 cm^{-1} transitions respectively. These values are consistent with the energy of the phonon peaks analysed by Richman [99]. Transitions emanating from the $^5D_1$ multiplet which terminate on $^7F_2$ are shown in Figure 6.37(b). As expected two transitions to all three $^7F_2$ states are observed with a common 15 cm^{-1} splitting.

Figure 6.38(a) shows transitions from $^5D_0$ to the $^7F_3$ multiplet in the 15600 - 15100 cm^{-1} region. Five transitions can be observed. The two strong transitions at 15459 and 15420 cm^{-1} have magnetic dipole π' and σ' polarisation dependences. From this, we assign these transitions as terminating on the $W_1\gamma_2$ and $W_2\gamma_3$ states at 1836 and 1875 cm^{-1} respectively. The next two transitions are twenty times weaker. We observe these at frequencies of 15361 and 15328 cm^{-1} corresponding to $^7F_3$ state energies of 1934 and 1967 cm^{-1} respectively. From the π polarisation of the 15361 cm^{-1} transition we can assign this as the $A_1\gamma_1 \rightarrow W_3\gamma_1$ transition. The latter transition is slightly weaker and no polarisation ratio could be measured. From the studies of Jouart et. al. we tentatively assign this transition as terminating on the $W_4\gamma_3$ state. The fifth transition at 15174 cm^{-1} is 285 cm^{-1} from the 15459 cm^{-1} transition and is assigned as a transition terminating on a vibronic level of the lattice. Transitions from $^5D_1$ to $^7F_3$ are more complicated as can be observed in Figure 6.38(b). This is due to the overlap of fluorescence transitions involving several multiplets. A weak transition at 17295 cm^{-1} is the $A_1\gamma_1 \rightarrow Z_1\gamma_1$ transition. Two extremely strong (and off scale) transitions are the two $^5D_0 \rightarrow ^7F_1$ transitions at frequencies of 16977 and 16898 cm^{-1}. The remaining transitions are $^5D_1 \rightarrow ^7F_3$ transitions. As with $^5D_0$ emission the first four $^7F_3$ states are observed however, no transition to the final state can be observed.

$^5D_0$ transitions to the $^7F_4$ multiplet occur in the 14500 - 14000 cm^{-1} region as shown in Figure 6.39(a). Two strong sharp transitions at 14435 and 14414 cm^{-1} display π' and σ' polarisation dependences respectively. We assign these transitions as terminating on γ_2 and γ_3 states at 2860 and 2881 cm^{-1}, as appropriate. This is confirmed in chapter 8 where an infrared absorption transition at 2881 cm^{-1}, splits under the influence of a magnetic field whilst that at 2860 cm^{-1} does not. Two weaker transitions at 14232 and 14211 cm^{-1} give σ and π polarisation dependences and are assigned as terminating on γ_3 and γ_1 states at 3063 and 3084 cm^{-1} respectively. Transitions to the $^7F_4$ multiplet from $^5D_1$ are shown in Figure 6.39(b). As with previous cases this is a complex spectrum due to overlapping intermultiplet transitions and related vibronics as indicated in Figure 6.39(b). Despite this, transitions to the 2860, 2881 and 3084 cm^{-1} states can be observed. An additional transition is observed at 16592 cm^{-1} which we assign as the $B_1\gamma_3 \rightarrow V_1\gamma_1$ transition placing the $V_1\gamma_1$ state at 2454 cm^{-1} - see Table 6.11.

Transitions to the $^7F_5$ multiplet from $^5D_0$ are shown in Figure 6.40(a) and are found to occur in the 13600 - 13000 cm^{-1} region. The spectrum is particularly simple

with only two strong transitions observed. The transition at 13504 cm^{-1} gives a π polarisation dependence consistent with a γ_1 singlet state at 3791 cm^{-1}. An additional transition at 13284 cm^{-1}, a spacing of 220 cm^{-1} from the 13504 cm^{-1} transition, is assigned as a transition terminating vibronic levels of the lattice. Figure 6.40(b) shows $^5D_1$ transitions to the $^7F_5$ multiplet. Transitions from both the $B_1\gamma_3$ and $B_2\gamma_2$ states are observed to the 3791 cm^{-1} state. Two additional transitions are observed which do not appear to be related to the J centre.

Figure 6.41(a) shows transitions from $^5D_0$ to the $^7F_6$ multiplet in the 12400 - 12100 cm^{-1} region. Four transitions are observed, the first two of which, are strong. We measure the transition frequencies to be 12333 and 12292 cm^{-1}. These transitions display π and σ' polarisation dependences respectively. They are assigned as terminating on states of γ_1 and γ_3 symmetry at energies of 4962 and 5003 cm^{-1}. No polarisation ratio could be measured for the weaker 12246 cm^{-1} transition. This transition terminates on a state at 5049 cm^{-1} which we tentatively assign as having γ_3 symmetry from crystal field analyses. The final transition at 12222 cm^{-1} displays a π' polarisation dependence consistent with a transition to a state of γ_2 symmetry at 5073 cm^{-1}. Figure 6.41(b) shows $^5D_1$ transitions to this multiplet. These lie in a band of vibronic transitions coupled to the $^5D_0 \rightarrow {}^7F_4$ transitions. Only one $^5D_1 \rightarrow {}^7F_6$ transition is observed at 14043 cm^{-1} corresponding to the $B_1\gamma_3 \rightarrow T_2\gamma_3$ transition.

6.4 Spectroscopy of BaF_2:Eu^{3+}

6.4.1 Optical Absorption and Excitation Spectra

The absorption spectra of transitions to the $^5D_1$, $^5D_2$ and $^5D_3$ multiplets were recorded for a 22.2 mm thick BaF_2:0.3%Eu^{3+} crystal. It was possible to use such high concentrations of the Eu^{3+} dopant without undue complication of the spectra, as the tendency for rare earth ions to cluster in BaF_2 crystals is significantly reduced from that of CaF_2. Figure 6.42 shows the spectra obtained. The dominant spectral features are due to the C_{3v} symmetry centre observed by Jouart et. al. [106] (that we label L). In the $^5D_1$ spectrum, a weak feature is observed that correlates with the BaF_2:Eu^{3+} cubic centre [92].

The $^5D_2$ absorption spectrum shows two L centre absorption transitions at 465.52 and 463.62 nm. These are assigned as the $Z_1 \rightarrow C_1$ and C_3 transitions from the work of Jouart et. al. [106]. The $^5D_3$ transitions are harder to explain as these have not been studied by laser selective excitation. Two transitions at frequencies of 409.10 and 409.07 nm are observed. As with CaF_2:Eu^{3+} and SrF_2:Eu^{3+} crystals,

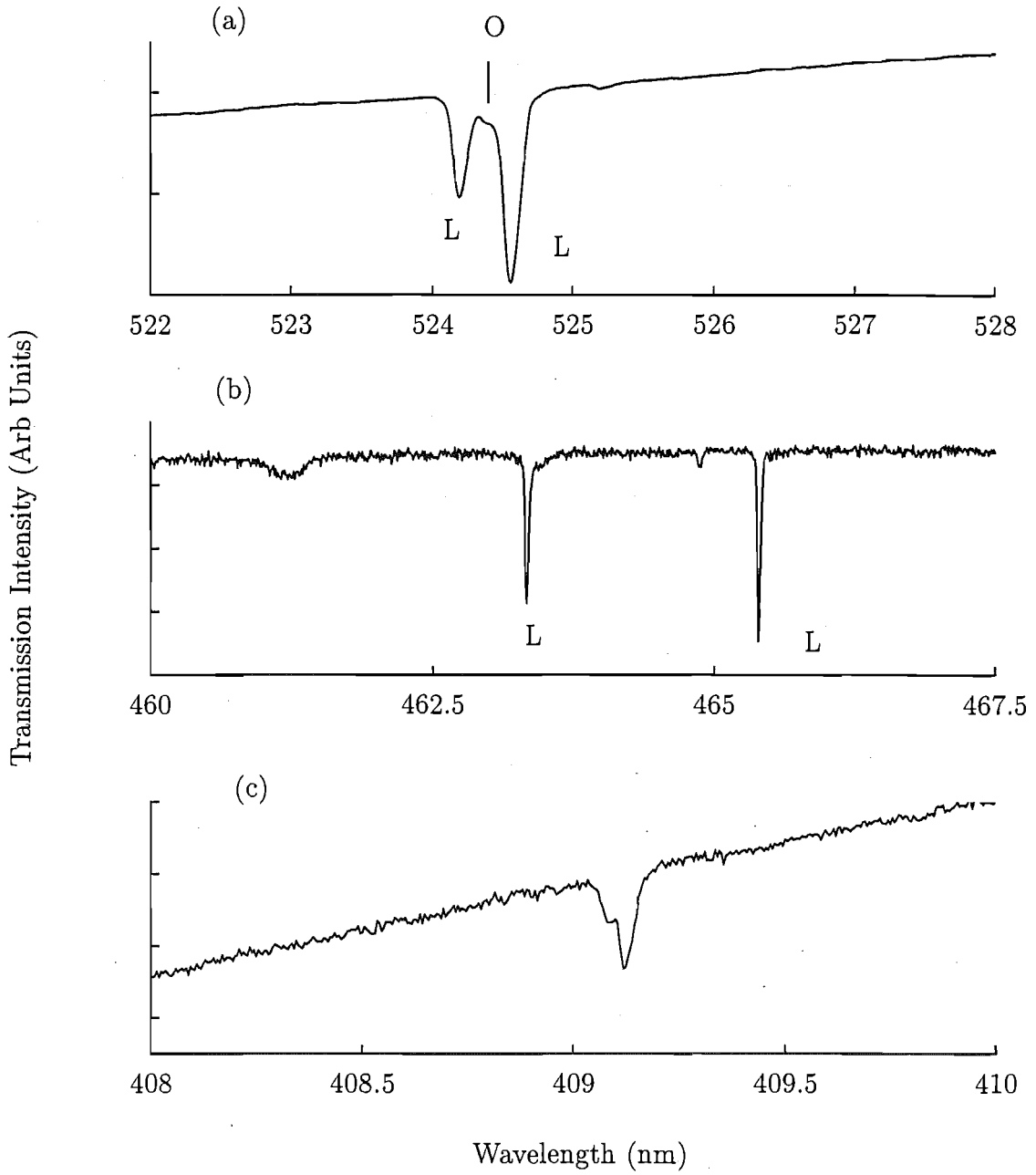

Figure 6.42: Absorption spectra for the (a) $^5D_1$, (b) $^5D_2$ and (c) $^5D_3$ multiplets in BaF_2:0.3%Eu^{3+}. The spectra were recorded at 16K.

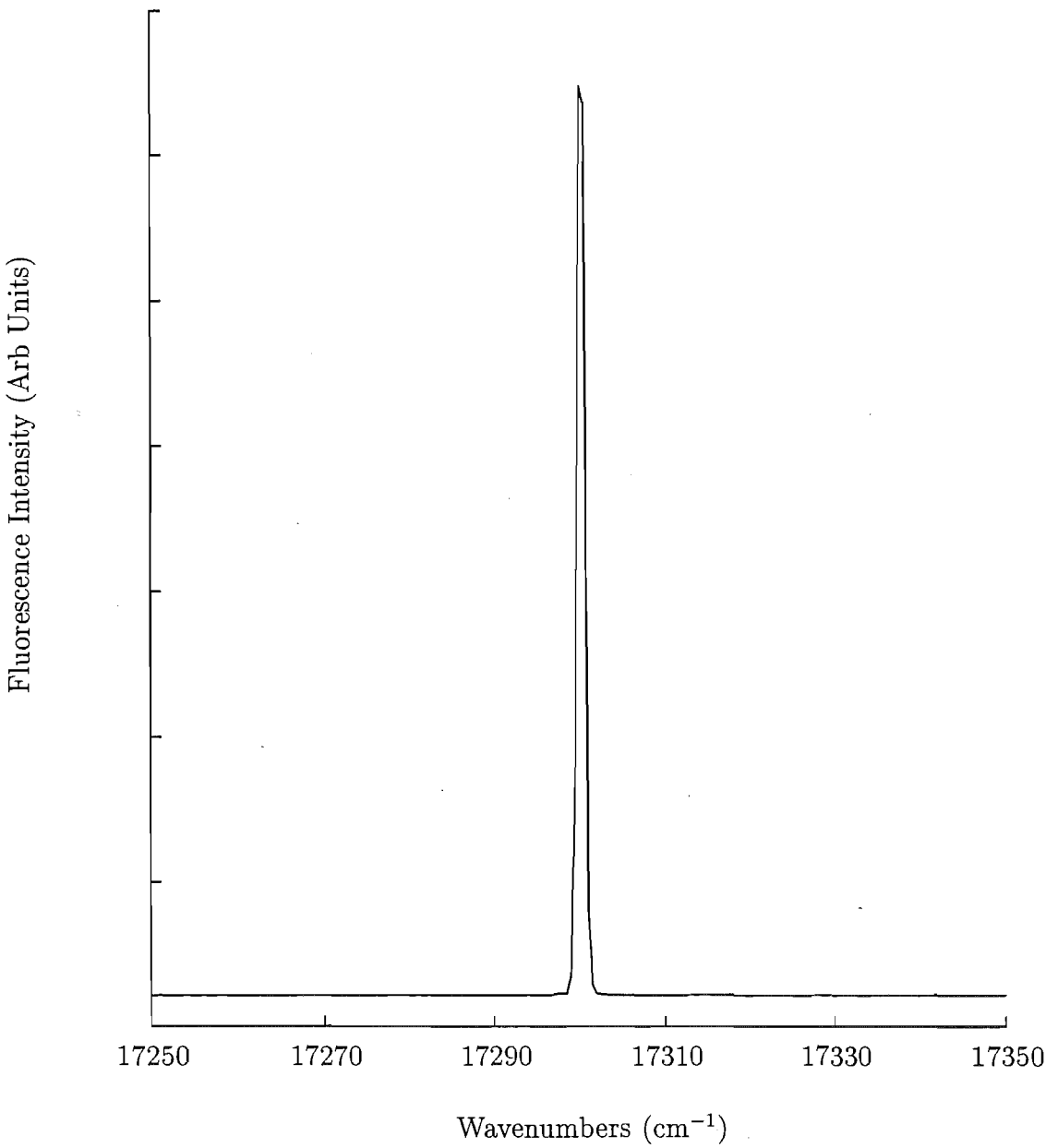

Figure 6.43: Excitation spectrum for the $^5D_0$ multiplet in BaF_2:0.05%Eu^{3+} monitoring all transitions at 630 nm. The spectra were recorded at 16K.

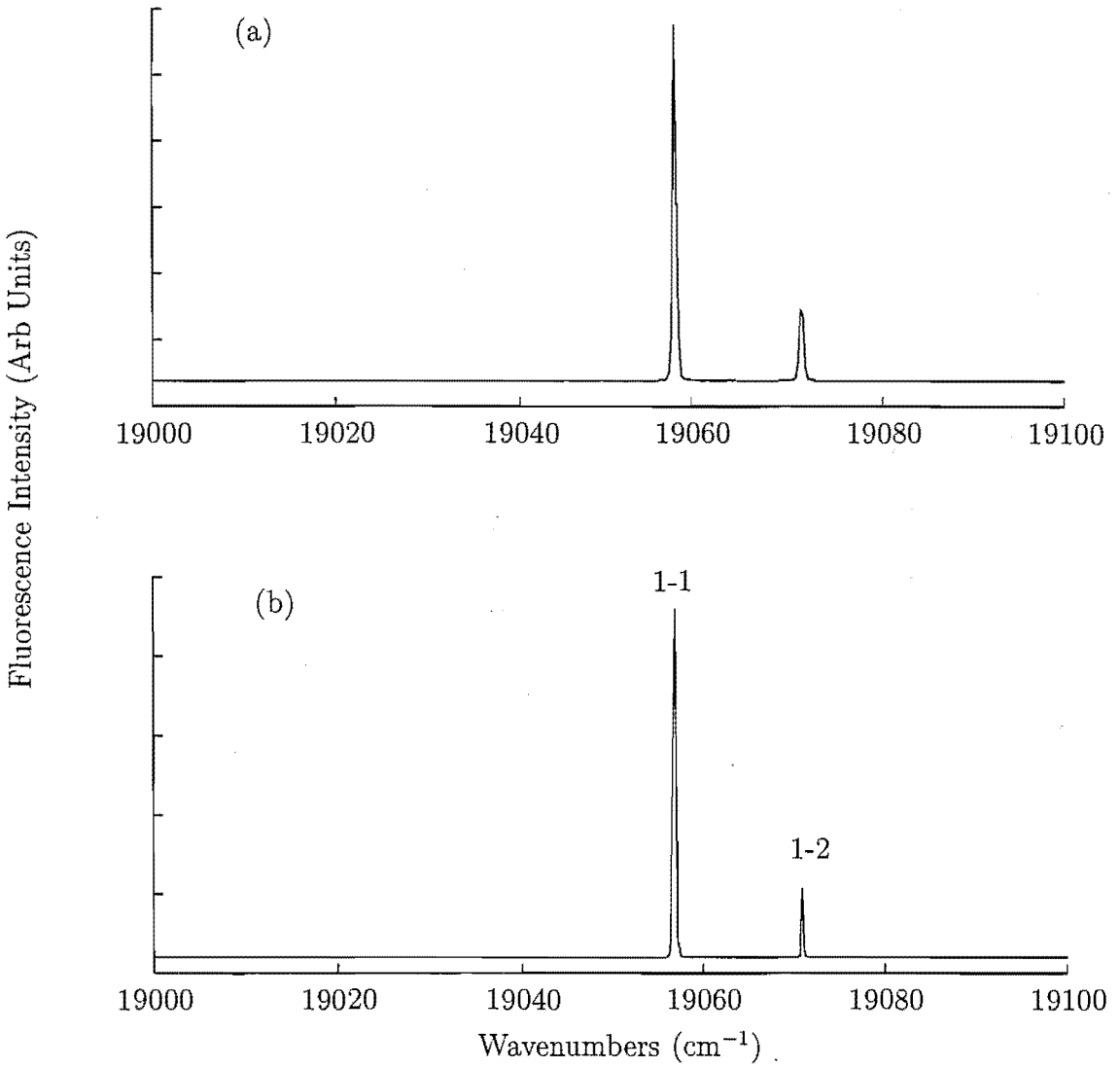

Figure 6.44: Excitation spectra for the $^5D_1$ multiplet in BaF_2:0.05%Eu^{3+} (a) monitoring all transitions at 630 nm and (b) monitoring the 16978 cm^{-1} transition of the L centre. The spectra were recorded at 16K.

no absorption could be detected for conventional transmission measurements to the $^5D_0$ multiplet for BaF_2:Eu^{3+}.

Laser excitation spectra for transitions to the $^5D_0$ and $^5D_1$ multiplets are shown in Figures 6.43 and 6.44 respectively. The $^5D_0$ spectrum is exceedly simple with only one transition present at 17303 cm^{-1}. This is associated with the L centre. The $^5D_1$ spectrum is equally clear with two transitions, both due to L centre absorption as shown in Figure 6.46(b), at frequencies of 19057 and 19061 cm^{-1}.

6.4.2 L Centre Fluorescence

The dominant centre in BaF_2:0.05%Eu^{3+} has been previously studied by Jouart et. al. [106]. They assign this centre trigonal C_{3v} symmetry from the observed number fluorescence lines. However, a study by Silversmith and Macfarlane [112] using hole-burning spectroscopy has reassigned the dominant centre as having tetragonal C_{4v} symmetry. We have studied this centre, that we label L, with both $\langle 100 \rangle$ and $\langle 111 \rangle$ oriented crystals. No observed polarisation dependence has been found for L centre fluorescence transitions in $\langle 100 \rangle$ oriented crystals. However, for $\langle 111 \rangle$ oriented crystals a polarisation dependence has been observed. This is given in Table 6.12. This is consistent with the symmetry assignment of Jouart et. al. that the centre is a trigonal C_{3v} symmetry RE^{3+} - F^- pair. From the low axial splittings observed, the most consistent charge compensation configuration is that of a next nearest neighbour $\langle 111 \rangle$ interstitial fluorine ion.

Excitation of the $^7F_0 \rightarrow ^5D_0$ absorption transition at 17303 cm^{-1} yields fluorescence to the ^7F_J multiplets. Fluorescence to the $^7F_1$ multiplet is observed in the 17000 - 16900 cm^{-1} region as shown in Figure 6.45(a). Two transitions are observed as is consistent with the C_{3v} symmetry assignment. These transitions are observed at frequencies of 16978 and 16912 cm^{-1}. From the respective magnetic dipole σ' and π' polarisations, they are assigned as transitions terminating on states of γ_3 and γ_2 symmetries, at energies of 325 and 391 cm^{-1} as respectively. Fluorescence from $^5D_1$ was obtained exciting the lowest frequency 19057 cm^{-1} transition. The L centre in BaF_2:Eu^{3+} is isostructural with the J centre in SrF_2:Eu^{3+} and from the observed $^7F_1$ and $^5D_1$ splittings appears to have a similar axial distortion to that centre. Therefore, we assign the $^5D_1$ transitions at 19057 and 19071 cm^{-1} as the $Z_1\gamma_1 \rightarrow B_1\gamma_3$ and $B_2\gamma_2$ transitions respectively, by analogy with those transitions in the SrF_2:Eu^{3+} J centre. Fluorescence transitions from $^5D_1$ to $^7F_1$ occur in the 18800 - 18500 cm^{-1} region as is shown in Figure 6.45(b). They appear more complex than those observed from $^5D_0$ for two reasons. Firstly, many of the transitions observed are to vibronic states of lattice. Features at 18807 and 18795 cm^{-1} are vibronics associated with the $^5D_1 \rightarrow ^7F_0$ transitions. Vibronic intervals of 250 and 262 cm^{-1}

are measured. The broad feature at 18543 cm^{-1} is a vibronic associated with the $^5D_1 \rightarrow ^7F_1$ transitions. This has a lattice energy of 196 cm^{-1}. Four electronic transitions are observed which come as two pairs with a common separation of 14 cm^{-1}. This corresponds to the $^5D_1$ splitting and arises as the $B_2\gamma_2$ level has a thermal population.

Fluorescence from $^5D_0$ to the $^7F_2$ multiplet is observed in the 16500 - 15600 cm^{-1} region as shown in Figure 6.46(a). This emission is typified by strong strong vibronics coupled to the electronic levels and is therefore difficult to analyse directly. Emission to $^7F_2$ from $^5D_1$ is clearer, as shown in Figure 6.46(b) and we discuss this first. Six transitions are observed from $^5D_1$ with the characteristic 14 cm^{-1} splitting. Transitions at 18218 and 18206 cm^{-1} terminate on the X_1 level. The corresponding $^5D_0$ fluorescence is observed as a weak feature at 16451 cm^{-1}. From the σ' polarisation of this fluorescence we assign this state as having γ_3 symmetry. It is located 852 cm^{-1} above the ground state. $^5D_1$ emission to the X_2 state is observed at 18190 and 18176 cm^{-1}. The corresponding $^5D_0$ emission is observed at 16420 cm^{-1} placing the X_2 state at 883 cm^{-1}. This transition is π polarised and the X_2 state is therefore, assigned as having γ_1 symmetry. The $^5D_0$ transition to the X_3 level is observed at 16015 cm^{-1} and this is confirmed by the $^5D_1 \rightarrow ^7F_2$ spectrum. The 16015 cm^{-1} transition is σ polarised and we assign the X_3 state as having γ_3 symmetry. The remaining transitions are to vibronic levels of the lattice. Transitions at 16194, 15819, 15762 and 15743 cm^{-1} give lattice vibrational frequencies of 196, 253 and 272 cm^{-1}. The transition at a frequency of 16431 is also a transition terminating on a vibronic level of the lattice. Specifically, it is assigned as a second order vibronic sideband associated with the 16978 cm^{-1}, $^5D_0A_1\gamma_1 \rightarrow Y_1\gamma_3$ transition. It is assigned for the following reasons; firstly it cannot be electronic as it not observed in emission from both $^5D_0$ and $^5D_1$ (nor is its polarisation behaviour consistent). Secondly, at a transition frequency of 16431 cm^{-1}, the observed emission feature is 547 cm^{-1} displaced from the 16978 cm^{-1} transition. This is approximately twice 273 cm^{-1}, a known vibrational frequency of the host lattice.

Transitions to the $^7F_3$ multiplet from $^5D_0$ are shown in Figure 6.49(a) and occur in the 15500 - 15300 cm^{-1} region. Four transitions are observed. The 15460, 15427 and 15354 cm^{-1} transitions are all of magnetic dipole character. The 15427 and 15354 cm^{-1} transitions are both σ' polarised and are assigned as terminating on γ_3 symmetry doublets at energies of 1875 and 1948 cm^{-1}. The 15460 cm^{-1} transition is π' polarised and is therefore, assigned as the $W_1\gamma_2$ state at 1842 cm^{-1}.

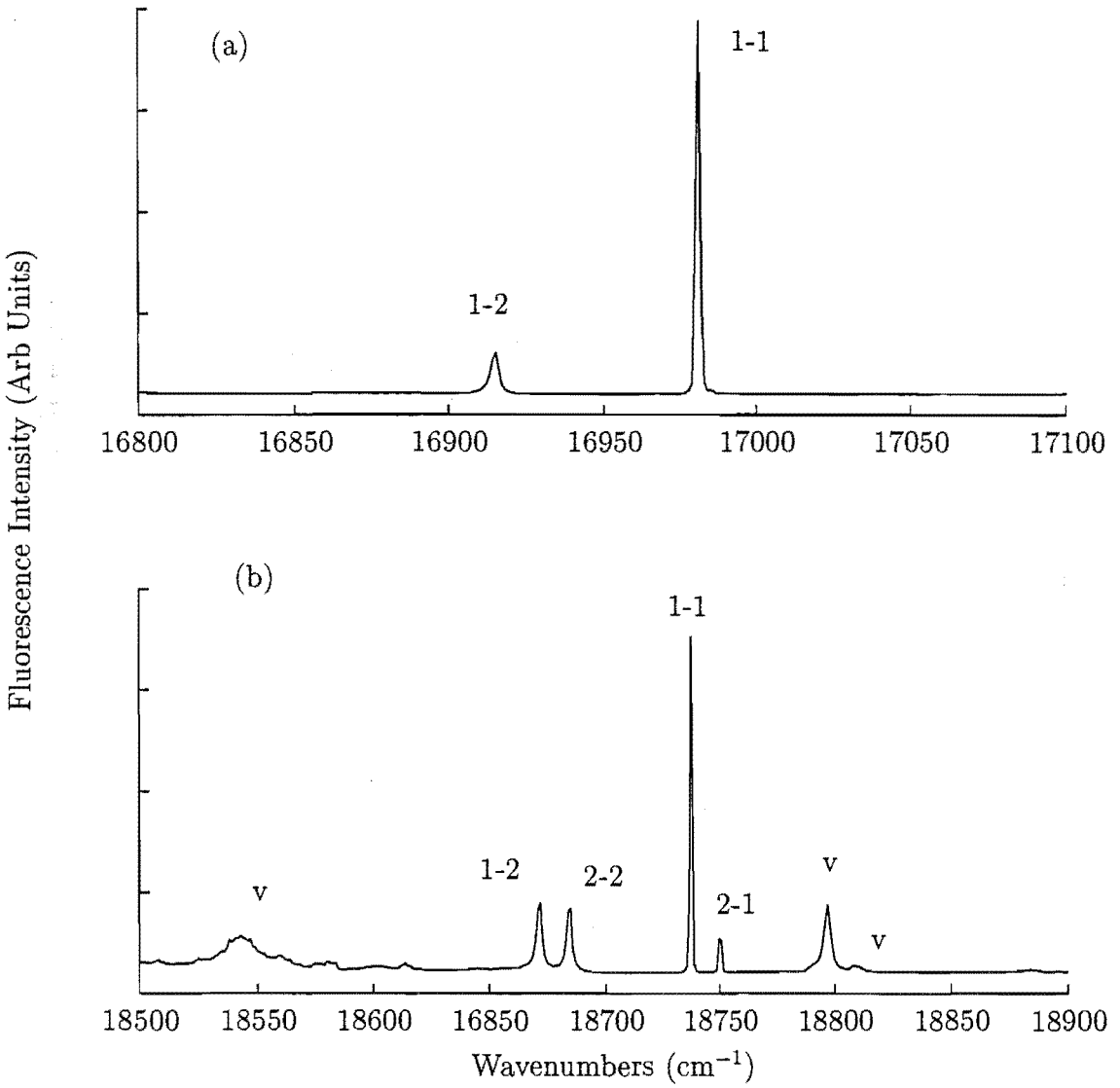

Figure 6.45: Unpolarised fluorescence from the (a) $^5D_0$ and (b) $^5D_1$ multiplets to the $^7F_1$ multiplet for the L centre in BaF_2:0.05%Eu^{3+}. The spectra were recorded at 16K.

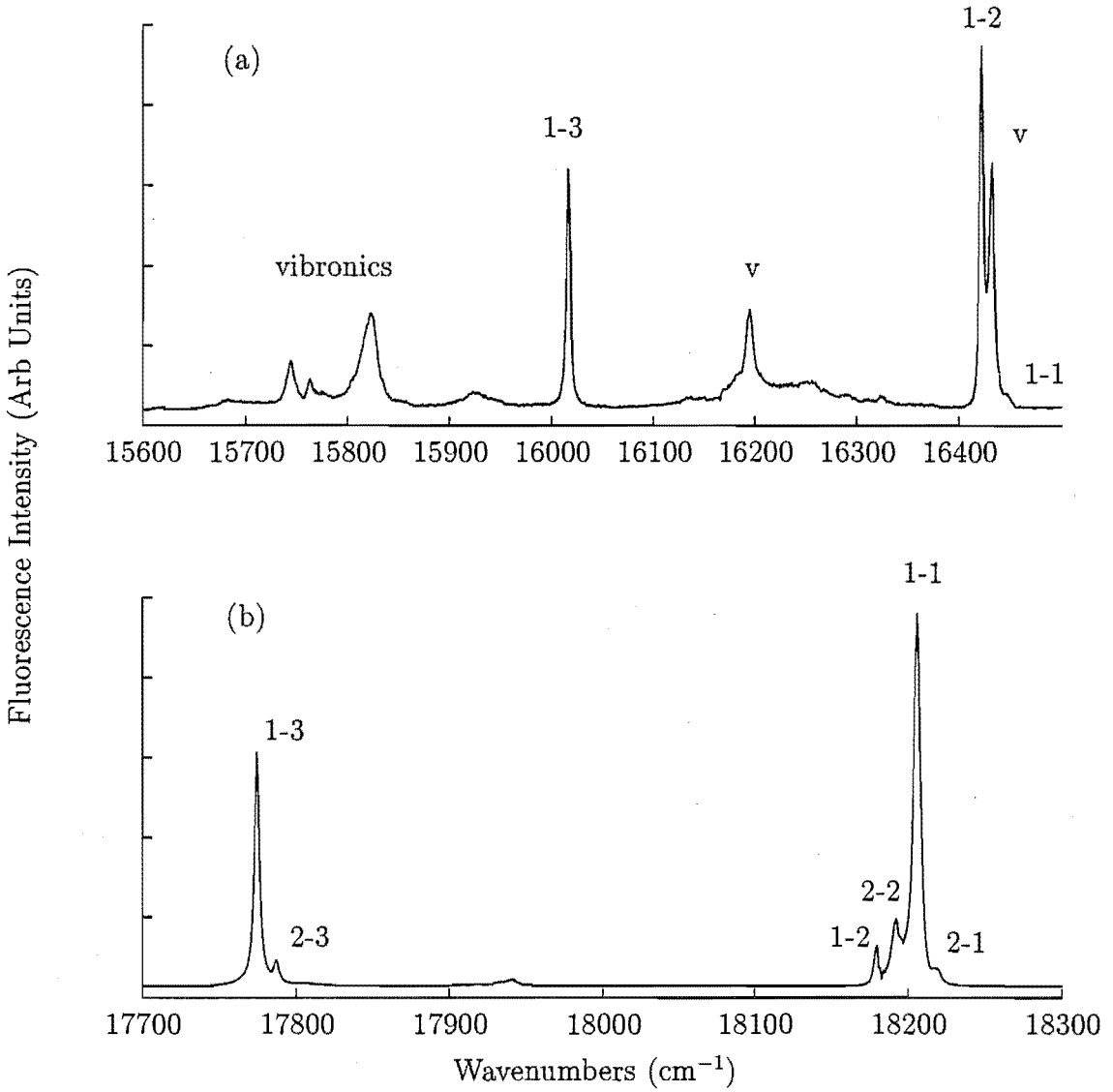

Figure 6.46: Unpolarised fluorescence from the (a) $^5D_0$ and (b) $^5D_1$ multiplets to the $^7F_2$ multiplet for the L centre in BaF_2:0.05%Eu^{3+}. The spectra were recorded at 16K.

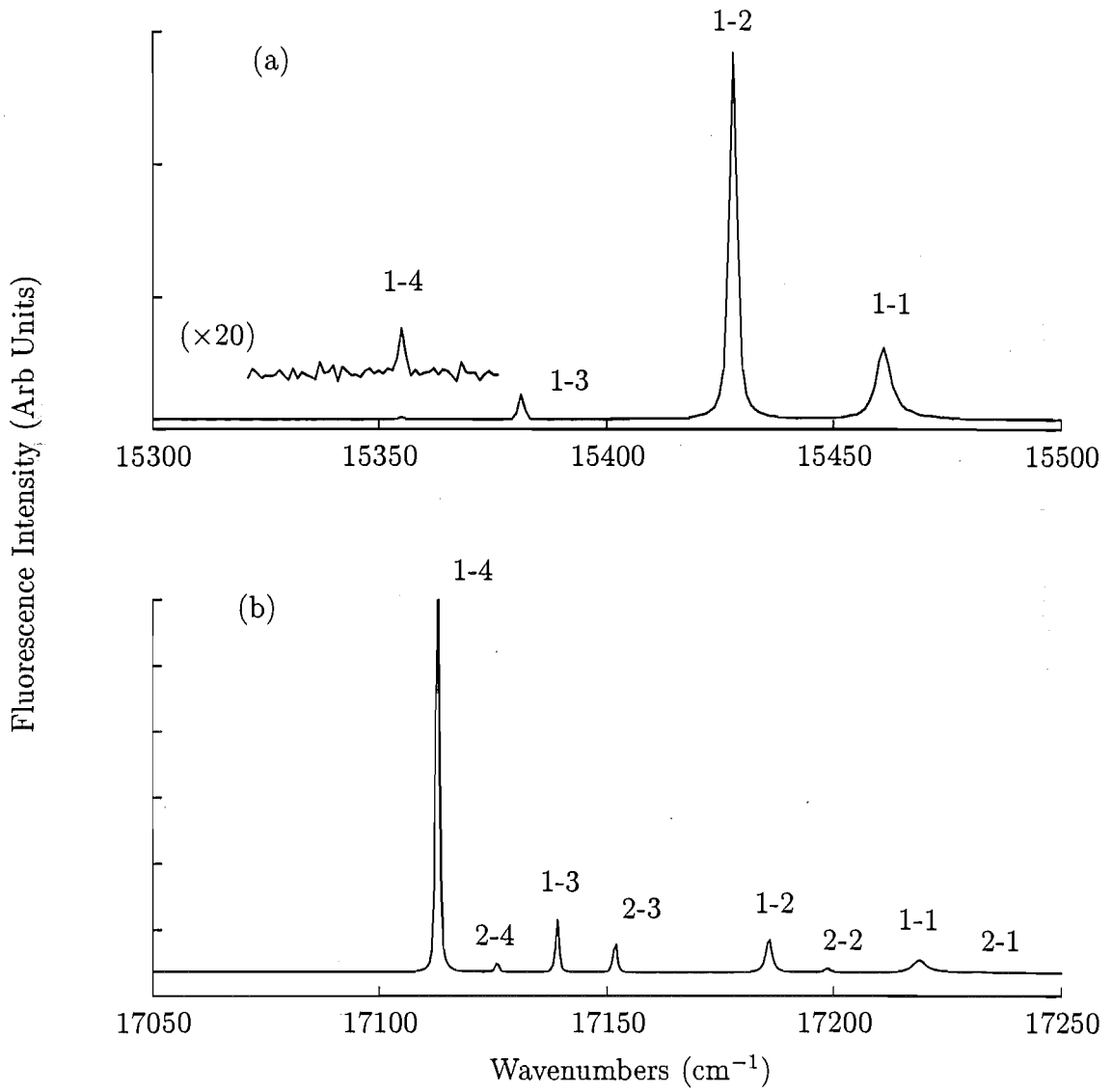

Figure 6.47: Unpolarised fluorescence from the (a) $^5D_0$ and (b) $^5D_1$ multiplets to the $^7F_3$ multiplet for the L centre in BaF_2:0.05%Eu^{3+}. The spectra were recorded at 16K.

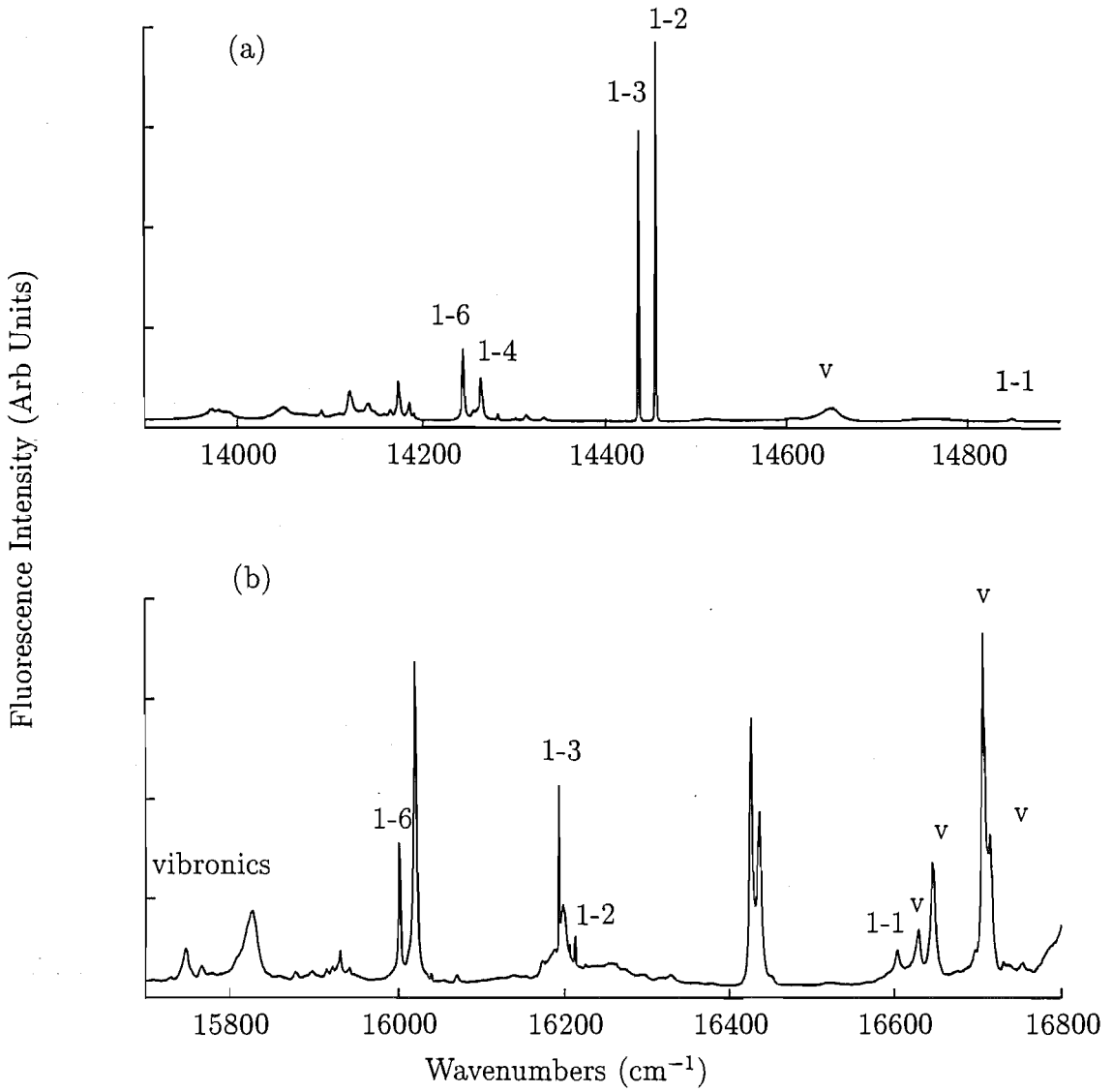

Figure 6.48: Unpolarised fluorescence from the (a) $^5D_0$ and (b) $^5D_1$ multiplets to the $^7F_4$ multiplet for the L centre in BaF_2:0.05%Eu^{3+}. The spectra were recorded at 16K.

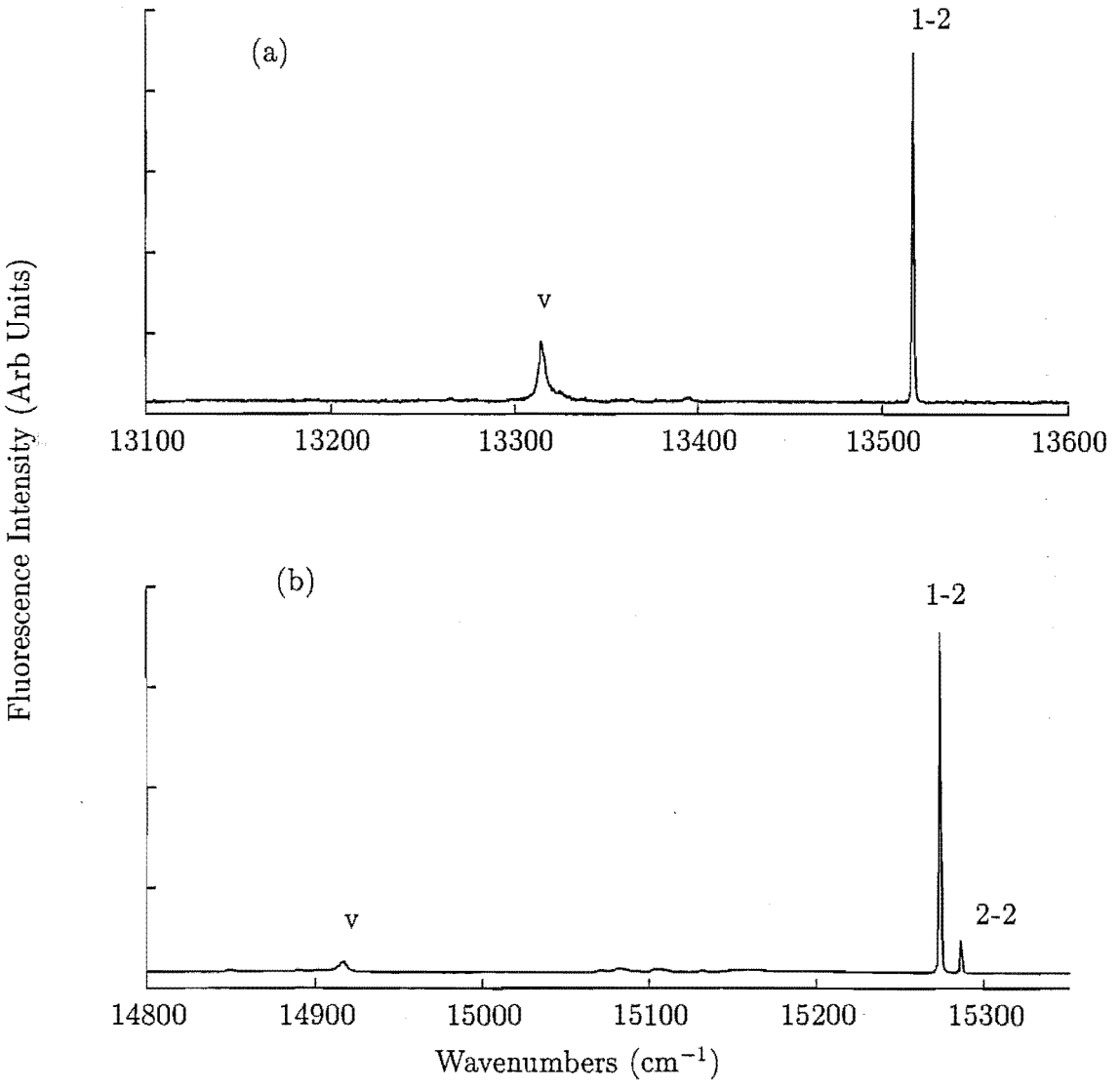

Figure 6.49: Unpolarised fluorescence from the (a) $^5D_0$ and (b) $^5D_1$ multiplets to the $^7F_5$ multiplet for the L centre in BaF_2:0.05%Eu^{3+}. The spectra were recorded at 16K.

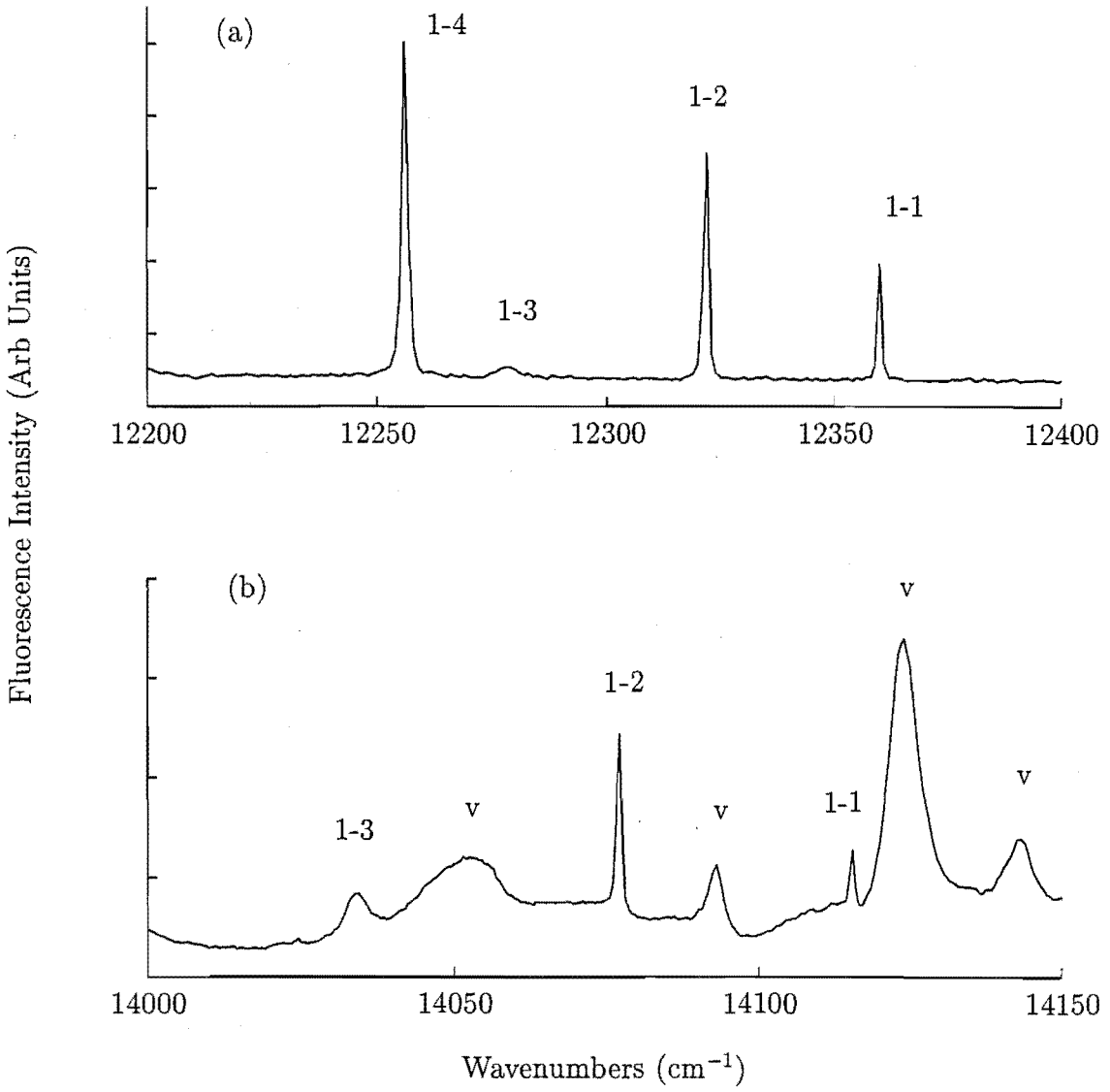

Figure 6.50: Unpolarised fluorescence from the (a) $^5D_0$ and (b) $^5D_1$ multiplets to the $^7F_6$ multiplet for the L centre in BaF_2:0.05%Eu^{3+}. Features labelled v are vibronics associated with the $^5D_0 \rightarrow {}^7F_4$ transitions. The spectra were recorded at 16K.

Table 6.12: Polarisation data, level assignments and energies for the L centre in BaF_2:0.05%Eu^{3+} obtained in emission from $^5D_0\gamma_1$ at 17303 cm^{-1}. Energies are measured in air cm^{-1} and have an uncertainty of ± 1 cm^{-1} unless otherwise stated.

Terminating Multiplet	State & Symmetry	Transition Frequency	State Energy	Polarisation (YY:YX)	Assignment
$^5F_1$	$Y_1\gamma_3$	16978	325	2.1:1	σ'
	$Y_2\gamma_2$	16912	391	1:2.6	π'
$^5F_2$	$X_1\gamma_3$	16451	852	2.4:1	σ'
	$X_2\gamma_1$	16420	883	2.5:1	π
	$X_3\gamma_3$	16015	1288	1:2	σ
$^5F_3$	$W_1\gamma_2$	15460	1842	1:2.6	π'
	$W_2\gamma_3$	15427	1875	2:1	σ'
	$W_3\gamma_1$	15380	1922	2.5:1	π
	$W_4\gamma_3$	15354	1948	2:1	σ'
$^5F_4$	$V_1\gamma_1$	14455	2458	3:1	π
	$V_2\gamma_2$	14455	2848	1:2.8	π'
	$V_3\gamma_3$	14436	2867	1.5:1	σ'
	$V_4\gamma_3$	14263	3040	2.2:1	σ'
	$V_6\gamma_3$	14244	3059	1:2.7	σ
$^5F_5$	$U_2\gamma_1$	13516	3787	2.2:1	π
$^5F_6$	$T_1\gamma_1$	12360	4943	3:1	π
	$T_2\gamma_3$	12321	4982	2:1	σ'
	$T_3\gamma_3$	12279	5024	-	-
	$T_4\gamma_2$	12256	5047	1:2.4	π'

Table 6.13: Fluorescence transitions from $^5D_1$ to the ^7F_J multiplets of the BaF_2:Eu^{3+} L Centre. Emission originates from the $B_1\gamma_3$ state at 19057 cm^{-1} and the $B_2\gamma_2$ state at 19071 cm^{-1}. All transition frequencies are as measured in air (cm^{-1},±1)

Multiplet	Transition		State
	Frequency	Assignment	Energy
$^7F_1$	18747	$B_2\gamma_2 \rightarrow Y_1\gamma_3$	324
	18733	$B_1\gamma_3 \rightarrow Y_1\gamma_3$	324
	18680	$B_2\gamma_2 \rightarrow Y_2\gamma_2$	391
	18666	$B_1\gamma_3 \rightarrow Y_2\gamma_2$	391
$^7F_2$	18218	$B_2\gamma_2 \rightarrow X_1\gamma_3$	853
	18206	$B_1\gamma_3 \rightarrow X_1\gamma_3$	851
	18190	$B_2\gamma_2 \rightarrow X_2\gamma_1$	881
	18176	$B_1\gamma_3 \rightarrow X_2\gamma_1$	881
	17785	$B_2\gamma_2 \rightarrow X_3\gamma_3$	1286
	17772	$B_1\gamma_3 \rightarrow X_3\gamma_3$	1285
$^7F_3$	17232	$B_2\gamma_2 \rightarrow W_1\gamma_2$	1841
	17217	$B_1\gamma_3 \rightarrow W_1\gamma_2$	1840
	17198	$B_2\gamma_2 \rightarrow W_2\gamma_3$	1873
	17185	$B_1\gamma_3 \rightarrow W_2\gamma_3$	1872
	17151	$B_2\gamma_2 \rightarrow W_3\gamma_1$	1920
	17137	$B_1\gamma_3 \rightarrow W_3\gamma_1$	1920
	17125	$B_2\gamma_2 \rightarrow W_4\gamma_3$	1946
	17110	$B_1\gamma_3 \rightarrow W_4\gamma_3$	1947
$^7F_4$	16599	$B_1\gamma_3 \rightarrow V_1\gamma_1$	2458
	16209	$B_1\gamma_3 \rightarrow V_2\gamma_2$	2848
	16190	$B_1\gamma_3 \rightarrow V_3\gamma_3$	2867
	15999	$B_1\gamma_3 \rightarrow V_5\gamma_1$	3058
$^7F_5$	15284	$B_2\gamma_2 \rightarrow U_2\gamma_1$	3787
	15270	$B_1\gamma_3 \rightarrow U_2\gamma_1$	3787
$^7F_6$	14115	$B_1\gamma_3 \rightarrow T_1\gamma_1$	4942
	14076	$B_1\gamma_3 \rightarrow T_2\gamma_3$	4981
	14034	$B_1\gamma_3 \rightarrow T_3\gamma_3$	5023

The 15380 cm^{-1} transition is electric dipole π polarised and is assigned as terminating on the $W_3\gamma_1$ state at 1922 cm^{-1}. Fluorescence to $^7F_3$ from $^5D_1$ is observed in the 17250 17100 cm^{-1} region as shown in Figure 6.47(b). All transitions to all four states observed from $^5D_0$ were observed however no transitions to the expected fifth state could be seen as was the case for the J centre in SrF_2:Eu^{3+}.

Figure 6.48(a) shows $^5D_0 \rightarrow ^7F_4$ fluorescence in the 14900 - 13900 cm^{-1} region. A weak transition at 14845 cm^{-1} is assigned as the $A_1\gamma_1 \rightarrow V_1\gamma_1$ from its π polarisation behaviour. A broad feature at 14649 cm^{-1} is displaced 196 cm^{-1} from the 14845 cm^{-1} transition. It is assigned as terminating on a lattice vibrational state. Two sharp transitions at 14455 and 14436 cm^{-1} are π' and σ' polarised respectively. From this, we assign them as the $A_1\gamma_1 \rightarrow V_2\gamma_2$ and $V_3\gamma_3$ transitions with the V_2 and V_3 states at 2848 and 2867 cm^{-1}. The 14400 - 13900 cm^{-1} region is difficult to analyse as complex vibronic structure is apparant. By analogy with the SrF_2 J centre we assign the 14263 and 14244 cm^{-1} transitions as terminating on the V_4 and V_6 states at 3040 and 3059 cm^{-1}. This assertion is supported by the σ' and σ polarisation dependence observed for these transitions leading to the assignment of both terminating states as γ_3 doublets. The $^5D_1 \rightarrow ^7F_4$ fluorescence is also complex as emission from $^5D_0$ overlaps the emission of interest. The $B_1\gamma_3 \rightarrow V_1\gamma_1$ transition is observed at 16599 cm^{-1} at a slightly lower frequency than lattice phonons associated with the $^5D_0 \rightarrow ^7F_1$ emission. $^5D_0 \rightarrow ^7F_2$ fluorescence is also present in this region and is left unlabelled. The $B_1\gamma_3 \rightarrow V_2\gamma_2$ and $V_3\gamma_3$ transitions are observed at frequencies of 16209 and 16190 cm^{-1}. The $B_1\gamma_3 \rightarrow V_6\gamma_3$ transition is observed at 15999 cm^{-1} which goes someway to confirming the tentative assignments made above.

By contrast the $^5D_0$ and $^5D_1$ emission to $^7F_5$ is extremely simple as shown in Figure 6.49(a) and (b). Transitions to only one $^7F_5$ state are observed. The 13516 cm^{-1} transition is π polarised leading to the assignment of the symmetry of the terminating state as γ_1, at an energy of 3787 cm^{-1} above the ground state. The weaker transition at 13314 cm^{-1} assigned as a vibronic from its 202 cm^{-1} displacement from the 13516 cm^{-1} transition.

As shown in Figure 6.50(a) the $^5D_0$ fluorescence to $^7F_6$ is also simple with four transitions observed. The 12360 and 12256 cm^{-1} transitions terminate on singlet states. From their respective π and π' polarisations we assign the $^7F_6$ states as $T_1\gamma_1$ at 4943 cm^{-1} and $T_4\gamma_2$ at 5047 cm^{-1}. Of the remaining transitions the 12321 cm^{-1} transition is observed to be σ' polarised leading to its assignment as terminating on the $T_3\gamma_3$ state. The final transition at 12279 cm^{-1} is too weak to obtain polarisation ratios. The corresponding $^5D_1$ fluorescence (Figure 6.50(b)) overlaps the vibronic bands associated with the $^5D_0 \rightarrow ^7F_4$ fluorescence. Despite this three transitions can be observed to the T_1, T_2 and T_3 states at 14115, 14079 and 14034 cm^{-1} as given

in Table 6.13.

6.5 Upconversion Fluorescence

Upconversion is a form of non-linear absorption in optically activated solids whereby long wavelength (low energy) radiation is converted into short wavelength (higher energy) radiation. There are several mechanisms through which this can be achieved [113]. Energy transfer upconversion between ions in neigbouring crystal sites, such as that observed in $Gd_3Ga_5O_{12}:Pr^{3+}$ [115], is probably the most common (and efficient) form of upconversion process. In this case, both an acceptor and donor ion undergo an absorption transition to an intermediate state (thereby utilising the absorption cross-section of both ions) from which the donor transfers its optical (or otherwise) excitation to the acceptor ion which is excited to a higher state. Another form of upconversion, which can be regarded as a hybrid of the excited state absorption and energy transfer processes, is the photon avalanche effect [116] [117]. The optically active ion is excited, typically by a laser light source (though not necessarily), into resonance with an excited state absorption transition. The terminating excited state absorption state decays via energy transfer to a non-excited neighbour, leaving both ions in an excited state. If the laser frequency is appropriate, both ions can then undergo excited state absorption transitions. If the excitation intensity is above a critical threshold the excited state absorber population can be sustained and strong upconversion fluorescence is observed.

Numerous studies of energy transfer upconversion in rare earth ion doped alkaline earth fluoride crystals have been reported, eg [114], [118], [119], [62] and it is these studies that dominate the literature. More recently it has been shown, that for low concentrations of around 0.01-0.05 molar % of the rare earth ion dopant, sequential absorption processes involving long-lived bottleneck states can dominate the upconversion process [120], [121], [122]. For the europium ion, sequential absorption processes have been observed for the divalent species [123]. Indeed in the case of the Eu^{2+} ion it is only this strong excited state absorption that prevents it from serving as a broadly tunable solid state laser source. Here we are only interested in the Eu^{3+} ion.

For resonant CW laser excitation of the $^7F_0 \rightarrow ^5D_0$ transition, upconversion fluorescence is observed from the $^5D_3$, $^5D_2$ and $^5D_1$ multiplet for the C_{4v} symmetry A centres in $CaF_2:Eu^{3+}$ and $SrF_2:Eu^{3+}$ and for the C_{3v} symmetry L centre in $BaF_2:Eu^{3+}$. However, for pulsed laser excitation of the $^7F_0 \rightarrow ^5D_0$ transition, no upconversion is observed at similar detection sensitivities. Based on this null result from the pulsed laser experiment and the low Eu^{3+} concentrations used here, energy transfer is ruled

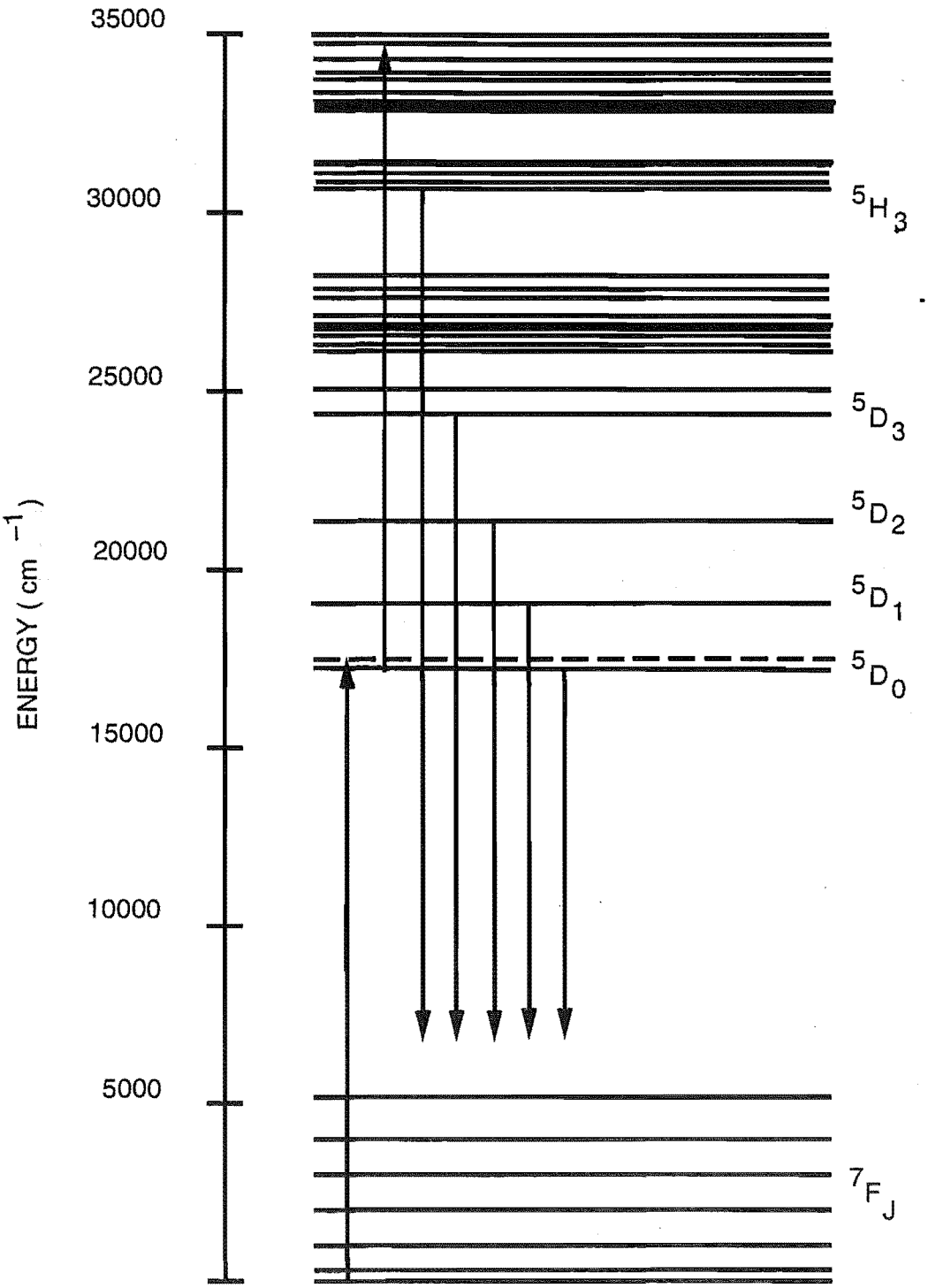

Figure 6.51: Schematic diagram of the Eu^{3+} upconversion process. The dotted lines indicate phonon sideband absorption.

out and the upconversion mechanism is assigned to be a sequential absorption of two photons placing the Eu^{3+} ions in states higher than $^5D_0$. Candidiates for the initial absorbing level for the second photon are the lower ^7F_J multiplets and the long lived $^5D_0$ level itself. Weak UV upconverted emission is observed emanating from the $^5H_3$ multiplet at 30000 cm^{-1} for SrF_2:Eu^{3+}. As the $^5D_0$ lifetime is sufficiently long (of the order of 10 millisecs) for the probability of absorption of a second photon to be high, the upconversion process is assigned to be a sequential absorption from the $^5D_0$ level itself. The absorption of a 17300 cm^{-1} photon from $^5D_0$ places the upper state of the excited state absorption transition (ESA) at high energy (around 34500 cm^{-1}). As shown in Figure 6.51, which indicates the positions of all of the higher energy multiplets of Eu^{3+} up to 35000 cm^{-1}, the density of electronic states in that spectral region is very high and there is a multitude of possible terminating levels for the ESA. Energy gaps in this region are small and the ion decays non-radiatively with most emission observed from the $^5D_3$, $^5D_2$, $^5D_1$ and $^5D_0$ multiplets.

Such multicolour upconversion emission as has been observed here is of great interest for the development of high-density optical storage and colour displays. Colour displays require red, green and blue emitters, thus, a single ion capable of producing one multiwavelength pixel can do the job of three and far greater resolution can be attained [124]. Lenth and Macfarlane [125] (1990) and later, Cockcroft [126] (1994) have reviewed various excitations mechanisms for the production of upconversion lasers.

6.5.1 Excitation and Temperature Dependence of the Eu^{3+} Upconversion Fluorescence

For resonant excitation of the $Z_1\gamma_1 \rightarrow A_1\gamma_1$ transitions of the C_{4v} symmetry A centres in CaF_2:0.05%Eu^{3+} and SrF_2:0.05%Eu^{3+} and the C_{3v} symmetry L centre in BaF_2:0.05%Eu^{3+}, upconversion fluorescence is observed from the lower multiplets of the ^5D term. As discussed above, this is assigned as a sequential absorption process out of $^5D_0$. Of the three alkaline earth fluoride host crystals the strongest Eu^{3+} upconversion fluorescence is observed for SrF_2:Eu^{3+}, this is due to the lower phonon energies of the SrF_2 host. Figures 6.52, 6.53 and 6.54 show upconversion excitation spectra for the aforementioned crystals at 16 and 200K with the appropriate resonant and non-resonant excitations indicated. Table 6.14 lists the upconversion excitation frequencies. Upconversion fluorescence for excitation of the $^7F_0 \rightarrow ^5D_0$ transition increases in intensity upon warming the crystal. The maximum efficiency is observed at approximately 80K for all three systems (see Figures 6.55, 6.56 and 6.57). The increase is accounted for as thermal phonons more efficiently bridge the energy mismatch for the ESA transition. The intensity decrease beyond 80K occurs because of thermal depletion of the ground state population. The profile of this

dropoff fits to a Boltzmann distribution with an activation energy that equates to the gap to the $^7F_1$ multiplet.

The warming of the crystal to 200K significantly populates the $^7F_1$ multiplet, 350 cm^{-1} above the ground state. Upconversion emission is observed for resonant excitation of the $^7F_1 \rightarrow ^5D_0$ transitions (see the upconversion excitation spectra). The $^7F_1 \rightarrow ^5D_0$ transitions are comparatively strong transitions of magnetic dipole character. A branching ratio of 0.71 has been obtained for fluorescence out of $^5D_0$ to $^7F_1$ by Hamers et. al. [104] for CaF_2:Eu^{3+}. As a consequence, absorption transitions from the two crystal field levels of the $^7F_1$ multiplet become increasing efficient at populating the $^5D_0$ state at higher temperatures. The thermal population of $^7F_1$ increasing with temperature, as determined from the appropriate Boltzmann factor. The lifetime of the $^5D_0$ state is not a significant contributing factor to the change in the upconversion fluorescence intensity. The measured lifetimes (see section 6.7) of 11.8, 13.4 and 14.6 ms in CaF_2:Eu^{3+}, SrF_2:Eu^{3+} and BaF_2:Eu^{3+} respectively are not observed to decrease with temperature up to 300K. The observed decrease is a function of the lifetime of $^5D_3$, fluorescence from which fluorescence is being monitored. Due to the increasing population of $^7F_1$, upconverted fluorescence intensity is observed to increase with temperature up to 240K and persists strongly through to room temperature as shown in Figures 6.58 through to 6.63.

Also apparent in the upconversion excitation spectra is emission obtained for resonant excitation of ESA transitions. For these transitions the $^5D_0$ multiplet is populated via phonon sideband absorption and ESA transitions are observed from typically 250 cm^{-1} and greater energies on the higher energy side of the $^7F_0 \rightarrow ^5D_0$ absorption transition. The ESA transition intensities begin to decay almost immediately upon warming the crystal. This is unexpected as higher temperatures should lead to increased vibronic activity more efficiently populating the $^5D_0$ state via phonon sideband absorption. Figure 6.64, 6.65 and 6.66 show representative ESA transition excitation thermal dependences.

For excitation of the $^5D_1$ multiplet (shown in Figure 6.67) weaker excitation powers of the 10-50 mW of the less efficient C540 dye are used. The $^7F_0 \rightarrow ^5D_1$ transitions are magnetic dipole allowed with comparably large absorption cross-sections. As such, the lower excitation powers used are sufficient to obtain upconverted fluorescence intensities similar to that of 200-400 mW excitation of $^5D_0$. These $^7F_0 \rightarrow ^5D_1$ transitions obtain their maximum intensity between 60-90K and thereafter the intensity reduces as thermally populated phonon modes compete more efficiently with radiative decay; the $^5D_1$ level decaying to $^5D_0$. These thermal dependences are shown in Figures 6.68 through to 6.73.

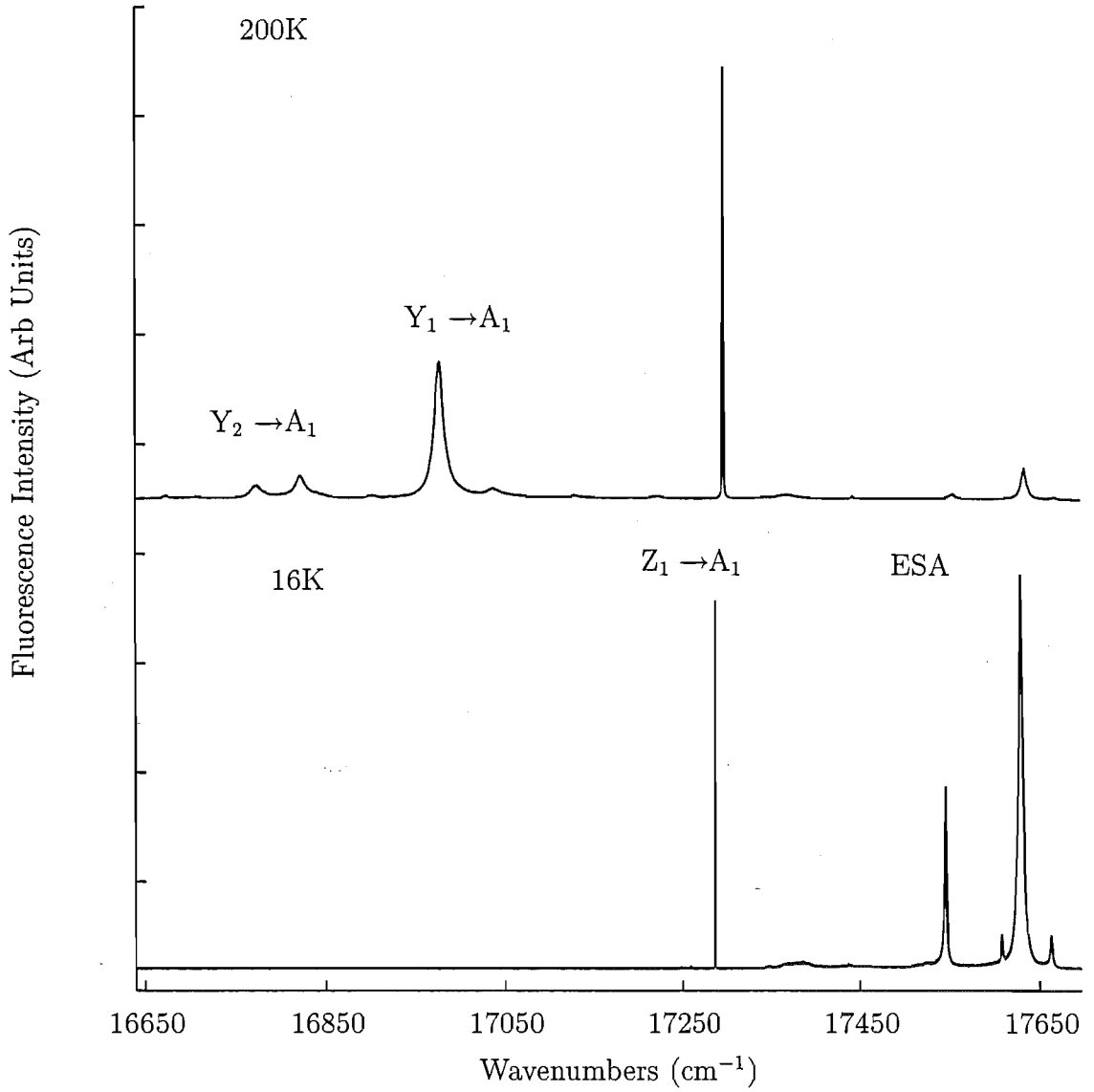

Figure 6.52: Upconversion excitation spectra for the $^5D_0$ multiplet in CaF_2:0.05%Eu^{3+} obtained whilst monitoring all transitions at 425 nm.

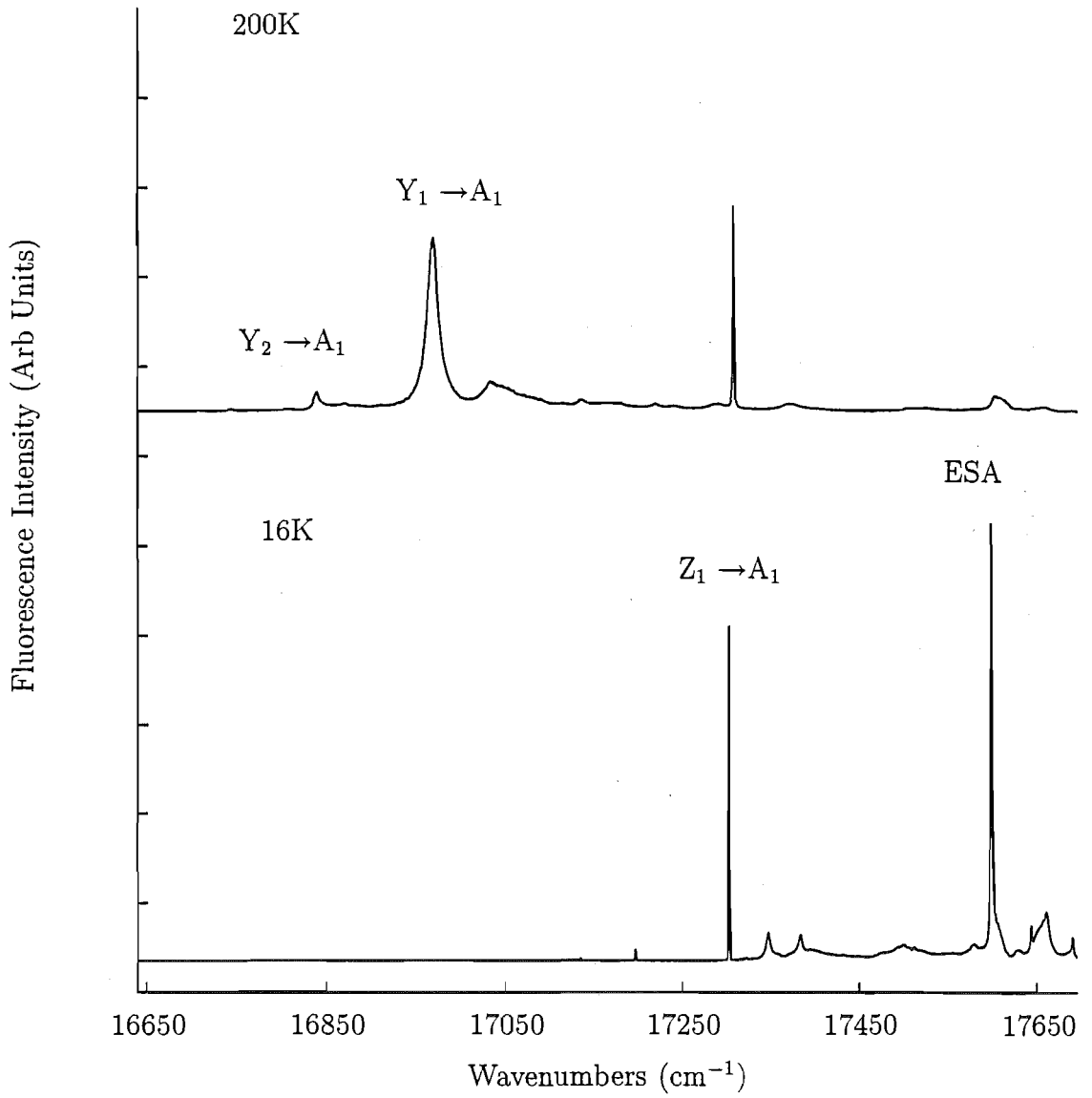

Figure 6.53: Upconversion excitation spectra for the $^5D_0$ multiplet in SrF_2:0.05%Eu^{3+} obtained whilst monitoring all transitions at 425 nm.

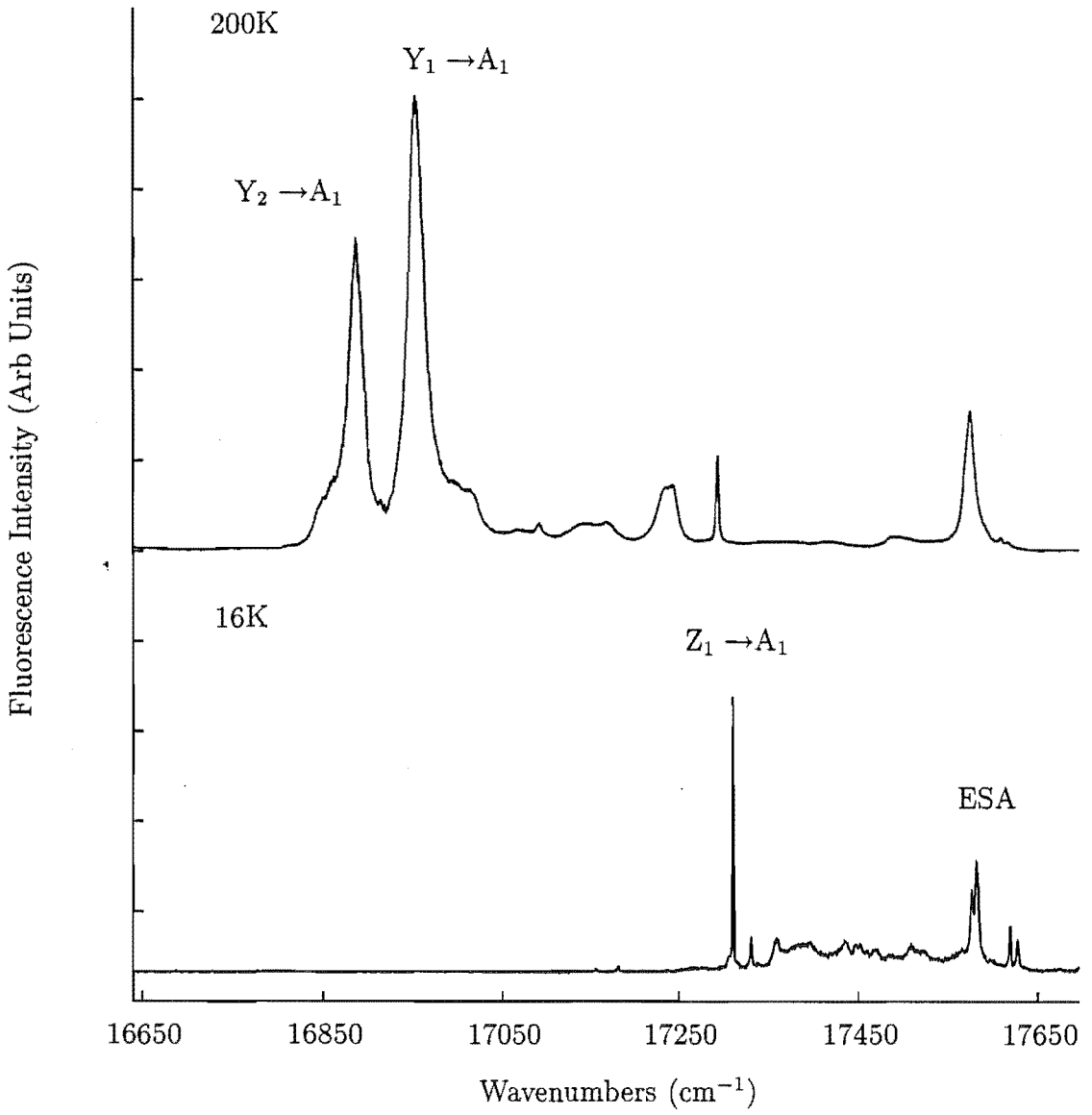

Figure 6.54: Upconversion excitation spectra for the $^5D_0$ multiplet in BaF_2:0.05%Eu^{3+} obtained whilst monitoring all transitions at 450 nm.

Table 6.14: Upconversion excitation frequencies (in air $cm^{-1}\pm1$) for the dominant centres in CaF_2, SrF_2 and BaF_2 doped with 0.05% Eu^{3+}

Crystal	Multiplet	Excitation Frequency	Transition
$CaF_2:Eu^{3+}$	$^5D_0$	16831	$Y_2\gamma_2 \rightarrow A_1\gamma_1$
C_{4v}		16979	$Y_1\gamma_5 \rightarrow A_1\gamma_1$
		17288	$Z_1\gamma_1 \rightarrow A_1\gamma_1$
		17541	ESA
		17608	ESA
		16629	ESA
		16660	ESA
	$^5D_1$	19029	$Z_1\gamma_1 \rightarrow B_1\gamma_5$
		17079	$Z_1\gamma_1 \rightarrow B_2\gamma_2$
$SrF_2:Eu^{3+}$	$^5D_0$	16870	$Y_2\gamma_2 \rightarrow A_1\gamma_1$
C_{4v}		16974	$Y_1\gamma_5 \rightarrow A_1\gamma_1$
		17298	$Z_1\gamma_1 \rightarrow A_1\gamma_1$
		17594	ESA
	$^5D_1$	19048	$Z_1\gamma_1 \rightarrow B_1\gamma_5$
		17082	$Z_1\gamma_1 \rightarrow B_2\gamma_2$
$BaF_2:Eu^{3+}$	$^5D_0$	16912	$Y_2\gamma_2 \rightarrow A_1\gamma_1$
C_{3v}		16978	$Y_1\gamma_3 \rightarrow A_1\gamma_1$
		17303	$Z_1\gamma_1 \rightarrow A_1\gamma_1$
		17572	ESA
		17578	ESA
		16616	ESA
		16625	ESA
	$^5D_1$	19057	$Z_1\gamma_1 \rightarrow B_1\gamma_3$
		17071	$Z_1\gamma_1 \rightarrow B_2\gamma_2$

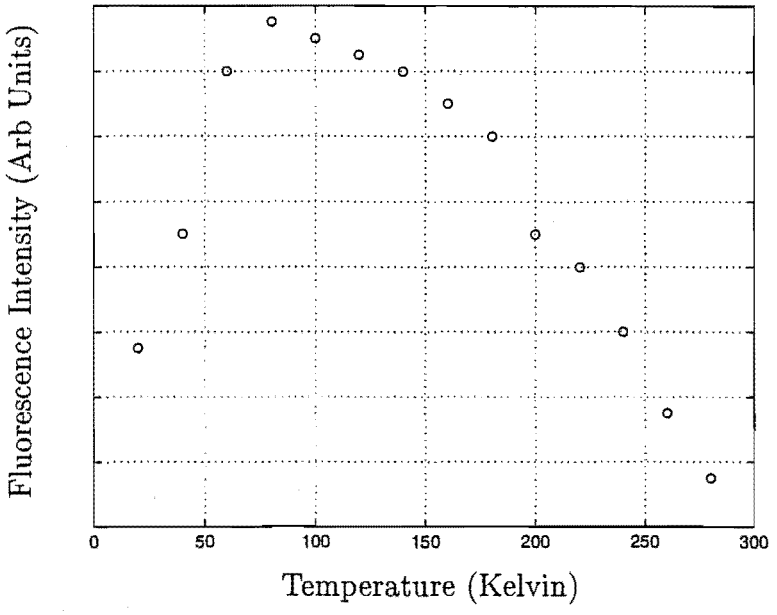

Figure 6.55: Temperature dependence of A centre upconverted emission for excitation of the $Z_1\gamma_1 \rightarrow A_1\gamma_1$ transition at 17288 cm^{-1} in CaF_2:0.05%Eu^{3+}. Emission was monitored at 425nm.

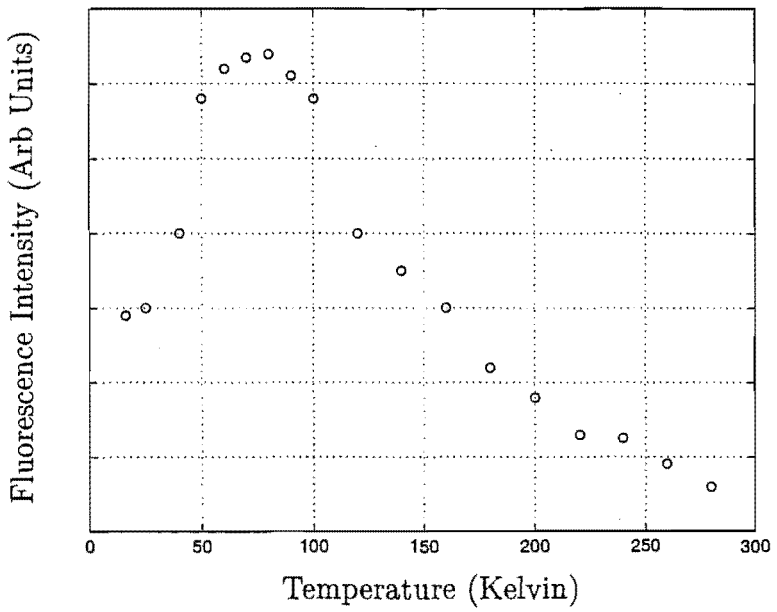

Figure 6.56: Temperature dependence of A centre upconverted emission for excitation of the $Z_1\gamma_1 \rightarrow A_1\gamma_1$ transition at 17298 cm^{-1} in SrF_2:0.05%Eu^{3+}. Emission was monitored at 425nm.

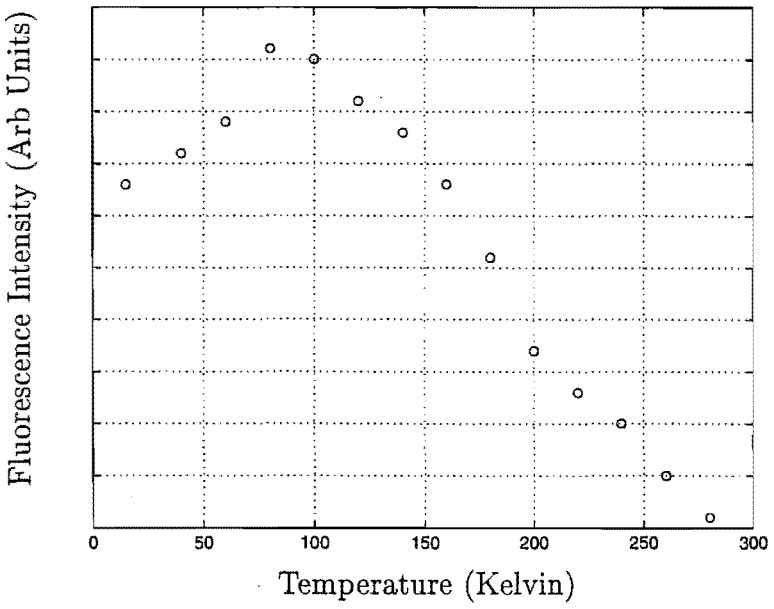

Figure 6.57: Temperature dependence of L centre upconverted emission for excitation of the $Z_1\gamma_1 \rightarrow A_1\gamma_1$ transition at 17303 cm^{-1} in BaF_2:0.05%Eu^{3+}. Emission was monitored at 450nm.

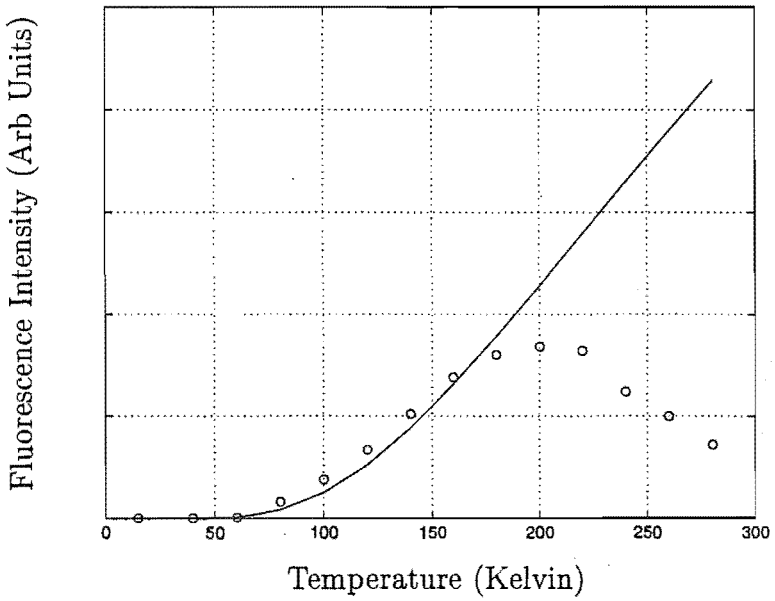

Figure 6.58: Temperature dependence of A centre upconverted emission for excitation of the $Y_1\gamma_5 \rightarrow A_1\gamma_1$ transition at 16981 cm^{-1} in CaF_2:0.05%Eu^{3+}. Emission was monitored at 425nm. The solid line is a fit of the Boltzmann distribution function to the experimental data, indicated with circles. ΔE, the $^7F_0$-$^7F_1Y_1$ splitting was held at the experimental value.

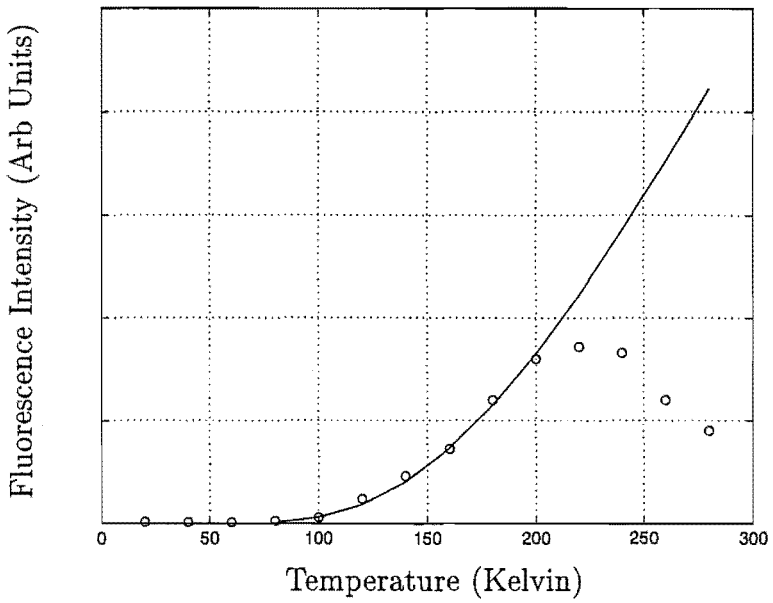

Figure 6.59: Temperature dependence of A centre upconverted emission for excitation of the $Y_2\gamma_2 \rightarrow A_1\gamma_1$ transition at 16832 cm^{-1} in CaF_2:0.05%Eu^{3+}. Emission was monitored at 425nm. The solid line is a fit of the Boltzmann distribution function to the experimental data, indicated with circles. ΔE, the $^7F_0$-$^7F_1Y_2$ splitting was held at the experimental value.

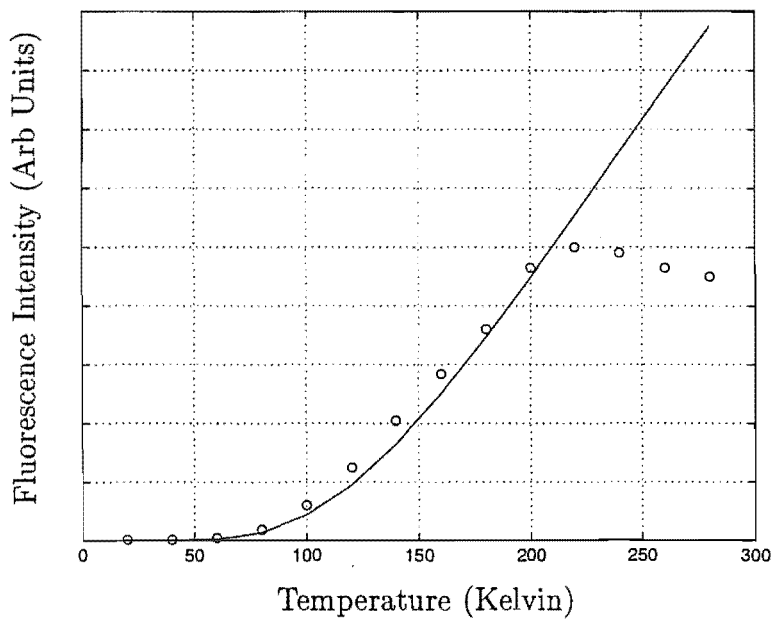

Figure 6.60: Temperature dependence of A centre upconverted emission for excitation of the $Y_1\gamma_5 \rightarrow A_1\gamma_1$ transition at 16974 cm^{-1} in SrF_2:0.05%Eu^{3+}. Emission was monitored at 425nm. The solid line is a fit of the Boltzmann distribution function to the experimental data, indicated with circles. ΔE, the $^7F_0$-$^7F_1Y_1$ splitting was held at the experimental value.

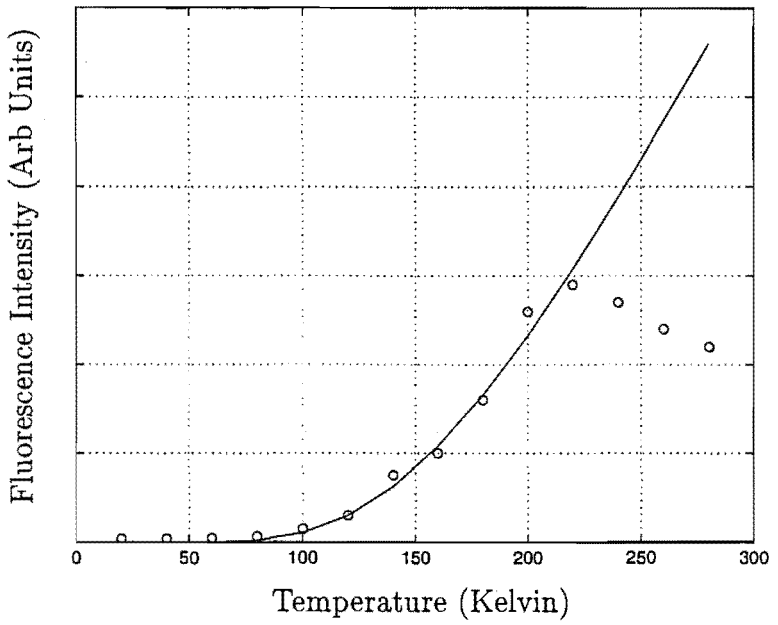

Figure 6.61: Temperature dependence of A centre upconverted emission for excitation of the $Y_2\gamma_2 \rightarrow A_1\gamma_1$ transition at 16870 cm^{-1} in SrF_2:0.05%Eu^{3+}. Emission was monitored at 425nm. The solid line is a fit of the Boltzmann distribution function to the experimental data, indicated with circles. ΔE, the $^7F_0$-$^7F_1Y_2$ splitting was held at the experimental value.

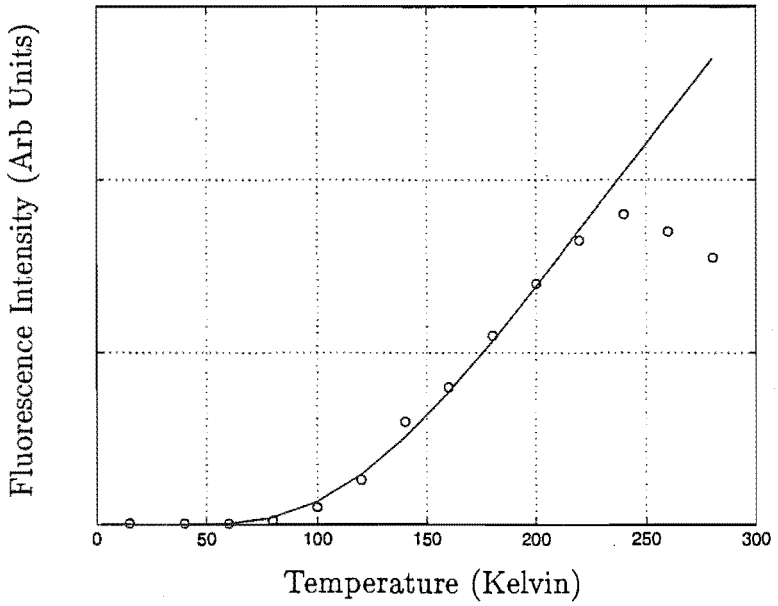

Figure 6.62: Temperature dependence of L centre upconverted emission for excitation of the $Y_1\gamma_3 \rightarrow A_1\gamma_1$ transition at 16979 cm^{-1} in BaF_2:0.05%Eu^{3+}. Emission was monitored at 450nm. The solid line is a fit of the Boltzmann distribution function to the experimental data, indicated with circles. ΔE, the $^7F_0$-$^7F_1Y_1$ splitting was held at the experimental value.

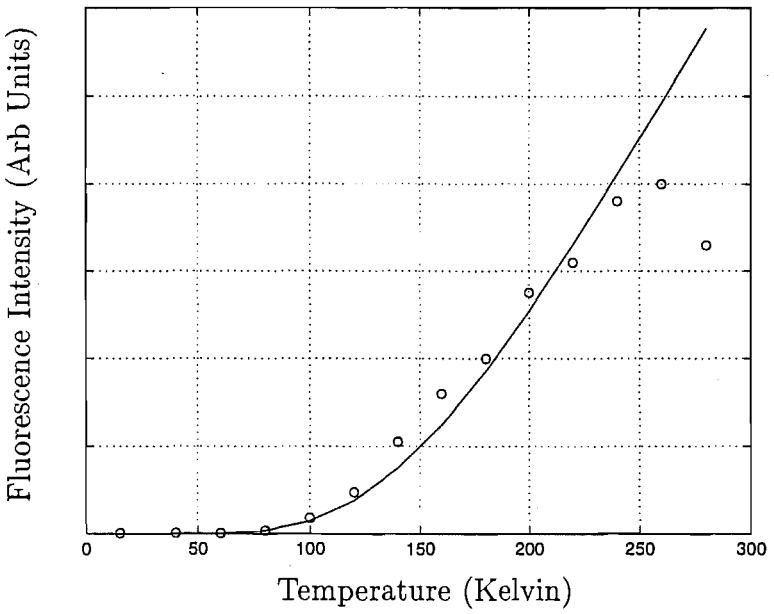

Figure 6.63: Temperature dependence of L centre upconverted emission for excitation of the $Y_2\gamma_2 \rightarrow A_1\gamma_1$ transition at 16912 cm^{-1} in BaF_2:0.05%Eu^{3+}. Emission was monitored at 450nm. The solid line is a fit of the Boltzmann distribution function to the experimental data, indicated with circles. ΔE, the $^7F_0$-$^7F_1Y_2$ splitting was held at the experimental value.

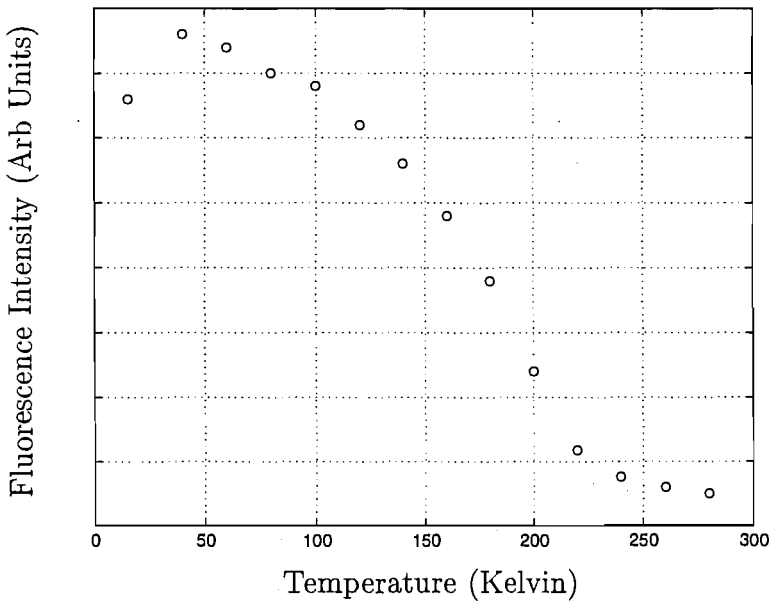

Figure 6.64: Temperature dependence of A centre upconverted emission for excitation of the 17629 cm^{-1} ESA transition in CaF_2:0.05%Eu^{3+}. Emission was monitored at 425nm.

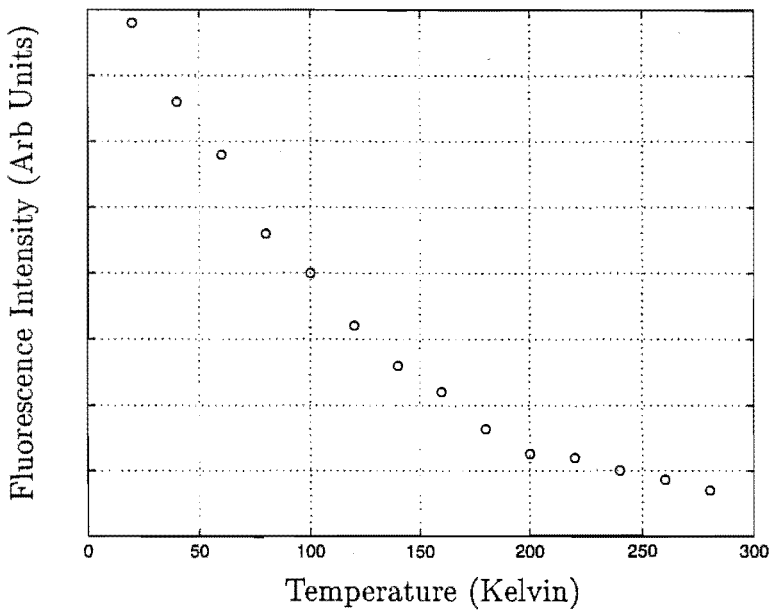

Figure 6.65: Temperature dependence of A centre upconverted emission for excitation of the ESA transition at 17594 cm^{-1} in SrF_2:0.05%Eu^{3+}. Emission was monitored at 425nm.

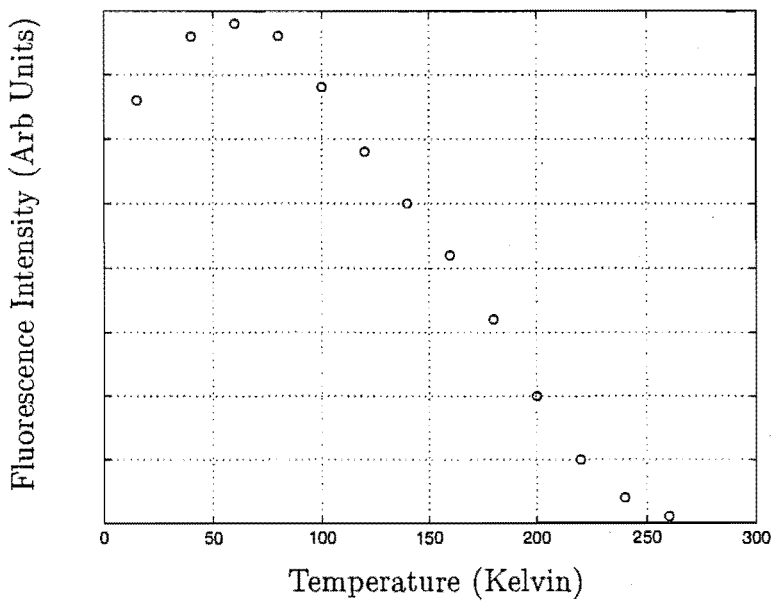

Figure 6.66: Temperature dependence of L centre upconverted emission for excitation of the 17578 cm^{-1} ESA transition in BaF_2:0.05%Eu^{3+}. Emission was monitored at 450nm.

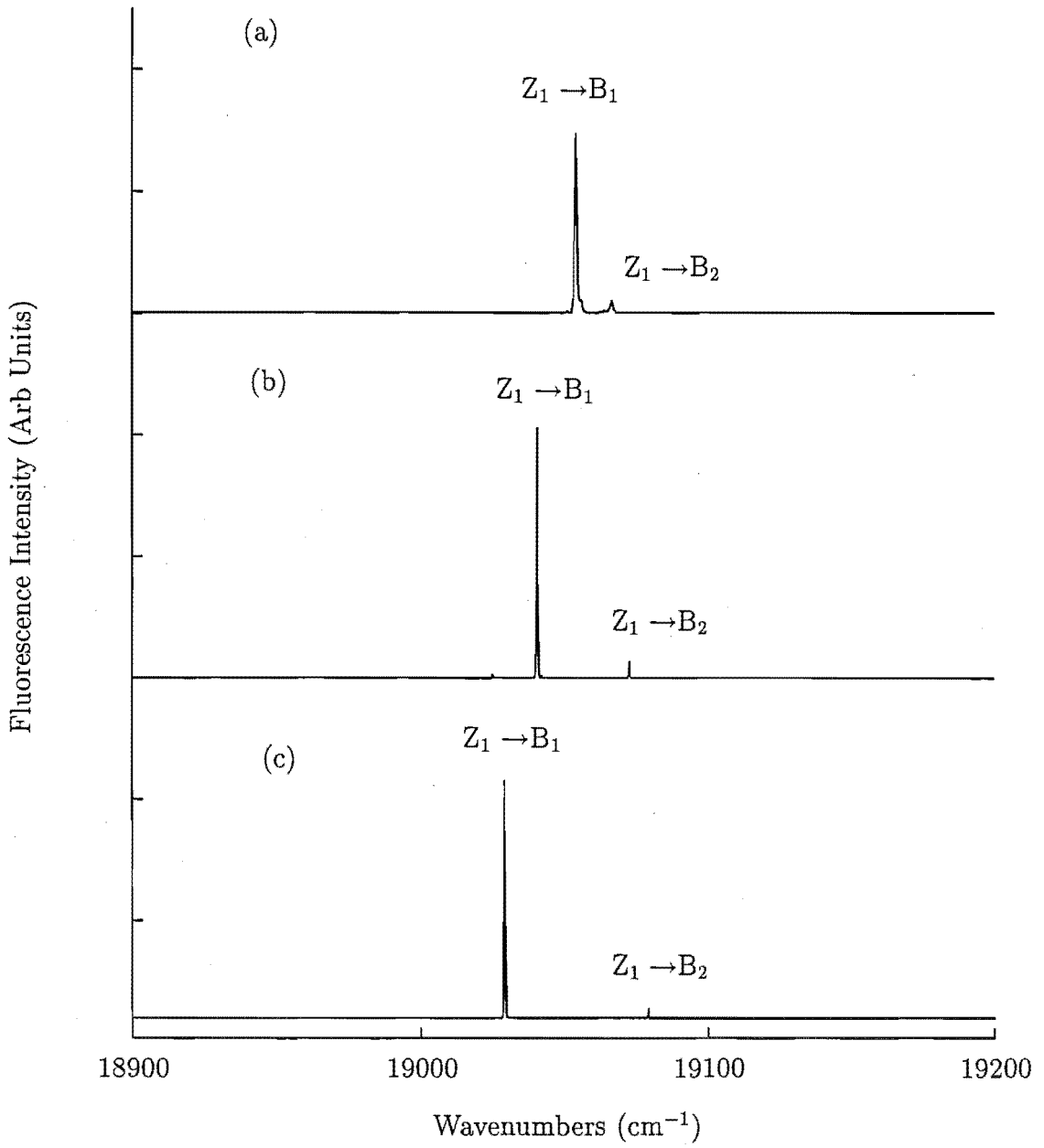

Figure 6.67: Upconversion excitation spectra of the $^5D_1$ multiplet for (a) the BaF_2:Eu^{3+} L centre (mon 450 nm), (b) the SrF_2:Eu^{3+} A centre (mon 425 nm) and (c) the CaF_2:Eu^{3+} A centre (mon 425 nm). The spectra were recorded at 16K.

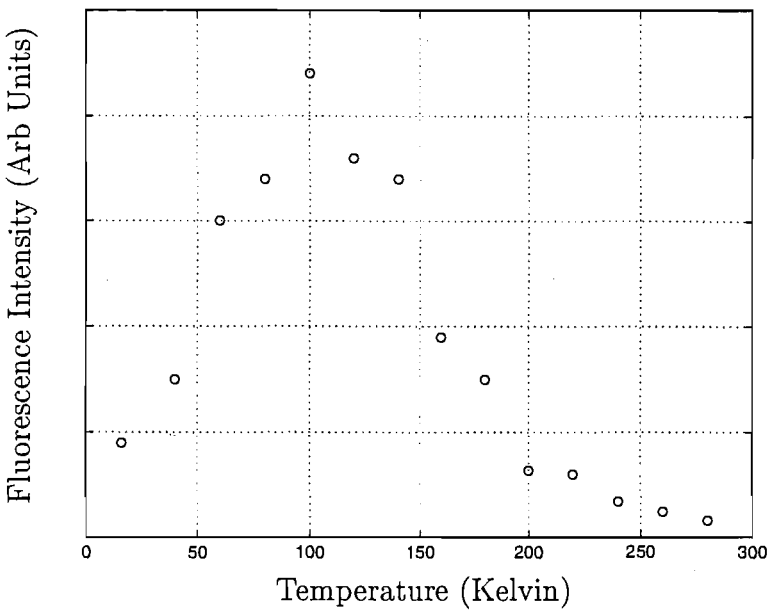

Figure 6.68: Temperature dependence of A centre upconverted emission for excitation of the 19029 cm^{-1} $Z_1\gamma_1 \rightarrow B_1\gamma_5$ transition in CaF_2:0.05%Eu^{3+}. Emission was monitored at 425nm.

Due to the low rare earth ion occupancy of minority centres, no upconversion fluorescence could be observed for centres such as the trigonal J centre in SrF_2:Eu^{3+} and the R and Q centres in CaF_2:Eu^{3+}. Of course, the R and Q centres are clusters and therefore we may not expect to observe upconversion as ion-pair processes leads to very rapid relaxation of the higher multiplets of the ^5D term to $^5D_0$.

For crystals treated in a dry oxygen atmosphere, O^{2-} charge compensated centres are present. The O^{2-} ion occupies a nearest neighbour substitutional position along the $\langle 111 \rangle$ direction thus providing a strong trigonal distortion. The $^7F_0 \rightarrow ^5D_0$ transitions for these centres in CaF_2, SrF_2 and BaF_2:Eu^{3+} are observed at frequencies of 17434, 17463 and 17457 cm^{-1} respectively and weak upconversion fluorescence can be detected for excitation of these transitions. Silversmith and Radlinski [127] have measured the lifetime of the CaF_2:Eu^{3+} $^5D_0\gamma_1$ state at 17434 cm^{-1} to be 1.8 ms. This sixfold reduction in the lifetime from the F^- centres can account for the considerably weaker intensity of the upconversion fluorescence observed.

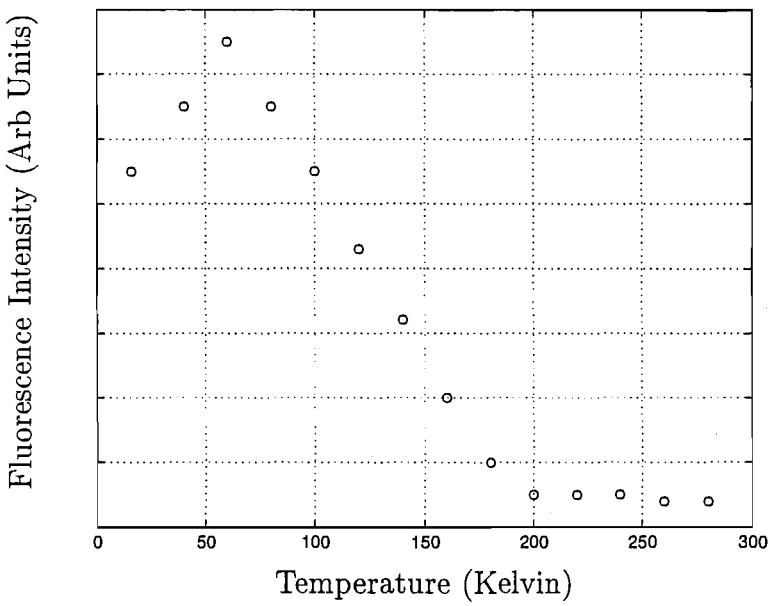

Figure 6.69: Temperature dependence of A centre upconverted emission for excitation of the 19079 cm^{-1} $Z_1\gamma_1 \rightarrow B_2\gamma_2$ transition in CaF_2:0.05%Eu^{3+}. Emission was monitored at 425nm.

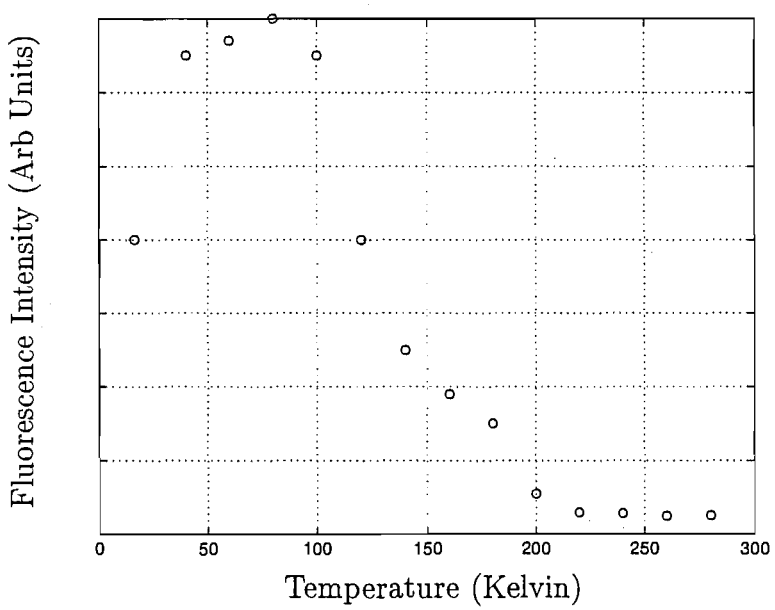

Figure 6.70: Temperature dependence of A centre upconverted emission for excitation of the 19048 cm^{-1} $Z_1\gamma_1 \rightarrow B_1\gamma_5$ transition in SrF_2:0.05%Eu^{3+}. Emission was monitored at 425nm.

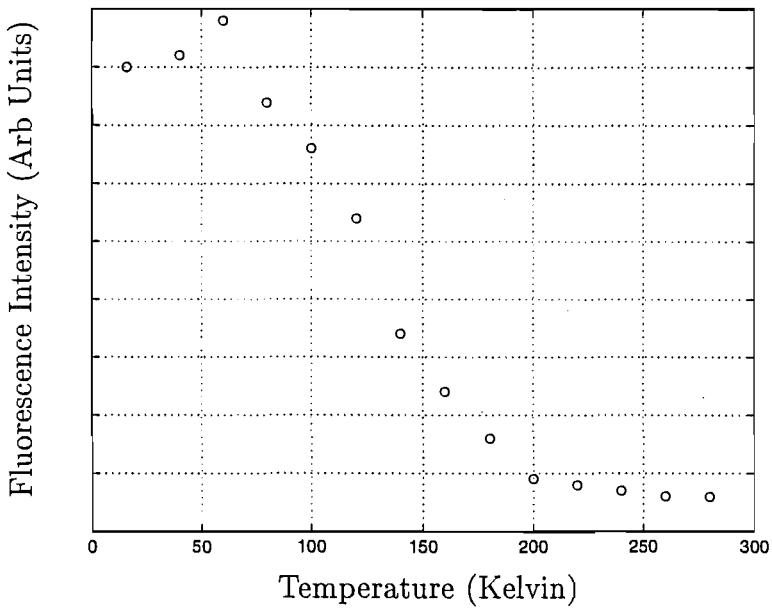

Figure 6.71: Temperature dependence of A centre upconverted emission for excitation of the 19082 cm^{-1} $Z_1\gamma_1 \rightarrow B_2\gamma_2$ transition in SrF_2:0.05%Eu^{3+}. Emission was monitored at 425nm.

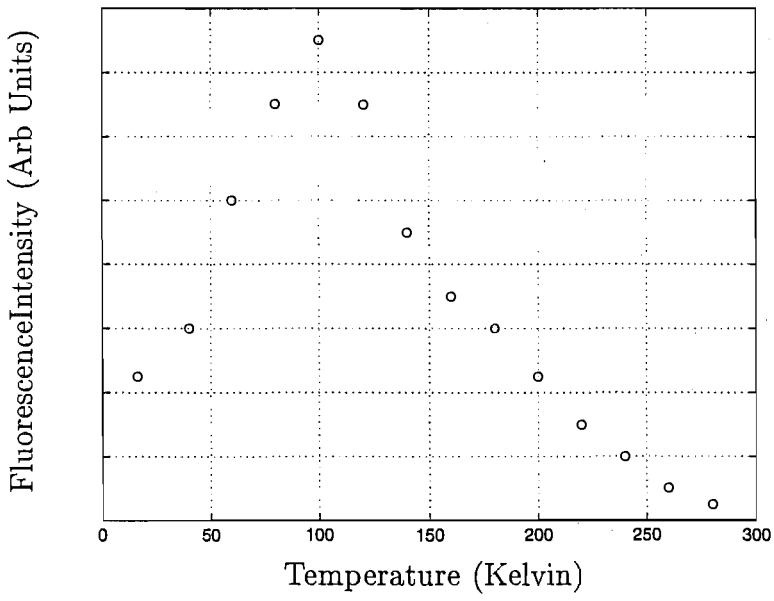

Figure 6.72: Temperature dependence of L centre upconverted emission for excitation of the 19057 cm^{-1} $Z_1\gamma_1 \rightarrow B_1\gamma_3$ transition in BaF_2:0.05%Eu^{3+}. Emission was monitored at 450nm.

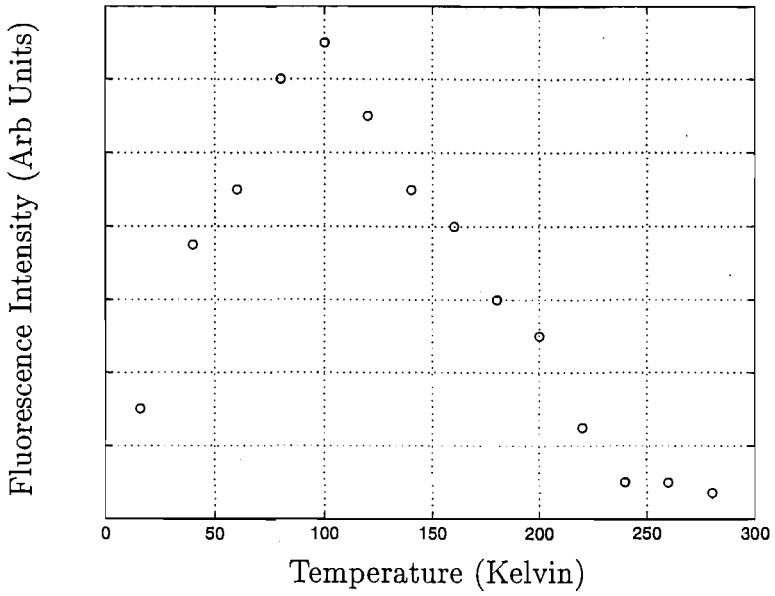

Figure 6.73: Temperature dependence of L centre upconverted emission for excitation of the 19071 cm^{-1} $Z_1\gamma_1 \rightarrow B_2\gamma_2$ transition in BaF_2:0.05%Eu^{3+}. Emission was monitored at 450nm.

6.5.2 CaF_2:Eu^{3+} - A Centre

For excitation of the 17288 cm^{-1} $Z_1\gamma_1 \rightarrow A_1\gamma_1$ transition, upconversion fluorescence is observed from $^5D_3$, $^5D_2$ and $^5D_1$ to the crystal field levels of the ^7F_J multiplets. No $^5D_3 \rightarrow ^7F_0$ emission could be detected and as a consequence, the highest frequency transitions observed are those to the $^7F_1$ multiplet levels.

Four electronic transitions are observed to the $^7F_1$ multiplet originating from the $^5D_3$ multiplet. These are shown in Figure 6.74. This fluorescence is observed in the 24100-23800 cm^{-1} region. The dominant feature at 24028 cm^{-1} is π polarised and is assigned as the $D_1\gamma_5 \rightarrow Y_1\gamma_5$ transition with $D_1\gamma_5$ at 24337 cm^{-1}. Two weaker transitions at the slightly higher frequencies of 24078 and 24055 cm^{-1} are both σ polarised. We assign these as transitions from thermally populated $^5D_3$ singlet levels at energies of 24362 and 24385 cm^{-1}. A σ polarised transition at 23875 cm^{-1} is assigned as the $D_1\gamma_5 \rightarrow Y_2\gamma_2$ transition. As with emission from $^5D_0$ and $^5D_1$, a vibronic state is observed 187 cm^1 from the $^5D_1\gamma_5 \rightarrow Y_1\gamma_5$ transition. The observation of the $^5D_3$ multiplet in the 24400 cm^{-1} region is in disagreement with the assignment of Hamers et. al. [104] who place this multiplet at around 25000 cm^{-1}.

Emission emanating from $^5D_3$ that terminates on the $^7F_2$ multiplet is observed in the 23600-23000 cm^{-1} region and is displayed in Figure 6.75. The highest frequency

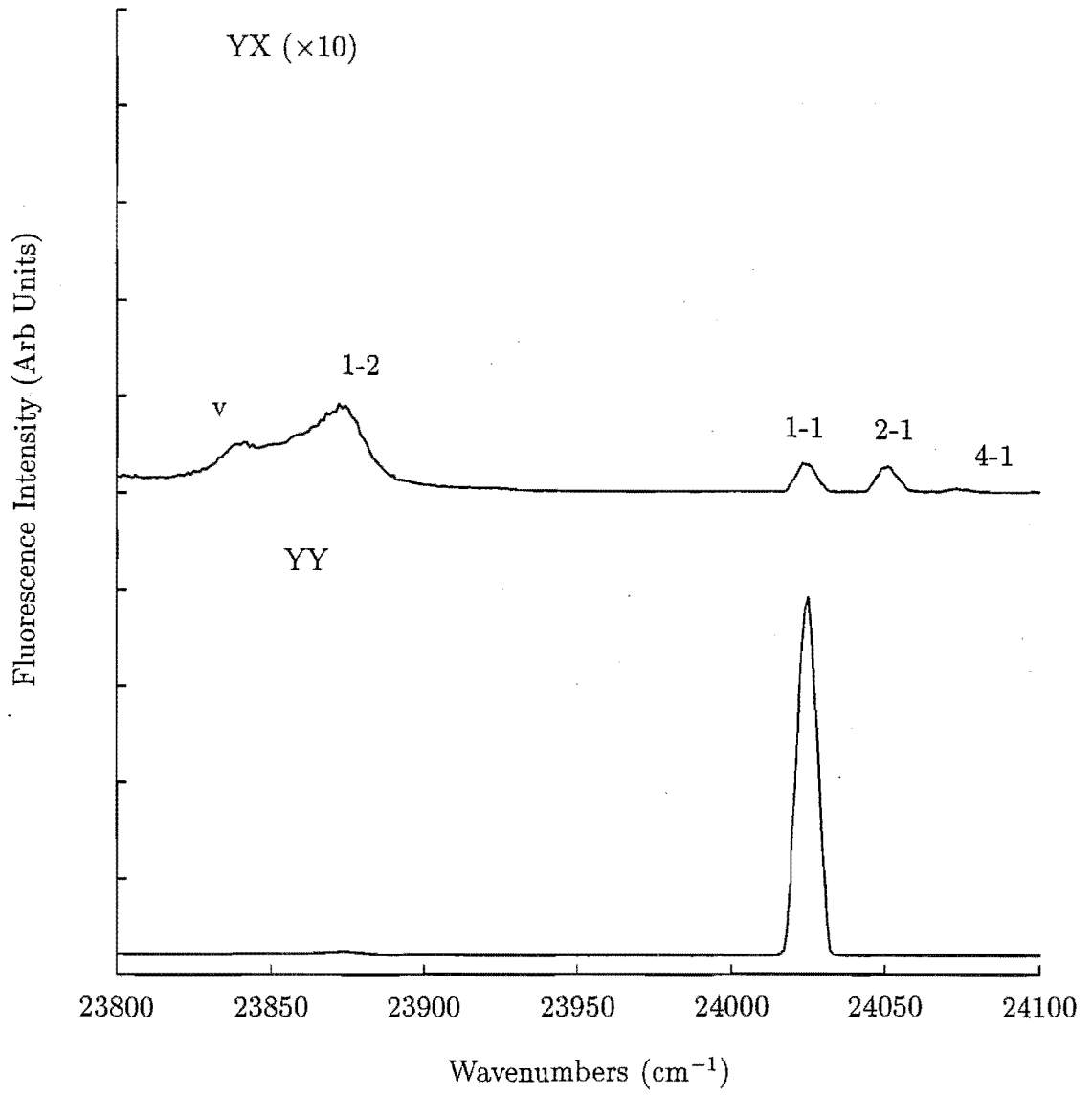

Figure 6.74: $^5D_3$ to $^7F_1$ polarised upconverted emission for the A centre in CaF_2:0.05%Eu^{3+}. v indicates a vibronic sideband. Excitation is at 17288 cm^{-1}. The spectra were recorded at 16K.

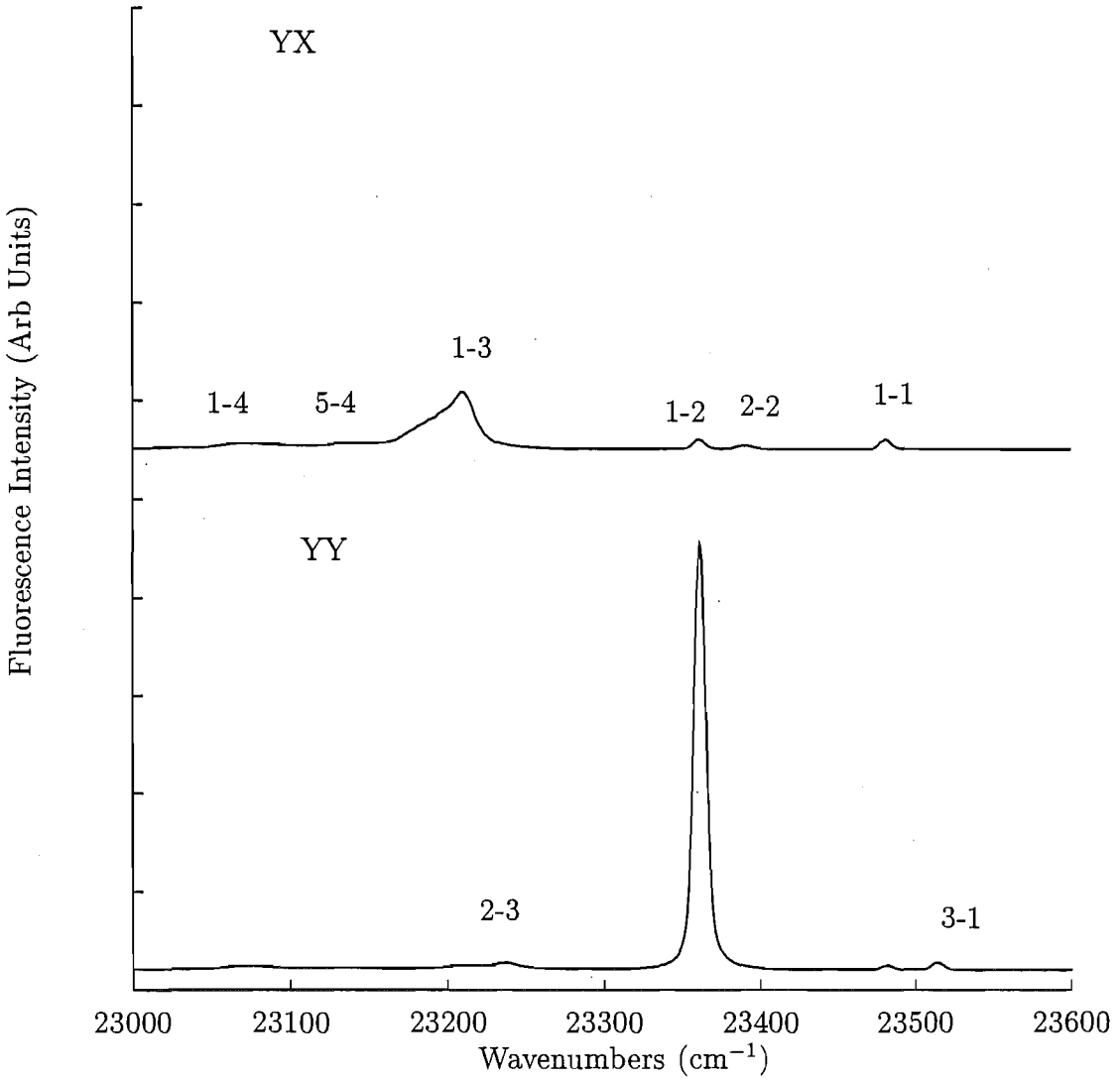

Figure 6.75: $^5D_3$ to $^7F_2$ polarised upconverted emission for the A centre in CaF_2:0.05%Eu^{3+}. Excitation is at 17288 cm^{-1}. The spectra were recorded at 16K.

transition, at 23519 cm^{-1}, is π polarised and originates from a thermally populated $^5D_3$ level. This transition terminates on the $X_1\gamma_4$ level at 852 cm^{-1} and thus we may assign the $^5D_3$ state as having γ_4 symmetry at 24371 cm^{-1}. We label this state D_3. The next transition at 23485 cm^{-1} is σ polarised consistent with the expected $D_1\gamma_5 \rightarrow X_1\gamma_4$ transition. The weak 23389 cm^{-1} transition is σ polarised emanating from the singlet state at 24360 cm^{-1} consistent with that observed from emission to $^7F_1$. The strong π polarised feature at 23365 cm^{-1} is the $D_1\gamma_5 \rightarrow X_2\gamma_5$ transition. The weak π polarised 23237 cm^{-1} transition terminates on the $X_3\gamma_3$ transition and originates from an upper state assigned as $D_2\gamma_3$ at 23360 cm^{-1}. The 23215 cm^{-1} transition is σ polarised and we assign this as the $D_1\gamma_5 \rightarrow X_3\gamma_3$ transition. The remaining observed transitions are both terminate on the $X_4\gamma_1$ state and are σ polarised. From this, we conclude that they originate from upper state doublets. The lower frequency transition at 23074 cm^{-1} is assigned as the $D_1\gamma_5 \rightarrow X_4\gamma_1$ transition. The broader higher frequency transition at 23136 cm^{-1} is assigned as emanating from the $D_5\gamma_5$ doublet state which is at 24397 cm^{-1}.

Upconversion fluorescence from the $^5D_3$ multiplet to $^7F_3$ multiplet is observed in the 22600-22100 cm^{-1} region as shown in Figure 6.76. Two small transitions at 22554 and 22534 cm^{-1} are observed to be σ and π polarised respectively. We assign these as the both originating from the $D_3\gamma_4$ state and terminating on the $W_1\gamma_5$ and $W_2\gamma_4$ states respectively. The stronger 22522 and 22503 cm^1 transitions are σ and π polarised and we assign these as the $D_1\gamma_5 \rightarrow W_1\gamma_5$ and $W_2\gamma_4$ transitions. The weak 22410 cm^{-1} transition has to be magnified 5 times to observe it clearly in the spectrum, it is σ polarised and terminates on the $W_3\gamma_5$ state. This is assigned as the $D_2\gamma_3 \rightarrow W_1\gamma_5$ transition. The strongest peak in the spectrum is π polarised $D_1\gamma_5 \rightarrow W_1\gamma_5$ emission at 22382 cm^{-1}, at the foot of which, lies a weak σ polarised transition which is assigned as the $D_1\gamma_5 \rightarrow W_4\gamma_2$ transition. Transitions from $D_2\gamma_3$ and $D_1\gamma_5$ are observed at 22226 and 22207 cm^{-1} repectively with π and σ polarisations consistent with this assignment.

Figure 6.77 shows $^5D_3$ emission to the $^7F_4$ multiplet in the 22000 - 21000 cm^{-1} region. Overlapping emission from the $^5D_2$ multiplet to both the $^7F_0$ and $^7F_1$ is observed, however this is relatively weak. The weak emission observed at 21876 cm^{-1} is π' polarised and terminates on the $V_1\gamma_1$ state. From this, we assign the upper level of this transition to be an unassigned state of $^5D_3$ at 24386 cm^{-1}. From its polarisation dependence, this state transforms as the γ_2 irrep of the C_{4v} symmetry point group. The 21825 cm^{-1} is σ' polarised and hence we assign this as the $D_1\gamma_5 \rightarrow V_1\gamma_1$ transition. Transitions at 21597 and 21569 cm^{-1} are π and σ' polarised, respectively. These are assigned as the $D_5\gamma_5 \rightarrow V_2\gamma_5$ and $D_3\gamma_4 \rightarrow V_2\gamma_5$ transitions. Strangely, no $D_1\gamma_5 \rightarrow V_2\gamma_5$ transition can be observed. A weak transition at 21493 is π polarised is assigned as the $C_2\gamma_1 \rightarrow Z_1$ transition. The 21388 cm^{-1} transition shows a mixed polarisation behaviour, despite this we assign this

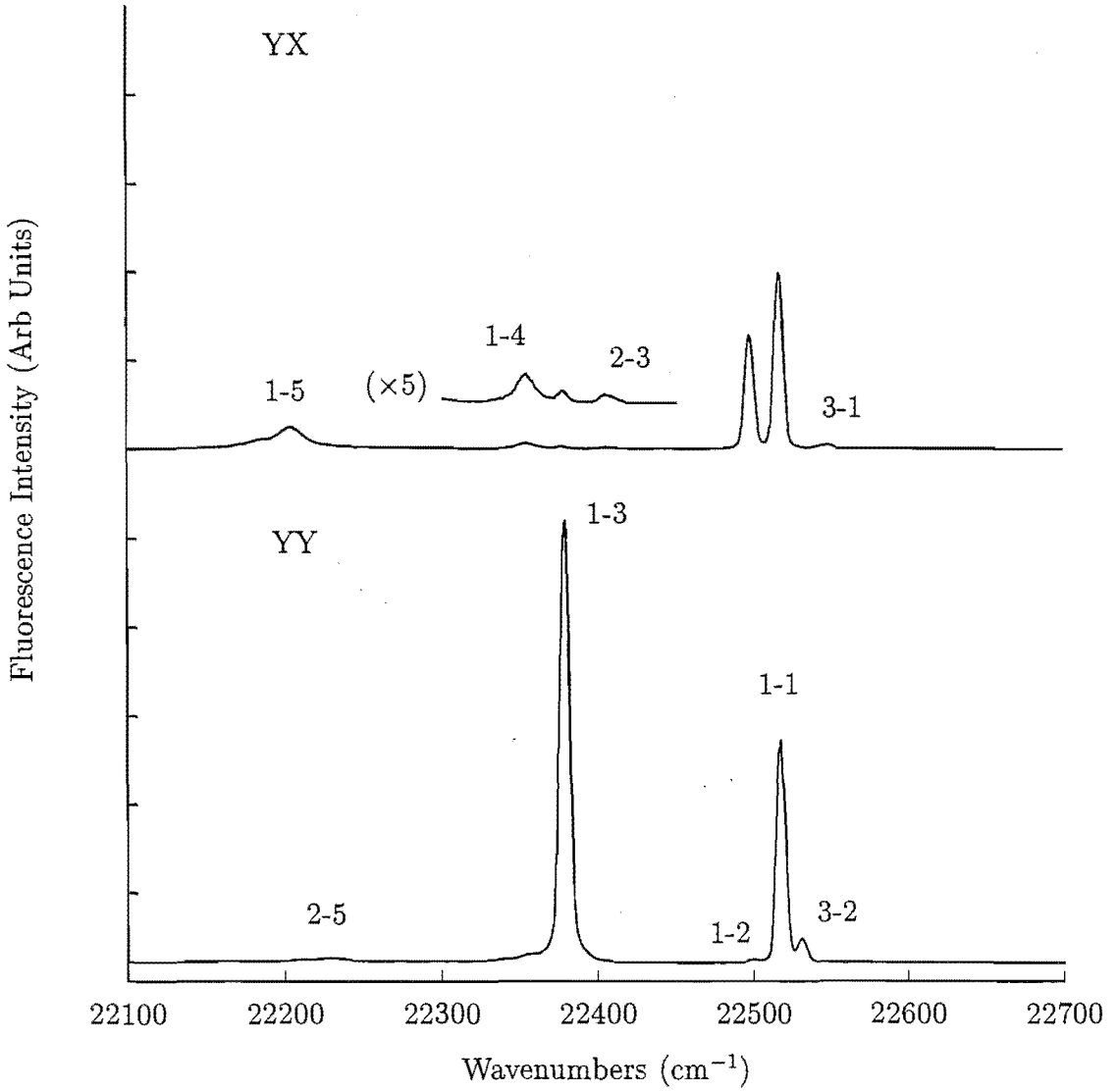

Figure 6.76: $^5D_3$ to $^7F_3$ polarised upconverted emission for the A centre in CaF_2:0.05%Eu^{3+}. Excitation is at 17288 cm^{-1}. The spectra were recorded at 16K.

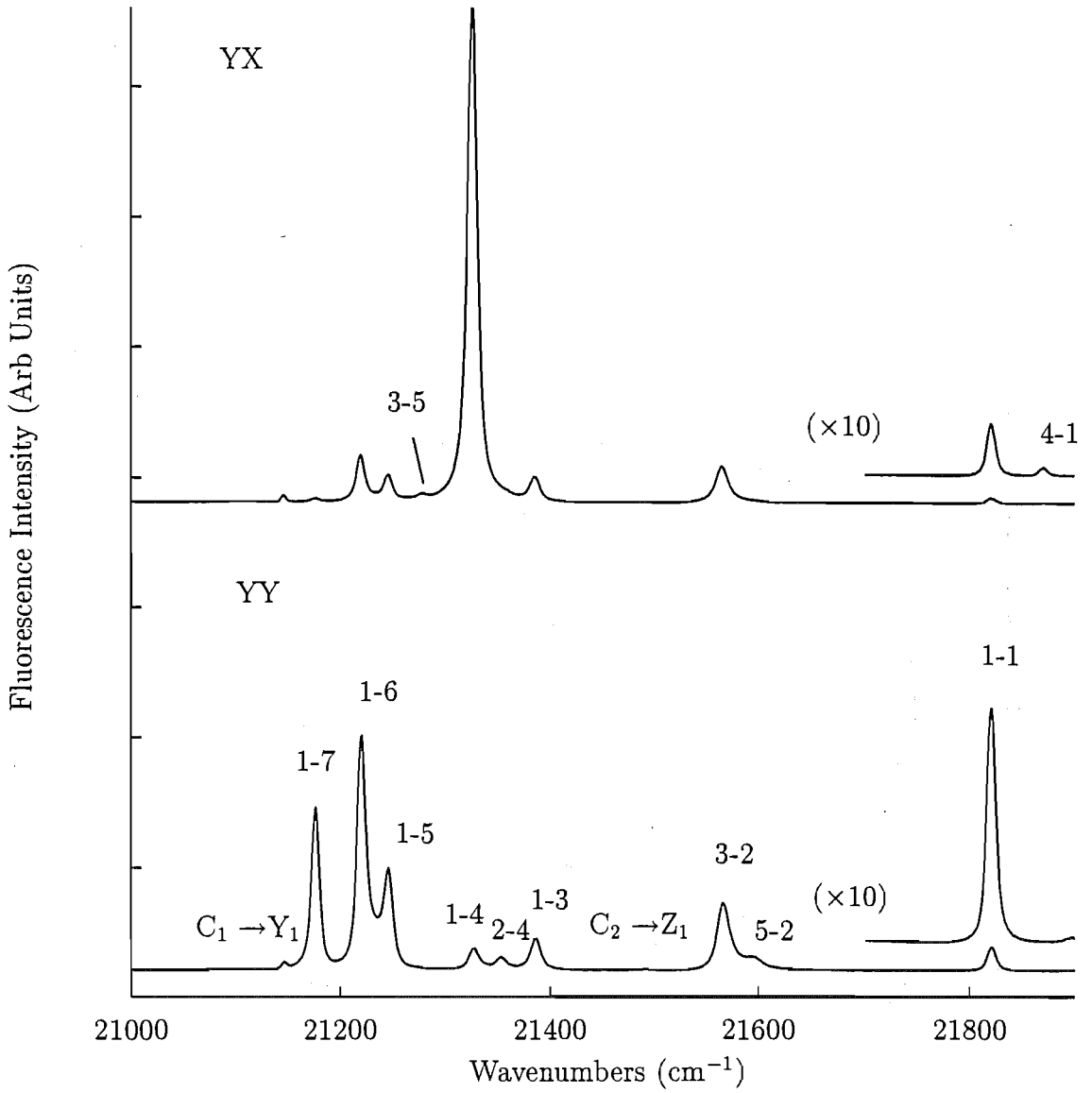

Figure 6.77: $^5D_3$ to $^7F_4$ polarised upconverted emission for the A centre in CaF_2:0.05%Eu^{3+}. Transitions emanating from $^5D_2$ are labelled appropriately. Excitation is at 17288 cm^{-1}. The spectra were recorded at 16K.

transition as $D_1\gamma_5 \rightarrow V_3\gamma_2$ from the good energy match this transition makes to the difference between these two levels. Transitions at 21348 and 21331 cm^{-1} are σ' and π' polarised respectively. These transitions emanate from the $D_2\gamma_3$ and $D_1\gamma_5$ states respectively, with them both terminating on the $V_4\gamma_5$ state. The next transition is π' polarised at a frequency of 21279 cm^{-1}, we assign this transition as $D_3\gamma_4 \rightarrow V_5\gamma_3$. The next three transitions all emanate from the $D_1\gamma_5$ level. They are observed at frequencies of 21249, 21223 and 21278 cm^{-1} and are σ' polarised indicating lower state singlets. We can assign these lower levels as the $V_5\gamma_3$, $V_6\gamma_4$ and $V_7\gamma_1$ states respectively. The lowest frequency transition in Figure 6.77 is at 21149 cm^{-1}. This displays no particularly strong polarisation dependence. It is assigned as emission from $^5D_2$ emanating from the lowest level of that multiplet at 21456 cm^{-1} (which is presumably a singlet of γ_3 or γ_4 symmetry as no emission to the ground state was observed). It is assigned as $C_1 \rightarrow Y_1\gamma_5$ because of the appropriate energy match.

Emission from $^5D_3$ to the $^7F_5$ multiplet is observed in the 20700 - 20100 cm^{-1} region. The spectrum is shown in Figure 6.78. This fluorescence overlaps with $^5D_2 \rightarrow ^7F_2$ transitions which occur in the same frequency region. The first two observed transitions are from thermally populated upper $^5D_3$ states and are very weak. These transitions are observed at frequencies of 20622 and 20613 cm^{-1}. From this, and the observed polarisation of these transitions of π and π' we assign these transitions as $D_3\gamma_4 \rightarrow U_1\gamma_4$ and $D_2\gamma_3 \rightarrow U_1\gamma_4$. The slightly stronger 20604 cm^{-1} transition emanates from $^5D_2$. It is π' polarised and is assigned as the $C_1\gamma_3 \rightarrow X_1\gamma_4$ transition. The dominant sharp transition is from the $^5D_3$ $D_1\gamma_5$ level to $X_1\gamma_4$ as determined from the measured transition energy of 20589 cm^{-1} and polarisation of σ. The 20556 and 20539 cm^{-1} transitions are weak and display a σ and σ' polarisation dependences. They are assigned as the $D_4\gamma_2 \rightarrow U_2\gamma_5$ and $D_3\gamma_4 \rightarrow U_2\gamma_5$ transitions as appropriate. An additional feature at 20533 cm^{-1} shows no particular polarisation dependence. From the frequency of this transition, we assign it as $D_2\gamma_3 \rightarrow U_2\gamma_5$. An extremely weak feature at 20521 cm^{-1} is determined to emanate from the $^5D_2$ multiplet. The observed σ polarisation dependence and appropriate frequency of the transition, leads to its assignment as the $C_2\gamma_1 \rightarrow X_2\gamma_5$ transition. The 20506 cm^{-1} transition is π polarised and can be assigned as the $D_1\gamma_5 \rightarrow U_2\gamma_5$ transition. The weaker broader transition at 20484 cm^{-1} is σ polarised. We assign this transition as $C_1\gamma_3 \rightarrow X_2\gamma_5$. The $D_1\gamma_5 \rightarrow U_3\gamma_2$ transition is observed at 20365 cm^{-1} and displays a σ polarisation dependence as expected. The observed lineshape of the transition at 20332 cm^{-1} is particularly asymmetrical. This is because of an underlying phonon structure which peaks 275 cm^{-1} displaced from the strong $D_1\gamma_5 \rightarrow U_1\gamma_4$ transition. This peak phonon energy is assigned as the (TO)L phonon peak by Ward and Whippy [89]. The 20332 cm^{-1} line is electronic and is π polarised. We assign this feature as $C_1\gamma_3 \rightarrow X_3\gamma_3$. A broad feature centred at 20256 cm^{-1} is assigned as the $D_3\gamma_4 \rightarrow U_6\gamma_5$ transition from its σ' polarisation dependence. The 20220 cm^{-1} is π' polarised from which we assign this transition as the $D_1\gamma_5 \rightarrow U_6\gamma_5$ transition.

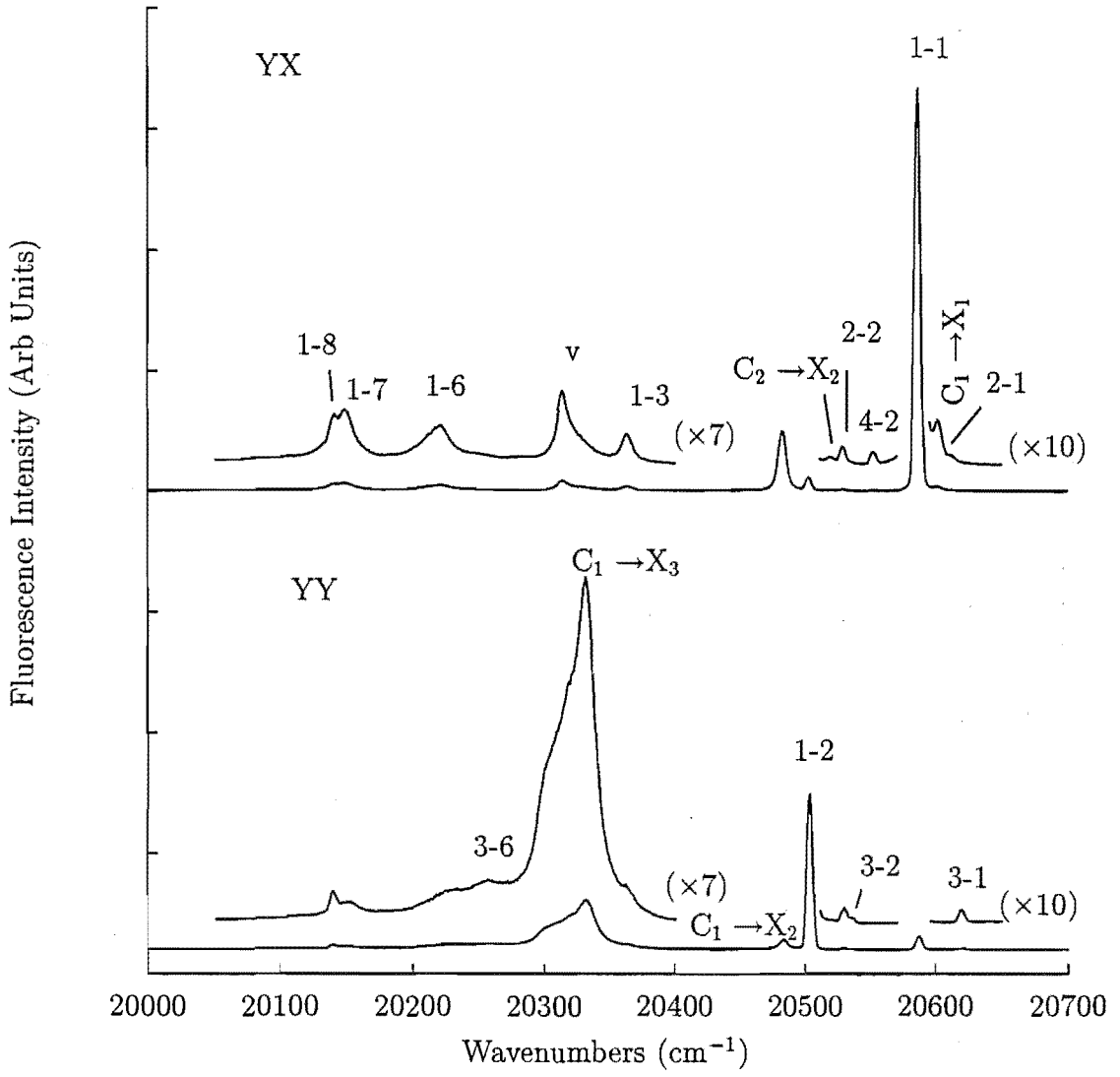

Figure 6.78: $^5D_3$ to $^7F_5$ polarised upconverted emission for the A centre in CaF_2:0.05%Eu^{3+}. Transitions emanating from $^5D_2$ are labelled appropriately. Excitation is at 17288 cm^{-1}. The spectra were recorded at 16K.

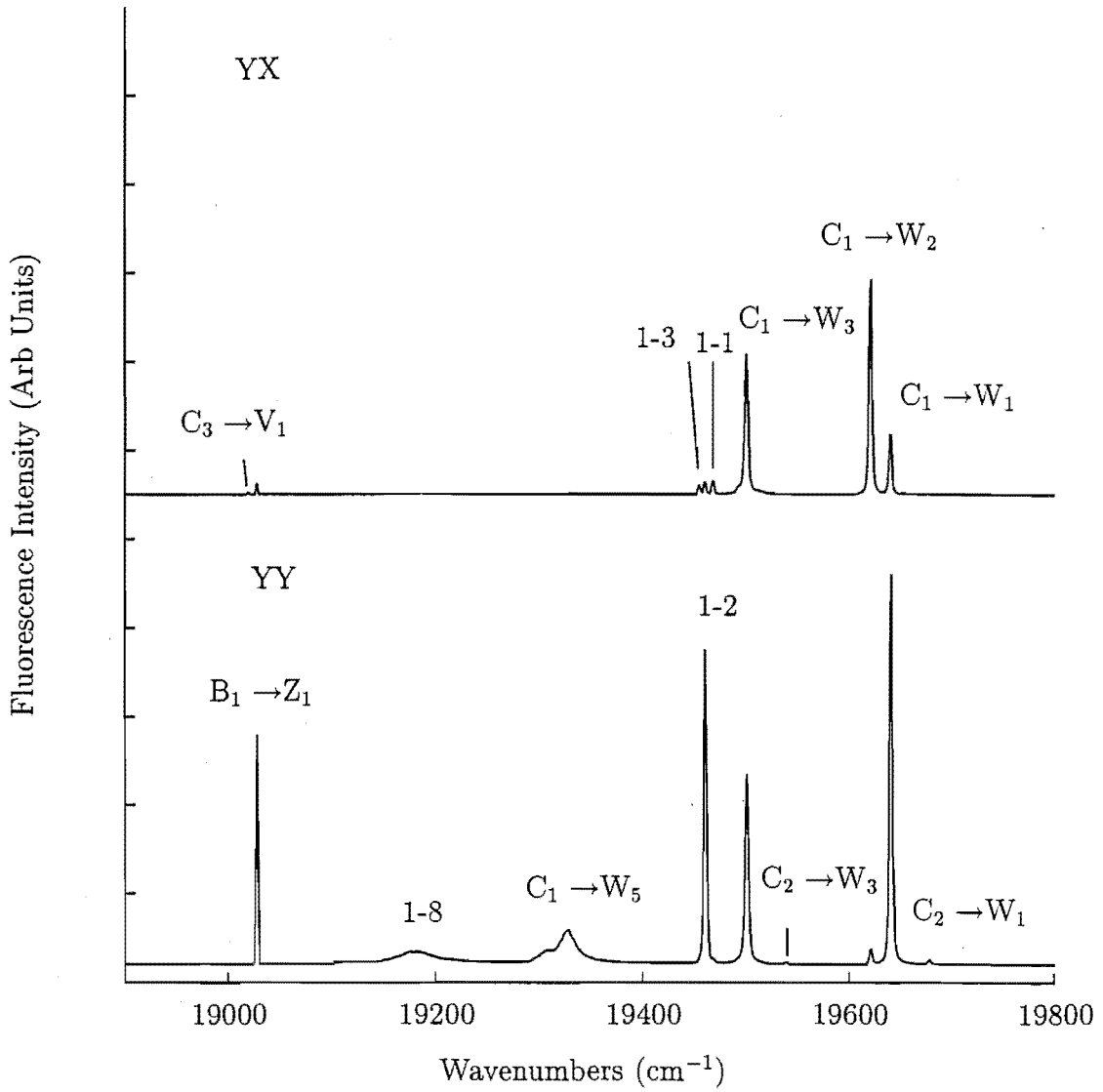

Figure 6.79: $^5D_3$ to $^7F_6$ polarised upconverted emission for the A centre in CaF_2:0.05%Eu^{3+}. Transitions emanating from $^5D_2$ and $^5D_1$ are labelled appropriately. Excitation is at 17288 cm^{-1}. The spectra were recorded at 16K.

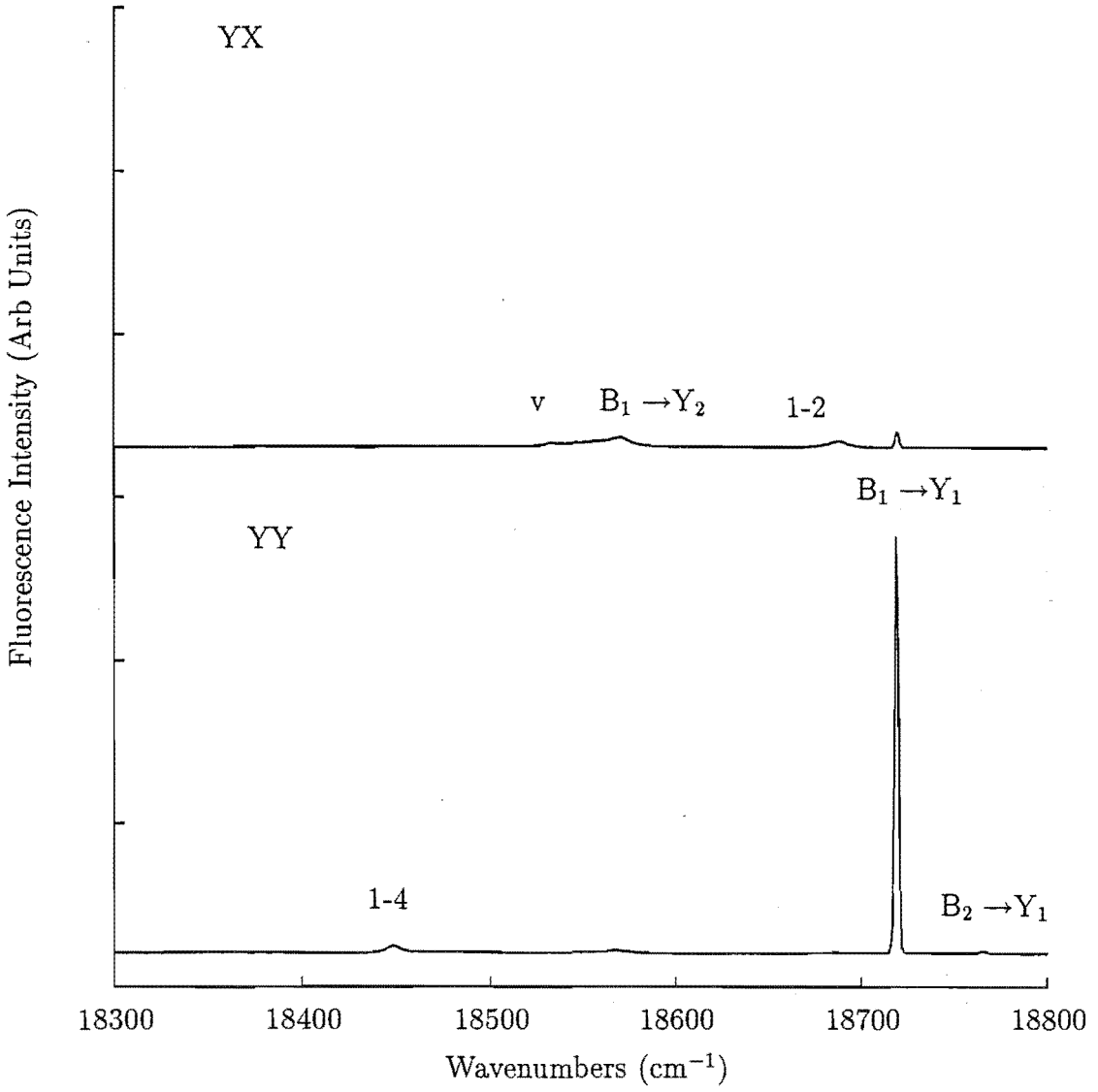

Figure 6.80: $^5D_2$ to $^7F_4$ polarised upconverted emission for the A centre in CaF_2:0.05%Eu^{3+}. Transitions emanating from $^5D_1$ are labelled appropriately. Excitation is at 17288 cm^{-1}. The spectra were recorded at 16K.

Table 6.15: Polarisation data, frequencies and transition assignments of upconverted fluorescence for the A centre in CaF_2:0.05%Eu^{3+}. Frequencies are in air cm^{-1} (± 1 unless otherwise stated). Excitation is at 17288 cm^{-1}.

Transition Frequency	Polarisation Assignment	Transition Assignment	Transition Frequency	Polarisation Assignment	Transition Assignment
24078	σ	$D_4\gamma_2 \rightarrow Y_1\gamma_5$	20604	π	$C_1\gamma_3 \rightarrow X_1\gamma_4$
24055	σ	$D_2\gamma_3 \rightarrow Y_1\gamma_5$	20589	σ	$D_1\gamma_5 \rightarrow U_1\gamma_4$
24028	π	$D_1\gamma_5 \rightarrow Y_1\gamma_5$	20556	σ	$D_4\gamma_2 \rightarrow U_2\gamma_5$
23873	σ	$D_1\gamma_5 \rightarrow Y_2\gamma_2$	20539	σ'	$D_3\gamma_4 \rightarrow U_2\gamma_5$
23519	π	$D_3\gamma_4 \rightarrow X_1\gamma_4$	20533	(mixed)	$D_2\gamma_3 \rightarrow U_2\gamma_5$
23485	σ	$D_1\gamma_5 \rightarrow X_1\gamma_4$	20521	σ	$C_2\gamma_1 \rightarrow X_2\gamma_5$
23389	σ	$D_2\gamma_5 \rightarrow X_2\gamma_5$	20506	π	$D_1\gamma_5 \rightarrow U_2\gamma_5$
23365	π	$D_1\gamma_5 \rightarrow X_2\gamma_5$	20484	σ	$C_1\gamma_3 \rightarrow X_2\gamma_5$
23237	π	$D_2\gamma_3 \rightarrow X_3\gamma_3$	20365	σ	$D_1\gamma_5 \rightarrow U_3\gamma_2$
23215	σ	$D_1\gamma_5 \rightarrow X_3\gamma_3$	20332	π	$C_1\gamma_3 \rightarrow X_3\gamma_3$
23074	σ	$D_1\gamma_5 \rightarrow X_4\gamma_1$	20256$\pm$2	σ'	$D_3\gamma_4 \rightarrow U_6\gamma_5$
22554	σ	$D_3\gamma_4 \rightarrow W_1\gamma_5$	20220	π'	$D_1\gamma_5 \rightarrow U_6\gamma_5$
22534	π	$D_3\gamma_4 \rightarrow W_2\gamma_4$	20152	σ	$D_1\gamma_5 \rightarrow U_7\gamma_1$
22522	π	$D_1\gamma_5 \rightarrow W_5\gamma_5$	20143	σ	$D_1\gamma_5 \rightarrow U_8\gamma_2$
22503	σ	$D_1\gamma_5 \rightarrow W_2\gamma_4$	19678	σ'	$C_2\gamma_1 \rightarrow W_1\gamma_5$
22410	σ	$D_2\gamma_3 \rightarrow W_3\gamma_5$	19642	σ'	$C_1\gamma_3 \rightarrow W_1\gamma_5$
22382	π	$D_1\gamma_5 \rightarrow W_3\gamma_5$	19622	π'	$C_1\gamma_3 \rightarrow W_2\gamma_4$
22359	σ	$D_1\gamma_5 \rightarrow W_4\gamma_2$	19540	σ'	$C_2\gamma_1 \rightarrow W_3\gamma_5$
22226	π	$D_2\gamma_3 \rightarrow W_5\gamma_3$	19502	σ'	$C_1\gamma_3 \rightarrow W_3\gamma_5$
22207	σ	$D_1\gamma_5 \rightarrow W_5\gamma_3$	19497	π'	$D_2\gamma_3 \rightarrow T_1\gamma_4$
21876	π'	$D_4\gamma_2 \rightarrow V_1\gamma_1$	19468	σ	$D_1\gamma_5 \rightarrow T_1\gamma_4$
21825	σ'	$D_1\gamma_5 \rightarrow V_1\gamma_1$	19462	π	$D_1\gamma_5 \rightarrow T_2\gamma_5$
21597	π	$D_5\gamma_5 \rightarrow V_2\gamma_5$	19459	σ	$D_1\gamma_5 \rightarrow T_3\gamma_1$
21569	σ'	$D_3\gamma_4 \rightarrow V_2\gamma_5$	19328	π	$C_1\gamma_3 \rightarrow W_5\gamma_3$
21493	π	$C_2\gamma_1 \rightarrow Z_1\gamma_1$	19179$\pm$5	π	$D_1\gamma_5 \rightarrow T_5\gamma_5$
21388	(mixed)	$D_1\gamma_5 \rightarrow V_3\gamma_2$	19030	σ'	$B_1\gamma_5 \rightarrow Y_1\gamma_5$
21348	σ'	$D_2\gamma_3 \rightarrow V_4\gamma_5$	19020	σ'	$C_3\gamma_5 \rightarrow V_1\gamma_1$
21331	π'	$D_1\gamma_5 \rightarrow V_4\gamma_5$	18770	σ'	$B_2\gamma_2 \rightarrow Y_1\gamma_5$
21279	π'	$D_3\gamma_4 \rightarrow V_5\gamma_3$	18722	π	$B_1\gamma_5 \rightarrow Y_1\gamma_5$
21249	σ'	$D_1\gamma_5 \rightarrow V_5\gamma_3$	18688	σ	$C_2\gamma_1 \rightarrow V_2\gamma_5$
21223	σ'	$D_1\gamma_5 \rightarrow V_6\gamma_4$	18570	σ	$B_1\gamma_5 \rightarrow Y_2\gamma_2$
21178	σ'	$D_1\gamma_5 \rightarrow V_7\gamma_1$	18449	σ'	$C_1\gamma_3 \rightarrow V_4\gamma_5$
21149	(mixed)	$C_1\gamma_3 \rightarrow Y_1\gamma_5$	18177	σ'	$B_1\gamma_5 \rightarrow X_1\gamma_4$
20622	π	$D_3\gamma_4 \rightarrow U_1\gamma_4$	18057	π'	$B_1\gamma_5 \rightarrow X_2\gamma_5$
20613	π'	$U_2\gamma_3 \rightarrow U_1\gamma_4$	17906	σ'	$B_1\gamma_5 \rightarrow X_3\gamma_3$

The overlapping transitions at 20152 and 20143 cm^{-1} both σ polarised. From this we infer that these are transitions from $D_1\gamma_5$ to the previously unobserved U_7 and U_8 states which are assigned to be singlets of γ_1 and γ_2 symmetry respectively as is consistent with crystal field calculations, fitting to all levels observed in down conversion.

Transitions from $^5D_3$ to $^7F_6$ and $^5D_2$ to $^7F_3$ occur in the 19800-19100 cm^{-1} region and are shown in Figure 6.79. We discuss the transitions emanating from $^5D_3$ first. Three transitions bunched together at 19468, 19462 and 19459 cm^{-1} are transitions from the $D_1\gamma_5$ level to the $T_1\gamma_4$, $T_2\gamma_5$ and $T_3\gamma_1$ states respectively, as is indicated by the respective σ, π and σ polarisation behaviour of these transitions. Only one additional transition from $^5D_3$ is observed at 19179 cm^{-1}. This is σ polarised and is assigned as the $D_1\gamma_5 \rightarrow T_5\gamma_5$ transition. The transitions from $^5D_2$ are, in general, the strongest features observed in Figure 6.79. The first of these transitions is very weak. It is observed at 19678 and is assigned as $C_2\gamma_1 \rightarrow W_1\gamma_5$ from the observed σ' polarisation dependence. The next two transitions are much stronger at frequencies of 19642 and 19622 cm^{-1}. These transitions display σ' and π' dependencies respectively. From this, we assign these transitions as $C_1\gamma_3 \rightarrow W_1\gamma_5$ and $W_2\gamma_4$. The next transition is weak. This is at a frequency of 19540 cm^{-1} and is σ' polarised. This transition is assigned as originating from the $C_2\gamma_1$ state and terminates on $W_3\gamma_5$. The transition at 19502 cm^{-1} does not give a clear polarisation ratio, but the transition frequency is in good agreement with the energy mismatch between $C_1\gamma_3$ and $W_3\gamma_5$ states . The significantly broader 18328 cm^{-1} transition is π polarised and assigned as the $C_1\gamma_3 \rightarrow W_5\gamma_3$ transition. A further emission feature from the $^5D_2$ multiplet is observed at 19020 cm^{-1}. This transition is σ' polarised indicating a transition from a doublet state. The final state is clearly the $V_1\gamma_1$ state due to its spectral isolation. Thus, it is concluded that there is a γ_5 doublet at an energy of 21530 $cm^{-1}(C_3\gamma_5)$. This in agreement with the study of Hamers et. al. [104] who found an excitation feature at approximately this frequency. The final emission feature observable in Figure 6.79 is at a frequency of 19030 cm^{-1} and is σ' polarised. This leaves no doubt that this is the $B_1\gamma_5 \rightarrow Z_1\gamma_1$ transition.

The remaining transitions from $^5D_2$ to the $^7F_4$ multiplet are shown in Figure 6.80. Also shown in Figure 6.80 are transitions from $^5D_1$ to the $^7F_1$ multiplet which have been discussed previously in the down converted spectra. Transitions at 18688 and 18449 cm^{-1} emanate from $^5D_2$. The first of these transitions is σ polarised and assigned as $C_1\gamma_3 \rightarrow V_2\gamma_5$. The second is σ polarised and we assign as $C_1\gamma_3 \rightarrow V_4\gamma_5$. No further emission features could be detected from $^5D_2$.

6.5.3 SrF_2:Eu^{3+} - A Centre

For excitation of the 17298 cm^{-1} $^7F_0 \rightarrow ^5D_0$ transition, the highest frequency emission observed emanates from the $^5H_3$ multiplet at around 29950 cm^{-1}, as shown in Figure 6.81. This fluorescence is extremely weak and the spectrometer slits were set at 3mm with 400 mW of R560 excitation. Due to the wide slit settings, little meaningful data could be collected from the observed fluorescence as the frequency resolution was low.

$^5D_3 \rightarrow ^7F_1$ emission is observed in the 24100-23900 cm^{-1} region. Three electronic transitions are observed. Two of these transitions are assigned to terminate on the $Y_1\gamma_5$ level at 324 cm^{-1}. These are at frequencies of 24067 and 24049 cm^{-1} and are σ and π polarised respectively. They are assigned as originating from the $D_2\gamma_3$ and $D_1\gamma_5$ states. This places these states at 24391 and 24373 cm^{-1}. The broader 23938 cm^{-1} transition is σ polarised and is assigned as the $D_1\gamma_5 \rightarrow Y_2\gamma_2$ transition (Figure 6.82). No $^5D_3 \rightarrow Z_1\gamma_1$ transition was observed. Upconverted transition energies and polarisation assignments are given in Table 6.16. A feature labelled v in Figure 6.82 is not listed in Table 6.16 because only electronic transitions have been given. This feature, at 23742 cm^{-1} is assigned as a transition terminating on vibronic levels of the SrF_2 host lattice.

It can be observed in Figure 6.83, that transitions from $^5D_3$, which terminate on $^7F_2$ are observed in the 23600-23100 cm^{-1} region. A number of transitions are observed. These correspond to emission from three different levels of the $^5D_3$ multiplet. The 23528 and 23498 cm^{-1} transitions terminate on the $X_1\gamma_4$ transition at 874 cm^{-1}. These transitions are electric dipole π and magnetic dipole σ' polarised respectively. In accordance with this, they have been assigned as the $D_3\gamma_4$ and $D_1\gamma_5 \rightarrow X_1\gamma_4$ transitions respectively. This places the $D_3\gamma_4$ state at 24402 cm^{-1}. Three transitions are observed to the $X_2\gamma_5$ state at 968 cm^{-1}. The two higher energy 23430 and 23422 cm^{-1} states are both σ polarised and are therefore assigned as transitions from the $D_3\gamma_4$ and $D_2\gamma_3$ states respectively. The 23404 cm^{-1} transition is π polarised and assigned to emanate from the $D_1\gamma_5$ state. Two broader transitions are observed at 23243 and 23201 cm^{-1}. These are assigned as the $D_3\gamma_4$ and $D_1\gamma_5 \rightarrow X_3\gamma_3$ transitions. The observed π' and σ polarisation for these transitions. It is noted by the author that the $D_2\gamma_3 \rightarrow X_3\gamma_3$ transition is missing here. This is unusual since its inverted polarisation behaviour to the two observed transitions should enable it to be observed clearly even if it is weak.

Eleven transitions are observed from the $^5D_3$ multiplet to $^7F_3$ in the 22600-22200 cm^{-1} region (Figure 6.84). The $W_1\gamma_5$ and $W_2\gamma_4$ states are separated by 18 cm^{-1} and transitions from the $^5D_3$ multiplet to these two levels overlap and form an initially

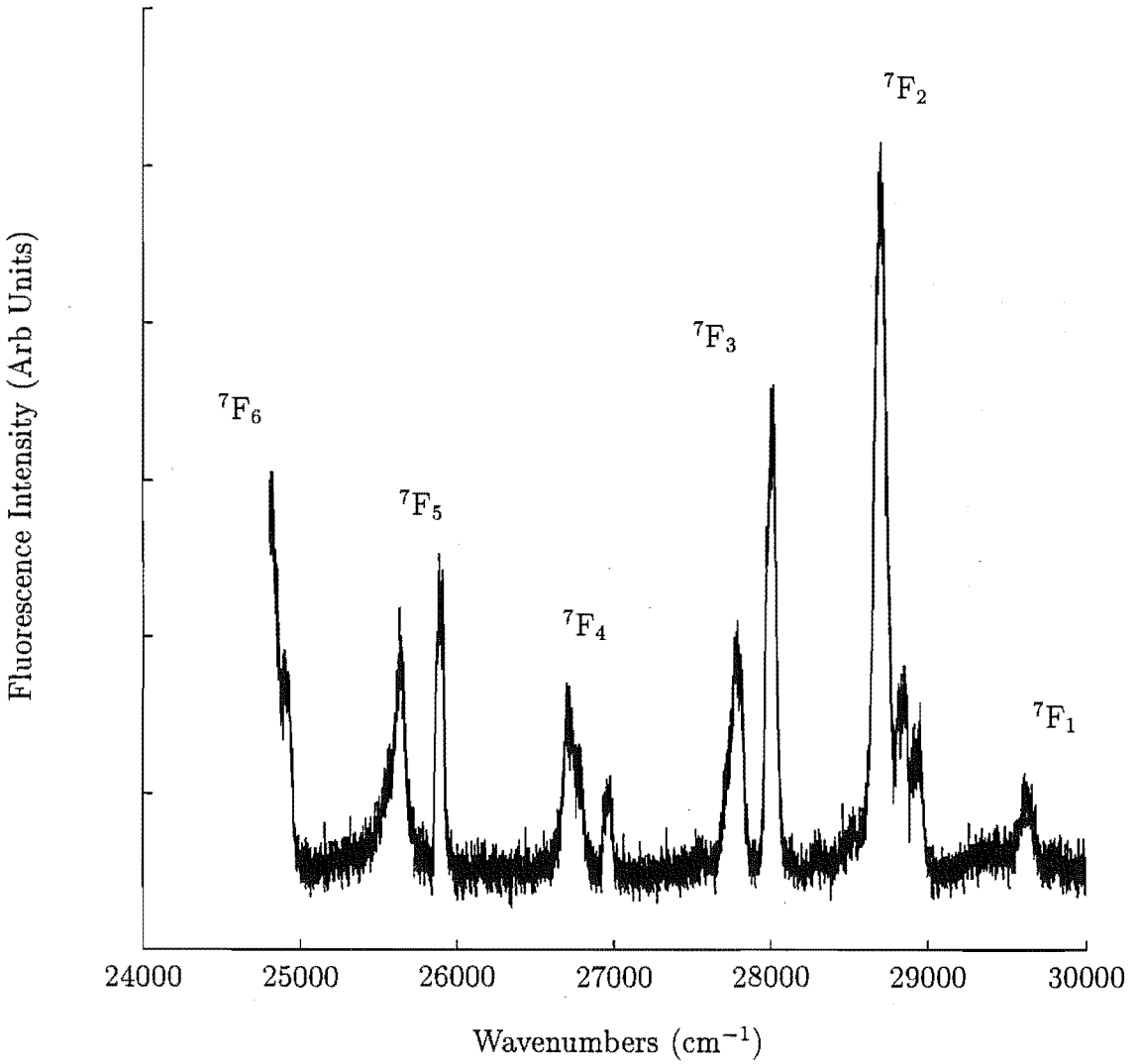

Figure 6.81: $^5H_3$ to ^7F_J multiplet upconverted emission for the A centre in SrF_2:0.05%Eu^{3+}. Excitation is at 17298 cm^{-1}. The spectra were recorded at 16K.

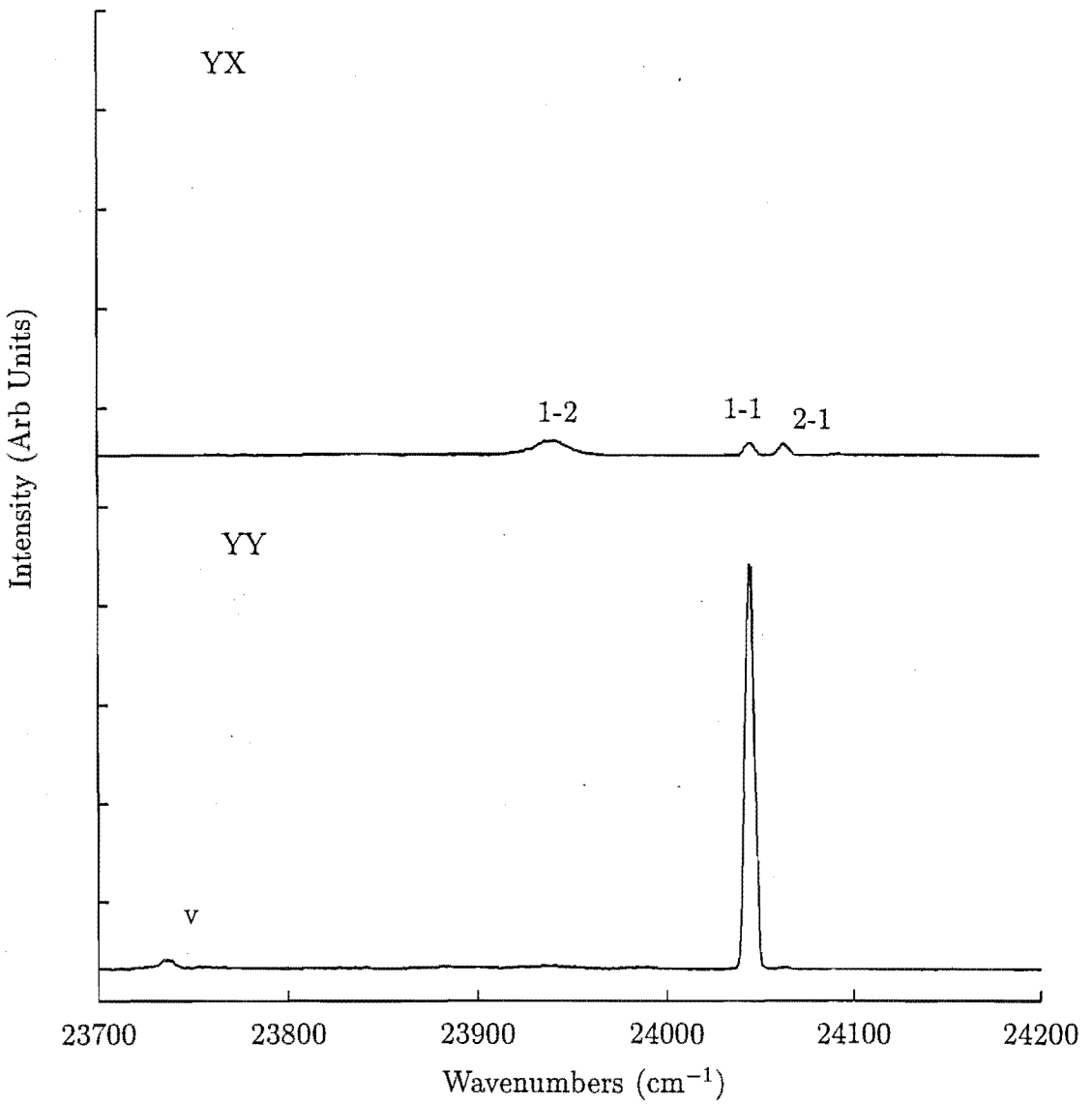

Figure 6.82: $^5D_3$ to $^7F_1$ polarised upconverted emission for the A centre in SrF_2:0.05%Eu^{3+}. v indicates a vibronic sideband. Excitation is at 17298 cm^{-1}. The spectra were recorded at 16K.

confusing pattern. An extremely weak transition at 22584 cm^{-1} is assigned as the $D_5\gamma_5 \rightarrow W_2\gamma_4$ transition. The σ' polarisation of this level is consistent with this and the $D_5\gamma_5$ level is assigned an energy 24437 cm^{-1} above the ground state. Immediately following this, are two σ polarised transitions which are assigned as terminating on the $W_1\gamma_5$ state. These transitions must therefore, emanate from singlet states. They are observed at energies of 22565 and 22556 cm^{-1} and are assigned as the $D_3\gamma_4$ $D_2\gamma_3 \rightarrow W_1\gamma_5$ transitions. The 22548 cm^{-1} transition is π polarised and consistent with a $D_3\gamma_4 \rightarrow W_2\gamma_4$ transition. A strong transition is observed at 22537 cm^{-1} which does not exhibit a well defined polarisation ratio. This is a good indication that at least one γ_5 is involved in the transition. Both D_1 and W_1 are γ_5 doublet states. This transition is a good match energetically for a transition between $D_1\gamma_5$ and $W_1\gamma_5$ and is assigned as such. The next observed transition at 22520 cm^{-1} displays a well defined polarisation behaviour and is σ polarised. This is assigned as a $D_1\gamma_5 \rightarrow W_2\gamma_4$ transition. Two transitions at 22458 and 22449 cm^{-1} are much weaker than the previous transition and are both σ polarised. They are assigned as the $D_3\gamma_4$ and $D_2\gamma_3 \rightarrow W_4\gamma_5$ transitions. The more intense transition at 22430 cm^{-1}, being the expected $D_1\gamma_5 \rightarrow W_4\gamma_5$. The π polarisation of this transition confirms this assignment. The next two transitions are broad and are not distinguishable prior to polarising the spectrum. These are the $D_2\gamma_3$ and $D_1\gamma_5 \rightarrow W_5\gamma_3$ transitions. The two transitions are observed at 22293 and 22284 cm^{-1} and are π and σ polarised.

Transitions from $^5D_3$ to the $^7F_4$ multiplet are shown in Figure 6.85 and are observed in the 22000-21200 cm^{-1} region. Two transitions are observed to the $V_1\gamma_1$ level. These are magnetic dipole π' and σ' polarised transitions and are assigned as the $D_4\gamma_2$ and $D_1\gamma_5 \rightarrow V_1\gamma_1$ transitions at 21886 and 21839 cm^{-1} respectively. This yields the $D_4\gamma_2$ state energy as 24417 cm^{-1}. Three transitions to the $V_2\gamma_5$ level are observed at 21620, 21609 and 21590 cm^{-1}. The first two transitions are both σ' polarised and are assigned as emanating from the $D_3\gamma_4$ and $D_2\gamma_3$ states respectively. The last transition to the $V_2\gamma_5$ state does not give a particularly well defined polarisation ratio and is assigned as the $D_1\gamma_5 \rightarrow V_2\gamma_5$ transition. The 21450 cm^{-1} transition is assigned as the $D_1\gamma_5 \rightarrow V_3\gamma_2$ transition because of the appropriate energy match. Two transitions to the $V_4\gamma_5$ state are observed at 21395 and 21385 cm^{-1}. They are σ' and π' polarised respectively and are assigned as emanating from $D_2\gamma_3$ and $D_1\gamma_5$. The 21347 cm^{-1} transition is observed as a foot on the $D_1\gamma_5 \rightarrow V_4\gamma_5$ transition and is π' polarised. It is assigned as the $D_3\gamma_4 \rightarrow V_5\gamma_3$ transition. The next observed transition is at 21322 cm^{-1} and is σ' polarised. This is the $D_1\gamma_5 \rightarrow V_5\gamma_3$ transition. The 21304 and 21292 cm^{-1} transitions terminate on the $V_6\gamma_4$ level. They are π' and σ' polarised respectively, and emanate from $D_2\gamma_3$ and $D_1\gamma_5$ in turn. The observation of the $D_3\gamma_4 \rightarrow V_5\gamma_3$ and $D_2\gamma_3 \rightarrow V_6\gamma_4$ transitions is interesting as no corresponding $D_2\gamma_3 \rightarrow V_5\gamma_3$ and $D_3\gamma_4 \rightarrow V_6\gamma_4$ transitions are observed. This indicates that the $^5D_3 \rightarrow {}^7F_4$ emission is dominated by magnetic dipole transitions. Finally, the 21255 cm^{-1} transition is assigned as $D_1\gamma_5 \rightarrow V_7\gamma_1$ as is consistent with the observed σ'

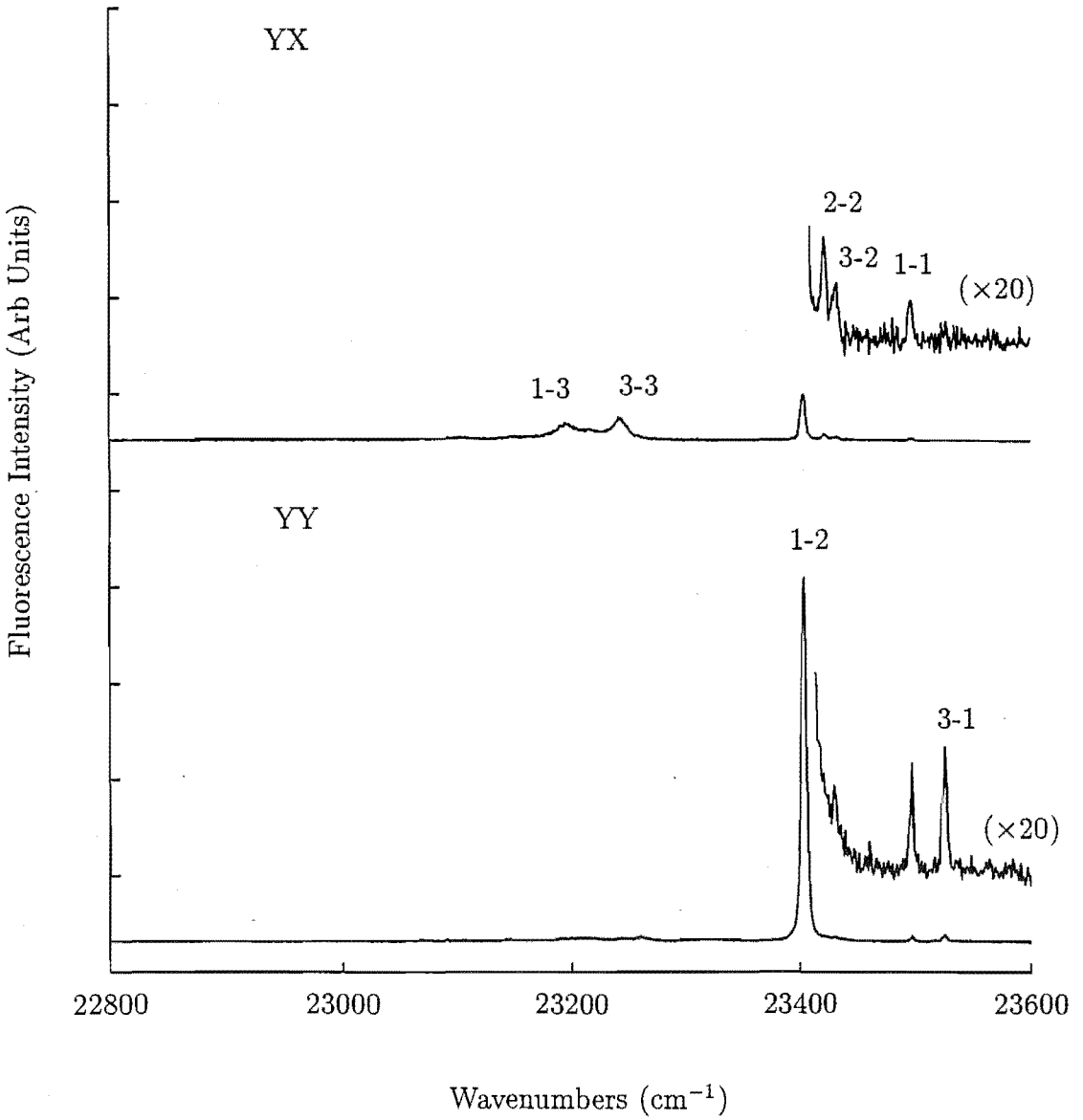

Figure 6.83: $^5D_3$ to $^7F_2$ polarised upconverted emission for the A centre in SrF_2:0.05%Eu^{3+}. Excitation is at 17298 cm^{-1}. The spectra were recorded at 16K.

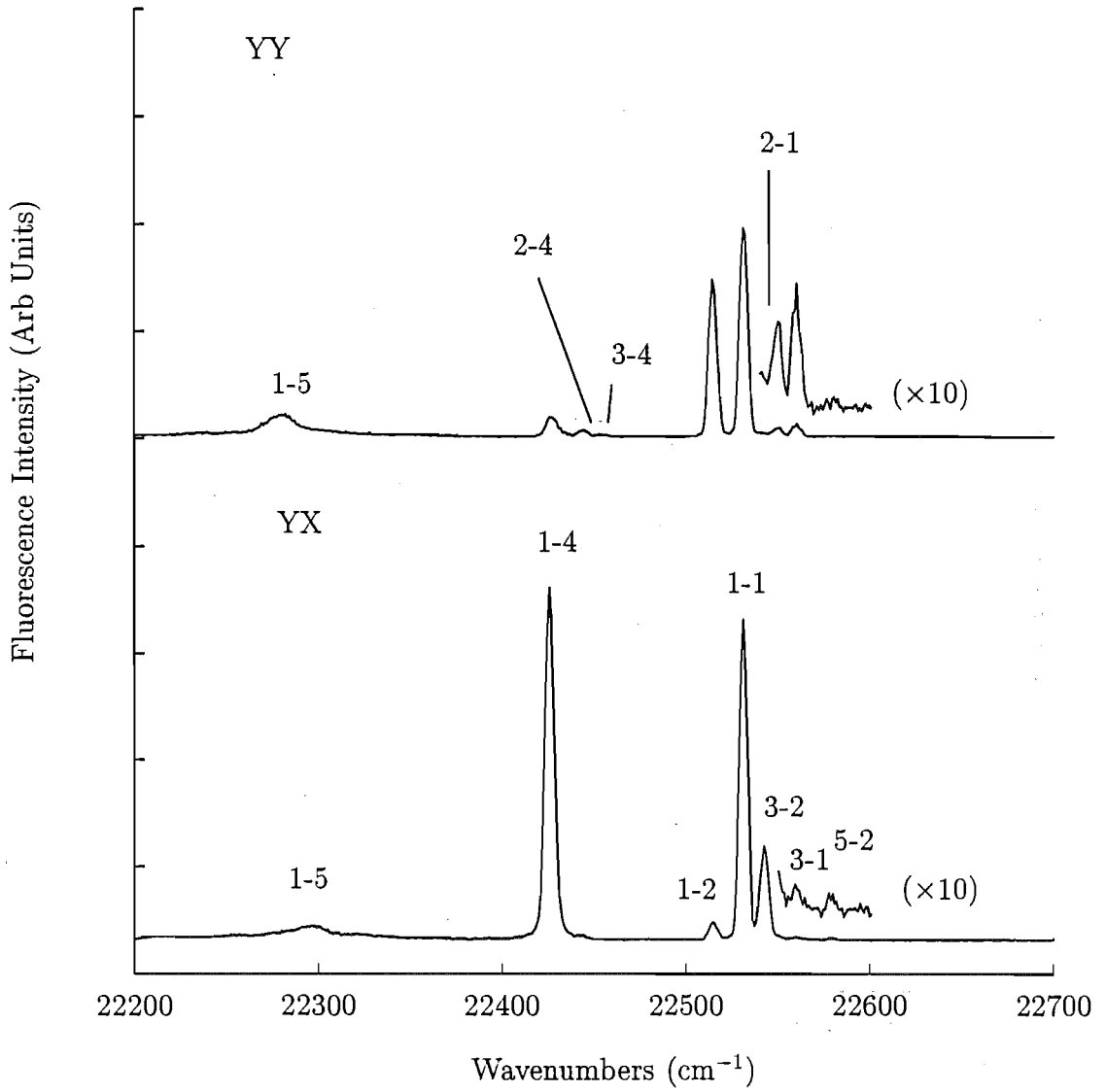

Figure 6.84: $^5D_3$ to $^7F_3$ polarised upconverted emission for the A in SrF_2:0.05%Eu^{3+}. Excitation is at 17298 cm^{-1}. The spectra were recorded at 16K.

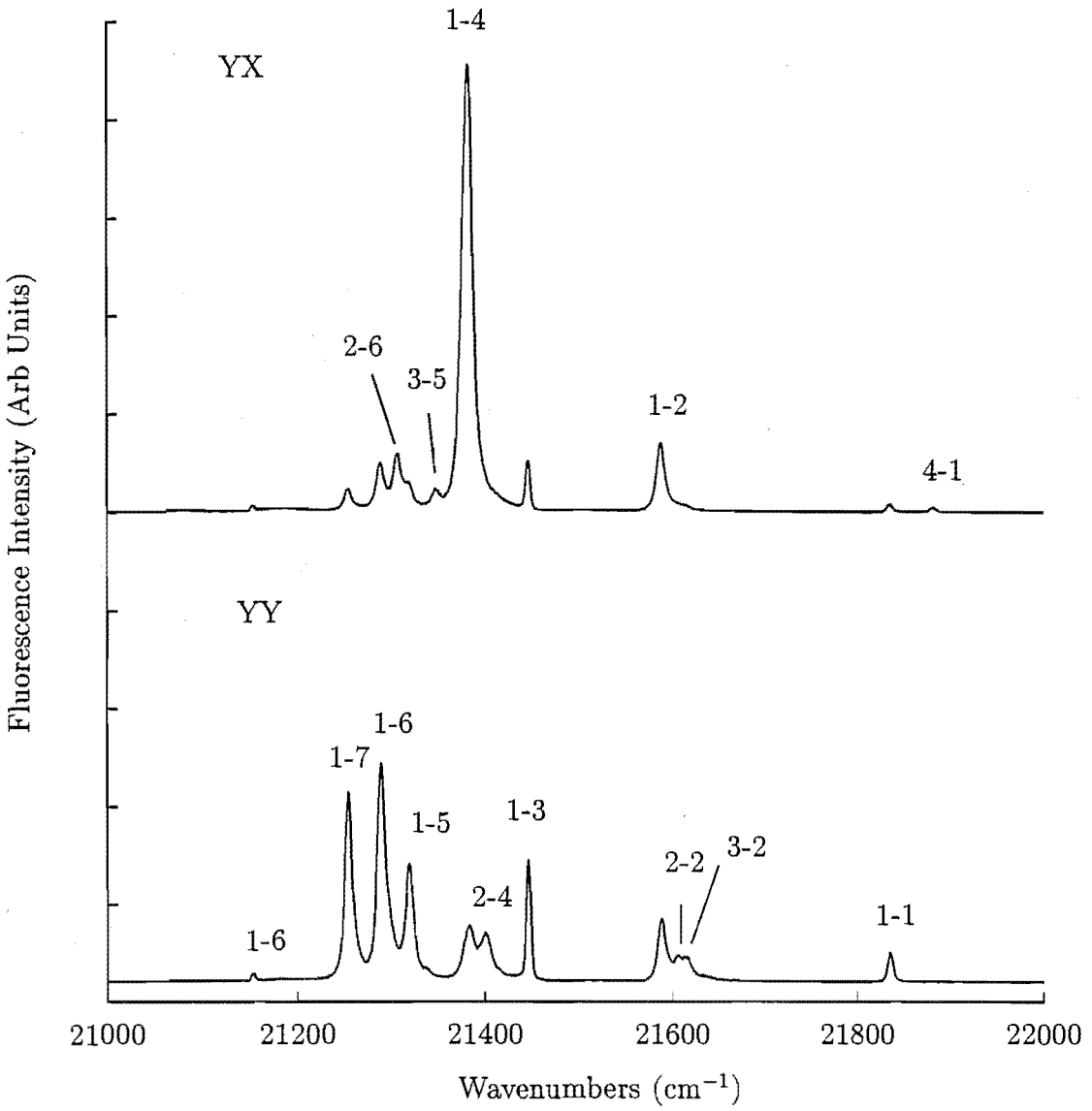

Figure 6.85: $^5D_3$ to $^7F_4$ polarised upconverted emission for the A centre in SrF_2:0.05%Eu^{3+}. Transitions emanating from $^5D_2$ are labelled appropriately. Excitation is at 17298 cm^{-1}. The spectra were recorded at 16K.

polarisation of this transition. An additional weak transition at 21156 cm^{-1} is the $C_1\gamma_3 \rightarrow Y_1\gamma_5$ transition. This places the $C_1\gamma_3$ state 21480 cm^{-1} above the ground state. No $C_1\gamma_3 \rightarrow Y_2\gamma_2$ transition would be expected to be observed due to the C_{4v} selection rules.

The $^5D_3$ to $^7F_5$ multiplet fluorescence is observed in the 20700-20200 cm^{-1} region and overlaps the $^5D_2 \rightarrow ^7F_2$ fluorescence. The spectrum is shown in Figure 6.86. Eleven distinct fluorescence transitions are observed from the $^5D_3$ multiplet to $^7F_5$. Two transitions are observed to $U_1\gamma_4$. These transitions are observed at energies 20653 and 20625 cm^{-1} and are π and σ polarised respectively. Accordingly they are assigned as emanating from $D_3\gamma_4$ and $D_1\gamma_5$ respectively. Four transitions are observed to the $U_2\gamma_5$ state at 3820 cm^{-1}. The only missing transition is that which emanates from $D_5\gamma_5$ and this could well be obscured by the transitions to the $U_1\gamma_4$ state. The four observed transitions are at frequencies of 20597, 20579, 20568 and 20550 cm^{-1}. They are assigned as emanating from the $D_4\gamma_2$, $D_3\gamma_4$, $D_2\gamma_3$ and $D_1\gamma_5$ states respectively. All, except the $D_2\gamma_3 \rightarrow U_2\gamma_5$ transition, show well defined polarisation behaviour as listed in Table 6.16. Transitions to the $U_4\gamma_5$ state are broader and only two are observed. These are the $D_2\gamma_3$ and $D_1\gamma_5 \rightarrow U_4\gamma_5$ transitions as assigned from their σ' and π respective polarisations. The 20352 cm^{-1} transition is σ' polarised and assigned as the $D_1\gamma_5 \rightarrow U_6\gamma_3$ transition. The broader 20300 cm^{-1} transition is assigned as the $D_1\gamma_5 \rightarrow U_6\gamma_5$ transition on the basis of the π polarisation of this transition. The final $^5D_3 \rightarrow ^7F_5$ transition observed is more difficult to assign as it could terminate on either of two levels. This transition is at a frequency of 20232 cm^{-1}. It is σ polarised and emanates from the $D_1\gamma_5$ state. The likely terminating states are the $U_7\gamma_1$ or $U_8\gamma_2$ states both of which will display a σ polarisation for emission from a γ_5 doublet. The crystal field analysis of section 6.6 places the $U_8\gamma_2$ state closer and thus this transition is assigned as the $D_1\gamma_5 \rightarrow U_8\gamma_2$ transition. The $U_8\gamma_2$ state is therefore, placed at 4141 cm^{-1} from $Z_1\gamma_1$. Two $^5D_2 \rightarrow ^7F_2$ transitions are also observed in this region of the spectrum as mentioned above. The first is at 20607 cm^{-1} and is π' polarised. It is assigned as the $C_1\gamma_3 \rightarrow X_1\gamma_4$ transition. The second is 20513 cm^{-1} and is σ polarised. This is the $C_1\gamma_3 \rightarrow X_2\gamma_5$ transition.

For transitions in the 19800-19000 cm^{-1} region, emission from three different multiplets is superimposed. The first set of transitions is the $^5D_2 \rightarrow ^7F_6$ emission. Six transitions are observed. The first pair of lines are the $C_2\gamma_1$ and $C_1\gamma_3 \rightarrow W_1\gamma_5$ transitions, as determined from the σ' polarisation behaviour that is displayed. The previously undetermined $C_2\gamma_1$ level is therefore, placed at 21512 cm^{-1} from the ground state. The 19627 cm^{-1} transition is assigned as the $C_1\gamma_3 \rightarrow W_2\gamma_4$ transition from the π' polarisation of this transition. The next two features are assigned as the $C_2\gamma_1$ and $C_1\gamma_3 \rightarrow W_4\gamma_5$ transitions and are at energies of 19572 and 19538 cm^{-1} respectively. The observed polarisation of σ' for the $C_1\gamma_4 \rightarrow W_4\gamma_5$ transition is consistent with this, however the $C_2\gamma_1 \rightarrow W_4\gamma_5$ transition did not yield well de-

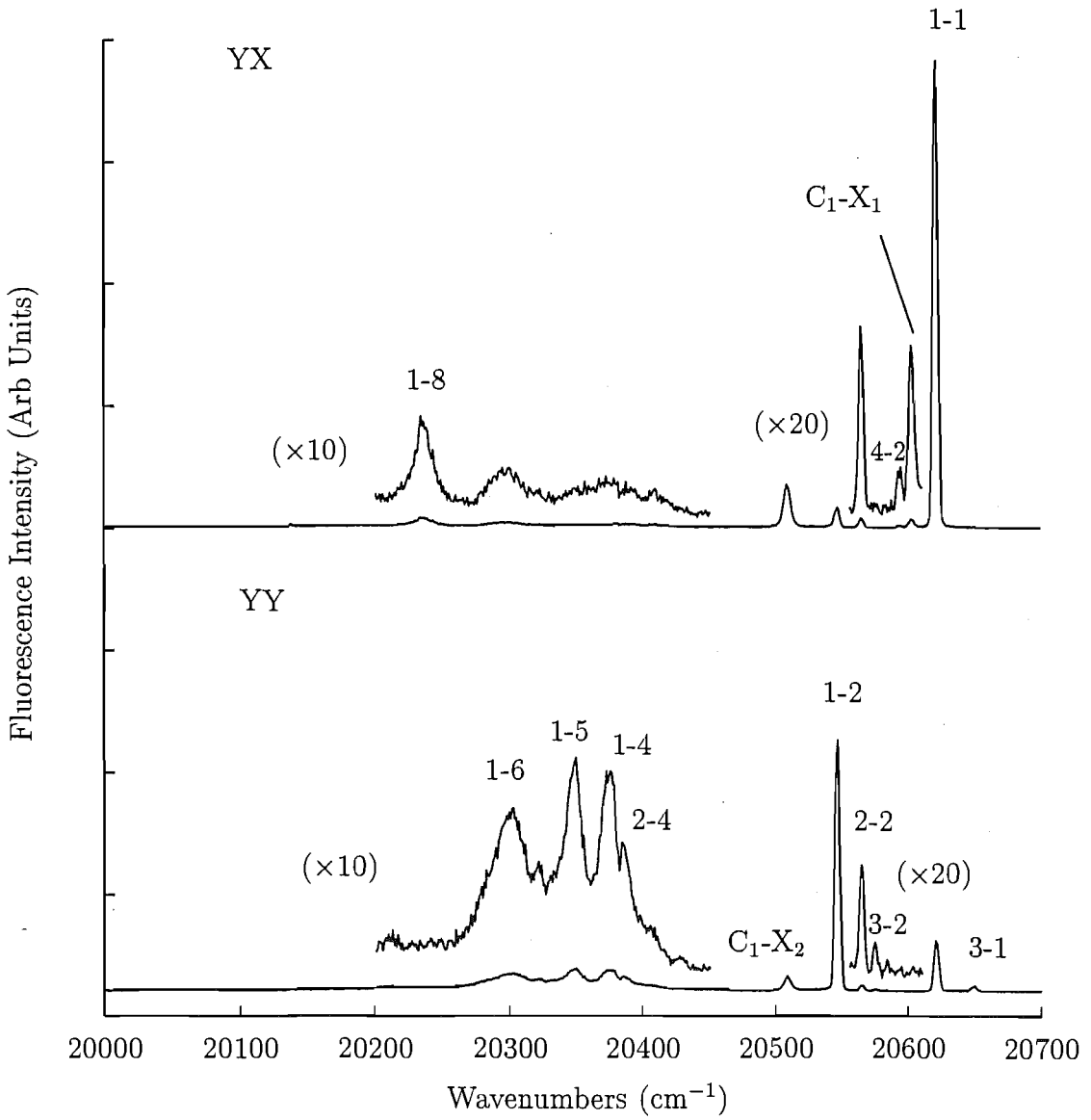

Figure 6.86: $^5D_3$ to $^7F_5$ polarised upconverted emission for the A centre in SrF_2:0.05%Eu^{3+}. Transitions emanating from $^5D_2$ are labelled appropriately. Excitation is at 17298 cm^{-1}. The spectra were recorded at 16K.

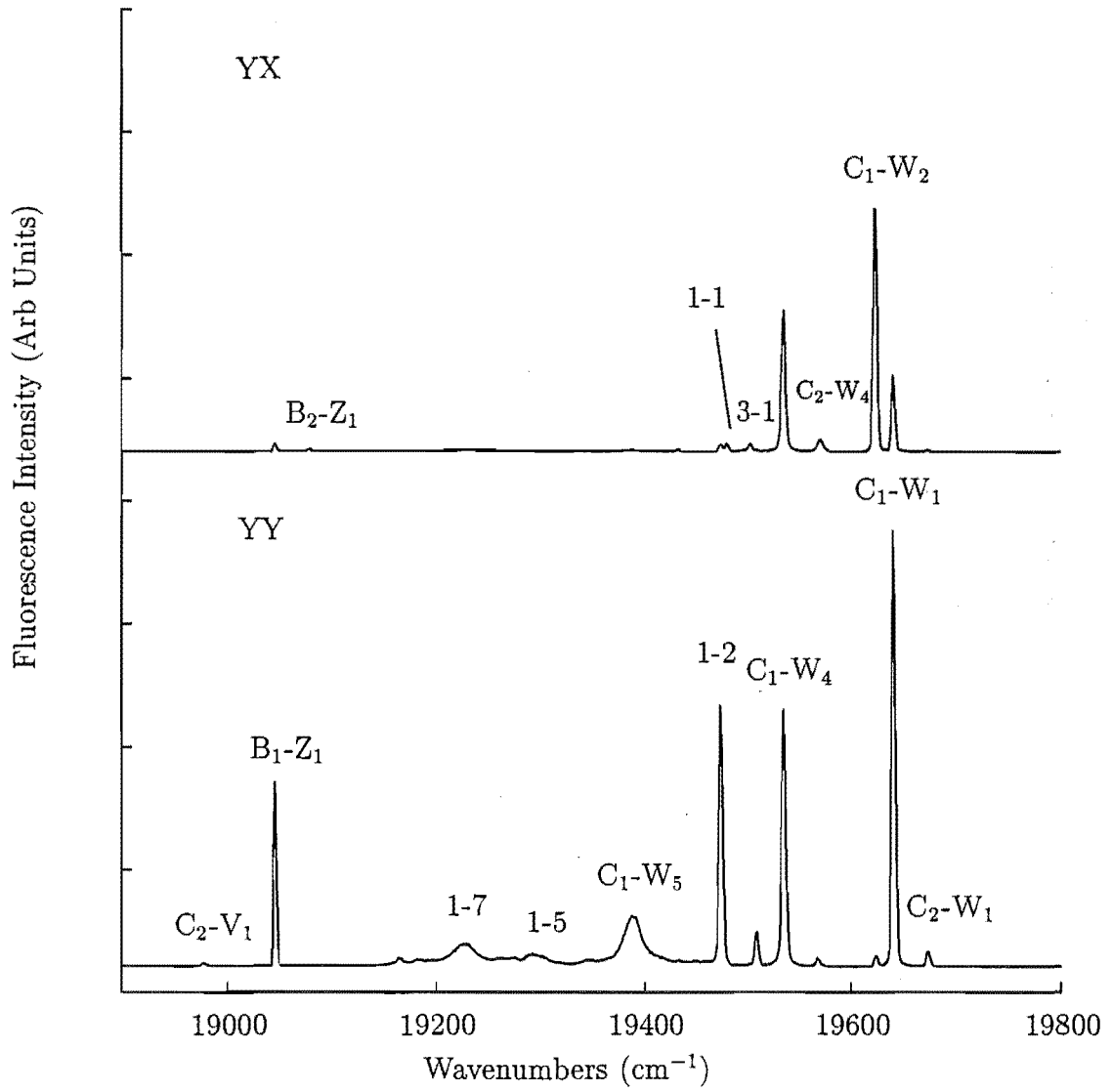

Figure 6.87: $^5D_3$ to $^7F_6$ polarised upconverted emission for the A centre in SrF_2:0.05%Eu^{3+}. Transitions emanating from $^5D_2$ or $^5D_1$ are labelled appropriately. Excitation is at 17298 cm^{-1}. The spectra were recorded at 16K.

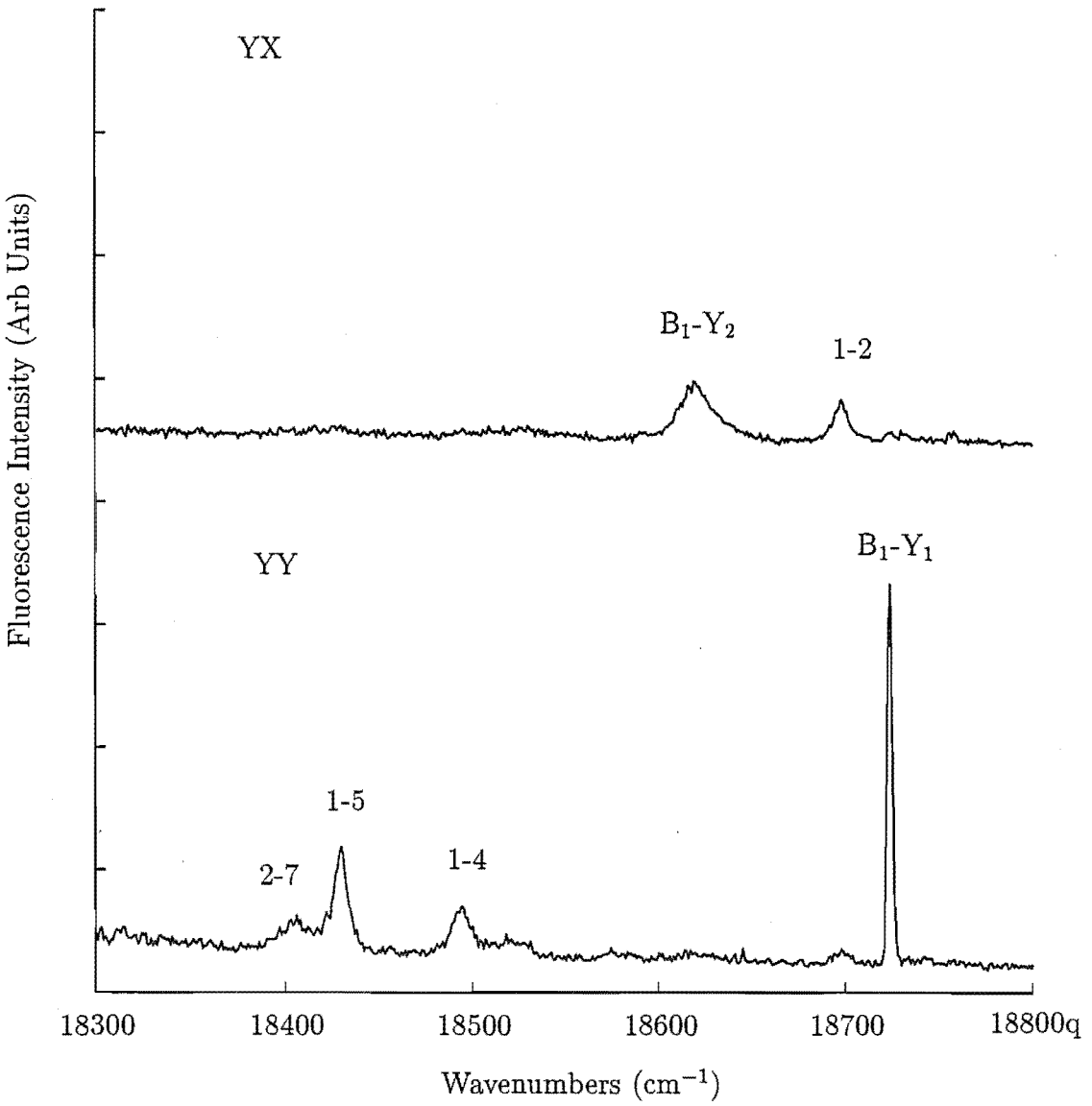

Figure 6.88: $^5D_2$ to $^7F_4$ polarised upconverted emission for the A centre in SrF_2:0.05%Eu^{3+}. Transitions emanating from $^5D_1$ are labelled appropriately. Excitation is at 17298 cm^{-1}. The spectra were recorded at 16K.

Table 6.16: Polarisation data, energies and transition assignments of upconverted fluorescence for the A centre in SrF_2:0.05%Eu^{3+}. Energies are in air cm^{-1} (±2 unless otherwise stated). Excitation is at 17298 cm^{-1}.

Transition Frequency	Polarisation Assignment	Transition Assignment	Transition Frequency	Polarisation Assignment	Transition Assignment
24067	σ	$D_2\gamma_3 \rightarrow Y_1\gamma_5$	20607	π'	$C_1\gamma_3 \rightarrow X_1\gamma_4$
24049	π	$D_1\gamma_5 \rightarrow Y_1\gamma_5$	20597	σ	$D_4\gamma_2 \rightarrow U_2\gamma_5$
23938±4	σ	$D_1\gamma_5 \rightarrow Y_2\gamma_2$	20579	σ'	$D_3\gamma_4 \rightarrow U_2\gamma_5$
23528	π	$D_3\gamma_4 \rightarrow X_1\gamma_4$	20568	(mixed)	$D_2\gamma_3 \rightarrow U_2\gamma_5$
23498	σ'	$D_1\gamma_5 \rightarrow X_1\gamma_4$	20550	π	$D_1\gamma_5 \rightarrow U_2\gamma_5$
23430	σ	$D_3\gamma_4 \rightarrow X_2\gamma_5$	20513	σ	$C_1\gamma_3 \rightarrow X_2\gamma_5$
23422	σ	$D_2\gamma_3 \rightarrow X_2\gamma_5$	20390	σ'	$D_2\gamma_3 \rightarrow U_4\gamma_5$
23404	π	$D_1\gamma_5 \rightarrow X_2\gamma_5$	20377	π	$D_1\gamma_5 \rightarrow U_4\gamma_5$
23243	π'	$D_3\gamma_4 \rightarrow X_3\gamma_3$	20352	σ'	$D_1\gamma_5 \rightarrow U_5\gamma_3$
23201	σ	$D_1\gamma_5 \rightarrow X_3\gamma_3$	20300±5	π	$D_1\gamma_5 \rightarrow U_6\gamma_5$
22584	σ'	$D_5\gamma_5 \rightarrow W_2\gamma_4$	20232	σ	$D_1\gamma_5 \rightarrow U_8\gamma_2$
22565	σ	$D_3\gamma_4 \rightarrow W_1\gamma_5$	19677	σ'	$C_2\gamma_1 \rightarrow W_1\gamma_5$
22556	σ	$D_2\gamma_3 \rightarrow W_1\gamma_5$	19645	σ'	$C_1\gamma_3 \rightarrow W_1\gamma_5$
22548	π	$D_3\gamma_4 \rightarrow W_2\gamma_4$	19627	π'	$C_1\gamma_3 \rightarrow W_2\gamma_4$
22537	(mixed)	$D_1\gamma_5 \rightarrow W_1\gamma_5$	19572	(mixed)	$C_2\gamma_1 \rightarrow W_4\gamma_5$
22520	σ	$D_1\gamma_5 \rightarrow W_2\gamma_4$	19538	σ'	$C_1\gamma_3 \rightarrow W_4\gamma_5$
22458	σ	$D_3\gamma_4 \rightarrow W_4\gamma_5$	19512	π	$D_3\gamma_4 \rightarrow T_1\gamma_4$
22449	σ	$D_2\gamma_3 \rightarrow W_4\gamma_5$	19484	σ	$D_1\gamma_5 \rightarrow T_1\gamma_4$
22430	π	$D_1\gamma_5 \rightarrow W_4\gamma_5$	19478	π	$D_1\gamma_5 \rightarrow T_2\gamma_5$
22293±4	π	$D_2\gamma_3 \rightarrow W_5\gamma_3$	19392	π	$C_1\gamma_3 \rightarrow W_5\gamma_3$
22284±4	σ	$D_1\gamma_5 \rightarrow W_5\gamma_3$	19296	π	$D_1\gamma_5 \rightarrow T_5\gamma_5$
21886	π'	$D_4\gamma_2 \rightarrow V_1\gamma_1$	19229	σ'	$D_1\gamma_5 \rightarrow T_6\gamma_1$
21839	σ'	$D_1\gamma_5 \rightarrow V_1\gamma_1$	19082	π'	$B_2\gamma_2 \rightarrow Z_1\gamma_1$
21620	σ'	$D_3\gamma_4 \rightarrow V_2\gamma_5$	19048	σ'	$B_1\gamma_5 \rightarrow Z_1\gamma_1$
21609	σ'	$D_2\gamma_3 \rightarrow V_2\gamma_5$	18978	π	$C_2\gamma_1 \rightarrow V_1\gamma_1$
21590	(mixed)	$D_1\gamma_5 \rightarrow V_2\gamma_5$	18724	π	$B_1\gamma_5 \rightarrow Y_1\gamma_5$
21450	(mixed)	$D_1\gamma_5 \rightarrow V_3\gamma_2$	18697	σ	$C_1\gamma_3 \rightarrow V_2\gamma_5$
21395	σ'	$D_2\gamma_3 \rightarrow V_4\gamma_5$	18619	σ	$B_1\gamma_5 \rightarrow Y_2\gamma_2$
21385	π'	$D_1\gamma_5 \rightarrow V_4\gamma_5$	18495	σ'	$C_1\gamma_3 \rightarrow V_4\gamma_5$
21347	π'	$D_3\gamma_4 \rightarrow V_5\gamma_3$	18430	π	$C_1\gamma_3 \rightarrow V_5\gamma_3$
21322	σ'	$D_1\gamma_5 \rightarrow V_5\gamma_3$	18405	π	$C_2\gamma_1 \rightarrow V_7\gamma_1$
21304	π'	$D_2\gamma_3 \rightarrow V_6\gamma_4$	18175	σ'	$B_1\gamma_5 \rightarrow X_1\gamma_4$
21292	σ'	$D_1\gamma_5 \rightarrow V_6\gamma_4$	18114	σ'	$B_2\gamma_2 \rightarrow X_2\gamma_5$
21255	σ'	$D_1\gamma_5 \rightarrow V_7\gamma_1$	18080	π'	$B_1\gamma_5 \rightarrow X_2\gamma_5$
21156	(mixed)	$C_1\gamma_3 \rightarrow Y_1\gamma_5$	17873	σ'	$B_1\gamma_5 \rightarrow X_3\gamma_3$
20653	π	$D_3\gamma_4 \rightarrow U_1\gamma_4$	17823	σ'	$B_1\gamma_5 \rightarrow X_4\gamma_1$
20625	σ	$D_1\gamma_5 \rightarrow U_1\gamma_4$			

fined polarisation ratios. The final $^5D_2 \rightarrow ^7F_6$ transition observed in this region was $C_1\gamma_3 \rightarrow W_5\gamma_3$ transition which showed π polarisation. Fluorescence from $^5D_3 \rightarrow ^7F_6$ is observed in the 19520-19200 cm^{-1} region. Two transitions are observed to the $T_1\gamma_4$ level. These emanate from the $D_3\gamma_4$ and $D_1\gamma_5$ states and are observed at 19512 and 19484 cm^{-1} respectively. The polarisation behaviour of π and σ for these transitions, is consistent with these assignments. The 19478 cm^{-1} transition is π polarised and is assigned as the $D_1\gamma_5 \rightarrow T_2\gamma_5$ transition. Two further transitions are observed to this multiplet at 19296 and 19229 cm^{-1}. They are π and σ' polarised respectively and are assigned as $D_1\gamma_5 \rightarrow T_5\gamma_5$ and $T_6\gamma_1$. This places the previously unobserved $T_5\gamma_5$ level at 5077 cm^{-1} above the ground state. As shown in Figure 6.87 the $B_2\gamma_2$ and $B_1\gamma_5$ transitions to $Z_1\gamma_1$ are observed at 19082 and 19048 cm^{-1} and show the expected π' and σ' polarisations. The final feature observed in Figure 6.87 is the $C_2\gamma_1 \rightarrow V_1\gamma_1$ transition at 18978 cm^{-1}. This transition is π polarised, consistent with its assignment.

In the 18800-18300 cm^{-1} region, $^5D_2 \rightarrow ^7F_4$ and $^5D_1 \rightarrow ^7F_1$ emission overlaps. The $^5D_1 \rightarrow ^7F_1$ transitions are observed at 18724 and 18619±4 cm^{-1} and are assigned (as with the downconverted spectrum) as the $B_1\gamma_5 \rightarrow Y_1\gamma_5$ and $B_1\gamma_5 \rightarrow Y_2\gamma_2$ transitions respectively, from the observed polarisation of π and σ. Four $^5D_2 \rightarrow ^7F_4$ emission features are observed in Figure 6.88. The 18697 cm^{-1} transition is σ polarised and is assigned as the $C_1\gamma_3 \rightarrow V_2\gamma_5$ transition. The $C_1\gamma_3 \rightarrow V_4\gamma_5$ is observed at 18495 cm^{-1} and displays a magnetic dipole σ' polarisation behaviour. The remaining two transitions are both σ polarised. They are observed at energies of 18430 and 18405 cm^{-1} respectively. We assign these as the $C_1\gamma_3 \rightarrow V_5\gamma_3$ and $C_2\gamma_1 \rightarrow V_7\gamma_1$ transitions.

Also listed in Table 6.16 are the $^5D_1 \rightarrow ^7F_2$ upconverted fluorescence transitions. As these are the same as that reported for the downconverted emission, no spectrum is given. Transitions from $^5D_2$ to the $^7F_5$ and $^7F_6$ multiplets were searched for but could not be observed.

6.5.4 The BaF_2:Eu^{3+} L Centre

For excitation of the 17303 cm^{-1} $Z_1\gamma_1 \rightarrow A_1\gamma_1$ transition, upconversion fluorescence is observed emanating from the $^5D_3$, $^5D_2$ and $^5D_1$ multiplets. The BaF_2:Eu^{3+} L centre is a C_{3v} symmetry centre with only a weak axial distortion. As such, the 17303 cm^{-1} transition is not as efficient as the equivalent transition in the C_{4v} symmetry centres, at populating the $^5D_0$ state. An overview of the upconversion fluorescence observed is shown in Figure 6.89.

Figure 6.90(a) shows fluorescence from $^5D_3$ to the $^7F_1$ multiplet. Only one transition

is observed and it is sufficiently weak that 400/3000/3000/400 μm spectrometer slits widths were necessary, at excitation powers of 400 mW, to record the given spectrum. The single observed transition, at a frequency of 24037 cm^{-1}, terminates on $Y_1\gamma_3$. This places the $^5D_3$ state at 24362 cm^{-1}. In Figure 6.90(b) the corresponding transitions to the $^7F_2$ multiplet are shown. Two transitions at 23508 and 23480 cm^{-1} orginate from the same $^5D_3$ level (at 24362 cm^{-1}). These transitions terminate on the $X_1\gamma_3$ and $X_2\gamma_1$ states at 852 and 883 cm^{-1}. A third transition at 23072 cm^{-1} terminates on the 1288 cm^{-1} $X_3\gamma_3$ transition. Transitions at 23313 and 22947 cm^{-1} are due to associated vibronic sidebands observed previously in emission from lower energy multiplets.

Transitions to the $^7F_3$ multiplet occur in the 22600-22400 cm^{-1} region as shown in Figure 6.92(a). Only three transitions are observed. Transitions at frequencies of 22521 and 22487 cm^{-1} emanate from the 24362 cm^{-1} $^5D_3$ state. The transitions terminate on the $^7F_3$ $W_1\gamma_2$ and $W_2\gamma_3$ states at 1842 and 1875 cm^{-1}. A third transition at 22534 cm^{-1} also terminates on the $W_1\gamma_2$ state at 1842 cm^{-1}. This originates from a higher, thermally populated level of the $^5D_3$ multiplet at 24376 cm^{-1}. By contrast transitions to the $^7F_4$ multiplet are reasonably intense and numerous. The 21905 cm^{-1} transition (shown amplified in Figure 6.92(b)) terminates on the 2458 cm^{-1} $V_1\gamma_1$ transition and unlike the rest of the spectrum was too weak to obtain a polarisation ratio. The 21529 cm^{-1} transition is π' polarised and terminates on the $V_2\gamma_2$ state at 2848 cm^{-1}. This indicates the upper state is a singlet of γ_2 irrep symmetry. Thus, we assign the 24376 cm^{-1} ($^5D_3$) state as $D_2\gamma_1$. The 21517 cm^{-1} cm^{-1} transition is σ' polarised and also terminates on the $V_2\gamma_2$ state. Therefore we assign the 24362 cm^{-1} ($^5D_3$) state as $D_1\gamma_3$. The 21508 cm^{-1} gives a poor polarisation ratio. This is consistent with its assignment as $D_1\gamma_3 \rightarrow V_3\gamma_3$. A smaller feature at 21482 cm^{-1} cannot be explained in terms of $^5D_3$ multiplet emission to known $^7F_4$ multiplet levels. The electric dipole σ polarisation of the transition indicates a transition involving both a doublet and a singlet. Thus, we are lead to conclude that this transition emanates from $^5D_2$ and is assigned as $C_1\gamma_3 \rightarrow Z_1\gamma_1$. A broad structure around 21320 cm^{-1} originates from $^5D_3$ and comprises four distinct transitions. The shoulder at 21335 cm^{-1} has σ polarisation and is assigned as $D_2\gamma_1 \rightarrow V_4\gamma_3$. The first peak is split by nine wavenumbers, the separation between the $D_1\gamma_3 \rightarrow V_4\gamma_3$ and $D_2\gamma_1 \rightarrow V_6\gamma_3$ transitions as evidenced by their polarisation behaviour (see Table 6.17) and the 21326 and 21317 cm^{-1} transition frequencies. The largest peak at 21305 cm^{-1} is assigned as the $D_1\gamma_3 \rightarrow V_6\gamma_3$ transition. The broader transitions in the 21270 - 21210 cm^{-1} region are assigned as vibronic sidebands.

Figure 6.92 shows transitions from $^5D_3$ to $^7F_5$ and from $^5D_2$ to $^7F_2$ in the 20700 - 19800 cm^{-1} region. A set of five transitions in close proximity form the first transition group centred around 20600 cm^{-1}. The strongest transition is the 20629 cm^{-1} $C_1\gamma_3 \rightarrow X_1\gamma_3$ transition. This gives a weak polarisation dependence as would

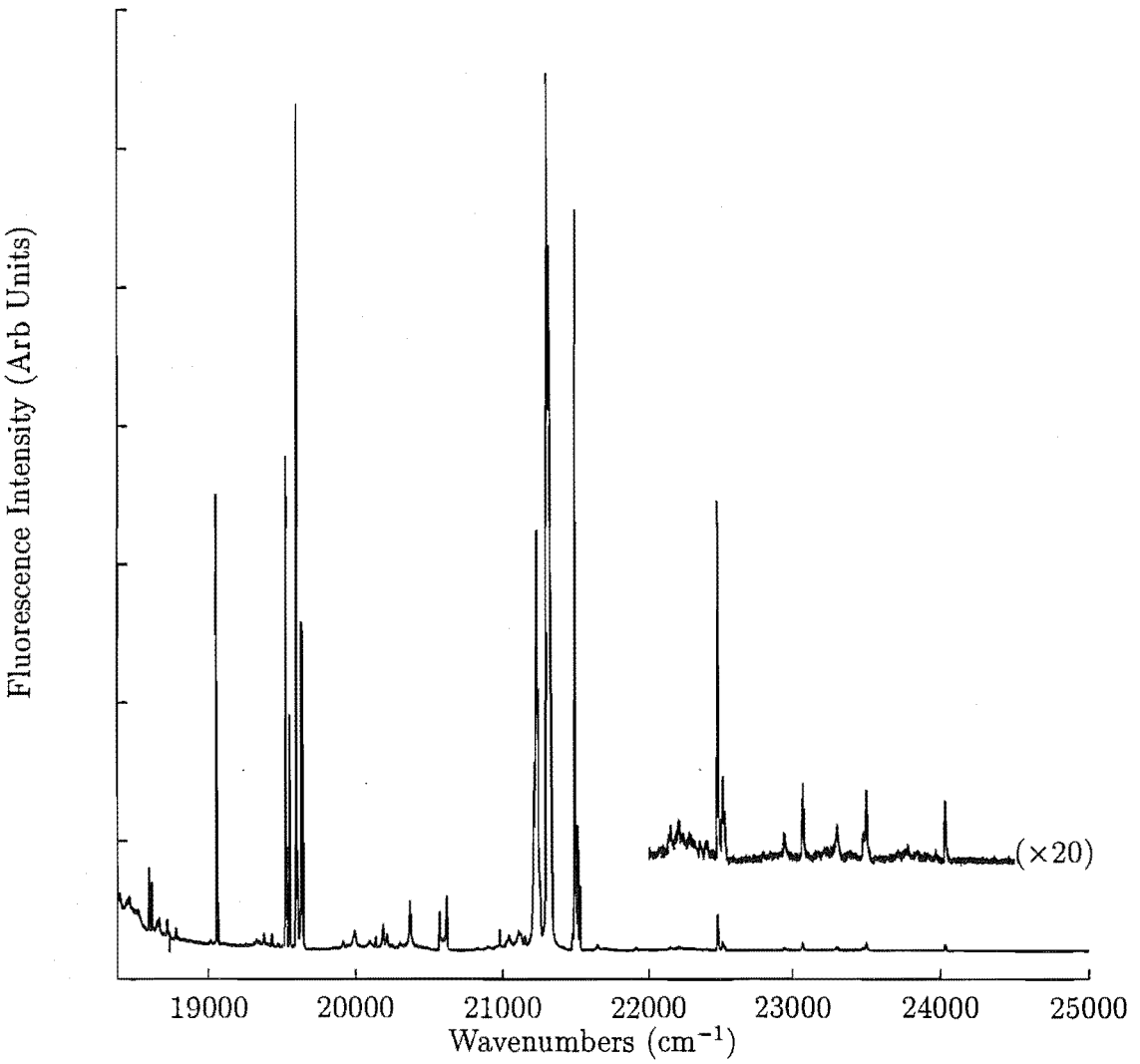

Figure 6.89: Overview of L centre upconversion fluorescence in BaF_2:0.05%Eu^{3+}

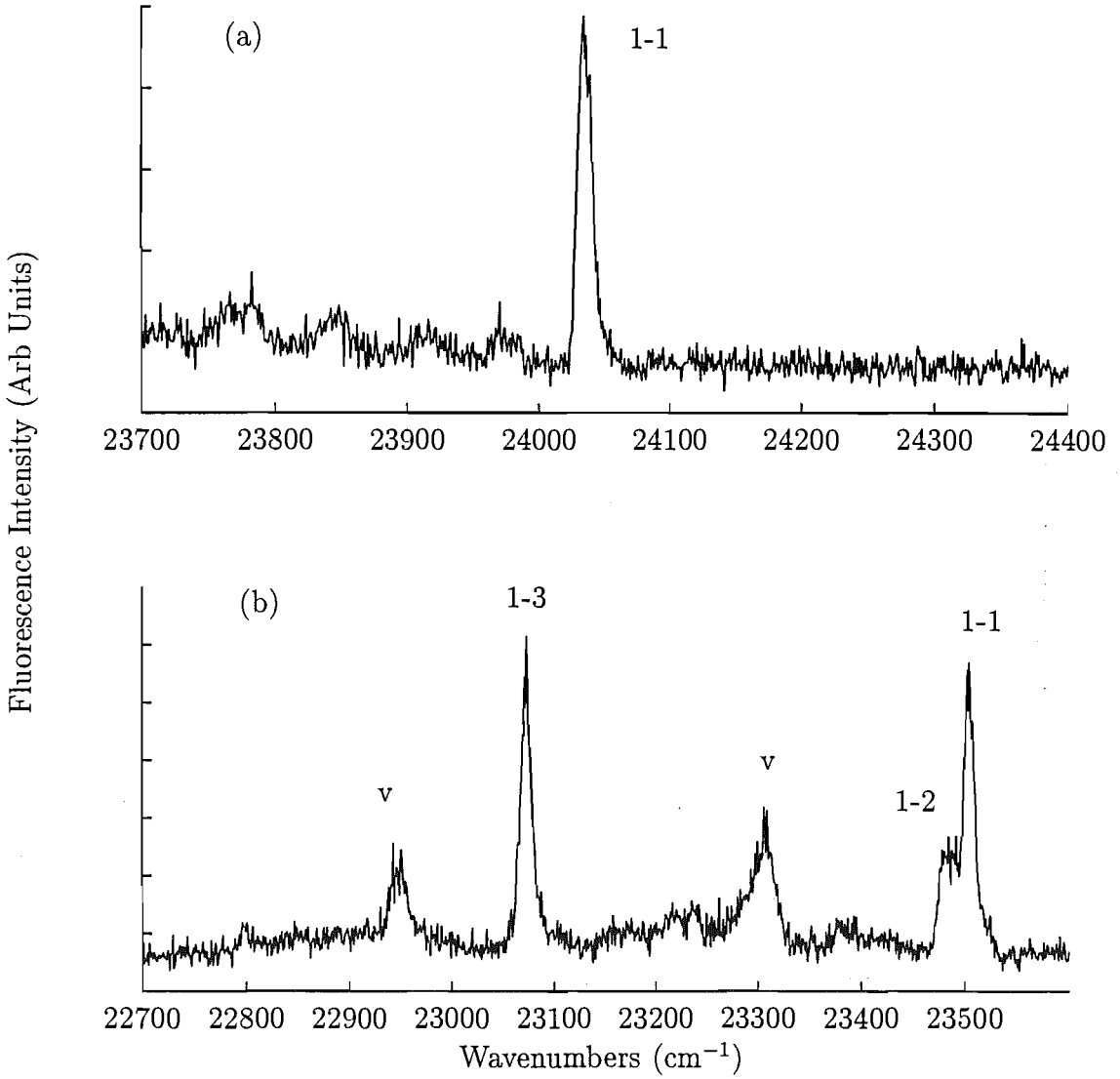

Figure 6.90: Upconversion fluorescence $^5D_3$ to (a) $^7F_1$ and (b) $^7F_2$ for the L centre in BaF_2:0.05%Eu^{3+}. The spectra were recorded at 16K.

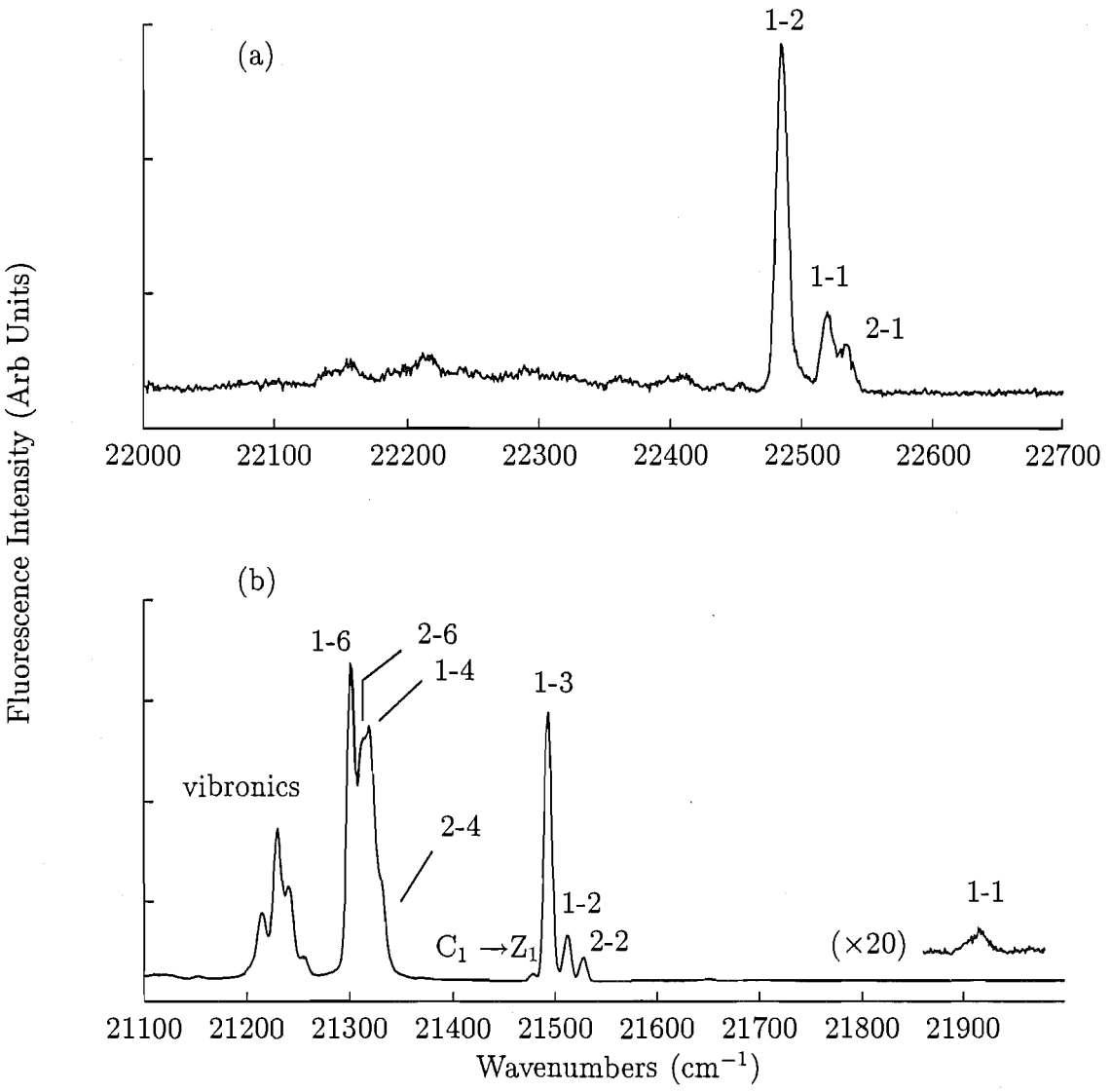

Figure 6.91: Upconversion fluorescence $^5D_3$ to (a) $^7F_3$ and (b) $^7F_4$ for the L centre in BaF_2:0.05%Eu^{3+}. The spectra were recorded at 16K.

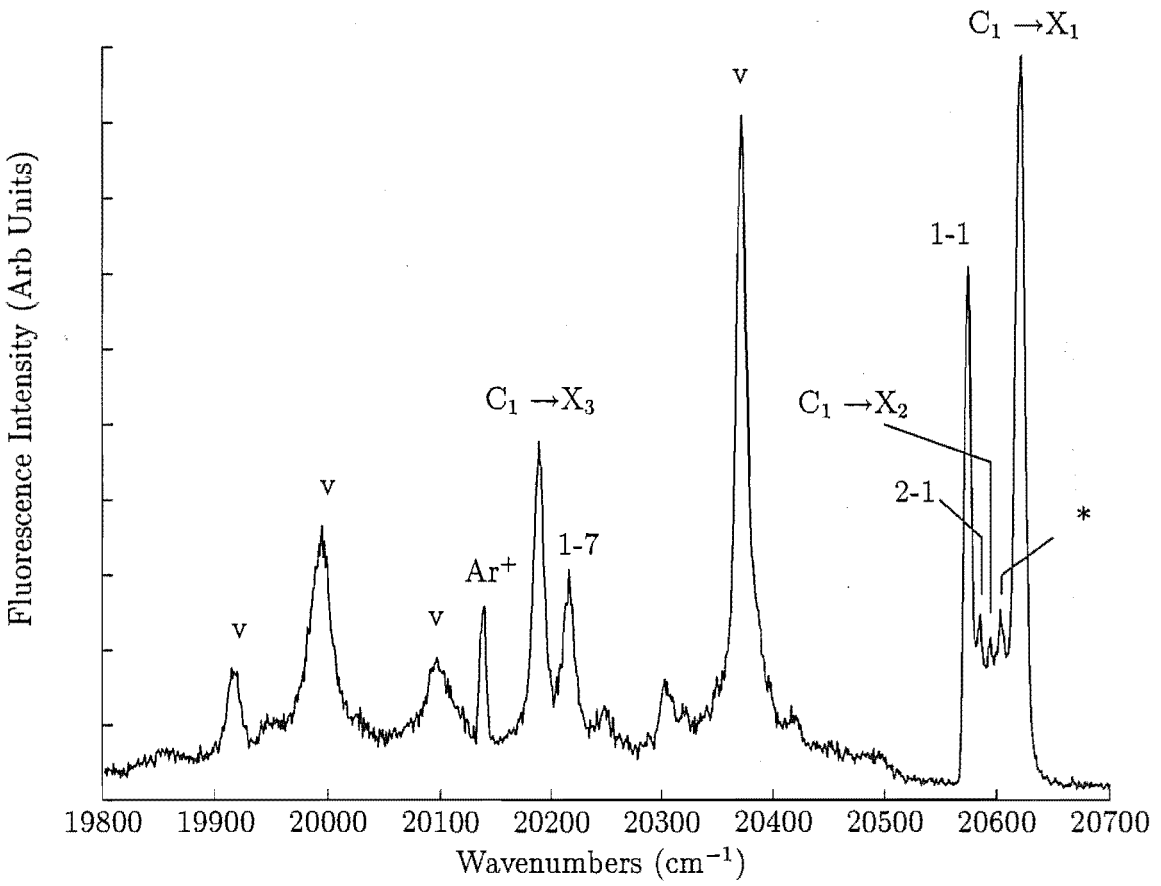

Figure 6.92: Upconversion fluorescence $^5D_3$ to $^7F_5$ for the L centre in BaF_2:0.05%Eu^{3+}. The transition labelled * is unassigned. The spectra were recorded at 16K.

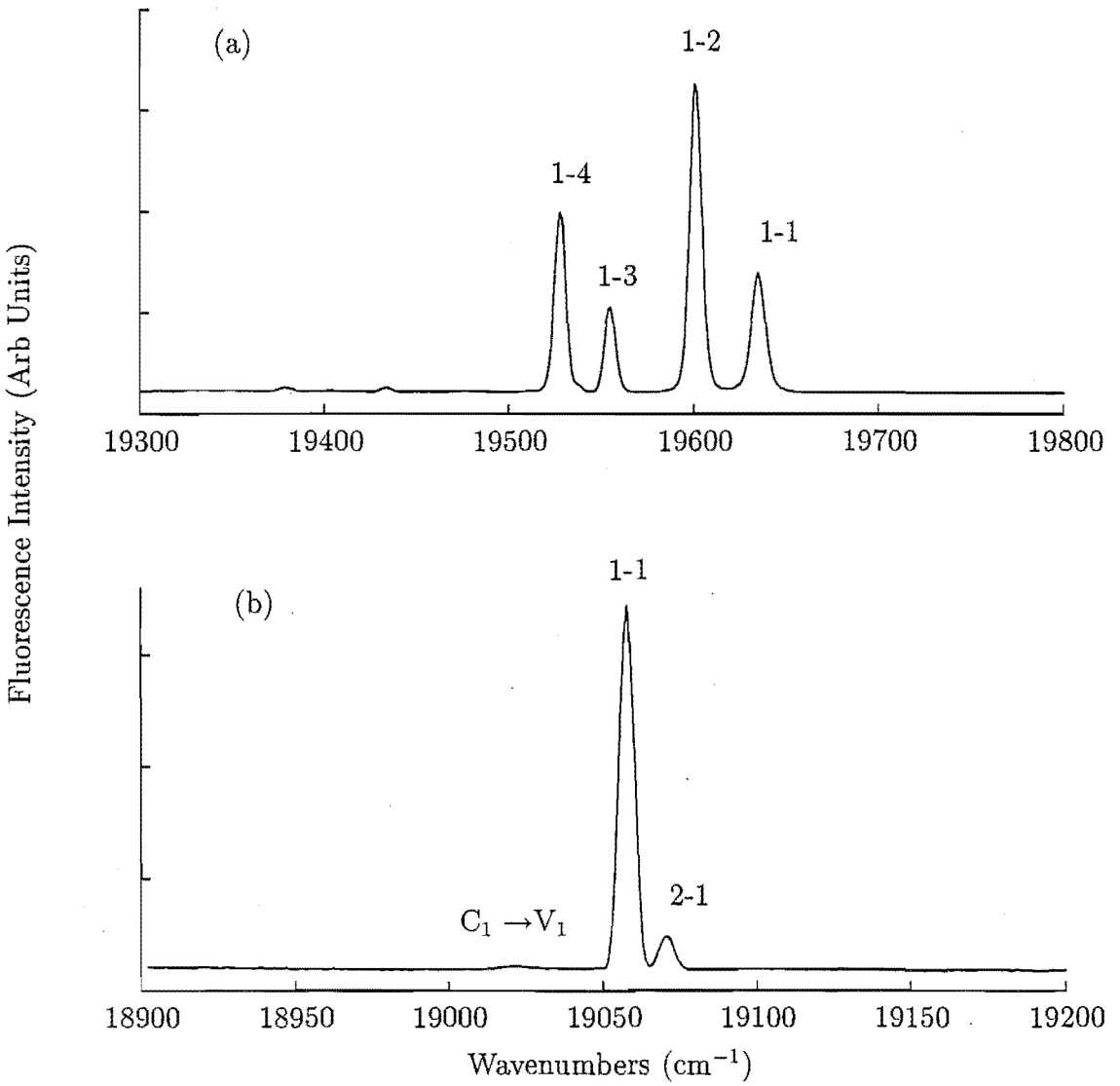

Figure 6.93: Upconversion fluorescence (a) $^5D_2 \rightarrow ^7F_1$ and (b) $^5D_1 \rightarrow ^7F_0$ for the L centre in BaF_2:0.05%Eu^{3+}. The spectra were recorded at 16K.

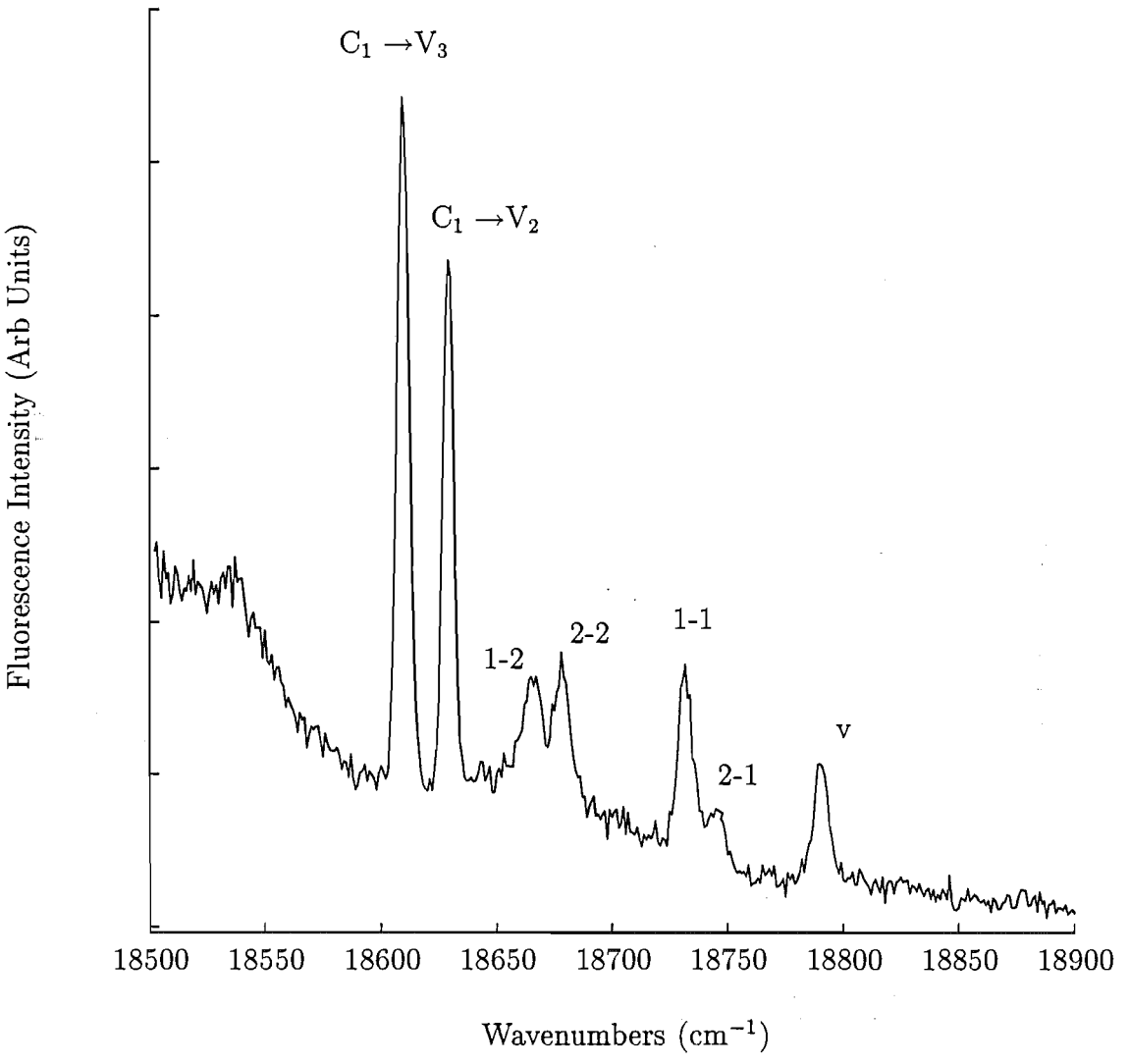

Figure 6.94: Upconversion fluorescence $^5D_1 \rightarrow ^7F_1$ for the L centre in BaF_2:0.05%Eu^{3+}. The spectra recorded at 16K.

Table 6.17: Upconversion fluorescence transition frequencies (air $cm^{-1}\pm1$) and polarisation for the L centre in BaF_2:0.05%Eu^{3+}. The † notation indicates a tentative assignment.

Transition		Polarisation	
Frequency	**Assignment**	**Ratio (YX:YY)**	**Assignment**
24037	$D_1\gamma_3 \rightarrow Y_1\gamma_3$	-	-
23501	$D_1\gamma_3 \rightarrow X_1\gamma_3$	-	-
23484	$D_1\gamma_3 \rightarrow X_2\gamma_1$	-	-
23072	$D_1\gamma_3 \rightarrow X_3\gamma_3$	-	-
22534	$D_2\gamma_1 \rightarrow W_1\gamma_2$	-	-
22521	$D_1\gamma_3 \rightarrow W_1\gamma_2$	-	-
22487	$D_1\gamma_3 \rightarrow W_2\gamma_3$	-	-
21905	$D_1\gamma_3 \rightarrow V_1\gamma_1$	-	-
21529	$D_2\gamma_1 \rightarrow V_2\gamma_2$	3:1	π'
21517	$D_1\gamma_3 \rightarrow V_2\gamma_2$	1:2.2	σ'
21508	$D_1\gamma_3 \rightarrow V_3\gamma_3$	1:1.4	Arb
21482	$C_1\gamma_3 \rightarrow Z_1\gamma_1$	2.3:1	σ
21335	$D_2\gamma_1 \rightarrow V_4\gamma_3$	2:1	σ
21326	$D_1\gamma_3 \rightarrow V_4\gamma_3$	1:2.1	Arb
21317	$D_2\gamma_1 \rightarrow V_6\gamma_3$	1:2.4	σ'
21305	$D_1\gamma_3 \rightarrow V_6\gamma_3$	2.6:1	Arb
20629	$C_1\gamma_3 \rightarrow X_1\gamma_3$	1:1.8	Arb
20599	$C_1\gamma_3 \rightarrow X_2\gamma_1$	-	-
20584	$D_2\gamma_1 \rightarrow U_2\gamma_1$	-	-
20574	$D_1\gamma_3 \rightarrow U_2\gamma_1$	1:1.1	mixed
20216	$D_1\gamma_3 \rightarrow U_7\gamma_3^{\dagger}$	-	-
20192	$C_1\gamma_3 \rightarrow X_3\gamma_3$	-	-
19638	$C_1\gamma_3 \rightarrow W_1\gamma_2$	1:2.3	σ'
19603	$C_1\gamma_3 \rightarrow W_2\gamma_3$	1.1:1	Arb
19558	$C_1\gamma_3 \rightarrow W_3\gamma_1$	1:2.3	σ'
19530	$C_1\gamma_3 \rightarrow W_4\gamma_3$	1:1	Arb
19070	$B_2\gamma_2 \rightarrow Z_1\gamma_1$	2.9:1	π'
19056	$B_1\gamma_3 \rightarrow Z_1\gamma_1$	1:2.3	σ'
19026	$C_1\gamma_3 \rightarrow V_1\gamma_1$	-	-
18748	$B_2\gamma_2 \rightarrow Y_1\gamma_3$	-	-
18732	$B_1\gamma_3 \rightarrow Y_1\gamma_3$	-	-
18680	$B_2\gamma_2 \rightarrow Y_2\gamma_2$	-	-
18667	$B_1\gamma_3 \rightarrow Y_1\gamma_3$	-	-
18633	$C_1\gamma_3 \rightarrow V_2\gamma_2$	-	-
18615	$C_1\gamma_3 \rightarrow V_3\gamma_3$	-	-

be expected from its selection rules. Nearby, at 20599 cm^{-1} is the $C_1\gamma_3 \rightarrow X_2\gamma_1$ transition which is too weak to polarise. At 20574 and 20584 cm^{-1} are the $D_1\gamma_3$ and $D_2\gamma_1$ to $U_2\gamma_1$ transitions. A further weak transition at 20610 cm^{-1} could terminate on the U_1 state, however without polarisation or a knowledge of the U_1 state energy this is difficult to assign. It remains unassigned. A strong transition at 20378 cm^{-1} is the familiar 196 cm^{-1} phonon associated with the 20574 cm^{-1} transition. A transition at 20192 cm^{-1} is assigned as the $C_1\gamma_3 \rightarrow X_3\gamma_3$ transition. A nearby sharp transition at 20140 cm^{-1} (or 496.5 nm) is noted to be coincident in frequency with an argon laser line presumably due to small amounts of scatter of the all lines (visible) pump source of the R590 dye used. A transition at 20216 cm^{-1} was too weak to polarise, however assuming emission from the $^5D_3D_1\gamma_3$ state yields a state at an appropriate energy (of 4115 cm^{-1}) to be assigned as the U_7 state.

Transitions from the $^5D_2$ multiplet to $^7F_3$ in the 19700 - 19450 cm^{-1} region (shown in Figure 6.93(a)) are less complex. Four transitions are observed at good signal intensities. The 19638 and 19558 cm^{-1} transitions give σ' polarisation ratios and are therefore assigned as the $C_1\gamma_3 \rightarrow W_1\gamma_2$ and $W_3\gamma_1$ transitions. The remaining two transitions at 19603 and 19530 cm^{-1} terminate on the $W_2\gamma_3$ and $W_4\gamma_3$ states and give essentially arbitrary polarisation ratios as consistent with $\gamma_3 \rightarrow \gamma_3$ transitions. Figure 6.93(b) shows transitions from the $^5D_1$ multiplet to the ground state. As would be expected two transitions are apparant at frequencies of 19070 and 19056 cm^{-1} with π' and σ' polarisation. These are the $B_2\gamma_2$ and $B_1\gamma_3 \rightarrow Z_1\gamma_1$ transitions. A weak transition at 19026 cm^{-1} is assigned as the $C_1\gamma_3 \rightarrow V_1\gamma_1$ transition from the appropriate energy mismatch.

Transitions from $^5D_1$ to $^7F_1$ are shown in Figure 6.94. The highest frequency transition is a vibronic sideband of the $^5D_1 \rightarrow ^7F_0$ transitions. The 18748 and 18732 cm^{-1} terminate on the $Y_1\gamma_3$ state and originate from the $B_2\gamma_2$ and $B_1\gamma_3$ states respectively. The 18680 and 18667 cm^{-1} terminate on the $Y_2\gamma_2$ state and have the same initial states. Two stronger transitions at 18633 and 18615 cm^{-1} are $^5D_2 \rightarrow ^7F_4$ transitions. They are assigned as $C_1\gamma_3 \rightarrow V_2\gamma_2$ and $V_3\gamma_3$ transitions.

6.6 Crystal Field Analyses for the C_{4v} and C_{3v} Symmetry Centres

Crystal field analyses were performed for tetragonal C_{4v} symmetry and trigonal C_{3v} symmetry Eu^{3+} ion centres in CaF_2, SrF_2 and BaF_2 crystals. The appropriate Hamiltonians for these symmetries have been given earlier in chapter two. As with the Sm^{3+} ion centres, the F-Shell Empirical programs of Dr Mike Reid were employed. The f^6 configuration is appropriate for the Eu^{3+} ion which consists of 3003

electronic states.

Crystal field analyses of Eu^{3+} ion centres have been reported in many hosts (eg $LiYF_4$:Eu^{3+} [107]). Amongst which a series of classic papers by Porcher and Caro [128] (1976), [129] [130] (1978) presented analyses for Eu^{3+} ions in KY_3F_{10}. In this crystal, the Eu^{3+} ions reside in a C_{4v} symmetry centre. The authors noted that the fluorescence was of a multipolar character, an observation which typifies Eu^{3+} fluorescence. The crystal field analysis presented in the work of Porcher and Caro was successful, although difficulty was had in accurately determining the free ion parameters as only levels of the ^7F_J and the three lowest ^5D term multiplets were fitted. These authors carried the analyses onto intensity parameterisation and non-radiative transition probabilities.

For the crystal field analyses presented here, the f^6 configuration has been truncated to the lowest 40 multiplets (400 electronic states) as an approximation to the entire configuration. Only the crystal field levels of the $^7F_0$, $^7F_1$, $^7F_2$, $^7F_3$, $^7F_4$, $^7F_5$ and $^7F_6$ multiplets of the ^7F term and the $^5D_0$, $^5D_1$, $^5D_2$ and $^5D_3$ multiplets of the ^5D term have been determined experimentally. As a consequence of this, the interactions within the 'free ion', other than the spin-orbit interaction, are not well accounted for. Generally the parameters representing these free ion interactions are not fitted but are held fixed at the values determined by Carnall et. al. [68]. The F^2 Slater radial parameter has been varied freely as the ^7F - ^5D splitting is known. However the F^4 and F^6 parameters are constrained to the ratios $\frac{F^4}{F^2}$=0.71 and $\frac{F^6}{F^2}$=0.51. These are the ratios obtained for Eu^{3+} doped LaF_3 by Carnall et. al.

The crystal field fits for the C_{4v} symmetry A centres in CaF_2 and SrF_2:Eu^{3+} are presented in Table 6.18 and 6.19 with the optimised parameters presented in Table 6.20. As can be observed, reasonable agreement between the fitted values and experimental values is obtained. These parameter values agree well with previously obtained parameters (tabulated in chapter nine) which confirm the RE^{3+}-F^- configuration for these centres as that of a nearest neighbour interstitial F^- ion situated along the $\langle 100 \rangle$ axis.

Table 6.18: C_{4v} symmetry crystal field fit to the ^7F term and the four lowest multiplets of the ^5D term energy levels of the A centre in CaF_2:Eu^{3+}.

State & Symmetry	Calculated Energy	Experimental Energy	State & Symmetry	Calculated Energy	Experimental Energy
$Z_1\gamma_1$	-2	0	$U_7\gamma_1$	4184	4183
$Y_1\gamma_5$	312	307	$U_8\gamma_2$	4185	4192
$Y_2\gamma_2$	495	456	$T_1\gamma_4$	4891	4866
$X_1\gamma_4$	839	852	$T_2\gamma_5$	4900	4873
$X_2\gamma_5$	969	971	$T_3\gamma_1$	4908	4879
$X_3\gamma_3$	1130	1123	$T_4\gamma_2$	5138	5150
$X_4\gamma_1$	1242	1261	$T_5\gamma_5$	5164	5158
$W_1\gamma_5$	1806	1814	$T_6\gamma_3$	5173	-
$W_2\gamma_4$	1826	1835	$T_7\gamma_1$	5183	5167
$W_3\gamma_5$	1952	1953	$T_8\gamma_5$	5223	5184
$W_4\gamma_2$	1976	1977	$T_9\gamma_4$	5398	-
$W_5\gamma_3$	2113	2130	$T_{10}\gamma_3$	5398	-
$V_1\gamma_1$	2503	2510	$A_1\gamma_1$	17315	17288
$V_2\gamma_5$	2764	2800	$B_1\gamma_5$	19022	19029
$V_3\gamma_2$	2936	2947	$B_2\gamma_2$	19089	19073
$V_4\gamma_5$	3001	3006	$C_1\gamma_3$	21453	21455
$V_5\gamma_3$	3071	3089	$C_2\gamma_1$	21490	21495
$V_6\gamma_4$	3104	3114	$C_3\gamma_5$	21521	21537
$V_7\gamma_1$	3136	3156	$C_4\gamma_4$	21522	-
$U_1\gamma_4$	3753	3747	$D_1\gamma_5$	24333	24335
$U_2\gamma_5$	3833	3829	$D_2\gamma_3$	24367	24362
$U_3\gamma_2$	3958	3970	$D_3\gamma_4$	24357	24371
$U_4\gamma_3$	4032	4020	$D_4\gamma_2$	24367	24385
$U_5\gamma_5$	4036	4035	$D_5\gamma_5$	24406	24397
$U_6\gamma_5$	4112	4115			

Table 6.19: C_{4v} symmetry crystal field fit to the ^7F term and the four lowest multiplets of the ^5D term energy levels of the A centre in SrF_2:Eu^{3+}.† indicates the data of Jouart et. al.

State & Symmetry	Calculated Energy	Experimental Energy	State & Symmetry	Calculated Energy	Experimental Energy
$Z_1\gamma_1$	-1	0	$U_7\gamma_1$	4133	-
$Y_1\gamma_5$	331	324	$U_8\gamma_2$	4133	-
$Y_2\gamma_2$	451	427	$T_1\gamma_4$	4915	4888
$X_1\gamma_4$	862	874	$T_2\gamma_5$	4921	4892
$X_2\gamma_5$	959	968	$T_3\gamma_1$	4923	4895
$X_3\gamma_3$	1148	1169	$T_4\gamma_2$	5083	5055
$X_4\gamma_1$	1201	1221	$T_5\gamma_5$	5123	5077
$W_1\gamma_5$	1823	1835	$T_6\gamma_1$	5147	5139
$W_2\gamma_4$	1846	1853	$T_7\gamma_5$	5160	5140
$W_3\gamma_2$	1933	1936	$T_8\gamma_3$	5154	5146
$W_4\gamma_5$	1936	1939	$T_9\gamma_4$	5295	-
$W_5\gamma_3$	2068	2084	$T_{10}\gamma_3$	5295	-
$V_1\gamma_1$	2525	2531	$A_1\gamma_1$	17343	17298
$V_2\gamma_5$	2774	2779	$B_1\gamma_5$	19055	19049
$V_3\gamma_2$	2904	2921	$B_2\gamma_2$	19098	19082
$V_4\gamma_5$	2977	2986	$C_1\gamma_3$	21482	21480
$V_5\gamma_3$	3029	3051	$C_2\gamma_1$	21510	21511
$V_6\gamma_4$	3073	3081	$C_3\gamma_5$	21542	21554
$V_7\gamma_1$	3079	3114	$C_4\gamma_4$	21547	21566†
$U_1\gamma_4$	3750	3748	$D_1\gamma_5$	24368	24373
$U_2\gamma_5$	3821	3820	$D_2\gamma_3$	24396	24391
$U_3\gamma_2$	3940	3960	$D_3\gamma_4$	24387	24401
$U_4\gamma_5$	3987	3994	$D_4\gamma_2$	24400	24419
$U_5\gamma_3$	4021	-	$D_5\gamma_5$	24424	24436
$U_6\gamma_5$	4067	4054			

Table 6.20: Crystal field parameters for the C_{4v} symmetry A centres in CaF_2:Eu^{3+} and SrF_2:Eu^{3+}. Quantities in square brackets were not varied. All parameter values are in cm^{-1}.

Parameter	SrF_2	CaF_2
F_{tot}	83406	83267
α	[20]	[20]
β	[-570]	[-570]
γ	[1450]	[1450]
T^2	[330]	[330]
T^3	[41.5]	[41.5]
T^4	[62]	[62]
T^6	[-295]	[-295]
T^7	[360]	[360]
T^8	[310]	[310]
M_{tot}	[3.03]	[3.03]
P_{tot}	[300]	[300]
ζ	1324	1325
B^2_A	469	718
B^4_A	364	442
B^6_A	463	545
B^4_C	-1176	-1209
B^6_C	552	656
n	44	45
σ	20	17

Table 6.21: C_{3v} symmetry crystal field fit to the ^7F term and the three lowest multiplets of the ^5D term energy levels of the J centre in SrF_2:Eu^{3+}.† indicates the data of Jouart et. al.

State & Symmetry	Calculated Energy	Experimental Energy	State & Symmetry	Calculated Energy	Experimental Energy
$Z_1\gamma_1$	-5	0	$U_4\gamma_3$	3963	-
$Y_1\gamma_3$	333	318	$U_5\gamma_2$	4134	-
$Y_2\gamma_2$	408	397	$U_6\gamma_3$	4139	-
$X_1\gamma_3$	837	831	$U_7\gamma_3$	4194	-
$X_2\gamma_1$	856	953	$T_1\gamma_1$	4945	4962
$X_3\gamma_3$	1289	1316	$T_2\gamma_3$	4990	5003
$W_1\gamma_2$	1838	1836	$T_3\gamma_3$	5054	5049
$W_2\gamma_3$	1883	1875	$T_4\gamma_2$	5058	5073
$W_3\gamma_1$	1949	1934	$T_5\gamma_1$	5068	-
$W_4\gamma_3$	1972	1967	$T_6\gamma_1$	5231	-
$W_5\gamma_2$	2139	-	$T_7\gamma_2$	5234	-
$V_1\gamma_1$	2438	2454	$T_8\gamma_3$	5240	-
$V_2\gamma_2$	2849	2860	$T_9\gamma_3$	5248	-
$V_3\gamma_3$	2854	2881	$A_1\gamma_1$	17282	17295
$V_4\gamma_3$	3086	3063	$B_1\gamma_3$	19036	19046
$V_5\gamma_1$	3107	-	$B_2\gamma_2$	19056	19061
$V_6\gamma_3$	3111	3084	$C_1\gamma_3$	21483	21454†
$U_1\gamma_3$	3780	-	$C_2\gamma_3$	21554	-
$U_2\gamma_1$	3799	3791	$C_3\gamma_2$	21564	-
$U_3\gamma_2$	3952	-			

Table 6.22: C_{3v} symmetry crystal field fit to the ^7F term and the four lowest multiplets of the ^5D term energy levels of the L centre in BaF_2:Eu^{3+}.† indicates the data of Jouart et. al.

State & Symmetry	Calculated Energy	Experimental Energy	State & Symmetry	Calculated Energy	Experimental Energy
$Z_1\gamma_1$	-3	0	$U_6\gamma_3$	4114	-
$Y_1\gamma_3$	346	325	$U_7\gamma_3$	4150	4146
$Y_2\gamma_2$	409	391	$T_1\gamma_1$	4931	4943
$X_1\gamma_3$	859	852	$T_2\gamma_3$	4970	4982
$X_2\gamma_1$	878	883	$T_3\gamma_3$	5023	5024
$X_3\gamma_3$	1265	1288	$T_4\gamma_2$	5031	5047
$W_1\gamma_2$	1841	1842	$T_5\gamma_1$	5040	-
$W_2\gamma_3$	1876	1875	$T_6\gamma_1$	5195	-
$W_3\gamma_1$	1936	1922	$T_7\gamma_2$	5198	-
$W_4\gamma_3$	1952	1948	$T_8\gamma_3$	5199	-
$W_5\gamma_2$	2116	-	$T_9\gamma_3$	5205	-
$V_1\gamma_1$	2446	2458	$A_1\gamma_1$	17301	17303
$V_2\gamma_2$	2837	2848	$B_1\gamma_3$	19046	19057
$V_3\gamma_3$	2845	2867	$B_2\gamma_2$	19063	19071
$V_4\gamma_3$	3056	3040	$C_1\gamma_3$	21486	21482
$V_5\gamma_1$	3066	-	$C_2\gamma_3$	21551	21565†
$V_6\gamma_3$	3089	3059	$C_3\gamma_2$	21558	21571†
$U_1\gamma_3$	3772	-	$D_1\gamma_3$	24383	24362
$U_2\gamma_1$	3785	3787	$D_2\gamma_1$	24398	24376
$U_3\gamma_2$	3943	-	$D_3\gamma_2$	24408	-
$U_4\gamma_3$	3948	-	$D_4\gamma_3$	24427	-
$U_5\gamma_2$	4106	-	$D_5\gamma_2$	24431	-

Table 6.23: Crystal field parameters for the C_{3v} symmetry J centre in SrF_2:Eu^{3+} and L centre in BaF_2:Eu^{3+}. Quantities in square brackets were not varied. All parameter values are in cm^{-1}. The corresponding crystal field parameters for the J and L centres in SrF_2:Er^{3+} and BaF_2:Er^{3+} respectively are given in round brackets. [131]

Parameter	SrF_2	BaF_2
F_{tot}	83811	83837
α	[20]	[20]
β	[-570]	[-570]
γ	[1450]	[1450]
T^2	[330]	[330]
T^3	[41.5]	[41.5]
T^4	[62]	[62]
T^6	[-295]	[-295]
T^7	[360]	[360]
T^8	[310]	[310]
M_{tot}	[3.03]	[3.03]
P_{tot}	[300]	[300]
ζ	1346	1341
B^2_A	221(118)	186(108)
B^4_A	171(-185)	95(-101)
B^6_A	-238(-258)	-156(-107)
$B^6_{\hat{A}}$	-59(-84)	-18(-59)
B^4_C	1227(1087)	1121(959)
B^6_C	1152(1023)	1121(862)
n	24	29
σ	19	17

The crystal field fits for the trigonal C_{3v} symmetry J and L centres in SrF_2 and BaF_2:Eu^{3+} are given in Tables 6.21 and 6.22 with the optimised parameters presented in Table 6.23. The agreement between the fitted values and experiment is good. The optimised parameter values are interesting as previously, trigonal centre parameters have only been known for the B, J and L centres in CaF_2, SrF_2 and BaF_2:Er^{3+} respectively [14] [131] and the B centres in CaF_2 and SrF_2:Ho^{3+} [15]. The J and L centres in SrF_2 and BaF_2:Er^{3+} have been reported by Dean [131] to comprise the familiar next nearest neighbour $\langle 111 \rangle$ interstitial F^- ion . In Table 6.23 the optimised parameters for the J and L centres in SrF_2 and BaF_2:Er^{3+} are given beside those for the SrF_2 and BaF_2:Eu^{3+} parameters. It is evident from the comparision between these parameter values that these centres are similar in their RE^{3+}-F^- configuration and thus the near cubic trigonal centre appears to exist throughout the rare earth series for doping into the SrF_2 and BaF_2 crystals. As has been stated earlier this centre is a minoritycentre in the SrF_2:RE^{3+} system until around Dy^{3+}.

6.7 Fluorescence Lifetimes

The fluorescence decay of the dominant C_{4v} symmetry A centres in $CaF_2:Eu^{3+}$ and $SrF_2:Eu^{3+}$ and the C_{3v} symmetry L centre in $BaF_2:Eu^{3+}$ have been recorded. These experiments were done with crystals cooled to 16K. The $^5D_2$, $^5D_1$ and $^5D_0$ multiplets were studied as listed in Table 6.24. The observed decay curves are shown in Figures 6.95 through to 6.103.

Table 6.24: 16K fluorescence lifetimes for the $^5D_2$, $^5D_1$ and $^5D_0$ multiplets of the A centres in $CaF_2:Eu^{3+}$ and $SrF_2:Eu^{3+}$ and L centre in $BaF_2:Eu^{3+}$. The values in brackets are those of Hamers et. al.

Crystal	Centre Symmetry	Manifold Lifetime $^5D_0$	$^5D_1$	$^5D_2$
$CaF_2:Eu^{3+}$	C_{4v}	11.8(11.8)	3.6(3.58)	1.6(1.62)
$SrF_2:Eu^{3+}$	C_{4v}	13.4	5.9	5.4
$BaF_2:Eu^{3+}$	C_{3v}	14.6	10.3	6.3

For measurement of the $^5D_0$ lifetimes, R590 dye was used at the high frequency end of its range for pumping with the PRA nitrogen laser. Thus the $^5D_0$ multiplet was excited directly. This could not be done for the $^5D_0$ multiplet of the L centre in $BaF_2:Eu^{3+}$ as the $^7F_0 \rightarrow {}^5D_0$ transition is too weak. Instead, this multiplet was indirectly excited from $^5D_1$. The same approach was employed by Hamers et. al. [104] for the A centre in $CaF_2:Eu^{3+}$. The results of Hamers for $CaF_2:Eu^{3+}$ are given in Table 6.24. The $^5D_0$ lifetimes obtained are of the order of tens of milliseconds and reflect the absence of non-radiative relaxation from the $^5D_0$ state due to the large energy gap (12000 cm^{-1}) to the $^7F_6$ multiplet. As such they reflect only the electronic wavefunctions of the respective $^5D_0$ states. The measured lifetimes for this state in the three host crystals are observed to increase as the ionic radius of the alkaline earth fluoride increases. Such an increase is entirely consistent with the proposed charge compensation configurations for these centres as the interstitial F^- ion (responsible for the predominantly electric dipole character of the emitted radiation) becomes progressively more distant as we proceed through the host cations from Ca^{2+} to Ba^{2+}.

The $^5D_1$ multiplet can be readily excited with the very efficent C500 dye. Under this excitation, a striking visible (yellow - red) fluorescence is observed. The measured lifetimes change dramatically for the different host crystals. This feature is due to a combination of the lowering phonon cutoff energies of the host crystal lattice and the differing composition of the electronic wavefunctions.

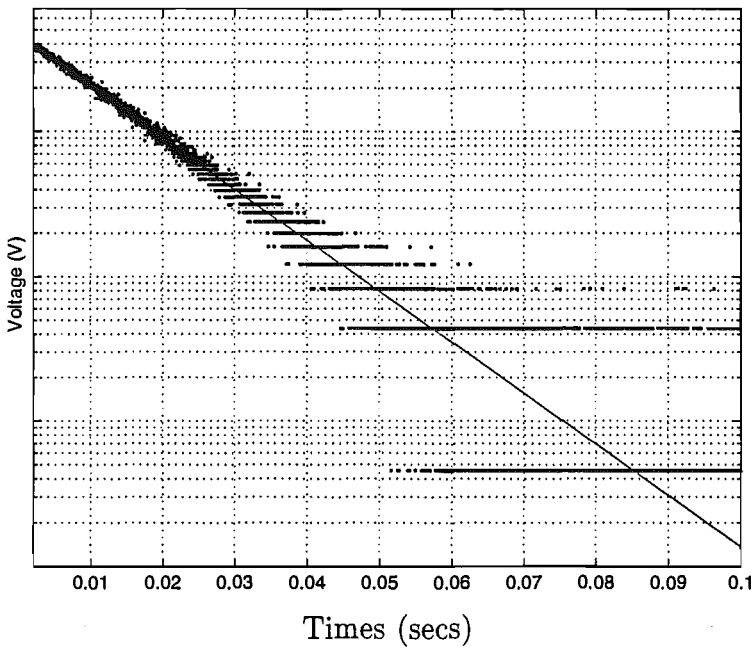

Figure 6.95: 16K $^5D_0$ fluorescence decay monitoring the 16979 cm^{-1} transition of the A centre in CaF_2:0.05%Eu^{3+}

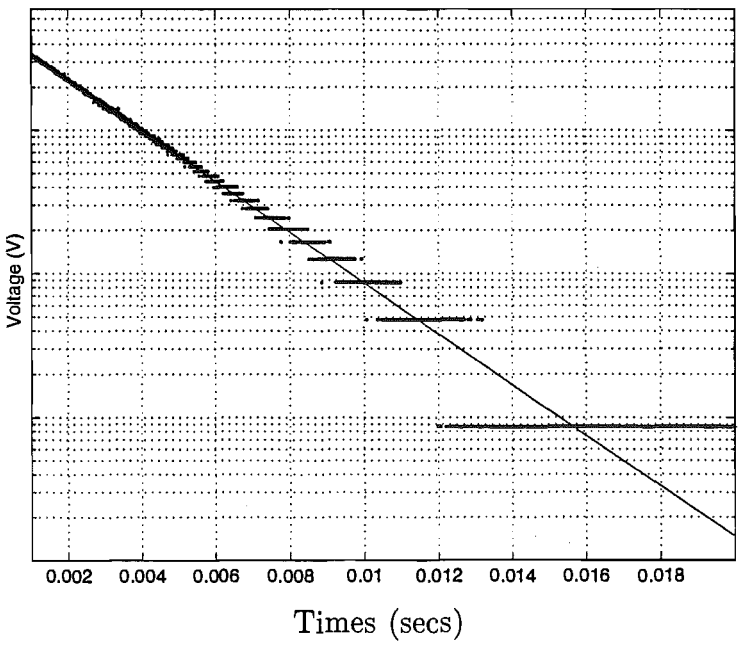

Figure 6.96: 16K $^5D_1$ fluorescence decay monitoring the 18177 cm^{-1} transition of the A centre in CaF_2:0.05%Eu^{3+}

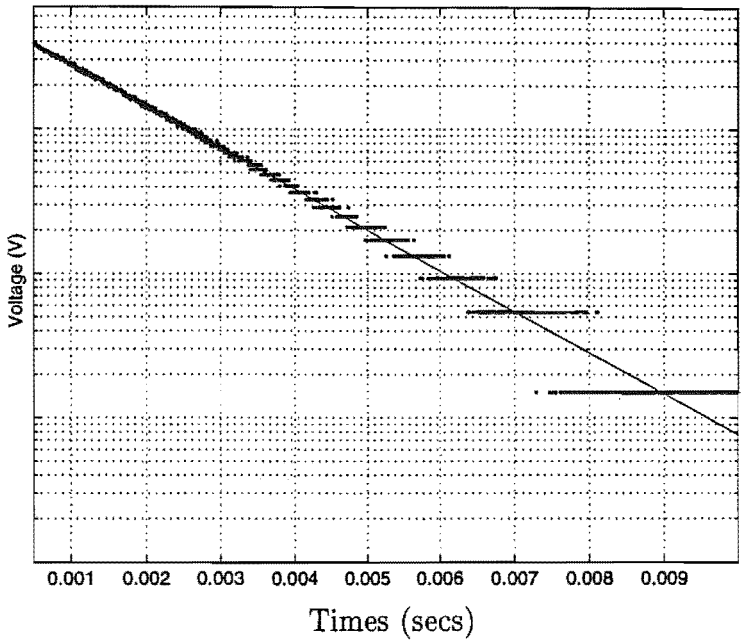

Figure 6.97: 16K $^5D_2$ fluorescence decay monitoring the 20484 cm^{-1} transition of the A centre in CaF_2:0.05%Eu^{3+}

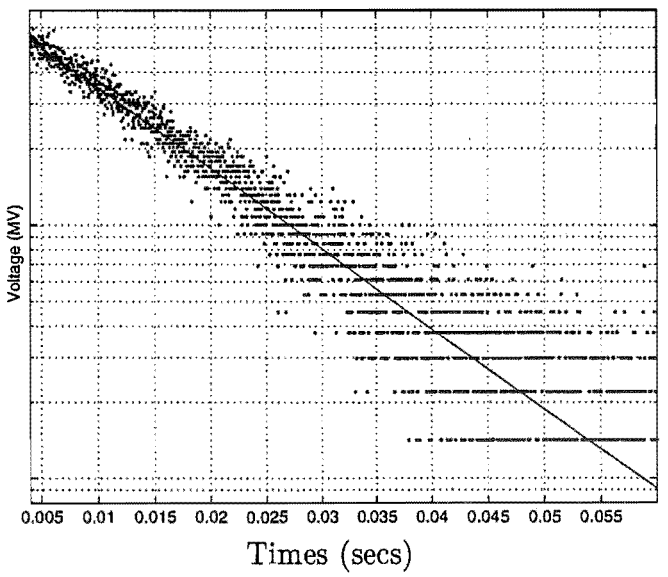

Figure 6.98: 16K $^5D_0$ fluorescence decay monitoring the 16974 cm^{-1} transition of the A centre in SrF_2:0.05%Eu^{3+}

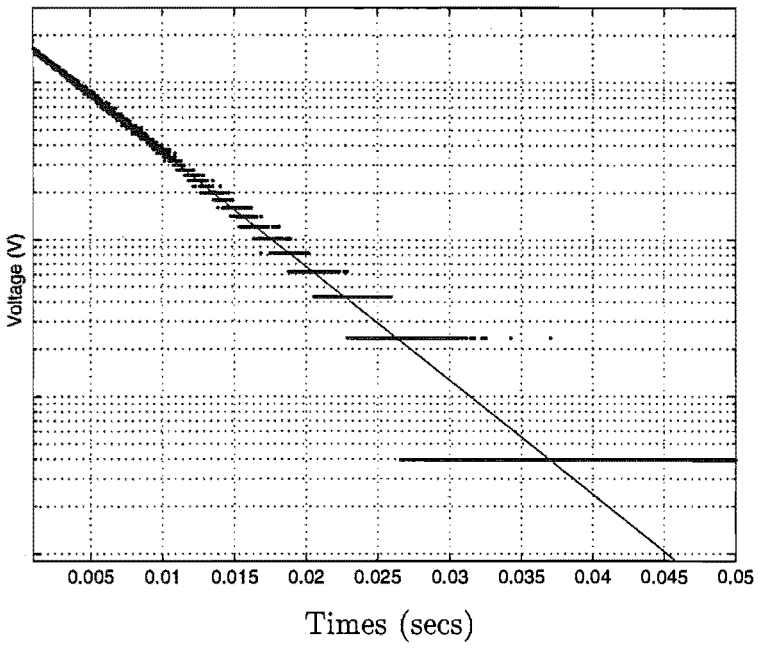

Figure 6.99: 16K $^5D_1$ fluorescence decay monitoring the 18175 cm^{-1} transition of the A centre in SrF_2:0.05%Eu^{3+}

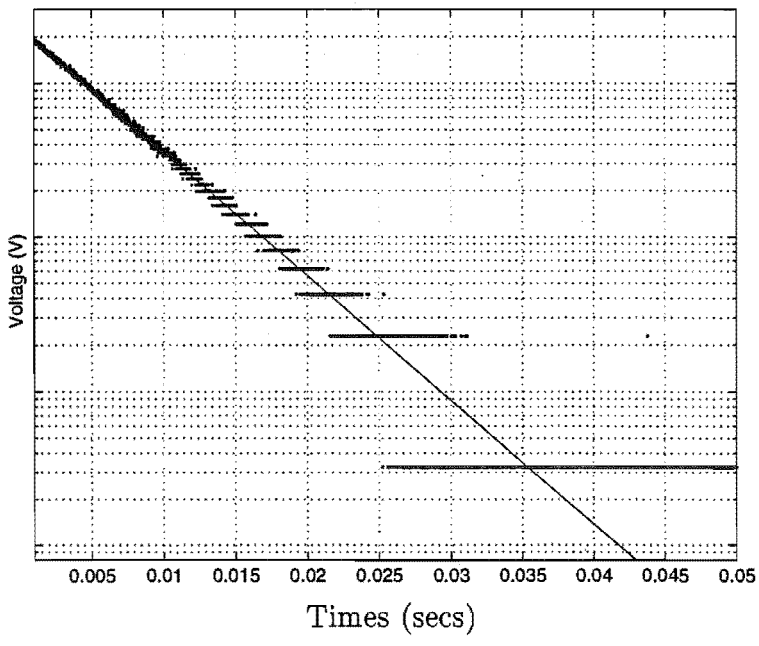

Figure 6.100: 16K $^5D_2$ fluorescence decay monitoring the 20513 cm^{-1} transition of the A centre in SrF_2:0.05%Eu^{3+}

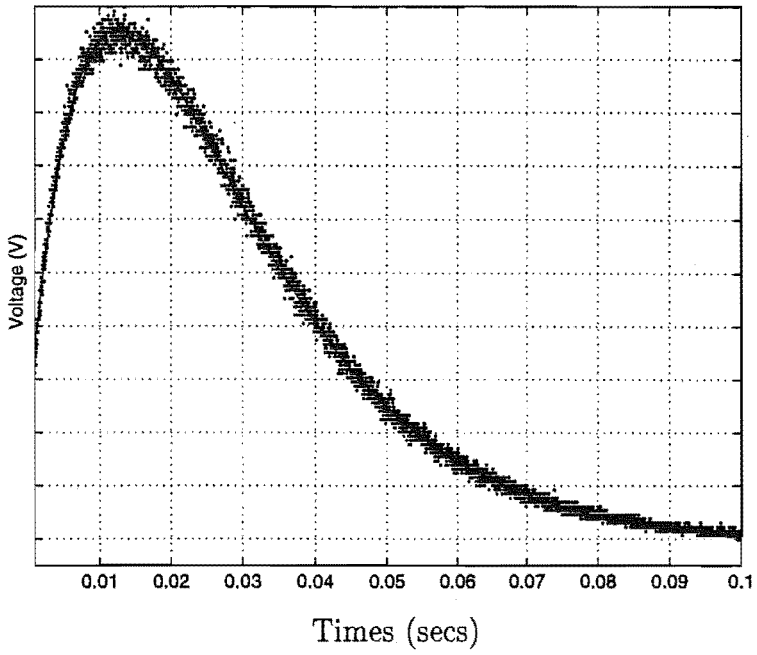

Figure 6.101: 16K $^5D_0$ fluorescence decay monitoring the 16978 cm^{-1} transition of the L centre in BaF_2:0.05%Eu^{3+}. The build up time is present because the $^5D_1$ multiplet was excited for measurement of this decay transient.

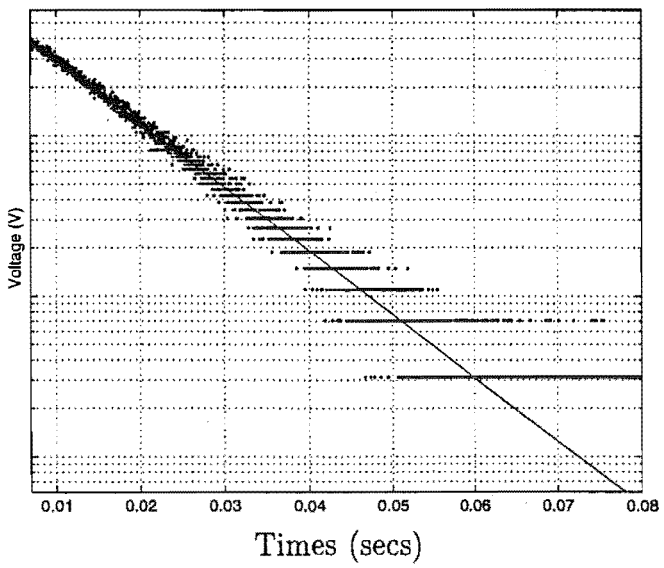

Figure 6.102: 16K $^5D_1$ fluorescence decay monitoring the 18206 cm^{-1} transition of the L centre in BaF_2:0.05%Eu^{3+}

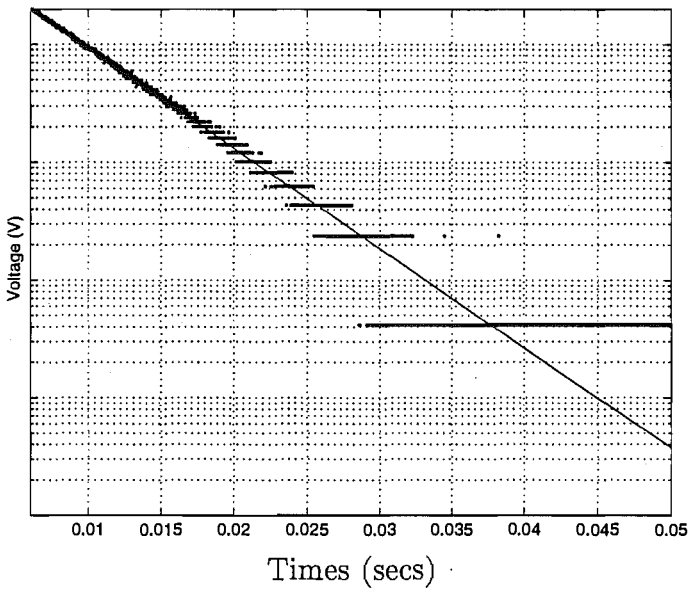

Figure 6.103: 16K $^5D_2$ fluorescence decay monitoring the 20629 cm^{-1} transition of the L centre in BaF_2:0.05%Eu^{3+}

Chapter 7

Laser Spectroscopy of Double Doped CaF_2:RE^{3+}:Sm^{3+}

7.1 Introduction

This chapter presents laser excitation and emission experiments on preferential cluster centres in CaF_2 crystals doubly doped with rare earth ions. Previous studies of cluster centres in rare earth doped CaF_2 crystals are reviewed below.

Some of the early evidence for the existence of preferential clustering in CaF_2 crystals, was obtained in the CaF_2:Nd^{3+} system. Both EPR and optical studies detected two centres that were interpreted as an orthorhombic dimer centre with two associated F^- ions (the M centre), and a more complex centre involving four Nd^{3+} ions (the N centre) Kask et. al. [132] (1965), Voronko et. al. [133] (1966). A further study, by Voronko et. al. [134] (1966) systematically analysed the optical absorption spectra of CaF_2 crystals doped with Pr^{3+}, Nd^{3+}, Eu^{3+} and Er^{3+} ions in turn. This was done using the concentration dependence of the absorption transitions. From the results presented there, it was apparant that at least two distinct cluster centres were formed at very low concentrations of the rare-earth dopant ion.

Corish et. al. [21] (1982) have theoretically examined the stability of monomer and dimer cluster centres in CaF_2 crystals containing trivalent rare-earth impurity ions. These authors have confirmed the stability of nearest neighbour dimer clusters containing two RE^{3+} ions and two F^- ions. It was also noted that such cluster centres form deep traps for any free interstitial F^- ions that might be present, thus forming an anion excess cluster centre.

The advent of up-to-date laser spectroscopic techniques allowed a more sensitive experimental determination of the extent to which clustering occurs in CaF_2:RE^{3+} crystals. Early work concentrated on the Er^{3+} ion (Tallant and Wright [22] 1975, Tallant, Moore and Wright [94] 1977, Moore and Wright [93] 1981). From these studies, a complex picture of 16 cluster centres was determined. Clustering was

proposed as the dominant mechanism for the control of the defect centre distribution in $CaF_2:RE^{3+}$ crystals. Miller and Wright [135] (1978) and Moore and Wright [136] (1979) supported a model of interstitial fluoride scavenging. This model was proposed by Yaney, Schaeffer and Wolf [82] (1975) to account for the behaviour of the non-locally charge compensated cubic symmetry centres in $SrF_2:Gd^{3+}:Ce^{3+}$ crystals. In this case, the cubic centres are observed to increase in proportion with the increasing dimer centre population as a function of concentration.

Higher order clusters have also been detected in $CaF_2:RE^{3+}$ crystals. A particularly beautiful example is presented by Seelbinder and Wright [137] (1981) for $CaF_2:Tb^{3+}:Yb^{3+}$ crystals. This study uses three-body energy transfer to identify trimer centres. Two Yb^{3+} ions are simultaneously excited, leading to higher frequency Tb^{3+} emission. Such a process cannot proceed by simple two body processes as two Yb^{3+} ions are required to bridge the energy mismatch between the appropriate $Yb^{3+}(^2F_{\frac{5}{2}})$ and $Tb^{3+}(^5D_4)$ states. Still more complex centre configurations have been reported by Kazanskii [138] (1984). This author studied the $CaF_2:Er^{3+}$ system, where the creation of superstructure regions in the host lattice was observed. This was proposed to be due to the formation of hexamers consisting of six rare earth ions surrounded by 12 or more interstitial F^- ions.

Various cluster centres have been observed by Tissue and Wright [62] (1987) for the $CaF_2:Pr^{3+}$ system. Of these, an assymmetric dimer centre was studied for energy transfer between the inequivalent Pr^{3+} ions. For an energy mismatch of around 150 cm^{-1} these authors showed that the dominant mechanism of energy transfer, at low temperatures (around 10K), was a one phonon emission process. At higher temperatures the transfer mechanism was determined to be a combination of a one phonon and several two-phonon resonant processes [114]. The effect of co-doping with additional rare earths was also explored to observe line shifts in the cluster centre absorption transitions.

In $CaF_2:Eu^{3+}$, asymmetric and symmetric dimer centres have been observed by Hamers et. al. [104] (1982). The symmetric dimer centre, labelled Q, has been assigned from its manifold degeneracy and concentration dependence as containing two coupled equivalent Eu^{3+} ions. For the asymmetric centre, labelled R, more than 2J+1 emission features were observed for each J manifold. Emission was studied from $^5D_0$. From analysis of emmission from $^5D_0$ and the dependence of the absorption intensity upon dopant concentration, the centre was assigned as a pair of inequivalent Eu^{3+} ions. Additional studies were undertaken by Cirillo-Penn and Wright [10] [110]. These authors reassigned the Q centre as a trimer centre from the annealing time dependence of the absolute centre concentrations. The co-doping of La^{3+}, Gd^{3+} and Lu^{3+} into the parent $CaF_2:Eu^{3+}$ system was also studied for the observation of line shifts of the cluster centre absorption transitions.

The observation of a pair of non-radiative Sm^{3+} centres in CaF_2:Sm^{3+} prompts a study of co-doped systems where additional RE^{3+} ions have been added to the CaF_2:Sm^{3+} parent. The objective is to create analogue centres, where the Sm^{3+} cross-relaxation processes have effectively been turned-off. This enables a study of the Sm^{3+} emission to be performed in order to better understand the nature of the observed centres.

7.2 Sm^{3+} Cross-Relaxation Processes

In the CaF_2:Sm^{3+} absorption and excitation spectra, it was discovered that there exist Sm^{3+} centres which are entirely non-radiative. As the energy gap between the $^4G_{\frac{5}{2}}$ multiplet and the highest energy ^6F multiplet is 7500 cm^{-1}, direct multiphonon processes will be negligible. Therefore, the optical excitation must be destroyed by energy transfer cross-relaxation processes between the Sm^{3+} ions of which the centre(s) are comprised. Naturally, this implies that there are multi-ion centres present, or at least, loosely coupled single ion centres.

Sm^{3+} energy transfer cross-relaxation has been previously observed in the rare-earth hexachloroelpasolite crystals by Luxbacher et. al. [139] [140]. Specifically, $Cs_2NaSm_xY_{1-x}Cl_6$ and $Cs_2NaSm_xGd_{1-x}Cl_6$ crystals were studied for $^4G_{\frac{5}{2}}$ fluorescent decay as a function of temperature. In the rare-earth hexachloroelpasolites, the RE^{3+} occupies a purely octahedral centre, surrounded by six chloride ions [141]. Due to the selection rules for octahedral centres, the excited state lifetimes are long. This offers possibilities for energy transfer and storage. Luxbacher and co-workers discovered that $^4G_{\frac{5}{2}} \rightarrow {}^6F_J$ cross-relaxation occured over a wide range of concentrations from x=0.001 to x=1. In addition, emission was observed from the $^4G_{\frac{5}{2}}$ state to levels of the ^6H_J and ^6F_J multiplets. The authors analysed the cross-relaxation in terms of a shell model [142]. This model assumes Förster-Dexter multipole-multipole interactions [143] between statisically distributed donor and acceptor ions. The difference here is that instead of the concept of a continuous range of distances between donor and acceptor ions, the acceptor ions are grouped into shells of a certain occupancy as appropriate for the crystal structure in question. This idea first put forward by Heber, Dornauf and Siebold [144] (1981).

The most probable Sm^{3+}-Sm^{3+} energy transfer relaxation pathways are shown in Figure 7.1. These pathways are taken from [140]. In the CaF_2:Sm^{3+} cluster centres discussed here, no $^4G_{\frac{5}{2}}$ emission is observed. Thus, it is concluded that the cross-relaxation energy transfer is all but total. As a result of the approximately 460 cm^{-1} phonon cutoff energy for the host lattice phonon spectrum, ions which end up in the

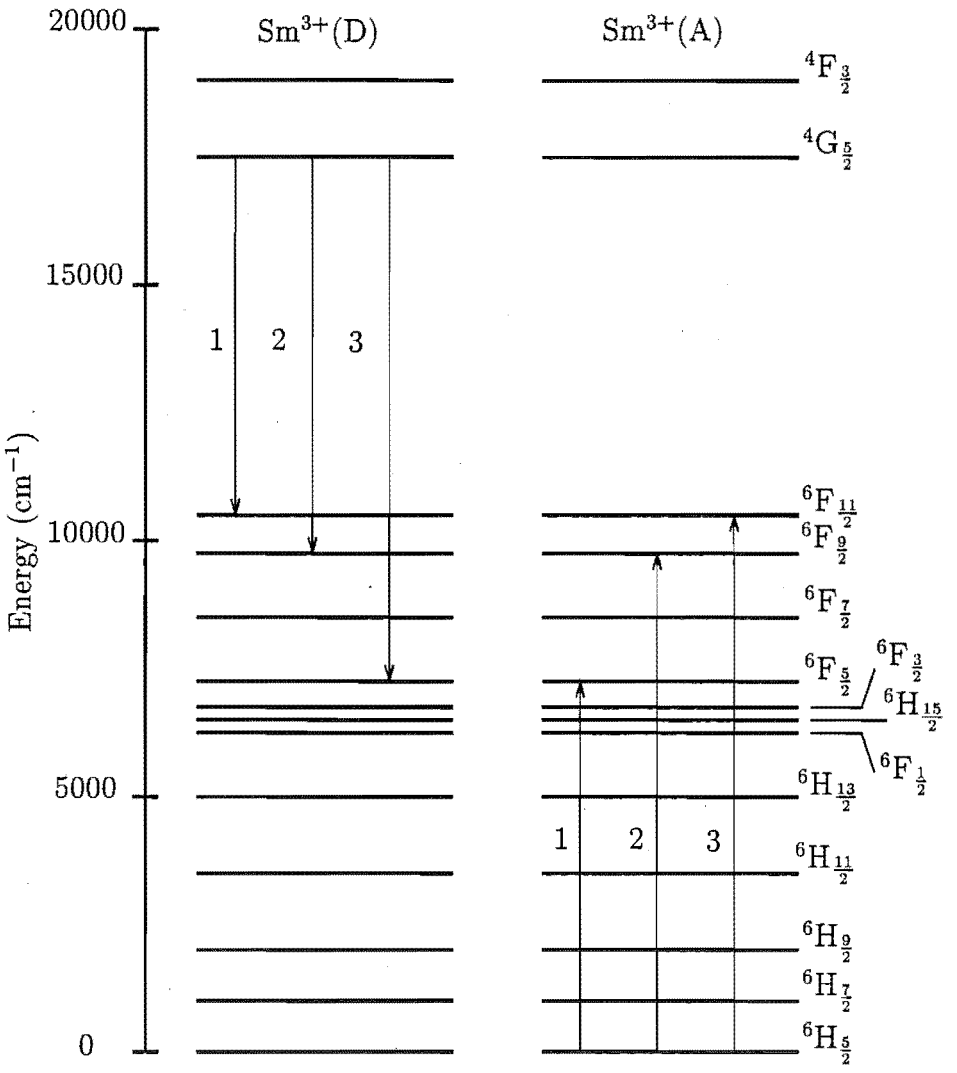

Figure 7.1: Possible Sm^{3+}-Sm^{3+} energy transfer relaxation pathways.

^6F_J states as a result of cross-relaxation, decay non-radiatively to the ground state with no possibility of monitoring emission from the ^6F_J states.

7.3 Excitation Spectra

The following notation is adopted in this chapter. Q(RE,Sm) indicates a heterogeneous Q centre, whilst R(RE,Sm) indicates a heterogeneous R centre. RE indicates the particular rare-earth ion introduced. No attempt is made to refer to the number of ions in the centre. Because of the particular crystal growth conditions used and the optical spectra observed it is apparent that the rare earth ions are trivalent.

$^4G_{\frac{5}{2}}$ excitation spectra have been measured for CaF_2:0.05%Sm^{3+} crystals co-doped with 0.15% of LaF_3, CeF_3, EuF_3, GdF_3, TbF_3, DyF_3, ErF_3, TmF_3 and YbF_3. The crystals were cooled to 16K. The recorded spectra are shown in Figures 7.2 through to 7.10. Both broad and narrow band frequency detection was employed. When recording broadband Sm^{3+} excitation spectra, either on the SPEX 1700 or 0.25m Bausch and Lomb monochromators, a 2-62-1 Corning glass filter was used to eliminate unwanted laser scatter.

It can be observed that the centre distributions come in two classes. For co-dopant ions prior to Dy^{3+}, the observed excitation spectra resemble the CaF_2:Sm^{3+} parent crystal absorption spectra for the $^4G_{\frac{5}{2}}$ multiplet. In these cases, the features labelled R and Q (in the $^4G_{\frac{5}{2}}$ absorption spectra) are observed. Note that the R and Q were not present in the parent crystal excitation spectra but are observed here because the Sm^{3+} - RE^{3+} clusters cannot cross-relax, as suitable energy matches are not available. This confirms that the R and Q centres do correspond to multi-ion centres. This is reinforced by the frequency shifts of the observed R and Q centre transitions, apparant for different co-dopant ions. The $^4G_{\frac{5}{2}}$ excitation frequencies for the heterogeneous R and Q centres are given in Tables 7.1 and 7.2. PrF_3 and NdF_3 were also added to the parent CaF_2:0.05%Sm^{3+} system. In these cases, R and Q centre emission was seached for, but none was observed. It is assumed that this is due to the availability of appropriate levels for cross-relaxation.

When ions smaller, and including, Dy^{3+} are included in the crystal melt, a centre distinct from either R or Q, is formed. Spectroscopically, this centre appears similar to both the R and Q centres. We arbitrarily label this centre S. Table 7.3 gives the measured transition frequencies for the S centre. The $^4G_{\frac{5}{2}}$ excitation frequencies of this centre do not change as the codopant ion is altered. Thus, it is concluded that this centre contains a single Sm^{3+} ion with no additional rare earth ions present.

Table 7.1: Excitation frequencies measured for the $^4G_{\frac{5}{2}}$ multiplet of the Q(RE,Sm) centre in CaF_2. All frequencies are as measured in air (cm^{-1}, ± 1).

State	(La^{3+}:Sm^{3+})	(Ce^{3+}:Sm^{3+})	(Eu^{3+}:Sm^{3+})	(Gd^{3+}:Sm^{3+})	(Tb^{3+}:Sm^{3+})
A_1	17810	17811	17813	17813	17812
A_2	17905	17900	17887	17885	17881
A_3	17965	17956	17960	17957	17954

Table 7.2: Excitation frequencies measured for the $^4G_{\frac{5}{2}}$ multiplet of the R(RE,Sm) centre in CaF_2. All frequencies are as measured in air (cm^{-1}, ± 1).

State	(La^{3+}:Sm^{3+})	(Ce^{3+}:Sm^{3+})	(Eu^{3+}:Sm^{3+})	(Gd^{3+}:Sm^{3+})	(Tb^{3+}:Sm^{3+})
A_1	17830	17830	17829	17828	17828
A_2	17894	17893	17891	17889	17888
A_3	17928	17920	17908	17906	17898
A_4	17938	17931	17922	17918	17913
A_5	17953	17947	17942	17941	17935

The $^4G_{\frac{5}{2}}$ excitation spectra were also measured for co-doping Ho^{3+} and Lu^{3+} ions. In the case of CaF_2:0.15%Ho^{3+}:0.05%Sm^{3+}, an anomalous centre distribution was found in which the cubic centre dominated the spectrum. Few additional centres, including the A centre, were apparant. The CaF_2:0.15%Lu^{3+}:0.05%Sm^{3+} spectrum was exceedingly complex with many centres apparant. In both of these cases it was beyond the scope of this study to pursue the investigation any further.

Table 7.3: Excitation frequencies measured for the $^4G_{\frac{5}{2}}$ multiplet of the S centre in CaF_2:RE^{3+}:Sm^{3+}. All frequencies are as measured in air (cm^{-1}, ± 1).

State	(Dy^{3+}:Sm^{3+})	(Er^{3+}:Sm^{3+})	(Tm^{3+}:Sm^{3+})	(Yb^{3+}:Sm^{3+})
A_1	17811	17812	17811	17811
A_2	17834	17833	17832	17833
A_3	17854	17855	17854	17854
A_4	17889	17889	17887	17887
A_5	17911	17911	17911	17912

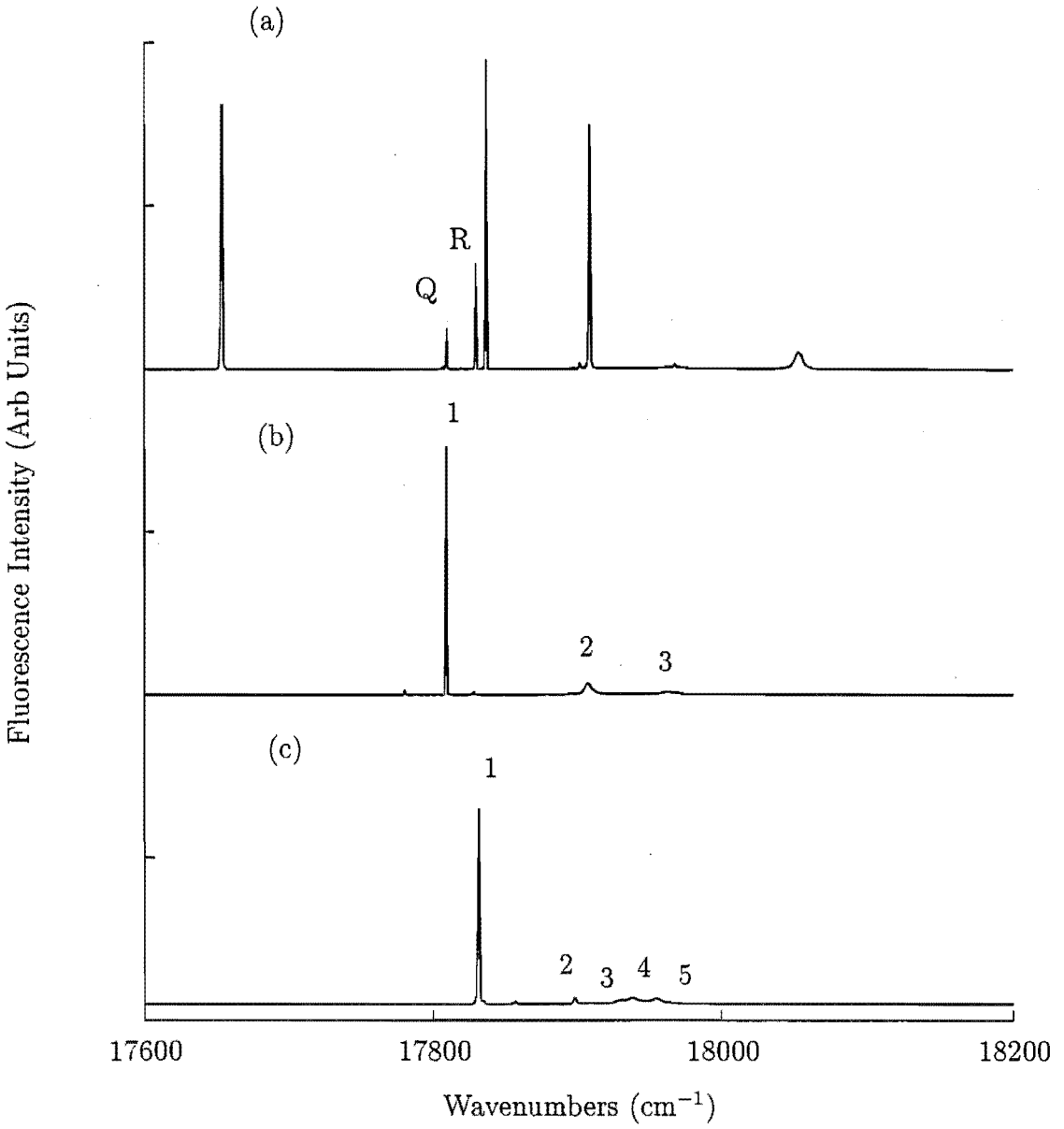

Figure 7.2: $^4G_{\frac{5}{2}}$ (Sm^{3+}) excitation spectra for CaF_2:0.15%La^{3+}:0.05%Sm^{3+}. (a) Broadband monitoring all fluorescence in zero order, (b) Q centre monitoring at 15601 cm^{-1} and (c) R centre monitoring at 15613 cm^{-1}. The spectra were recorded at 16K.

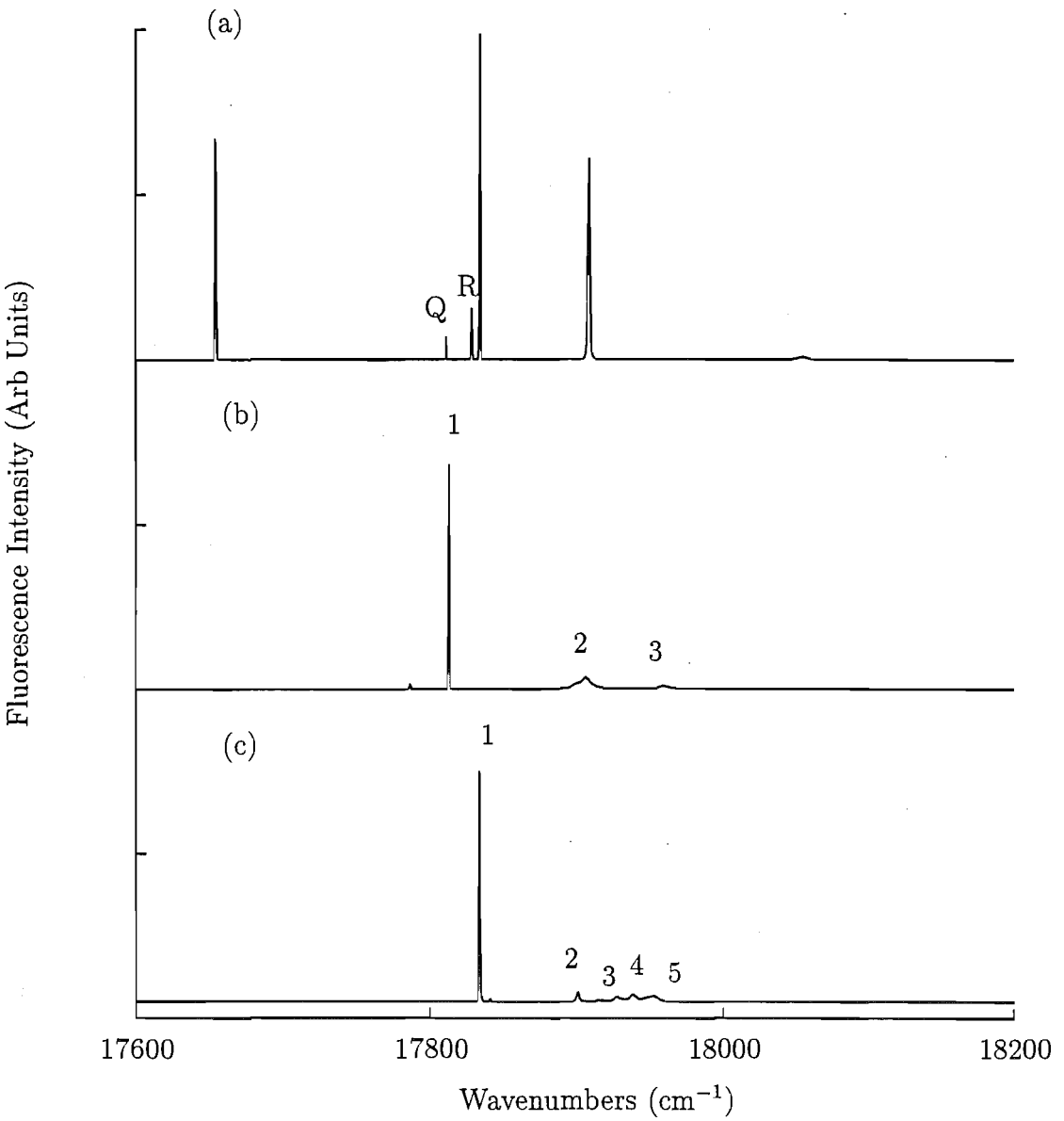

Figure 7.3: $^4G_{\frac{5}{2}}$ (Sm^{3+}) excitation spectra for CaF_2:0.15%Ce^{3+}:0.05%Sm^{3+}. (a) Broadband monitoring all fluorescence in zero order, (b) Q centre monitoring at 15607 cm^{-1} and (c) R centre monitoring at 15617 cm^{-1}. The spectra were recorded at 16K.

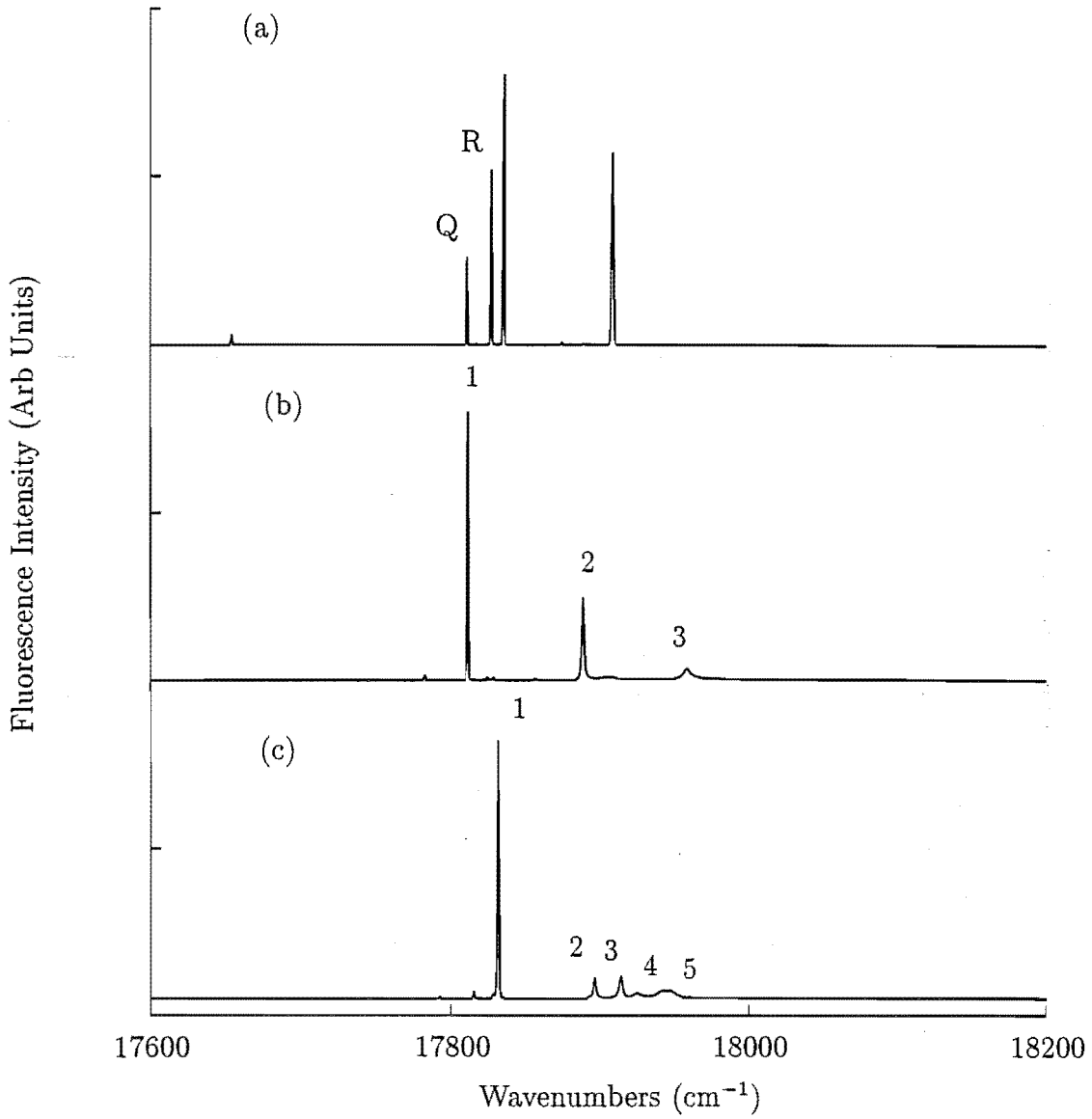

Figure 7.4: $^4G_{\frac{5}{2}}$ (Sm^{3+}) excitation spectra for CaF_2:0.15%Eu^{3+}:0.05%Sm^{3+}. (a) Broadband monitoring all fluorescence in zero order, (b) Q centre monitoring at 16934 cm^{-1} and (c) R centre monitoring at 16942 cm^{-1}. The spectra were recorded at 16K.

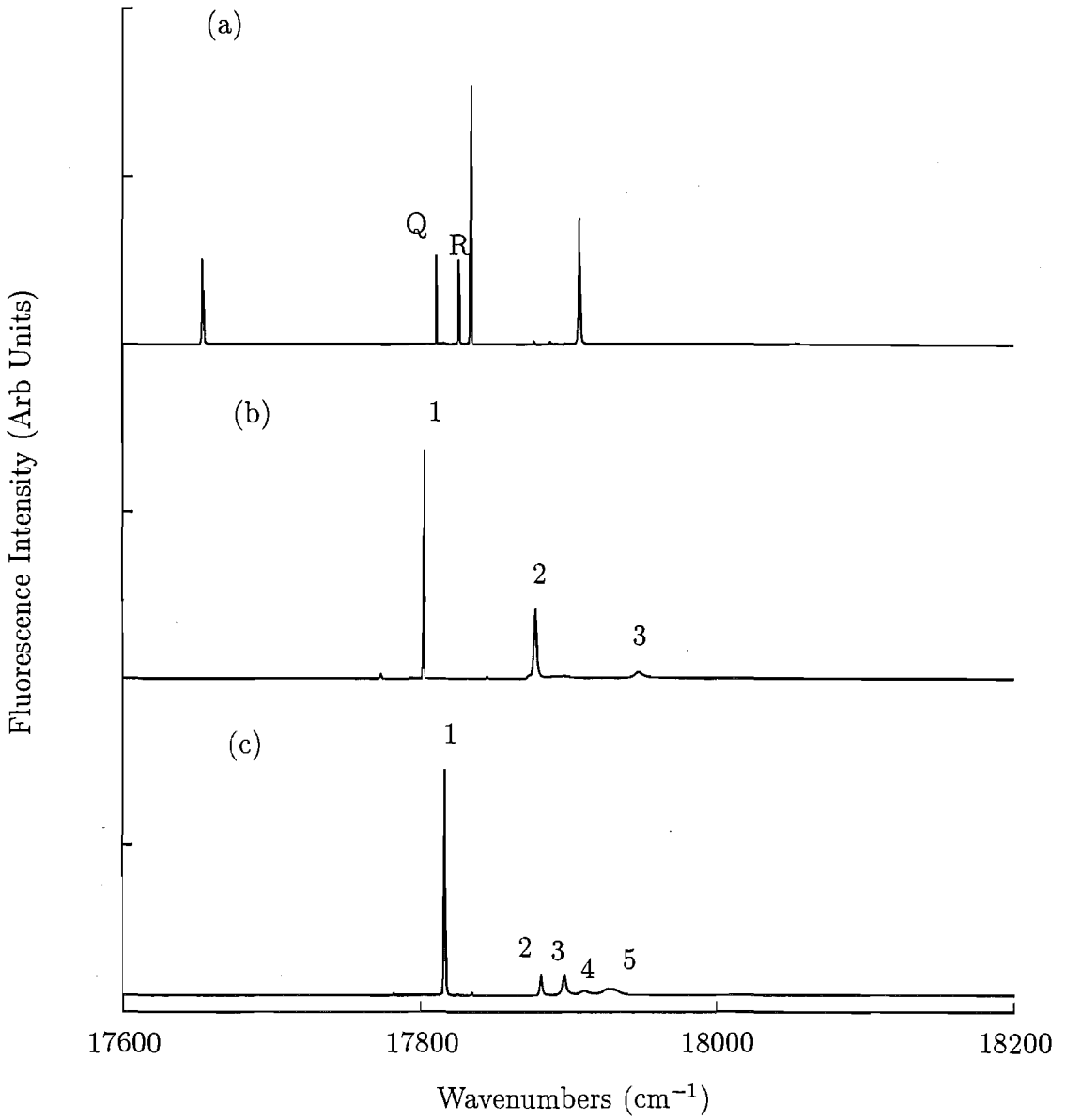

Figure 7.5: $^4G_{\frac{5}{2}}$ (Sm^{3+}) excitation spectra for CaF_2:0.15%Gd^{3+}:0.05%Sm^{3+}. (a) Broadband monitoring all fluorescence in zero order, (b) Q centre monitoring at 15614 cm^{-1} and (c) R centre monitoring at 15628 cm^{-1}. The spectra were recorded at 16K.

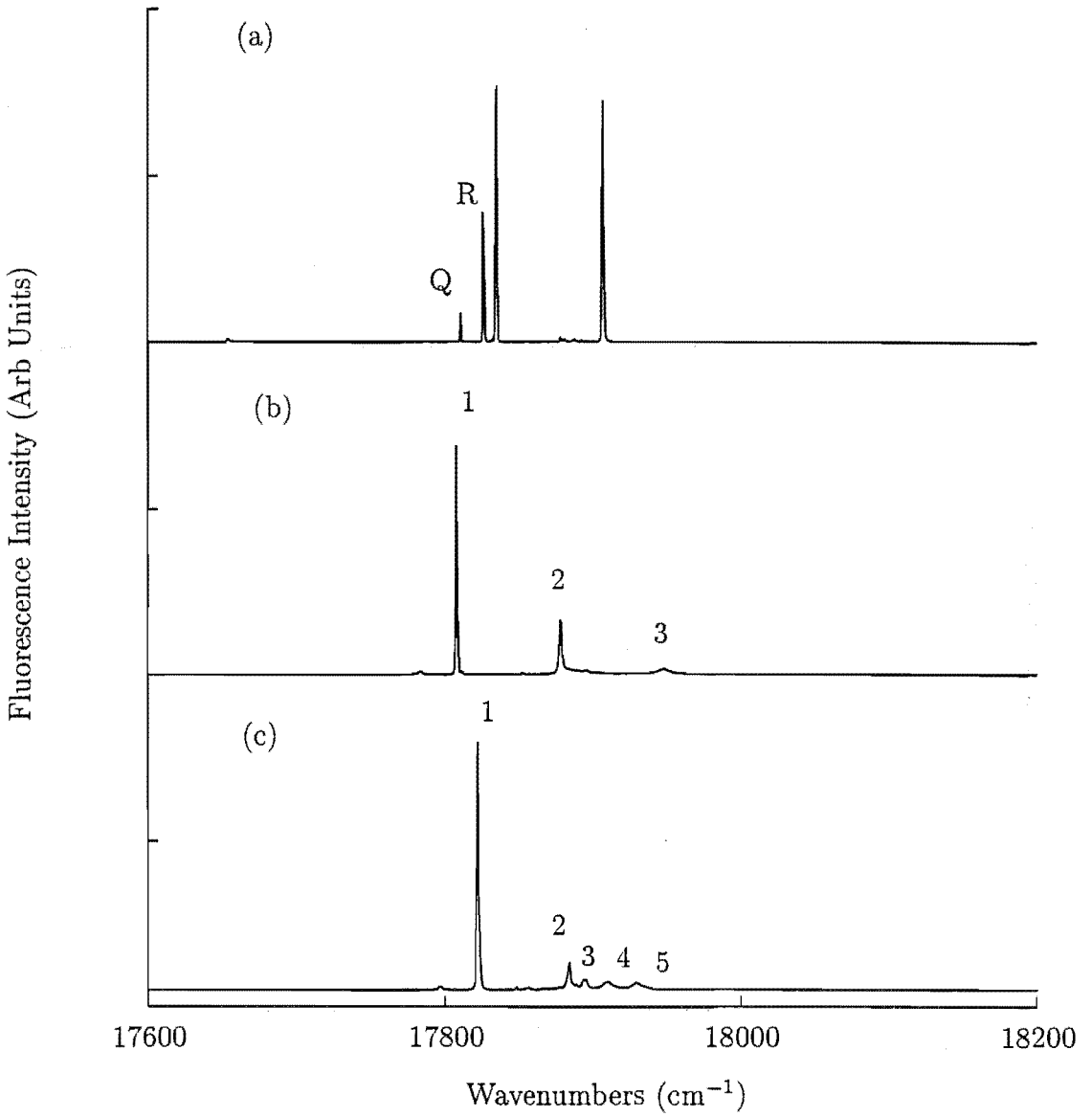

Figure 7.6: $^4G_{\frac{5}{2}}$ (Sm^{3+}) excitation spectra for CaF_2:0.15%Tb^{3+}:0.05%Sm^{3+}. (a) Broadband monitoring all fluorescence in zero order, (b) Q centre monitoring at 15620 cm^{-1} and (c) R centre monitoring at 15637 cm^{-1}. The spectra were recorded at 16K.

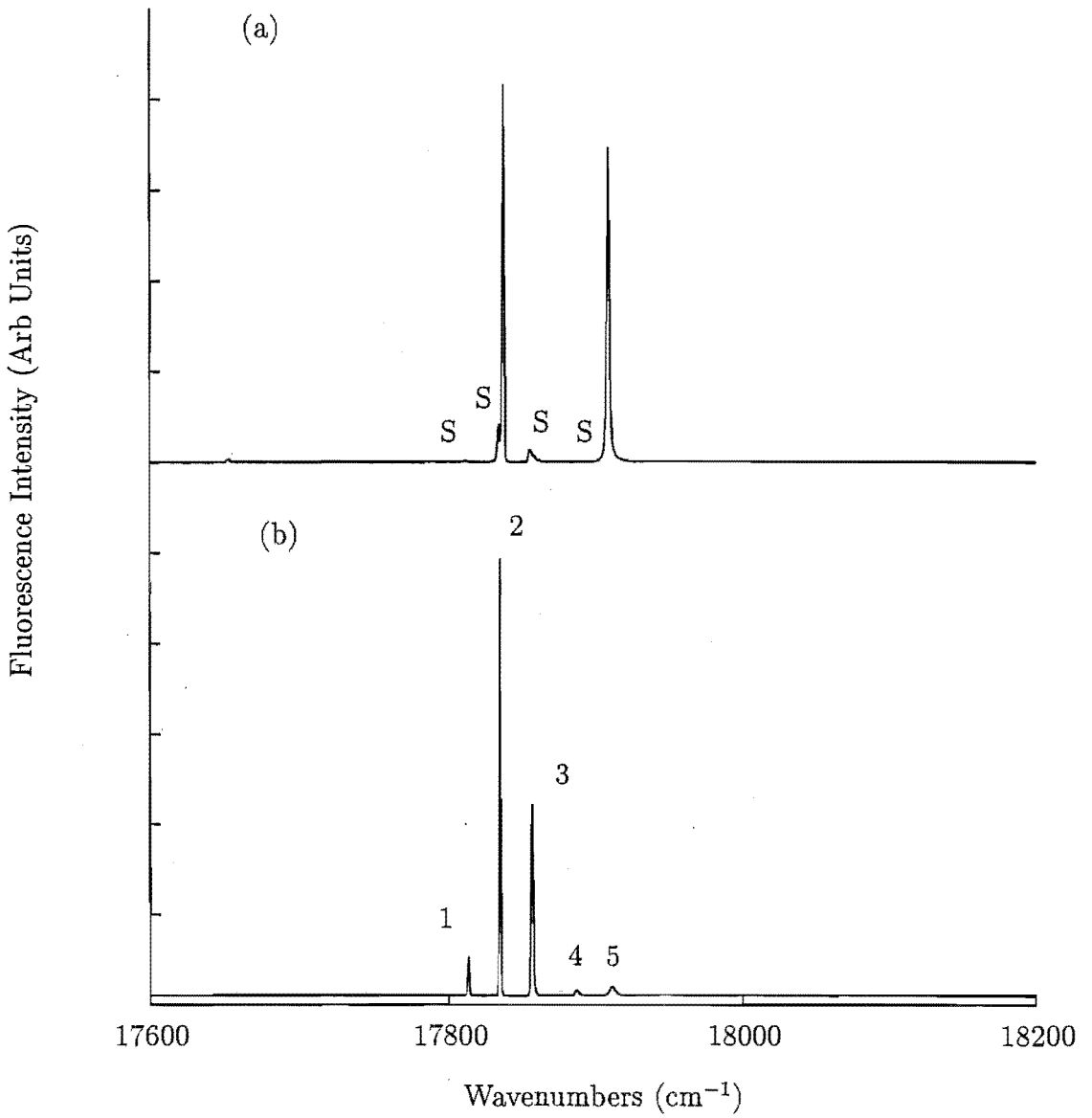

Figure 7.7: $^4G_{\frac{5}{2}}$ (Sm^{3+}) excitation spectra for CaF_2:0.15%Dy^{3+}:0.05%Sm^{3+}. (a) Broadband monitoring all fluorescence in zero order and (b) S centre monitoring at 16868 cm^{-1}. The spectra were recorded at 16K.

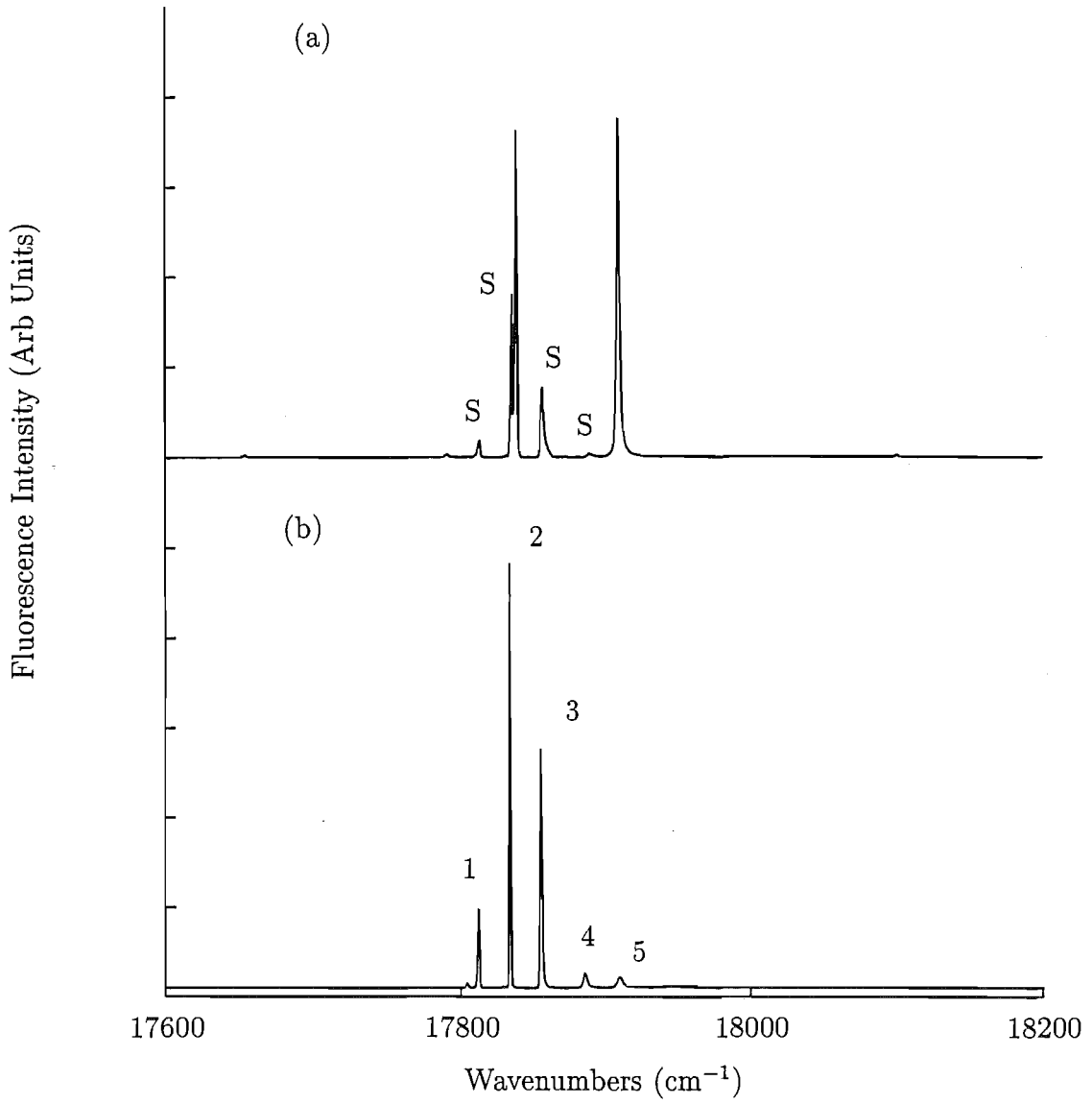

Figure 7.8: $^4G_{\frac{5}{2}}$ (Sm^{3+}) excitation spectra for CaF_2:0.15%Tm^{3+}:0.05%Sm^{3+}. (a) Broadband monitoring all fluorescence in zero order and (b) S centre monitoring at 16867 cm^{-1}. The spectra were recorded at 16K.

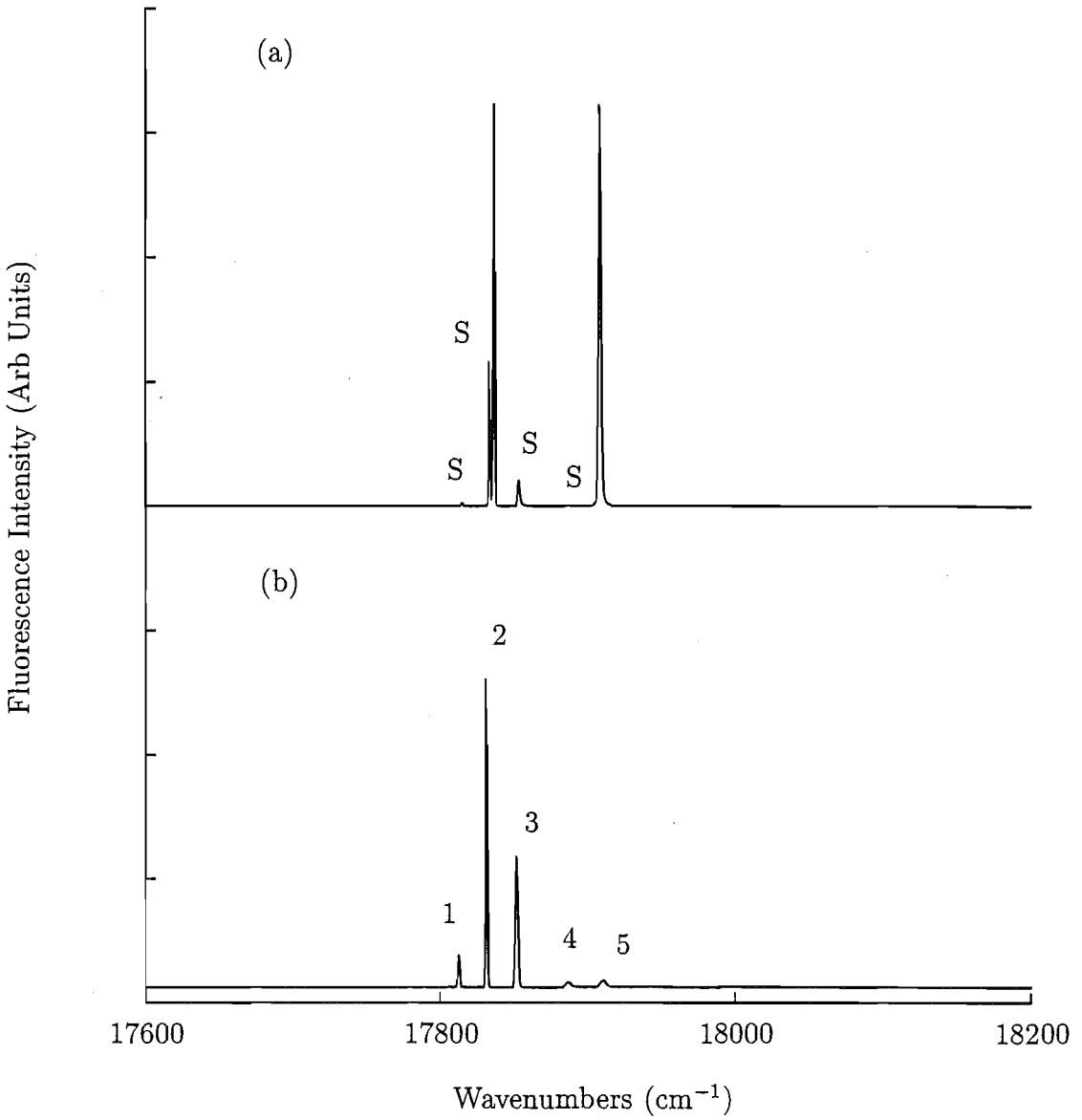

Figure 7.9: $^4G_{\frac{5}{2}}$ (Sm^{3+}) excitation spectra for CaF_2:0.15%Er^{3+}:0.05%Sm^{3+}. (a) Broadband monitoring all fluorescence in zero order and (b) S centre monitoring at 16868 cm^{-1}. The spectra were recorded at 16K.

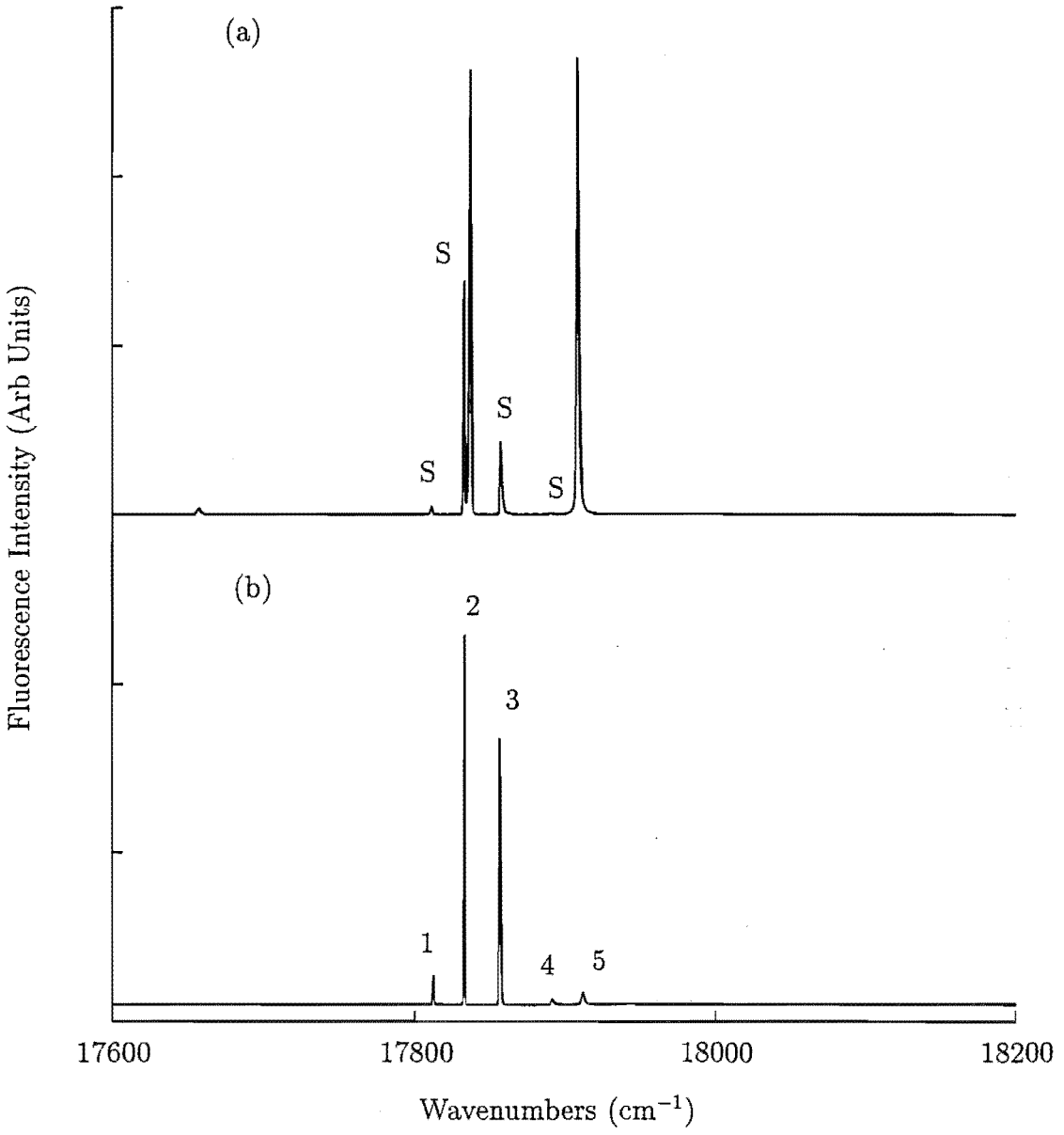

Figure 7.10: $^4G_{\frac{5}{2}}$ (Sm^{3+}) excitation spectra for CaF_2:0.15%Yb^{3+}:0.05%Sm^{3+}. (a) Broadband monitoring all fluorescence in zero order and (b) S centre monitoring at 16867 cm^{-1}. The were recorded at 16K.

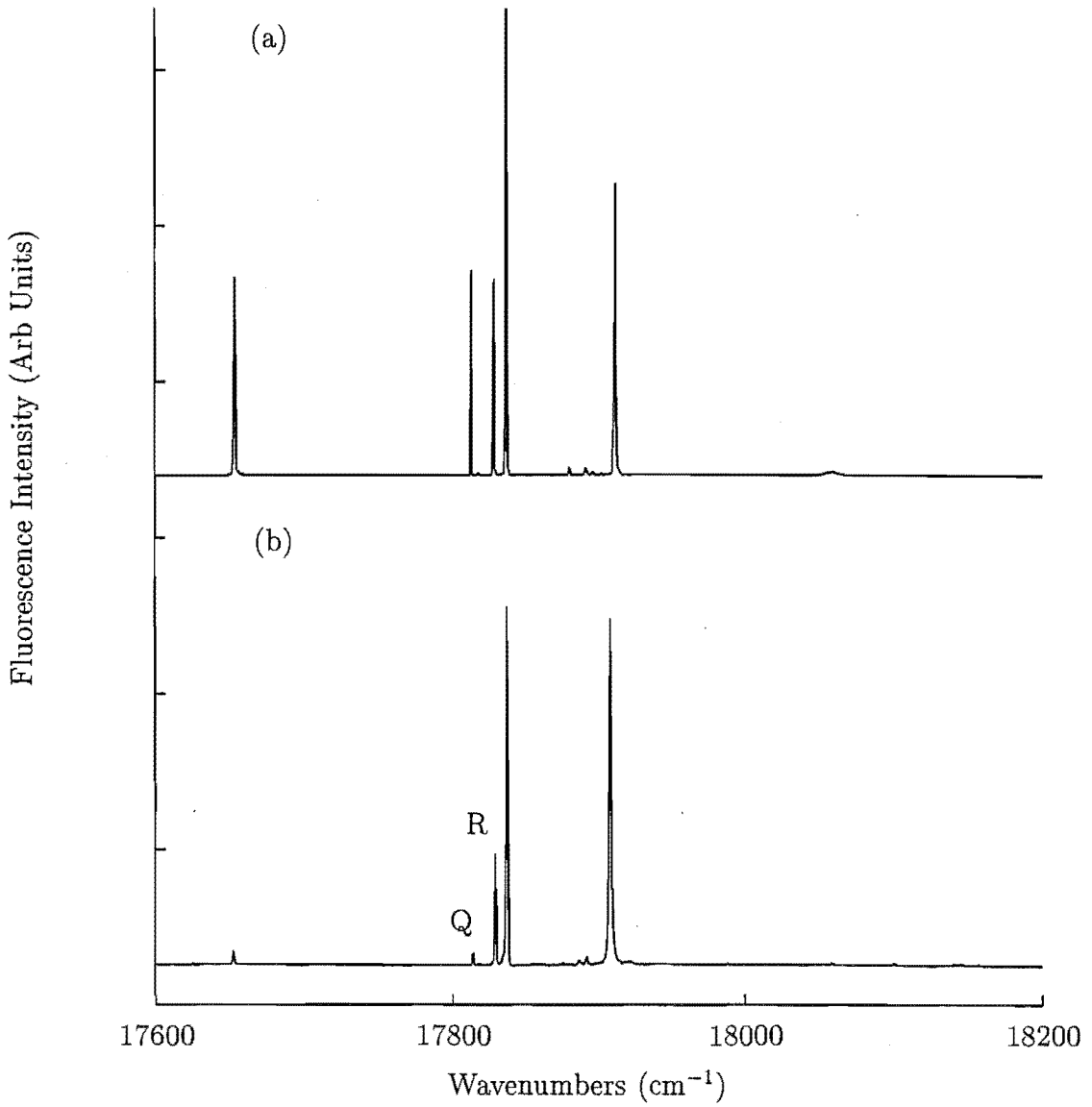

Figure 7.11: $^4G_{\frac{5}{2}}$ (Sm^{3+}) excitation spectra for (a) CaF_2:0.15%Gd^{3+}:0.05%Sm^{3+} and (b) CaF_2:0.15%Sm^{3+}:0.05%Gd^{3+}. The spectra were recorded at 16K.

For most cluster centres studied, the crystals grown were doped in the ratio one Sm^{3+} ion for every three co-dopant ions. This was done, in order to ensure that even for centres comprising more than two rare earth ions, fluorescence would be detectable. However, in order to determine whether the cluster centres observed here contain more than two ions, the dopant ratios were reversed. A CaF_2:0.15%Sm^{3+}:0.05%Gd^{3+} crystal was grown and its $^4G_{\frac{5}{2}}$ excitation spectrum recorded. The spectrum is given in Figure 7.11. By comparision with the CaF_2:0.15%Gd^{3+}:0.05Sm^{3+} $^4G_{\frac{5}{2}}$ excitation spectrum, it is observed that the Q centre fluorescence decreases by more than a factor of three. This is judged from the intensity of the 17813 cm^{-1} transition. A possible explanation is that the Q centre contains more than two rare earth ions. The Q(Gd,Sm) centre fluorescence intensity would decrease because there is a higher probability for Sm^{3+} - Sm^{3+} cross-relaxation in a higher order cluster, in mixed crystals where more Sm^{3+} is added than Gd^{3+}. Cirillo-Penn and Wright [10] [110] assign the Q centre in CaF_2:Eu^{3+} as a trimer. These results appear consistent with this assignment.

7.4 Fluorescence Spectroscopy

7.4.1 The Q and R Centres in CaF_2:Eu^{3+}:Sm^{3+}

(a) Q Centre Fluorescence

In CaF_2:0.15%Eu^{3+}:0.05%Sm^{3+} crystals, fluorescence is observed upon optical excitation of the either the Eu^{3+} or Sm^{3+} absorption transitions of the heterogeneous Q(Eu,Sm) centre. For excitation of the Sm^{3+} ion $Z_1 \rightarrow A_1$ transition, at 17813 cm^{-1}, strong emission is observed. The recorded fluorescence spectra are shown in Figures 7.12 through to 7.14. Table 7.4 gives the measured transition frequencies.

It is readily apparent that the emission emanates from the Eu^{3+} ion with the initial state being the single $^5D_0A_1$ level at 17259 cm^{-1}. Thus, energy has been transferred from the $Sm^{3+}(^4G_{\frac{5}{2}})$ ion to the $Eu^{3+}(^5D_0)$ ion. This energy transfer requires lattice mediation between the two electronic levels. This is achieved via the emission of at least two phonons since the 554 cm^{-1} gap is beyond the 460 cm^{-1} cutoff energies for the CaF_2 host lattice.

Detection sensitivities greater than 1000 times that, required to observe the Eu^{3+} $^5D_0 \rightarrow ^7F_1$ transitions, were employed in an attempt to observe Sm^{3+} $^4G_{\frac{5}{2}}$ emission.

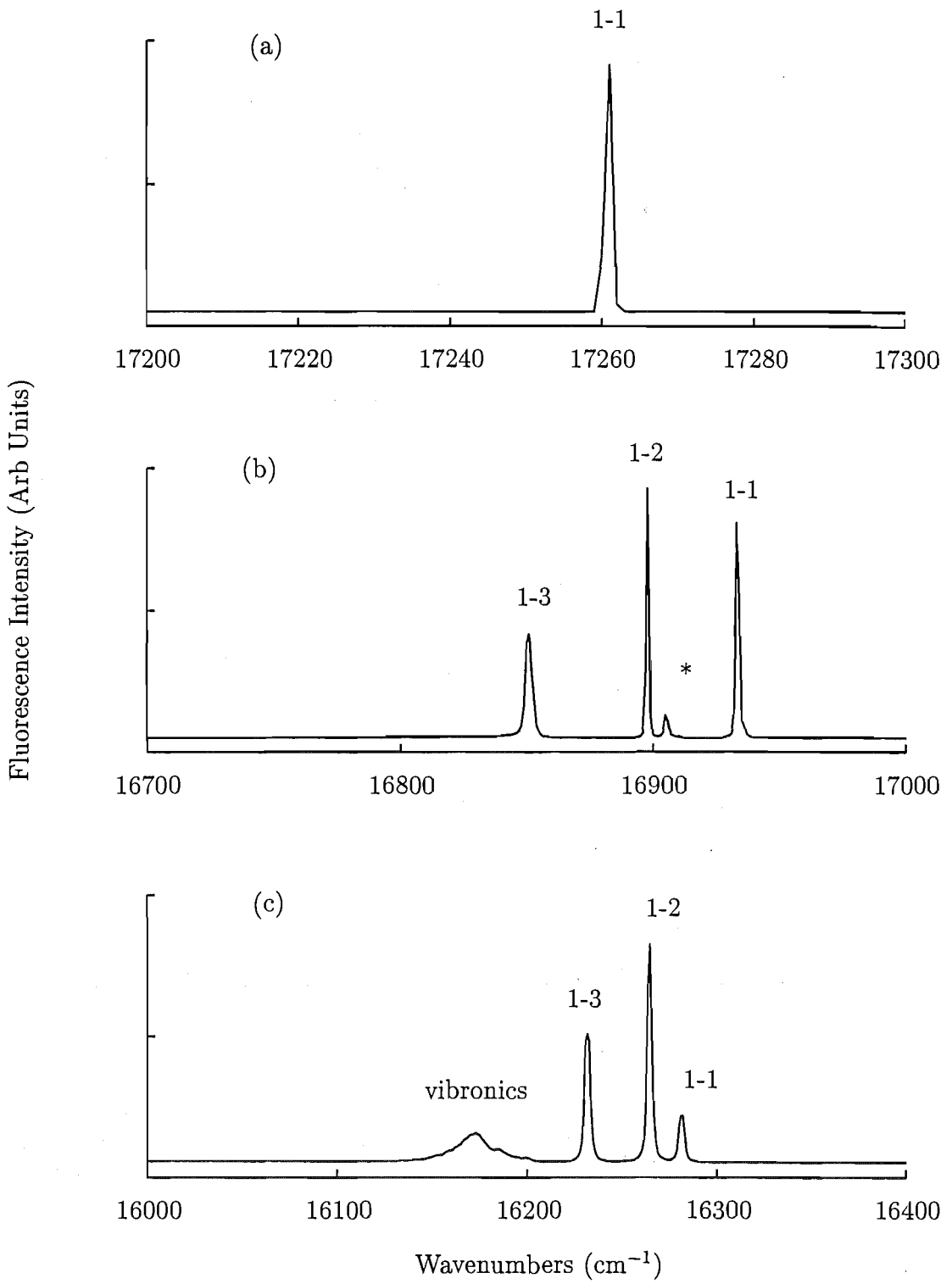

Figure 7.12: Fluorescence spectrum of the Q(Eu,Sm) centre for transitions from $^5D_0$ to (a) the $^7F_0$ multiplet, (b) the $^7F_1$ multiplet and (c) the $^7F_2$ multiplet in CaF_2:0.15%Eu^{3+}:0.05%Sm^{3+}. All spectra were obtained exciting the 17813 cm^{-1} $Z_1 \rightarrow A_1$ transition of Sm^{3+}. * denotes an unidentified transition. The spectra were recorded at 16K.

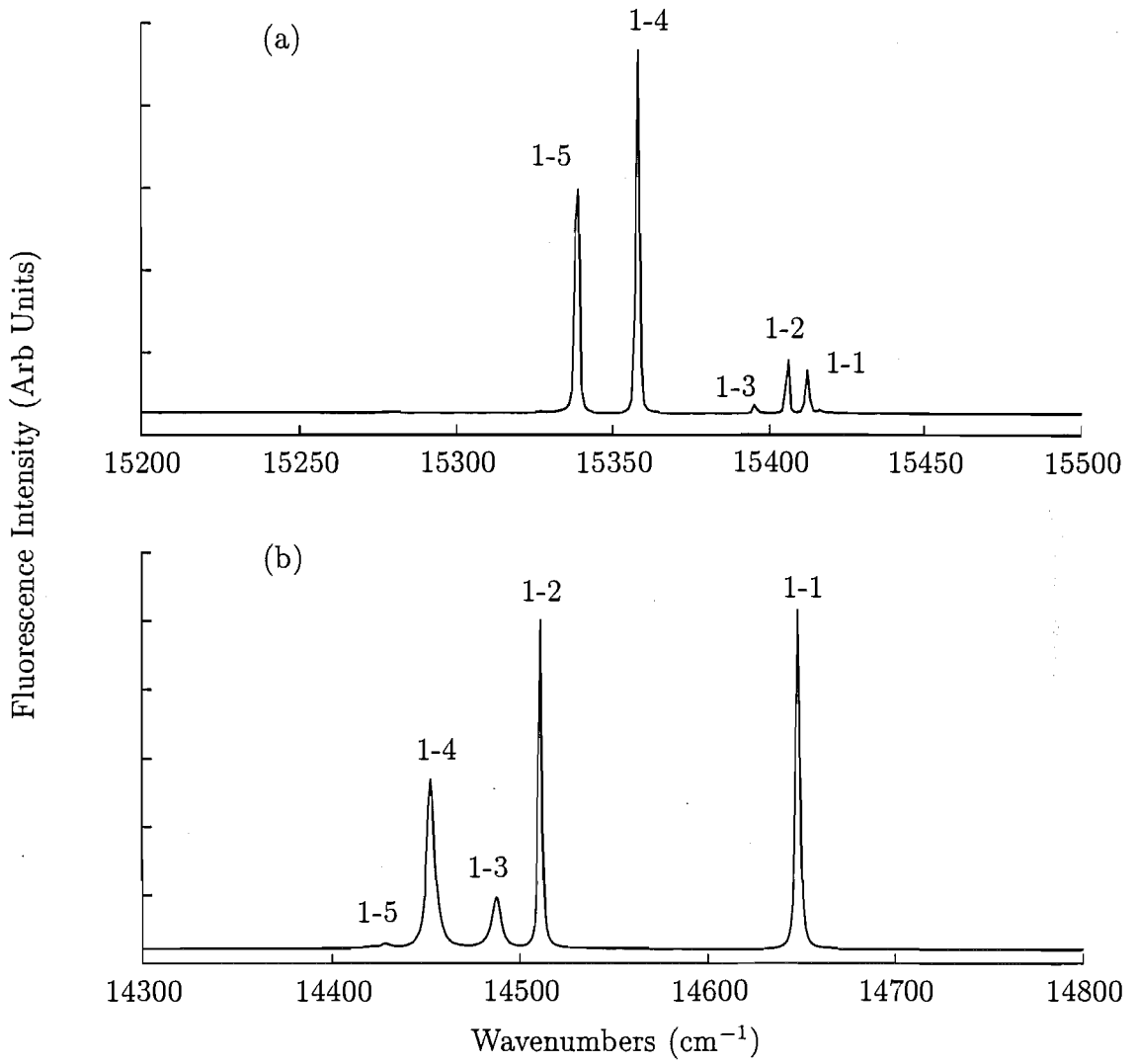

Figure 7.13: Fluorescence spectrum of the Q(Eu,Sm) centre for transitions from $^5D_0$ to (a) the $^7F_3$ multiplet and (b) the $^7F_4$ multiplet in CaF_2:0.15%Eu^{3+}:0.05%Sm^{3+}. All spectra were obtained exciting the 17813 cm^{-1} $Z_1 \rightarrow A_1$ transition of Sm^{3+}. The spectra were recorded at 16K.

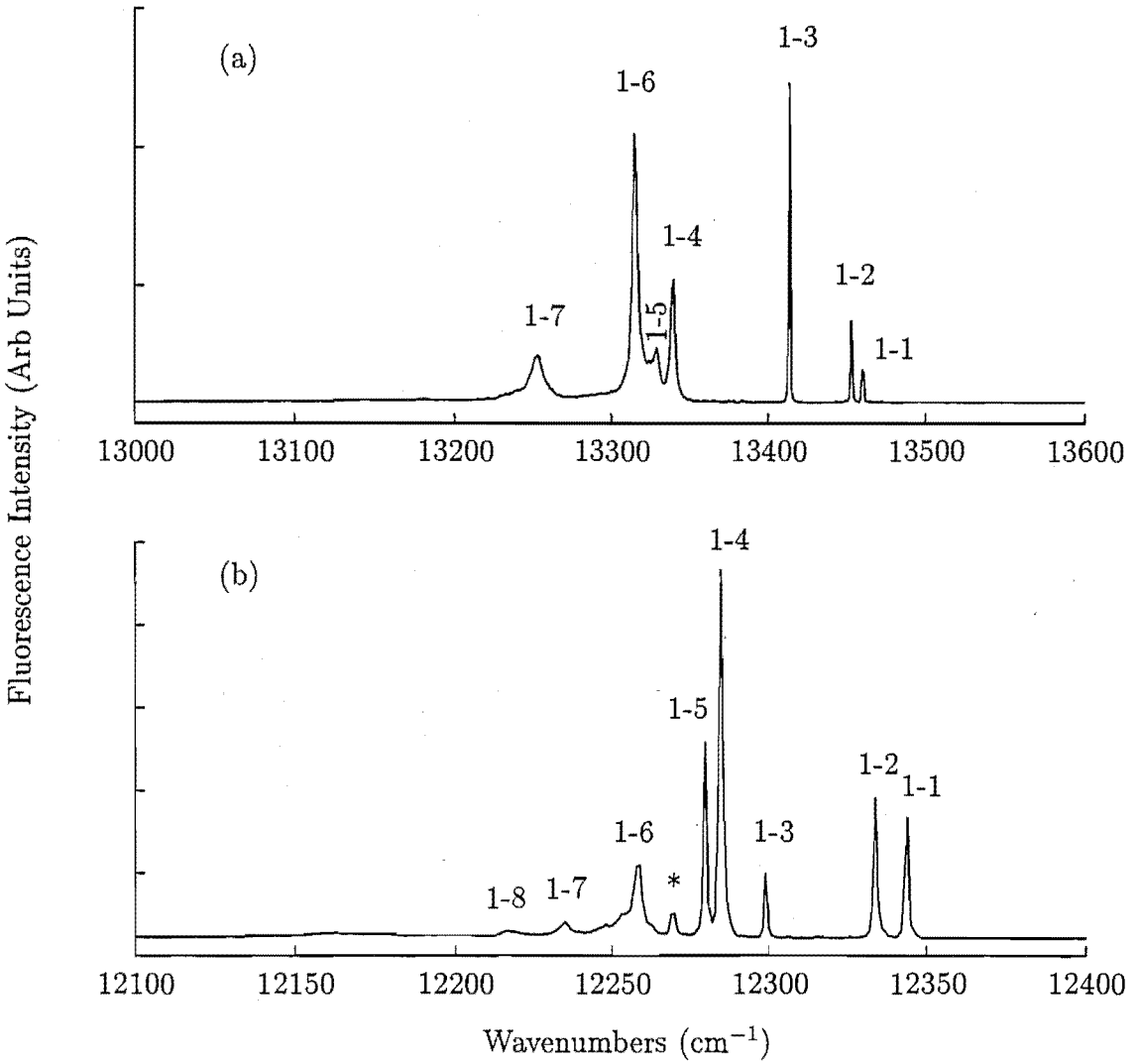

Figure 7.14: Fluorescence spectrum of the Q(Eu,Sm) centre for transitions from $^5D_0$ to (a) the $^7F_5$ multiplet and (b) the $^7F_6$ multiplet in CaF_2:0.15%Eu^{3+}:0.05%Sm^{3+}. All spectra were obtained exciting the 17813 cm^{-1} $Z_1 \rightarrow A_1$ transition of Sm^{3+}. * denotes an unidentified transition. The spectra were recorded at 16K.

Table 7.4: Transition frequencies (cm^{-1}, ± 1) and energy levels of the Eu^{3+} ions in the Q(Eu,Sm) centre in CaF_2:0.15%Eu^{3+}:0.05%Sm^{3+}.

Multiplet	State Label	Transition Frequency	State Energy
$^7F_0$	Z_1	17259	0
$^7F_1$	Y_1	16934	325
	Y_2	16905	354
	Y_3	16894	364
$^7F_2$	X_1	16282	977
	X_2	16265	994
	X_3	16232	1027
$^7F_3$	W_1	15412	1847
	W_2	15406	1853
	W_3	15395	1863
	W_4	15358	1901
	W_5	15338	1920
$^7F_4$	V_1	14649	2610
	V_2	14510	2749
	V_3	14488	2771
	V_4	14452	2806
	V_5	14428	2830
$^7F_5$	U_1	13462	3797
	U_2	13454	3805
	U_3	13415	3844
	U_4	13340	3918
	U_5	13330	3929
	U_6	13316	3943
	U_7	13253	4005
$^7F_6$	T_1	12347	4912
	T_2	12334	4924
	T_3	12300	4958
	T_4	12286	4973
	T_5	12281	4978
	T_6	12257	5001
	T_7	12233	5025
	T_8	12218	5040

None could be observed to originate from the 17813 cm^{-1} level. Conversely, for direct excitation of the Eu^{3+} $^5D_0A_1$ (17259 cm^{-1}) level, only Eu^{3+} $^5D_0$ emission is observed. It is apparent that the Q centre in observed in $CaF_2:Sm^{3+}$ is analogous to the trimer centre labelled Q in $CaF_2:Eu^{3+}$.

The observed Q(Eu,Sm) centre transition frequencies are only slightly shifted from those of the $CaF_2:Eu^{3+}$ Q centre. This is due to the altered crystal field created by the Sm^{3+} ion. The $^5D_0 \rightarrow ^7F_1$ emission shown in Figure 7.12(b), has transitions at 16934, 16905 and 16894 cm^{-1}. These are assigned as the $A_1 \rightarrow Y_1$, Y_2 and Y_3 transitions. The observation of three fluorescence transitions indicates that all remaining degeneracy of the crystal field levels has been removed for J=1 multiplet. An additional feature is observed at 16902 cm^{-1}. It is not associated with the Eu^{3+} emission of this centre and cannot be ascribed to any of the known Sm^{3+} emission lines. It remains unassigned at this point.

(b) R Centre Fluorescence

The R centre is thought to comprise two rare earth ions in asymmetrical sites within the centre. The asymmetry most likely arising from the placement of interstitial anions. Therefore, when examining heterogeneous R centres such as R(Eu,Sm) the possibility arises that each RE^{3+} has a chance of occupying either asymmetrical site leading to 2 types of R centre: R(Eu,Sm) and R(Sm,Eu). Of course, in a singly doped crystal such types are indistinguishable but the manifestation was the observation of more than 2J+1 energy levels. The same applies in the heterogeneous centres but the extent of which the site occupation probability is 50:50 for different rare-earth ions and whether there is sufficient frequency resolution to distinguish the two types remains unclear.

In CaF_2:0.15%Eu^{3+}:0.05%Sm^{3+} crystals, fluorescence is observed upon optical excitation of the either the Eu^{3+} or Sm^{3+} absorption transitions of the heterogeneous R(Eu,Sm) centre. For excitation of the Sm^{3+} absorption transition at 17829 cm^{-1}, only Eu^{3+} emission is detected, the originating level being $^5D_0$ at 17261 cm^{-1}. The energy gap between the lowest $^4G_{\frac{5}{2}}$ level of the Sm^{3+} ion and the $^5D_0$ level of the Eu^{3+} ion is 568 cm^{-1}. As with the Q(Eu,Sm) centre, this energy gap is larger than the phonon cutoff energy of the CaF_2 host lattice at 460 cm^{-1} and at least two lattice phonons are required to conserve energy.

The observation of emission at 17261 cm^{-1}, and the subsequent ^7F_J levels inferred from this emission, confirms that the R centres in $CaF_2:Sm^{3+}$, are the analogues of those in $CaF_2:Eu^{3+}$. The recorded fluorescence spectra are shown in Figures 7.15 to 7.17. Table 7.5 gives the measured transition energies.

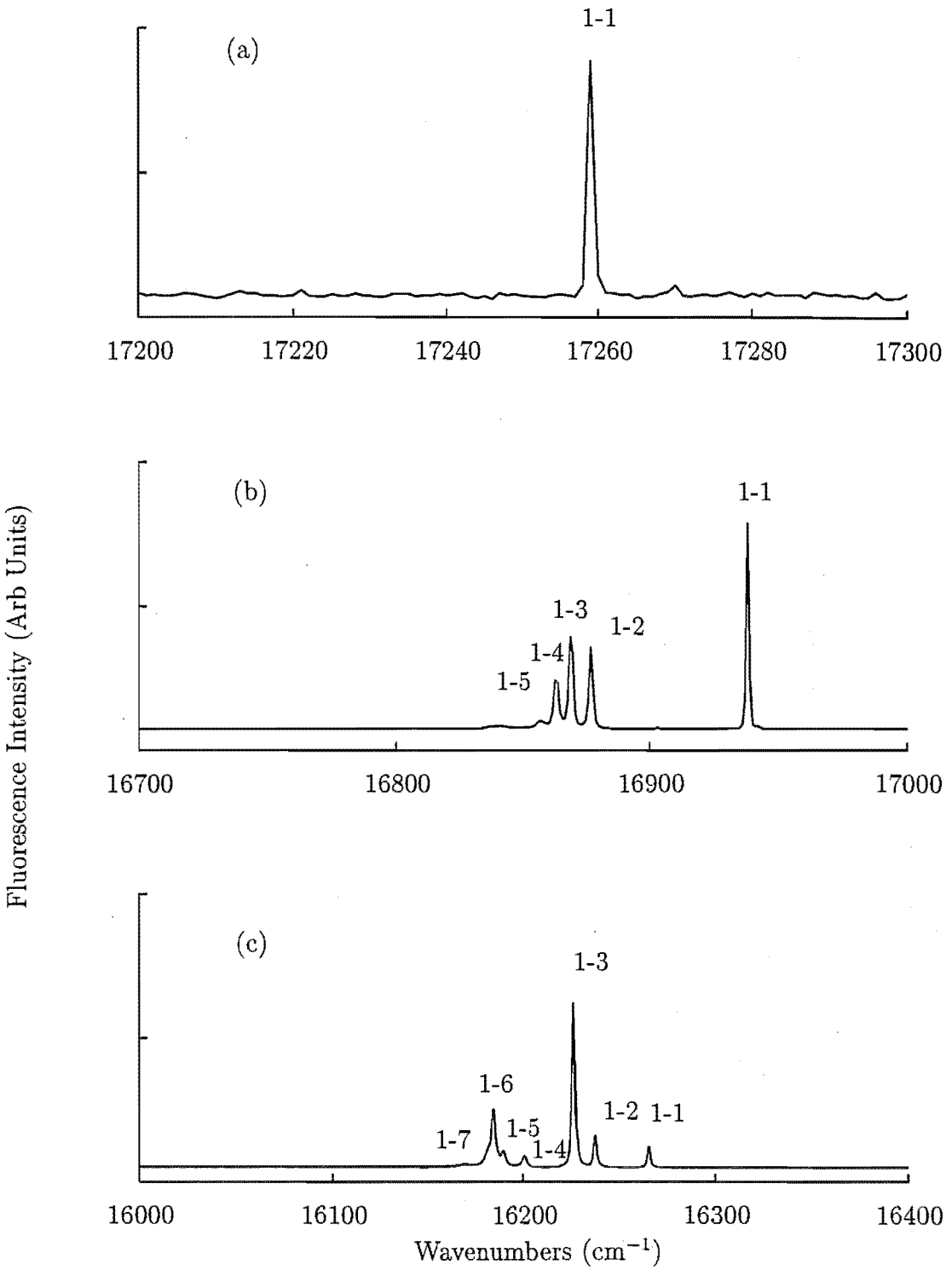

Figure 7.15: Fluorescence spectrum of the R(Eu,Sm) centre for transitions from $^5D_0$ to (a) the $^7F_0$ multiplet, (b) the $^7F_1$ multiplet and (c) the $^7F_2$ multiplet in CaF_2:0.15%Eu^{3+}:0.05%Sm^{3+}. All spectra were obtained exciting the 17829 cm^{-1} $Z_1 \rightarrow A_1$ transition of Sm^{3+}. * denotes an unidentified transition. The spectra were recorded at 16K.

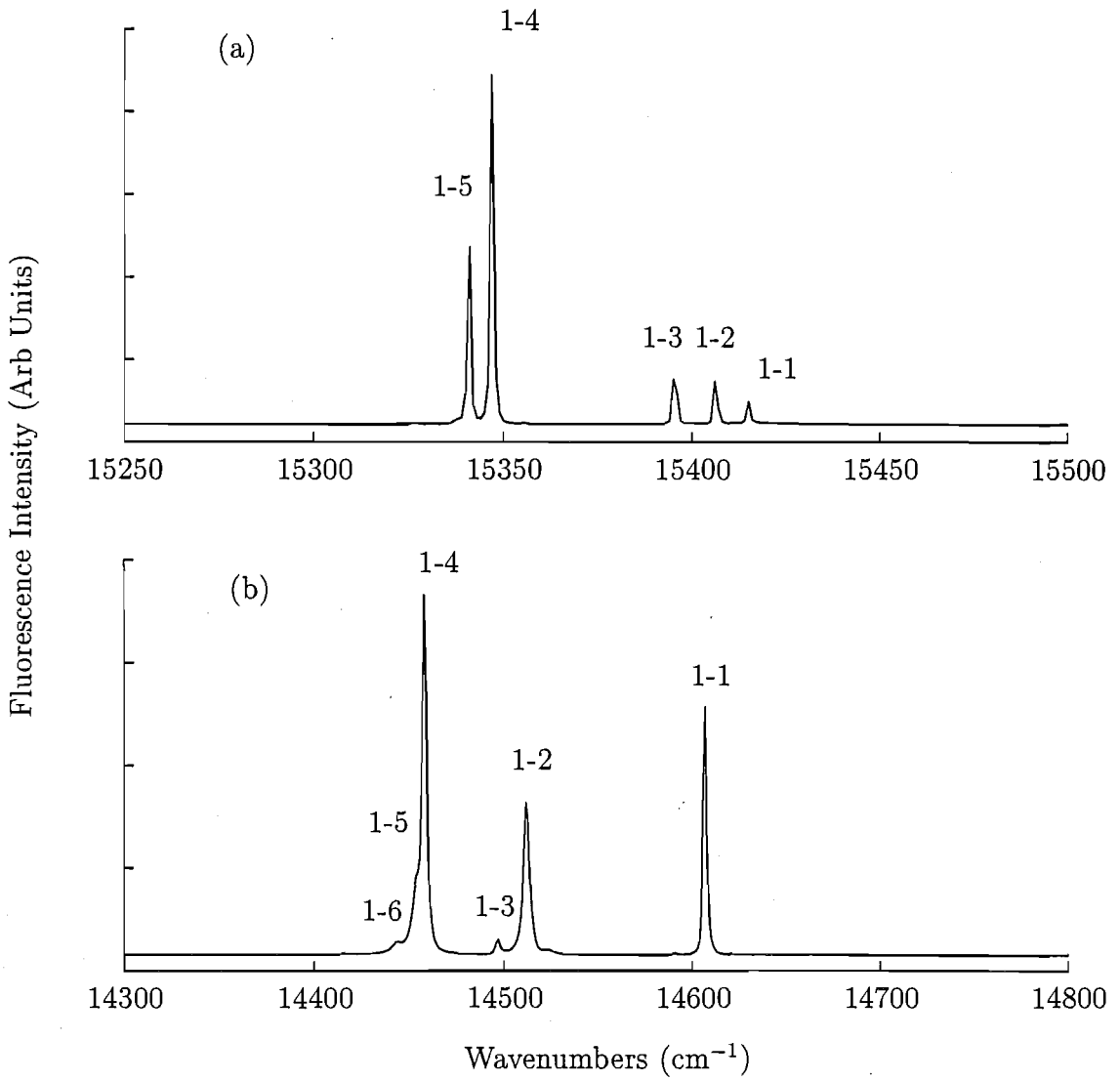

Figure 7.16: Fluorescence spectrum of the R(Eu,Sm) centre for transitions from $^5D_0$ to (a) the $^7F_3$ multiplet and (b) the $^7F_4$ multiplet in CaF_2:0.15%Eu^{3+}:0.05%Sm^{3+}. All spectra were obtained exciting the 17829 cm^{-1} $Z_1 \rightarrow A_1$ transition of Sm^{3+}. The spectra were recorded at 16K.

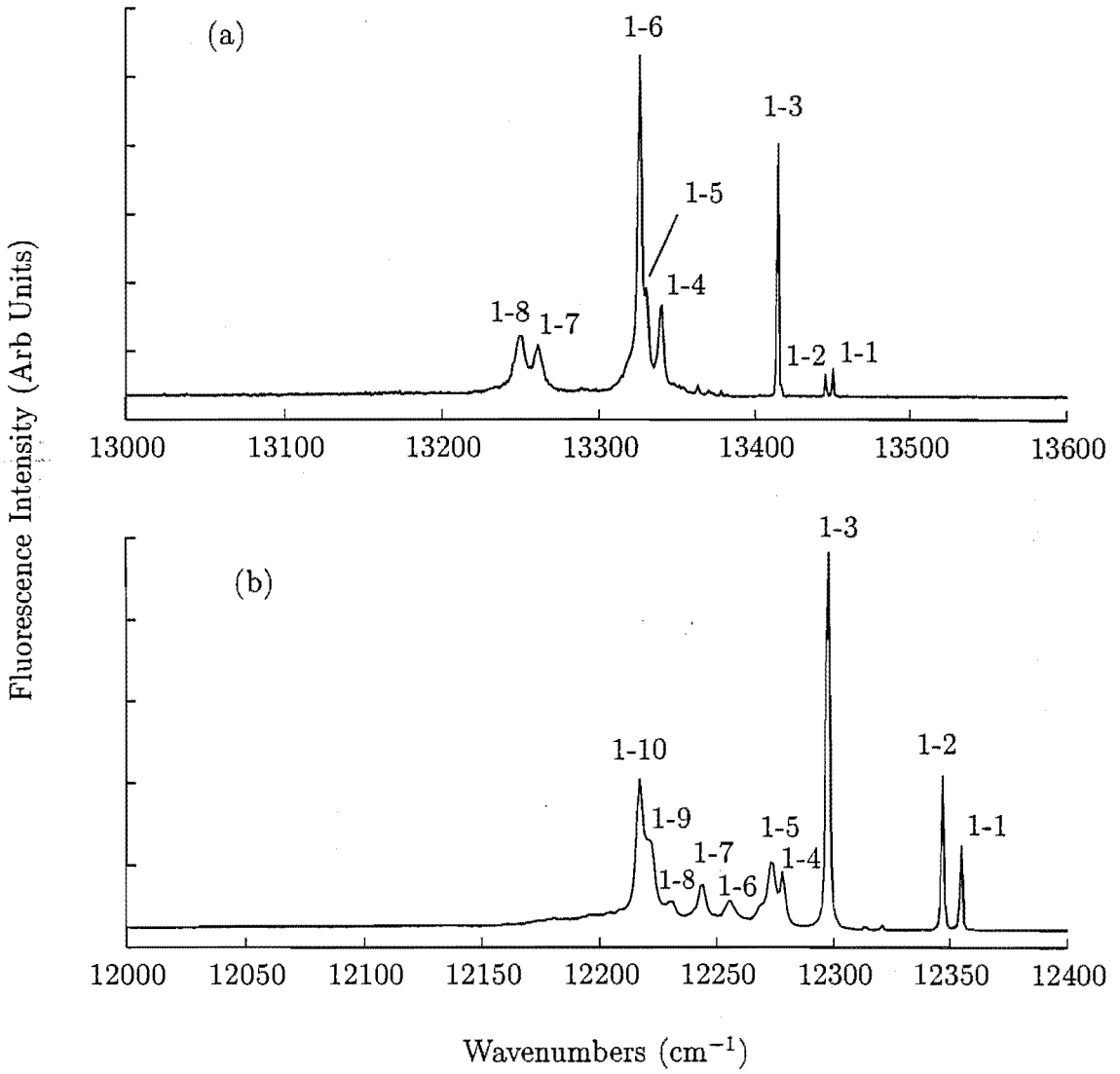

Figure 7.17: Fluorescence spectrum of the R(Eu,Sm) centre for transitions from $^5D_0$ to (a) the $^7F_5$ multiplet and (b) the $^7F_6$ multiplet in CaF_2:0.15%Eu^{3+}:0.05%Sm^{3+}. All spectra were obtained exciting the 17829 cm^{-1} $Z_1 \rightarrow A_1$ transition of Sm^{3+}. The spectra were recorded at 16K

Table 7.5: Fluorescence energies (cm^{-1}, ± 1) and energy levels of the Eu^{3+} ions in the R(Eu,Sm) centre in CaF_2:0.15%Eu^{3+}:0.05%Sm^{3+}.

Multiplet	State Label	Transition Frequency	State Energy
$^7F_0$	Z_1	17261	0
$^7F_1$	Y_1	16942	319
	Y_2	16884	377
	Y_3	16877	384
	Y_4	16870	391
	Y_5	16863	398
$^7F_2$	X_1	16242	996
	X_2	16238	1023
	X_3	16227	1034
	X_4	16201	1060
	X_5	16189	1071
	X_6	16184	1077
	X_7	16168	1093
$^7F_3$	W_1	15415	1845
	W_2	15407	1854
	W_3	15396	1865
	W_4	15347	1914
	W_5	15341	1920
$^7F_4$	V_1	14607	2654
	V_2	14513	2748
	V_3	14497	2764
	V_4	14458	2802
	V_5	14457	27603
	V_6	14446	2815
$^7F_5$	U_1	13450	3811
	U_2	13446	3815
	U_3	13415	3846
	U_4	13340	3921
	U_5	13330	3931
	U_6	13326	3935
	U_7	13261	4000
	U_8	13250	4011
$^7F_6$	T_1	12355	4906
	T_2	12347	4913
	T_3	12298	4963
	T_4	12278	4983
	T_5	12273	4987
	T_6	12256	5005
	T_7	12243	5017
	T_8	12229	5031
	T_9	12221	5039
	T_{10}	12217	5043

Fluorescence transitions to the $^7F_1$ multiplet of the Eu^{3+} ion are shown in Figure 7.15(b). Five transitions have been observed. The dominant feature is the strong line at the highest frequency of 16942 cm^{-1}. This is assiged as the $A_1 \rightarrow Y_1$ transition. The line is separated by 58 cm^{-1} from a bunched set of four transitions. These are assigned as the $A_1 \rightarrow Y_2$, Y_3, Y_4 and Y_5 transitions. They are at the measured energies of 16884, 16877, 16870 and 16863 cm^{-1}. The transitions observed are consistent, yet slightly shifted, with respect to those observed for the parent R(Eu,Eu) centre.

A weak, broader transition at 16837 cm^{-1} is assigned as a vibronic sideband. This is due to a pseudo-localised mode of vibration of the rare earth ions in the cluster. A similar vibrational mode was observed for the homogeneous cluster centre in CaF_2:0.05%Eu^{3+}. In that case, the inferred vibrational frequency was 96 cm^{-1}. In the heterogeneous centre, this vibrational frequency is modified to 105 cm^{-1}. This effect is apparantly due to the replacement of one Eu^{3+} ion with a lighter Sm^{3+} ion, leading to a slightly higher frequency of vibration for the complex. Such 90-100 cm^{-1} vibrational frequencies of rare earth ion centres have been observed previously in far infrared absorption (Ward and Clayman [145] (1975)) and 4f→5d absorption spectra (Hayes et. al. [146] (1973)). In these cases, the vibrational mode has been associated with the C_{4v} A centres present in CaF_2:RE^{3+} crystals. No such vibrational modes could be observed as sidebands from the C_{4v} symmetry A centre fluorescence. In these cases, only vibrational intervals corresponding to band modes of the lattice were observed.

7.4.2 Fluorescence of the Q and R centres in CaF_2:Sm^{3+}:RE^{3+}, where RE^{3+}=La^{3+}, Ce^{3+}, Gd^{3+}, Tb^{3+}

Crystals of CaF_2:0.05%Sm^{3+} that are grown with 0.15 molar % of La^{3+}, Ce^{3+}, Gd^{3+} or Tb^{3+} also give rise to heterogeneous R and Q cluster centres. In these cases, only Sm^{3+} emission is observed when the $^4G_{\frac{5}{2}}(Sm^{3+})$ multiplet is excited. This happens because the non-Sm^{3+} co-dopant is either non-paramagnetic, as with the case of the La^{3+} ion, or does not have suitable energy levels for transfer of the optical excitation to occur. The latter, is true for the addition of Ce^{3+}, Gd^{3+} or Tb^{3+} ions.

(a) Q Centre Fluorescence

CaF_2:0.05%Sm^{3+} crystals co-doped with either La^{3+}, Ce^{3+}, Gd^{3+} or Tb^{3+}, have

been studied. Excitation of Q(RE,Sm) centre $^4G_{\frac{5}{2}}(Sm^{3+})$ absorption transitions, yields fluorescence to the ^6H_J and ^6F_J multiplets of Sm^{3+}. The recorded fluorescence spectra are shown in Figures 7.18 through to 7.29. We deal with the fluorescence to these multiplets below.

Fluorescence to the $^6H_{\frac{5}{2}}$ multiplet is detected in the 17850-17600 cm^{-1} region. The second crystal field level of the $^4G_{\frac{5}{2}}$ multiplet is excited here ($Z_1 \rightarrow A_2$) so that emission can be detected from the lowest level (A_1) without interference from scattered laser light. Typically, these fluorescence spectra are complex showing lines originating from the Q, A and O centres. The O centres are excited due to an overlap of a vibronic absorption band and the absorption transition of the Q centre itself. The A centre is excited due to the overlap of the $Z_1 \rightarrow A_2$ transitions of both the A and Q centres. This is only significant for the Q(La,Sm) and Q(Ce,Sm) centres. Three fluorescence transitions are observed for the respective Q(RE,Sm) centres. This is consistent with the conclusions of Hamers et. al. [104], in that the ions which make up the cluster appear to experience similar crystal fields.

For measurement of fluorescence transitions to the $^4H_{\frac{7}{2}}$ multiplet around 16800 cm^{-1}, the $Z_1 \rightarrow A_1$ transition of the $^4G_{\frac{5}{2}}$ multiplet was excited as the laser frequency is now well removed from the detection region. Four electronic transitions are assigned consistent with the J=$\frac{7}{2}$ of the terminating multiplet. A feature at 16468-16472 cm^{-1}, corresponds to a transition terminating on a vibronic level. The frequency shift of 360 cm^{-1} corresponds to the energy of the transverse optical phonon of the CaF_2 host lattice. Transitions involving this phonon are commonly observed coupled to the sharpest "zero-phonon" electronic transitions. For the Q(La,Sm) and Q(Ce,Sm) centres all four expected electronic transitions are also observed. The $A_1 \rightarrow Y_3$ transition is not observed in either the Q(Gd,Sm) or Q(Tb,Sm) centres. Table 7.6 gives the observed transition frequencies for fluorescence to this multiplet.

Transitions to the $^6H_{\frac{9}{2}}$ multiplet are observed in the 15700-15200 cm^{-1} region. All five transitions expected to a J=$\frac{9}{2}$ multiplet, are observed. Two strong sharp transitions are observed at the highest frequencies which are assigned as the $A_1 \rightarrow X_1$ and X_2 transitions. Three broad transitions, which are roughly ten times weaker, are observed in the 15470-15330 cm^{-1} region which are assigned as the $A_1 \rightarrow X_3$, X_4 and X_5 transitions.

For transitions to the $^6H_{\frac{11}{2}}$ multiplet, the six expected transitions are observed, except in the case of the Q(Tb,Sm) centre. Here there is an accidental overlap of the $A_1 \rightarrow W_5$ transition with the characteristic 14115 cm^{-1}, interconfigurational $4f^{N-1}5d \rightarrow 4f^N$ transition of the Sm^{2+} ion.

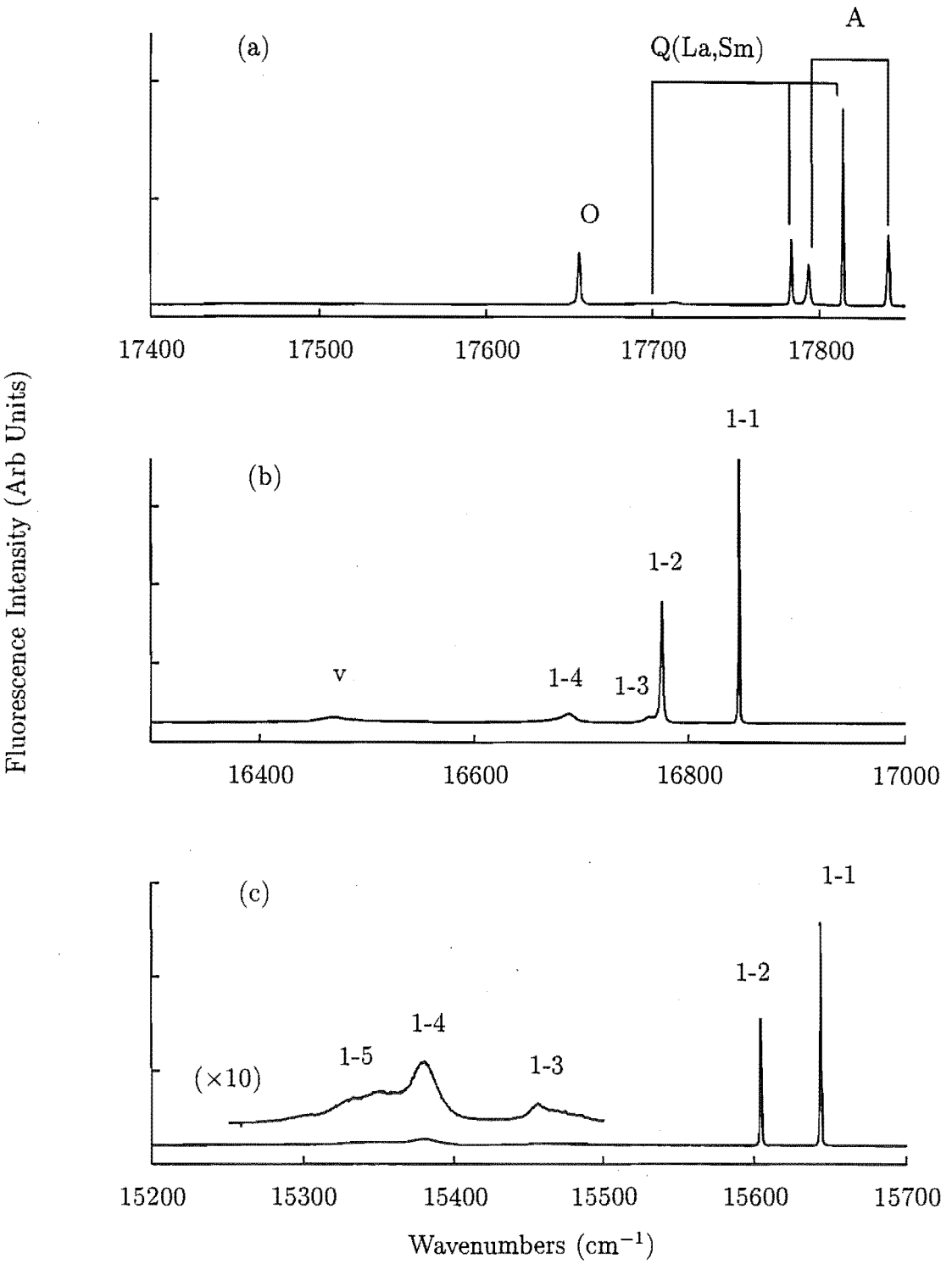

Figure 7.18: Fluorescence spectrum of the Q(La,Sm) centre for transitions from $^4G_{\frac{5}{2}}$ to (a) the $^6H_{\frac{5}{2}}$ multiplet, (b) the $^6H_{\frac{7}{2}}$ multiplet and (c) the $^6H_{\frac{9}{2}}$ multiplet in CaF_2:0.15%La^{3+}:0.05%Sm^{3+}. For measurement of the $^4G_{\frac{5}{2}} \rightarrow {}^6H_{\frac{5}{2}}$ spectrum the 17905 cm^{-1} $Z_1 \rightarrow A_2$ absorption transition was excited, while for all others the 17810 cm^{-1} transition was excited. The spectra were recorded at 16K.

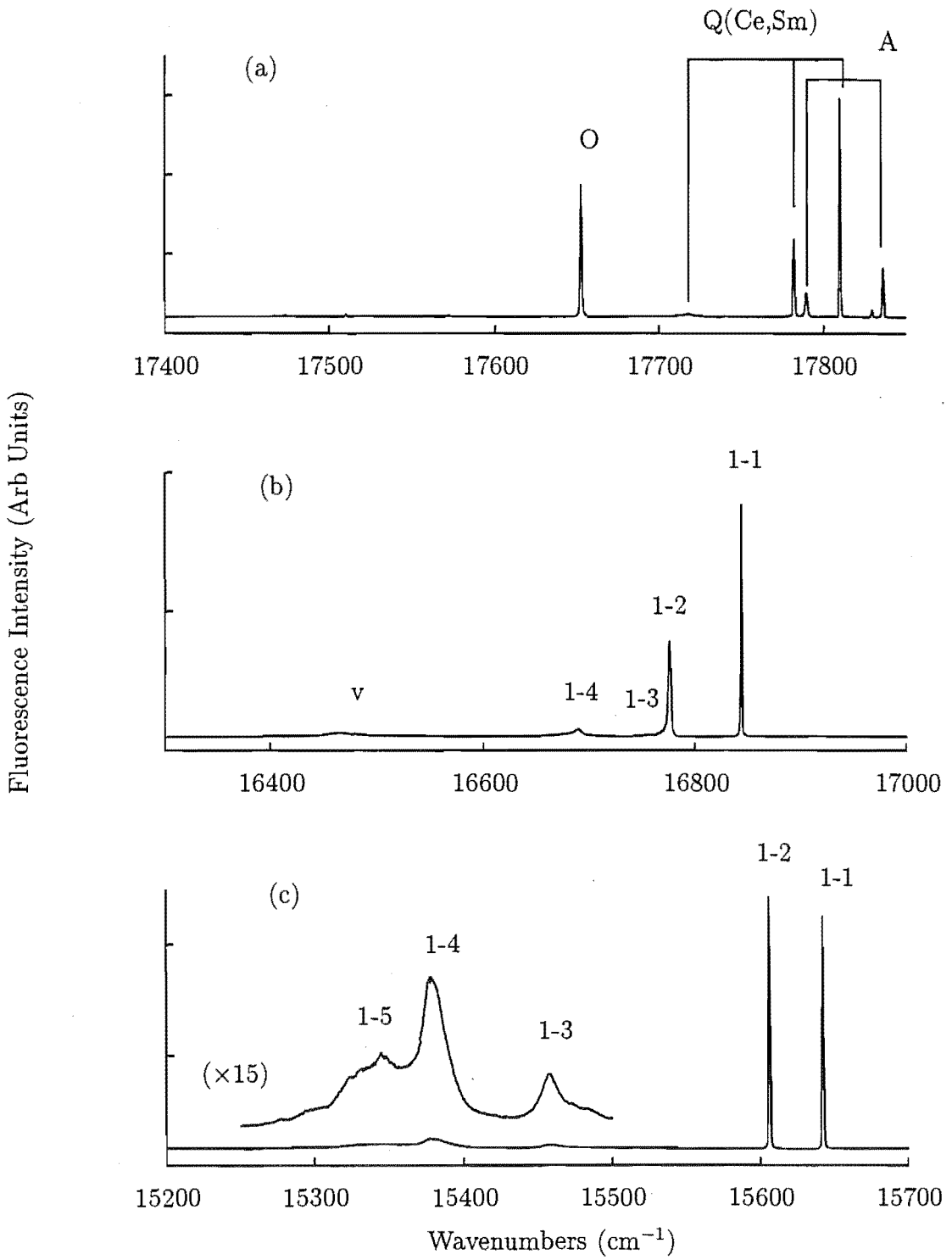

Figure 7.19: Fluorescence spectrum of the Q(Ce,Sm) centre for transitions from $^4G_{\frac{5}{2}}$ to (a) the $^6H_{\frac{5}{2}}$ multiplet, (b) the $^6H_{\frac{7}{2}}$ multiplet and (c) the $^6H_{\frac{9}{2}}$ multiplet in CaF_2:0.15%Ce^{3+}:0.05%Sm^{3+}. For measurement of the $^4G_{\frac{5}{2}} \rightarrow {}^6H_{\frac{5}{2}}$ spectrum the 17900 cm^{-1} $Z_1 \rightarrow A_2$ absorption transition was excited, while for all others the 17811 cm^{-1} transition was excited. The spectra were recorded at 16K.

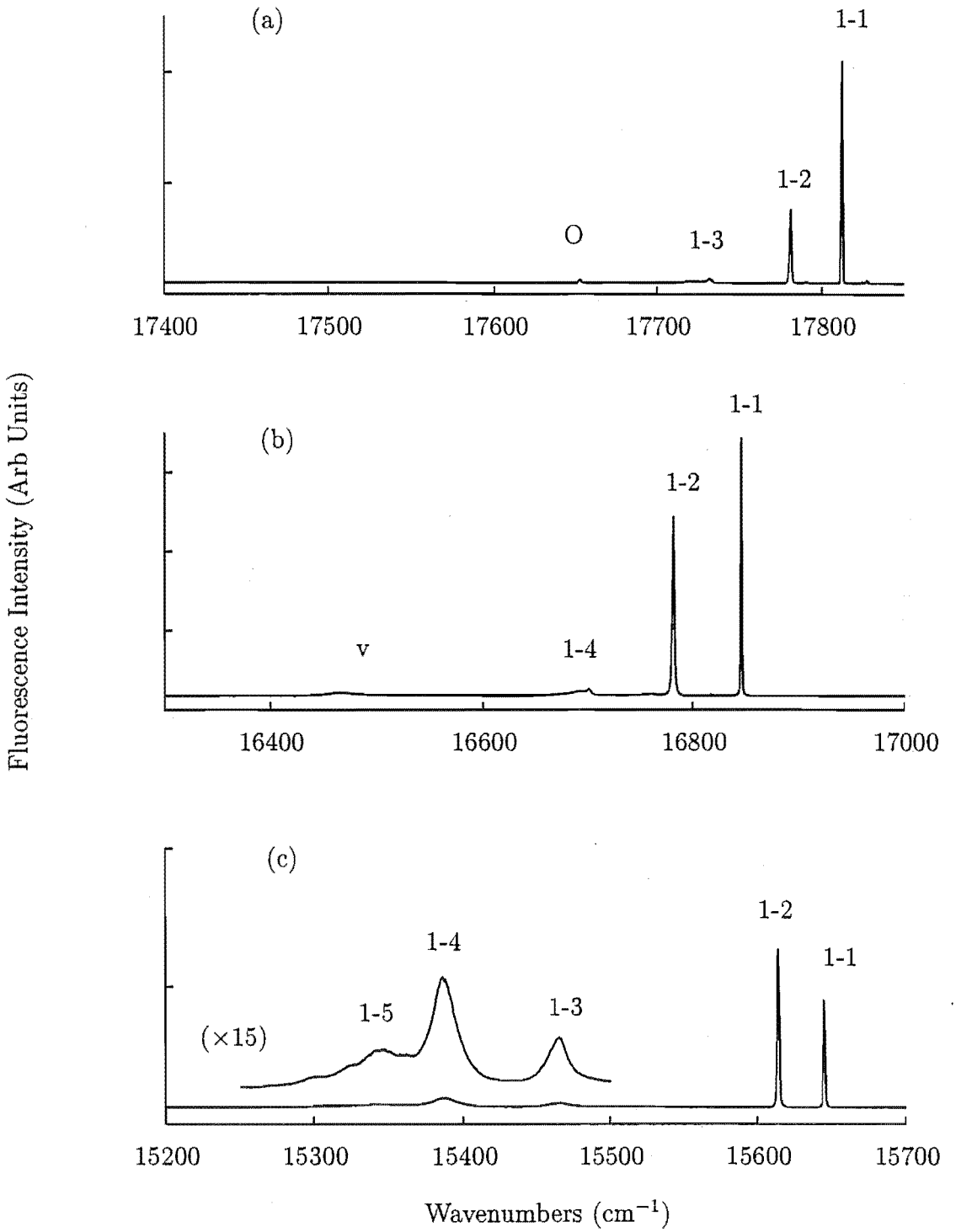

Figure 7.20: Fluorescence spectrum of the Q(Gd,Sm) centre for transitions from $^4G_{\frac{5}{2}}$ to (a) the $^6H_{\frac{5}{2}}$ multiplet, (b) the $^6H_{\frac{7}{2}}$ multiplet and (c) the $^6H_{\frac{9}{2}}$ multiplet in CaF_2:0.15%Gd^{3+}:0.05%Sm^{3+}. For measurement of the $^4G_{\frac{5}{2}} \rightarrow {}^6H_{\frac{5}{2}}$ spectrum the 17885 cm^{-1} $Z_1 \rightarrow A_2$ absorption transition was excited, while for all others the 17813 cm^{-1} transition was excited. The spectra were recorded at 16K.

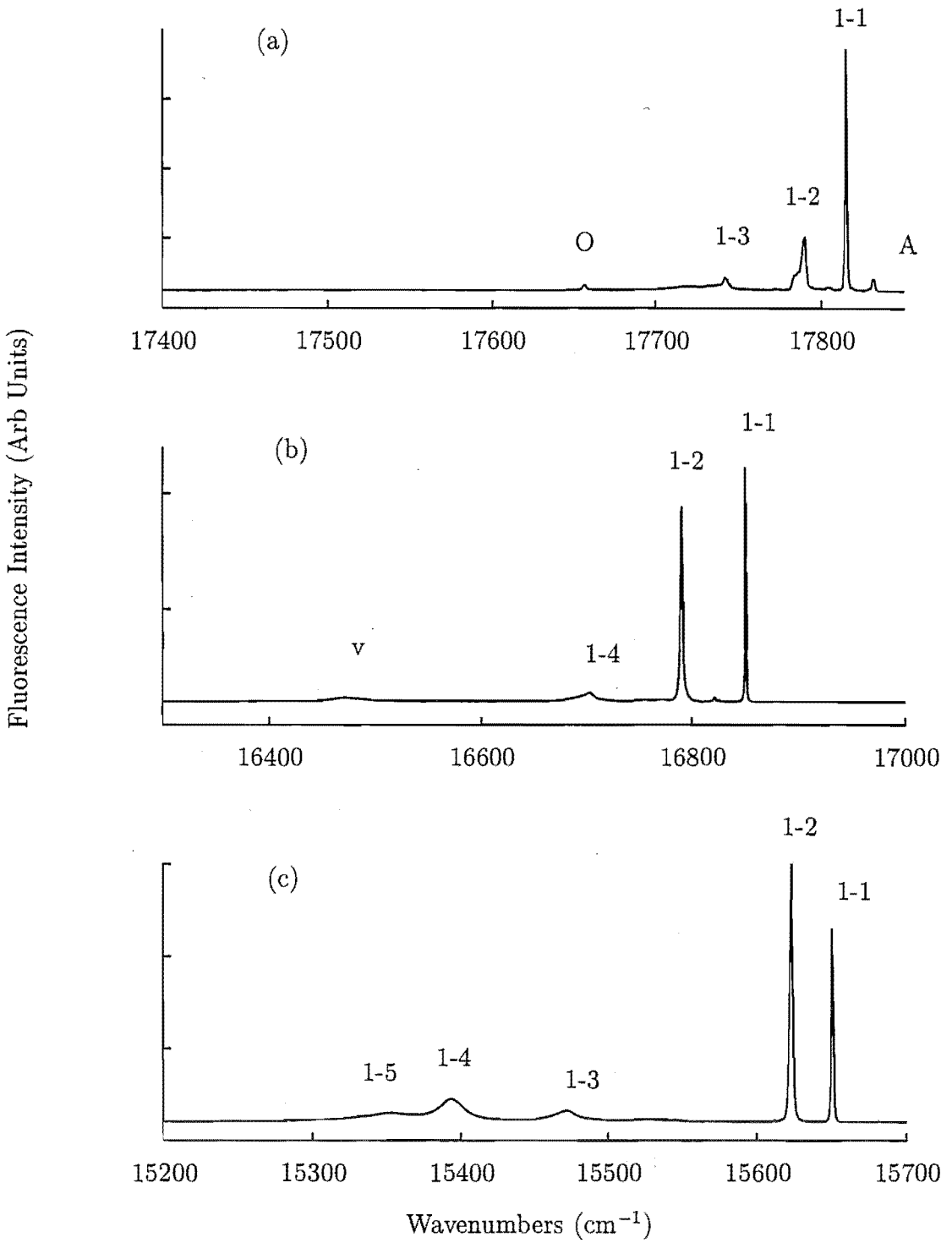

Figure 7.21: Fluorescence spectrum of the Q(Tb,Sm) centre for transitions from $^4G_{\frac{5}{2}}$ to (a) the $^6H_{\frac{5}{2}}$ multiplet, (b) the $^6H_{\frac{7}{2}}$ multiplet and (c) the $^6H_{\frac{9}{2}}$ multiplet in CaF_2:0.15%Tb^{3+}:0.05%Sm^{3+}. For measurement of the $^4G_{\frac{5}{2}} \rightarrow {}^6H_{\frac{5}{2}}$ spectrum the 17881 cm^{-1} $Z_1 \rightarrow A_2$ absorption transition was excited, while for all others the 17812 cm^{-1} transition was excited. The spectra were recorded at 16K.

Table 7.6: Fluorescence transitions for the $^6H_{\frac{5}{2}}$, $^6H_{\frac{7}{2}}$ and $^6H_{\frac{9}{2}}$ multiplets of the Q centre in CaF_2:0.15%La^{3+}:0.05%Sm^{3+}, CaF_2:0.15%Ce^{3+}:0.05%Sm^{3+}, CaF_2:0.15%Gd^{3+}:0.05%Sm^{3+} and CaF_2:0.15%Tb^{3+}:0.05%Sm^{3+}. All frequencies are as measured in air (cm^{-1},±1).

Multiplet	State Label	(La^{3+}:Sm^{3+}) Transition Frequency	(La^{3+}:Sm^{3+}) State Energy	(Ce^{3+}:Sm^{3+}) Transition Frequency	(Ce^{3+}:Sm^{3+}) State Energy	(Gd^{3+}:Sm^{3+}) Transition Frequency	(Gd^{3+}:Sm^{3+}) State Energy	(Tb^{3+}:Sm^{3+}) Transition Frequency	(Tb^{3+}:Sm^{3+}) State Energy
	Z_1	17810	0	17811	0	17813	0	17812	0
$^6H_{\frac{5}{2}}$	Z_2	17780	30	17783	29	17782	31	17786	26
	Z_3	17708	102	17721	90	17733	80	17739	73
	Y_1	16843	968	16845	966	16846	966	16848	964
$^6H_{\frac{7}{2}}$	Y_2	16771	1039	16778	1034	16782	1031	16787	1025
	Y_3	16760	1050	16758	1053	-	-	-	-
	Y_4	16684	1126	16691	1120	16702	1111	16701	1111
	X_1	15641	2169	15644	2167	15645	2167	15649	2163
	X_2	15601	2209	15607	2204	15614	2198	15620	2191
$^6H_{\frac{9}{2}}$	X_3	15456	2355	15461	2350	15467	2346	15470	2342
	X_4	15379	2431	15382	2428	15387	2426	15392	2420
	X_5	15350±5	2460	15348	2463	15348	2465	15351	2461

Fluorescence transitions to the remaining ^6H_J and ^6F_J multiplets were recorded in their relevant spectral regions and using the infrared sensitive spectrometer and photomultiplier where appropriate. The expected number of electronic transitions as dictated by the lifting of the total $J+\frac{1}{2}$ degeneracy were observed for all but the overlapping $^6H_{\frac{15}{2}}$, $^6F_{\frac{1}{2}}$ and $^6F_{\frac{3}{2}}$ multiplets. Here, relaxation via spontaneous phonon emission between closely lying levels tends to broaden the optical transitions making a complete assignment difficult.

Tables 7.7 and 7.8 give the relevant transition frequencies and corresponding energies for the crystal field levels of these multiplets.

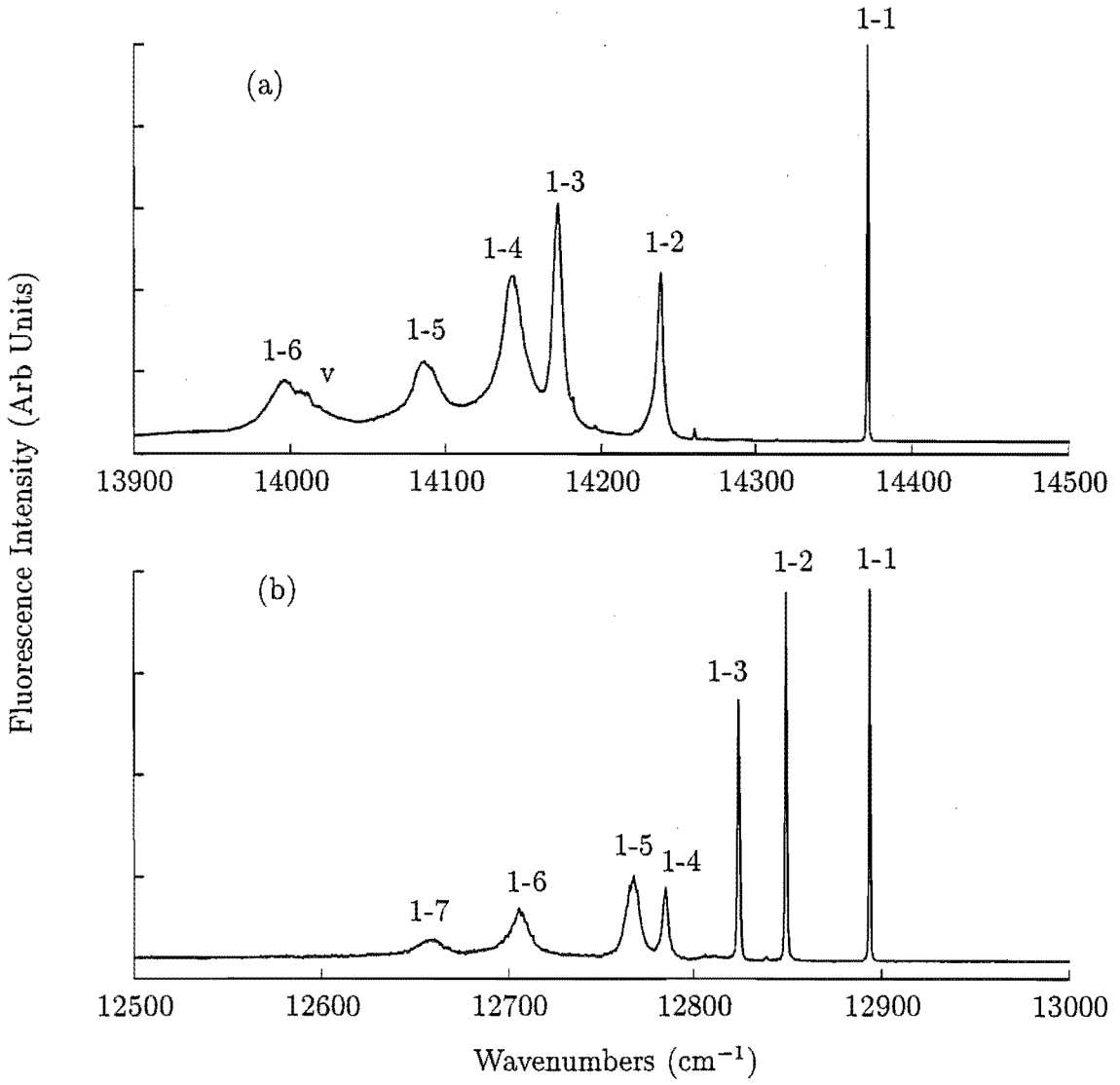

Figure 7.22: Fluorescence spectrum of the Q(La,Sm) centre for transitions from $^4G_{\frac{5}{2}}$ to (a) the $^6H_{\frac{11}{2}}$ multiplet and (b) the $^6H_{\frac{13}{2}}$ multiplet in CaF_2:0.15%La^{3+}:0.05%Sm^{3+}. The spectra were recorded at 16K.

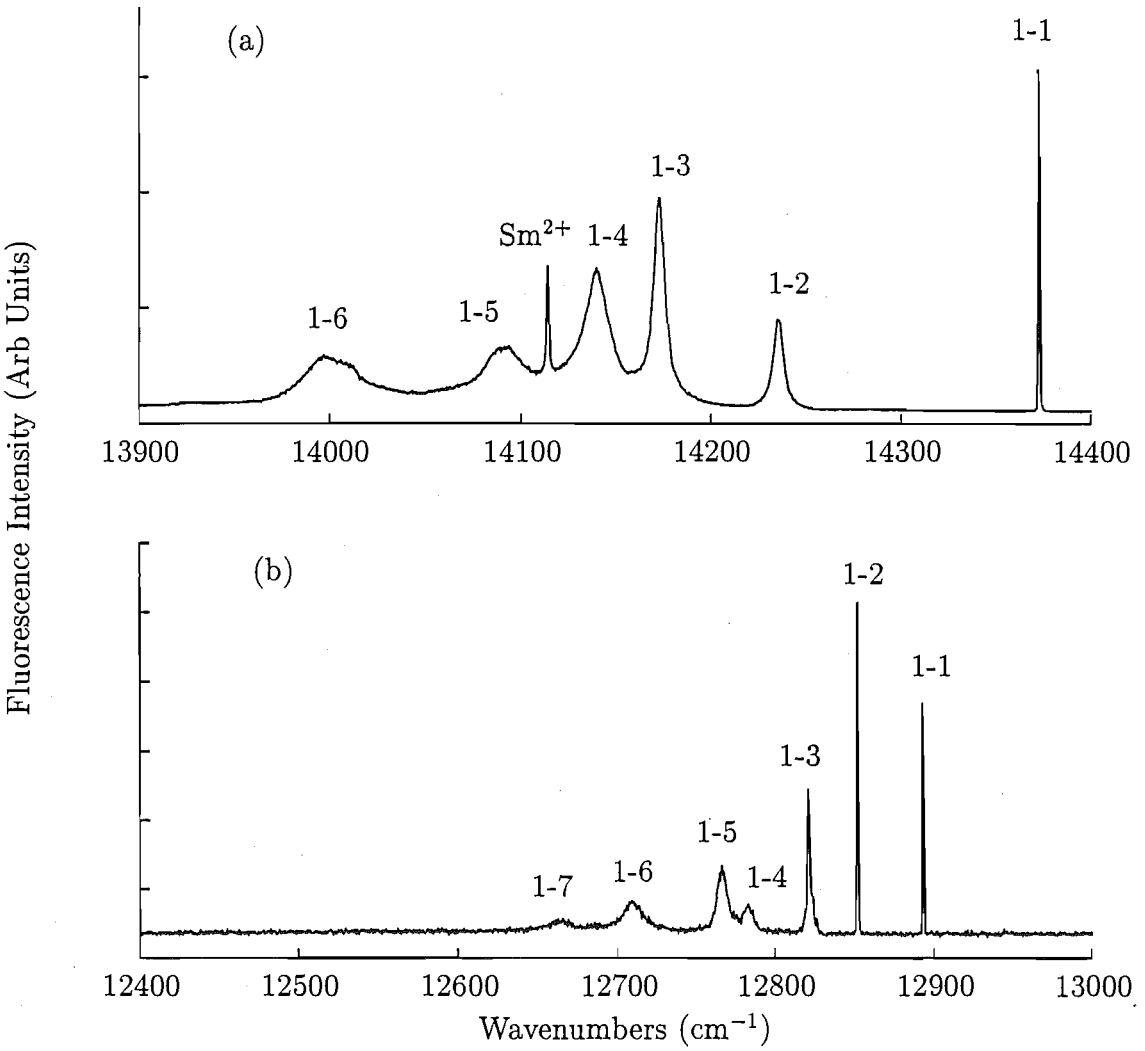

Figure 7.23: Fluorescence spectrum of the Q(Ce,Sm) centre for transitions from $^4G_{\frac{5}{2}}$ to (a) the $^6H_{\frac{11}{2}}$ multiplet and (b) the $^6H_{\frac{13}{2}}$ multiplet in CaF_2:0.15%Ce^{3+}:0.05%Sm^{3+}. The spectra were recorded at 16K.

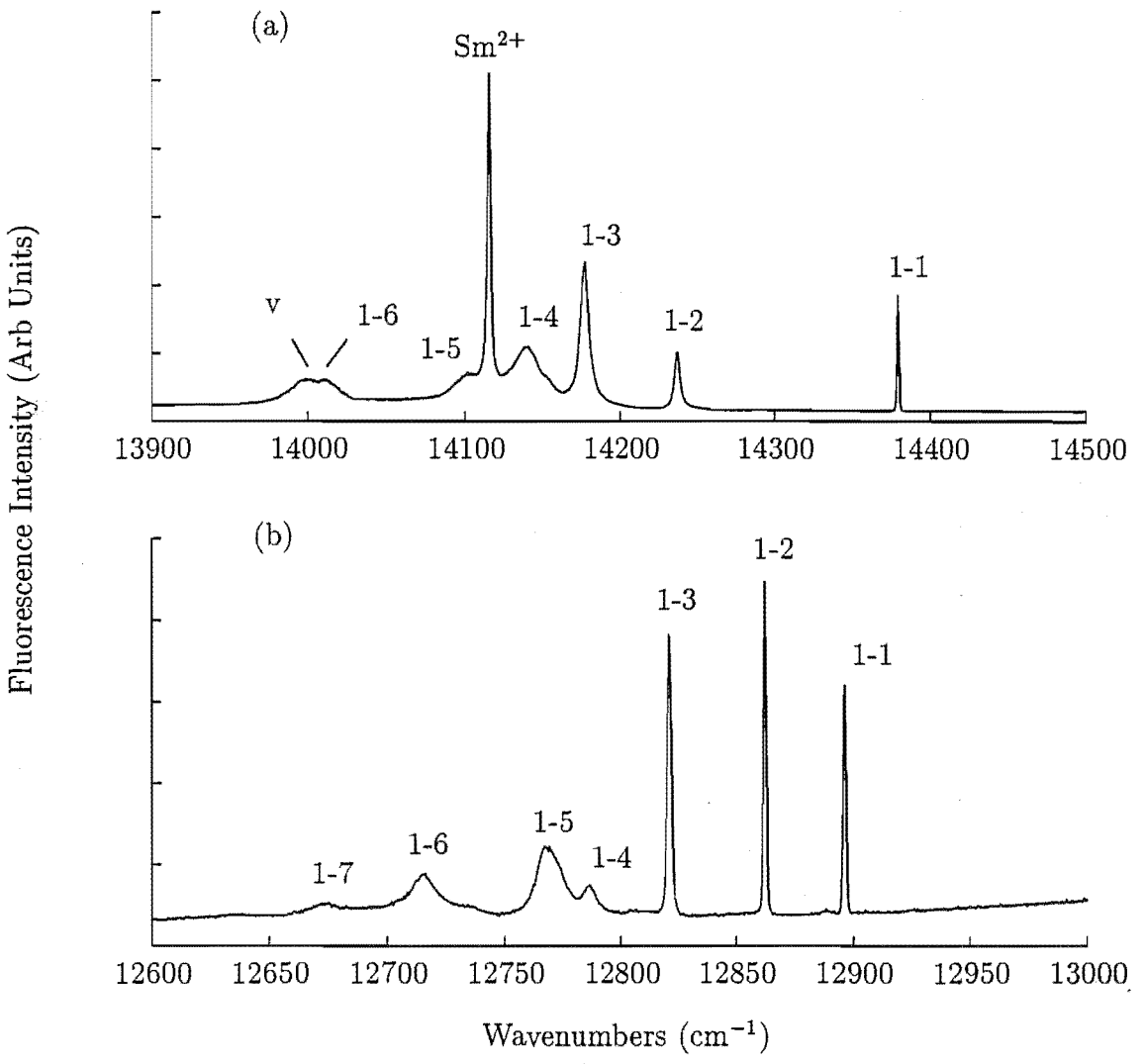

Figure 7.24: Fluorescence spectrum of the Q(Gd,Sm) centre for transitions from $^4G_{\frac{5}{2}}$ to (a) the $^6H_{\frac{11}{2}}$ multiplet and (b) the $^6H_{\frac{13}{2}}$ multiplet in CaF_2:0.15%Gd^{3+}:0.05%Sm^{3+}. The spectra were recorded at 16K.

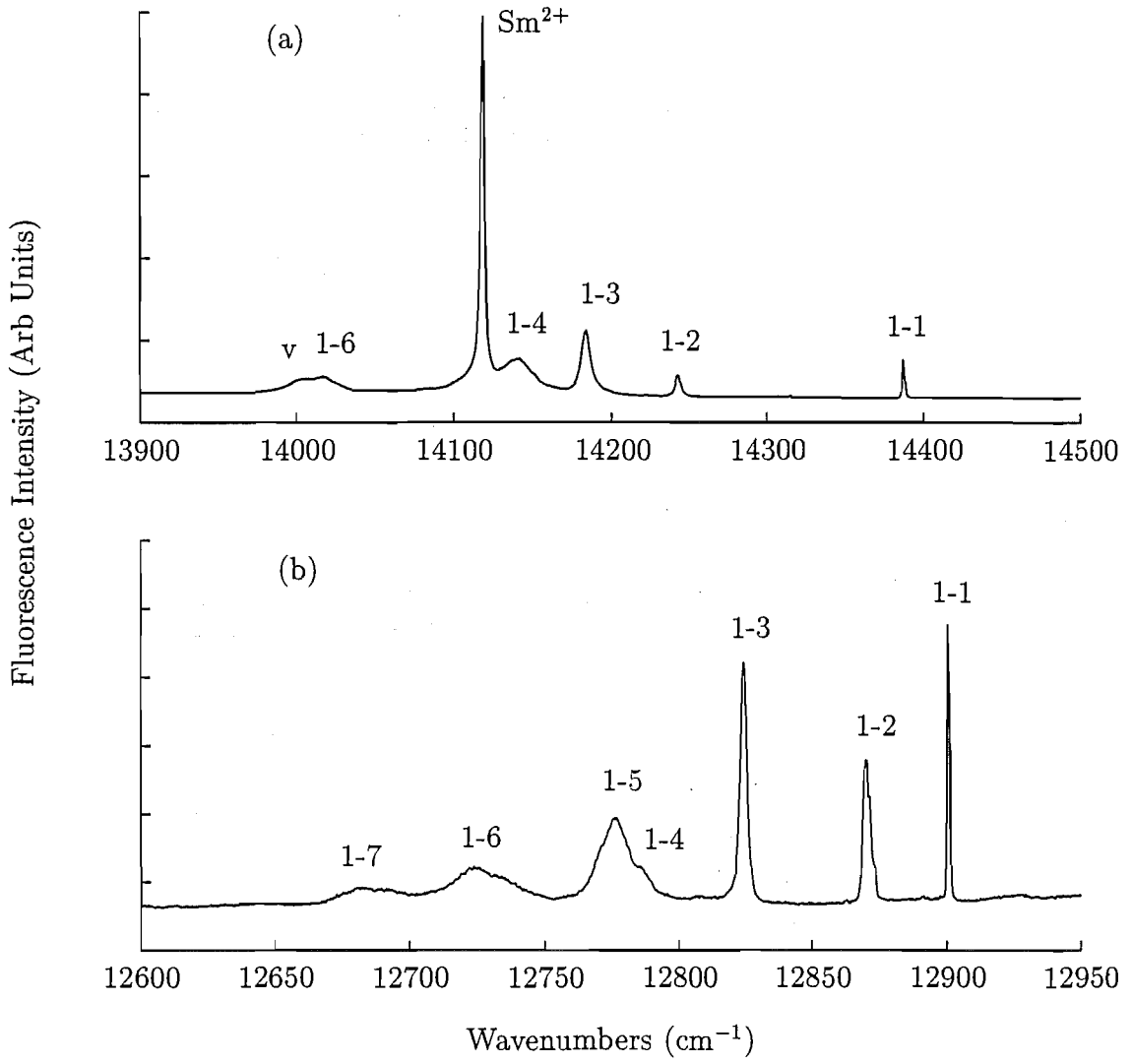

Figure 7.25: Fluorescence spectrum of the Q(Tb,Sm) centre for transitions from $^4G_{\frac{5}{2}}$ to (a) the $^6H_{\frac{11}{2}}$ multiplet and (b) the $^6H_{\frac{13}{2}}$ multiplet in CaF_2:0.15%Tb^{3+}:0.05%Sm^{3+}. The spectra were recorded at 16K.

Table 7.7: Fluorescence transitions for the $^6H_{\frac{11}{2}}$ and $^6H_{\frac{13}{2}}$ multiplets of the Q centre in CaF_2:0.15%La^{3+}:0.05%Sm^{3+}, CaF_2:0.15%Ce^{3+}:0.05%Sm^{3+}, CaF_2:0.15%Gd^{3+}:0.05%Sm^{3+} and CaF_2:0.15%Tb^{3+}:0.05%Sm^{3+}. All frequencies are as measured in air (cm^{-1},±1).

Multiplet	State Label	(La^{3+}:Sm^{3+}) Transition Frequency	(La^{3+}:Sm^{3+}) State Energy	(Ce^{3+}:Sm^{3+}) Transition Frequency	(Ce^{3+}:Sm^{3+}) State Energy	(Gd^{3+}:Sm^{3+}) Transition Frequency	(Gd^{3+}:Sm^{3+}) State Energy	(Tb^{3+}:Sm^{3+}) Transition Frequency	(Tb^{3+}:Sm^{3+}) State Energy
$^6H_{\frac{11}{2}}$	W_1	14368	3442	14373	3438	14380	3433	14384	3428
	W_2	14236	3575	14237	3578	14238	3574	14239	3572
	W_3	14168	3642	14173	3638	14178	3635	14181	3631
	W_4	14141	3669	14140	3670	14142±2	3671	14141	3671
	W_5	14084	3726	14092	3718	14103±2	3710	14115±5	3697
	W_6	13995	3815	14002	3808	14012	3801	14004	3808
$^6H_{\frac{13}{2}}$	V_1	12891	4919	12894	4917	12896	4916	12898	4914
	V_2	12847	4964	12853	4958	12863	4950	12869	4943
	V_3	12822	4989	12824	4987	12821	4991	12822	4990
	V_4	12782	5028	12787	5024	12786	5026	12783	5029
	V_5	12765	5046	12767	5044	12769	5044	12775	5037
	V_6	12705	5105	12711	5100	12715	5098	12724	5088
	V_7	12660	5151	12667	5144	12676	5137	12682	5130

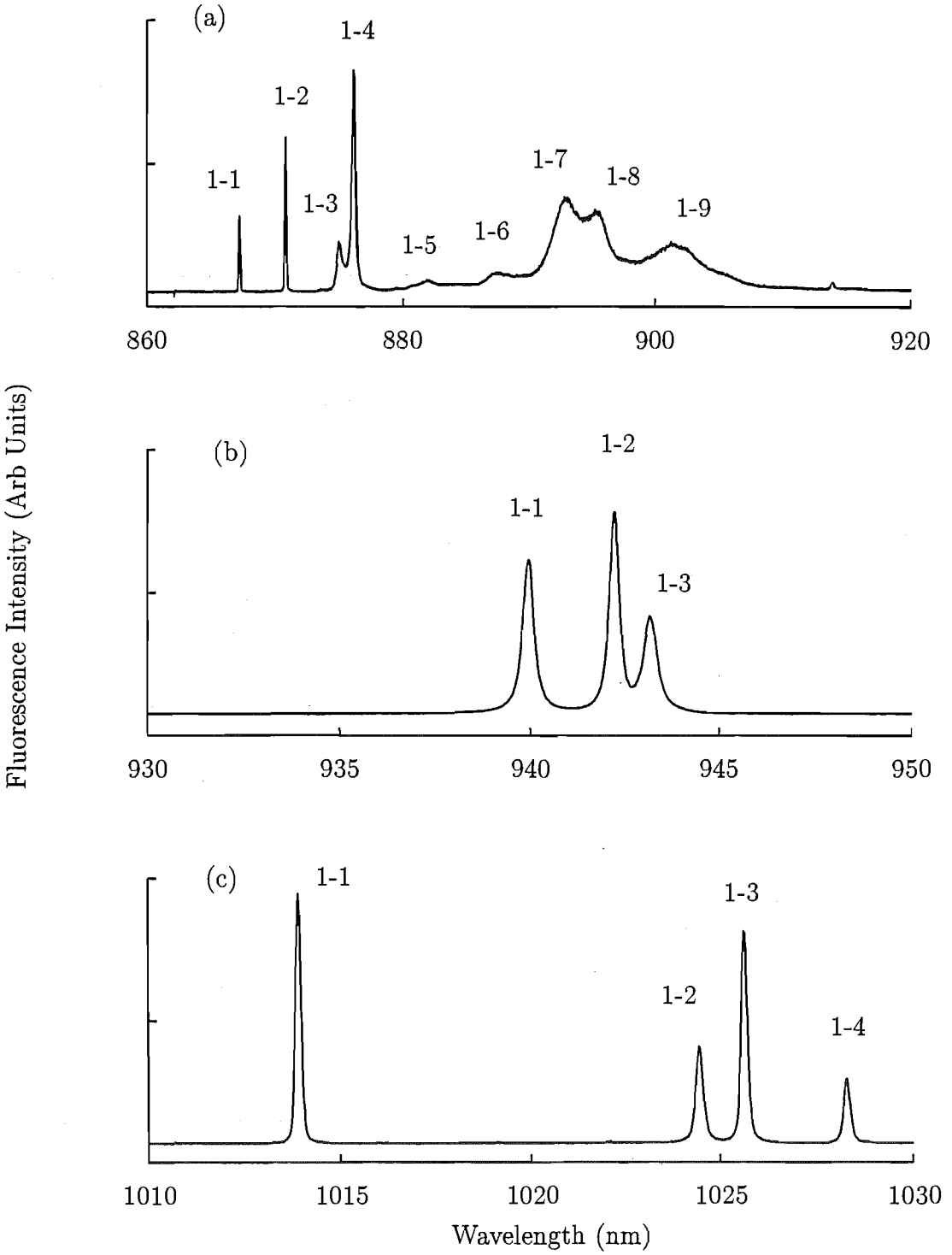

Figure 7.26: Fluorescence spectrum of the Q(La,Sm) centre for transitions from $^4G_{\frac{5}{2}}$ to (a) the $^6H_{\frac{15}{2}}$, $^6F_{\frac{1}{2}}$ and $^6F_{\frac{3}{2}}$ multiplets, (b) the $^6F_{\frac{5}{2}}$ multiplet and (c) the $^6F_{\frac{7}{2}}$ multiplet in CaF_2:0.15%La^{3+}:0.05%Sm^{3+}. The spectra were recorded at 16K.

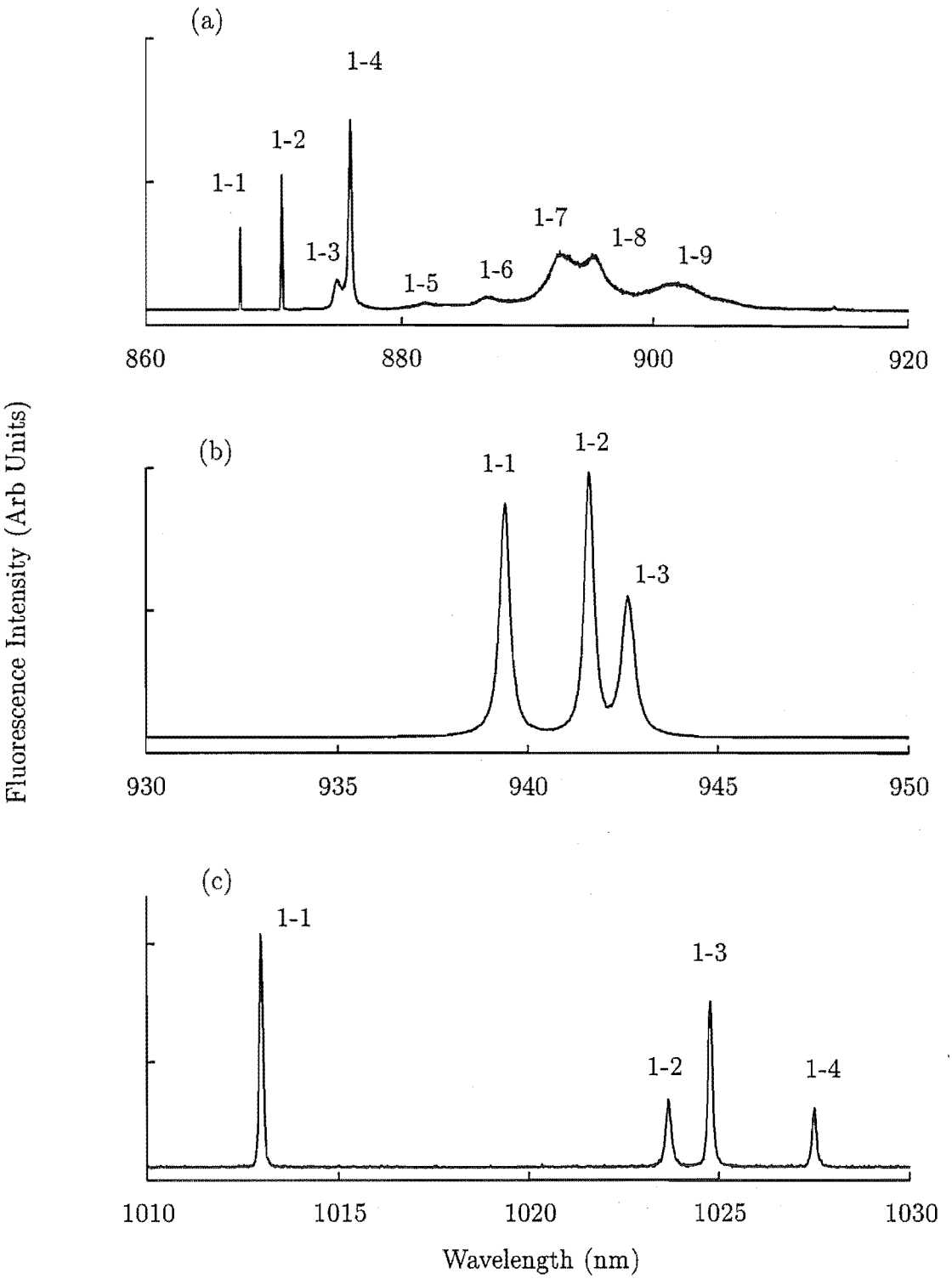

Figure 7.27: Fluorescence spectrum of the Q(Ce,Sm) centre for transitions from $^4G_{\frac{5}{2}}$ to (a) the $^6H_{\frac{15}{2}}$, $^6F_{\frac{1}{2}}$ and $^6F_{\frac{3}{2}}$ multiplets, (b) the $^6F_{\frac{5}{2}}$ multiplet and (c) the $^6F_{\frac{7}{2}}$ multiplet in CaF_2:0.15%Ce^{3+}:0.05%Sm^{3+}. The spectra were recorded at 16K.

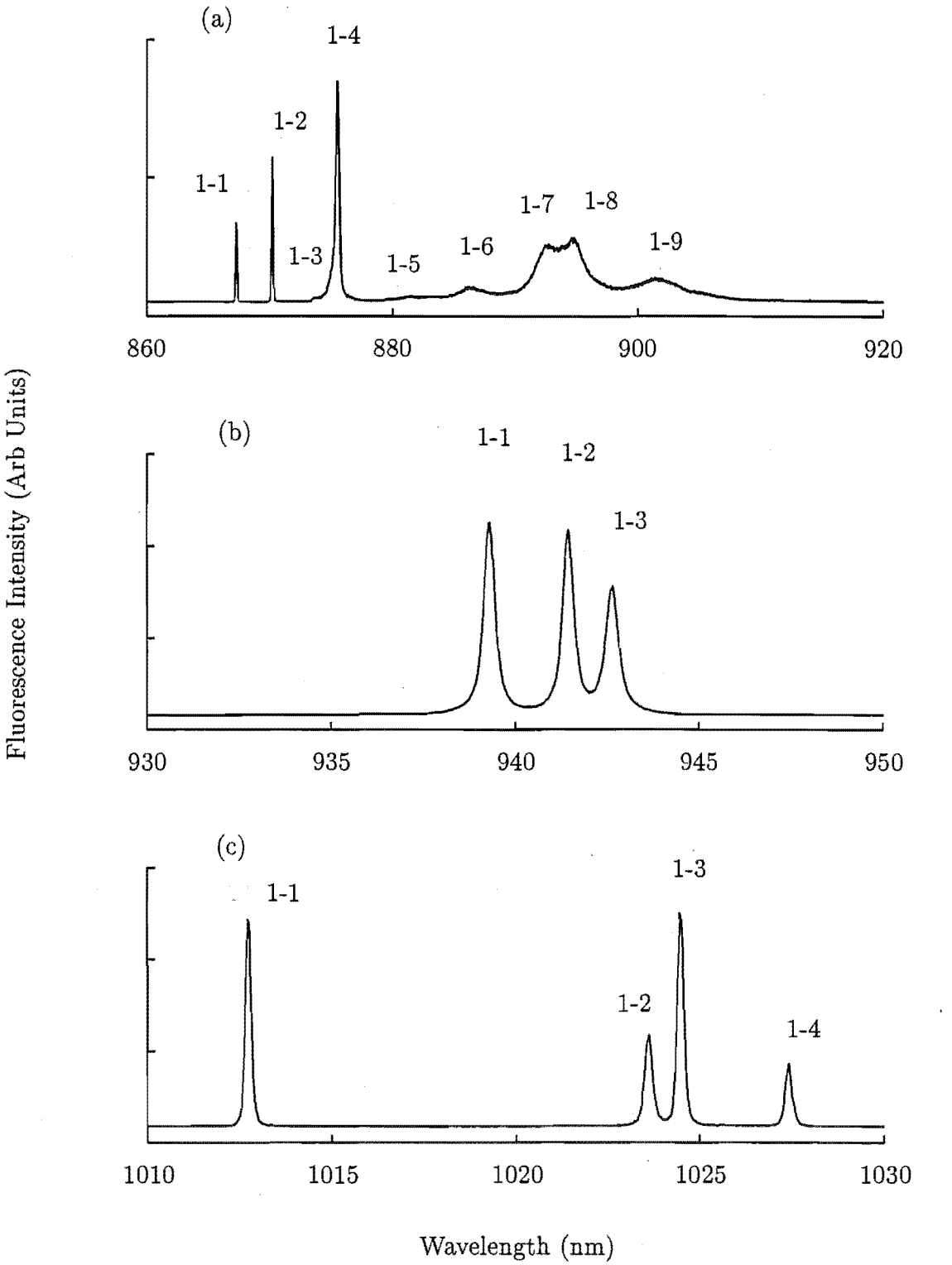

Figure 7.28: Fluorescence spectrum of the Q(Gd,Sm) centre for transitions from $^4G_{\frac{5}{2}}$ to (a) the $^6H_{\frac{15}{2}}$, $^6F_{\frac{1}{2}}$ and $^6F_{\frac{3}{2}}$ multiplets, (b) the $^6F_{\frac{5}{2}}$ multiplet and (c) the $^6F_{\frac{7}{2}}$ multiplet in CaF_2:0.15%Gd^{3+}:0.05%Sm^{3+}. The spectra were recorded at 16K.

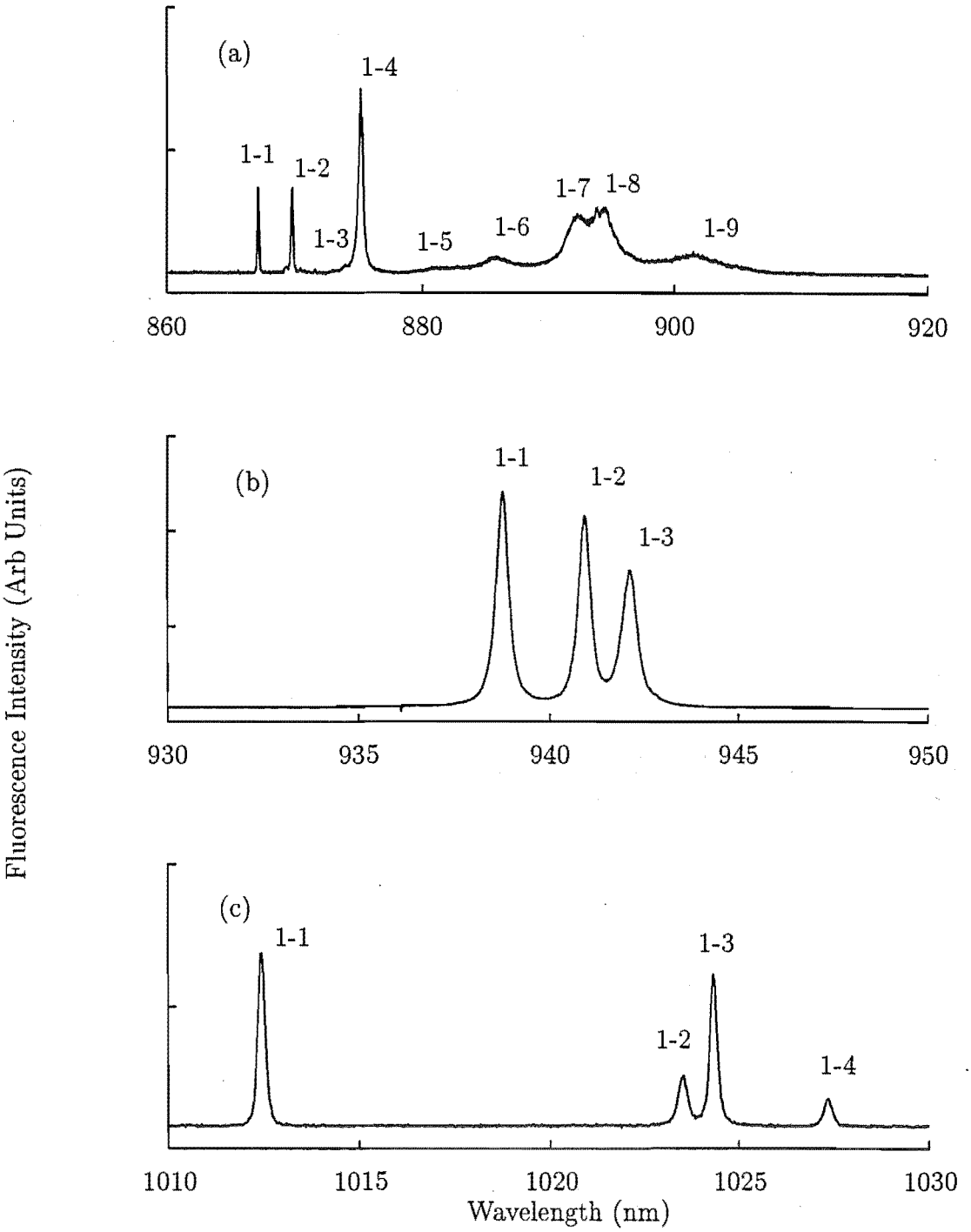

Figure 7.29: Fluorescence spectrum of the Q(Tb,Sm) centre for transitions from $^4G_{\frac{5}{2}}$ to (a) the $^6H_{\frac{15}{2}}$, $^6F_{\frac{1}{2}}$ and $^6F_{\frac{3}{2}}$ multiplets, (b) the $^6F_{\frac{5}{2}}$ multiplet and (c) the $^6F_{\frac{7}{2}}$ multiplet in CaF_2:0.15%Tb^{3+}:0.05%Sm^{3+}. The spectra were recorded at 16K.

Table 7.8: Fluorescence transitions for the $^6H_{\frac{15}{2}}$, $^6F_{\frac{1}{2}}$, $^6F_{\frac{3}{2}}$, $^6F_{\frac{5}{2}}$ and $^6F_{\frac{7}{2}}$ multiplets of the Q centre in CaF_2:0.15%La^{3+}:0.05%Sm^{3+}, CaF_2:0.15%Ce^{3+}:0.05%Sm^{3+}, CaF_2:0.15%Gd^{3+}:0.05%Sm^{3+} and CaF_2:0.15%Tb^{3+}:0.05%Sm^{3+}. All frequencies are as measured in air (cm^{-1},±1).

Multiplet	State Label	(La^{3+}:Sm^{3+}) Transition Frequency	(La^{3+}:Sm^{3+}) State Energy	(Ce^{3+}:Sm^{3+}) Transition Frequency	(Ce^{3+}:Sm^{3+}) State Energy	(Gd^{3+}:Sm^{3+}) Transition Frequency	(Gd^{3+}:Sm^{3+}) State Energy	(Tb^{3+}:Sm^{3+}) Transition Frequency	(Tb^{3+}:Sm^{3+}) State Energy
	S_1	11529	6281	11525	6286	11529	6284	11529	6282
	S_2	11481	6329	11481	6330	11490	6322	11494	6318
	S_3	11426	6384	11426	6385	11443	6370	-	-
$^6H_{\frac{15}{2}}$,	S_4	11411	6399	11412	6399	11420	6393	11423	6389
$^6F_{\frac{1}{2}}$ &	S_5	11335	6475	11336	6475	11348	6464	11356	6456
$^6F_{\frac{3}{2}}$	S_6	11267	6543	11273	6538	11282	6530	11287	6525
	S_7	11198	6612	11199	6612	11201	6612	11200	6612
	S_8	11167	6643	11169	6642	11177	6636	11183	6628
	S_9	11089	6721	11086	6725	11084	6729	11091	6721
	R_1	10642	7168	10643	7168	10650	7163	10649	7163
$^6F_{\frac{5}{2}}$	R_2	10617	7194	10618	7193	10625	7188	10625	7187
	R_3	10605	7205	10606	7205	10611	7201	10611	7201
	Q_1	9865	7945	9868	7943	9875	7938	9877	7935
	Q_2	9762	8048	9766	8045	9771	8042	9769	8043
$^6F_{\frac{7}{2}}$	Q_3	9751	8059	9755	8056	9762	8051	9762	8050
	Q_4	9726	8085	9729	8082	9733	8080	9736	8076

(b) R Centre Fluorescence

Excitation of R(RE,Sm) centre $^4G_{\frac{5}{2}}(Sm^{3+})$ absorption transitions, yields fluorescence to the Sm^{3+} ^6H_J and ^6F_J multiplets. The recorded fluorescence spectra are shown in Figures 7.30 to 7.41. We deal with fluorescence to these multiplets below.

Fluorescence to the $^6H_{\frac{5}{2}}$ multiplet is detected in the 17850-17600 cm^{-1} region. Typically, transitions to five $^6H_{\frac{5}{2}}$ states are observed rather than 3 expected from $J+\frac{1}{2}$. This reflects the statistical occupation of two asymmetrical sites in the cluster by the Sm^{3+} ions and the distinct crystal field at each. For the CeF_3 codoped sample, a 3 cm^{-1} splitting is observed for the $A_1 \rightarrow Z_2$ transition. To check that this was not due to overlap with an additional centre, the laser was tuned through the 17830 cm^{-1} absorption transition. No intensity variation was observed, relative to the other transitions assigned to the R(Ce,Sm) centre.

Transitions to the $^6H_{\frac{7}{2}}$ multiplet occur in the 16900-16400 cm^{-1} region. Six transitions are observed in this case. Emission to this multiplet is characterised by two strong transitions labelled $A_1 \rightarrow Y_1$ and Y_3. The remaining transitions are weak, but clearly observable. A broad feature is observed approximately 360 cm^{-1} from the $A_1 \rightarrow Y_1$ transition. This is assigned as a transition terminating on the TO(X) lattice vibrational mode.

Transitions to the $^6H_{\frac{9}{2}}$ multiplet are detected in the 15700-15200 cm^{-1} region. These spectra are very clear. No additional transitions above the 5 from $J+\frac{1}{2}$ are observed in this case.

Fluorescence to the $^6H_{\frac{11}{2}}$ multiplet can be observed in the 14500-13900 region. Up to ten fluorescence transitions are observed to $^6H_{\frac{11}{2}}$. The transition to the lowest state is typically sharp and intense. The $A_1 \rightarrow W_2$, W_3 and W_4 transitions are much weaker but can be clearly observed. The remaining transitions are broadened by non-radiative decay to the lowest states of the multiplet. The sharp d→f transition of the Sm^{2+} ion can be observed at a frequency of 14115 cm^{-1}. A broad feature is observed to be displaced 300-400 cm^{-1} from the $A_1 \rightarrow W_1$ transition. This is assigned as phonon sideband structure. The measured transition frequencies for emission to these multiplets are given in Table 7.9.

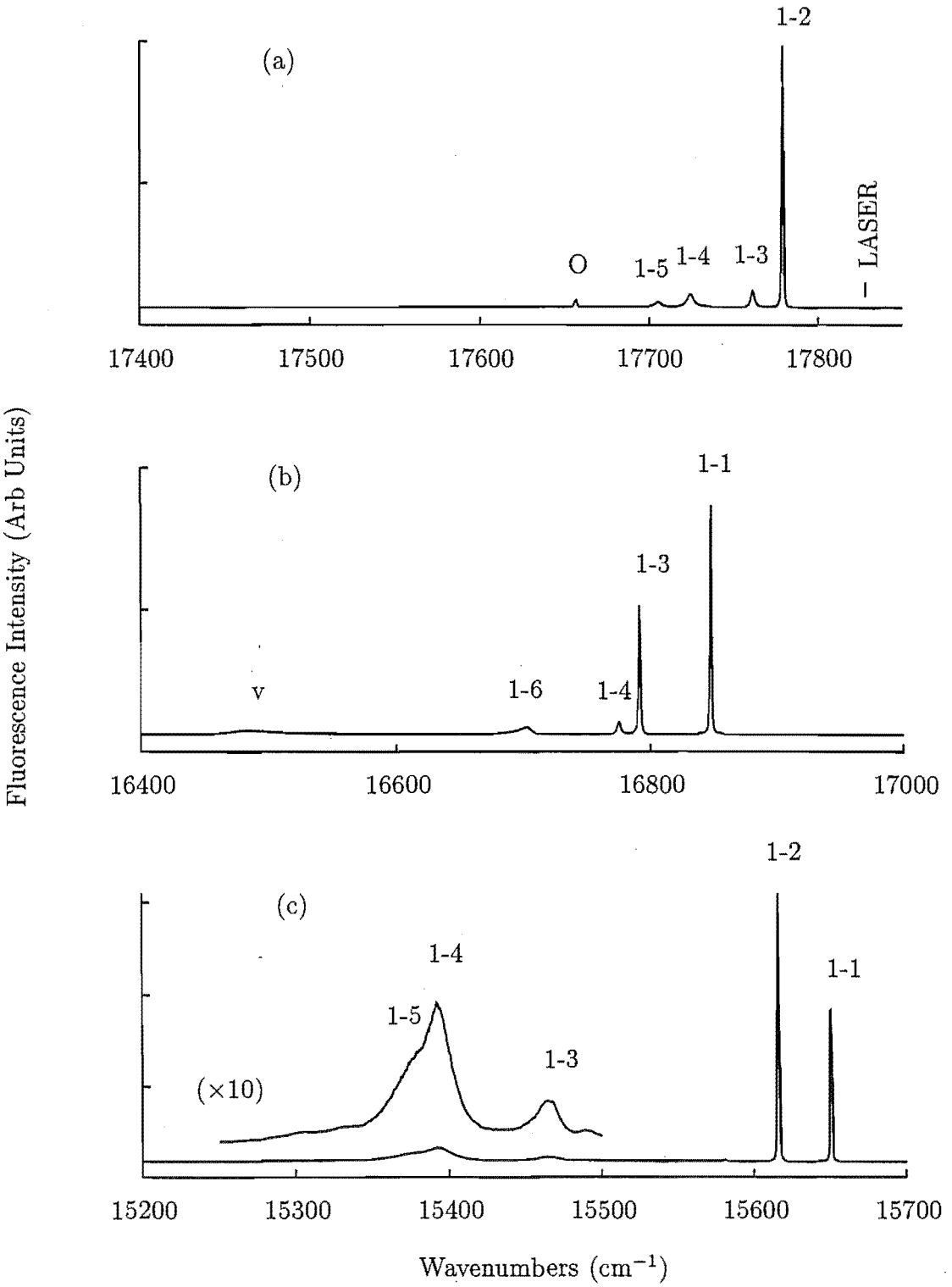

Figure 7.30: Fluorescence spectrum of the R(La,Sm) centre for transitions from $^4G_{\frac{5}{2}}$ to (a) the $^6H_{\frac{5}{2}}$ multiplet, (b) the $^6H_{\frac{7}{2}}$ multiplet and (c) the $^6H_{\frac{9}{2}}$ multiplet in CaF_2:0.15%La^{3+}:0.05%Sm^{3+}. For all spectra the 17830 cm^{-1} $Z_1 \rightarrow A_1$ transition was excited. The spectra were recorded at 16K

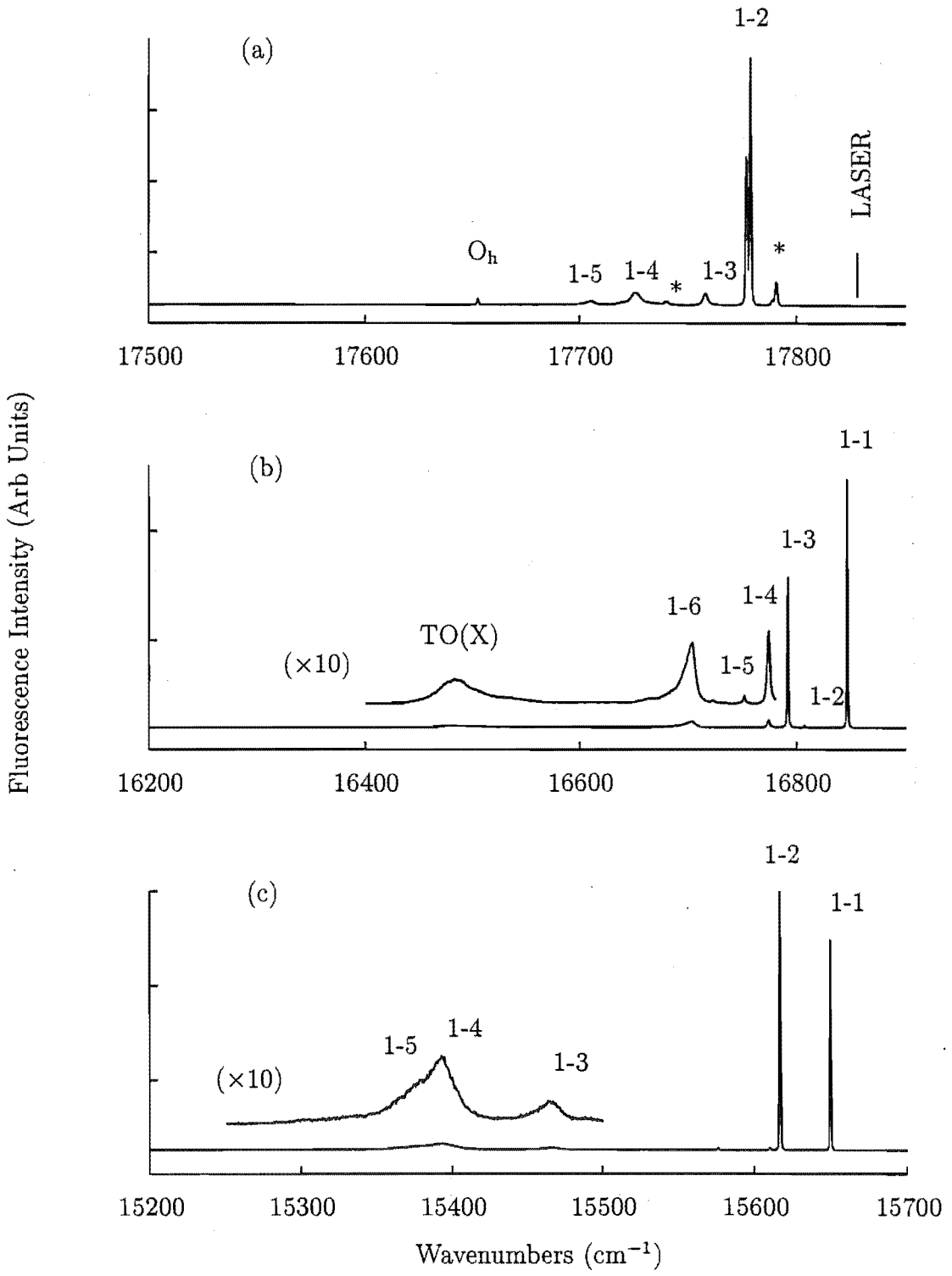

Figure 7.31: Fluorescence spectrum of the R(Ce,Sm) centre for transitions from $^4G_{\frac{5}{2}}$ to (a) the $^6H_{\frac{5}{2}}$ multiplet, (b) the $^6H_{\frac{7}{2}}$ multiplet and (c) the $^6H_{\frac{9}{2}}$ multiplet in CaF_2:0.15%Ce^{3+}:0.05%Sm^{3+}. For all spectra the 17830 cm^{-1} $Z_1 \rightarrow A_1$ transition was excited. The spectra were recorded at 16K. The * notation denotes unrelated features.

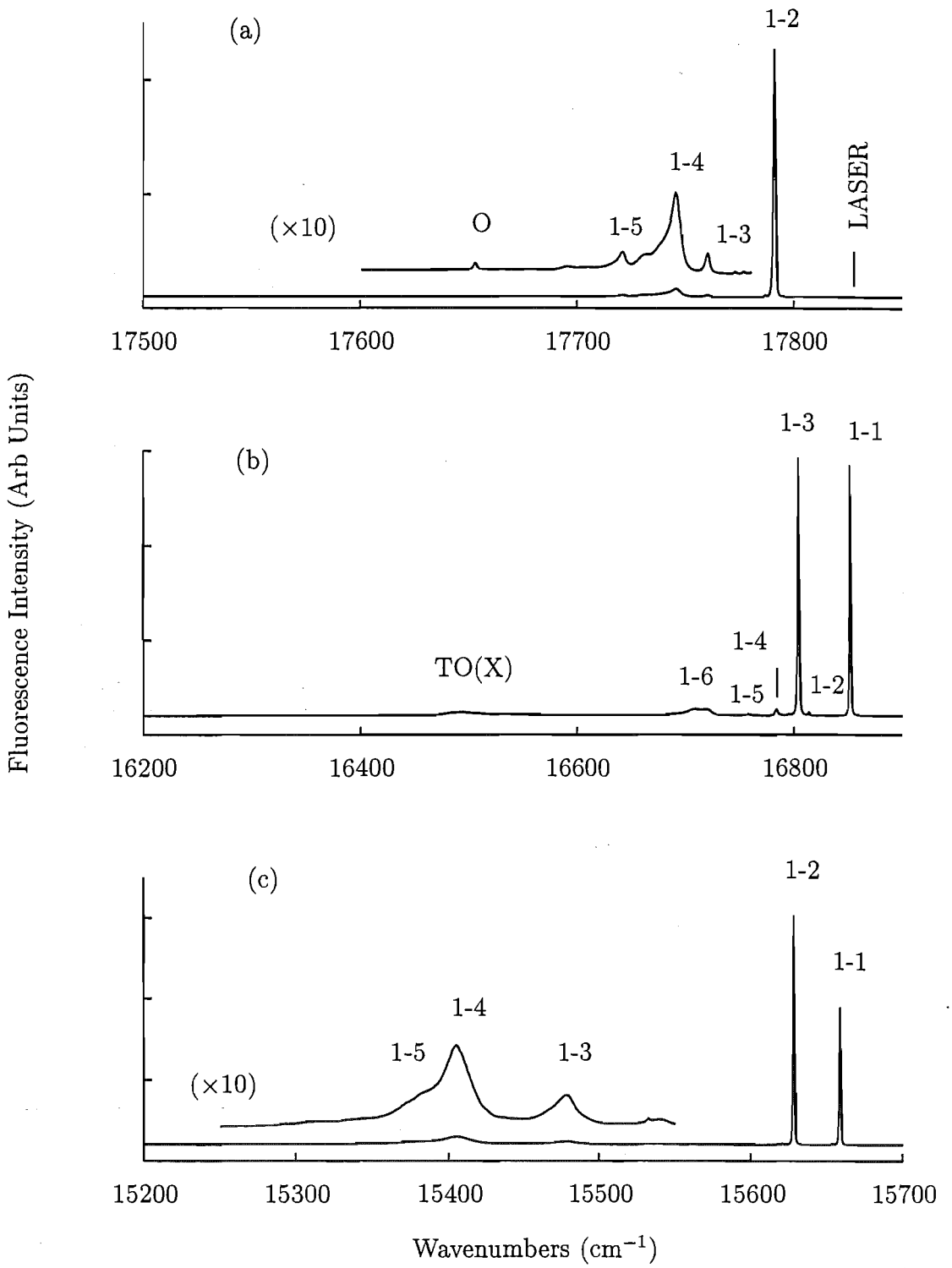

Figure 7.32: Fluorescence spectrum of the R(Gd,Sm) centre for transitions from $^4G_{\frac{5}{2}}$ to (a) the $^6H_{\frac{5}{2}}$ multiplet, (b) the $^6H_{\frac{7}{2}}$ multiplet and (c) the $^6H_{\frac{9}{2}}$ multiplet in CaF_2:0.15%Gd^{3+}:0.05%Sm^{3+}. For all spectra the 17828 cm^{-1} $Z_1 \rightarrow A_1$ transition was excited. The spectra were recorded at 16K.

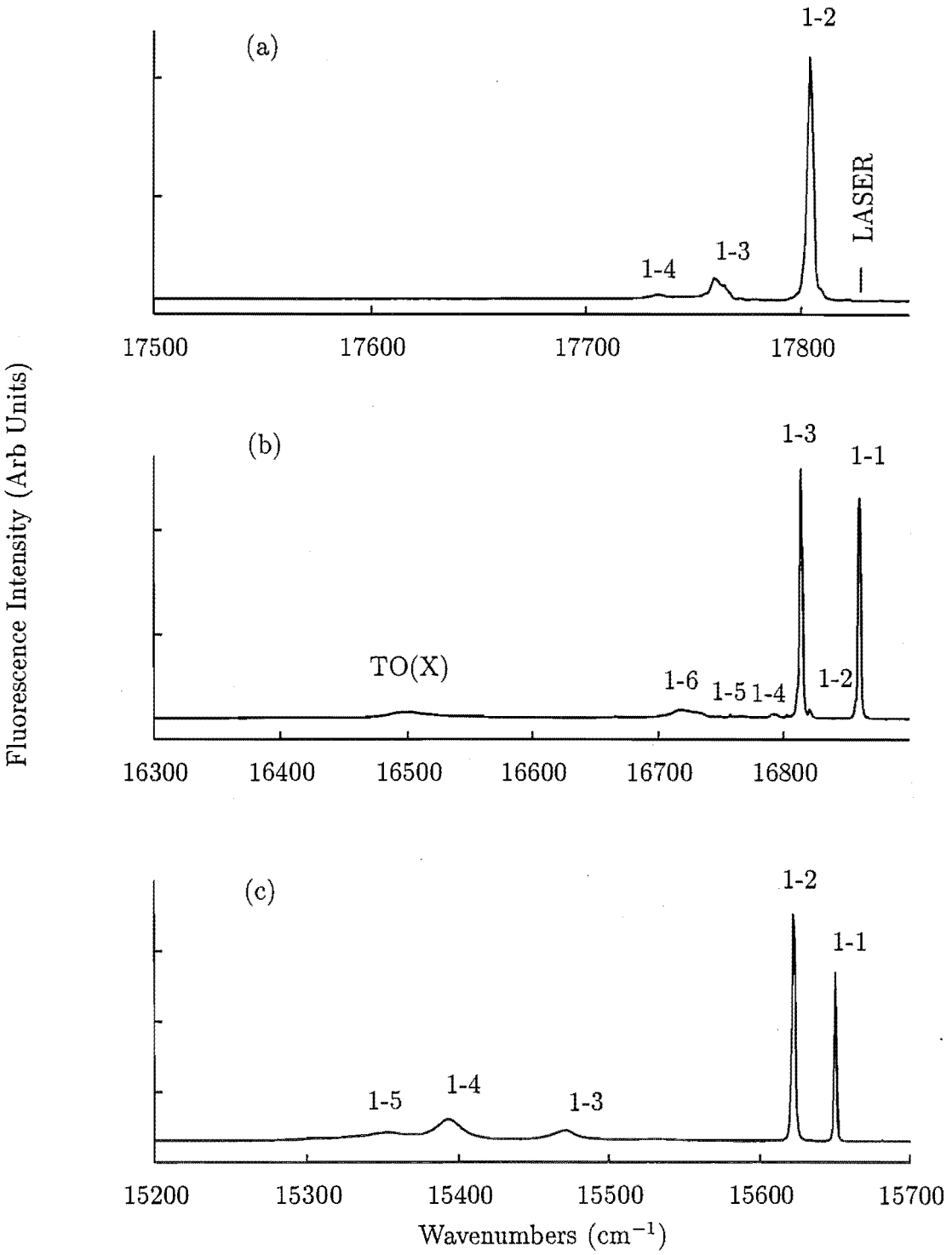

Figure 7.33: Fluorescence spectrum of the R(Tb,Sm) centre for transitions from $^4G_{\frac{5}{2}}$ to (a) the $^6H_{\frac{5}{2}}$ multiplet, (b) the $^6H_{\frac{7}{2}}$ multiplet and (c) the $^6H_{\frac{9}{2}}$ multiplet in CaF_2:0.15%Tb^{3+}:0.05%Sm^{3+}. For all spectra the 17828 cm^{-1} $Z_1 \rightarrow A_1$ transition was excited. The spectra were recorded at 16K.

Table 7.9: Fluorescence transitions for the $^6H_{\frac{5}{2}}$, $^6H_{\frac{7}{2}}$ and $^6H_{\frac{9}{2}}$ multiplets of the R centre in CaF_2:0.15%La^{3+}:0.05%Sm^{3+}, CaF_2:0.15%Ce^{3+}:0.05%Sm^{3+}, CaF_2:0.15%Gd^{3+}:0.05%Sm^{3+} and CaF_2:0.15%Tb^{3+}:0.05%Sm^{3+}. All frequencies are as measured in air (cm^{-1},±1).

Multiplet	State Label	(La^{3+}:Sm^{3+}) Transition Frequency	(La^{3+}:Sm^{3+}) State Energy	(Ce^{3+}:Sm^{3+}) Transition Frequency	(Ce^{3+}:Sm^{3+}) State Energy	(Gd^{3+}:Sm^{3+}) Transition Frequency	(Gd^{3+}:Sm^{3+}) State Energy	(Tb^{3+}:Sm^{3+}) Transition Frequency	(Tb^{3+}:Sm^{3+}) State Energy
$^6H_{\frac{5}{2}}$	Z_1	17830	0	17830	0	17828	0	17828	0
	Z_2	17776	54	$\frac{17781}{17778}$	$\frac{49}{52}$	17791	37	17806	22
	Z_3	17758	72	17760	70	17761	67	17760	68
	Z_4	17721	109	17727	103	17746	82	17730	98
	Z_5	17702	127	17707	123	17722	106	-	-
$^6H_{\frac{7}{2}}$	Y_1	16845	985	16846	983	16852	976	16859	969
	Y_2	-	-	16808	1022	16817	1011	16818	1010
	Y_3	16788	1042	16792	1037	16804	1024	16810	1018
	Y_4	16772	1058	16774	1155	16783	1045	16791	1037
	Y_5	-	-	16752	1077	16761	1067	16727	1101
	Y_6	16698	1132	16704	1126	16721±2	1107	16716	1112
$^6H_{\frac{9}{2}}$	X_1	15650	2180	15650	2180	15659	2169	15665	2163
	X_2	15613	2217	15617	2213	15628	2200	15637	2191
	X_3	15463	2367	15468	2362	15481±2	2347	15485	2343
	X_4	15391	2439	15396	2434	15408	2420	15413	2415
	X_5	15377	2453	15379	2451	15348±5	2444	15393	2435

Fluorescence transitions to the remaining ^6H_J and ^6F_J multipletrs were recorded in the appropriate spectral regions. For these measurements the SPEX 1700 series single monochromator and the liquid nitrogen cooled, RCA 7102 PMT were used to recorded the spectra. J+$\frac{1}{2}$ transiitons were observed exception for the overlapping $^6H_{\frac{15}{2}}$, $^6F_{\frac{1}{2}}$ and $^6F_{\frac{3}{2}}$ multiplets. The transition frequencies are given in Tables 7.10 and 7.11.

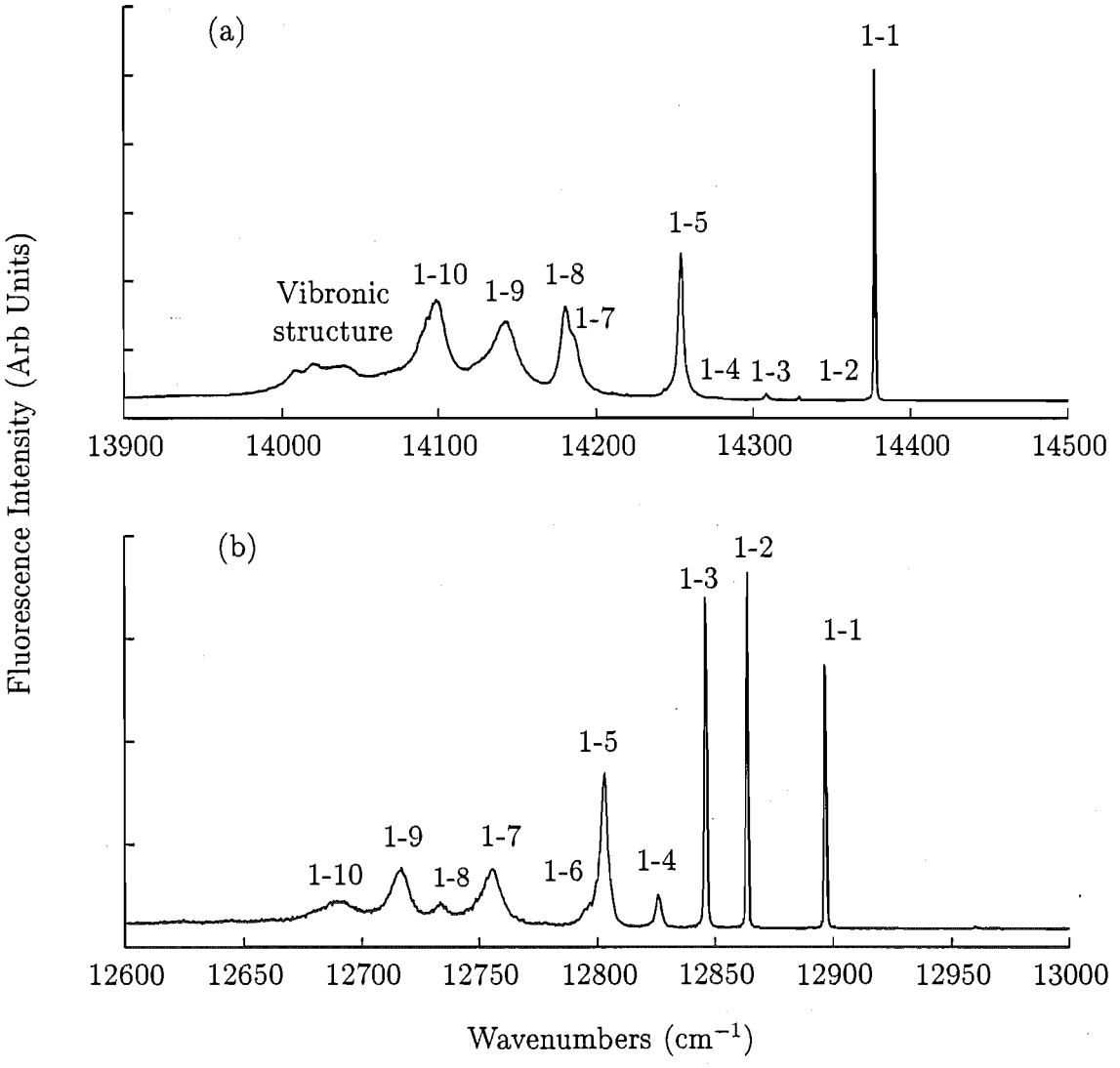

Figure 7.34: Fluorescence spectrum of the R(La,Sm) centre for transitions from $^4G_{\frac{5}{2}}$ to (a) the $^6H_{\frac{11}{2}}$ multiplet and (b) the $^6H_{\frac{13}{2}}$ multiplet in CaF_2:0.15%La^{3+}:0.05%Sm^{3+}. The spectra were recorded at 16K.

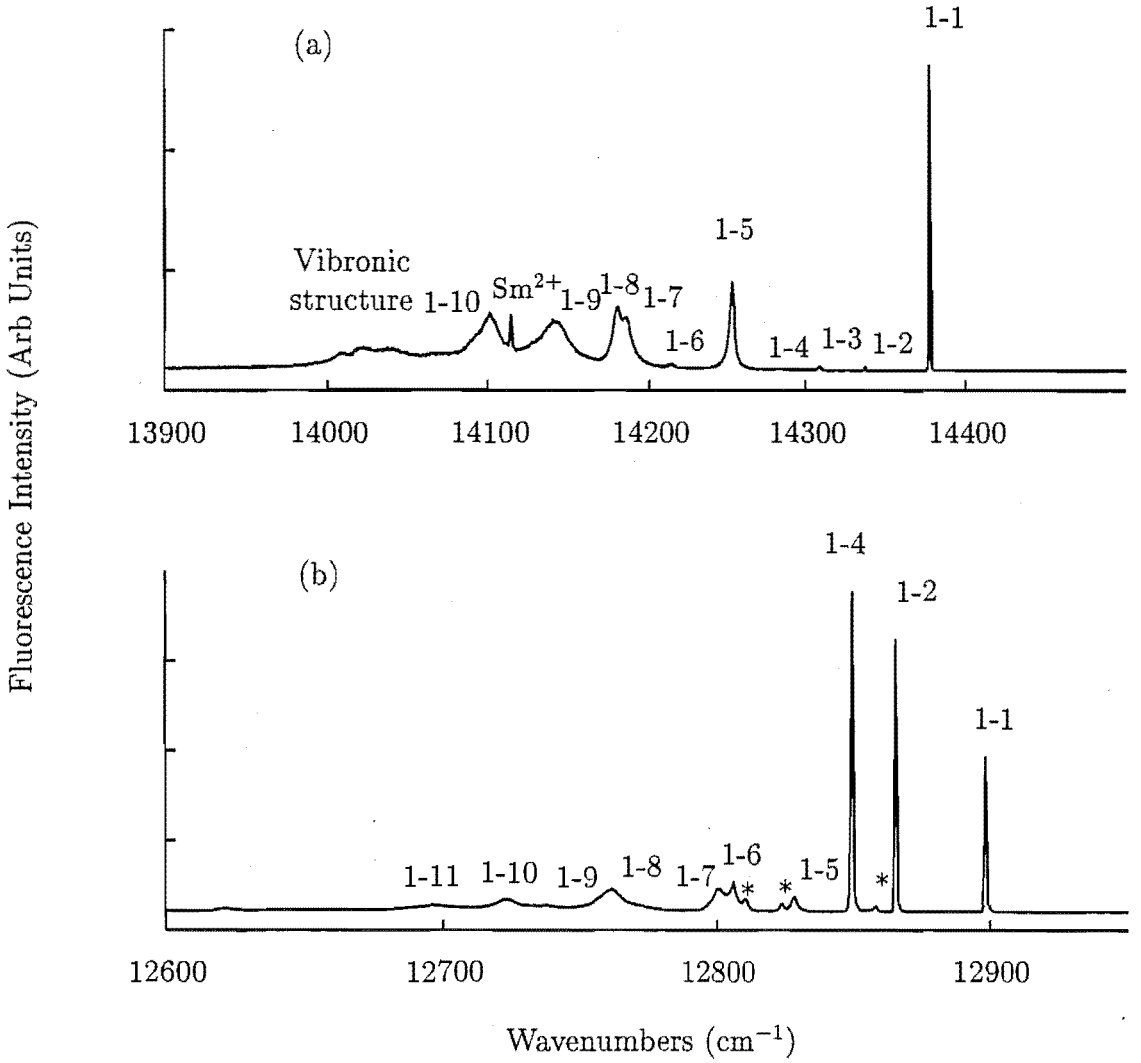

Figure 7.35: Fluorescence spectrum of the R(Ce,Sm) centre for transitions from $^4G_{\frac{5}{2}}$ to (a) the $^6H_{\frac{11}{2}}$ multiplet and (b) the $^6H_{\frac{13}{2}}$ multiplet in CaF_2:0.15%Ce^{3+}:0.05%Sm^{3+}. The spectra were recorded at 16K. The * notation denotes unrelated features.

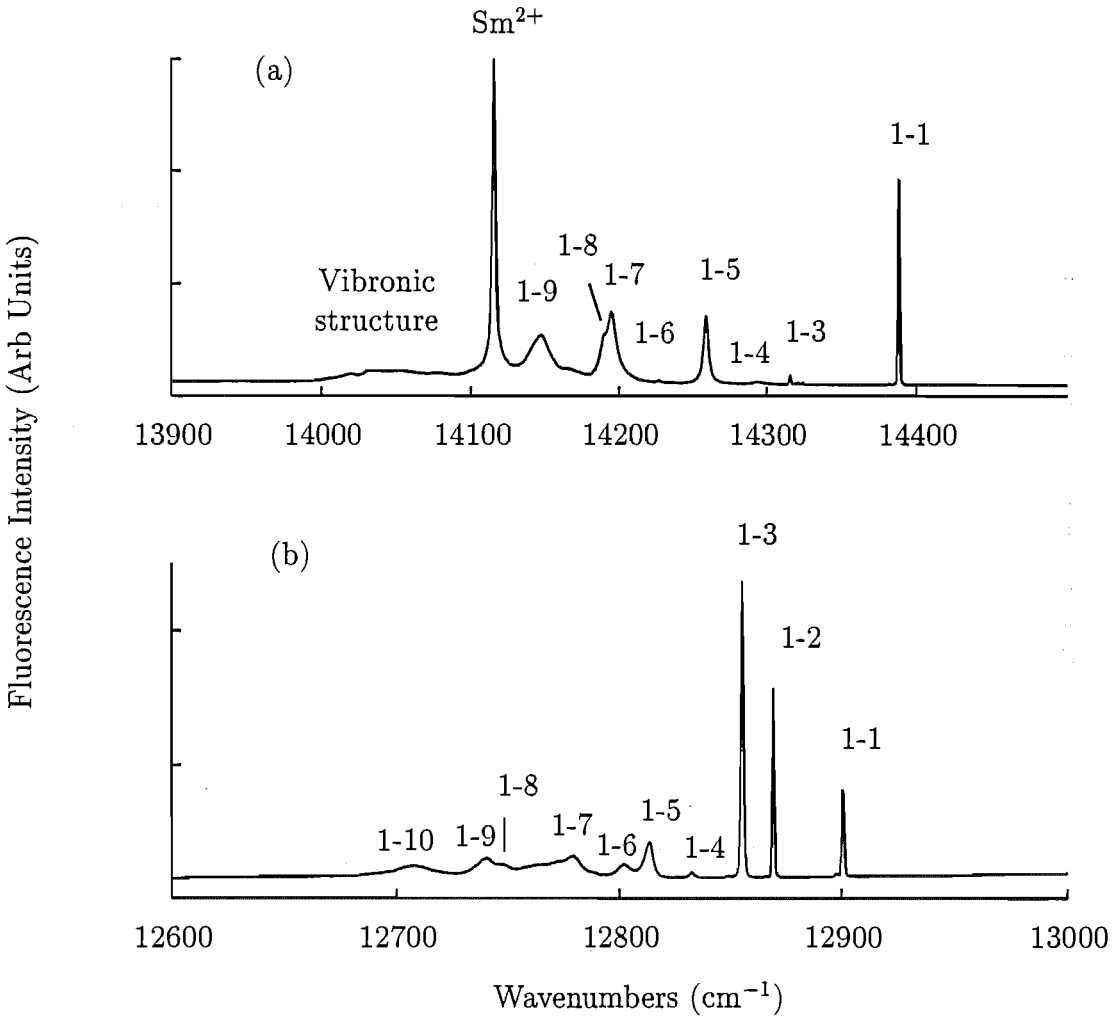

Figure 7.36: 16K fluorescence spectrum of the R(Gd,Sm) centre for transitions from $^4G_{\frac{5}{2}}$ to (a) the $^6H_{\frac{11}{2}}$ multiplet and (b) the $^6H_{\frac{13}{2}}$ multiplet in CaF_2:0.15%Gd^{3+}:0.05%Sm^{3+}.

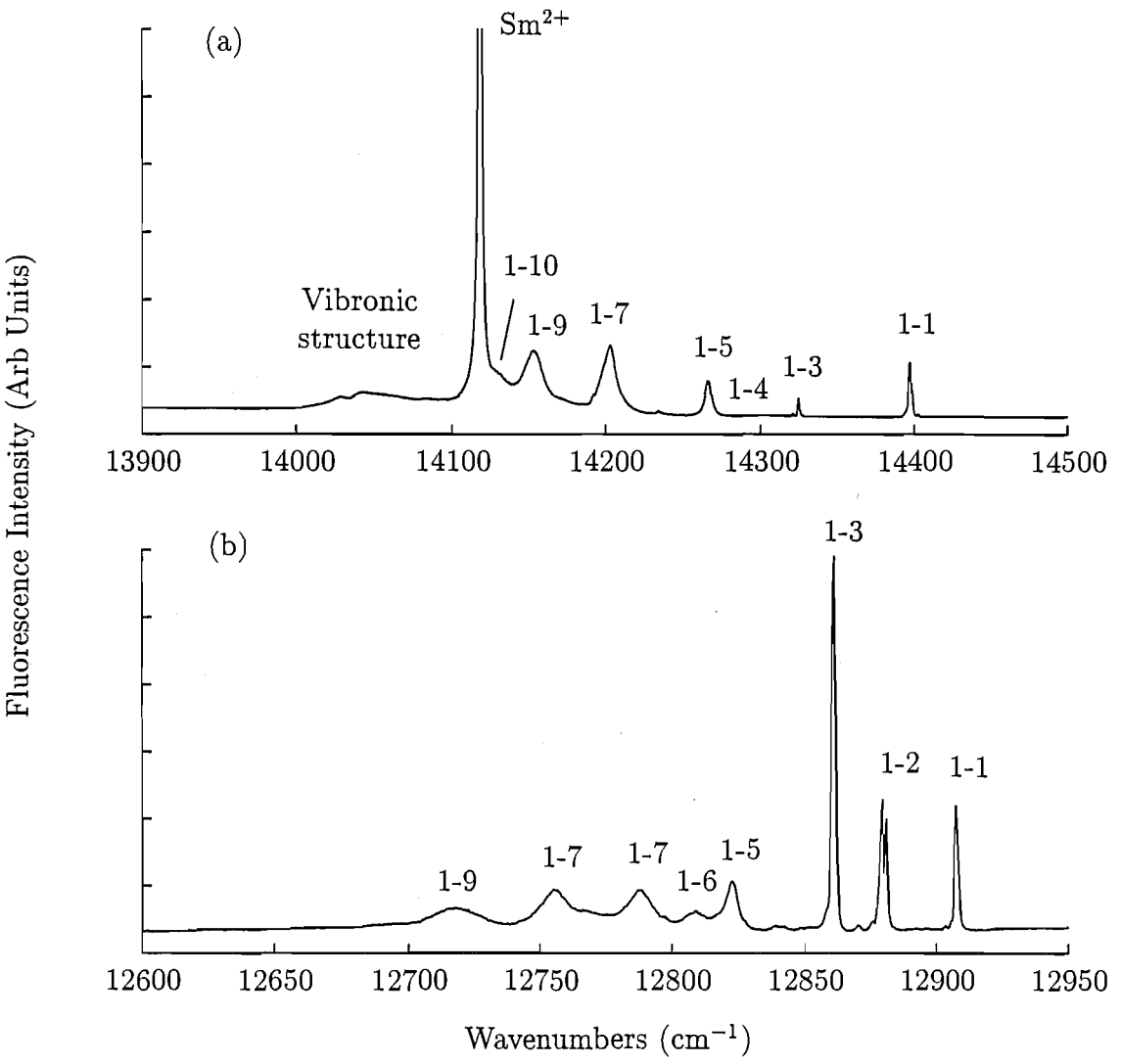

Figure 7.37: Fluorescence spectrum of the R(Tb,Sm) centre for transitions from $^4G_{\frac{5}{2}}$ to (a) the $^6H_{\frac{11}{2}}$ multiplet and (b) the $^6H_{\frac{13}{2}}$ multiplet in CaF_2:0.15%Tb^{3+}:0.05%Sm^{3+}. The spectra were recorded at 16K.

Table 7.10: Fluorescence transitions for the $^6H_{\frac{11}{2}}$ and $^6H_{\frac{13}{2}}$ multiplets of the R centre in CaF_2:0.15%La^{3+}:0.05%Sm^{3+}, CaF_2:0.15%Ce^{3+}:0.05%Sm^{3+}, CaF_2:0.15%Gd^{3+}:0.05%Sm^{3+} and CaF_2:0.15%Tb^{3+}:0.05%Sm^{3+}. All frequencies are as measured in air (cm^{-1},±1).

Multiplet	State Label	(La^{3+}:Sm^{3+}) Transition Frequency	(La^{3+}:Sm^{3+}) State Energy	(Ce^{3+}:Sm^{3+}) Transition Frequency	(Ce^{3+}:Sm^{3+}) State Energy	(Gd^{3+}:Sm^{3+}) Transition Frequency	(Gd^{3+}:Sm^{3+}) State Energy	(Tb^{3+}:Sm^{3+}) Transition Frequency	(Tb^{3+}:Sm^{3+}) State Energy
$^6H_{\frac{11}{2}}$	W_1	14374	3456	14379	3451	14388	3440	14396	3432
	W_2	14329	3501	14339	3591	-	-	-	-
	W_3	14305	3525	14310	3520	14316	3512	14324	3504
	W_4	14277	3553	14283	3547	14295	3533	14303	3525
	W_5	14251	3579	14254	3576	14260	3568	14264	3564
	W_6	-	-	14215	3614	14229	3599	-	-
	W_7	14181	3649	14187	3642	14195	3633	14201	3627
	W_8	14177	3653	14182	3648	14192	3636	-	-
	W_9	14140	3690	14144	3686	14146	3682	14152	3676
	W_{10}	14096	3734	14100	3729	-	-	14130	3698
$^6H_{\frac{13}{2}}$	V_1	12894	4936	12896	4934	12901	4927	12905	4923
	V_2	12861	4969	12863	4967	12869	4959	$\frac{12878}{12877}$	$\frac{4950}{4951}$
	V_3	12844	4987	12847	4983	12855	4973	12858	4970
	V_4	12823	5007	12825	5005	12833	4995	-	-
	V_5	12800	5030	12807	5023	12814	5014	12820	5008
	V_6	12797	5033	12801	5029	12802	5026	12806	5022
	V_7	12754	5076	12758	5072	12781	5047	12787	5041
	V_8	12733	5097	12738	5092	12748	5080	-	-
	V_9	12716	5114	12723	5107	12741	5087	12755	5074
	V_{10}	12689	5141	12696	5134	12709	5119	12716	5112

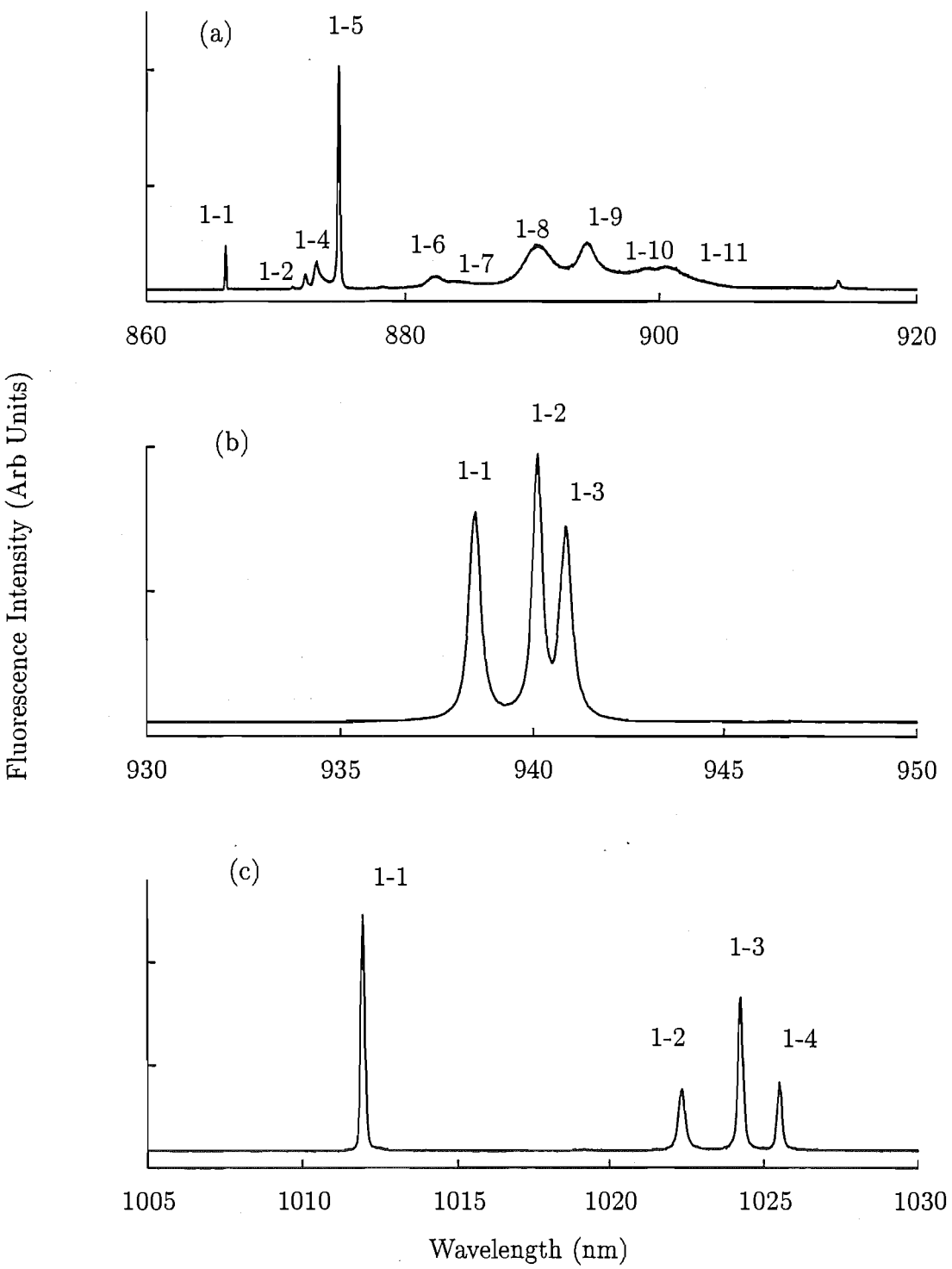

Figure 7.38: Fluorescence spectrum of the R(La,Sm) centre for transitions from $^4G_{\frac{5}{2}}$ to (a) the $^6H_{\frac{15}{2}}$, $^6F_{\frac{1}{2}}$ and $^6F_{\frac{3}{2}}$ multiplets, (b) the $^6F_{\frac{5}{2}}$ multiplet and (c) the $^6F_{\frac{7}{2}}$ multiplet in CaF_2:0.15%La^{3+}:0.05%Sm^{3+}. The spectra were recorded at 16K.

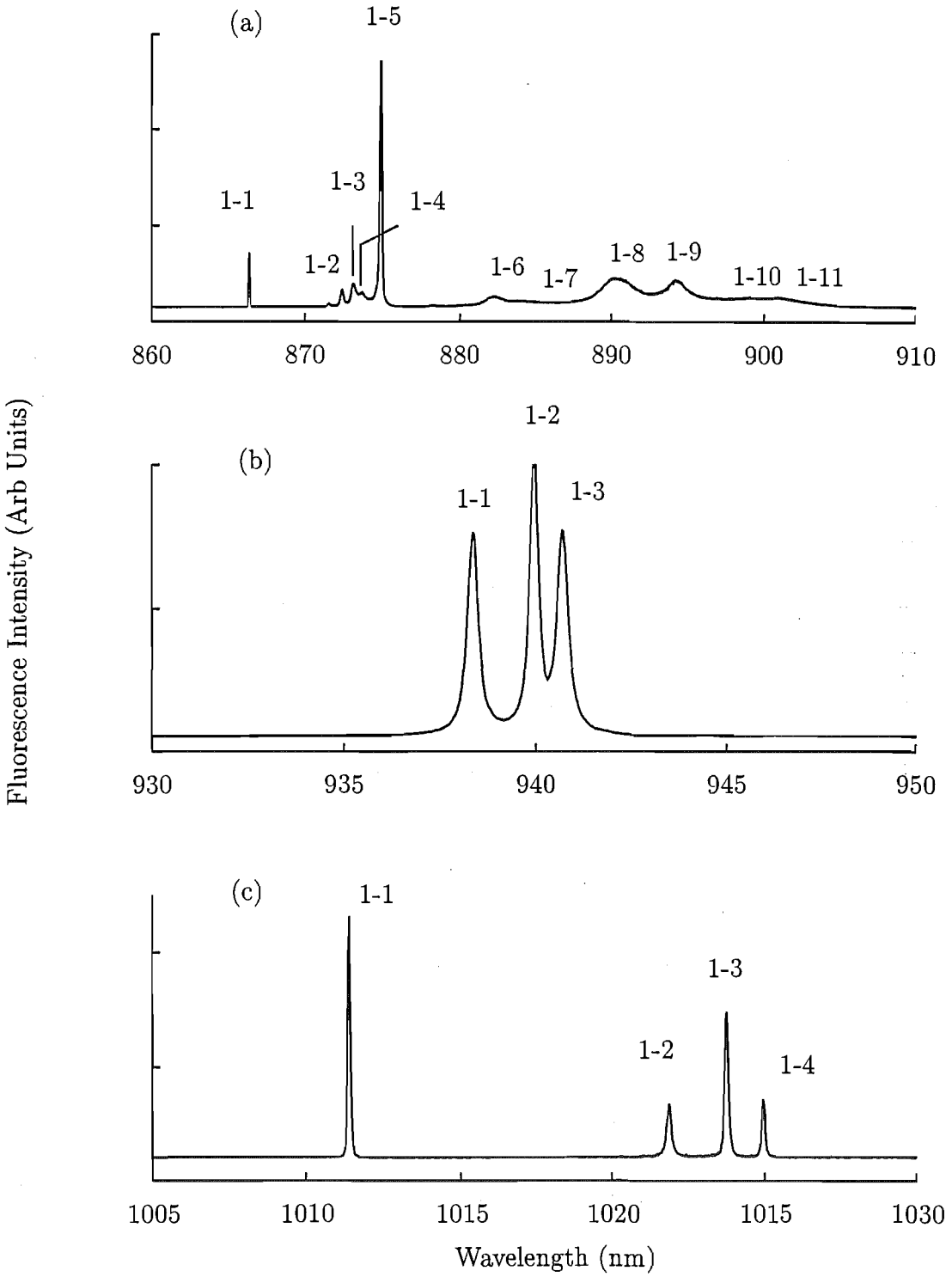

Figure 7.39: Fluorescence spectrum of the R(Ce,Sm) centre for transitions from $^4G_{\frac{5}{2}}$ to (a) the $^6H_{\frac{15}{2}}$, $^6F_{\frac{1}{2}}$ and $^6F_{\frac{3}{2}}$ multiplets, (b) the $^6F_{\frac{5}{2}}$ multiplet and (c) the $^6F_{\frac{7}{2}}$ multiplet in CaF_2:0.15%Ce^{3+}:0.05%Sm^{3+}. The spectra were recorded at 16K.

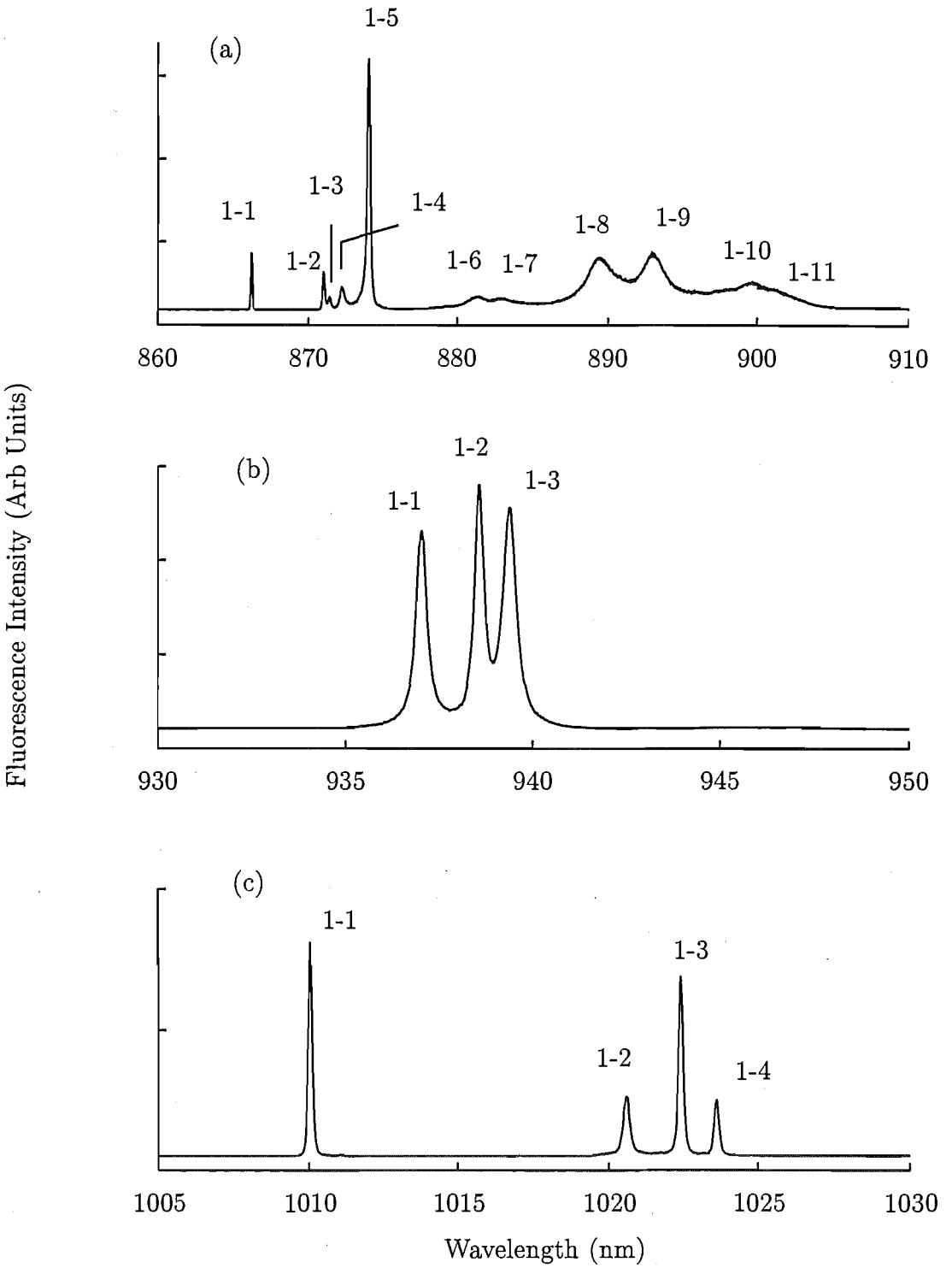

Figure 7.40: Fluorescence spectrum of the R(Gd,Sm) centre for transitions from $^4G_{\frac{5}{2}}$ to (a) the $^6H_{\frac{15}{2}}$, $^6F_{\frac{1}{2}}$ and $^6F_{\frac{3}{2}}$ multiplets, (b) the $^6F_{\frac{5}{2}}$ multiplet and (c) the $^6F_{\frac{7}{2}}$ multiplet in CaF_2:0.15%Gd^{3+}:0.05%Sm^{3+}. The spectra were recorded at 16K.

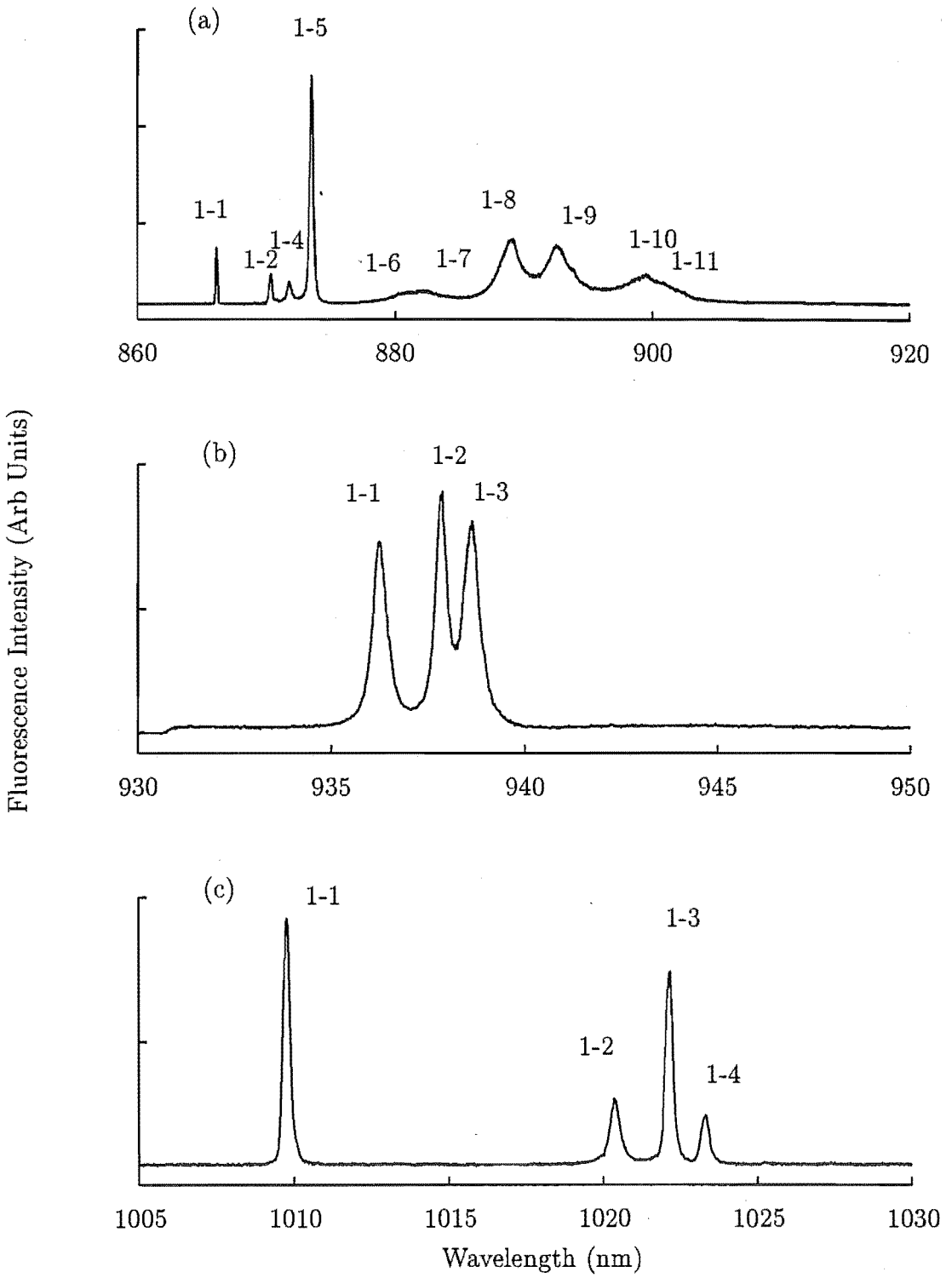

Figure 7.41: Fluorescence spectrum of the R(Tb,Sm) centre for transitions from $^4G_{\frac{5}{2}}$ to (a) the $^6H_{\frac{15}{2}}$, $^6F_{\frac{1}{2}}$ and $^6F_{\frac{3}{2}}$ multiplets, (b) the $^6F_{\frac{5}{2}}$ multiplet and (c) the $^6F_{\frac{7}{2}}$ multiplet in CaF_2:0.15%Tb^{3+}:0.05%Sm^{3+}. The spectra were recorded at 16K.

Table 7.11: Fluorescence transitions for the $^6H_{\frac{15}{2}}$, $^6F_{\frac{1}{2}}$, $^6F_{\frac{3}{2}}$, $^6F_{\frac{5}{2}}$ and $^6F_{\frac{7}{2}}$ multiplets of the R centre in CaF_2:0.15%La^{3+}:0.05%Sm^{3+}, CaF_2:0.15%Ce^{3+}:0.05%Sm^{3+}, CaF_2:0.15%Gd^{3+}:0.05%Sm^{3+} and CaF_2:0.15%Tb^{3+}:0.05%Sm^{3+}. All frequencies are as measured in air (cm^{-1},±1).

Multiplet	State Label	(La^{3+}:Sm^{3+}) Transition Frequency	(La^{3+}:Sm^{3+}) State Energy	(Ce^{3+}:Sm^{3+}) Transition Frequency	(Ce^{3+}:Sm^{3+}) State Energy	(Gd^{3+}:Sm^{3+}) Transition Frequency	(Gd^{3+}:Sm^{3+}) State Energy	(Tb^{3+}:Sm^{3+}) Transition Frequency	(Tb^{3+}:Sm^{3+}) State Energy
	S_1	11543	6287	11537	6293	11542	6286	11543	6285
	S_2	11461	6369	11460	6370	11479	6349	11487	6341
	S_3	-	-	11450	6380	11474	6354	-	-
$^6H_{\frac{15}{2}}$,	S_4	11450	6380	11442	6388	11464	6364	11469	6359
$^6F_{\frac{1}{2}}$ &	S_5	11425	6405	11427	6403	11440	6388	11446	6382
$^6F_{\frac{3}{2}}$	S_6	11329	6501	11331	6499	11347	6481	11353	6475
	S_7	11316	6514	11301	6529	11327	6501	11331	6497
	S_8	11230	6600	11234	6595	11244	6584	11246	6582
	S_9	11177	6653	11186	6643	11200	6628	11205	6624
	S_{10}	11117	6713	11126	6704	11116	6712	11117	6711
	S_{11}	11102	6728	11104	6726	11099	6729	11104	6724
	R_1	10657	7173	10660	7170	10673	7155	10677	7151
$^6F_{\frac{5}{2}}$	R_2	10640	7190	10642	7188	10655	7173	10661	7167
	R_3	10631	7199	10634	7196	10647	7181	10652	7176
	Q_1	9883	7947	9888	7942	9901	7927	9904	7924
	Q_2	9785	8045	9787	8043	9799	8029	9801	8027
$^6F_{\frac{7}{2}}$	Q_3	9764	8066	9769	8061	9781	8047	9784	8044
	Q_4	9754	8076	9758	8072	9770	8058	9778	8056

7.5 Fluorescence Lifetimes and Energy Transfer

7.5.1 The Fluorescent Transients

The $^4G_{\frac{5}{2}}$ fluorescence decay transients of the R and Q centres in La^{3+}, Ce^{3+}, Eu^{3+}, Gd^{3+} and Tb^{3+} codoped CaF_2 crystals has been recorded. The fluorescence lifetime was then determined by fitting the recorded luminescence decay curve to a single or double exponential function, as was appropriate.

As the concentrations used to study the cluster centres were around 0.2 mol %, it was often difficult to obtain decay curves that could be represented by single exponential functions. This is due to the overlap of Q and R centre transitions with those of other centres. Often, the laser was tuned down either side of the inhomogeneous profile of the absorption transition being excited. The measured exponentials for the Q centres are presented in Figures 7.42 - 7.46 whilst the R centre exponentials are presented in Figures 7.47 - 7.51 with the measured lifetimes for both centres presented in Table 7.12.

Table 7.12: 16K $^4G_{\frac{5}{2}}$ fluorescence lifetimes for the R and Q centres in CaF_2:0.15%La^{3+}:0.05%Sm^{3+}, CaF_2:0.15%Ce^{3+}:0.05%Sm^{3+}, CaF_2:0.15%Gd^{3+}:0.05%Sm^{3+} and CaF_2:0.15%Tb^{3+}:0.05%Sm^{3+}, and 16K $^5D_0$ lifetimes of the R and Q centres in CaF_2:0.15%Eu^{3+}:0.05%Sm^{3+}. All lifetimes are in milliseconds (±0.1) unless otherwise stated. The bracketed values given in the R,Q(Eu,Sm) cases are the R,Q(Eu,Eu) $^5D_0$ lifetimes measured by Hamers et. al. [104].

Centre	Multiplet	Lifetime
Q(La,Sm)	$^4G_{\frac{5}{2}}$	7.8
Q(Ce,Sm)	$^4G_{\frac{5}{2}}$	7.7
Q(Eu,Sm)	$^5D_0$	8.4 (10.1±0.1)
Q(Gd,Sm)	$^4G_{\frac{5}{2}}$	7.7
Q(Tb,Sm)	$^4G_{\frac{5}{2}}$	7.8±0.2
R(La,Sm)	$^4G_{\frac{5}{2}}$	7.3
R(Ce,Sm)	$^4G_{\frac{5}{2}}$	7.3
R(Eu,Sm)	$^5D_0$	10.5 (10.4±0.1)
R(Gd,Sm)	$^4G_{\frac{5}{2}}$	7.4
R(Tb,Sm)	$^4G_{\frac{5}{2}}$	7.5±0.2

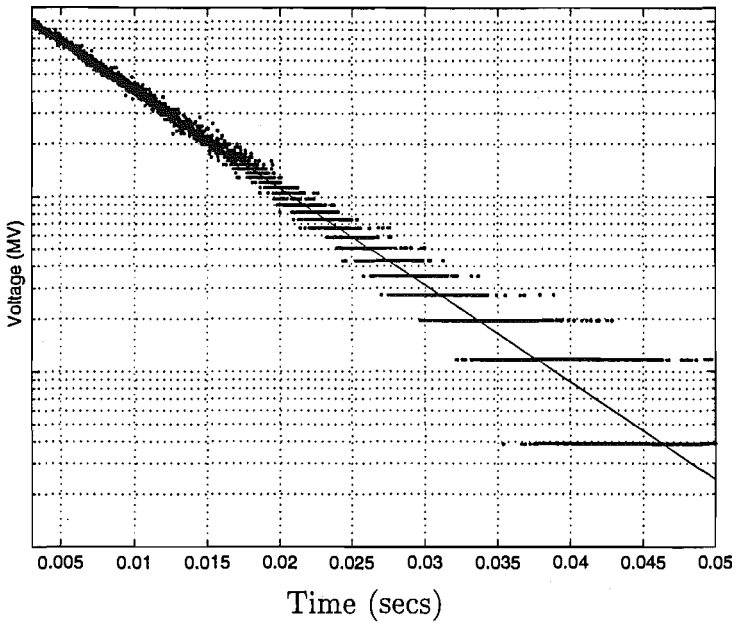

Figure 7.42: 16K $^4G_{\frac{5}{2}}$ fluorescence decay curve for the Q(La,Sm) centre

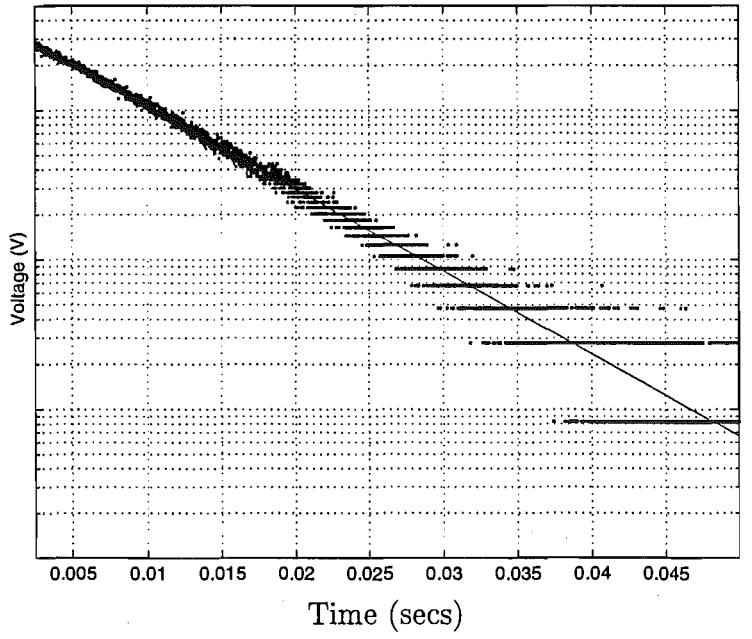

Figure 7.43: 16K $^4G_{\frac{5}{2}}$ fluorescence decay curve for the Q(Ce,Sm) centre

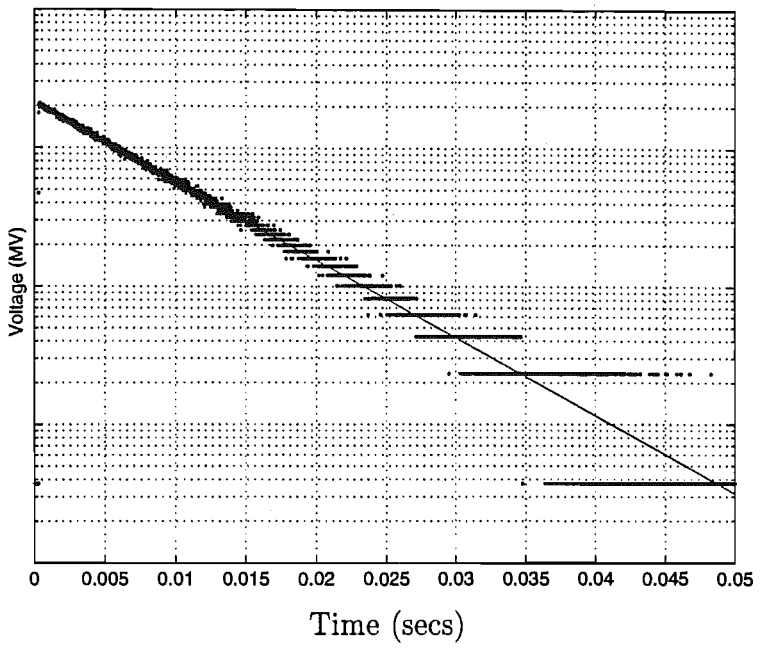

Figure 7.44: 16K $^4G_{\frac{5}{2}}$ fluorescence decay curve for the Q(Gd,Sm) centre

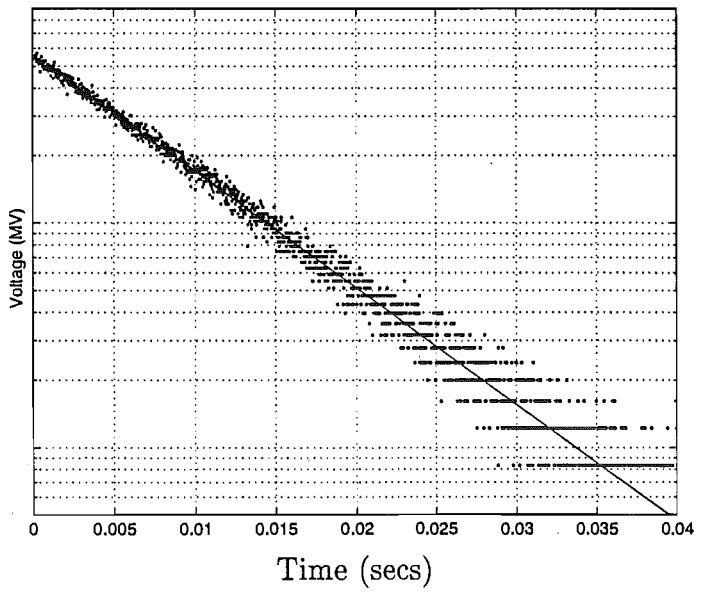

Figure 7.45: 16K $^5D_0$ fluorescence decay curve for the Q(Eu,Sm) centre

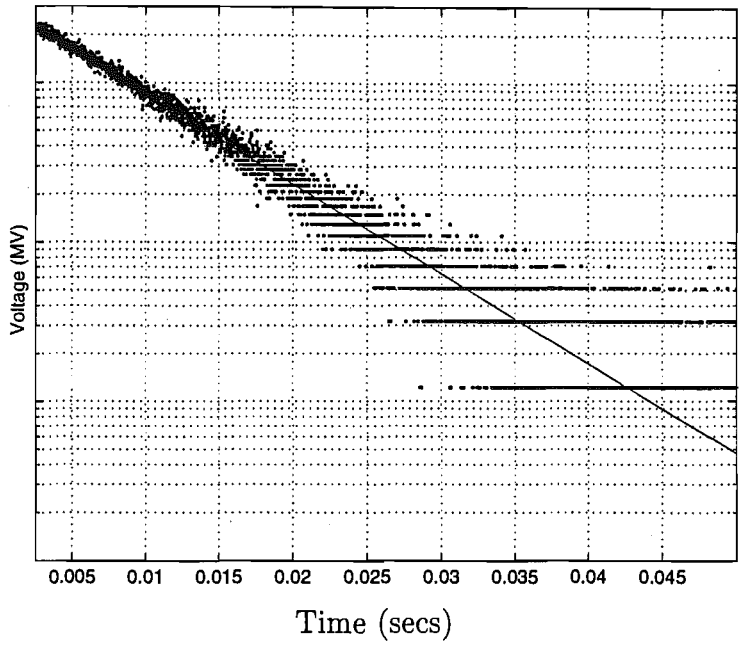

Figure 7.46: 16K $^4G_{\frac{5}{2}}$ fluorescence decay curve for the Q(Tb,Sm) centre

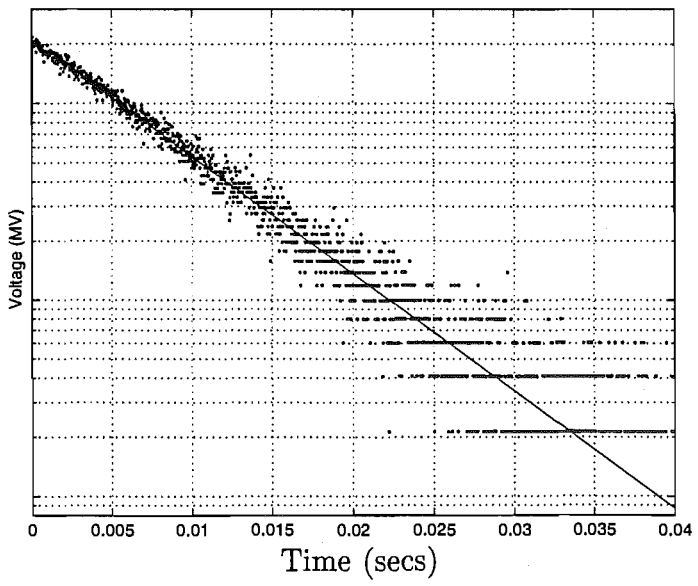

Figure 7.47: 16K $^4G_{\frac{5}{2}}$ fluorescence decay curve for the R(La,Sm) centre

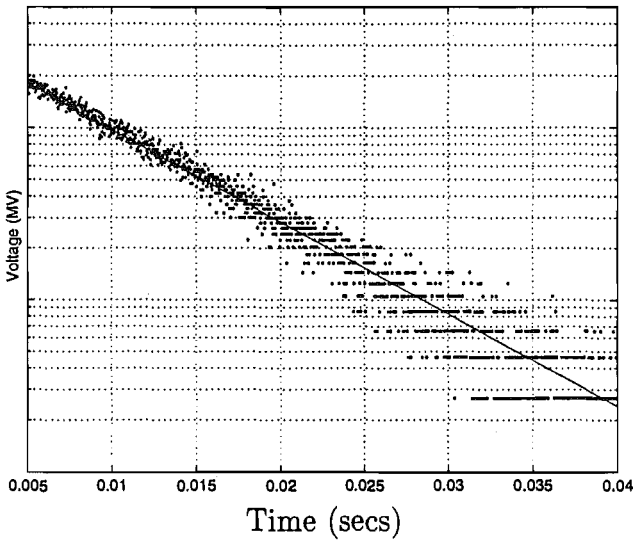

Figure 7.48: 16K $^4G_{\frac{5}{2}}$ fluorescence decay curve for the R(Ce,Sm) centre

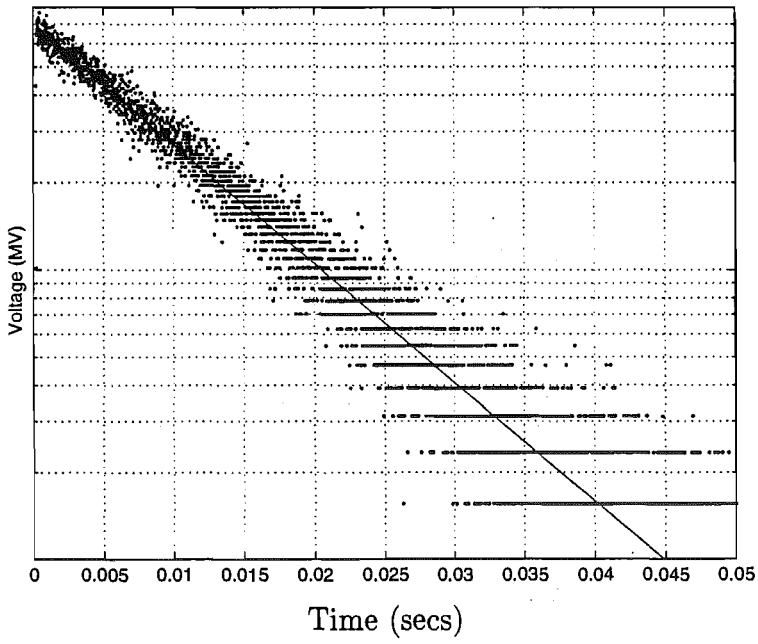

Figure 7.49: 16K $^4G_{\frac{5}{2}}$ fluorescence decay curve for the R(Eu,Sm) centre

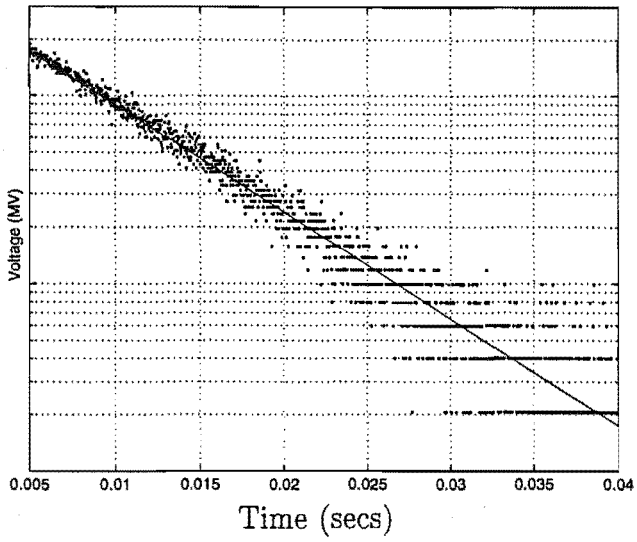

Figure 7.50: 16K $^4G_{\frac{5}{2}}$ fluorescence decay curve for the R(Gd,Sm) centre

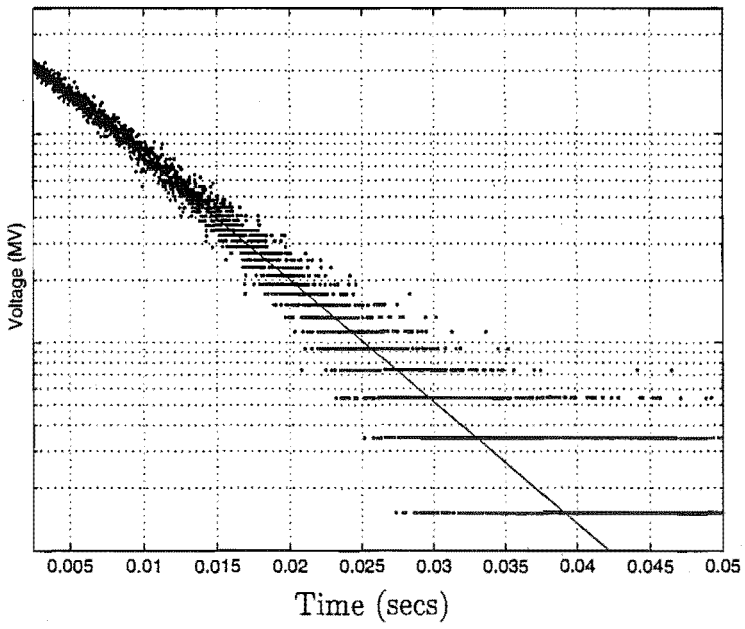

Figure 7.51: 16K $^4G_{\frac{5}{2}}$ fluorescence decay curve for the R(Tb,Sm) centre

The measured Eu^{3+} $^5D_0$ lifetimes for the R and Q centres deserve discussion. For the R(Eu,Sm) centre, the $^5D_0$ lifetime is 10.5 ms in reasonable agreement with the value measured by Hamers et. al. [104] for the equivalent CaF_2:Eu^{3+} R(Eu,Eu) centre of 10.4 ms. However, the Q(Eu,Sm) centre value, of 8.4 ms, is significantly different from the Q(Eu,Eu) centre value (of 10.1 ms). An explanation for this difference, is that the interionic separation of the RE^{3+} ions is less for the Q centres than for the R centres. This could lead to additional transfer mechanisms for the heterogeneous Sm^{3+}-Eu^{3+} centres. An example of such a mechanism is de-excitation of the $^5D_0$ multiplet through excitation of the Sm^{3+} $^6F_{\frac{11}{2}}$ multiplet at 10500 cm^{-1}. The Eu^{3+} ion could then de-excite to the $^7F_6$ multiplet at 5100 cm^{-1}. Such a process would require the emission of lattice phonons to conserve energy.

Additional evidence supporting a smaller interionic separation for the ions of the Q centre is provided by the risetimes observed for the Q(Eu,Sm) and R(Eu,Sm) centre, $^5D_0$ transients. The risetimes are 3.4μs for the Q(Eu,Sm) centre and 6.5μs for the R(Eu,Sm) centre. These are inversely proportional to the $^4G_{\frac{5}{2}} \rightarrow ^5D_0$ energy transfer rates. In addition, they are the only contribution to the $^4G_{\frac{5}{2}}$ lifetime. These energy transfer rates are, for the Q(Eu,Sm) centre W_{ET}^{16K}=294 ms^{-1} and for the R(Eu,Sm) centre W_{ET}^{16K}=154 ms^{-1}. This Q(Eu,Sm) centre value is nearly twice that of the R(Eu,Sm) centre. This indicates that the overlap of the Sm^{3+} and Eu^{3+} wavefunctions is much greater for the Q(Eu,Sm) centre due to the closer proximity of the Sm^{3+} and Eu^{3+} ions in that centre.

7.5.2 Temperature Dependence of Q(Eu,Sm) and R(Eu,Sm) Centre Energy Transfer

The Q(Eu,Sm) and R(Eu,Sm) centres in CaF_2:Eu^{3+}:Sm^{3+}, exhibit extremely efficient energy transfer between the heterogeneous ions in the cluster. This is evidenced by the lack of Sm^{3+} fluorescence from the $^4G_{\frac{5}{2}}$ level being excited and the intense Eu^{3+} emission. The process is mediated by lattice phonons. The high efficiency is perhaps surprising, since the direct energy gap between the $^4G_{\frac{5}{2}}(Sm^{3+})$ and $^5D_0(Eu^{3+})$ levels, is greater than the lattice phonon cutoff energy for the CaF_2 host crystal. Further, electron-phonon coupling is expected to be weaker for rare earth ions in the middle of the 4f-series [147] (1995) [148] (1997). Thus, the high transfer efficiency reflects a large site-site coupling of the Eu^{3+} and Sm^{3+} ions. This is largely attributable to the proximity of the rare earth ions in the cluster.

The measurement of energy transfer rates is, in general, a difficult experimental problem necessitating, in some cases, a knowledge of the non-radiative quantum ef-

ficiency. The measured fluorescence decay rate of an excited state W_T, is determined by the sum of the radiative rate W_R, the multiphonon relaxation rate W_{MPH} and the rate of energy transfer W_{ET}

$$\frac{1}{\tau_T} = W_T = W_R + W_{MPH} + W_{ET} \tag{7.1}$$

For the $^4G_{\frac{5}{2}}$ multiplet of the Q(Eu,Sm) and R(Eu,Sm) centres, the lack of Sm^{3+} emission indicates the W_R rate is negligible and the large $^4G_{\frac{5}{2}}$-$^6F_{\frac{11}{2}}$ gap eliminates the W_{MPH} contribution to the total lifetime. Thus, we can measure the energy transfer directly, as a risetime on the recorded $^5D_0$ decay profile. The recorded decay transients are shown in Figures 7.52 and 7.53.

Energy transfer between the $^4G_{\frac{5}{2}}$ multiplet of Sm^{3+} and the $^5D_0$ multiplet of Eu^{3+}, has been observed previously by Reisfeld and Boehm [149] in phosphate glass. In that study, analysis of the energy transfer process was complicated by the necessity to model the radial dependence of the transfer process. This is a consequence of the statistical distribution of the Sm^{3+} and Eu^{3+} ions in the host material. For the Q(Eu,Sm) and R(Eu,Sm) dimer centres, there is no necessity to model the radial dependence of acceptor ions as the donor-acceptor interionic distance is fixed.

The temperature dependence of phonon assisted energy transfer up to several hundred degrees Kelvin, is dominated by the thermal population of the lattice phonon modes. A general form of the temperature dependence of the multiphonon assisted energy transfer rate can be written as

$$W_{ET}(T) = W_{if}^{ET,0}(n+1)^p \tag{7.2}$$

where n is the occupation number of the phonon mode involved, p is the order of the process ($=\frac{\Delta E}{\hbar\omega}$, where ΔE is the energy mismatch to be bridged by the phonons) and $W_{if}^{ET,0}$ is the spontaneous multiphonon emission rate at 0K. The i and f notation designates the upper level as i, and the lower level as f, Replacing the occupation number of the phonon mode, by its Bose-Einstein average [150]

$$n = [exp(\frac{\hbar\omega}{kT}) - 1]^{-1} \tag{7.3}$$

we have the temperature dependent multiphonon assisted energy transfer rate for a single frequency p-phonon process

$$W^{ET}(T) = W_{if}^{ET,0}\left(\frac{exp(\frac{\hbar\omega}{kT})}{exp(\frac{\hbar\omega}{kT}) - 1}\right)^p \tag{7.4}$$

It has been pointed out by Riseberg and Weber [150], that the critical feature is

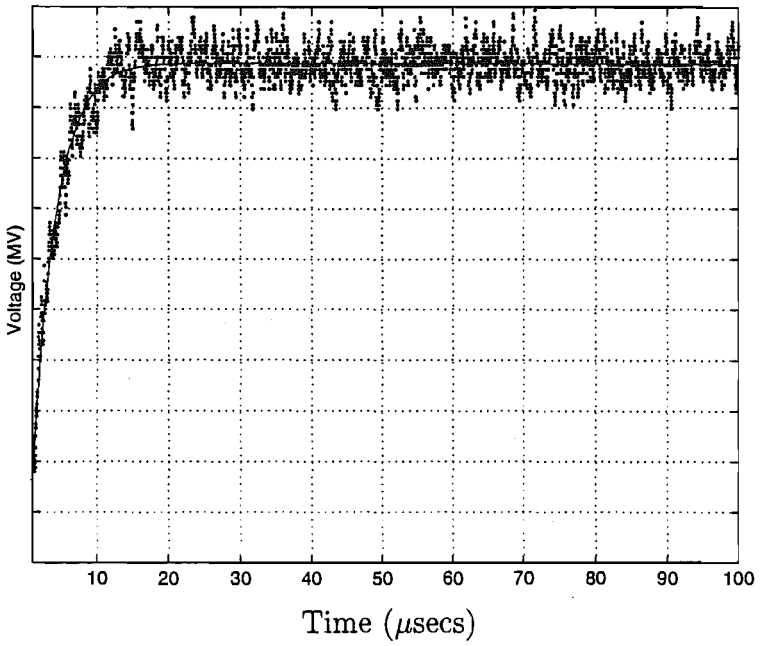

Figure 7.52: 16K energy transfer exponential for the $^4G_{\frac{5}{2}} \rightarrow {}^5D_0$ process in the Q(Eu,Sm) centre

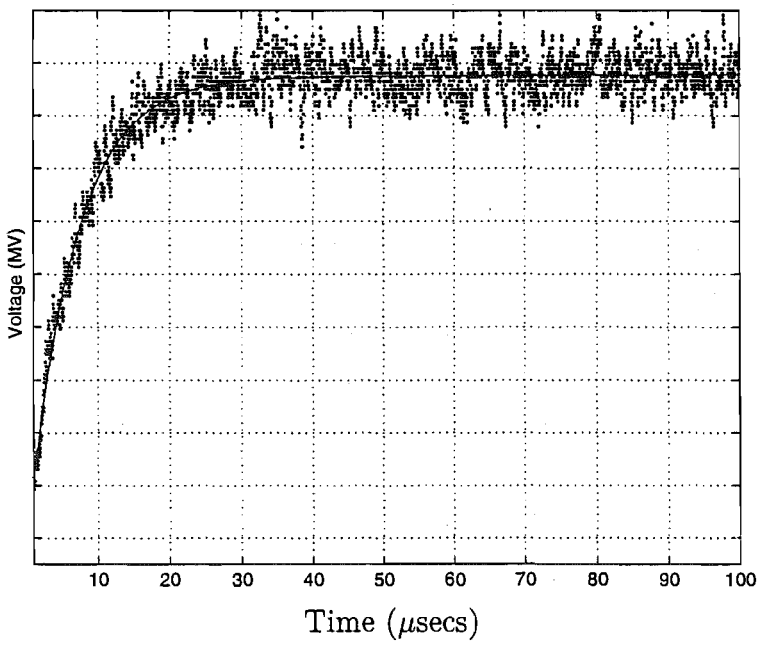

Figure 7.53: 16K energy transfer exponential for the $^4G_{\frac{5}{2}} \rightarrow {}^5D_0$ process in the R(Eu,Sm) centre

the order of the process rather than the precise phonon energy distribution which governs the temperature dependence. It should be realised, that eqn 7.4 assumes a simple process involving transfer between two discrete crystal field levels, whereas each multiplet generally comprises several levels. If we designate the levels of the upper multiplet by i, and the levels of the lower multiplet by f, then the total transfer rate from one of the upper levels is $\Sigma_f W_{if}$. As the levels of the multiplet are in thermal equilibrium, the combined rate is a Boltzmann average from the separate levels

$$W_{ET} = \frac{\Sigma_i \Sigma_f g_i W_{if}(T) exp(-\frac{\Delta_i}{kT})}{\Sigma_i g_i exp(-\frac{\Delta_i}{kT})} \tag{7.5}$$

where W_{if} is an individual decay rate from upper multiplet level i to lower multiplet level f, g_i is the degeneracy and Δ_i is the energy separation of the ith level from the bottom level of the upper multiplet.

The measured temperature dependence, of the energy transfer rate, is plotted for the Q(Eu,Sm) and R(Eu,Sm) centres in Figure 7.54. The general features of the data can be explained as follows. The flat section, to 50 K, is due to the spontaneous emission of phonons from the lowest level of $^4G_{\frac{5}{2}}$. The thermal depopulation of this lowest level, is responsible for the dip in the transfer rate (or lengthening of the lifetime), in the 50-150K region. Beyond 150 K, additional lattice phonon modes become thermally populated. This leads to stimulated emission of phonons from all of the $^4G_{\frac{5}{2}}$ levels. This gives rise to the steep increase in energy transfer rate at higher temperatures.

There are three crystal field levels (19813, 17887 and 17960 cm^{-1}) of the $^4G_{\frac{5}{2}}$ multiplet of Sm^{3+} for the Q(Eu,Sm) centre and five (17829, 17891, and 17908, 17922 and 17942 cm^{-1}) for the R(Eu,Sm) centre. Using eqn 7.6, the thermal population of the excited $^4G_{\frac{5}{2}}$ states are accounted for. We adopt the approximation of a non-vanishing W^0_{ET} only for the lowest Sm^{3+} crystal field level.

For the Q(Eu,Sm) centre, the total $^4G_{\frac{5}{2}}$-$^5D_0$ energy gap to be bridged is 554 cm^{-1}. The measured 16K value of the transfer rate (=294 ms^{-1}) was used as an approximation to $W^{ET,0}$. This appears justified by the flat nature of the data below 20K. Fourth, third and second order phonon process were calculated. The particular phonon frequency used, was chosen to fulfil energy conservation. It can be seen from Figure 7.54, that a third order process approximates the temperature dependence most adequately. The agreement between theory and experiment can be seen to be reasonable. However, at higher temperatures the predicted increase in the energy transfer rate appears too low.

For the R(Eu,Sm) center, the total $^4G_{\frac{5}{2}}$-$^5D_0$ energy gap to be bridged is 568 cm^{-1}. Again, $W^{ET,0}$ has been set to the 16K experimentally determined value of 154 ms^{-1}. Figure 7.54 shows the comparision between the predicted and experimental temperature dependences. For the R(Eu,Sm) centre, higher order processes were tried as the energy transfer rate had a greater dependence upon temperature. A fourth order process gives the best agreement. However the higher temperature experimental energy transfer rate is not at all well accounted for.

Overall, it appears that the single frequency model gives quite acceptable agreement at low temperatures (10-150K). It is clear, that the lattice phonons do not act to minimise the order of the process as was speculated in early studies of multiphonon decay and phonon assisted energy transfer [150]. This observation has been made previously, by Miller and Wright [151] (1979) and Weber [152] (1973).

Clearly further work is required to fully account for the temperature dependence of the energy transfer rate. Tissue and Wright [119] (1989) analysed the temperature dependence of the energy transfer rate between dimerised Er^{3+} ions in SrF_2:Er^{3+} in terms of resonant, two-phonon (Orbach) processes. However, these processes could not explain the large enhancements in the energy transfer rate as a function of an applied magnetic field. It would be interesting to repeat these experiments for the systems under study here. This was not experimentally possible in this work as the magnets available did not have sample temperature control, independent of the solenoid.

A further complication arises in that it is not clear that lattice phonon modes are responsible for mediating the energy transfer. It is possible that pseudo-localised modes of the rare earth ions are more important.

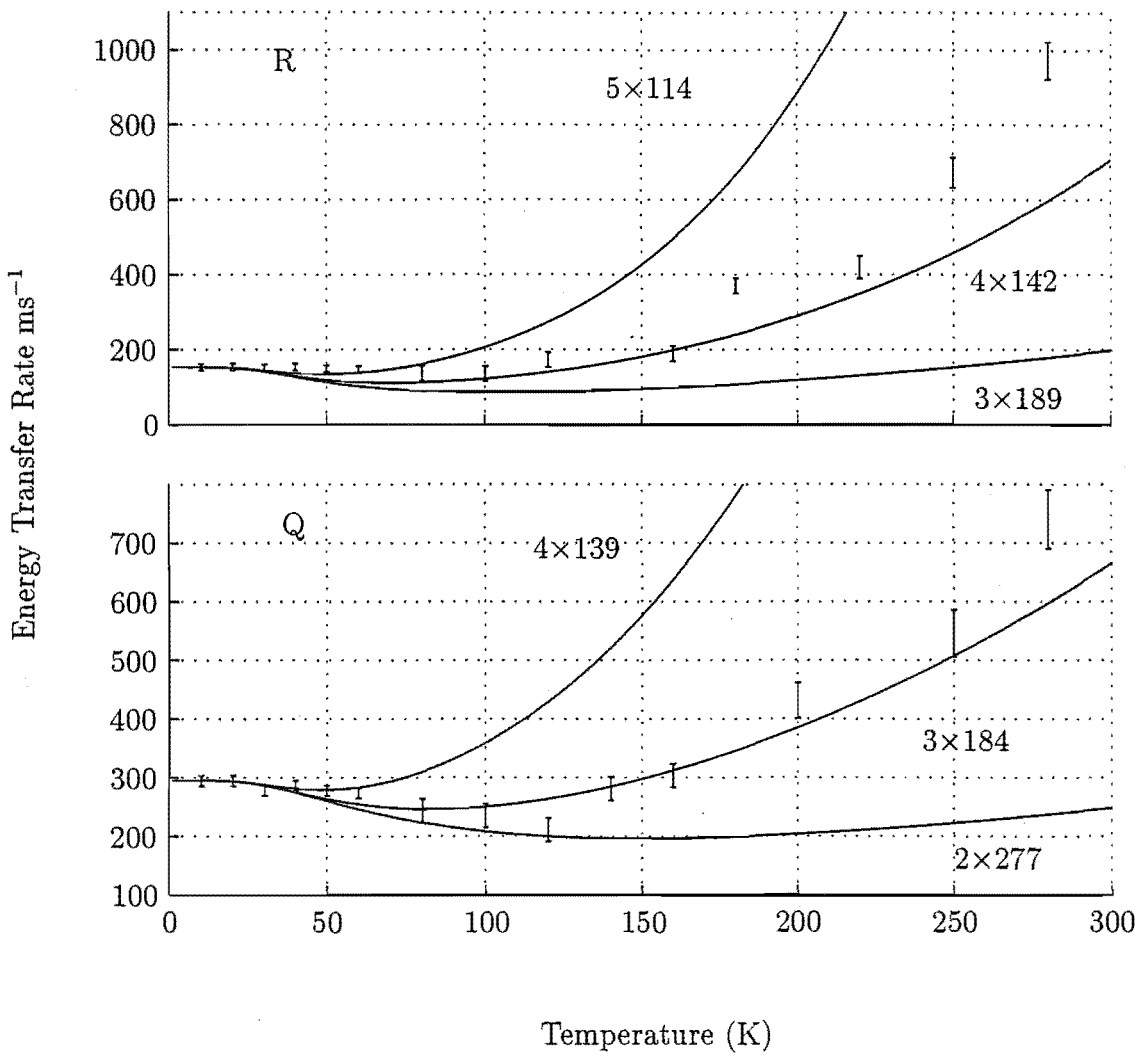

Figure 7.54: Experimental and calculated temperature dependence of the $^4G_{\frac{5}{2}}$-$^5D_0$ energy transfer rates for the Q(Eu,Sm) and R(Eu,Sm) centres in CaF_2:0.15%Eu^{3+}:0.05%Sm^{3+}. The solid lines are the calculated dependences.

Chapter 8

Zeeman Infrared Spectroscopy for Sm^{3+} and Eu^{3+} Doped into Alkaline Earth Fluoride Crystals

Infrared absorption transitions are rarely studied in spectroscopic analyses of RE^{3+} doped solids due to their inaccessibilty with commonly employed photomultipliers. However, these transitions are often stronger than those observed optically as transitions between levels of the same $^{(2S+1)}L$ term will be spin-allowed. The Eu^{3+} and Sm^{3+} ions give rise to a plethora of electronic structure accessible with the Digilab FTIR spectrometer used in this study. This is because the respective $^7F_0 \rightarrow {}^7F_{2,3,4,5,6}$ and $^6H_{\frac{5}{2}} \rightarrow {}^6H_{\frac{7}{2},\frac{9}{2},\frac{11}{2},\frac{13}{2},\frac{15}{2}}$ and $^6F_{\frac{1}{2},\frac{3}{2},\frac{5}{2},\frac{7}{2},\frac{9}{2},\frac{11}{2}}$ transitions occur in the 900 - 11000 cm^{-1} region .

In all crystals studied in this work, the absorption transitions observed are assigned by comparision with the corresponding laser selective excitation studies. This provides a check on the electronic states inferred from laser excited fluorescence. The influence of a magnetic field upon the sharper absorption lines has also been recorded and analysed. For transitions of the C_{4v} symmetry A centre in CaF_2 and SrF_2 crystals doped with Sm^{3+}, this is particularly interesting as no well defined polarisation ratios could be obtained from the laser selective excitation studies of chapter 5. A consequence of this has been that no experimental data was available to assign irrep symmetry labels to the electronic energy levels. Instead, this been done by comparision with preliminary crystal field calculations. Analysis of the Zeeman effect for those levels goes some way to remedy this, as the experimentally measured splittings may be compared with those expected from the crystal field calculations.

8.1 CaF_2:Sm^{3+}

8.1.1 Infrared Spectroscopy

The infrared absorption spectrum for a 26.5 mm thick CaF_2:0.05%Sm^{3+} crystal has been recorded. For these experiments the crystal was cooled to a temperature of 10K. Spectra for the individual multiplets of the ^6H and ^6F terms are shown in Figures 8.1 through to 8.5. The spectra are complicated by the co-existence of preferential cluster centres. The transitions associated with these centres are of comparable intensity to the A centre transitions, at concentrations of 0.05 molar %.

For transitions from the $^6H_{\frac{5}{2}}$ ground multiplet to the $^6H_{\frac{7}{2}}$, $^6H_{\frac{9}{2}}$ and $^6H_{\frac{11}{2}}$ multiplets, a globar source, KBr beamsplitter and mercury cadmium telluride detector combination has been used in the Digilab FTIR spectrometer. These transitions occur in the 900-4000 cm^{-1} region. Features of the spectra to the particular multiplets are discussed in turn below.

Transitions to $^6H_{\frac{7}{2}}$ fall just above the multiphonon edge of the CaF_2 host crystal. They are often detected with low transmission intensities for crystal lengths above 1 cm. Thinner crystals may be used to optimise the transmission intensities whilst maintaining good absorption strengths. Absorption due to both grease contaminants on the crystal faces and residual atmospheric moisture in the spectrometer, are observed amongst the absorption transitions to the $^6H_{\frac{7}{2}}$ multiplet. The broad absorption feature associated with grease is at a frequency of 1260.2 cm^{-1}. The spectrum is given in Figure 8.1.

For transitions to the $^6H_{\frac{9}{2}}$ multiplet, better signal strengths are obtained. Absorption transitions corresponding to the A, Q, R and near cubic O centres are observed. The absorption frequencies, linewidths and relative intensities are given in Tables 8.1, 8.2 and 8.3. The assignment of one transition at 2161.9 cm^{-1} as originating from the O centre is tentative but the level energy is consistent with that assigned from laser selective excitation. In Figure 8.3, the 2160 - 2200 cm^{-1} absorption is enlarged. This reveals a 0.3 cm^{-1} splitting of the infrared absorption transitions of the R centre. These splittings have their origin in exchange interactions between the two Sm^{3+} ions that comprise the cluster. Such splittings have been observed in $CsCdBr_3$:RE^{3+} (where preferential dimer formation occurs) by Cockcroft et. al. [153] (1989) and Mujaji et. al. [154] (1992), [155] (1993).

Transitions to the $^6H_{\frac{11}{2}}$ multiplet overlap with a strong, broad atmospheric absorption band. Only one transition to each of the A, R and Q centres is observed.

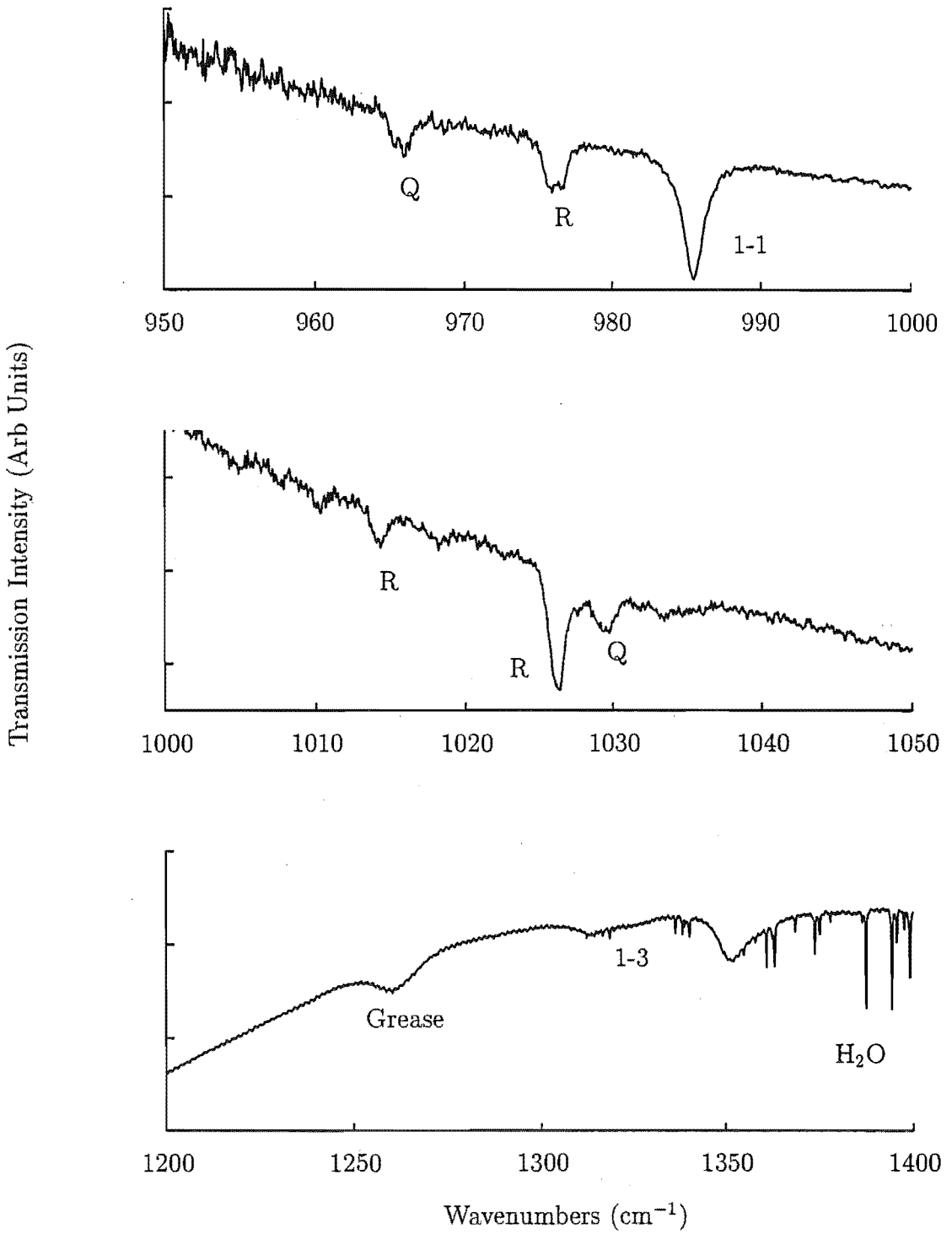

Figure 8.1: Infrared absorption transitions to the $^6H_{\frac{7}{2}}$ multiplet in CaF_2:0.05%Sm^{3+}. Spectra were recorded at 10K. The A centre transitions are labelled by their arbitrary numerical labels.

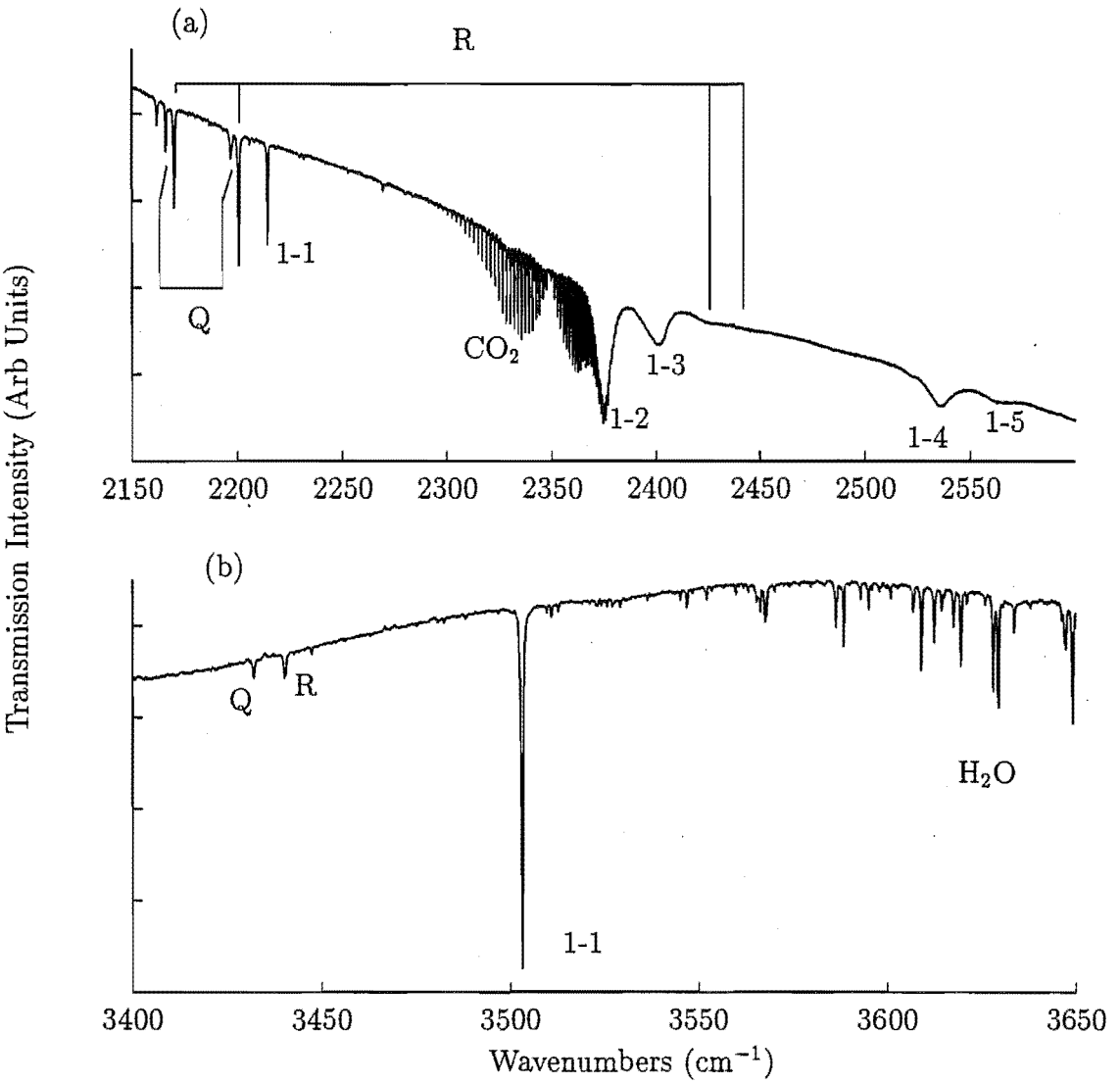

Figure 8.2: Infrared absorption transitions to the (a) $^6H_{\frac{9}{2}}$ and (b) $^6H_{\frac{11}{2}}$ multiplets, for CaF_2:0.05%Sm^{3+}. Spectra were recorded at 10K. The A centre transitions are labelled by their arbitrary numerical labels.

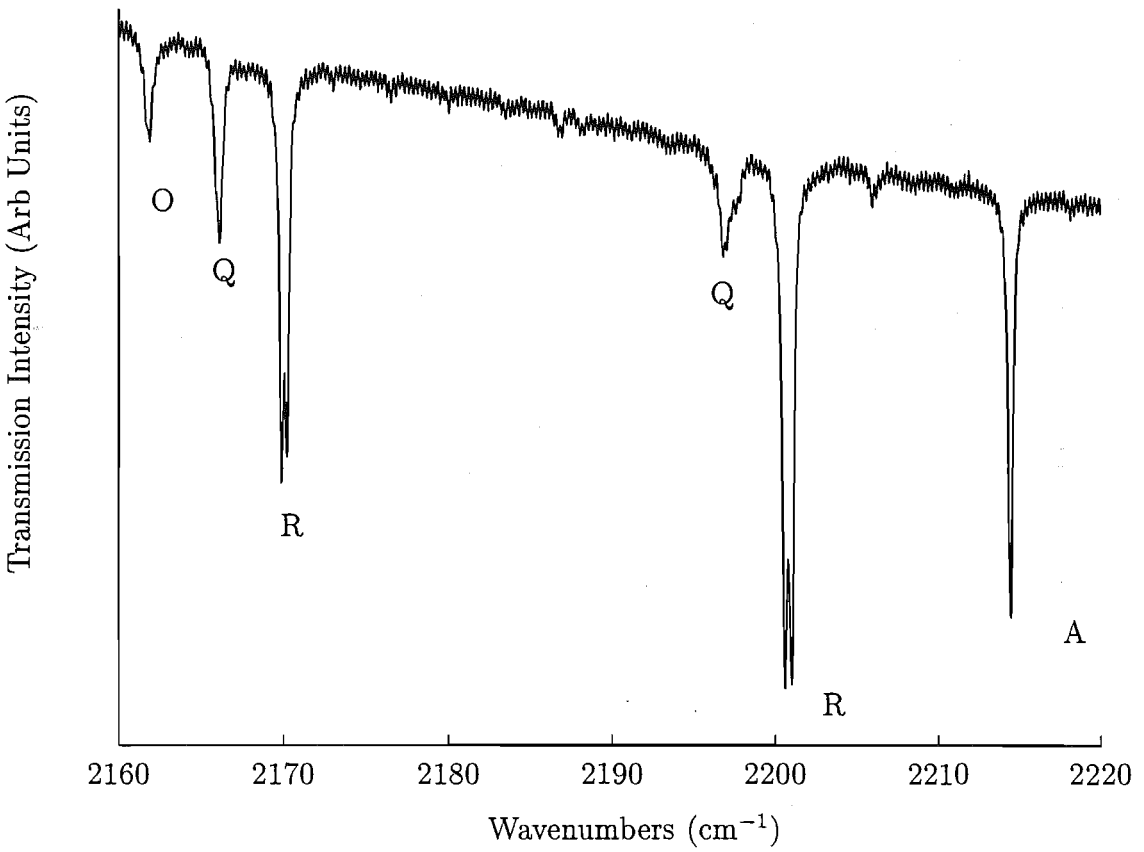

Figure 8.3: Infrared absorption transitions to the $^6H_{\frac{9}{2}}$ multiplet for CaF_2:0.05%Sm^{3+} on a enlarged scale showing R centre pair splittings.

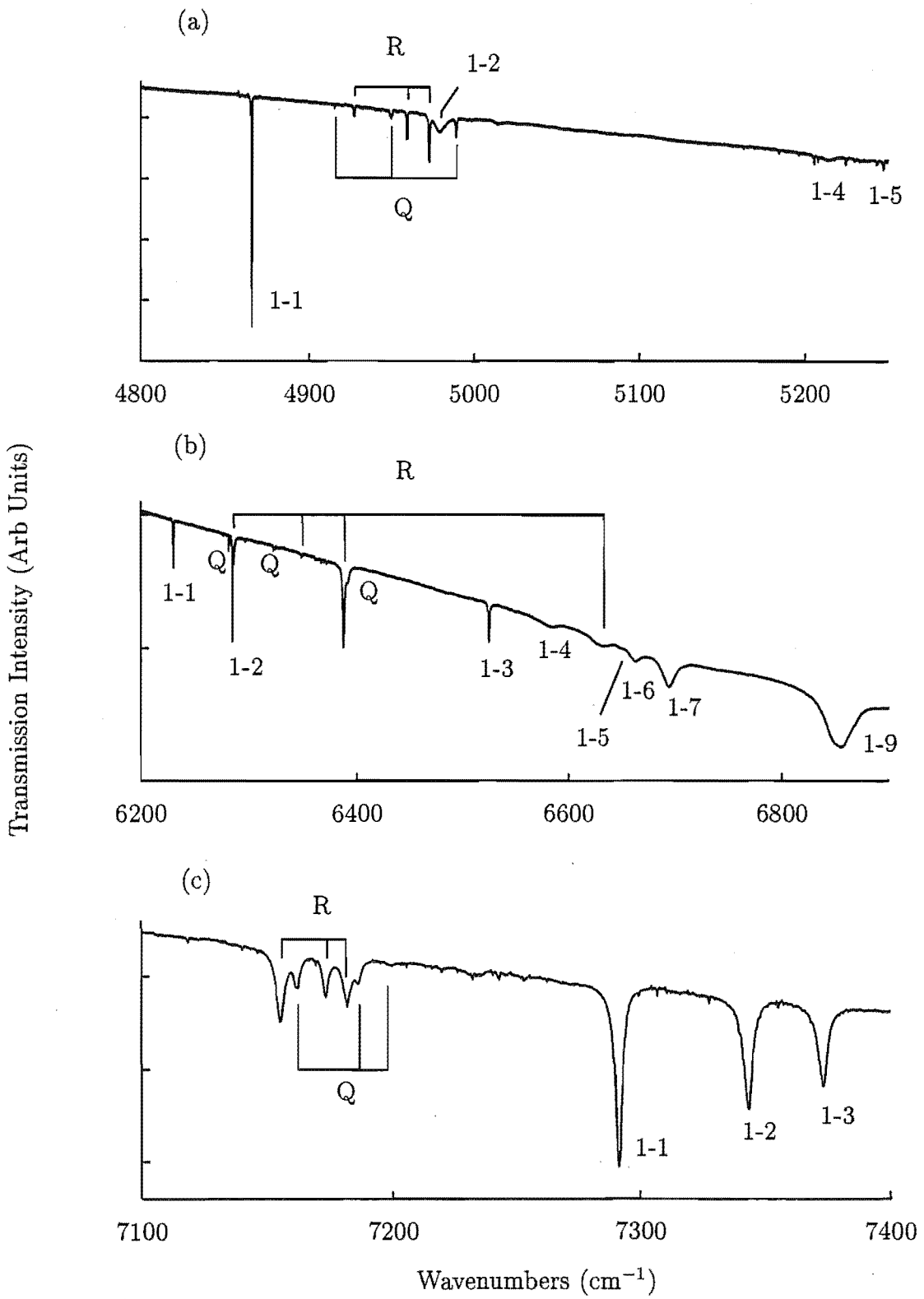

Figure 8.4: Infrared absorption transitions to the (a) $^6H_{\frac{13}{2}}$, (b) $^6H_{\frac{15}{2}}$, $^6F_{\frac{1}{2}}$ and $^6F_{\frac{3}{2}}$ and (c) $^6F_{\frac{5}{2}}$ multiplets for CaF_2:0.05%Sm^{3+}. Spectra were recorded at 10K. The A centre transitions are labelled by their arbitrary numerical labels.

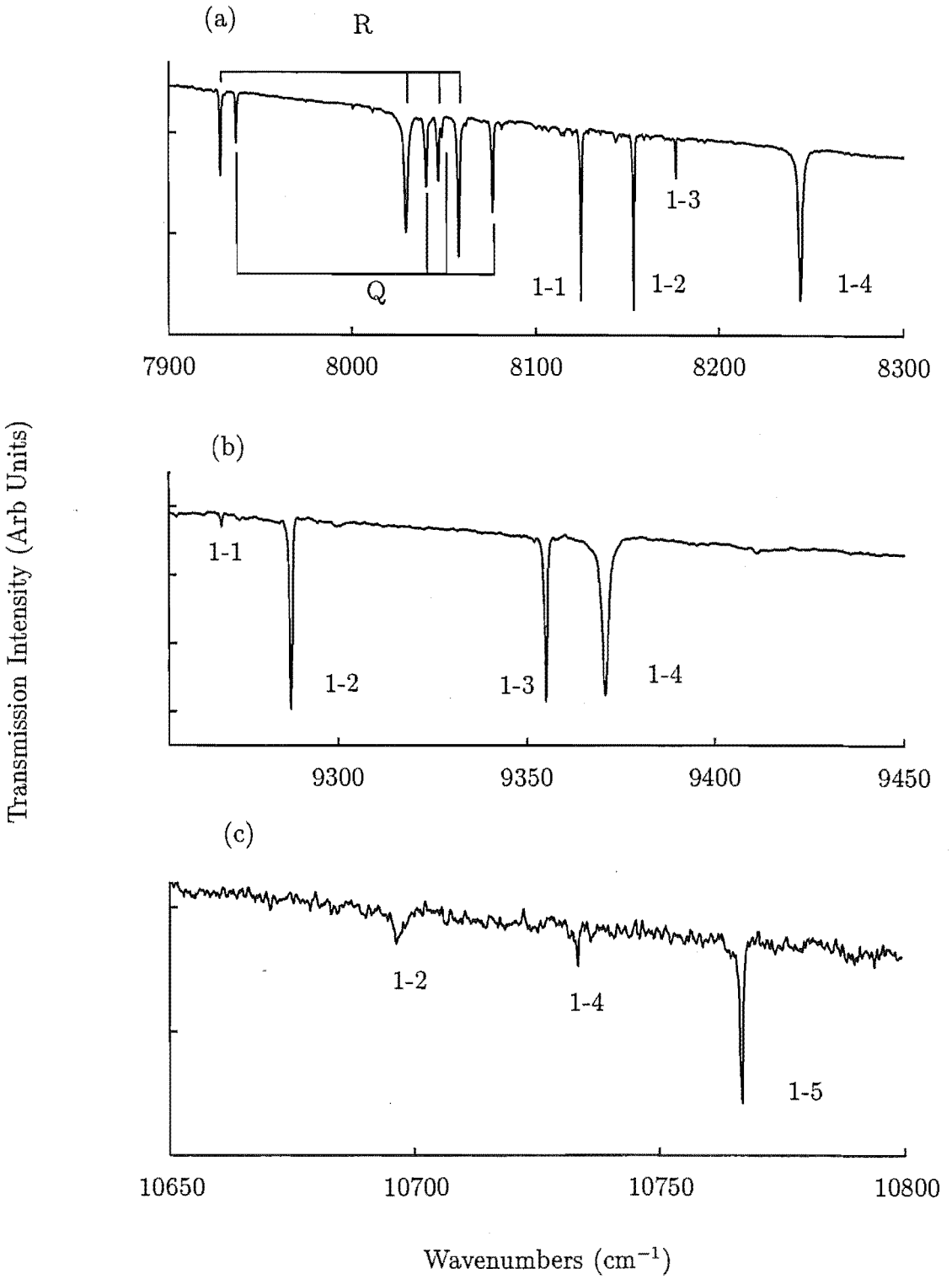

Figure 8.5: Infrared absorption transitions to the (a) $^6F_{\frac{7}{2}}$, (b) $^6F_{\frac{9}{2}}$ and (c) $^6F_{\frac{11}{2}}$ multiplets for CaF_2:0.05%Sm^{3+}. Spectra were measured at 10K. The A centre transitions are labelled by their arbitrary numerical labels.

Transitions to other crystal field levels of the $^6H_{\frac{11}{2}}$ multiplet were searched for, however none could be found. The unobserved features are difficult to identify as they are located amidst the region in which the atmospheric absorption is strongest.

For recording the absorption transitions to the $^6H_{\frac{13}{2}}$ multiplet a quartz beamsplitter, quartz-halogen souce and indium antimonide detector combination is employed in the Digilab FTIR spectrometer. This gives extended range over the 2800 - 11000 cm^{-1} region. Transitions to the $^6H_{\frac{13}{2}}$ multiplet, also overlap an atmospheric absorption band. In this case, vigorous flushing of the spectrometer with dry nitrogen gas can eliminate the problem, as the absorption due to water vapour is weaker. This shown in Figure 8.4(a). All but one of the A centre transitions to the $^6H_{\frac{15}{2}}$, $^6F_{\frac{1}{2}}$ and $^6F_{\frac{3}{2}}$ multiplets are observed. Significantly fewer of the R and Q transitions can be identified. This can, in some part, be attributed to the slightly stronger A centre transitions obscuring them. In Figure 8.4(c) transitions to the $^6F_{\frac{5}{2}}$ multiplet are shown.

Transitions to the $^6F_{\frac{7}{2}}$ multiplet are very strong. Here, the cluster centre transitions occur at lower frequencies than the A centre transitions and this makes the spectrum simpler to interpret. For each of the centres, transitions to all levels assigned from laser excited fluorescence are observed. No intensely absorbing features remain unassigned.

Absorption transitions to the $^6F_{\frac{9}{2}}$ and $^7F_{\frac{11}{2}}$ multiplets are observed in the 9000 - 9450 cm^{-1} and 10500 - 10800 cm^{-1} regions respectively. Laser excited fluorescence transitions to these levels have not been observed. This is because the photomultiplier employed cannot reach significantly further into the infrared than 9000 cm^{-1} (1.1 μm). We attempt assignment of the A centre levels only, as these can be compared against the predictions of the crystal field analysis presented in chapter 5. The observed transitions can also be compared with the analogous spectra for SrF_2:0.05%Sm^{3+}. This gives a good contrast as few centres (other than the A centre) are present in absorption for SrF_2:0.05%Sm^{3+}. Four transitions have been observed to the $^6F_{\frac{9}{2}}$ multiplet which are assigned as belonging to the A centre. The frequencies of these transitions are 9269.9, 9288.4, 9356.4 and 9372.3 cm^{-1}. They are assigned as transitions to the $P_1\gamma_6$, $P_2\gamma_6$, $P_3\gamma_7$ and $P_4\gamma_6$ states respectively. For the $^6F_{\frac{11}{2}}$ multiplet, transitions to only three of the expected six levels are observed. The frequencies of these transitions are 10396.6, 10733.6 and 10767.2 cm^{-1}. The $^6F_{\frac{11}{2}}$ states are assigned as $O_2\gamma_6$, $O_4\gamma_6$ and $O_5\gamma_6$ from comparision with the crystal field analysis.

Table 8.1: Energy levels (in vacuum cm^{-1}, ±0.2), intensities (relative to the strongest line in the spectrum (=100.00), ±0.50) and linewidths (in cm^{-1}, ±0.2) as measured in absorption to A centre crystal field levels of the ^6H and ^6F terms in CaF_2:0.05%Sm^{3+}

Multiplet	Transition	Energy	Intensity	Linewidth
	$Z_1\gamma_6 \rightarrow Y_1\gamma_6$	985.6	36.7	1.3
$^6H_{\frac{7}{2}}$	$\rightarrow Y_3\gamma_7$	1324±3	5.1±1.0	6.5±0.3
	$\rightarrow X_1\gamma_6$	2214.8	0.6	0.2
	$\rightarrow X_2\gamma_6$	2375.6	15.9	5.0
$^6H_{\frac{9}{2}}$	$\rightarrow X_3\gamma_7$	2402.0	8.9	8.0
	$\rightarrow X_4\gamma_7$	2537.2	7.1	9.1
	$\rightarrow X_5\gamma_6$	2563.2	3.5	13.6
$^6H_{\frac{11}{2}}$	$\rightarrow W_1\gamma_6$	3503.6	26.0	0.3
	$\rightarrow V_1\gamma_6$	4865.9	7.0	0.3
	$\rightarrow V_2\gamma_7$	4979.6	8.3	5.3
$^6H_{\frac{13}{2}}$	$\rightarrow V_4\gamma_7$	5215.3	3.1	6.0
	$\rightarrow V_5\gamma_6$	5237±1	1.3	6.5±0.4
	$\rightarrow S_1\gamma_7$	6230.2	0.6	0.5
	$\rightarrow S_2\gamma_6$	6285.0	4.0	0.4
	$\rightarrow S_3\gamma_6$	6526.4	4.0	1.1
	$\rightarrow S_4\gamma_6$	6587.1	4.0	7.4
$^6H_{\frac{15}{2}}$, $^6F_{\frac{1}{2}}$	$\rightarrow S_5\gamma_6$	6652.2	2.5	5.3±0.4
and $^6F_{\frac{3}{2}}$	$\rightarrow S_6\gamma_7$	6664.15	9.0	7.4
	$\rightarrow S_7\gamma_6$	6695.9	23.6	7.9
	$\rightarrow S_9\gamma_7$	6857.4	81.5	13.8±0.2
	$\rightarrow R_1\gamma_7$	7292.4	67.6	2.5
$^6F_{\frac{5}{2}}$	$\rightarrow R_2\gamma_6$	7344.7	37.8	2.6
	$\rightarrow R_3\gamma_7$	7374.5	29.4	2.8
	$\rightarrow Q_1\gamma_7$	8125.5	33.5	0.5
	$\rightarrow Q_2\gamma_6$	8154.7	47.7	0.6
$^6F_{\frac{7}{2}}$	$\rightarrow Q_3\gamma_7$	8178.0	3.0	0.3
	$\rightarrow Q_4\gamma_6$	8245.5	100.0	1.6
	$\rightarrow P_1\gamma_6$	9269.9	0.9	0.5
	$\rightarrow P_2\gamma_6$	9288.4	31.3	0.6
$^6F_{\frac{9}{2}}$	$\rightarrow P_3\gamma_6$	9356.4	34.7	0.8
	$\rightarrow P_4\gamma_7$	9372.3	51.4	1.3
	$\rightarrow O_2\gamma_6$	10696.6	3.9	1.6
$^6F_{\frac{11}{2}}$	$\rightarrow O_4\gamma_6$	10733.7	1.7	0.5
	$\rightarrow O_5\gamma_6$	10767.4	10.2	0.6

Table 8.2: Energy levels (in vacuum cm^{-1}, ± 0.2), intensities (relative to the strongest line in the spectrum (=100.00), ± 0.50) and linewidths (in cm^{-1}, ± 0.2) as measured in absorption to R centre crystal field levels of the ^6H and ^6F terms in CaF_2:0.05%Sm^{3+}

Multiplet	Transition	Energy	Intensity	Linewidth
	$Z_1 \rightarrow Y_1$	975.9	28.9	1.5
$^6H_{\frac{7}{2}}$	$\rightarrow Y_2$	1014.4	3.0	0.9
	$\rightarrow Y_3$	1026.3	11.0	0.8
	$\rightarrow X_1$	2170.6	5.4	0.6
	$\rightarrow X_2$	2200.9	9.0	0.6
$^6H_{\frac{9}{2}}$	$\rightarrow X_4$	2426±3	29±1	10.1±5
	$\rightarrow X_5$	2442±3	14±1	10.1±0.5
$^6H_{\frac{11}{2}}$	$\rightarrow W_1$	3440.8	1.8	0.6
	$\rightarrow V_1$	4927.5	3.2	1.7
$^6H_{\frac{13}{2}}$	$\rightarrow V_2$	4959.7	8.3	5.3
	$\rightarrow V_4$	4972.9	5.8	0.6
	$\rightarrow S_1$	6285.8	3±1	0.7±0.3
$^6H_{\frac{15}{2}}$, $^6F_{\frac{1}{2}}$	$\rightarrow S_2$	6349.0	0.9	1.5
and $^6F_{\frac{3}{2}}$	$\rightarrow S_5$	6388.6	19.8	1.2
	$\rightarrow S_9$	6633.6	20.1	10.5
	$\rightarrow R_1$	7155.4	49.4	2.8
$^6F_{\frac{5}{2}}$	$\rightarrow R_2$	7173.5	17.6	1.8
	$\rightarrow R_3$	7182.9	27.7	2.3
	$\rightarrow Q_1$	7928.4	25.3	0.7
	$\rightarrow Q_2$	8030.4	100.0	1.5
$^6F_{\frac{7}{2}}$	$\rightarrow Q_3$	8048.1	24.4	0.8
	$\rightarrow Q_4$	8059.2	88.5	1.0

Table 8.3: Energy levels (in vacuum cm^{-1}, ± 0.2), intensities (relative to the strongest line in the spectrum (=100.00), ± 0.50) and linewidths (in cm^{-1}, ± 0.2) as measured in absorption to Q centre crystal field levels of the ^6H and ^6F terms in CaF_2:0.05%Sm^{3+}

Multiplet	Transition	Energy	Intensity	Linewidth
	$Z_1 \rightarrow Y_1$	966.0	35.3	1.2
$^6H_{\frac{7}{2}}$	$\rightarrow Y_2$	1029.8	21.7	1.4
	$\rightarrow X_1$	2166.2	6.0	0.4
$^6H_{\frac{9}{2}}$	$\rightarrow X_2$	2197.2	7.6	0.9
$^6H_{\frac{11}{2}}$	$\rightarrow W_1$	3432.4	2.8	0.4
	$\rightarrow V_1$	4915.7	1.4	0.8
$^6H_{\frac{13}{2}}$	$\rightarrow V_2$	4949.8	8.6	2.3
	$\rightarrow V_3$	4989.5	7.0	0.7
	$\rightarrow S_1$	6281.4	2.7	0.4
$^6H_{\frac{15}{2}}$, $^6F_{\frac{1}{2}}$	$\rightarrow S_2$	6323	0.3	1.3
and $^6F_{\frac{3}{2}}$	$\rightarrow S_4$	6392.3	18±1	2.3±0.3
	$\rightarrow R_1$	7162.0	54.6	2.6
$^6F_{\frac{5}{2}}$	$\rightarrow R_2$	7186.6	31.9	2.2
	$\rightarrow R_3$	7200.0	5.7	2.5
	$\rightarrow Q_1$	7937.0	30.5	0.6
	$\rightarrow Q_2$	8041.4	74.2	0.9
$^6F_{\frac{7}{2}}$	$\rightarrow Q_3$	8050.3	21.1	1.0
	$\rightarrow Q_4$	8077.6	100.0	0.9

8.1.2 Zeeman Infrared Spectroscopy

For Zeeman measurements on the infrared absorption transitions, a 17.4 mm thick CaF_2:0.05%Sm^{3+} crystal, oriented along its $\langle 111 \rangle$ planes has been used. Wells [64] has measured the Zeeman spectra of CaF_2:Sm^{3+} for many of the infrared transitions in the 900 - 4000 cm^{-1} region. In this study, that work is extended to the Zeeman splittings of the A centre transitions in the 4500 - 10000 cm^{-1} region.

The $Z_1\gamma_6 \rightarrow W_1\gamma_6$ transition at 3503.6 cm^{-1} is in the region of overlap of the KBr and indium antimonide beamsplitters available in this study. The spectrum of this transition has been remeasured for comparision with that of Wells. The spectra at fields of 0, 2 and 4 Tesla are shown in Figure 8.6. The Zeeman splitting of the ground state is quite small. From electron paramagnetic resonance measurements, it is measured to be $g_{\|}=0\pm0.06$ and $g_{\perp}=0.823\pm0.003$ [78]. Because of this, the Zeeman effect in the ground state is often observed as a small splitting, superimposed on the splitting of the upper state. For a magnetic field applied along the $\langle 111 \rangle$ direction, the ground state g value for the A centre in CaF_2:Sm^{3+} is measured to be 0.64. This is in good agreement with the value inferred from EPR of 0.67.

Of the transitions observed to the $^6H_{\frac{13}{2}}$ multiplet only the $Z_1\gamma_6 \rightarrow V_1\gamma_6$ transition at 4865.9 cm^{-1} gives a clear splitting (Figure 8.7). The $Z_1\gamma_6 \rightarrow V_2\gamma_7$ transition at 4979.6 cm^{-1} is observed to broaden but no splitting could be observed. The spectrum is additionally complicated by overlapping R and Q centre lines.

Figures 8.8 and 8.10 show clear splittings of the $S_1\gamma_6$ and $S_3\gamma_6$ states at 6230.2 and 6526.4 cm^{-1} respectively. However, in Figure 8.9 the splitting of the $Z_1\gamma_6 \rightarrow S_2\gamma_6$ transition at 6285.0 cm^{-1} is complicated by cluster centre lines. In this case, the notation $S_2^{l,u}$ is used to indicate the higher and lower energy Zeeman levels of the S_2 state. These can be identified by the symmetrical broadening of these transitions due to the (unresolved) ground state splitting.

For transitions to the $^6H_{\frac{15}{2}}$, $^6F_{\frac{1}{2}}$ and $^6F_{\frac{3}{2}}$ multiplet levels, shown in Figure 8.11, the linewidths are so broad that no distinct Zeeman splittings are observed (up to magnetic field strengths of 4 Tesla). Obviously, in this case very few conclusions can be drawn.

Figure 8.12 shows transitions to the $^6F_{\frac{5}{2}}$ multiplet. The $^6F_{\frac{5}{2}}$ states decay via spontaneous multiphonon emission to the lower energy $^6H_{\frac{15}{2}}$, $^6F_{\frac{1}{2}}$ and $^6F_{\frac{3}{2}}$ multiplets. As a consequence, the linewidths for transitions to this multiplet are broader and the Zeeman splittings are less well resolved.

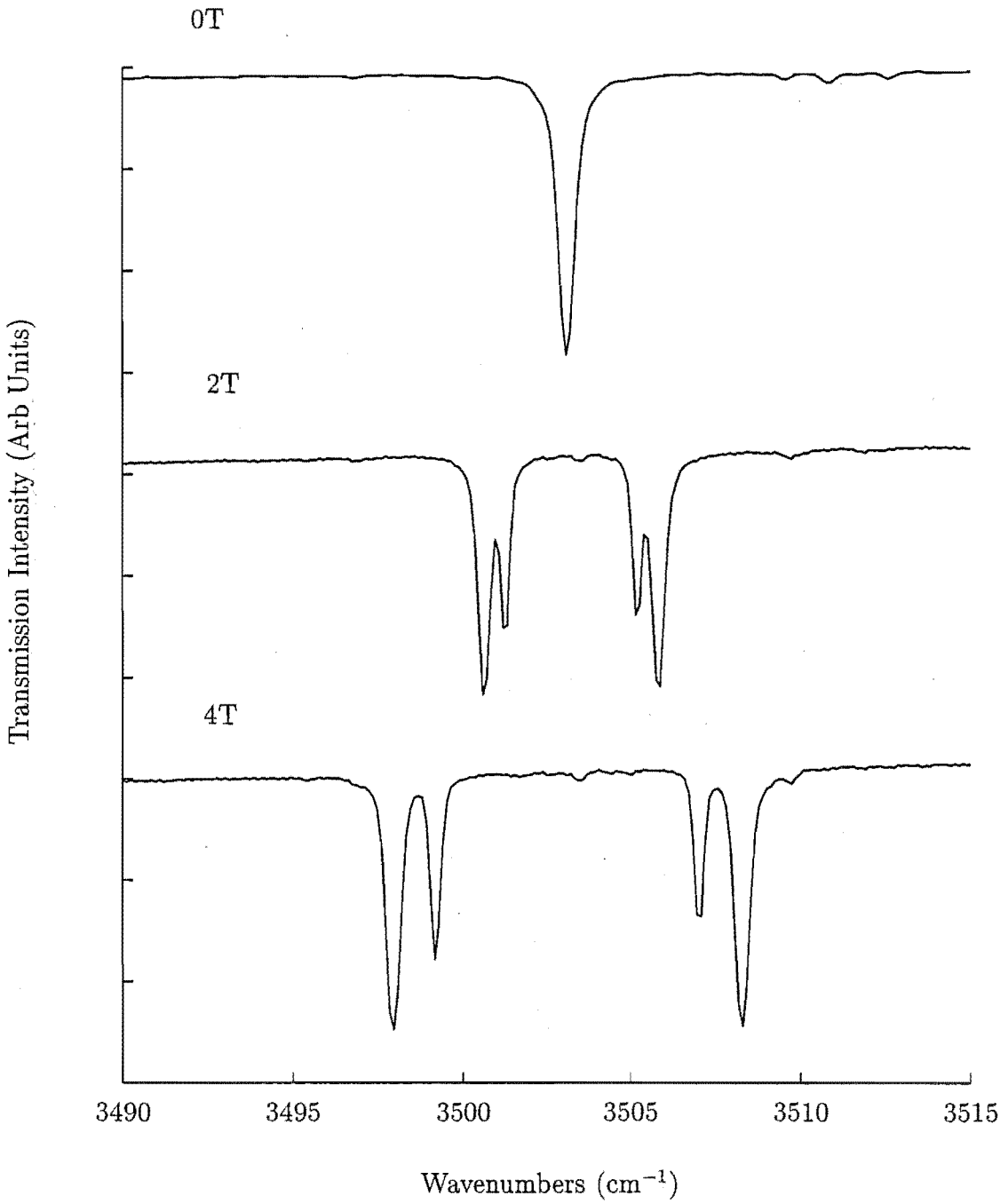

Figure 8.6: 4.2K splitting of the CaF_2:0.05%Sm^{3+} A centre ${}^6H_{\frac{5}{2}}(Z_1\gamma_6) \rightarrow {}^6H_{\frac{11}{2}}(W_1\gamma_6)$ transition as a function of magnetic field directed along a $\langle 111 \rangle$ axis.

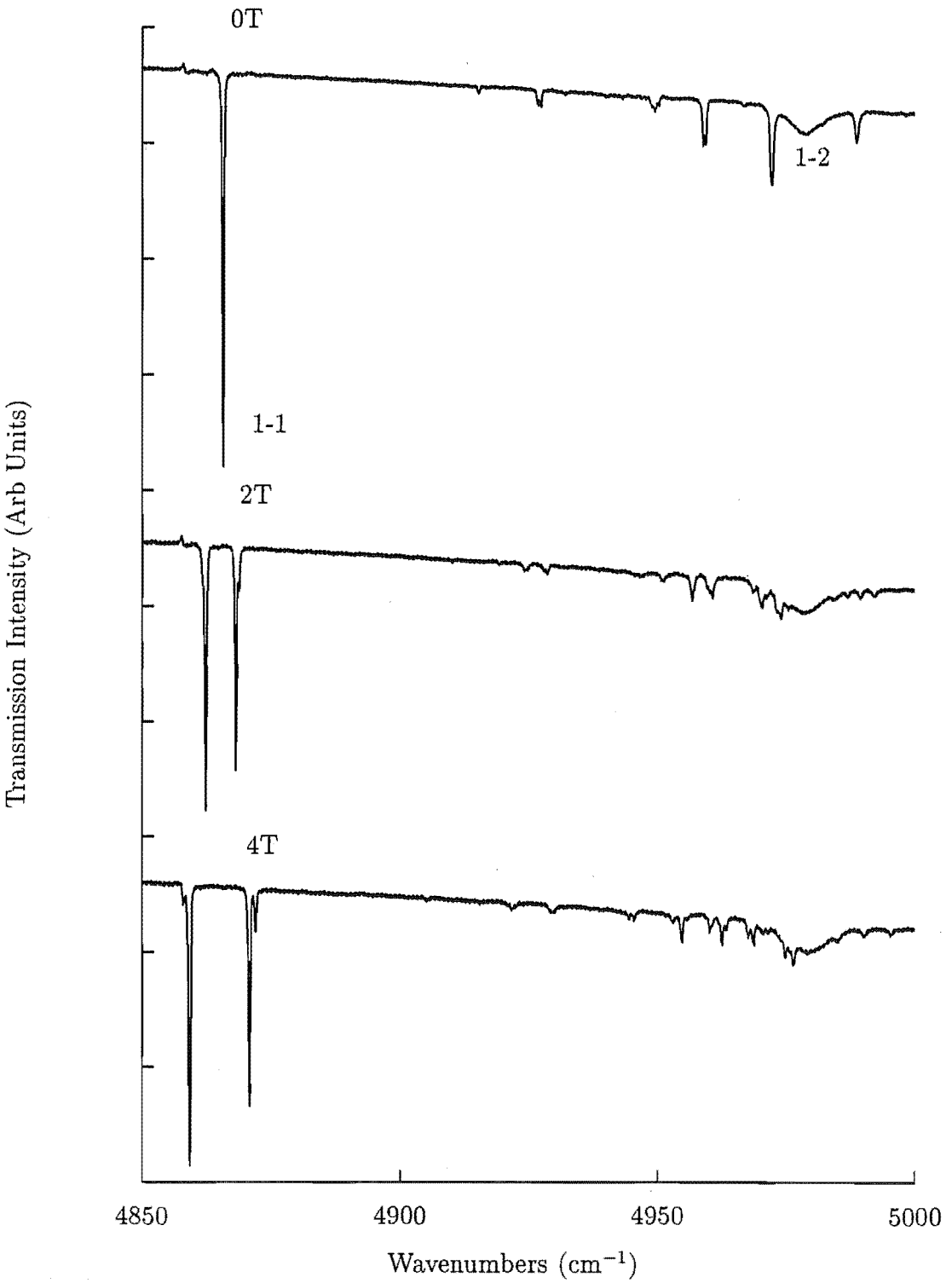

Figure 8.7: 4.2K splitting of the CaF_2:0.05%Sm^{3+} A centre ${}^6H_{\frac{5}{2}}(Z_1\gamma_6) \rightarrow {}^6H_{\frac{13}{2}}(V_1\gamma_6)$ and $(V_2\gamma_7)$ transitions as a function of magnetic field directed along a $\langle 111 \rangle$ axis.

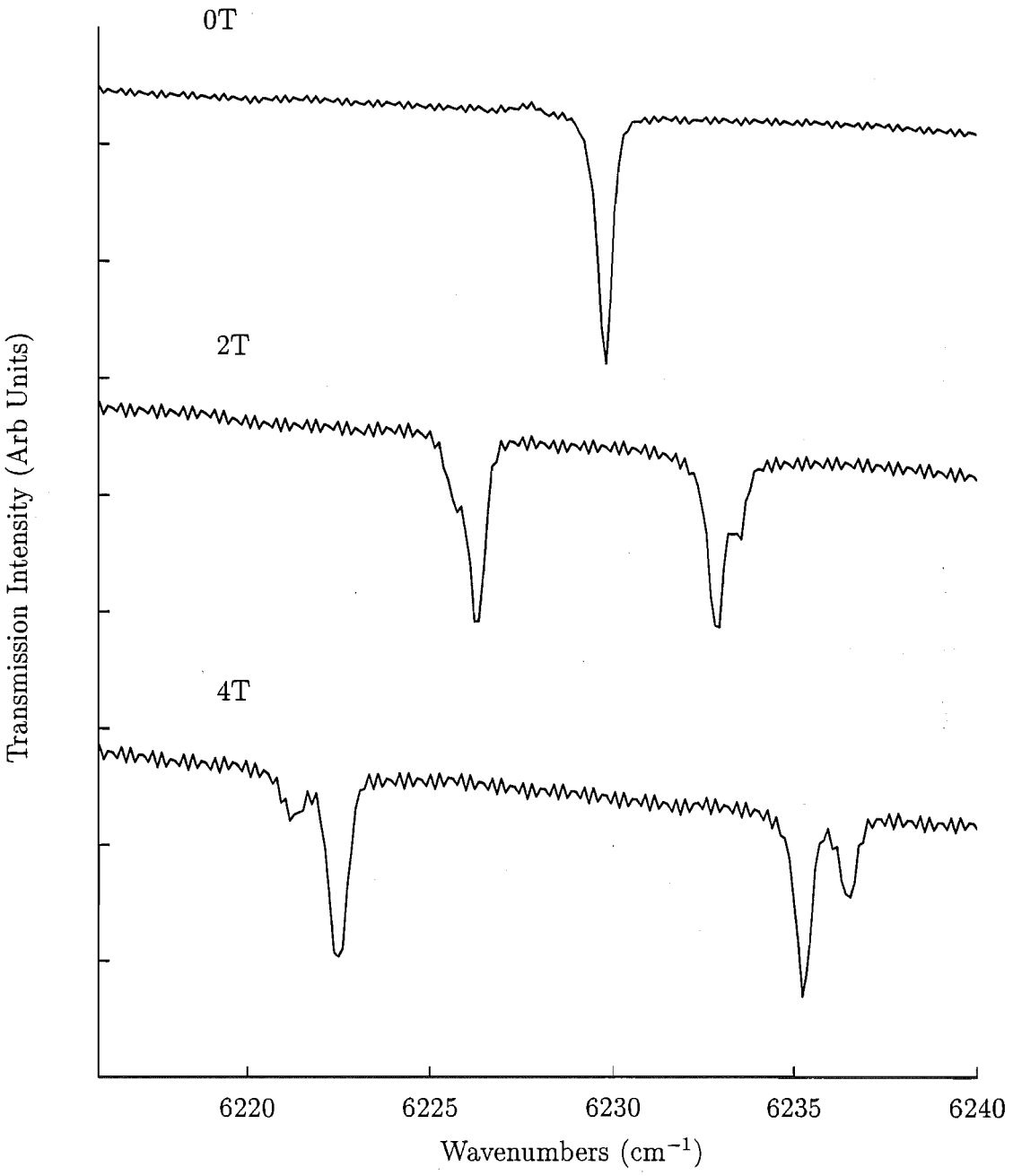

Figure 8.8: 4.2K splitting of the CaF_2:0.05%Sm^{3+} A centre $^6H_{\frac{5}{2}}(Z_1\gamma_6)\rightarrow(S_1\gamma_7)$ transition as a function of magnetic field directed along a ⟨111⟩ axis.

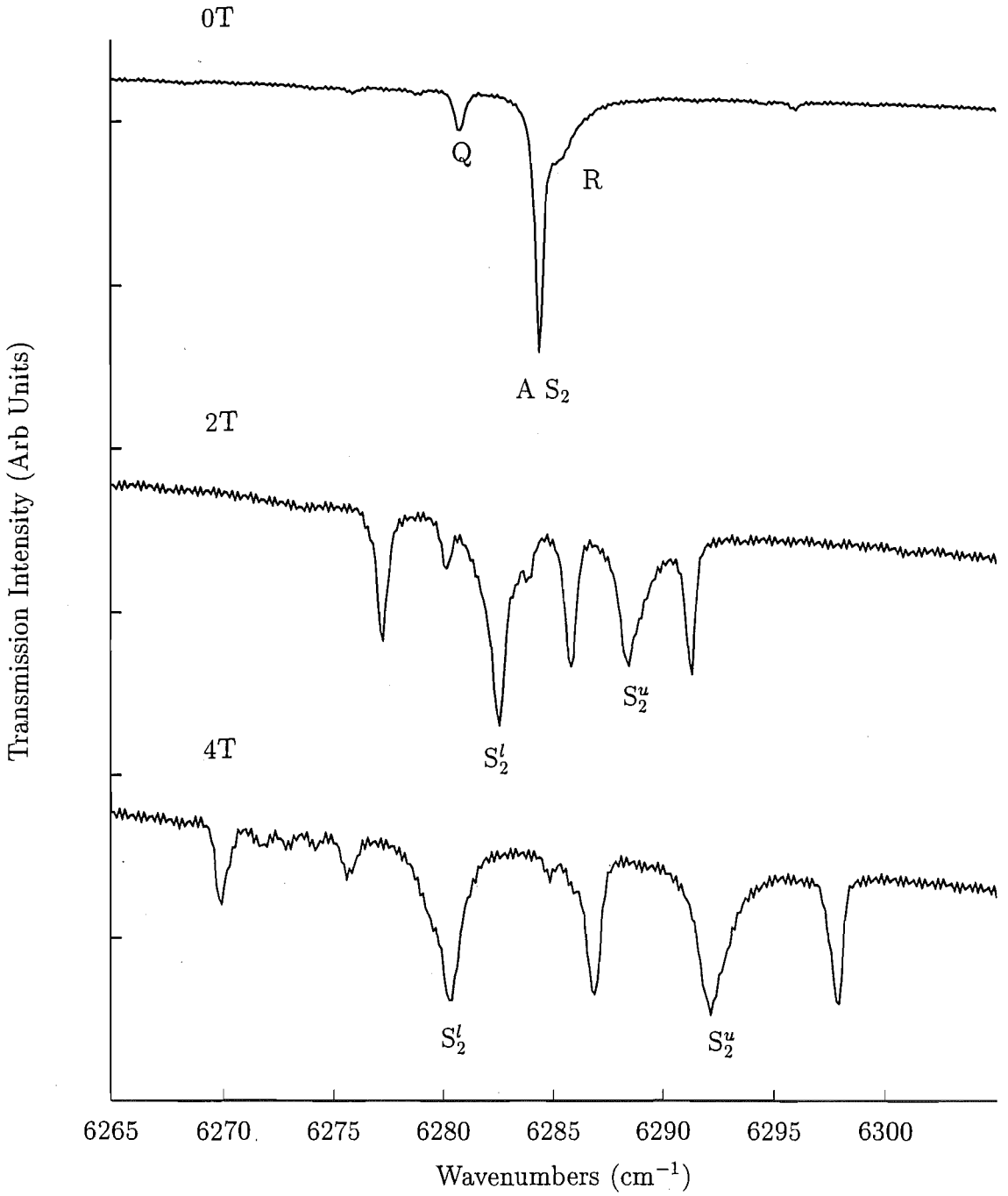

Figure 8.9: 4.2K splitting of the CaF_2:0.05%Sm^{3+} A centre ${}^6H_{\frac{5}{2}}(Z_1\gamma_6) \rightarrow (S_2\gamma_6)$ transition as a function of magnetic field directed along a $\langle 111 \rangle$ axis. The spectrum is complicated by the presence of nearby cluster centre lines. The notation $S_2^{l,u}$ denotes the lower and upper components of the S_2 state.

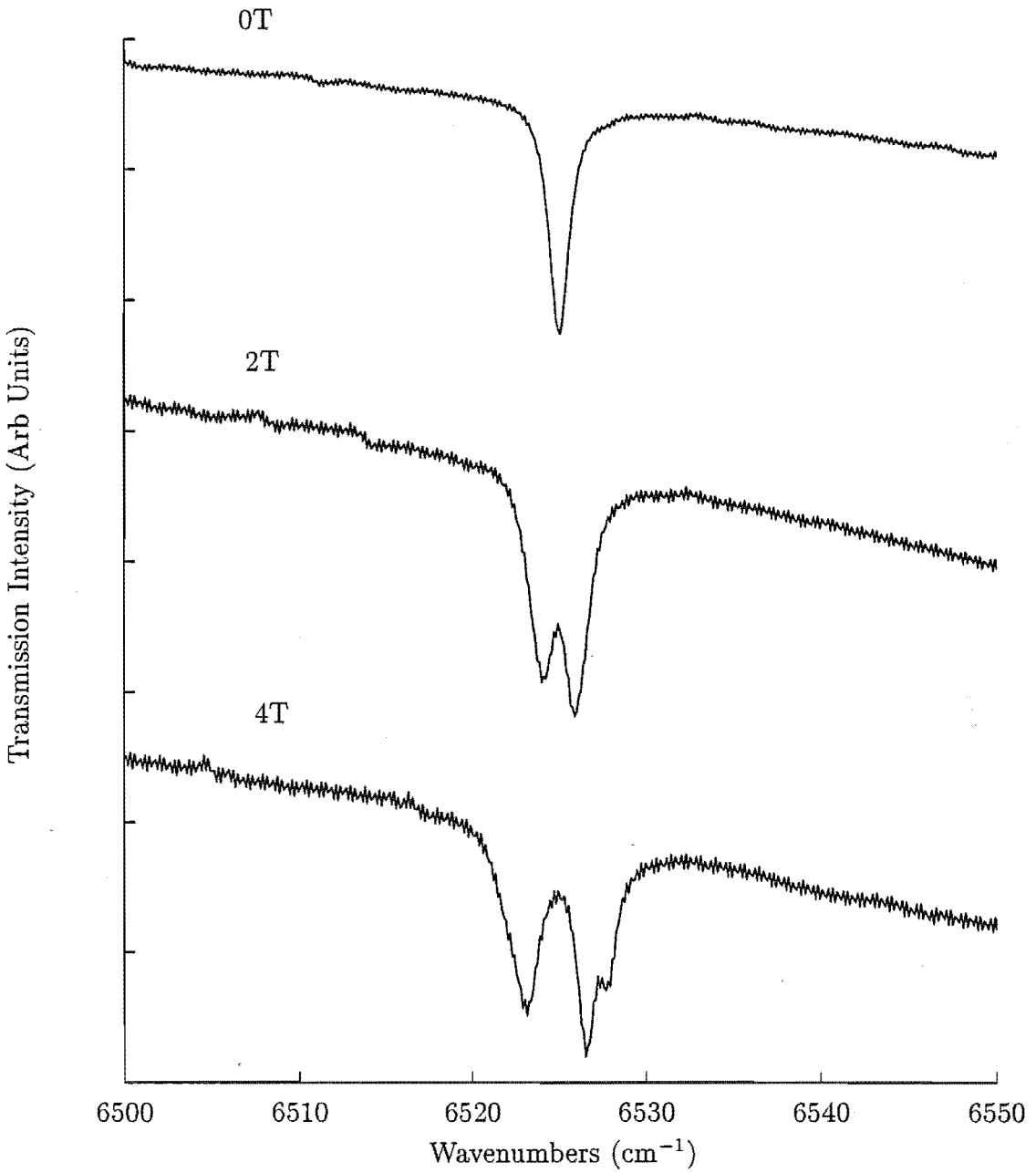

Figure 8.10: 4.2K splitting of the CaF_2:0.05%Sm^{3+} A centre ${}^6H_{\frac{5}{2}}(Z_1\gamma_6)\rightarrow(S_3\gamma_6)$ transition as a function of magnetic field directed along a $\langle 111 \rangle$ axis.

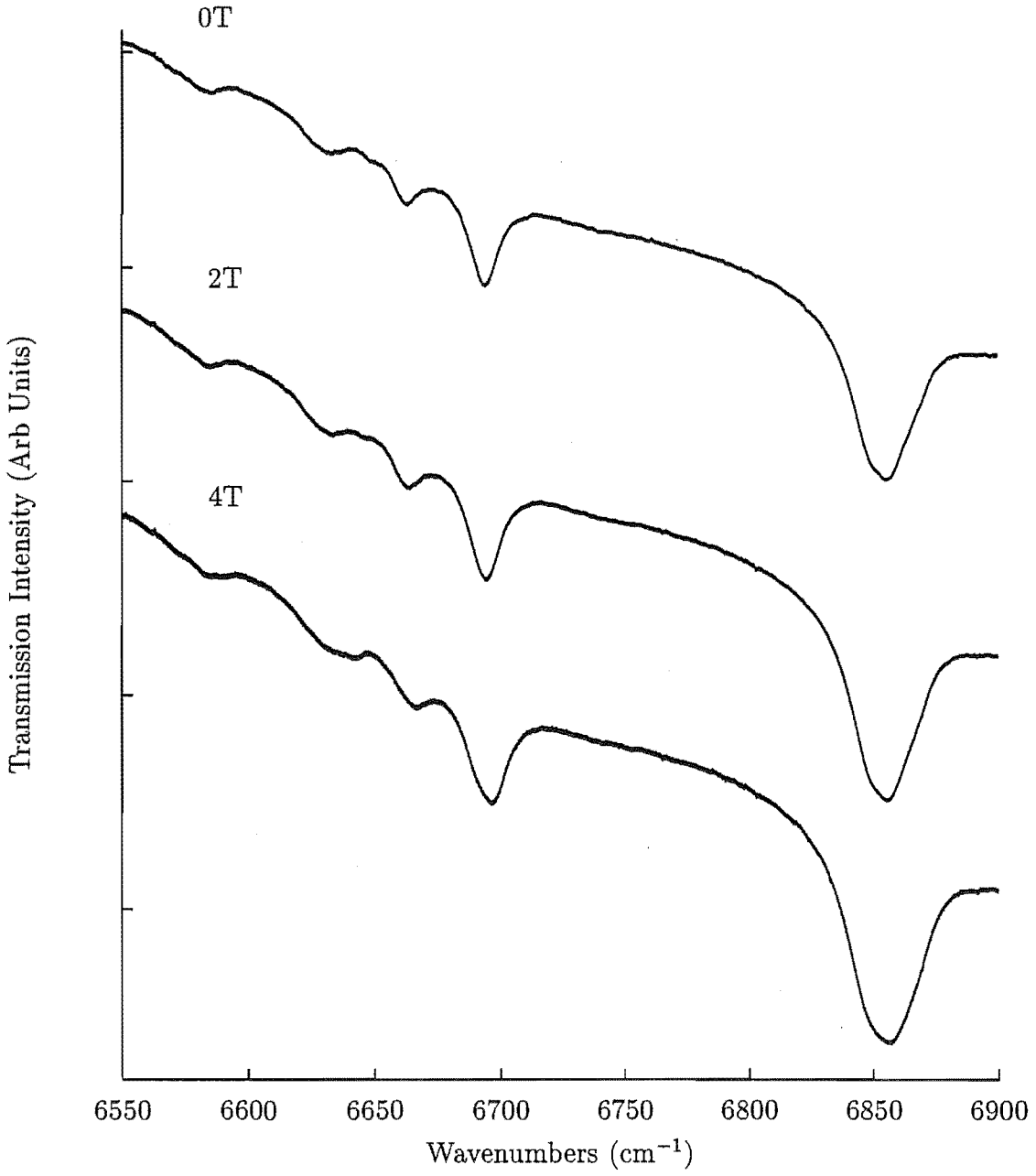

Figure 8.11: 4.2K splitting of the CaF_2:0.05%Sm^{3+} A centre $^6H_{\frac{5}{2}}(Z_1\gamma_6) \rightarrow (S_4\gamma_6)$, $(S_5\gamma_6)$, $(S_6\gamma_7)$, $(S_7\gamma_6)$ and $(S_9\gamma_7)$ transitions as a function of magnetic field directed along a $\langle 111 \rangle$ axis.

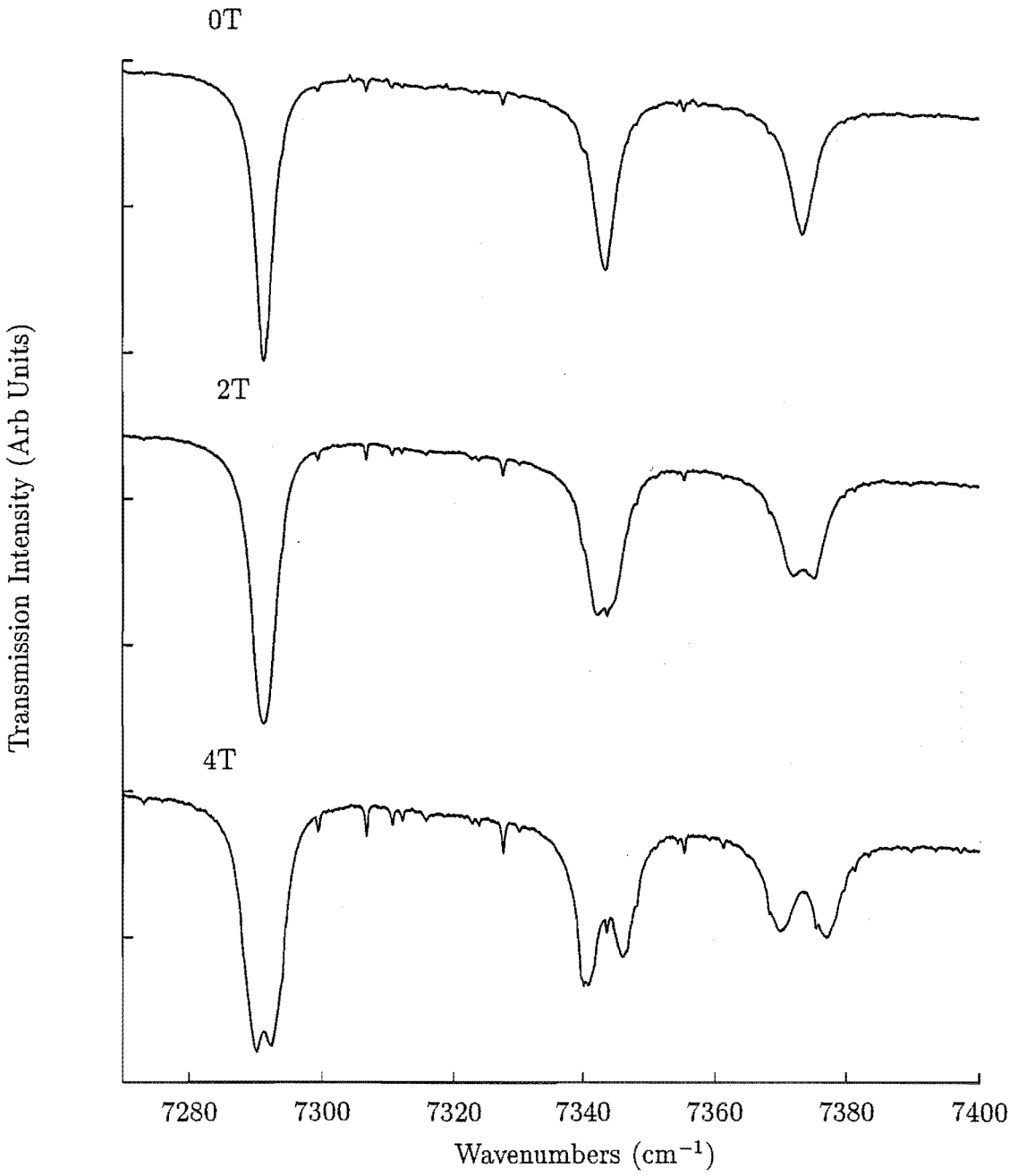

Figure 8.12: 4.2K splitting of the CaF_2:0.05%Sm^{3+} A centre $^6H_{\frac{5}{2}}(Z_1\gamma_6) \rightarrow {}^6F_{\frac{5}{2}}(R_1\gamma_7)$, $(R_2\gamma_6)$ and $(R_3\gamma_7)$ transitions as a function of magnetic field directed along a $\langle 111 \rangle$ axis.

Transitions to both the $^6F_{\frac{7}{2}}$ and $^6F_{\frac{9}{2}}$ multiplets, shown in Figures 8.14 and 8.15, are sharper and give well resolved Zeeman patterns for all but the highest frequency transitions. In Figure 8.14 the weak $Z_1\gamma_6 \rightarrow P_1\gamma_6$ transition at 9269.9 cm^{-1} is seen to gain in intensity as the strength of the magnetic field is increased. This results from mixing of the $P_1\gamma_6$ and $P_2\gamma_6$ state wavefunctions, in the applied magnetic field.

Transitions to the $^6F_{\frac{11}{2}}$ multiplet are observed as weak features because of low transmission signals at 10000 cm^{-1} and above. The application of a magnetic field lifts the Kramers degeneracy of the states. As such, the Zeeman subtransitions are weaker and few transitions could be detected.

The measured Zeeman splitting factors are given in Table 8.4 where they are compared with those calculated using Dr Mike Reid's *F-Shell Empiricial Programs* . On the whole, these give good agreement with the measured values.

There is a particularly poorly duplicated set of splittings, namely those of the $P_1\gamma_6$ and $P_2\gamma_6$ states. This arises because the crystal field analysis places these two states only 2.9 cm^{-1} apart however, they are experimentally measured to be separated by 18 cm^{-1}. Therefore, the calculated second order Zeeman interaction between these states, will be larger than it actually is. This will distort the calculated splitting factors. A better assessment of the Zeeman effects between these states will be possible if the calculation is repeated by a simple, back of the envelope type calculation. This is presented below.

Here, we neglect the mixing of the two wavefunctions. The output of the crystal field analysis gives wavefunctions of the $\mid J_z\rangle$ form:

$$P_1\gamma_6^{\pm} \quad 0.2525 \mid \mp\tfrac{7}{2}\rangle - 0.4185 \mid \pm\tfrac{1}{2}\rangle - 0.8616 \mid \pm\tfrac{9}{2}\rangle$$

$$P_2\gamma_6^{\pm} \quad 0.9515 \mid \mp\tfrac{7}{2}\rangle + 0.0488 \mid \pm\tfrac{1}{2}\rangle + 0.2518 \mid \pm\tfrac{9}{2}\rangle$$

The Zeeman matrix elements within the states of the Kramers doublet are:

$$H_z = \mu_B B_z(L_z + 2S_z) = \mu_B g_L B_z \langle \gamma_6^+ \mid J_z \mid \gamma_6^+ \rangle$$

for the parallel effect and for the perpendicular effect:

$$H_x = \mu_B B_x(L_x + 2S_x) = \frac{\mu_B g_L}{2} \langle \gamma_6^- \mid J_- \mid \gamma_6^+ \rangle$$

Where g_L, the Lande g-factor, is equal to 1.657 for the $^6F_{\frac{9}{2}}$ multiplet of Sm^{3+} . From the above matrix elements the splitting factors are:

$$s_{\parallel} = 2g_L \langle \gamma_6^+ \mid J_z \mid \gamma_6^+ \rangle$$

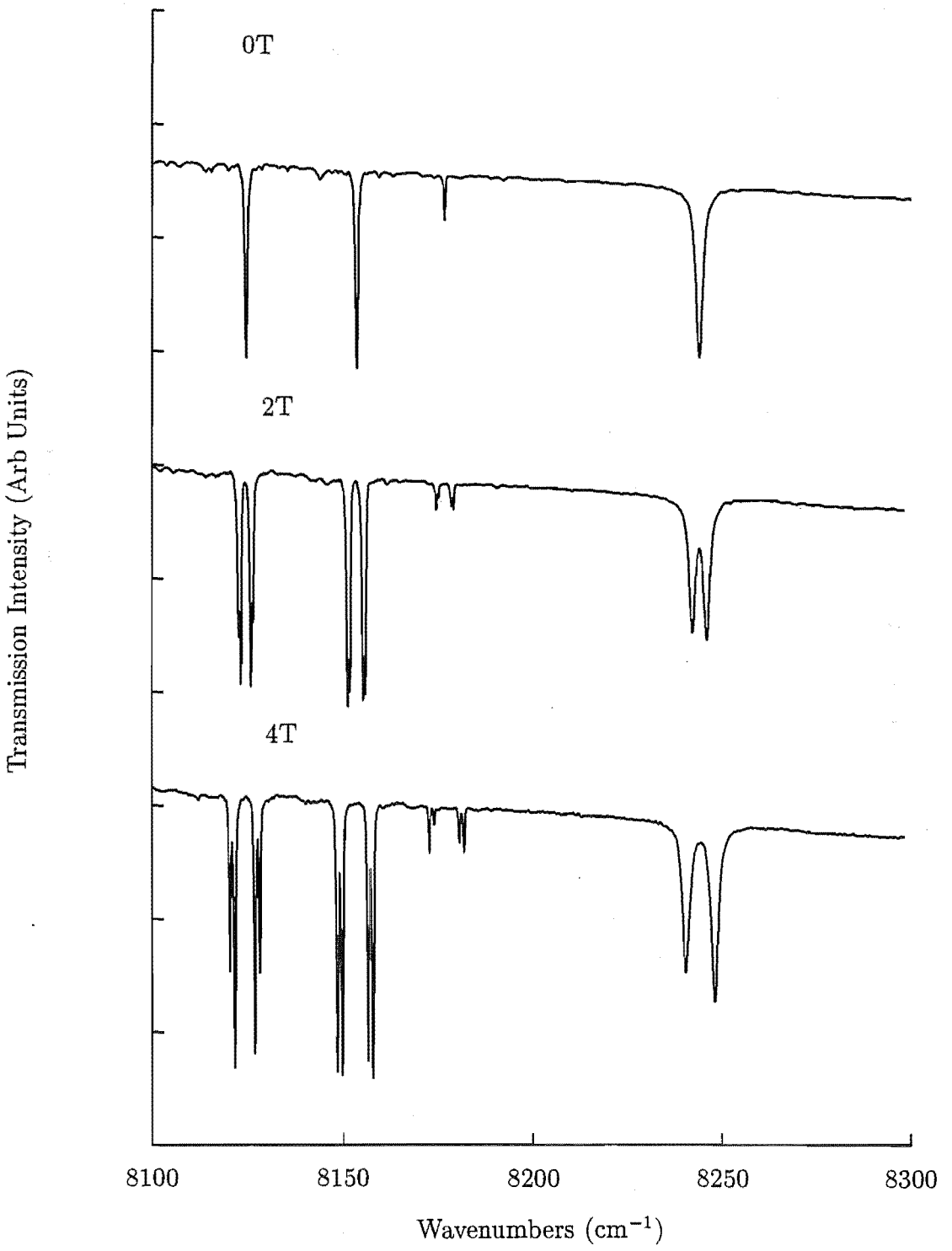

Figure 8.13: 4.2K splitting of the CaF_2:0.05%Sm^{3+} A centre $^6H_{\frac{5}{2}}(Z_1\gamma_6) \rightarrow {}^6F_{\frac{7}{2}}(Q_1\gamma_7)$, $(Q_2\gamma_6)$, $(Q_3\gamma_7)$ and $(Q_4\gamma_6)$ transitions as a function of magnetic field directed along a $\langle 111 \rangle$ axis.

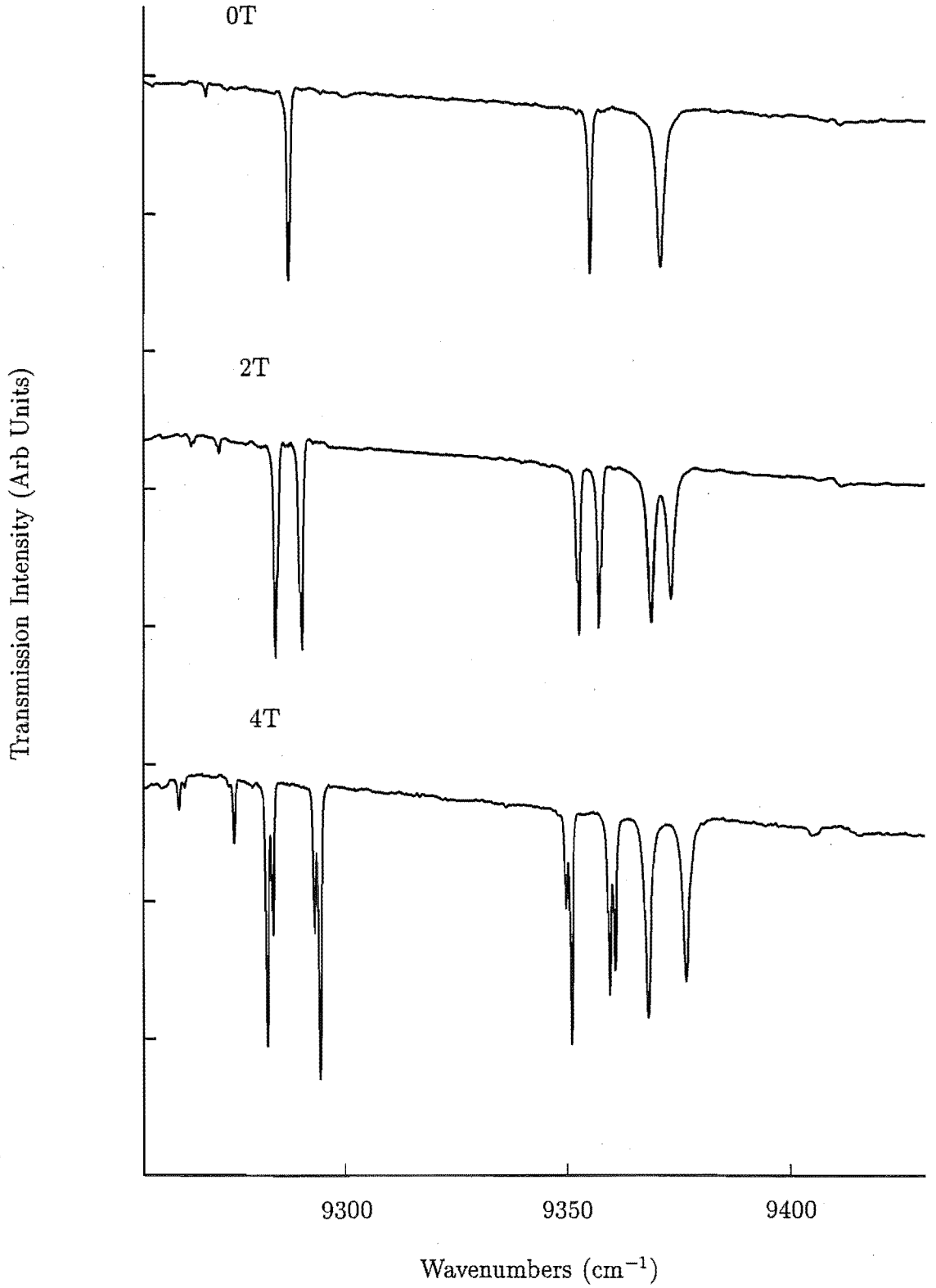

Figure 8.14: 4.2K splitting of the CaF_2:0.05%Sm^{3+} A centre $^6H_{\frac{5}{2}}(Z_1\gamma_6) \rightarrow {}^6F_{\frac{9}{2}}(P_1\gamma_6)$, $(P_2\gamma_6)$, $(P_3\gamma_7)$ and $(P_4\gamma_6)$ transitions as a function of magnetic field directed along a $\langle 111 \rangle$ axis.

Table 8.4: Calculated and experimental Zeeman splitting factors for the C_{4v} A centre in CaF_2:0.05%Sm^{3+}. Experimental uncertainties are ±0.2 unless otherwise stated. The † notation indicates the data of Wells [64]. The superscript *a* denotes calculated splitting factors which have been hand calculated neglecting second order Zeeman interactions.

State & Symmetry	Field (Tesla)	Zeeman Splitting Factor			
		Calculated			Experimental
		$S_\perp$	$S_\parallel$	$S_{[111]}$	$S_{[111]}$
$Z_1\gamma_6$	4	0.93	0.07	0.77	0.6
$X_1\gamma_6$	3	4.48	1.48	3.76	3.72±0.10†
$W_1\gamma_6$	3	6.06	1.93	5.07	4.89±0.10†
$V_1\gamma_6$	4	8.49	1.41	7.00	6.9
$S_1\gamma_7$	4	9.68	1.13	7.66	7.6
$S_2\gamma_6$	4	8.23	2.07	6.47	6.4
$S_3\gamma_6$	4	0.16	3.22	1.84	2.4±0.3
$R_1\gamma_7$	4	1.68	2.35	1.94	1.2±0.5
$R_2\gamma_6$	4	4.24	1.54	3.59	2.9±0.5
$R_3\gamma_7$	4	2.77	5.21	3.75	3.8±0.5
$Q_1\gamma_7$	4	0.94	4.26	2.57	3.5
$Q_2\gamma_6$	4	1.91	4.02	3.79	4.4
$Q_3\gamma_7$	4	1.05	4.60	4.07	4.3
$Q_4\gamma_6$	4	3.68	1.69	3.17	4.2±0.5
$P_1\gamma_6$	4	0.71^a	10.62^a	6.16^a	6.0
$P_2\gamma_6$	4	2.41^a	9.56^a	5.86^a	5.3
$P_3\gamma_7$	4	6.20	2.04	5.40	5.4
$P_4\gamma_6$	4	5.26	3.28	4.90	4.5±0.5

$$s_\perp = g_L \langle \gamma_6^- \mid J_- \mid \gamma_6^+ \rangle$$

We start with the $P_1\gamma_6$ state at 9269.9 cm^{-1}, calculating the magnitude of $\langle J_z \rangle$:

$$\langle J_z \rangle = -(0.2525)^2 \frac{7}{2} + (-0.4185)^2 \frac{1}{2} + (-0.8616)^2 \frac{9}{2} = 3.21$$

Therefore $s_\parallel$=10.62. Now calculating the matrix elements of the perpendicular splitting:

$$\langle -\frac{1}{2} \mid J_- \mid \frac{1}{2} \rangle = \sqrt{\frac{9}{2}(\frac{9}{2}+1) - \frac{1}{2}(\frac{1}{2}-1)} = 5$$

$$\langle \frac{7}{2} \mid J_- \mid \frac{9}{2} \rangle = \sqrt{\frac{9}{2}(\frac{9}{2}+1) - \frac{9}{2}(\frac{9}{2}-1)} = 3 = \langle -\frac{9}{2} \mid J_- \mid -\frac{7}{2} \rangle$$

Thus

$$\langle \gamma_6^- \mid J_- \mid \gamma_6^+ \rangle = (-0.4185)^2 5 - 2(0.8616)(0.2525)3 = -0.4296$$

and $s_\perp$=0.71. Calculating $s_{[111]}$ from

$$s_{[111]} = \sqrt{\frac{s_\parallel^2 + 2s_\perp^2}{3}}$$

we obtain a value of 6.16. This value is in significantly better agreement with the measured value of 6.0 than the value calculated by the program of 3.20.

Repeating the calculation for the $P_2\gamma_6$ state at 9288.4 cm^{-1}, we obtain a $\langle J_z \rangle$ value of 2.88 yielding $s_\parallel$=9.56. Whilst a $\langle J_- \rangle$ value of 1.45 yields $s_\perp$=2.41. These give $s_{[111]}$=5.86. Once again, a significantly better approximation to the measured value of 5.3 is obtained than the value of 3.10 calculated by the program.

Finally, we wish to consider the splitting of the R and Q cluster centres. Figure 8.15 shows the spectrum of the $Z_1 \rightarrow Q_1$ transitions of the R and Q centres as a function of magnetic field strength. These transitions are chosen as representative of the cluster centre lines since they are stronger, isolated and reasonably sharp. As can be seen from Figure 8.15, the splitting is simple although not clearly resolved. In neither case are more than four lines observed. This observation is true of all the cluster centre transitions observed in the Zeeman spectra. This suggests that all of the possible orientations of the cluster centres are magnetically equivalent along the $\langle 111 \rangle$ direction. However, with the small splitting factors possessed by the Sm^{3+} ion, it is possible that not all Zeeman sub-transitions can be observed. Even so, the simplicity of the observed patterns hints at a high symmetry for the R and Q centres observed in CaF_2 doped RE^{3+} crystals.

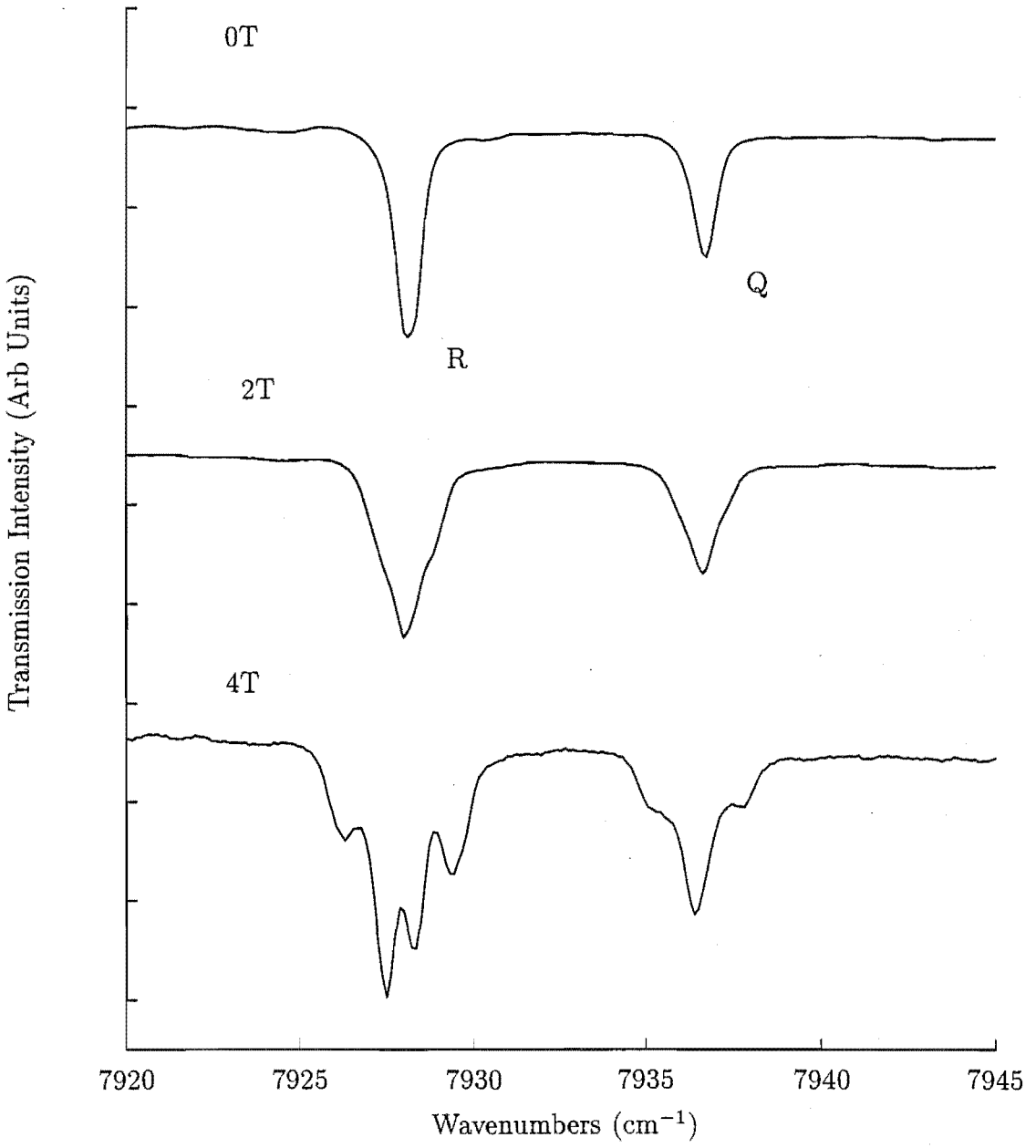

Figure 8.15: 4.2K splitting of the CaF_2:0.05%Sm^{3+} R and Q centre $^6H_{\frac{5}{2}}(Z_1) \rightarrow {}^6F_{\frac{7}{2}}(Q_1)$ transitions at 7928.4 and 7937.0 cm^{-1} respectively as a function of magnetic field directed along a $\langle 111 \rangle$ axis.

8.2 SrF_2:Sm^{3+}

8.2.1 Infrared Spectroscopy

The infrared absorption spectra of a 21mm thick SrF_2:0.05%Sm^{3+} crystal was measured on the Bio-Rad Digilab FTIR spectrometer. The crystal was cooled to 10K. All measurements were made at 0.25 cm^{-1} resolution. Light transmitted through the crystal was detected from the multiphonon absorption edge of the host crystal, at 800 cm^{-1}, through to the limits of the indium antimonide detector at 10500 cm^{-1}. An earlier study by Wells [64], employed Zeeman techniques for absorption transitions to the $^6H_{\frac{7}{2}}$, $^6H_{\frac{9}{2}}$ and $^6H_{\frac{11}{2}}$ multiplets. The range of that work was limited by the transmission of the KBr beamsplitter in use at that time. In addition, analysis was hindered by limited knowledge of the crystal field wavefunctions of the dominant centre. We are now in a position to reanalyse the infrared absorption of the Sm^{3+} ion in SrF_2 crystals.

As for CaF_2:0.05%Sm^{3+}, the KBr beamsplitter, mercury-cadmium-telluride detector and globar source combination was used to study absorption transitions to the $^6H_{\frac{7}{2}}$, $^6H_{\frac{9}{2}}$ and $^6H_{\frac{11}{2}}$ multiplets. These spectra are shown in Figure 8.16. As with the other SrF_2:RE^{3+} crystals studied in this thesis, the simplicity of the spectra with respect to those observed in CaF_2:RE^{3+} systems is noted here also. For both the $^6H_{\frac{7}{2}}$ and $^6H_{\frac{9}{2}}$ transitions, all levels assigned by laser selective excitation are detected. However, for the $^6H_{\frac{11}{2}}$ multiplet transitions, the strong atmospheric absorption band in the 3500-3900 cm^{-1} region makes transition assignments difficult. The spectrometer was flushed with dry nitrogen gas, however it is difficult to eliminate these unwanted absorption features. As a consequence of this problem, only one level of the $^6H_{\frac{11}{2}}$ multiplet has been assigned. This is given in Table 8.5.

Four absorption transitions are observed to the $^6H_{\frac{13}{2}}$ multiplet in the 4850-5210 cm^{-1} region. Again, an atmospheric absorption band overlaps these transitions. As the features associated with the water vapour are weaker than those in the 3600 - 3900 cm^{-1} region, the nitrogen purge gas can clear these unwanted features. Transitions to the $^6H_{\frac{15}{2}}$, $^6F_{\frac{1}{2}}$ and $^6F_{\frac{3}{2}}$ multiplets are clear and all levels observed via laser excited fluorescence are observed in absorption. These transitions follow the same pattern as those in fluorescence, with the higher lying levels significantly broadened due to relaxation to the lower levels. As a consequence of this, no candidates for the $S_{10}\gamma_6$ and $S_{11}\gamma_7$ transitions are observed. The $^6H_{\frac{5}{2}} \rightarrow ^6F_{\frac{5}{2}}$ and $^6F_{\frac{7}{2}}$ transitions are particularly strong. The measured frequencies of these transitions are given in Table 8.5. As in the CaF_2:Sm^{3+} case, additional features are observed in the 9200-9350 and 10600-10750 cm^{-1} regions which correspond to the $^6H_{\frac{5}{2}} \rightarrow ^6F_{\frac{9}{2}}$ and $^6F_{\frac{11}{2}}$

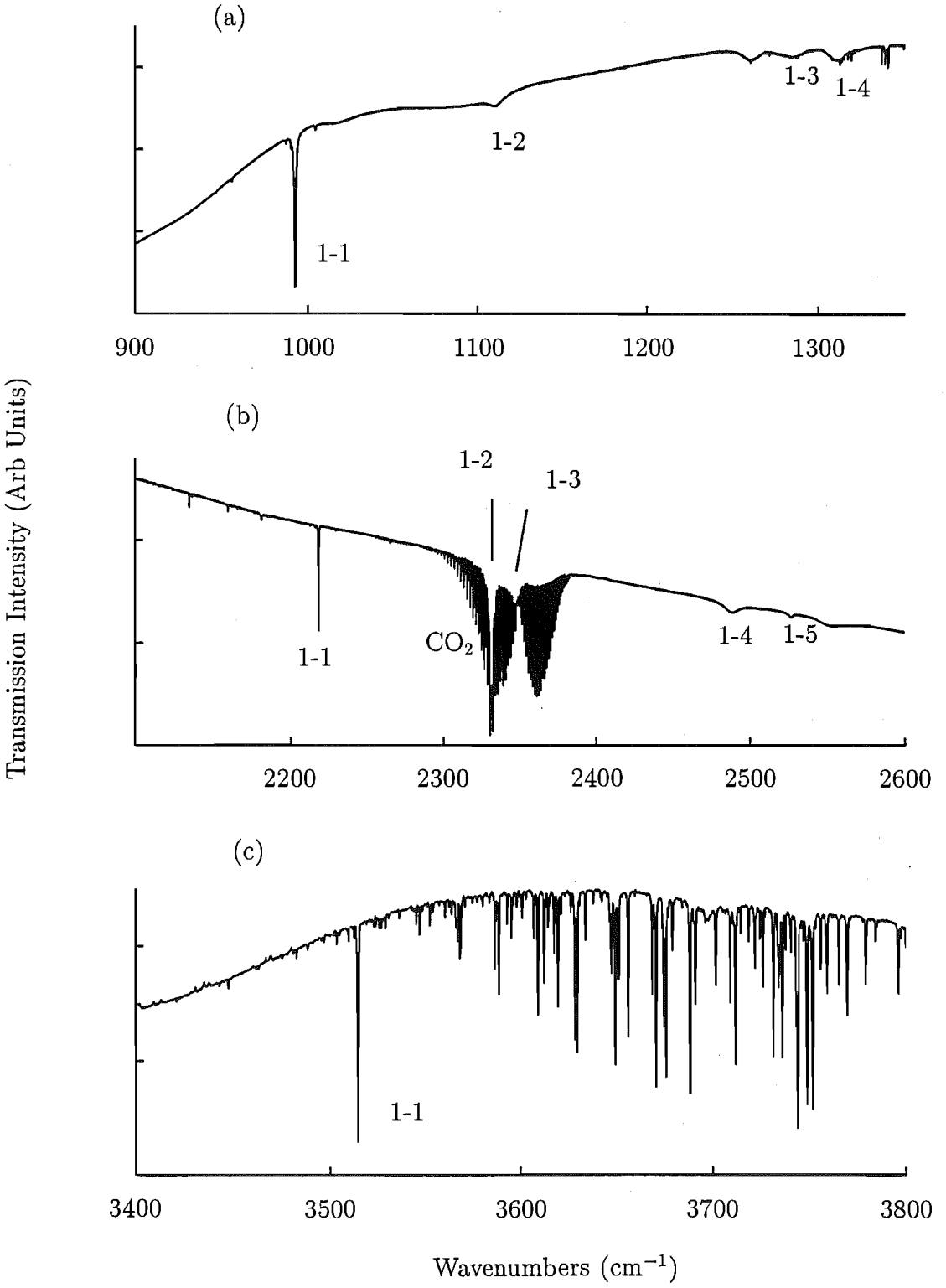

Figure 8.16: Infrared absorption to the (a) $^6H_{\frac{7}{2}}$, (b) $^6H_{\frac{9}{2}}$ and (c) $^6H_{\frac{11}{2}}$ multiplets in SrF_2:0.05%Sm^{3+}. The spectra were recorded at 10K. The A centre levels are given an arbitrary numerical label.

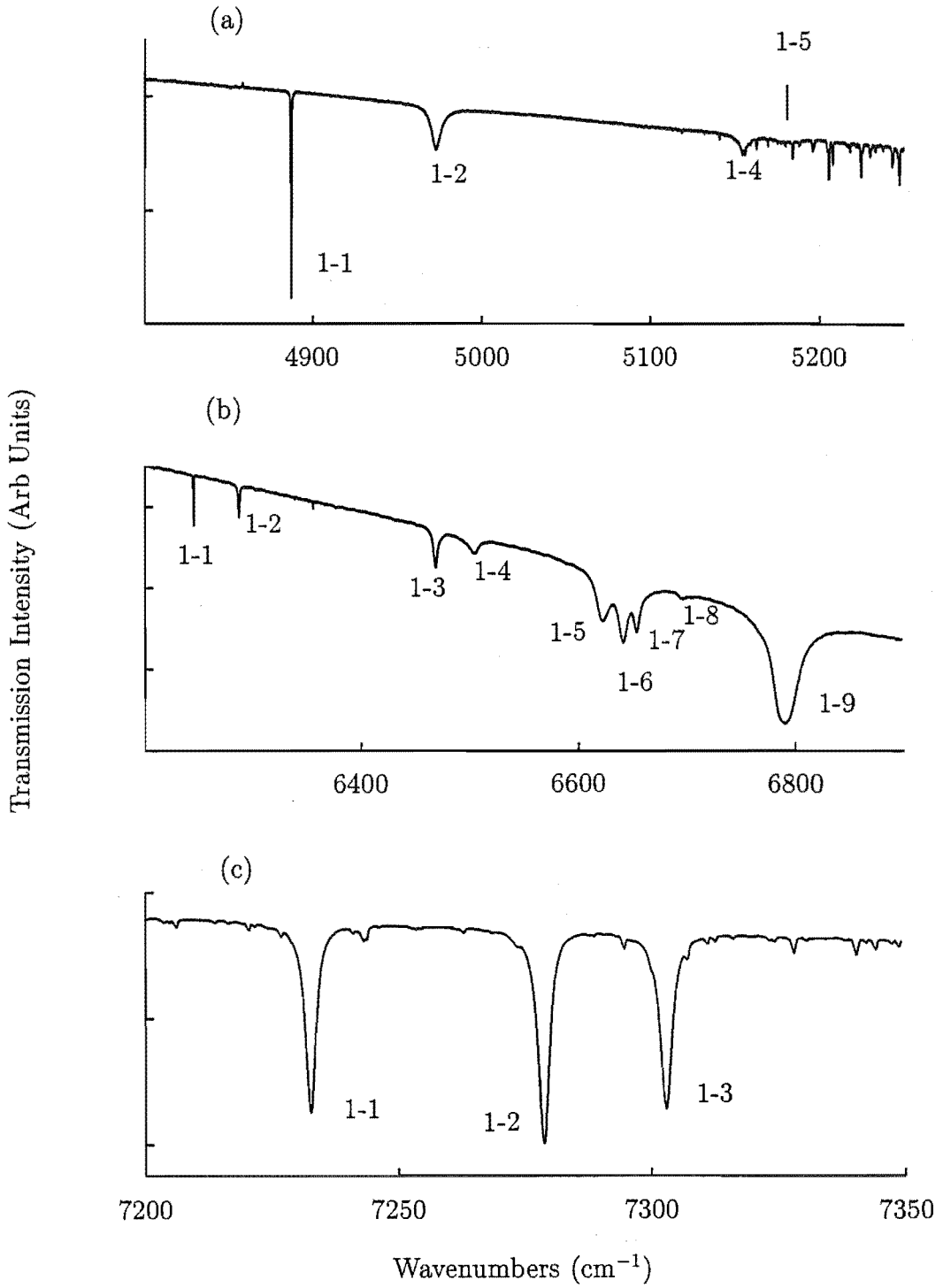

Figure 8.17: Infrared absorption to the (a) $^6H_{\frac{13}{2}}$, (b) $^6H_{\frac{15}{2}}$, $^6F_{\frac{1}{2}}$, $^6F_{\frac{3}{2}}$ and (c) $^6F_{\frac{5}{2}}$ multiplets in SrF_2:0.05%Sm^{3+}. The spectra were recorded at 10K. The A centre levels are given an arbitrary numerical label.

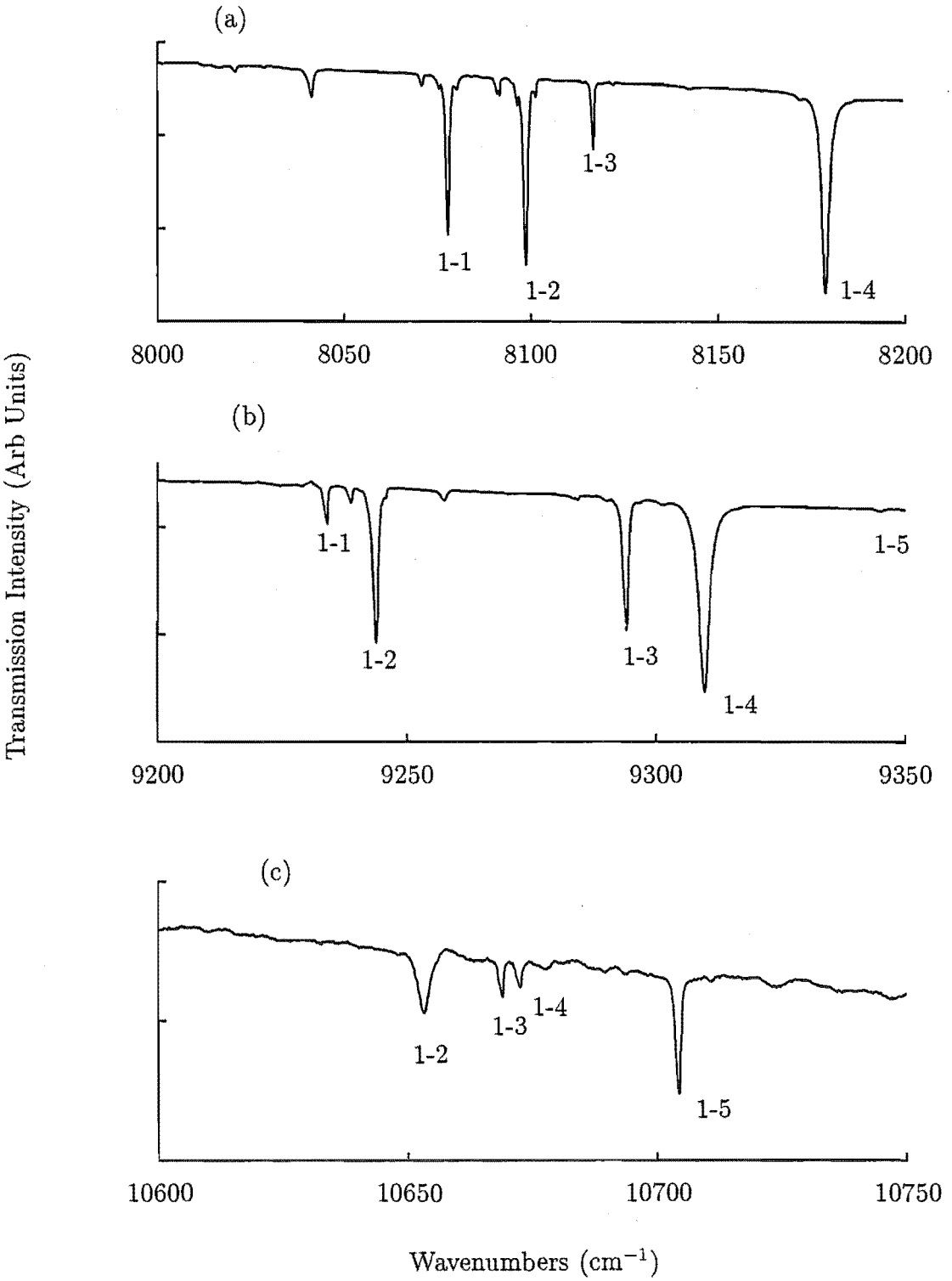

Figure 8.18: Infrared absorption to the (a) $^6F_{\frac{7}{2}}$, (b) $^6F_{\frac{9}{2}}$ and (c) $^6F_{\frac{11}{2}}$ multiplets in SrF_2:0.05%Sm^{3+}.The spectra were recorded at 10K. The A centre levels are given an arbitrary numerical label.

Table 8.5: Energy levels (in vacuum cm^{-1}, ± 0.2), intensities (relative to the strongest line in the spectrum (=100.00), ± 0.50) and linewidths (in cm^{-1}, ± 0.2) as measured in absorption to A centre crystal field levels of the ^6H and ^6F terms in SrF_2:0.05%Sm^{3+}

Multiplet	Transition	Energy	Intensity	Linewidth
	$Z_1\gamma_6 \rightarrow Y_1\gamma_6$	992.5	50.2	0.8
$^6H_{\frac{7}{2}}$	$\rightarrow Y_2\gamma_7$	1110.0	3.1	3.8
	$\rightarrow Y_3\gamma_7$	1285.6	9.0	13.1
	$\rightarrow Y_4\gamma_6$	1312.0	8.8	7.5
	$\rightarrow X_1\gamma_6$	2218.0	1.8	0.2
	$\rightarrow X_2\gamma_6$	2331.8	21.3	2.2
$^6H_{\frac{9}{2}}$	$\rightarrow X_3\gamma_7$	2348.0	9.6	4.7
	$\rightarrow X_4\gamma_7$	2489.2	6.9	9.5
	$\rightarrow X_5\gamma_6$	2527.6	0.9	2.9
$^6H_{\frac{11}{2}}$	$\rightarrow W_1\gamma_6$	3514.9	15.0	0.3
	$\rightarrow V_1\gamma_6$	4887.4	4.6	0.6
	$\rightarrow V_2\gamma_7$	4973.9	7.3	5.0
$^6H_{\frac{13}{2}}$	$\rightarrow V_4\gamma_7$	5157.0	2.2	3.5
	$\rightarrow V_5\gamma_6$	5181.7	3.9	10.7±0.5
	$\rightarrow S_1\gamma_7$	6245.2	1.0	0.6
	$\rightarrow S_2\gamma_6$	6288.8	1.4	1.2
	$\rightarrow S_3\gamma_6$	6469.6	3.9	2.6
	$\rightarrow S_4\gamma_6$	6505.1	4.6	7.9
$^6H_{\frac{15}{2}}$, $^6F_{\frac{1}{2}}$	$\rightarrow S_5\gamma_6$	6623.7	24.0	10.8
and $^6F_{\frac{3}{2}}$	$\rightarrow S_6\gamma_7$	6643.2	17.9	5.8
	$\rightarrow S_7\gamma_7$	6655.9	13.2	5.3
	$\rightarrow S_8\gamma_7$	6698.0	4.4	7.9
	$\rightarrow S_9\gamma_6$	6792.8	100.0	17.1
	$\rightarrow R_1\gamma_7$	7233.1	31.3	1.3
$^6F_{\frac{5}{2}}$	$\rightarrow R_2\gamma_6$	7279.2	58.2	1.8
	$\rightarrow R_3\gamma_7$	7303.6	41.6	1.9
	$\rightarrow Q_1\gamma_7$	8078.1	21.2	1.0
	$\rightarrow Q_2\gamma_6$	8099.1	34.6	1.2
$^6F_{\frac{7}{2}}$	$\rightarrow Q_3\gamma_7$	8117.3	1.9	0.3
	$\rightarrow Q_4\gamma_6$	8179.4	65.7	1.6
	$\rightarrow P_1\gamma_6$	9234.2	2.4	0.8
	$\rightarrow P_2\gamma_6$	9244.0	16.7	0.9
$^6F_{\frac{9}{2}}$	$\rightarrow P_3\gamma_7$	9294.5	14.8	0.9
	$\rightarrow P_4\gamma_6$	9310.0	59.7	1.9
	$\rightarrow P_5\gamma_7$	9345.7	0.3	1.2
	$\rightarrow O_2\gamma_6$	10653.5	4.7	1.7
$^6F_{\frac{11}{2}}$	$\rightarrow O_3\gamma_7$	10669.4	1.8	0.7
	$\rightarrow O_4\gamma_6$	10672.9	1.3	0.8
	$\rightarrow O_5\gamma_6$	10704.8	4.9	0.8

transitions. Assignments are made by comparision with the $CaF_2:Sm^{3+}$ case and, where possible, the Zeeman spectroscopy to follow in this section. Five transitions have been observed to the $^6F_{\frac{9}{2}}$ multiplet at frequencies of 9234.18, 9244.03, 9294.51, 9310.02 and 9345.67 cm^{-1}. These are assigned as the $P_1\gamma_6$, $P_2\gamma_6$, $P_3\gamma_7$, $P_4\gamma_6$ and $P_5\gamma_7$ states respectively. The irrep symmetry labels have been determined from the crystal field analysis and should therefore be regarded as tentative, having not been inferred from polarisation studies. The $^6F_{\frac{11}{2}}$ multiplet levels lie in the tail of the transmission response of the FTIR and signal intensities are quite low. Only four of the expected six transitions are observed at frequencies of 10653.47, 10669.36, 10672.94 and 10704.82 cm^{-1}. These are assigned as the $O_2\gamma_6$, $O_3\gamma_7$, $O_4\gamma_6$ and $O_5\gamma_6$ states.

8.2.2 Zeeman Infrared Spectroscopy

As the sample used for infrared absorption was already [111] oriented, the same boule was then used for Zeeman spectroscopy in the 3000-10000 cm^{-1} region. Wells [64] has already measured the Zeeman effect of many lines in the 900-3500 cm^{-1} region. These were not remeasured but this data was included for completeness in Table 8.6 . The $Z_1\gamma_6 \rightarrow W_1\gamma_6$ transition at 3514.86 cm^{-1} is in the overlap region for the two beamsplitters available and this splitting has been remeasured for direct comparision between the two studies.

All sharp lines show the splitting of the ground state for 4 Tesla fields. From this common splitting, the ground state [111] splitting factor of 0.65 is found to be in good agreement with the value inferred from the EPR data of Antipin et. al. [156] of 0.68 ($g_{\|}=0\pm0.06$ and $g_{\perp}=0.829\pm0.002$). As the ground state splitting is so small, the Zeeman splitting of the lines is dominated by the behaviour of the terminating states of the transitions. Often, the line-profiles are dominated by the contribution from the homogeneous linewidth (phonon broadened). In these cases, four distinct lines are not observed. We can estimate the Zeeman splitting of such states directly, ignoring the superimposed ground state contribution. This leads to additional uncertainties in the splitting factors. From Table 8.6, we see general agreement is obtained with the calculated values obtained from the crystal field wavefunctions.

Some notable exceptions arise. The $Z_1\gamma_6 \rightarrow V_2\gamma_7$ transition at 4973.85 cm^{-1} is an example of this. The calculated splitting factor is almost twice as large as that measured from the spectra. One should note that the two line splitting observed, is barely resolved. Also, that the linewidths are large. Therefore, large uncertainties are introduced to the measurement and the value of 1.8 ± 1.0 should be treated as extremely tentative. Further cases such as this are the $Z_1\gamma_6 \rightarrow S_5\gamma_6$ and $S_7\gamma_7$

transitions at 6623.68 and 6655.94 cm^{-1}. In this region, not only are the lines broad but they are further obscured by the $Z_1\gamma_6 \rightarrow S_6\gamma_7$ transition at 6643.17 cm^{-1}. Figure 8.25 plots the observed Zeeman subtransitions from which the measured splitting factors in Table 8.6 are inferred.

Table 8.6: Calculated and experimental Zeeman splitting factors for the A centre in SrF_2:0.05%Sm^{3+}. Experimental uncertainties are ±0.2 unless otherwise stated. The † notation indicates the data of Wells [64].

State & Symmetry	Field (Tesla)	Zeeman Splitting Factor			
		Calculated			Experimental
		$S_\perp$	$S_\parallel$	$S_{[111]}$	$S_{[111]}$
$Z_1\gamma_6$	4	0.93	0.01	0.76	0.65
$Y_1\gamma_6$	3	2.76	0.73	2.30	2.06±0.10†
$X_1\gamma_6$	3	4.46	1.66	3.76	3.65±0.10†
$X_2\gamma_6$	3	0.14	7.46	4.28	4.5±0.4†
$W_1\gamma_6$	3	5.85	2.31	4.98	4.80±0.10†
$V_1\gamma_6$	4	8.51	1.46	6.99	6.8
$V_2\gamma_7$	4	2.64	4.30	3.24	1.8±1.0
$V_4\gamma_7$	4	1.92	9.70	5.94	6.4±0.3
$S_1\gamma_7$	4	9.76	1.09	7.45	7.4
$S_2\gamma_6$	4	8.49	2.07	6.35	6.5
$S_3\gamma_6$	4	0.11	6.31	3.58	3.7±0.3
$S_5\gamma_6$	4	6.57	1.26	5.32	6.5±0.4
$S_7\gamma_7$	4	4.40	9.38	5.90	6.6±0.5
$R_1\gamma_7$	4	1.92	2.05	1.99	1.3±0.3
$R_2\gamma_6$	4	4.20	1.52	3.56	2.8±0.3
$R_3\gamma_7$	4	2.95	4.81	3.67	3.9±0.3
$Q_1\gamma_7$	4	2.47	3.15	2.87	3.2
$Q_2\gamma_6$	4	2.18	5.30	3.37	4.0
$Q_3\gamma_7$	4	2.35	5.24	3.78	4.1
$Q_4\gamma_6$	4	3.48	2.22	3.09	3.9±0.3
$P_1\gamma_6$	4	1.16	4.17	4.27	5.2
$P_2\gamma_6$	4	3.52	3.57	4.48	5.1
$P_3\gamma_7$	4	6.42	1.80	5.26	4.9
$P_4\gamma_6$	4	4.47	4.38	4.44	4.1±0.3

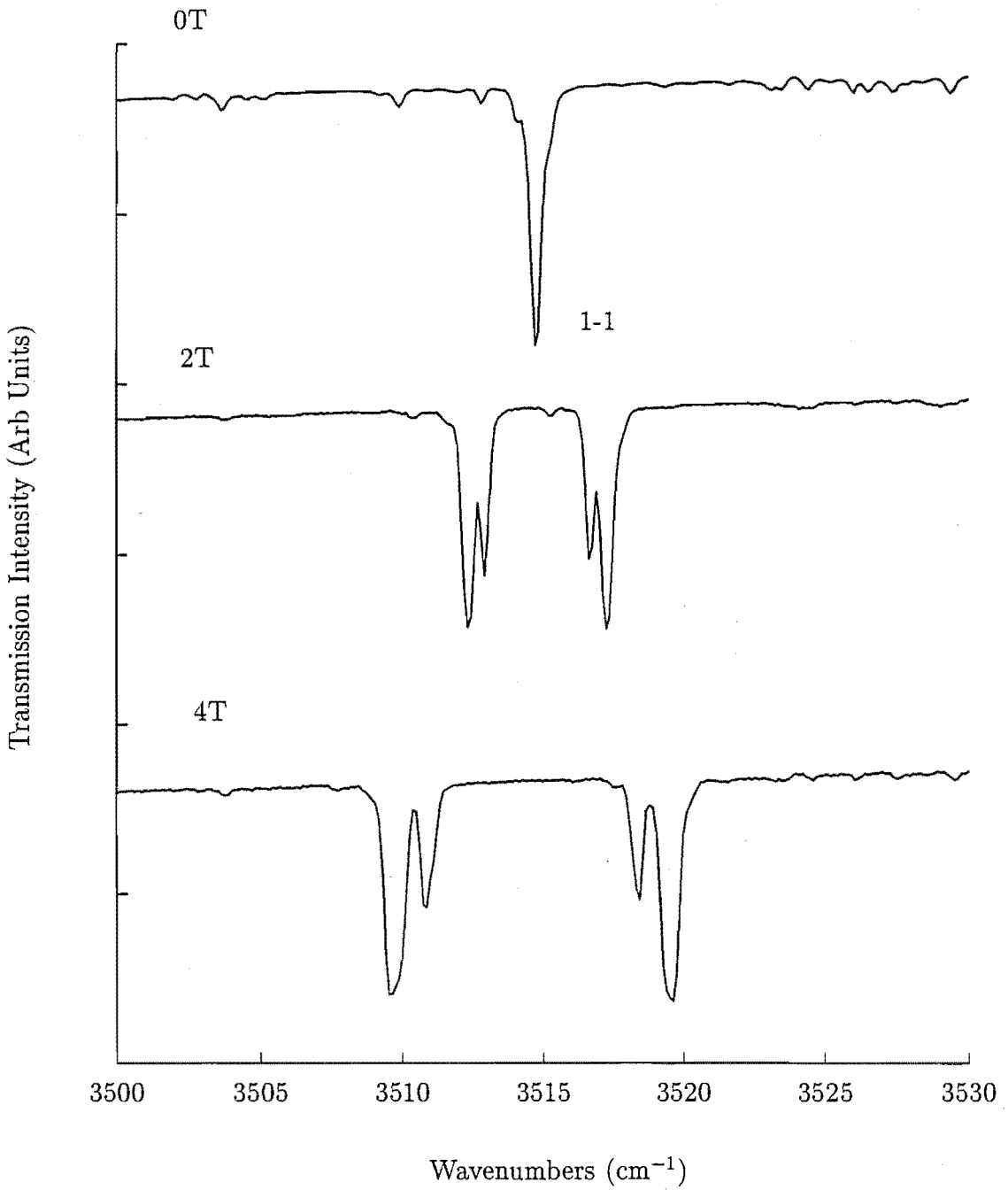

Figure 8.19: 4.2K splitting of the SrF_2:0.05%Sm^{3+} A centre ${}^6H_{\frac{5}{2}}(Z_1\gamma_6) \rightarrow {}^6H_{\frac{11}{2}}(W_1\gamma_6)$ transition as a function of magnetic field directed along a $\langle 111 \rangle$ axis.

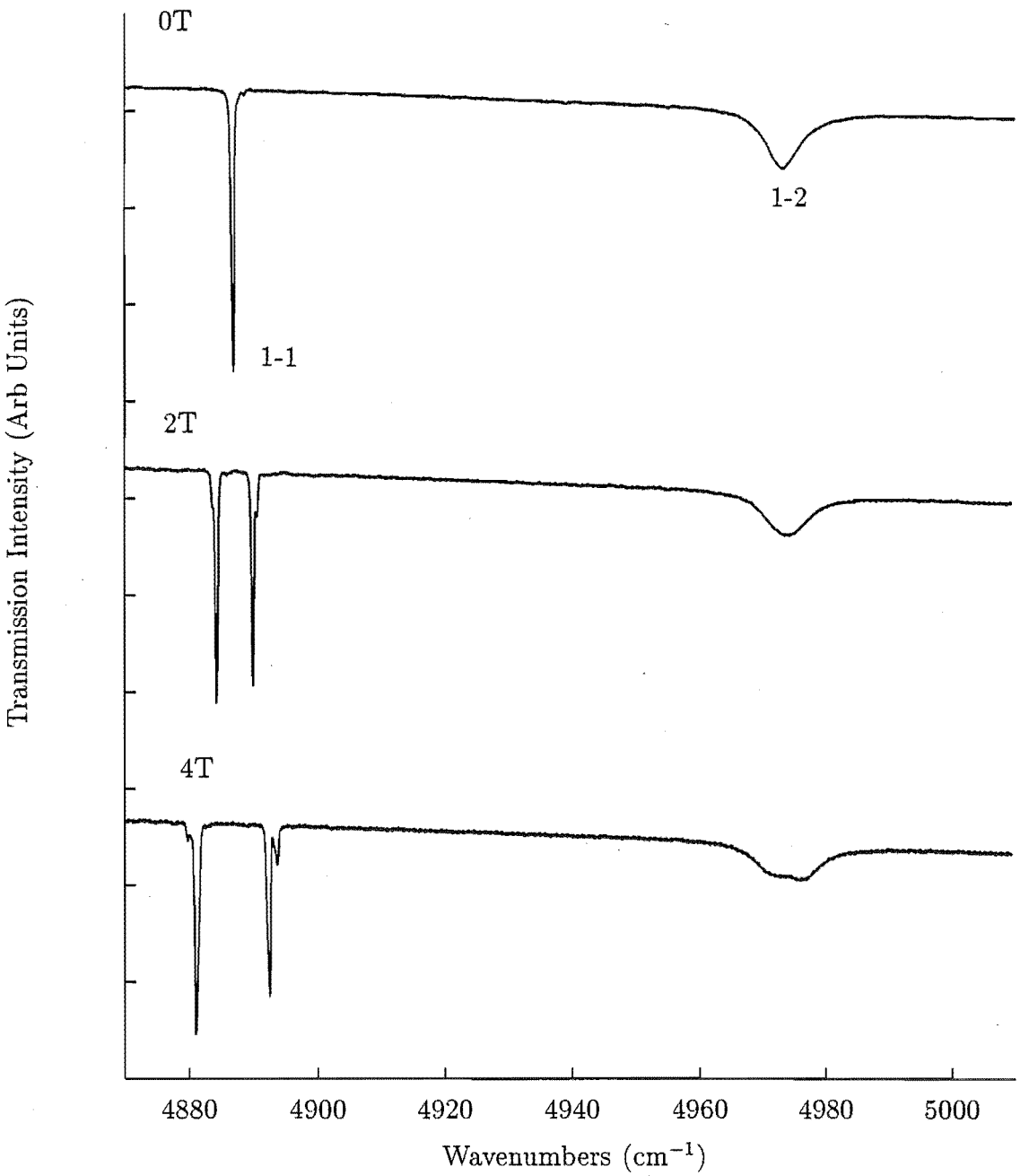

Figure 8.20: 4.2K splitting of the SrF_2:0.05%Sm^{3+} A centre ${}^6H_{\frac{5}{2}}(Z_1\gamma_6) \rightarrow {}^6H_{\frac{13}{2}}(V_1\gamma_6)$ and $(V_2\gamma_7)$ transitions as a function of magnetic field directed along a $\langle 111 \rangle$ axis.

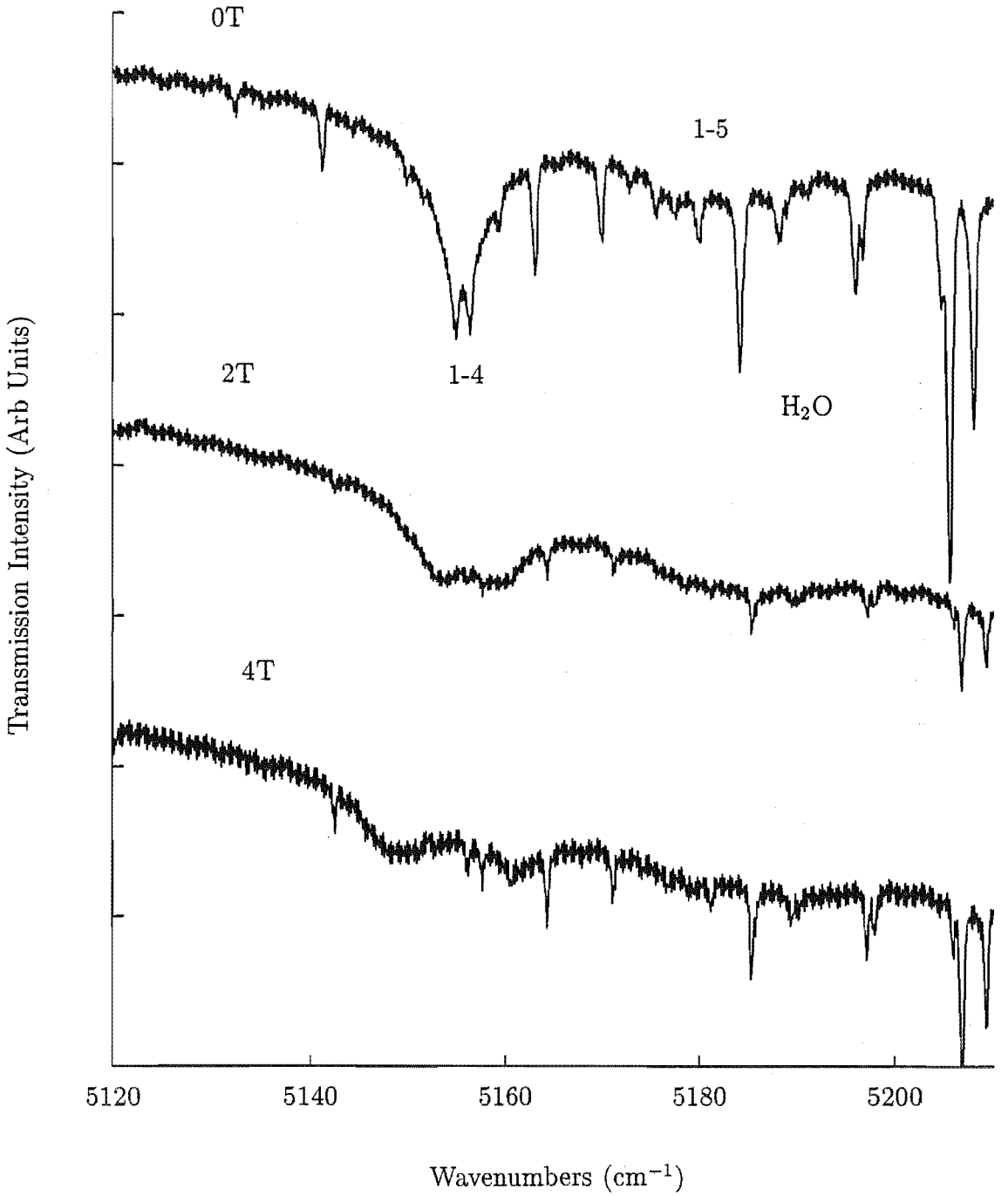

Figure 8.21: 4.2K splitting of the SrF_2:0.05%Sm^{3+} A centre ${}^6F_{\frac{5}{2}}(Z_1\gamma_6) \rightarrow {}^6H_{\frac{13}{2}}(V_4\gamma_7)$ and $(V_5\gamma_6)$ transitions as a function of magnetic field directed along a $\langle 111 \rangle$ axis.

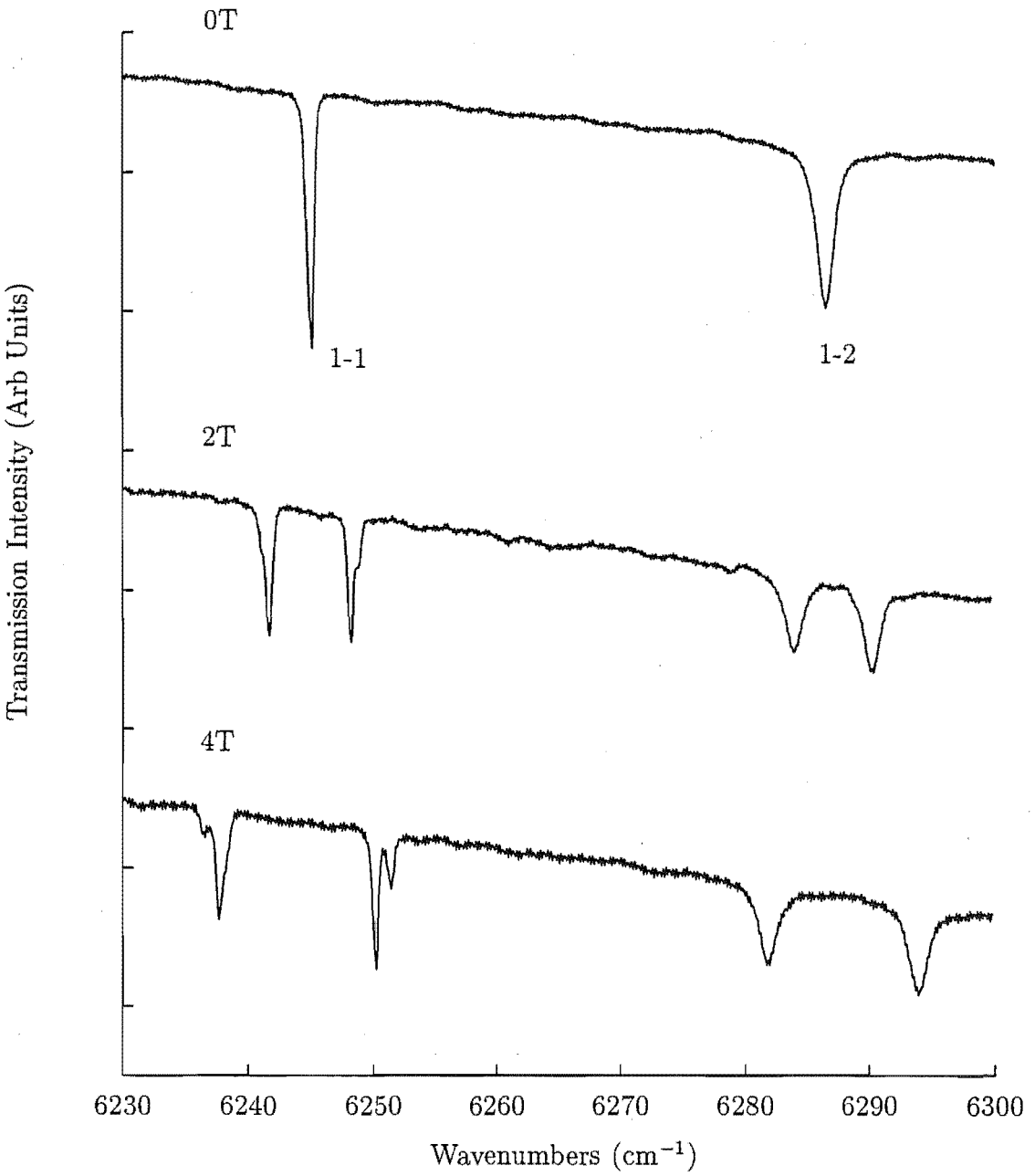

Figure 8.22: 4.2K splitting of the SrF_2:0.05%Sm^{3+} A centre $^6H_{\frac{5}{2}}(Z_1\gamma_6)\rightarrow(S_1\gamma_7)$ and $(S_2\gamma_6)$ transitions as a function of magnetic field directed along a $\langle 111\rangle$ axis.

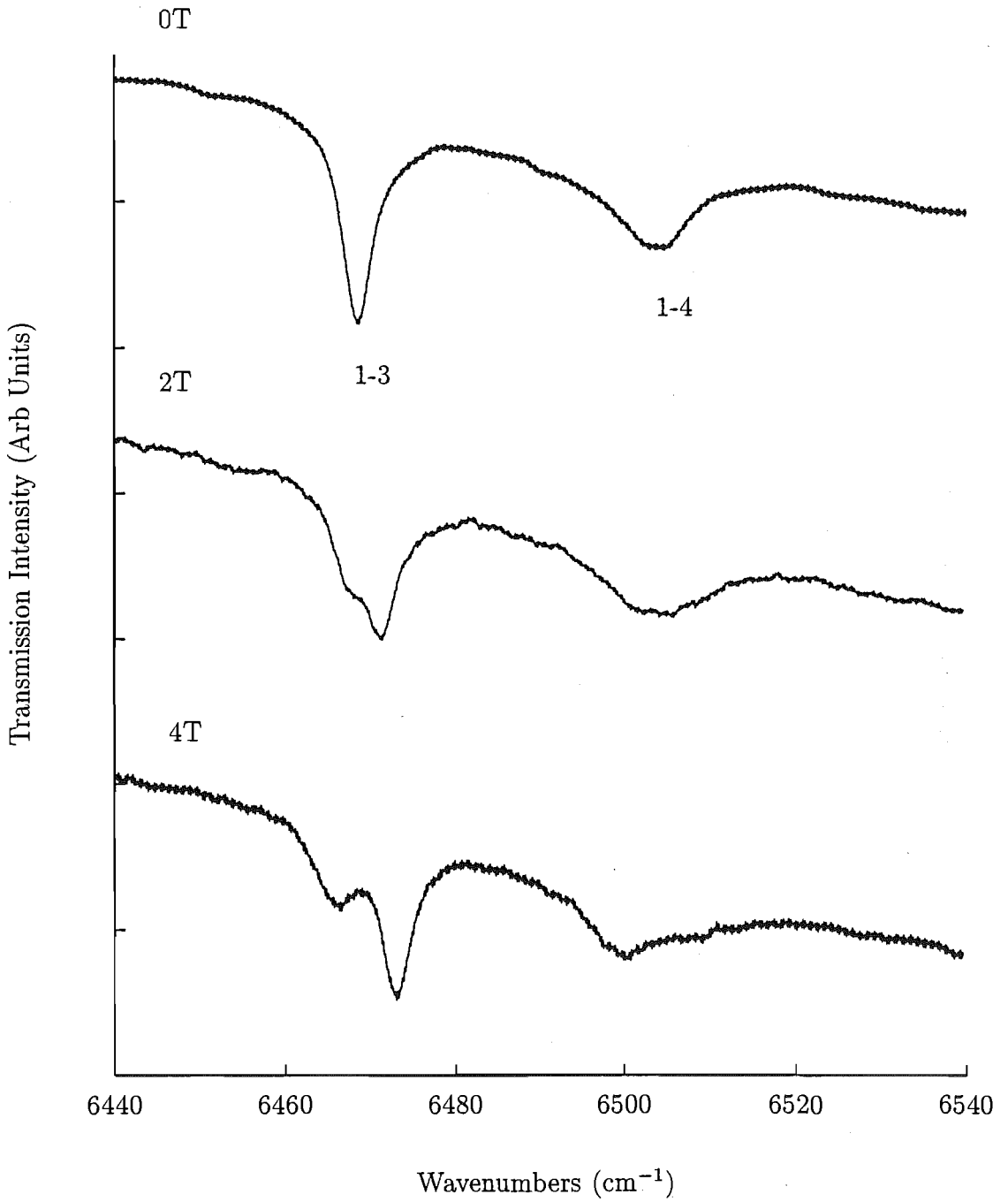

Figure 8.23: 4.2K splitting of the SrF_2:0.05%Sm^{3+} A centre $^6H_{\frac{5}{2}}(Z_1\gamma_6)\rightarrow(S_3\gamma_6)$ and $(S_4\gamma_6)$ transitions as a function of magnetic field directed along a $\langle 111\rangle$ axis.

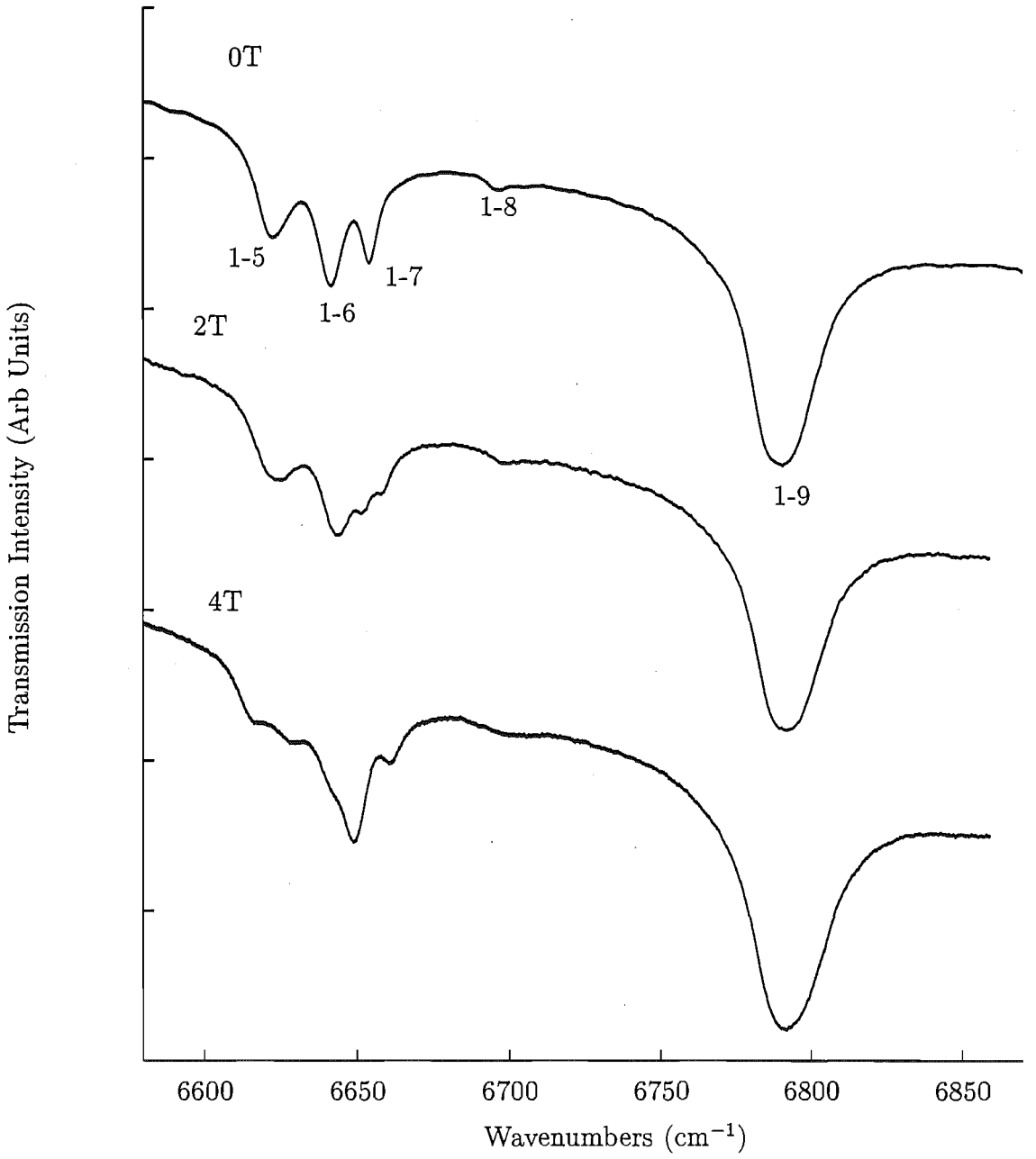

Figure 8.24: 4.2K splitting of the SrF_2:0.05%Sm^{3+} A centre $^6H_{\frac{5}{2}}(Z_1\gamma_6)\rightarrow(S_5\gamma_6)$, $(S_6\gamma_7)$, $(S_7\gamma_7)$, $(S_8\gamma_7)$ and $(S_9\gamma_6)$ transitions as a function of magnetic field directed along a $\langle 111\rangle$ axis.

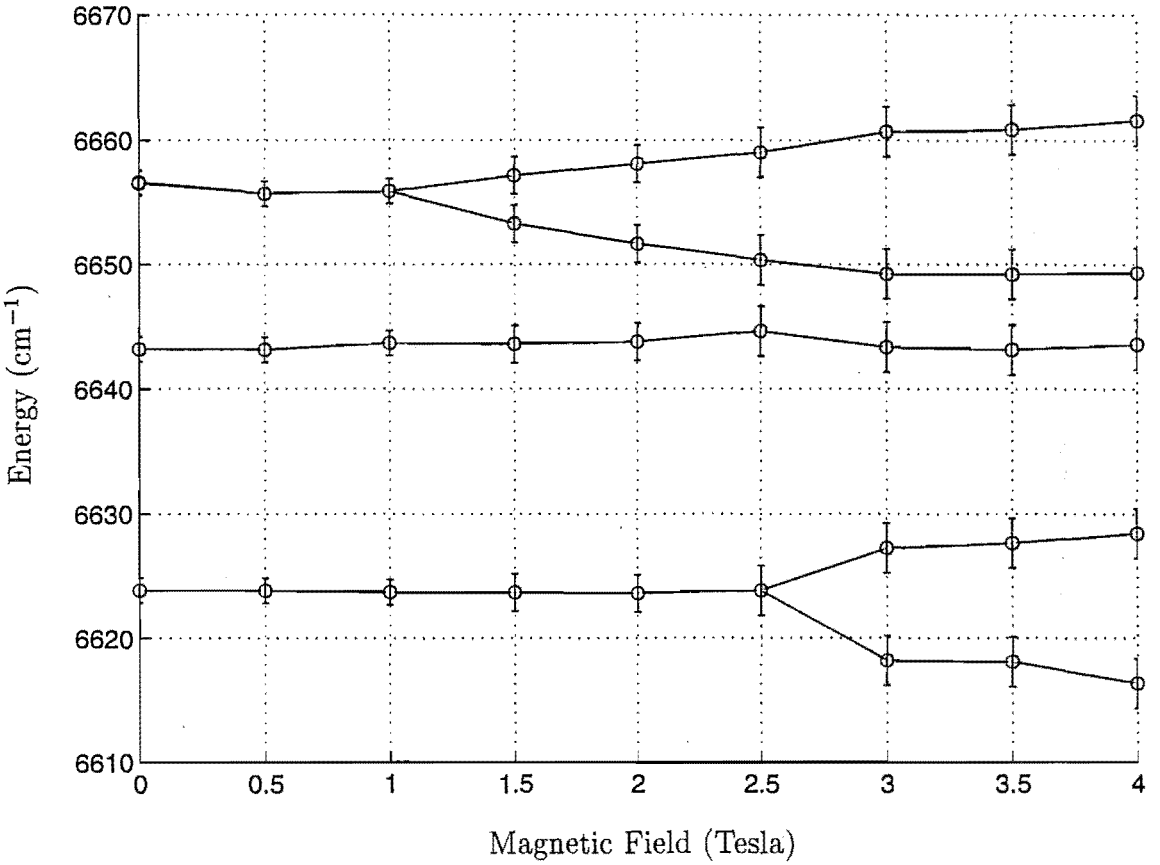

Figure 8.25: Splitting pattern of the SrF_2:0.05%Sm^{3+} A centre $Z_1\gamma_6 \rightarrow S_5\gamma_6$, $S_6\gamma_7$ and $S_7\gamma_7$ transitions as a function of magnetic field directed along a ⟨111⟩ axis. The solid lines are to guide the eye.

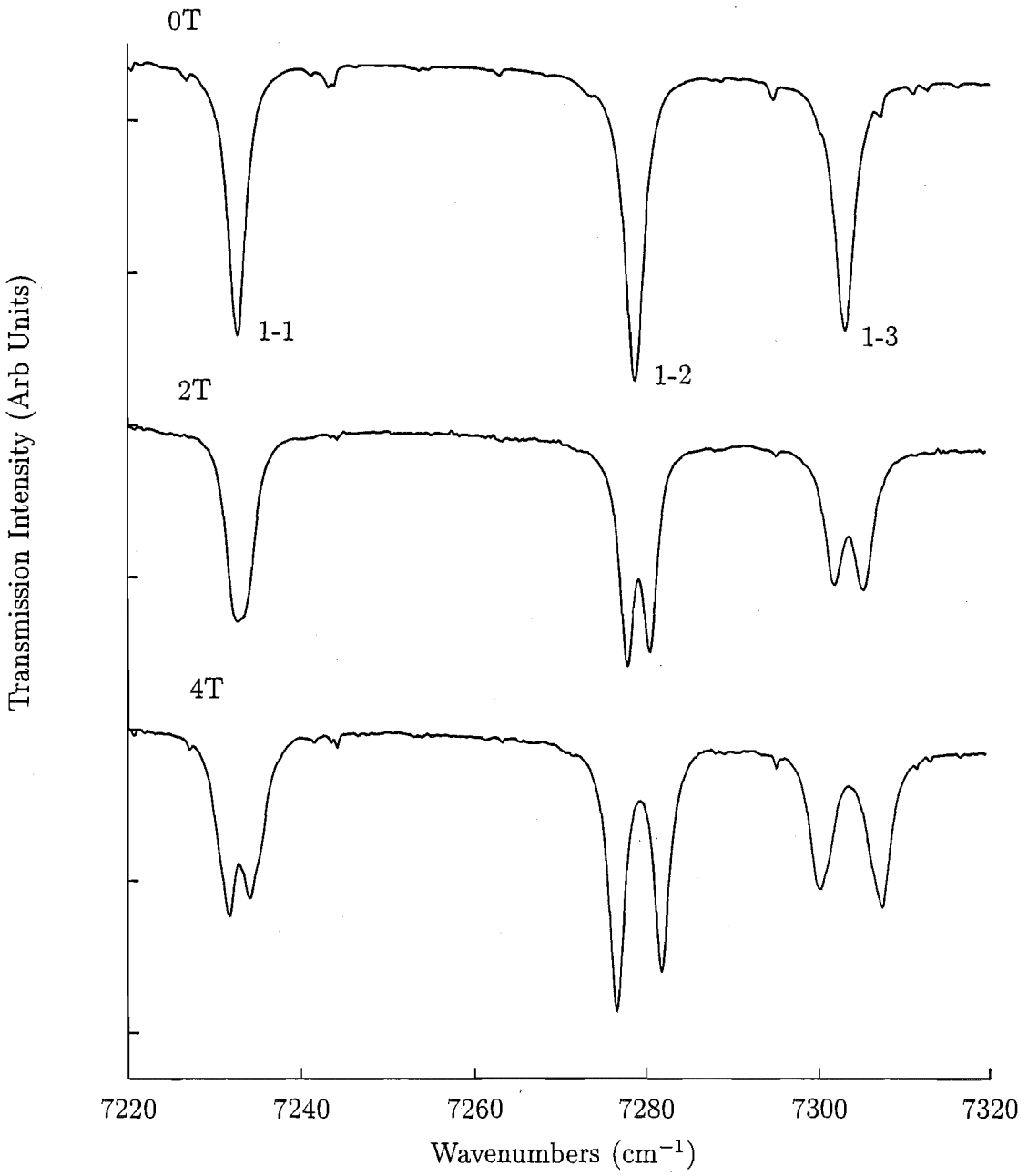

Figure 8.26: 4.2K splitting of the SrF_2:0.05%Sm^{3+} A centre ${}^6H_{\frac{5}{2}}(Z_1\gamma_6) \rightarrow {}^6F_{\frac{5}{2}}(R_1\gamma_7)$, $(R_2\gamma_6)$ and $(R_3\gamma_7)$ transitions as a function of magnetic field directed along a $\langle 111 \rangle$ axis.

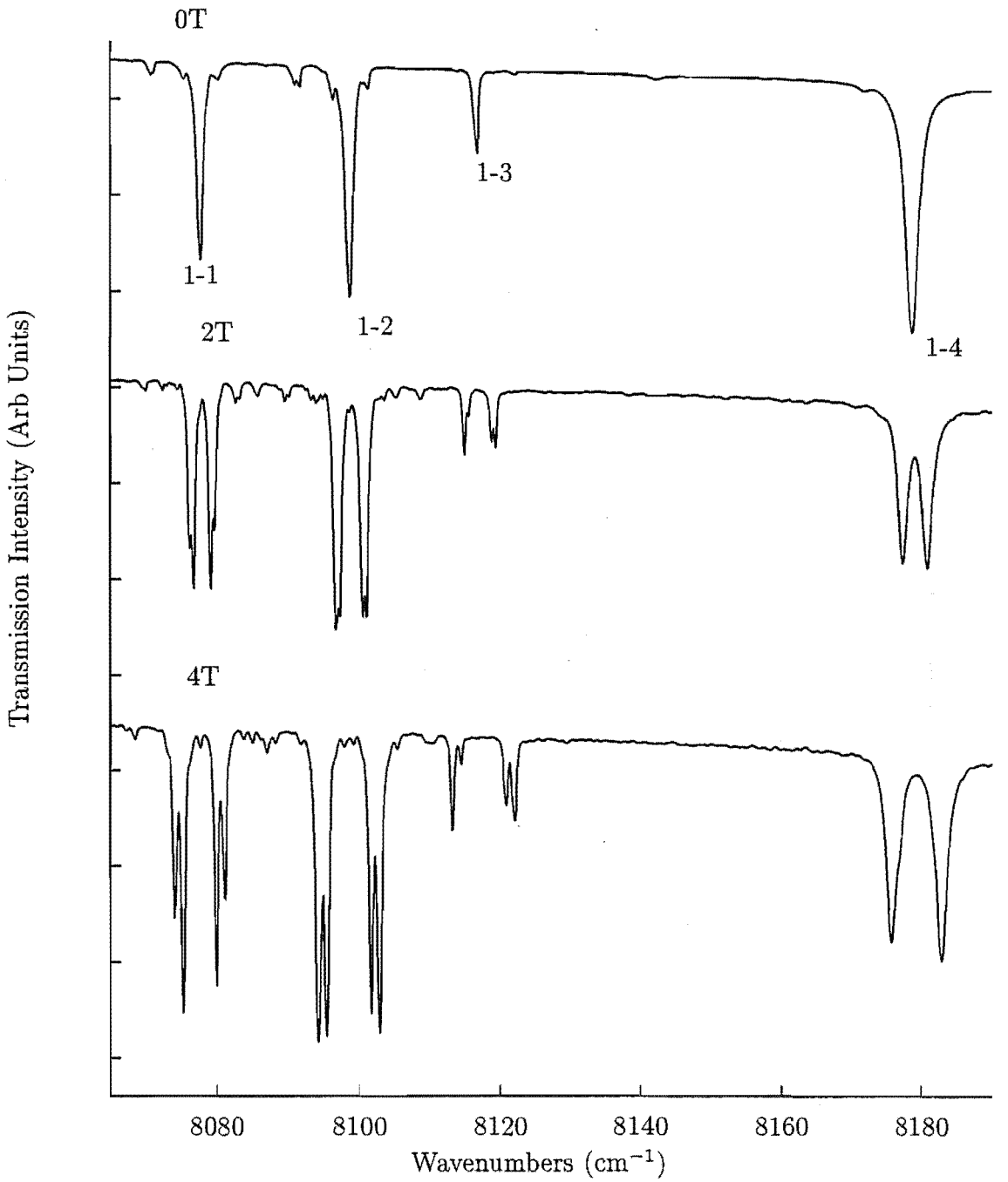

Figure 8.27: 4.2K splitting of the SrF_2:0.05%Sm^{3+} A centre ${}^6H_{\frac{5}{2}}(Z_1\gamma_6) \rightarrow {}^6F_{\frac{7}{2}}(Q_1\gamma_7)$, $(Q_2\gamma_6)$, $(Q_3\gamma_7)$ and $(Q_4\gamma_6)$ transitions as a function of magnetic field directed along a $\langle 111 \rangle$ axis.

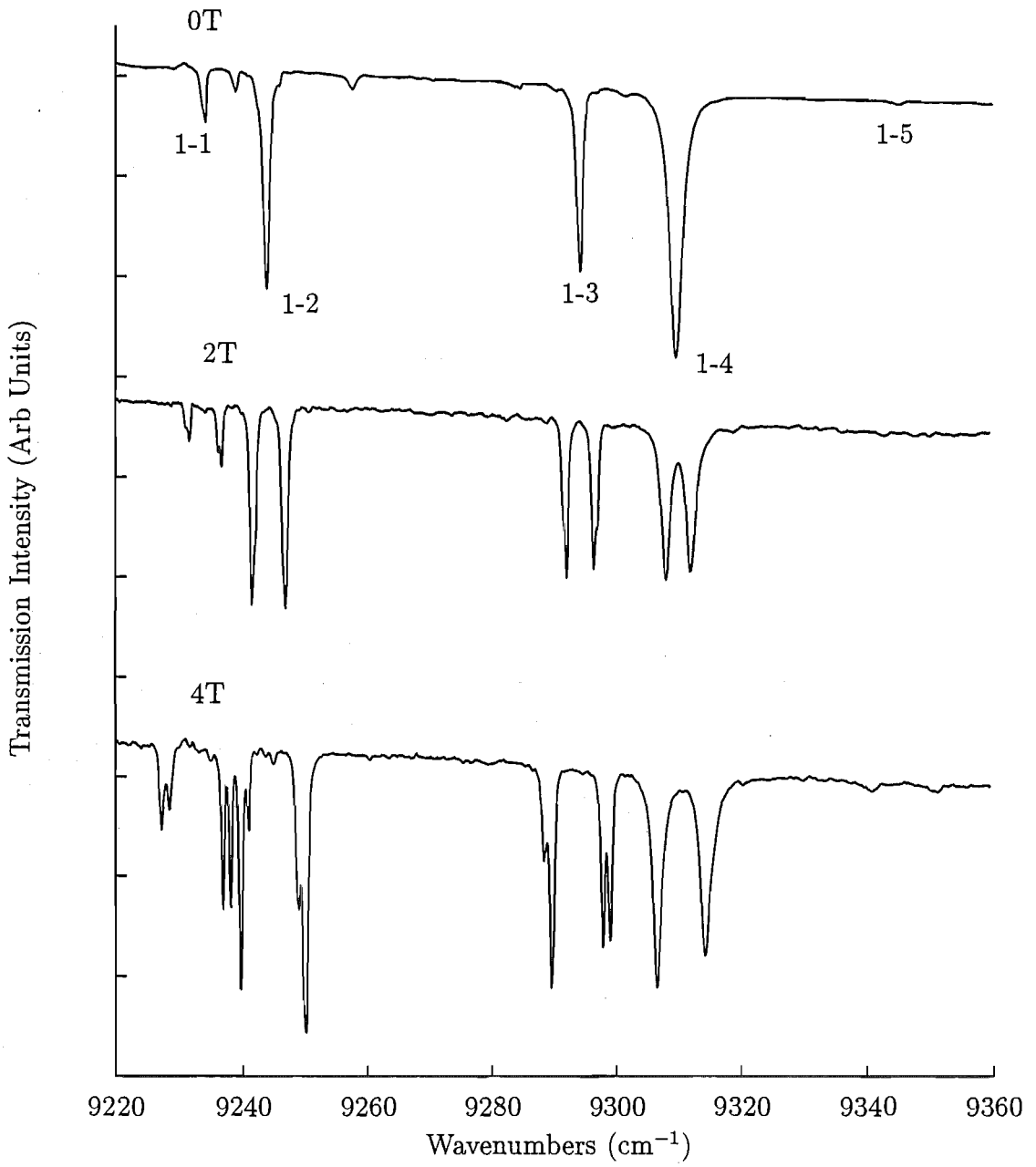

Figure 8.28: 4.2K splitting of the SrF_2:0.05%Sm^{3+} A centre $^6H_{\frac{5}{2}}(Z_1\gamma_6) \rightarrow {}^6F_{\frac{9}{2}}(P_1\gamma_6)$, $(P_2\gamma_6)$, $(P_3\gamma_7)$ and $(P_4\gamma_6)$ transitions as a function of magnetic field directed along a $\langle 111 \rangle$ axis.

8.3 $CaF_2:Eu^{3+}$

8.3.1 Infrared Spectroscopy

The infrared absorption spectra of a 25 mm thick CaF_2:0.05%Eu^{3+} crystal have been recorded. The crystal was cooled to 10K. Absorption transitions to the $^7F_2$, $^7F_3$, $^7F_4$ and $^7F_6$ multiplets have been studied. No transitions to the $^7F_5$ multiplet could be observed. This is because strong absorption due to atmospheric water vapour dominates the 3600 - 3900 cm^{-1} region. The recorded spectra are shown in Figures 8.29 and 8.30.

Only one transition to the $^7F_2$ multiplet can be observed at 971.3 cm^{-1}. This is to the $X_2\gamma_5$ state of the tetragonal symmetry A centre. The spectrum is shown in Figure 8.29(a).

Transitions to the $^7F_3$ multiplet are difficult to observe. This is because they occur in a region of intense atmospheric absorption (1300 - 2000 cm^{-1}). In addition to this, they are weak due to the $\Delta J=2, 4, 6$ electric dipole selection rule for an initial state of J=0. Thus, they can only occur through admixtures of states of different J. This is provided by the crystal field. To help identify these transitions, the spectrum recorded at 10K was ratioed against a spectrum recorded at room temperature. This isolates the transitions that increase in intensity, as the crystal gets colder (see Figure 8.29(b)). Two transitions are observed. Both of these are A centre transitions. This information is presented in Table 8.7. Transition energies, relative intensities and linewidth data is given for the R and Q centres in Tables 8.8 and 8.9.

Absorption transitions to the $^7F_4$ and $^7F_6$ multiplets occur in the 2500 - 3200 cm^{-1} and 4800 - 5200 cm^{-1} regions, respectively. The recorded spectra are considerably more complicated than those for the $^7F_2$ and $^7F_3$ multiplets. As with CaF_2:0.05%Sm^{3+}, the complexity arises because of transitions associated with cluster centres. The spectra are shown in Figure 8.30. Several aspects of these spectra deserve discussion. Three absorption features at 2846.9, 2915.8 and 2964.2 cm^{-1} are due to contamination of the crystal surfaces with grease. This is largely due to contact with human tissue. These absorption features are known to increase considerably if grease based copper putties are used to attach the sample, to the sampleholder. Another interesting feature, is the observation of a transition to the near cubic O centre level at 2884.2 cm^{-1}. $\Delta J=4$ transitions are magnetic dipole forbidden. Therefore, this centre must have a small electric dipole moment. This indicates that the charge compensating fluorine ion is nearby. This assertion is supported by the observation of the $^5D_0 \rightarrow ^7F_0$ transition by Jouart et. al. [92] .

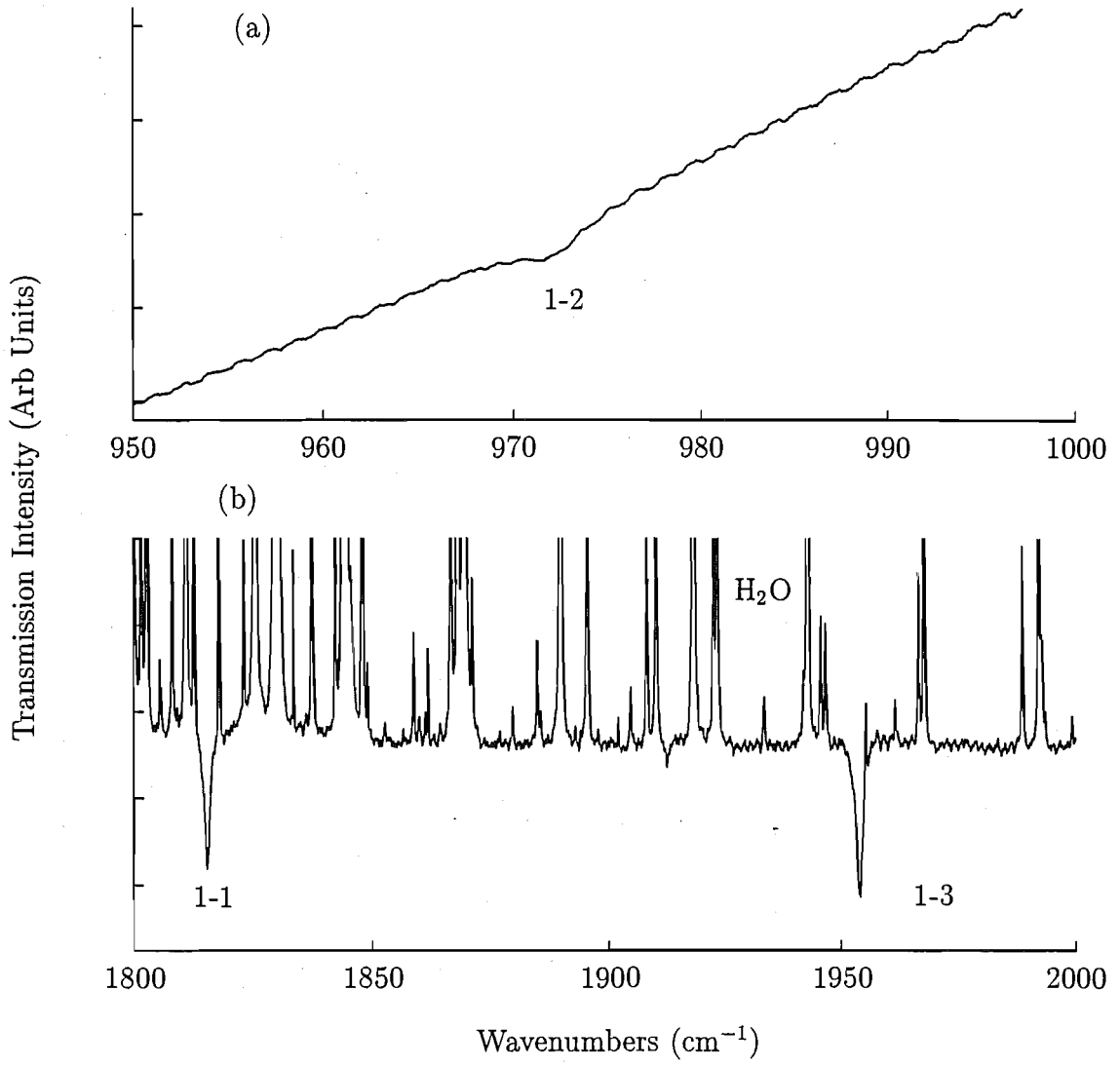

Figure 8.29: Infrared absorption spectra for the (a) $^7F_2$ and (b) $^7F_3$ multiplets in CaF_2:0.05%Eu^{3+}. The spectra were recorded at 10K. Transitions to crystal field levels of the A centre are labelled by their arbitrary numerical labels. The $^7F_3$ multiplet spectrum has been ratioed against a room temperature spectrum.

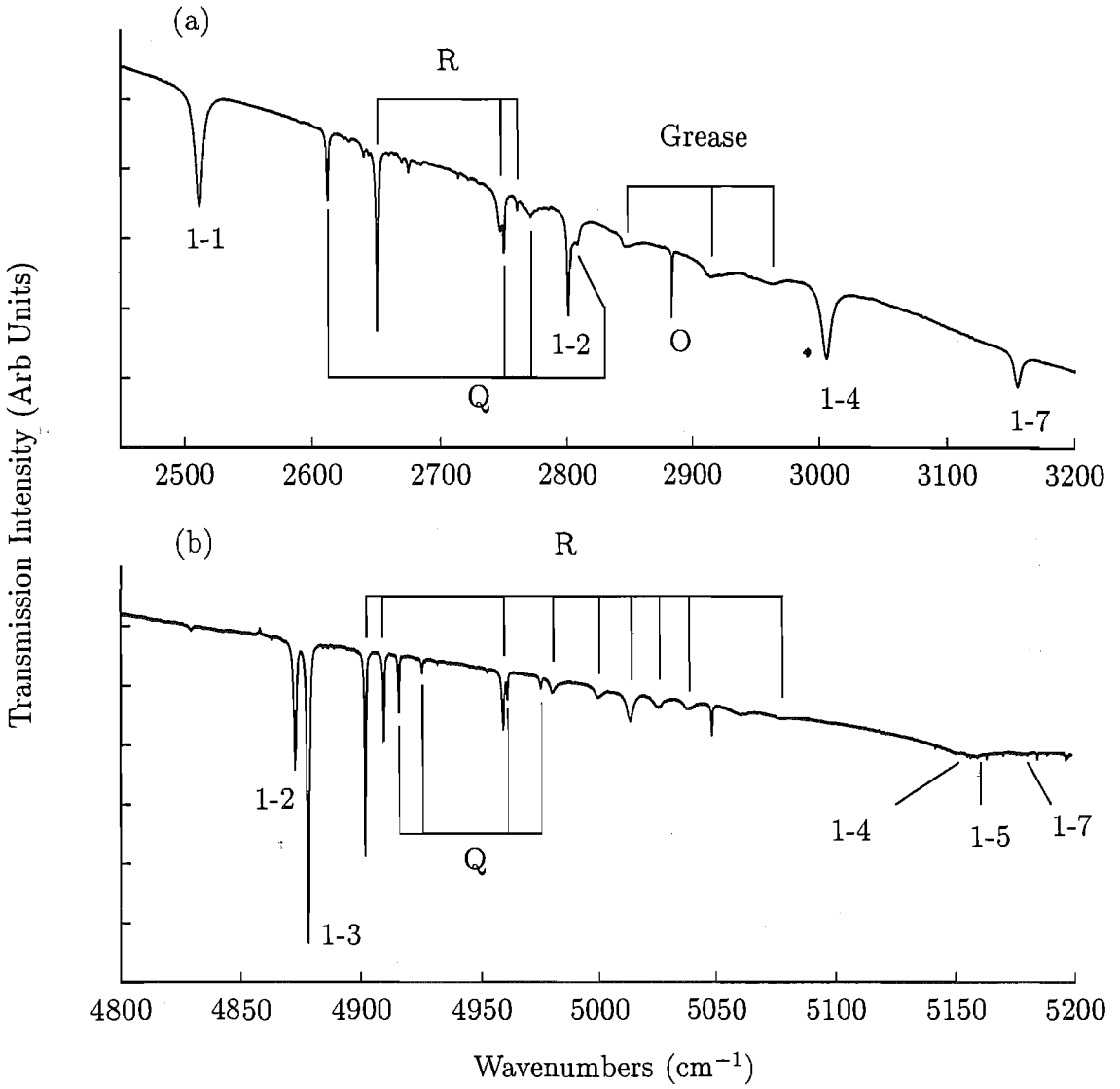

Figure 8.30: Infrared absorption spectra for the (a) $^7F_4$ and (b) $^7F_6$ multiplets in CaF_2:0.05%Eu^{3+}. The spectra were recorded at 10K. Transitions to crystal field levels of the A centre are labelled by their arbitrary numerical labels.

Table 8.7: Energy levels (in vacuum cm^{-1}, ± 0.2), intensities (relative to the strongest line in the spectrum (=100.00), ± 0.50) and linewidths (in cm^{-1}, ± 0.2) as measured in absorption to A centre crystal field levels of the $^7F_2$, $^7F_3$, $^7F_4$ and $^7F_6$ multiplets in CaF_2:0.05%Eu^{3+}

Multiplet	Transition	Energy	Intensity	Linewidth
$^7F_2$	$Z_1\gamma_1 \rightarrow X_2\gamma_5$	971.3	27.3	2±0.3
$^7F_3$	$\rightarrow W_1\gamma_5$	1815.3	2.3	0.9
	$\rightarrow W_3\gamma_5$	1954.1	4.1	4.2
$^7F_4$	$\rightarrow V_1\gamma_1$	2511.7	82.6	4.0
	$\rightarrow V_2\gamma_5$	2801.4	18.7	1.0
	$\rightarrow V_4\gamma_5$	3006.5	83.6	4.5
	$\rightarrow V_7\gamma_1$	3156.3	45.30	3.0
$^7F_6$	$\rightarrow T_2\gamma_5$	4872.9	27.5	0.7
	$\rightarrow T_3\gamma_1$	4878.5	100.0	0.7
	$\rightarrow T_4\gamma_2$	5151.4	79.8	16.9
	$\rightarrow T_5\gamma_5$	5160.7	67.9	14.4
	$\rightarrow T_7\gamma_1$	5180.1	21.4	9.4

Table 8.8: Energy levels (in vacuum cm^{-1}, ± 0.2), intensities (relative to the strongest line in the spectrum (=100.00), ± 0.50) and linewidths (in cm^{-1}, ± 0.2) as measured in absorption to Q centre crystal field levels of the $^7F_4$ and $^7F_6$ multiplets in CaF_2:0.05%Eu^{3+}

Multiplet	Transition	Energy	Intensity	Linewidth
$^7F_4$	$\rightarrow V_1$	2612.5	67.2	1.0
	$\rightarrow V_3$	2749.7	98.8	1.5
	$\rightarrow V_4$	2771.1	100.0	7.1
	$\rightarrow V_5$	2808.6	97.7	3.5
$^7F_6$	$\rightarrow T_1$	4916.1	30.8	0.4
	$\rightarrow T_2$	4925.8	11.6	0.6
	$\rightarrow T_3$	4961.4	14.7	0.4
	$\rightarrow T_4$	4975.7	14.7	0.7

Table 8.9: Energy levels (in vacuum cm^{-1}, ± 0.2), intensities (relative to the strongest line in the spectrum (=100.00), ± 0.50) and linewidths (in cm^{-1}, ± 0.2) as measured in absorption to R centre crystal field levels of the $^7F_4$ and $^7F_6$ multiplets in CaF_2:0.05%Eu^{3+}

Multiplet	Transition	Energy	Intensity	Linewidth
	$\rightarrow V_1$	2651.3	100.0	1.3
$^7F_4$	$\rightarrow V_2$	2746.9	55.5	3.5
	$\rightarrow V_3$	2760.4	5.70	1.0
	$\rightarrow T_1$	4902.2	59.2	0.5
	$\rightarrow T_2$	4909.9	20.6	0.5
	$\rightarrow T_3$	4959.5	23.1	0.8
	$\rightarrow T_4$	4980.6	10.6	1.7
$^7F_6$	$\rightarrow T_5$	5000.2	12.6	2.4
	$\rightarrow T_6$	5013.9	33.5	2.2
	$\rightarrow T_7$	5025.9	22.2	3.8
	$\rightarrow T_8$	5038.6	13.7	3.1
	$\rightarrow T_9$	5077.9	5.9	3.1

8.3.2 Zeeman Infrared Spectroscopy

Zeeman measurements have been performed for a CaF_2:0.05%Eu^{3+} sample. The crystal was 11.83 mm in length. The magnetic field was directed along the $\langle 111 \rangle$ axis of the crystal. The field strength was varied up to the maximum available field, of 4 Tesla.

The only observable transition to the $^7F_2$ multiplet has been noted to be broad. No Zeeman splittings for this 971.3 cm^{-1} transition could be obtained.

Two transitions have been observed to the $^7F_3$ multiplet. These transitions have measured frequencies of 1815.3 and 1954.1 cm^{-1}. They are assigned as terminating on the $W_1\gamma_5$ and $W_3\gamma_5$ doublet states by comparision with the polarised laser selective excitation studies of chapter 6. The spectra of these transitions, as a function of magnetic field, is shown in Figure 8.31. Only the 1954.1 cm^{-1} transition is observed to split. A two-fold splitting is observed. This is consistent with the tetragonal C_{4v} symmetry assigned for the A centre as the ground state is a singlet. A magnetic splitting factor of 2.2 is measured. This is in reasonable agreement with the calculated value of 2.60. The 1815.3 cm^{-1} transition does not split but broadens considerably upon application of the field. This is expected because the calculated splitting factor of 0.71 is small.

The Zeeman spectrum of absorption transitions to the $^7F_4$ multiplet is shown in Figure 8.32. Four transitions associated with the C_{4v} symmetry A centre are observed. Of these, the 2511.7 and 3156.3 cm^{-1} transitions have been assigned as singlets from polarised laser selective excitation. No Zeeman effect would be expected for these transitions. It can be seen in Figure 8.32, that these assignments are confirmed by the Zeeman experiments. The 3006.52 cm^{-1} transition is assigned as terminating on a doublet state. In conflict with this, no Zeeman splitting can be observed for this transition. This can be explained if the zero-field linewidth of 4.5 cm^{-1} is considered. The calculated magnetic splitting factor is 0.93. Thus, we would not expect to see a splitting in this line-profile. The behaviour of the 2801.4 cm^{-1} transition is more difficult to analyse. This is due to the presence of a nearby Q centre transition at 2808.6 cm^{-1}. In addition, there is an overlapping R transition not directly observable at zero field. At 4 Tesla, the Q centre line has moved to higher energy and splits into two lines. The R centre line is now directly observable. It is 2.1 cm^{-1} higher in energy than the A centre line which appears unsplit. A cubic centre line at 2884.2 cm^{-1} can also be observed. This is split into two lines. The magnetic splitting factor for this state is 0.8.

Figure 8.33 shows the Zeeman spectrum for the 4872.9 and 4878.5 cm^{-1} transitions of the A centre. The 4872.9 cm^{-1} state has been assigned as the $T_2\gamma_5$ doublet, whilst the 4878.5 cm^{-1} state is assigned as $T_3\gamma_1$. At 4 Tesla, the 4872.9 cm^{-1} transition has broadened, but no resolvable splitting is apparant. From this, we infer that the [111] magnetic splitting factor is close to 0.3. This is consistent with the calculated value, of 0.21. From 1.5 Tesla onward, an additional feature is observed on the low frequency side of the 4872.9 cm^{-1} transition. It can be seen to grow in intensity as the magnetic field strength is increased. This is a transition to the $T_1\gamma_4$ state. Such a transition is forbidden under C_{4v} symmetry because the ground state has γ_1 irrep symmetry. It can be observed due to a non-linear Zeeman effect between the γ_4 state and the nearby γ_5 state, 7.5 cm^{-1} higher in energy. This interaction has the effect of mixing the wavefunctions of the two states thereby allowing the $T_1\gamma_4$ transition to occur. Figure 8.34 shows the Zeeman splitting diagram for the three states. The non-linearity of the splittings observed indicates a mixing of the crystal field wavefunctions due to the perturbing magnetic field. An additional transition is observed to the high frequency end of the displayed spectrum. This is a Zeeman split sublevel of a nearby R centre transition. Figure 8.35 shows the splitting of higher frequency transitions of the A centre. These transitions terminate on the $T_4\gamma_2$ 5151.4 cm^{-1}, $T_5\gamma_5$ 5160.7 cm^{-1} and the $T_7\gamma_1$ 5180.1 cm^{-1} states. In this case, the linewidths are phonon broadened and no splitting is resolvable when a magnetic field is applied.

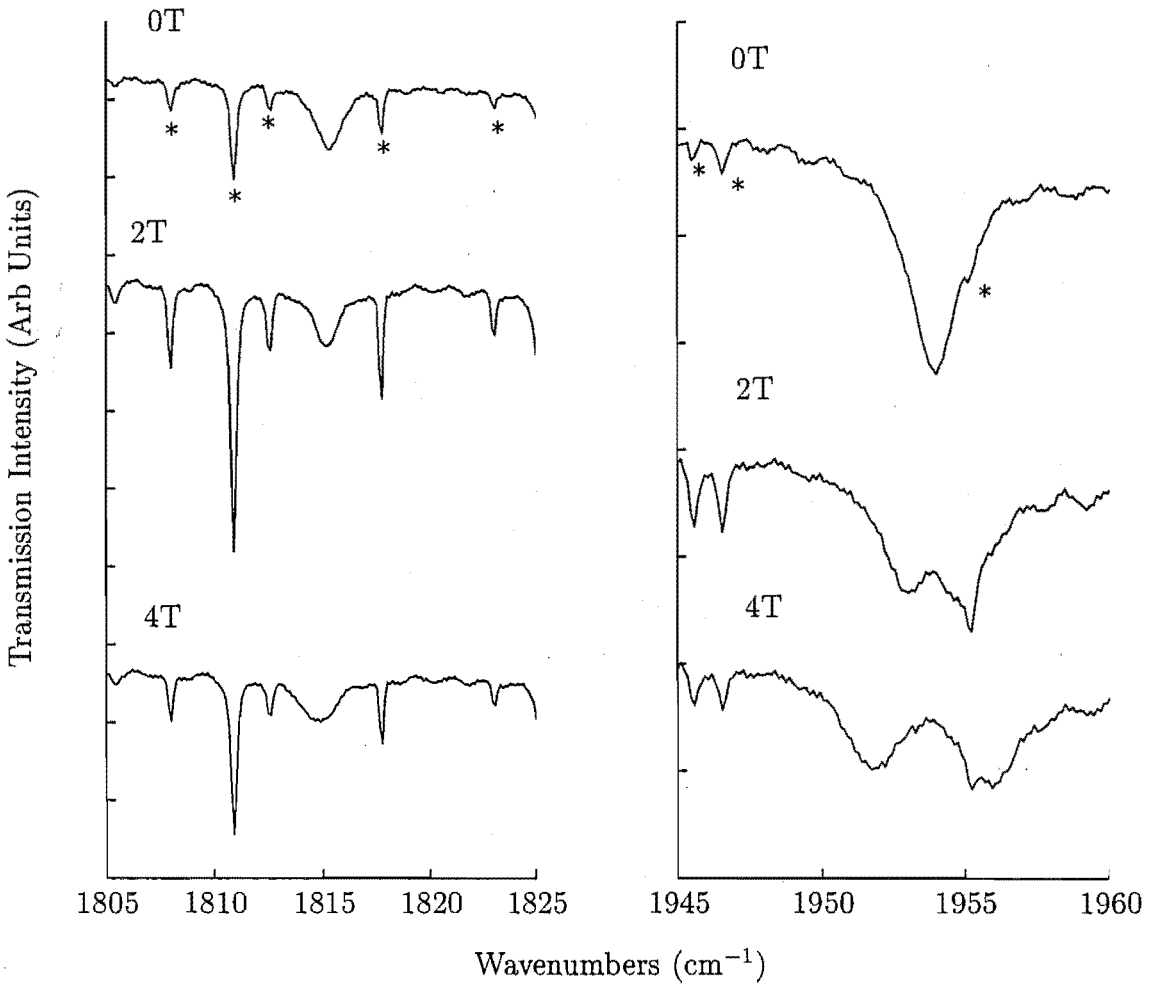

Figure 8.31: 4.2K splitting of the CaF_2:0.05%Eu^{3+} A centre $^7F_3$ transitions as a function of the magnetic field directed along a ⟨111⟩ axis. The * notation indicates atmospheric absorption.

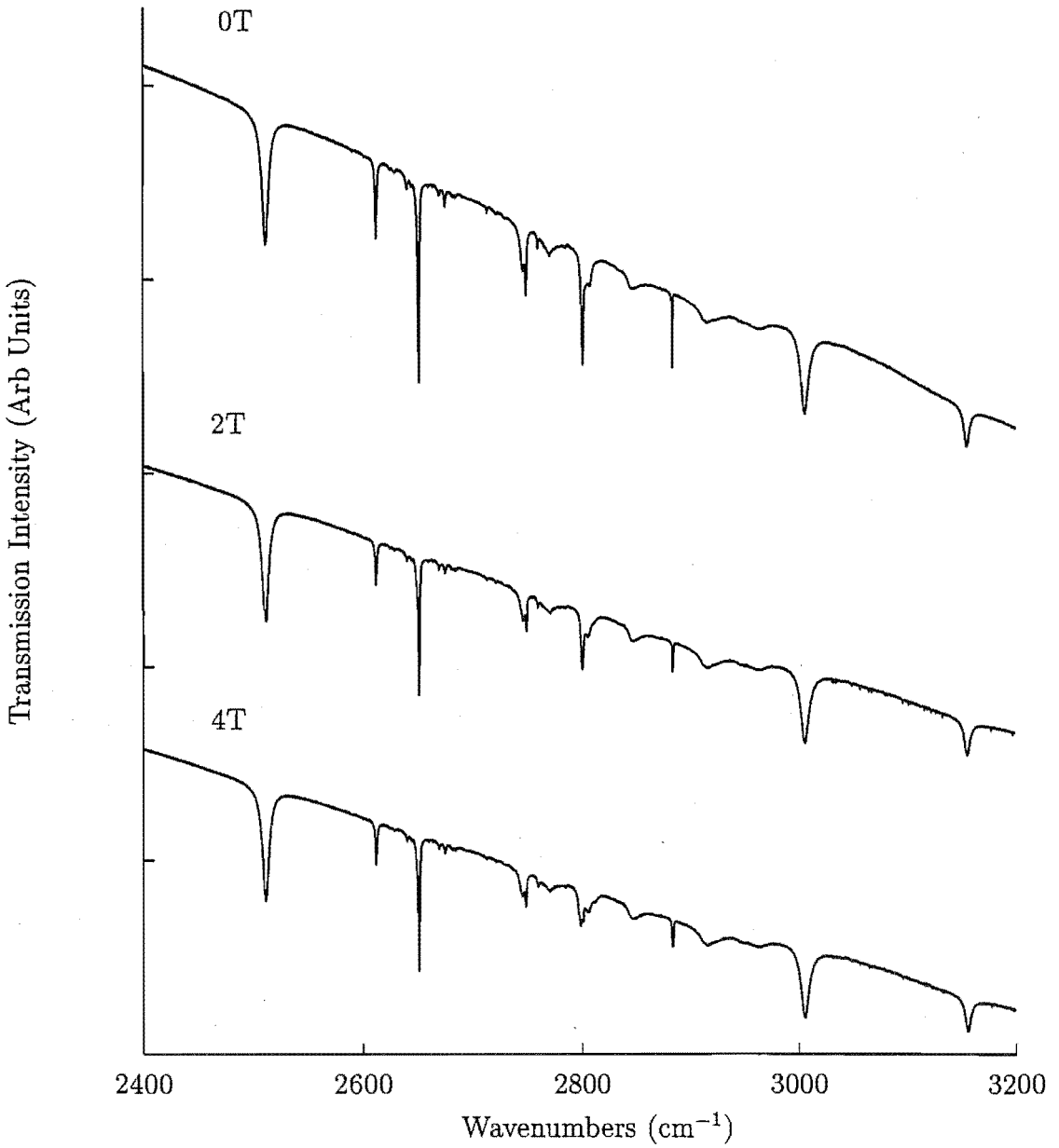

Figure 8.32: 4.2K splitting of the CaF_2:0.05%Eu^{3+} $^7F_4$ transitions as a function of the magnetic field directed along a ⟨111⟩ axis.

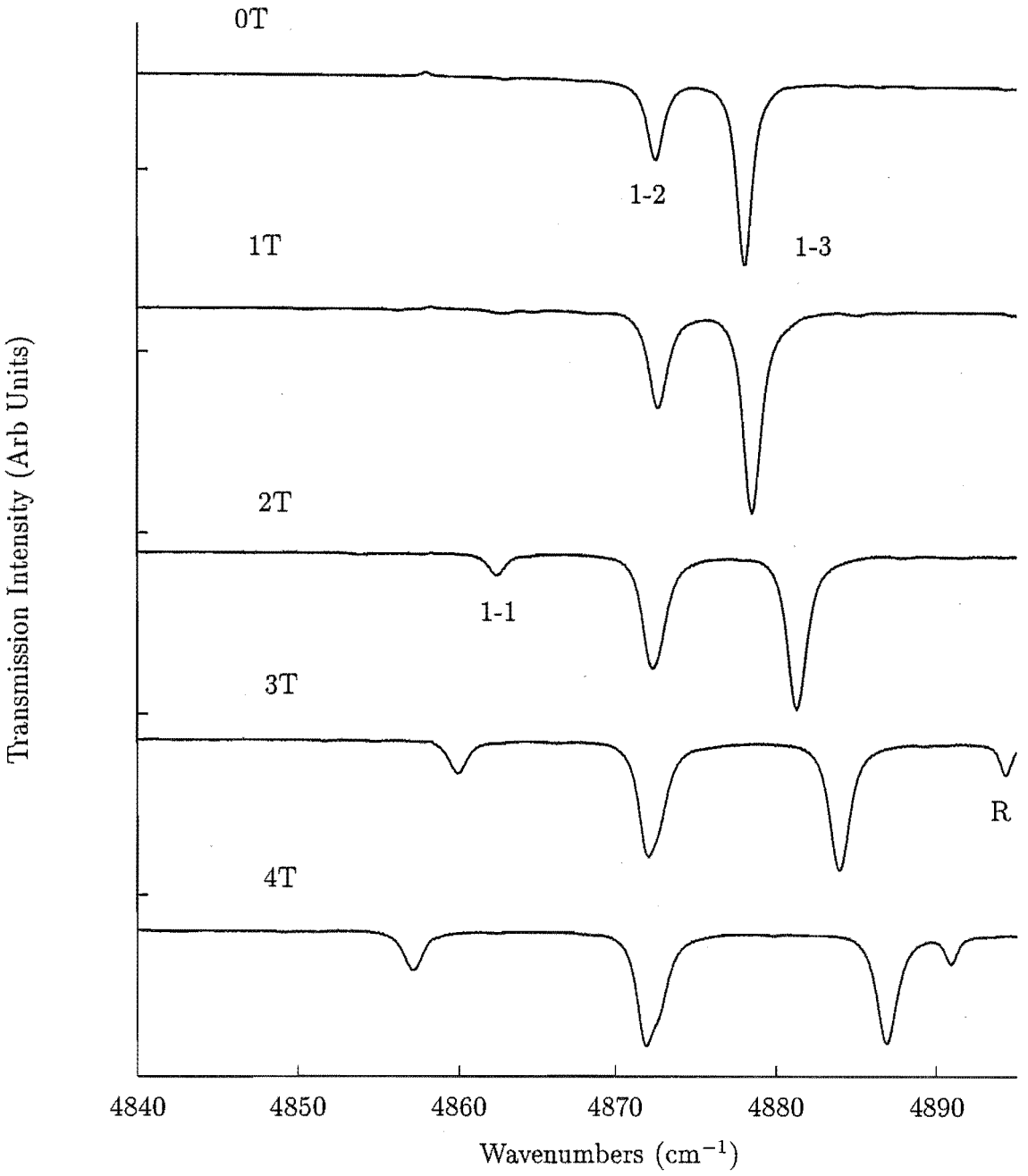

Figure 8.33: 4.2K splitting of the CaF_2:0.05%Eu^{3+} A centre $^7F_6(T_1\gamma_4)$, $(T_2\gamma_5)$ and $(T_3\gamma_1)$ states as a function of the magnetic field directed along a ⟨111⟩ axis. R indicates a Zeeman split sublevel of a nearby R centre line.

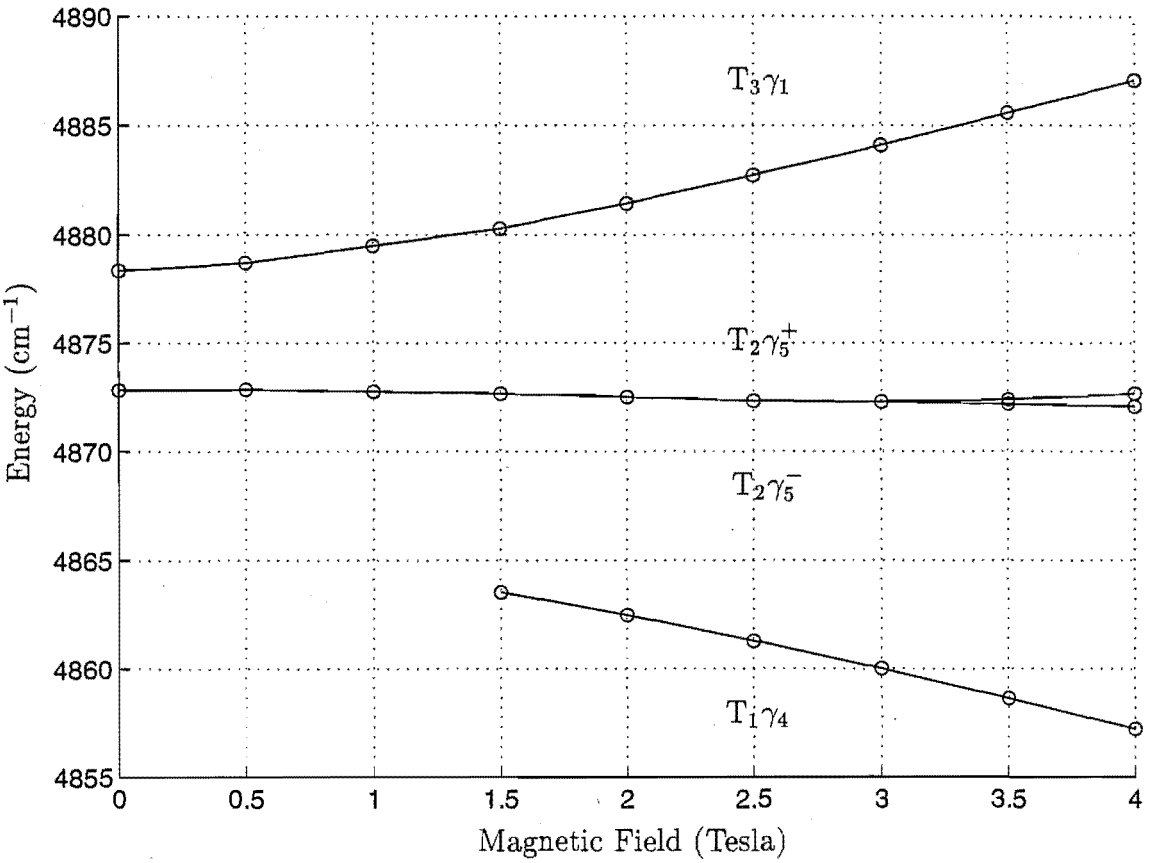

Figure 8.34: Zeeman splitting diagram for the CaF_2:Eu^{3+} A centre $^7F_6(T_1\gamma_4)$, $(T_2\gamma_5)$ and $(T_3\gamma_1)$ levels in a (111) applied magnetic field. The open circles are the experimental points and the solid lines are to guide the eye.

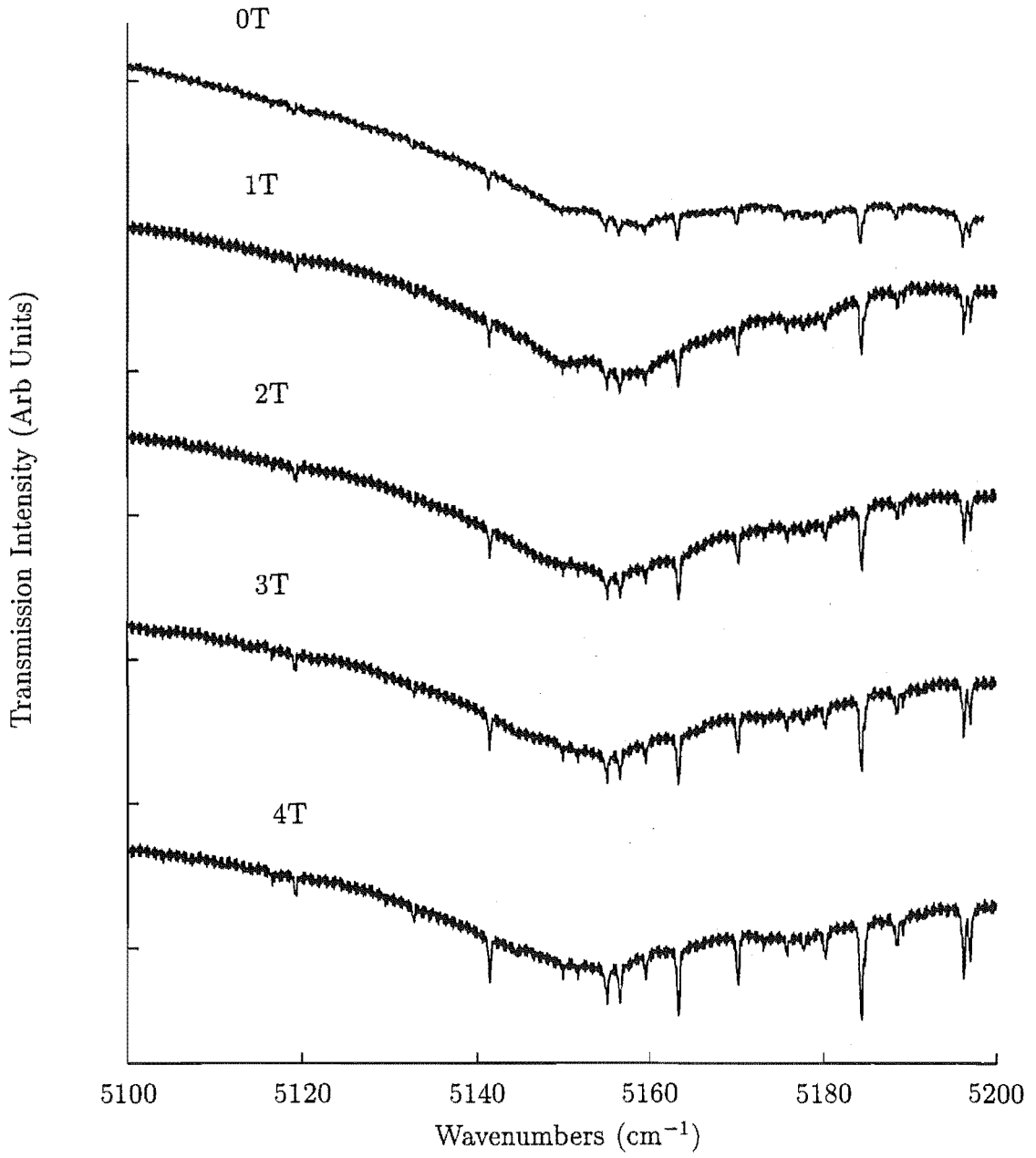

Figure 8.35: 4.2K splitting of the CaF_2:0.05%Eu^{3+} A centre $^7F_6(T_4\gamma_2)$, $(T_5\gamma_5)$ and $(T_7\gamma_1)$ states as a function of the magnetic field directed along a $\langle 111 \rangle$ axis.

8.4 SrF_2:Eu^{3+}

8.4.1 Infrared Spectroscopy

The infrared absorption spectra of a 29 mm thick SrF_2:0.05%Eu^{3+} crystal have been recorded. The crystal was cooled to 10K. Transitions to the $^7F_2$, $^7F_3$, $^7F_4$ and $^7F_6$ multiplets were studied. These spectra are shown in Figures 8.36 and 8.37.

The transitions to the $^7F_2$ and $^7F_3$ multiplets are very similar to those observed for CaF_2:Eu^{3+}. Only the $Z_1 \rightarrow X_2\gamma_5$ transition at 967.9 cm^{-1} is observed to the $^7F_2$ multiplet. For the $^7F_3$ multiplet, two transitions at 1835.6 and 1941.6 cm^{-1} are observed. These correspond to the $Z_1\gamma_1 \rightarrow W_1\gamma_5$ and $W_4\gamma_5$ transitions. Both are associated with the A centre.

Transitions to the $^7F_4$ and $^7F_6$ multiplets are much simplier than those observed for CaF_2:Eu^{3+}. This due to the absence of clustering in the SrF_2:Eu^{3+} system at concentrations of 0.05 molar %. Table 8.10 gives the A centre transition energies, relative intensities and linewidth data.

Table 8.10: Energy levels (in vacuum cm^{-1}, ±0.2), intensities (relative to the strongest line in the spectrum (=100.00), ±0.50) and linewidths (in cm^{-1}, ±0.2) as measured in absorption to A centre crystal field levels of the $^7F_2$, $^7F_3$, $^7F_4$ and $^7F_6$ multiplets in SrF_2:0.05%Eu^{3+}

Multiplet	Transition	Energy	Intensity	Linewidth
$^7F_2$	$Z_1 \rightarrow X_2\gamma_5$	967.9	8.6	1.5
$^7F_3$	$\rightarrow W_1\gamma_5$	1835.63	1.5	0.5
	$\rightarrow W_4\gamma_5$	1941.6	1.6	1.0
$^7F_4$	$\rightarrow V_1\gamma_1$	2532.4	100.0	3.0
	$\rightarrow V_2\gamma_5$	2780.8	7.7	4.0
	$\rightarrow V_3$	2921.8	13.0	2.5
	$\rightarrow V_4\gamma_5$	2985.7	64.1	7.4
	$\rightarrow V_7\gamma_1$	3114.9	28.9	3.5
$^7F_6$	$\rightarrow T_2\gamma_5$	4892.9	18.0	0.8
	$\rightarrow T_2\gamma_1$	4894.1	67.5	0.8
	$\rightarrow T_6\gamma_1$	5140.6	53.4	10.6

In Figure 8.38, the 2840 - 2900 cm^{-1} portion of Figure 8.37(a) is amplified. In this spectrum, transitions to both the trigonal J and cubic O centres are observed. The J centre transitions are at frequencies of 2859.7 and 2881.2 cm^{-1}. These are assigned as the $Z_1\gamma_1 \rightarrow V_2\gamma_2$ and $V_3\gamma_3$ transitions. The cubic centre transition is at a frequency of 2867.7 cm^{-1}.

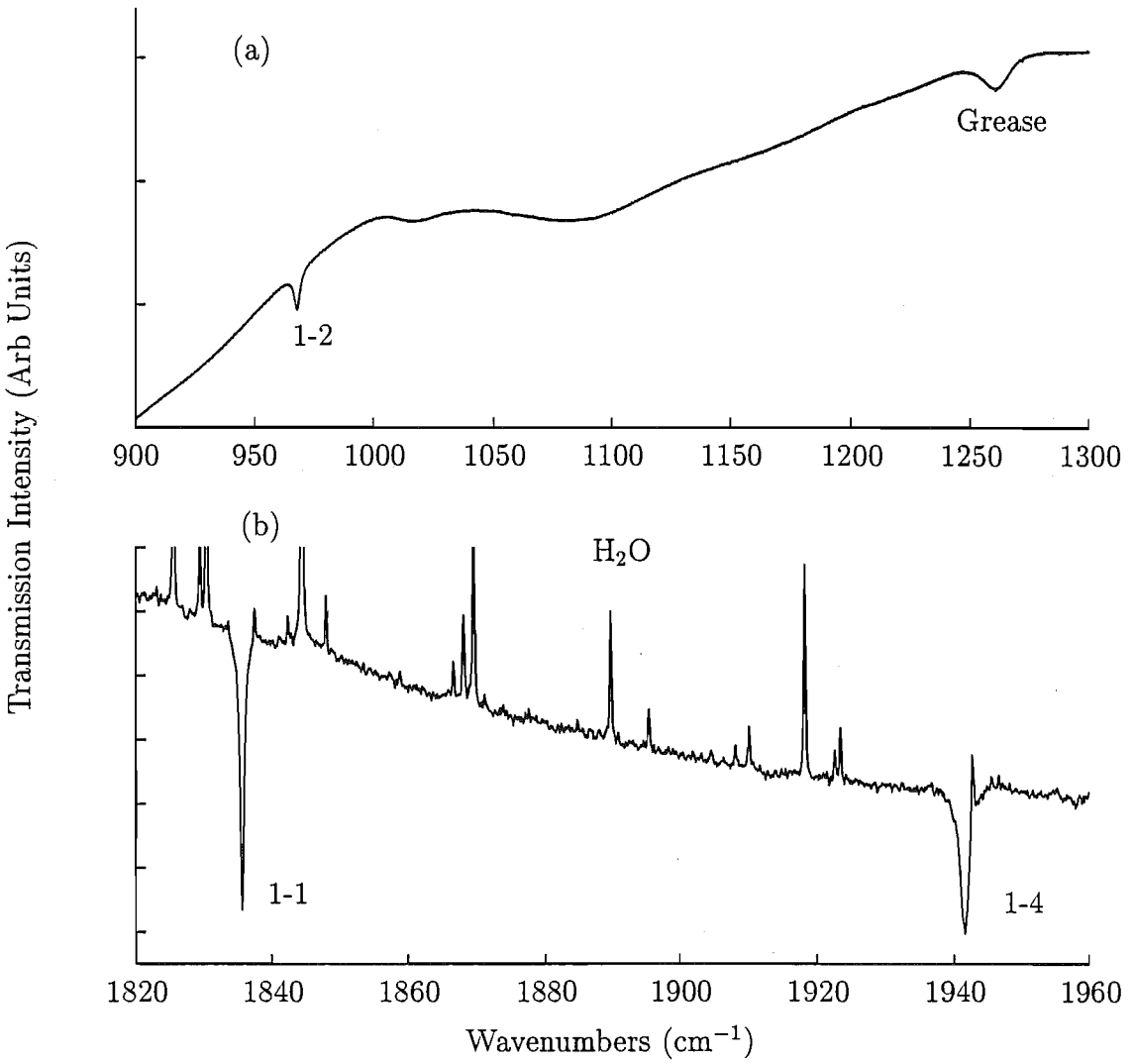

Figure 8.36: Infrared absorption spectra for the (a) $^7F_2$ and (b) $^7F_3$ multiplets in SrF_2:0.05%Eu^{3+}. The spectra were recorded at 10K. Transitions to crystal field levels of the A centre are labelled by their arbitrary numerical labels. The $^7F_3$ multiplet spectrum has been ratioed against a room temperature spectrum.

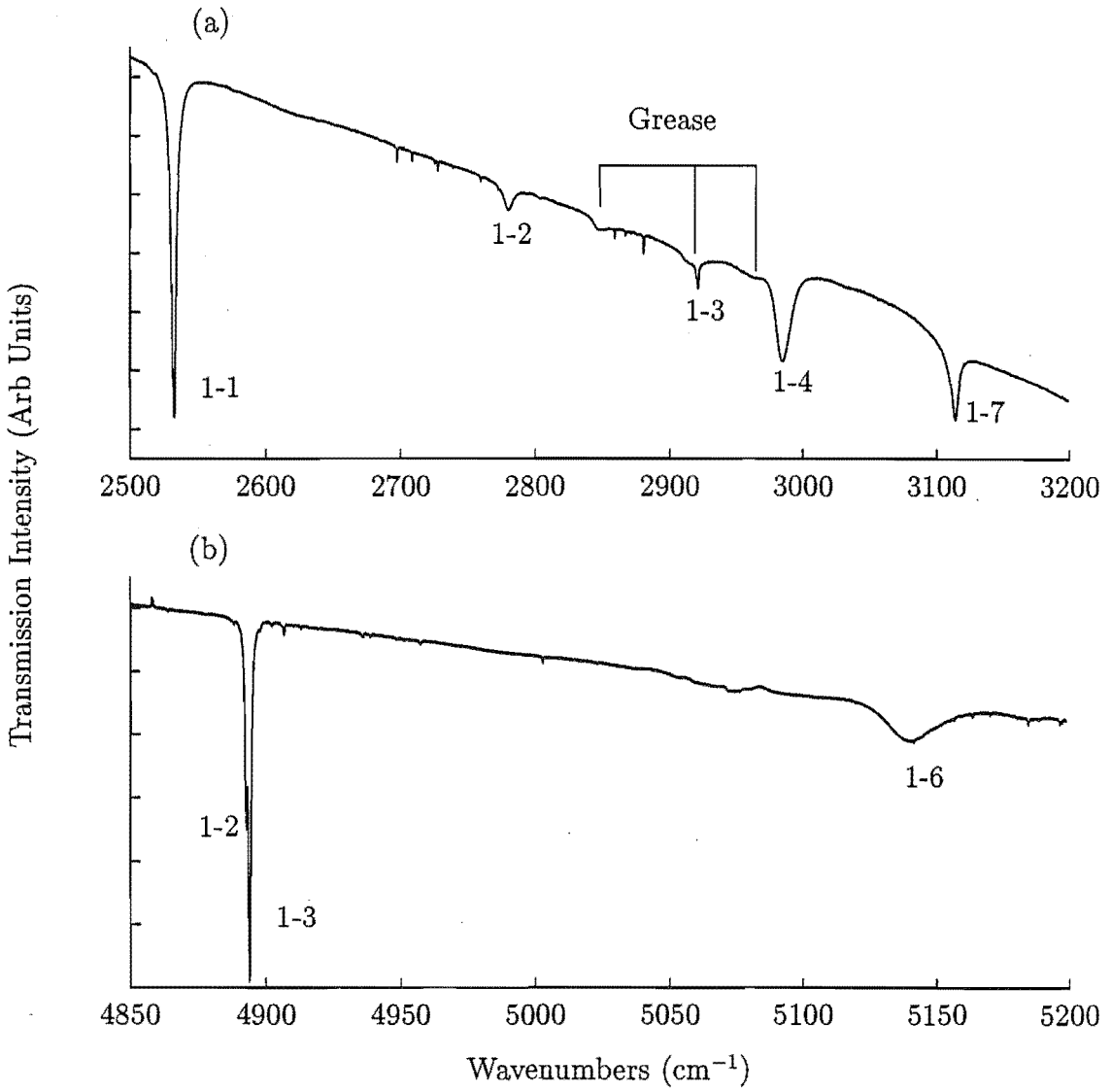

Figure 8.37: Infrared absorption spectra for the (a) $^7F_4$ and (b) $^7F_6$ multiplets in SrF_2:0.05%Eu^{3+}. The spectra were recorded at 10K. Transitions to crystal field levels of the A centre are labelled by their arbitrary numerical labels.

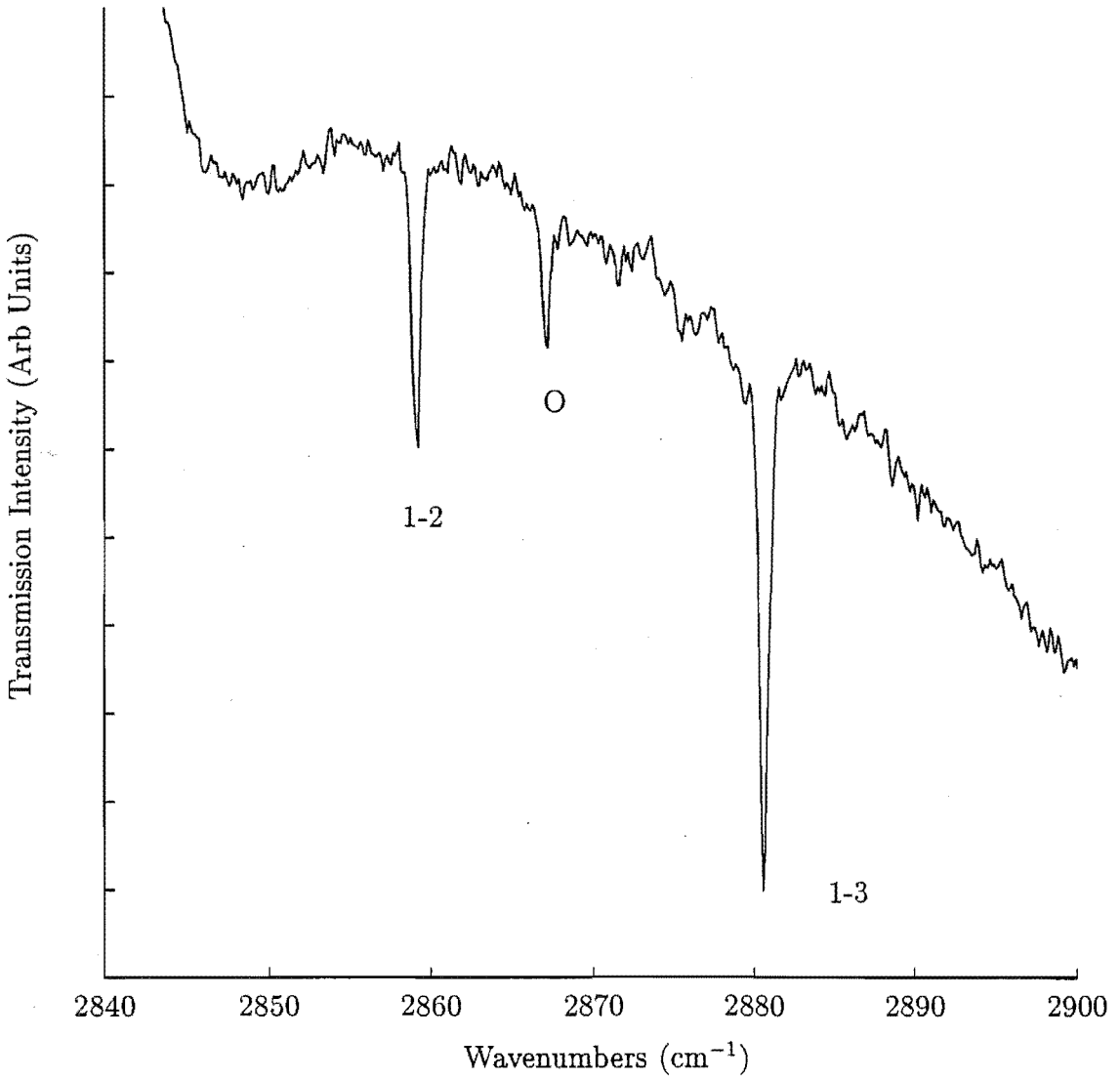

Figure 8.38: $^7F_4$ multiplet infrared absorption spectra for the J and O centres in SrF_2:0.05%Eu^{3+}. The spectra were recorded at 10K. The J centre levels are labelled with the usual arbitrary numerical label.

8.4.2 Zeeman Infrared Spectroscopy

The Zeeman spectra of a 8.4 mm thick SrF_2:0.05%Eu^{3+} sample was recorded on the Digilab FTIR spectrometer. The magnetic field was applied along the ⟨111⟩ axis of the crystal. The recorded spectra are presented in Figures 8.39 through to 8.45.

The splitting of the $^7F_2(X_1\gamma_5)$ and $^7F_3(W_1\gamma_5)$ and $(W_4\gamma_5)$ levels are two-fold. This confirms that the symmetry of the A centre is C_{4v}. It also confirms the assignment (from laser selective excitation) of these levels as doublets. Analysis of the $^7F_3$ levels is rendered difficult due to their low absorption strengths, and the presence of atmospheric absorption in the same spectral region. Table 8.11 compares the experimentally determined splitting factors with those calculated using the F-Shell Empirical Program of Dr M F Reid. The agreement is favourable giving confidence in the crystal field wavefunctions.

Table 8.11: Experimental and calculated Zeeman splitting factors for the C_{4v} symmetry A centre in SrF_2:Eu^{3+}. All experimentally measured splitting factors are ±0.2 unless otherwise stated.

State	Field (Tesla)	Magnetic Splitting Factors			
		Theoretical			Experimental
		$S_{\parallel}$	$S_{\perp}$	$S_{[111]}$	$S_{[111]}$
X_1	4	3.46	0.13	1.99	2.0
W_1	4	0.23	0.72	0.44	0.6
W_4	3	5.11	0.89	2.70	2.3±0.3
T_2	4	1.17	0.70	1.08	1.0

The Zeeman spectrum of the $^7F_4$ multiplet is shown in Figure 8.41. No distinct splittings are observed for transitions to this multiplet. The 2532.4, 2921.8 and 3114.9 cm^{-1} transitions have all been assigned as singlets from polarised laser selective excitation. Therefore, no splittings are expected in these cases. However, both the 2780.8 and 2985.7 cm^{-1} transitions should split under the influence of a magnetic field because they are doublets. The 2780.8 cm^{-1} transition can be observed to broaden in the field. Clearly, the field strength is insufficient to observe a distinct splitting as the zero field, phonon-broadened linewidth is 4 cm^{-1}. Since the calculated [111] splitting factor is only 3.99, it is reasonable that only a broadening effect is observed. The 2985.7 cm^{-1} transition is virtually unaffected by the application of a 4 Tesla magnetic field. The zero-field linewidth in this case is 7.4 cm^{-1} and we calculate the splitting factor for the $V_4\gamma_5$ state to be 1.54. This explains the absence of a splitting for this assigned doublet state.

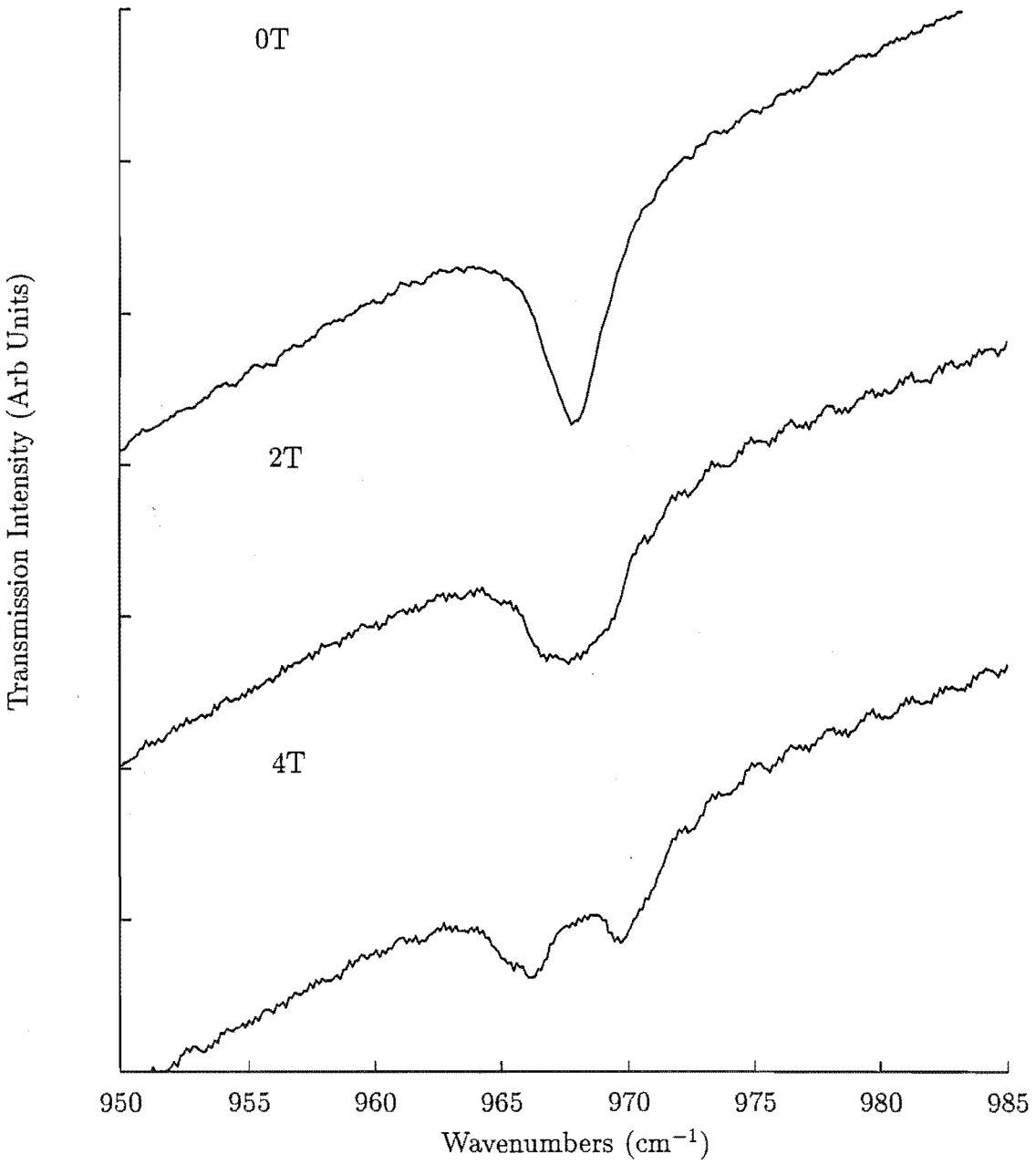

Figure 8.39: 4.2K splitting of the SrF_2:0.05%Eu^{3+} A centre $^7F_2$ transitions as a function of magnetic field directed along a ⟨111⟩ axis.

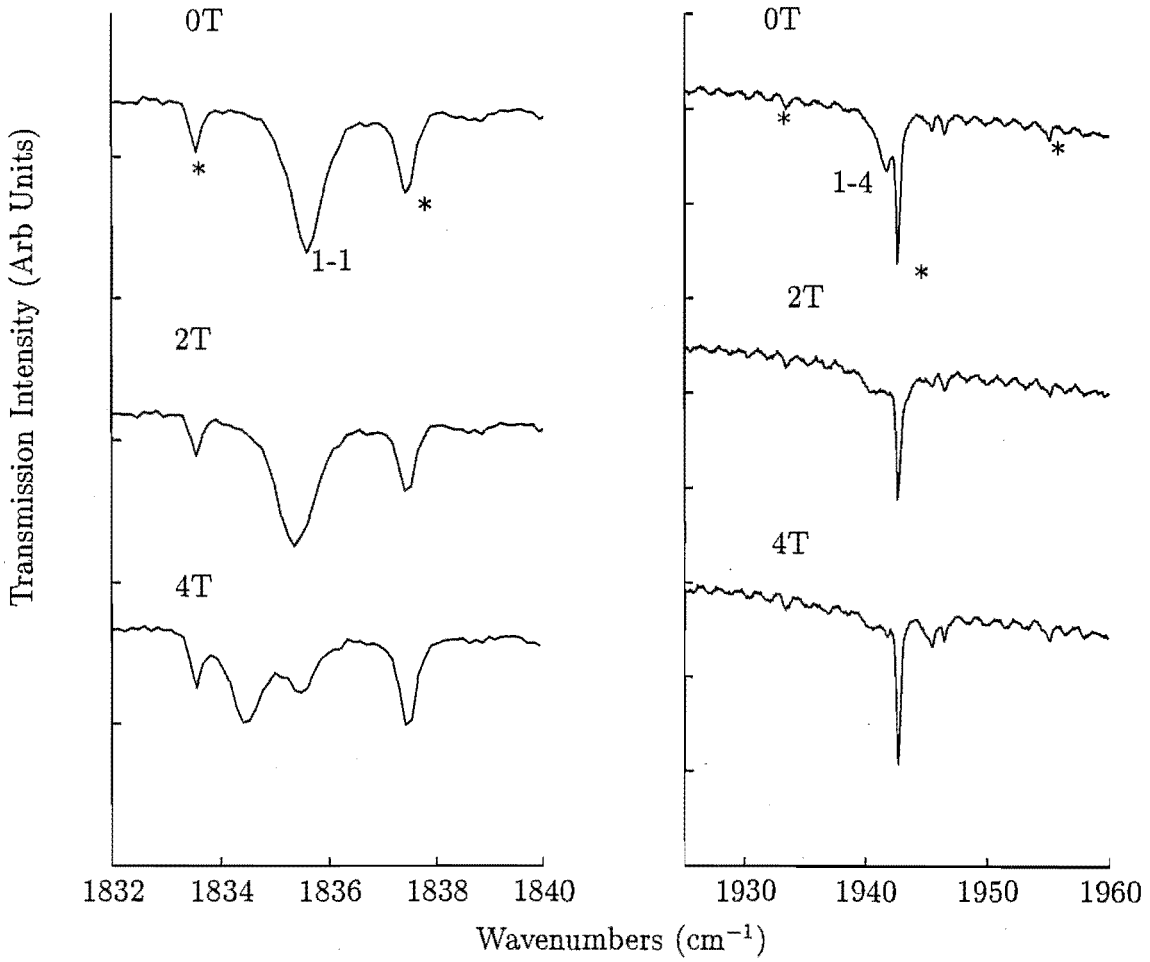

Figure 8.40: 4.2K splitting of the SrF_2:0.05%Eu^{3+} A centre $^7F_3$ transitions as a function of the magnetic field directed along a ⟨111⟩ axis. The * notation indicates atmospheric absorption.

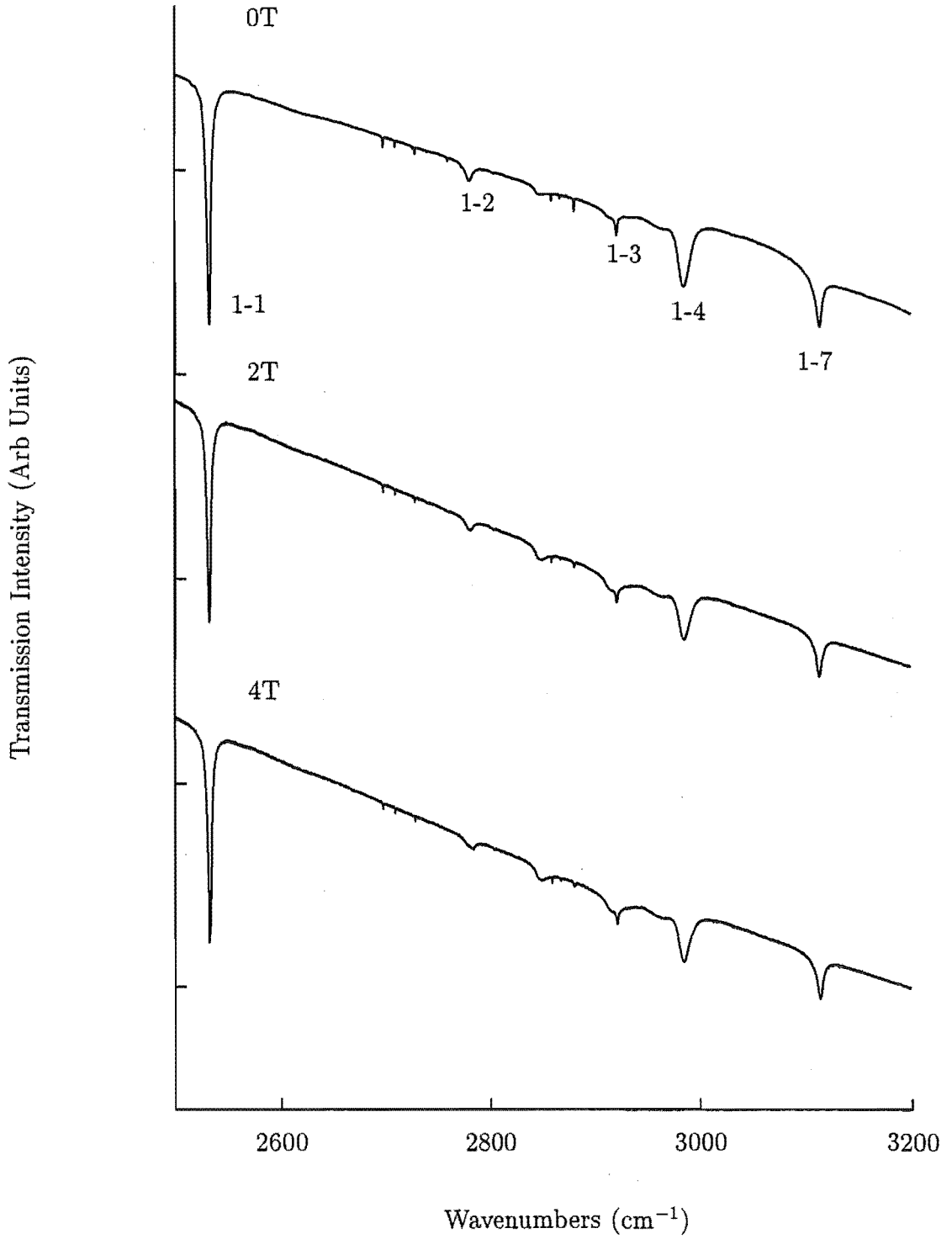

Figure 8.41: 4.2K splitting of the SrF_2:0.05%Eu^{3+} A centre $^7F_4$ transitions as a function of magnetic field directed along a ⟨111⟩ axis.

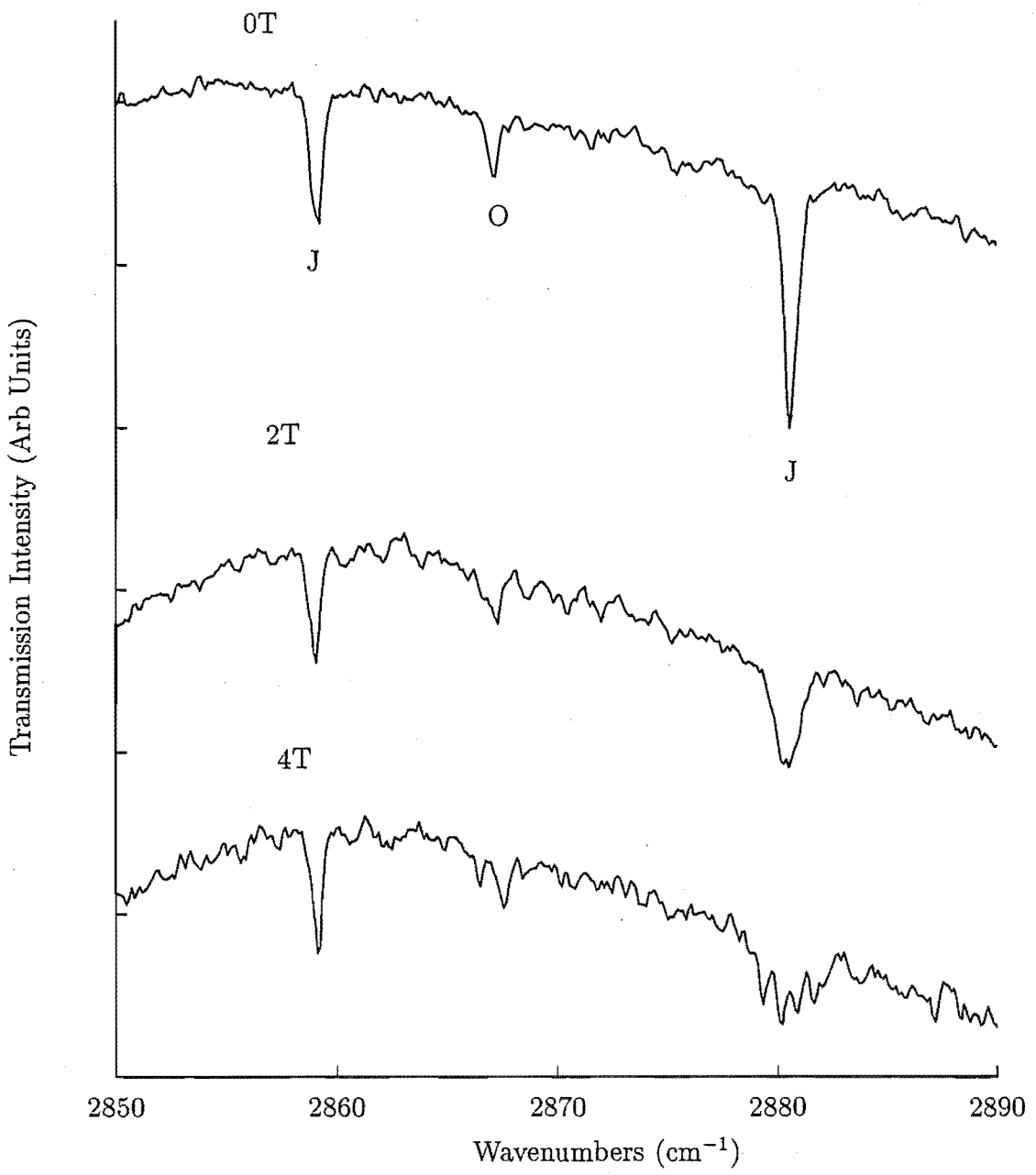

Figure 8.42: 4.2K splitting of the SrF_2:0.05%Eu^{3+} J and O centre $^7F_4$ transitions as a function of magnetic field directed along a ⟨111⟩ axis.

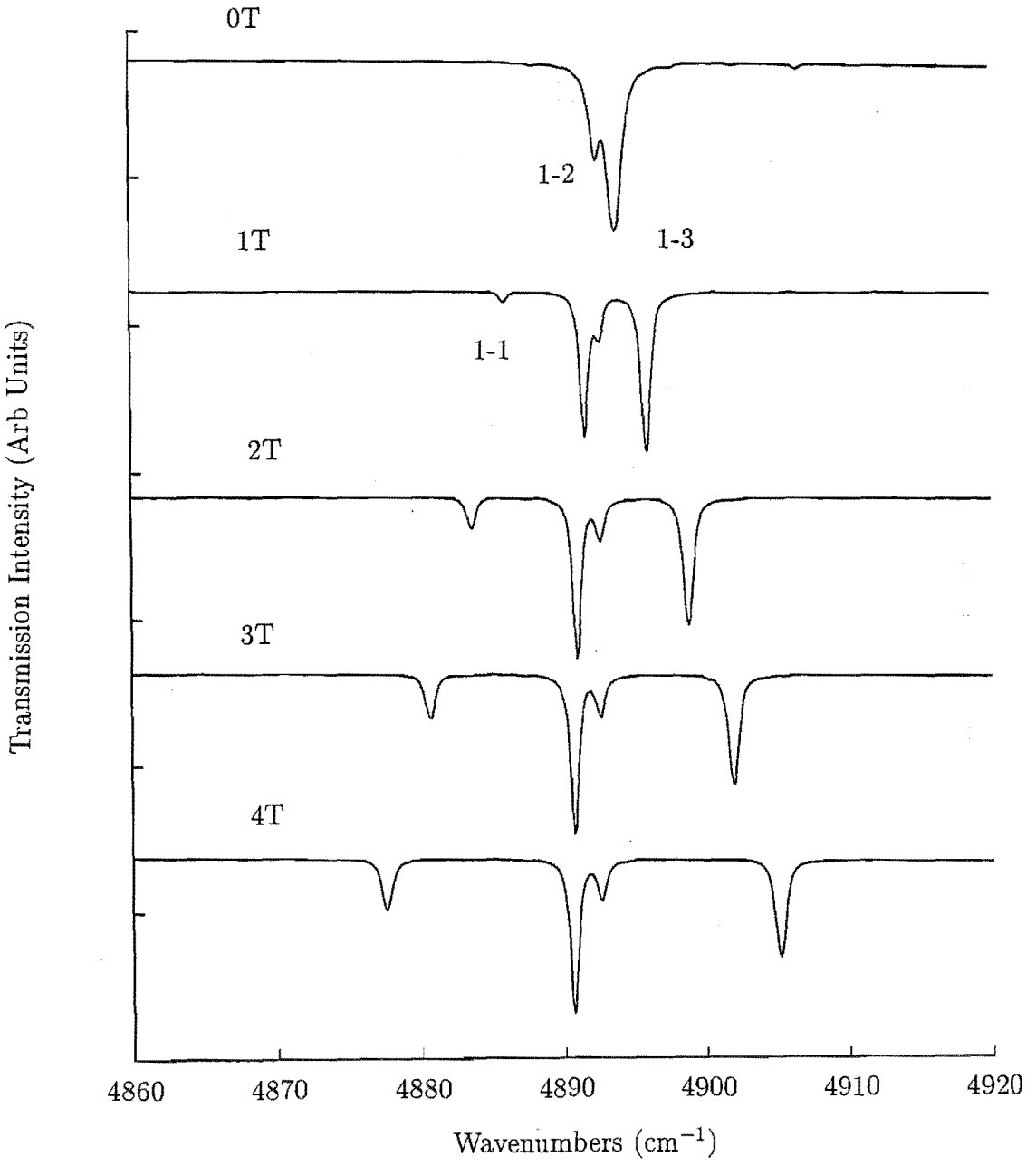

Figure 8.43: 4.2K splitting of the SrF_2:0.05%Eu^{3+} A centre $^7F_6(T_1\gamma_4)$, $(T_2\gamma_5)$ and $(T_3\gamma_1)$ levels as a function of magnetic field directed along a $\langle 111 \rangle$ axis.

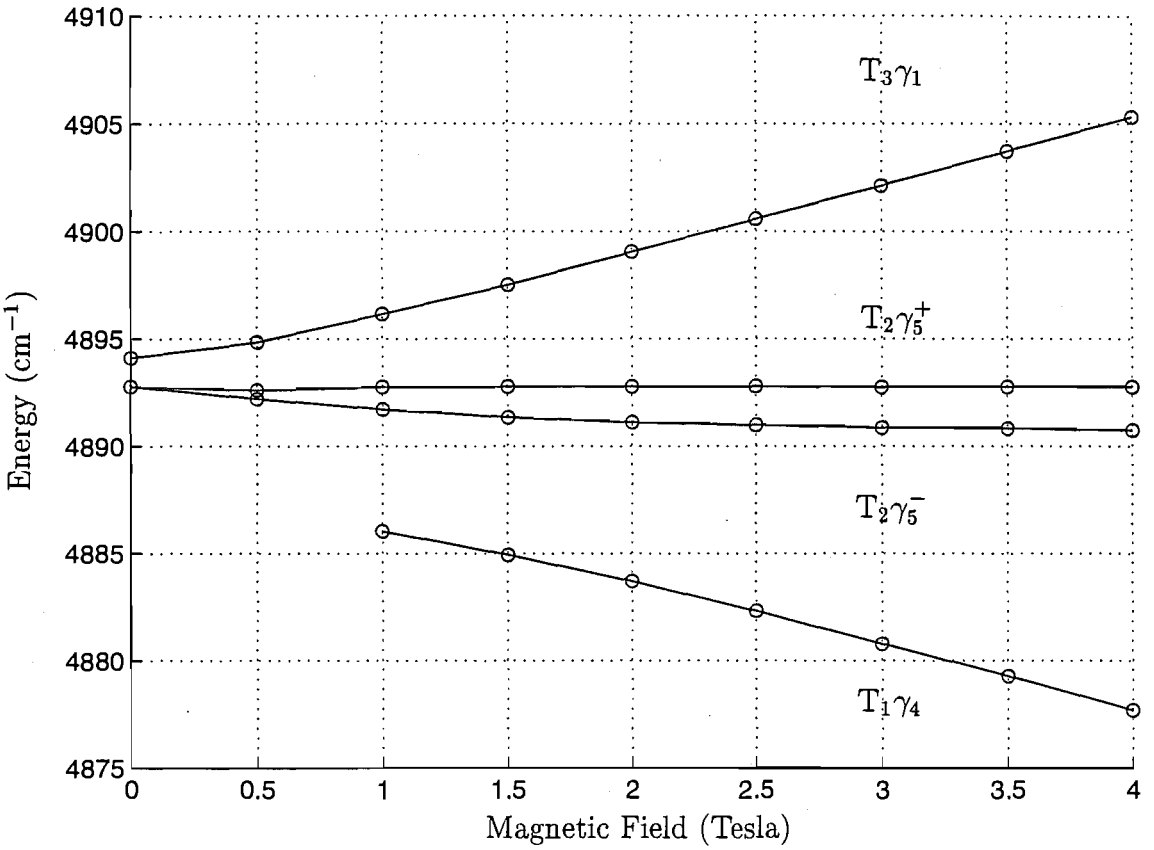

Figure 8.44: Zeeman splitting diagram for the SrF_2:Eu^{3+} A centre $^7F_6(T_1\gamma_4)$, $(T_2\gamma_5)$ and $(T_3\gamma_1)$ levels in a $\langle 111 \rangle$ applied magnetic field. The open circles are the experimental points and the solid lines are to guide the eye.

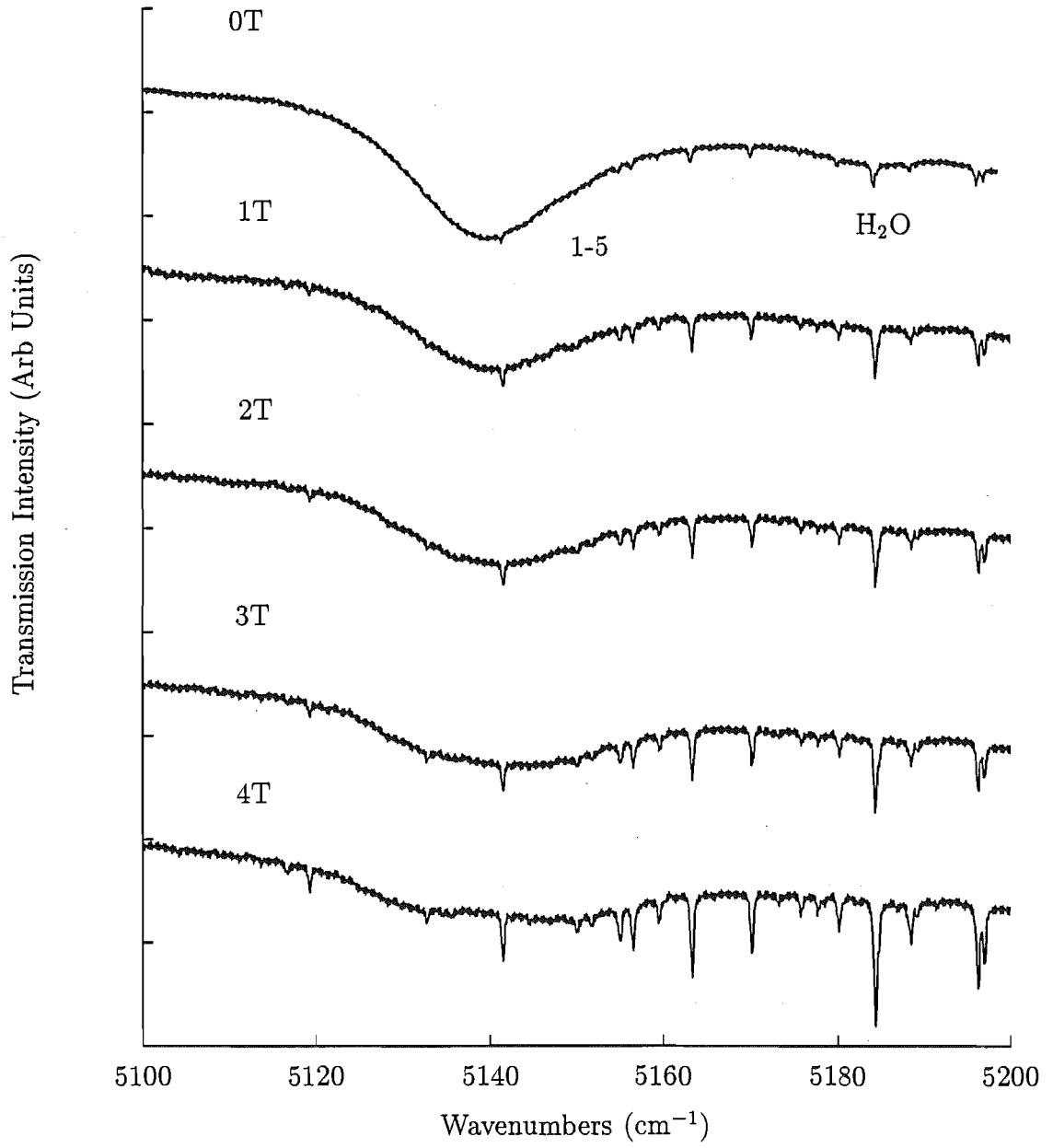

Figure 8.45: 4.2K splitting of the SrF_2:0.05%Eu^{3+} A centre $^7F_6(T_5\gamma_5)$ level as a function of magnetic field directed along a ⟨111⟩ axis.

In Figure 8.42, a small portion of the $^7F_4$ absorption spectrum is amplified to show the splitting of transitions associated with the trigonal J centre. These transitions are barely observable above the noise. Despite this, a four line splitting is observed for the 2881.2 cm^{-1} J centre transition. This consistent with the trigonal symmetry of the centre. Magnetic splitting factors of $s_{||}$=1.22 and $s_{[111]}$=0.39 can be derived from this four fold pattern. The 2859.7 cm^{-1} transition is not observed to split in the applied magnetic field. This is consistent with its assignment as terminating on an upper state of γ_2 symmetry.

The Zeeman spectra of transitions to the $^7F_6$ multiplet are given in Figures 8.43 and 8.45. Figure 8.43 shows the splitting of the 4892.9 and 4894.1 cm^{-1} states. Of these, only the 4892.9 cm^{-1} T_2 state is assigned as a doublet. The splitting observed in Figure 8.43 is interesting as an additional transition appears and grows in intensity as the magnetic strength is increased. The transition observed is assigned to the $T_1\gamma_4$ state. This state should not be observed from the $Z_1\gamma_1$ ground state. It is observed in the field as the magnetic field mixes in components of the $T_2\gamma_5$ state. This effect is also responsible for the movement of both the $T_1\gamma_4$ and $T_3\gamma_1$ states. This is shown in Figure 8.44, which plots the Zeeman splitting patterns. The measured splitting factor of the $T_2\gamma_5$ state, is 0.98. This in good agreement with the calculated value of 1.08. The $T_7\gamma_5$ state is only observed to broaden in the field, as is shown in Figure 8.45.

8.5 Infrared and Zeeman Infrared Spectroscopy of BaF_2:Eu^{3+}

Absorption measurements have been made for an 11.1 mm thick BaF_2:0.1%Eu^{3+} crystal. The crystal was cooled to 10K. Only transitions to the $^7F_4$ and $^7F_6$ multiplets are observed. These are shown in Figure 8.46.

Three absorption transitions are observed to the $^7F_4$ multiplet. The features at 2850.0 and 2869.2 cm^{-1} are assigned as transitions associated with the dominant L centre in this crystal. These assignments are made by comparision with the laser excited fluorescence studies of chapter 6. The additional transition is ascribed to a near cubic centre present in these crystals and discussed in chapter 6.

For transitions to the $^7F_6$ multiplet only L centre transitions are observed as given in Table 8.12.

The dominant centre in BaF_2:0.05%Eu^{3+} has been determined by Jouart et. al. [106] to be of trigonal C_{3v} symmetry from laser selective excitation studies. No

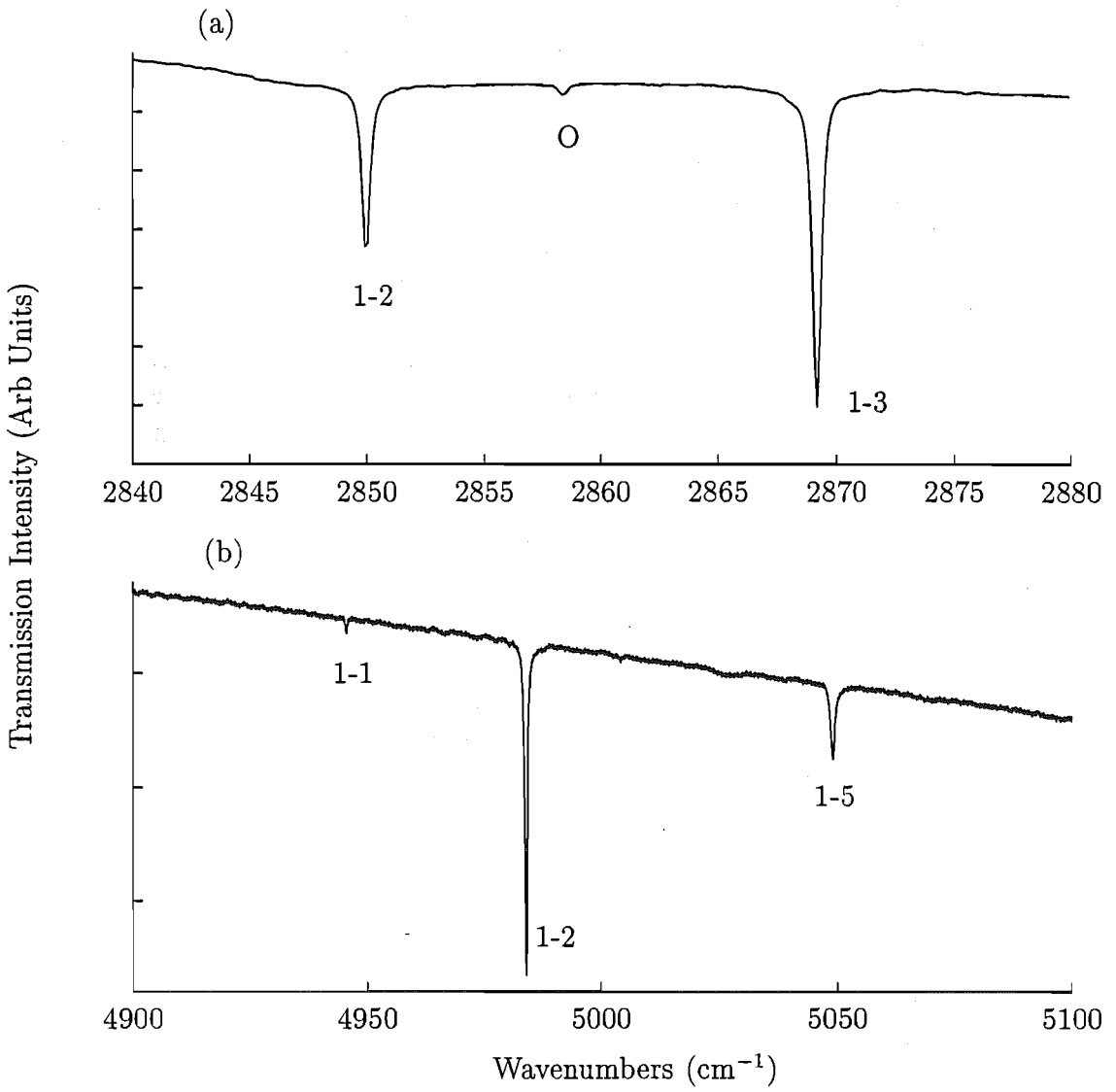

Figure 8.46: Infrared absorption spectra for the (a) $^7F_4$ and (b) $^7F_6$ multiplets in BaF_2:0.1%Eu^{3+}. The spectra were recorded at 10K. Transitions to crystal field levels of the L centre are labelled by their arbitrary numerical labels.

justification for this assignment was given. It has been challenged by Silversmith and Macfarlane [112] who assign the symmetry as tetragonal C_{4v}. Once again, no justification was given. The polarised laser excited fluorescence studies of chapter 6, gave results consistent with the findings of Jouart et. al. The derived energy level scheme could be readily fitted to a C_{3v} symmetry crystal field Hamiltonian. In this section, we conclusively test the trigonal C_{3v} assignment with Zeeman infrared measurements on the observed transitions. For this purpose two crystals were oriented.

Table 8.12: 10K energy levels (in vacuum cm^{-1}, ± 0.2), intensities (relative to the strongest line in the spectrum (=100.00), ± 0.50) and linewidths (in cm^{-1}, ± 0.2) as measured in absorption to L centre crystal field levels of the $^7F_4$ and $^7F_6$ multiplets in BaF_2:0.1%Eu^{3+}

Multiplet	Transition	Energy	Intensity	Linewidth
$^7F_4$	$Z_1 \rightarrow V_2\gamma_2$	2850.0	68.7	0.3
	$\rightarrow V_3\gamma_3$	2869.2	100.0	0.4
	$\rightarrow T_1\gamma_1$	4945.8	1.1	0.3
$^7F_6$	$\rightarrow T_2\gamma_3$	4984.7	24.1	0.5
	$\rightarrow T_4\gamma_2$	5049.7	7.3	0.7

A 11.1 mm thick, $\langle 100 \rangle$ oriented BaF_2:0.1%Eu^{3+} crystal and a 7.3 mm thick, $\langle 111 \rangle$ oriented BaF_2:0.1%Eu^{3+} crystal were used to study the Zeeman splittings of the observed $^7F_4$ and $^7F_6$ multiplet transitions. The recorded Zeeman spectra for the $^7F_4$ multiplet are shown in Figures 8.47 and 8.48. Figures 8.49 and 8.50 show the Zeeman spectra for the $^7F_6$ multiplet transitions.

The 2850.0, 4945.8 and 5049.7 cm^{-1} transitions have been assigned as singlets from polarised laser selective excitation studies. Thus, no splitting is expected and it is not observed. The 2869.2 and 4984.7 cm^{-1} transitions are observed to split in the field. This confirms their assignments from chapter 6 as doublet states. Four- and two-fold line splittings are observed for magnetic fields applied along the [111] and [100] directions, respectively. This is consistent with the C_{3v} selection rules. For a centre of C_{4v} symmetry, we would have expected four transitions for the field along the [100] direction due to the superposition of transitions from the magnetic C_4 and C_s sub-centres. Two transitions would be observed for the field directed along the [111] direction. From these results, the dominant centre in BaF_2:0.05%Eu^{3+} is assigned as having C_{3v} symmetry.

The 2850.0 cm^{-1} transition, splits into four evenly spaced lines in a [111] directed magnetic field. The C_{3v} symmetry, L centre reduces to two magnetic subgroups for a magnetic field along the a $\langle 111 \rangle$ axis. A C_3 symmetry centre along the field and

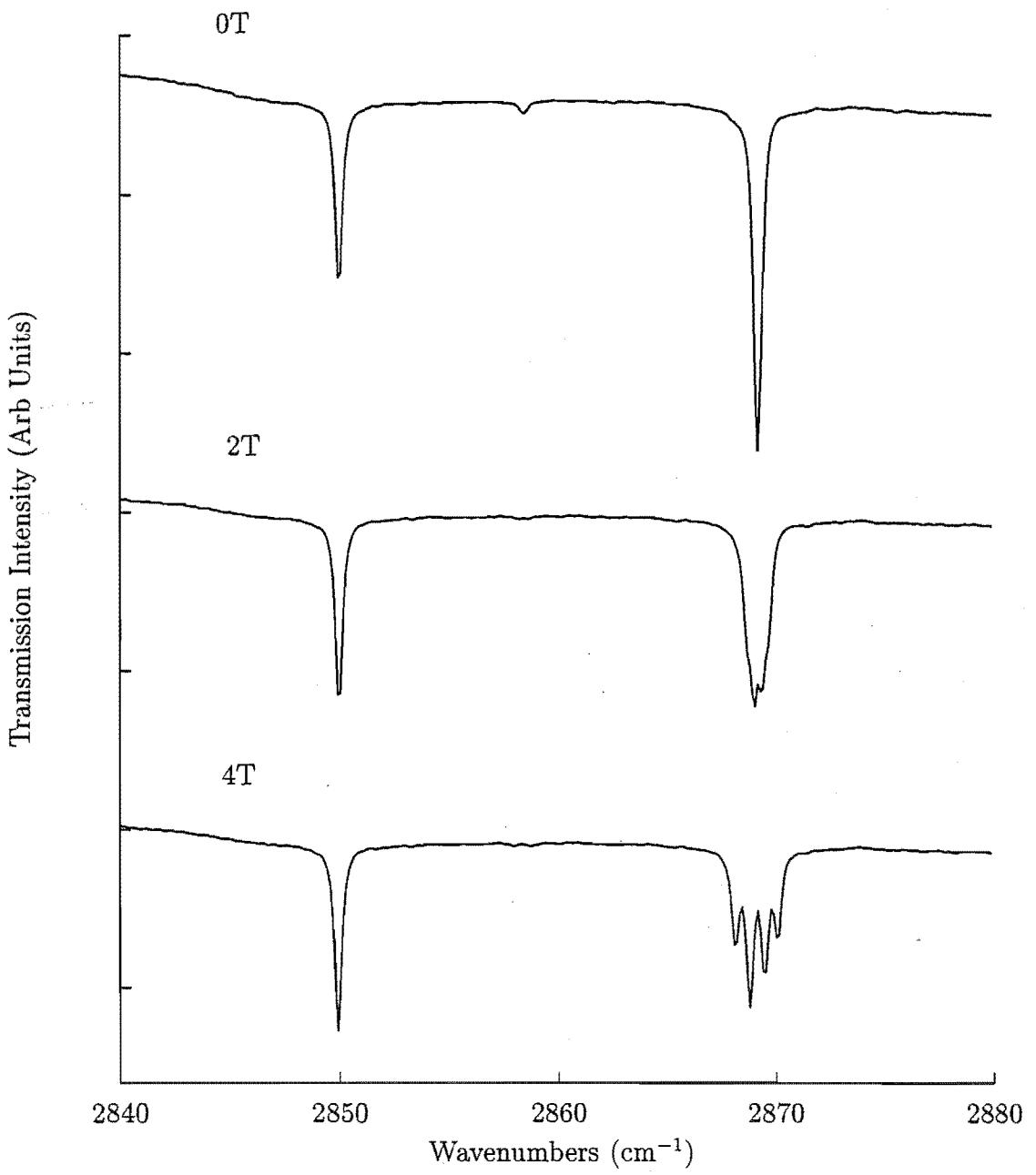

Figure 8.47: 4.2K splitting of the BaF_2:0.1%Eu^{3+} L centre $^7F_4$ transitions as a function of magnetic field directed along a ⟨111⟩ axis.

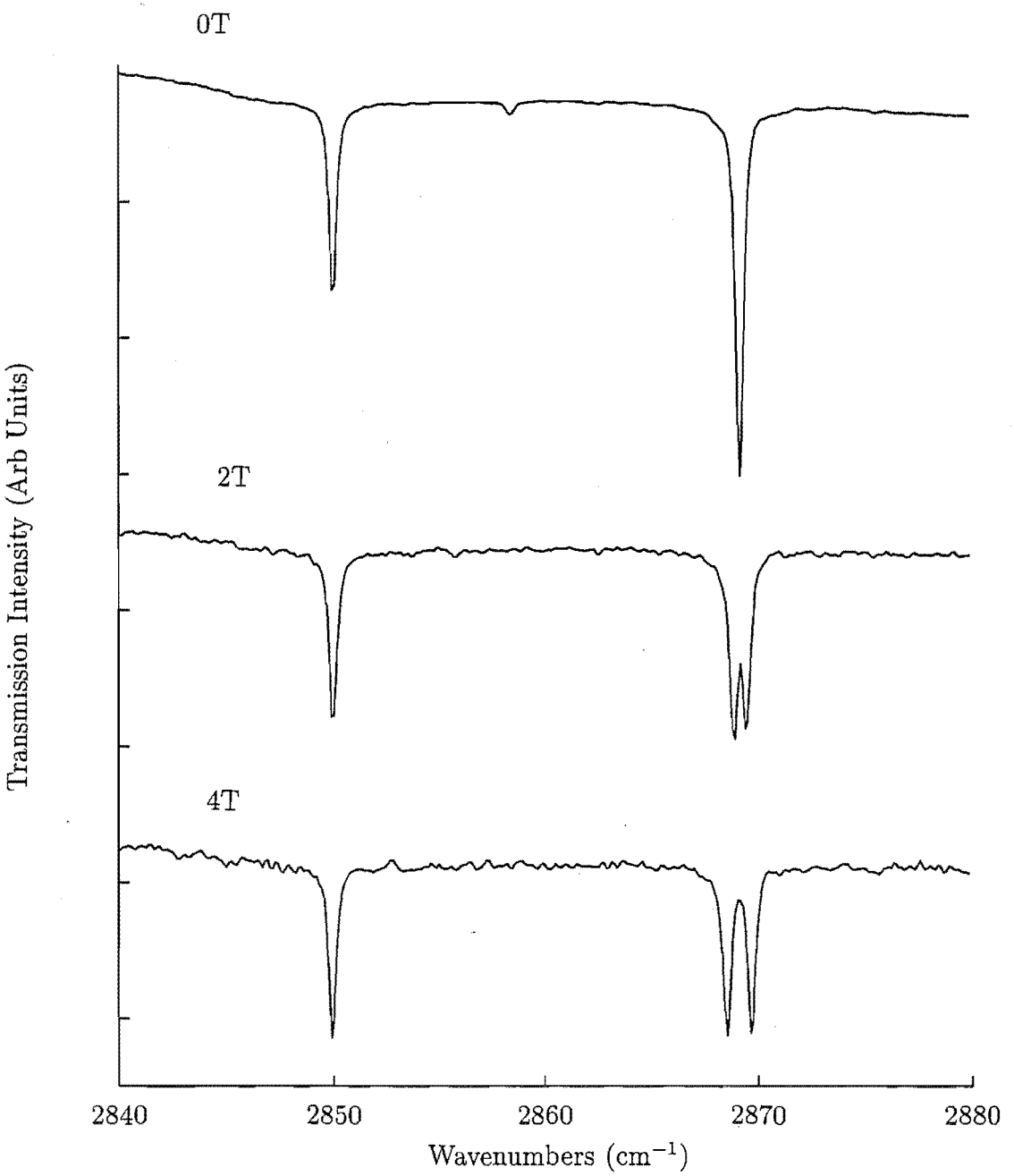

Figure 8.48: 4.2K splitting of the BaF_2:0.1%Eu^{3+} L centre $^7F_4$ transitions as a function of magnetic field directed along a ⟨100⟩ axis.

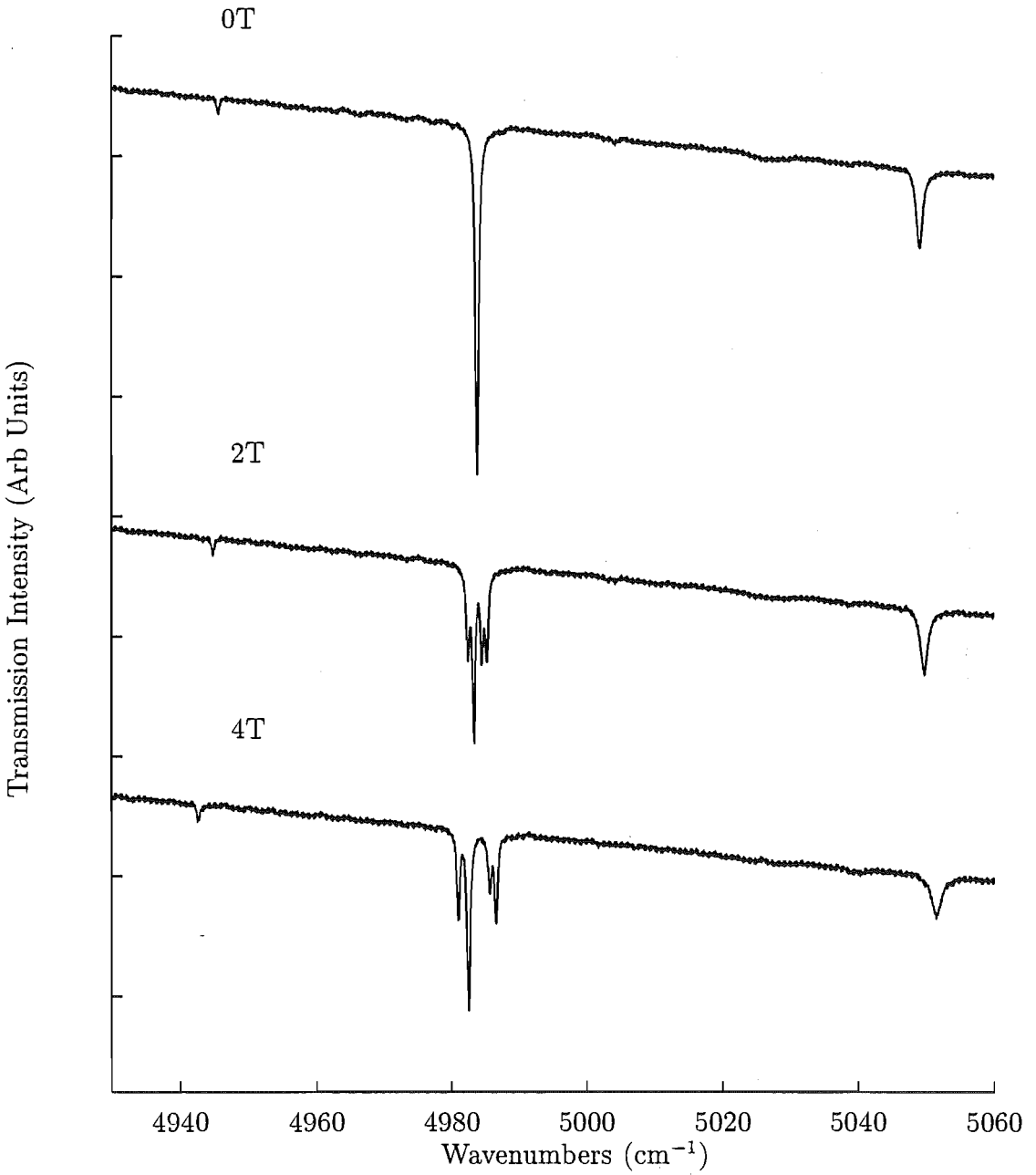

Figure 8.49: 4.2K splitting of the BaF_2:0.1%Eu^{3+} L centre $^7F_6$ transitions as a function of magnetic field directed along a ⟨111⟩ axis.

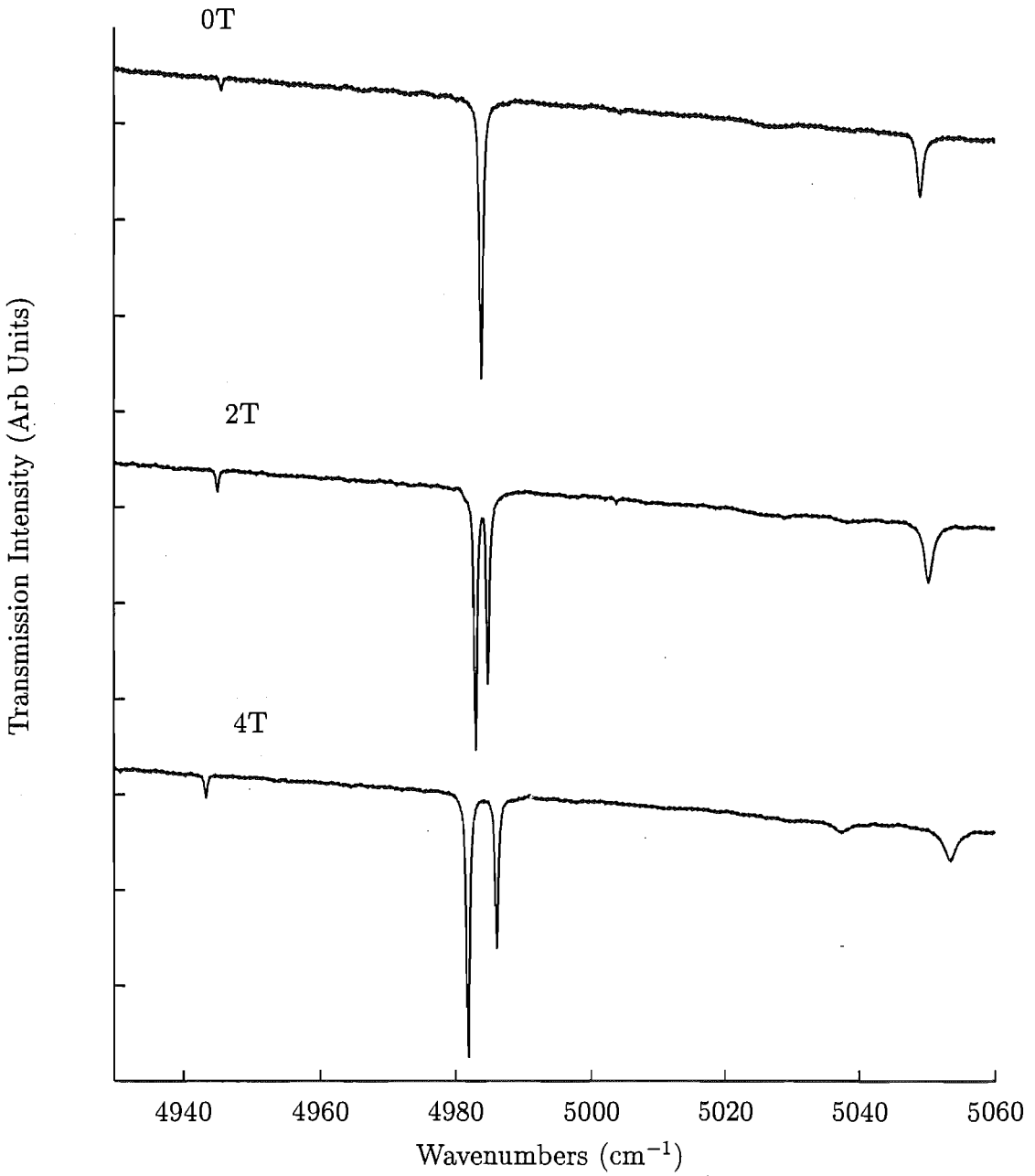

Figure 8.50: 4.2K splitting of the BaF_2:0.1%Eu^{3+} L centre $^7F_4$ transitions as a function of magnetic field directed along a ⟨100⟩ axis.

three C_1 symmetry centres along the $[\bar{1}11]$, $[1\bar{1}1]$ and $[\bar{1}\bar{1}1]$ directions, each with one third of the field projected along their principal axis. Defining the splitting factor of the C_3 site as $s_{\|}$ and that of the C_1 centres as $s_{[111]}$, we have the relationship

$$s_{\|} = 3s_{[111]}$$

The 4 Tesla experimental values bear out this relationship, giving $s_{\|}$=1.03 and $s_{[111]}$=0.35 (here more significant figures than the stated uncertainty of these measurements (of $\pm$0.2) strictly allows, has been used to illustrate the point).

For a magnetic field along the [100] axis, a two line splitting is observed. A 4 Tesla splitting factor of $s_{[100]}$=0.6 is measured. For a magnetic field applied along an arbitrary axis:

$$s_\theta = \sqrt{s_{\|}^2 \cos^2\theta + s_{\perp}^2 \sin^2\theta}$$

where θ is the angle between the magnetic field and the principal symmetry axis of the centre. For the [100] case, θ=$\cos^{-1}(\frac{1}{\sqrt{3}})$. As $s_{\perp}$ is essentially zero for non-Kramers ions we can write:

$$s_{[100]} = \frac{1}{\sqrt{3}} s_{\|}$$

For the 2850.0 cm^{-1} $s_{\|}$ value of 1.03, this yields $s_{[100]}$=0.59. This is in excellent agreement with the experimentally measured value.

The observed four-fold [111] splitting of the 4984.7 cm^{-1} transition does not have constant line spacings. This is an indication that for this state, the magnetic field has induced sufficient mixing into the crystal field wavefunctions for the angular momentum ladder operators to connect the states of the doublet. As a result, $s_{\perp}$ is now non-zero. From the observed splittings, we measure $s_{\|}$=3.0 and $s_{[111]}$=1.6. The [100] splitting is two lines. This is consistent with the symmetry of the centre. The measured value of $s_{[100]}$ is 2.3.

An additional feature of the spectrum is the movement, in the field, of the 5049.7 cm^{-1} singlet level. In the [111] field it has moved 2.5 cm^{-1} and in the [100] field it shifts by 4 cm^{-1} to the higher frequency. This arises from non-linear Zeeman interactions between this singlet level ($T_4\gamma_1$) and a nearby singlet transforming as a γ_2. As such, these levels can be connected by the parallel Zeeman operator and have matrix elements in J_z. The difficulty in analysing the splitting is that the exact position of the γ_2 level is unknown from either laser or infrared spectroscopy.

The crystal field analysis of chapter 6 predicts the splittings of the $V_3\gamma_3$ state to be $s_{\|}$=1.44. The $T_2\gamma_3$ state is predicted to have $s_{\|}$=2.82 (with $s_{\perp}$=1.22). These $s_{\|}$ values match the measured experimental values of 1.0 and 3.0 reasonably well giving some confidence in the overall assignments made for the L centre in BaF_2:Eu^{3+}.

Chapter 9

Discussion and Conclusions

The techniques of laser selective excitation and fluorescence, and optical and Zeeman infrared absorption have been applied to the experimental investigation of rare earth ion centres in alkaline earth fluoride crystals.

High resolution infrared absorption spectroscopy has been used to study hyperfine splittings of sharp infrared absorption lines for Pr^{3+}, Tb^{3+} and Ho^{3+} ions in CaF_2 and SrF_2 crystals. The ground state of the C_{4v} symmetry centre in both CaF_2:Pr^{3+} and SrF_2:Pr^{3+} is a γ_5 doublet state. Magnetic hyperfine interactions in the ground state are readily observed as structure in the $^3H_4 \rightarrow ^3H_5$ and $^3H_6$ infrared absorption transitions. The lowest energy $^3H_5$ states are singlets with linewidths dominated by their inhomogeneous contributions. As such, the structure observed in these transitions reflects only the ground state hyperfine interactions. A deeper central dip in the recorded six-line hyperfine pattern is indicative of non-axial strain. This arises from a random distribution of non-C_{4v} distortions. The lowest level of the $^3H_5$ multiplet is a γ_5 doublet. Thus, the observed hyperfine pattern is a superposition of the hyperfine structure of the ground state and the $^3H_5$ excited state. These hyperfine patterns have been analysed using the crystal field wavefunctions for the appropriate Pr^{3+} electronic states and calculated magnetic hyperfine interaction constants. This well accounts for the observed structure.

The ground state of the C_{4v} centre in CaF_2:Tb^{3+} comprises two close lying singlet states of γ_3 and γ_4 symmetry, separated by 0.18 cm^{-1}. These states are mixed by the parallel hyperfine interaction giving rise to a pseudo-quadrupole hyperfine interaction in the ground state. These interactions are observed as hyperfine structure in transitions to a singlet state of the $^7F_4$ multiplet. Calculations, based on crystal field wavefunctions and magnetic hyperfine interaction constants can account for the observed two-fold hyperfine splittings. In the same centre in SrF_2:Tb^{3+}, no hyperfine splittings are observed. Here the γ_3-γ_4 splitting is 0.48 cm^{-1} making the hyperfine splitting 3 times smaller and unresolved in the present experiments.

The CaF_2:Ho^{3+} C_{4v} centre ground state is also a pseudo-degenerate state compris-

ing γ_1 and γ_2 singlet levels, separated by 1.7 cm^{-1}. As with the CaF_2:Tb^{3+} and SrF_2:Tb^{3+} C_{4v} centre ground states, the γ_1 and γ_2 states are mixed by the parallel hyperfine interaction. Infrared absorption transitions to γ_5 doublets of both the $^5I_7$ and $^5I_6$ multiplets show two sets of eight line hyperfine patterns separated by approximately 1.7 cm^{-1}. A feature of these patterns is the interesting intensity distribution amongst the hyperfine transitions arising from mixing of the ground state wavefunctions. Simulated spectra calculated from the electron-nuclear wavefunctions and assuming a Boltzmann population distribution well accounted for the spacing and intensities of the hyperfine levels.

A more complex hyperfine pattern is observed for absorption transitions to the close lying $Y_2\gamma_3$, $Y_3\gamma_5$ and $Y_4\gamma_2$ states of the $^5I_7$ multiplet. In this case, the hyperfine splittings of the doublet are perturbed by the presence of the nearby singlets. Both singlets interact with the doublet via the perpendicular hyperfine interaction, however they do not interact with each other. Transitions to these states show the ground state hyperfine splittings superimposed upon the hyperfine structure of the excited states. In the absence of any hyperfine interactions, the absorption transition to the $Y_2\gamma_3$ state is forbidden but due to the mixing with the $Y_3\gamma_5$ electron-nuclear wavefunctions, $Y_2\gamma_3$ hyperfine transitions become weakly allowed.

To account for this hyperfine pattern, the full 32×32 perturbation matrix of the excited states was diagonalised yielding an energy level scheme for the 32 hyperfine levels. Simulation of the observed hyperfine transition intensity distribution adequately accounts for the gross features of the spectrum but some anomalies remain. The observed $Z_1\gamma_1 \rightarrow Y_3\gamma_5$ hyperfine pattern is not at all well accounted for. Interactions from the $Y_1\gamma_5$ state 17 cm^{-1} away and varying the optical transition parameters from unity, were incorporated into the hyperfine perturbation matrix but had negligible effect. A more direct solution to the problem could be obtained with higher spectral resolution, coupled with Zeeman effect experiments on the hyperfine transitions. In this case, the additional perturbation is tunable and, since the electronic Zeeman splittings will lift the degeneracy of the I_z states, this may prove an effective means of level assignment.

Laser selective excitation and fluorescence has been used, in conjunction with optical and Zeeman infrared absorption, to study CaF_2 and SrF_2 crystals doped with Sm^{3+} and Eu^{3+} ions. For CaF_2:Sm^{3+} and CaF_2:Eu^{3+} crystals, very similar defect centre distributions have been observed. The spectrum is dominated by C_{4v} symmetry RE^{3+}-F^- pairs for concentrations lower than 0.05 molar % of the rare-earth dopant. As the concentration is increased, the centre distribution exhibits a preference for the formation of cluster centres. For CaF_2:Sm^{3+}, these cluster centres are shown to be entirely non-radiative due to cross-relaxation processes between the constituent Sm^{3+} ions. In CaF_2:Eu^{3+}, suitable energy levels are not available for non-radiative

annihilation of the optical excitation and fluorescence is observed from the $^5D_0$ multiplet.

As the $^6H_{\frac{5}{2}} \rightarrow ^4G_{\frac{5}{2}}(Sm^{3+})$ and $^7F_0 \rightarrow ^5D_1(Eu^{3+})$ transitions are magnetic dipole allowed, transitions of cubic symmetry centres can be observed. The intensity of these transitions has been seen to increase proportionally to the increase in cluster centre transitions. This observation supports the assertion by Yaney [82] that the cluster centres scavenge interstitial F^- ions from the single RE^{3+}-F^- pairs, thereby creating non-locally charge compensated RE^{3+} ions.

The spectra of SrF_2 crystals doped with Sm^{3+} and Eu^{3+} ions are more simple to interpret. In these cases the effects of clustering are not apparent at the concentrations studied here. In SrF_2:Sm^{3+}, only C_{4v} and cubic symmetry centres are observed. In SrF_2:Eu^{3+} the spectra are dominated by the C_{4v} centre. A very weak C_{3v} symmetry centre is present. This centre is shown to be equivalent to the dominant centre in BaF_2:Eu^{3+} which consists of a Eu^{3+}-F^- pair with the interstitial F^- ion occupying a nearest neighbour interstitial position along the $\langle 111 \rangle$ direction.

Oxygen readily diffuses into CaF_2 and SrF_2 crystals. The O^{2-} ion can charge compensate RE^{3+} ions doped into these crystals by replacing a nearby lattice F^- ion. Laser selective excitation and fluorescence studies of the CaF_2:Sm^{3+}:O^{2-} and SrF_2:Sm^{3+}:O^{2-} systems show that for short oxygenation periods a C_{3v} symmetry centre comprising Sm^{3+}-O^{2-} pairs is the dominant form of O^{2-} associated RE^{3+} centre.

Upconversion fluorescence has been observed for the C_{4v} centres in CaF_2:Eu^{3+} and SrF_2:Eu^{3+}, and the C_{3v} centre in BaF_2:Eu^{3+}. In these cases, the upconversion mechanism is assigned as a sequential absorption process, with $^5D_0$ as the intermediate state. Excitation resonant with the $^7F_0 \rightarrow ^5D_0$ transition, and separately the excited state absorption transition, is observed to produce fluorescence at higher frequencies than that of the laser excitation source. At higher temperatures, excitation of the $^7F_1 \rightarrow ^5D_0$ transitions also yields upconverted fluorescence, which persists strongly through to 300K.

Polarisation of the observed fluorescence transitions has been used to analyse the energy level structure of the C_{4v} and C_{3v} symmetry centres in CaF_2, SrF_2 and BaF_2 crystals doped with Eu^{3+}. This has led to irrep label assignments of the individual crystal field states. Polarisation of the observed transitions for centres in CaF_2 and SrF_2 crystals doped with Sm^{3+}, yields polarisation ratios that are not as distinct. This partly arises from the less well defined selection rules for Kramers ions in C_{4v} symmetry centres, but the dominant reason is the multipolar

character of the $^4G_{\frac{5}{2}} \rightarrow ^6H_J$ and ^6F_J emission. This is caused by J-mixing from the crystal field, leading to comparable electric and magnetic dipole contributions to the emissive linestrengths. A result of this is that polarisation gives minimal assistance in assigning irrep labels to the crystal field states.

Crystal field analyses have been done for all F^- compensated C_{4v} and C_{3v} symmetry centres studied here. For the Eu^{3+} centres, these analyses were based on the experimentally determined irrep labels. For the Sm^{3+} C_{4v} symmetry centres, interpolated crystal field parameters were used as a starting point which enabled assignments of irrep labels to crystal field states. Table 9.1 shows the fitted crystal field parameters. The parameters obtained in this study appear consistent with those obtained for other rare earth ions.

Table 9.1: Optimised crystal field parameters for RE^{3+} ions in C_{4v} symmetry centres in CaF_2 and SrF_2 crystals

Crystal	B^2_A	B^4_A	B^6_A	B^4_C	B^6_C	Ref
CaF_2:Ce^{3+}	906	692	569	-2082	1127	[11]
CaF_2:Pr^{3+}	838	586	411	-1841	904	[12],[65]
CaF_2:Nd^{3+}	813	585	613	-1602	837	[13],[64]
CaF_2:Sm^{3+}	749	616	617	-1208	669	This Study
CaF_2:Eu^{3+}	718	442	545	-1209	656	This Study
CaF_2:Tb^{3+}	807	504	445	-1330	624	[16]
CaF_2:Ho^{3+}	678	345	420	-1075	559	[15], This Study
CaF_2:Er^{3+}	608	409	403	-1172	505	[11]
CaF_2:Tm^{3+}	567	393	386	-1101	489	[158]
SrF_2:Ce^{3+}	730	665	365	-1859	991	[11]
SrF_2:Pr^{3+}	636	601	447	-1713	769	[12], [65]
SrF_2:Nd^{3+}	585	509	503	-1509	713	[13],[64]
SrF_2:Sm^{3+}	472	545	489	-1204	562	This Study
SrF_2:Eu^{3+}	469	364	463	-1176	552	This Study
SrF_2:Tb^{3+}	482	450	334	-1101	474	[16]
SrF_2:Ho^{3+}	338	297	325	-1030	488	[15]

Table 9.2 presents the optimised crystal field parameters for the trigonal C_{3v} symmetry centres in CaF_2, SrF_2 and BaF_2. From this data it can be seen that two distinct types of centre have been observed. In both SrF_2:RE^{3+} and BaF_2:RE^{3+}, the J and L C_{3v} centres have similar crystal field parameters the relative size of which indicates there is a weak axial distortion. This is consistent with the model of a rare earth ion compensated by a nearest neighbour $\langle 111 \rangle$ interstitial F^- ion. It can be seen in Table 9.2 that the axial parameters decrease as the lattice parameter increases from

SrF_2 and BaF_2. The B centres observed in CaF_2:RE^{3+} and SrF_2:Ho^{3+} appear to have a different configuration. Judging from the magnitude of the cubic parameters for that centre there may be lattice vacancies in the cube around the rare-earth ion. The observation of a B centre for SrF_2:Ho^{3+} is difficult to explain as both SrF_2:Eu^{3+} and SrF_2:Er^{3+} possess J centres.

Table 9.2: Optimised crystal field parameters for RE^{3+} ions in C_{3v} symmetry centres in CaF_2, SrF_2 and BaF_2 crystals. The J and L centres are equivalent.

Crystal	Centre	B^2_A	B^4_A	B^6_A	$B^6_{\hat{A}}$	B^4_C	B^6_C	Ref
CaF_2:Ho^{3+}	B	197	-72	-676	-223	46	681	[15]
CaF_2:Er^{3+}	B	141	77	-531	-342	83	581	[14]
SrF_2:Eu^{3+}	J	221	171	-238	-59	1227	1152	This Study
SrF_2:Ho^{3+}	B	52	-184	-526	-149	-58	605	[15]
SrF_2:Er^{3+}	J	118	-185	-258	-84	1087	1023	[14],[131]
BaF_2:Eu^{3+}	L	186	95	-156	-18	1121	1121	This Study
BaF_2:Er^{3+}	L	108	-101	-107	-59	959	862	[131]

As the R and Q centres observed in CaF_2:Sm^{3+} were found to have no optical radiative decay, a study CaF_2:Sm^{3+} codoped with additional RE^{3+} ions has been completed. Fluorescence has been observed from the heterogeneous R and Q centres for codoping of La^{3+}, Ce^{3+}, Eu^{3+}, Gd^{3+} and Tb^{3+}. This has allowed a determination of the Sm^{3+} energy levels for these centres. For the R(Eu,Sm) and Q(Eu,Sm) centres efficient $^4G_{\frac{5}{2}}(Sm^{3+}) \rightarrow {}^5D_0(Eu^{3+})$ energy transfer has been observed. This has been analysed in terms of the thermal population of the phonon modes mediating the transfer.

Simple Zeeman splitting patterns are observed for the R and Q centres with magnetic fields applied along the $\langle 111 \rangle$ direction. This indicates that there is only one magnetically equivalent centre for the field applied along this crystallographic axis. Thus, the centres have a high symmetry axis along the $\langle 111 \rangle$. From the measured energy transfer rates, it appears that the ions are in closer spatial proximity for the Q centre than the R centre. Further to this, the ions in the Q trimer centre are equivalent and therefore experience the same crystal field, whilst those in the R dimer centre are inequivalent. Thus, some restrictions on the centre configuration are provided by the studies presented here.

When ions heavier than Tb^{3+} are added to CaF_2:Sm^{3+}, the R and Q centres are not apparent. Instead, a new centre labelled S has been observed. This centre appears to be due to a single isolated Sm^{3+} ion as the measured $^4G_{\frac{5}{2}}$ excitation frequencies do not change as the ionic radius of the codopant ion changes.

Zeeman infrared absorption studies have been carried out for CaF_2 and SrF_2 crystals doped with Sm^{3+} and Eu^{3+} ions and BaF_2:Eu^{3+}. These experiments not only confirm the centre symmetries assigned from laser selective excitation and fluorescence, but the measured magnetic splitting factors have been used to test the crystal field analyses performed for these centres. This is particularly useful for the C_{4v} symmetry centres in CaF_2:Sm^{3+} and SrF_2:Sm^{3+} as in these cases the crystal field calculations have been performed without experiment irrep symmetry labels. On the whole, good agreement between the calculated and experimental splitting factors has been obtained giving confidence in the analyses performed.

Appendix A

The Calculation of Magnetic Hyperfine Constants, A_J for Ho^{3+}, Pr^{3+} and Tb^{3+}

In order to accurately analyse the hyperfine patterns observed for Pr^{3+}, Tb^{3+} and Ho^{3+} ions in CaF_2 and SrF_2 one must obtain an accurate set of nuclear hyperfine constants for the magnetic hyperfine interactions. We restrict ourselves to the magnetic interaction only, as there is no evidence for any quadrupole splittings in the spectra measured here.

To calculate the magnetic hyperfine structure constants we use formula 5-19 of Wybourne [25]

$$A_J = a_l \left[2 - g + 2 \left(\frac{14(2J+1)}{J(J+1)} \right)^{\frac{1}{2}} (f^N \alpha S L \,||\, V^{(12)} \,||\, f^N \alpha' S' L') \begin{Bmatrix} S & S' & 1 \\ L & L' & 2 \\ J & J & 1 \end{Bmatrix} \right]$$

$$= a_l(\Re + \Im)$$

where $\Re$=2-g and $\Im$ represents the remainder of the expression. Such a calculation proceeds by first determining a value for a_l given by:

$$2\mu_B \mu_N g_I \langle r^{-3} \rangle$$

where μ_B is the Bohr magneton, μ_N is the nuclear magneton and g_I is the nuclear g-factor. Since a_l depends upon $\langle r^{-3} \rangle$, the inverse cube of the electron orbital, this quantity is best determined from experimental data. Abragham and Bleaney (pg 298) give A_J values for the ground multiplets of most rare earth ions as determined from magnetic resonance measurements.

One then calculates the spin and orbital contributions to the magnetic hyperfine constant for the ground multiplet. This necessitates a knowledge of the intermediate-coupled free-ion wavefunctions. In this study the free ion wavefunctions of Mujaji for Ho^{3+} in CaF_2 were used while for Tb^{3+} and Pr^{3+} the LaF_3 [Carnall et. al. (1977)] free ion wavefunctions were used since free ion wavefunctions for the CaF_2:Tb^{3+} and CaF_2:Pr^{3+} systems have not been determined. It is pertinent to use intermediate-coupled wavefunctions in the calculation of the spin moments contribution to the

Table A.1: Intermediate-coupled free-ion wavefunctions and Lande g factors for CaF_2:Ho^{3+}

Multiplet	Wavefunction	Lande g Factor
$^5I_8$	$0.9673\vert\ ^5I_8\ \rangle + 0.1159\vert\ ^3K_8^1\ \rangle - 0.2206\vert\ ^3K_8^2\ \rangle$	1.24
$^5I_7$	$0.9855\vert\ ^5I_7\ \rangle + 0.0715\vert\ ^3K_7^1\ \rangle - 0.1448\vert\ ^3K_7^2\ \rangle$	1.17
$^5I_6$	$0.9748\vert\ ^5I_6\ \rangle - 0.0899\vert\ ^3H_6^1\ \rangle - 0.0878\vert\ ^3H_6^3\ \rangle$ $+0.1406\vert\ ^3H_6^4\ \rangle - 0.0758\vert\ ^3K_6^2\ \rangle$	1.07
$^5I_5$	$0.0717\vert\ ^5F_5\ \rangle - 0.9504\vert\ ^5I_5\ \rangle - 0.0867\vert\ ^3G_5^2\ \rangle$ $+0.1163\vert\ ^3H_5^1\ \rangle + 0.1420\vert\ ^3H_5^3\ \rangle - 0.1999\vert\ ^3H_5^4\ \rangle$	0.92
$^5I_4$	$-0.9460\vert\ ^5I_4\ \rangle + 0.1285\vert\ ^3H_4^1\ \rangle + 0.1655\vert\ ^3H_4^3\ \rangle$ $-0.2292\vert\ ^3H_4^4\ \rangle$	0.62
$^5F_5$	$-0.8937\vert\ ^5F_5\ \rangle + 0.1087\vert\ ^5G_5\ \rangle - 0.1347\vert\ ^5I_5\ \rangle$ $+ 0.1823\vert\ ^3G_5^1\ \rangle + 0.3174\vert\ ^3G_5^2\ \rangle - 0.1640\vert\ ^3G_5^3\ \rangle$	1.36
$^5S_2$	$0.8290\vert\ ^5S_2\ \rangle + 0.2482\vert\ ^5F_2\ \rangle + 0.3772\vert\ ^3P_2^2\ \rangle$ $+ 0.1036\vert^3P_2^3\rangle + 0.2325\vert^3D_2^1\rangle + 0.1096\vert^3D_2^2\rangle$ $+ 0.0866\vert^1D_2^2\rangle - 0.0948\vert^1D_2^3\rangle$	1.79

hyperfine interaction because of the sensitivity of $\Im$ to departure from LS coupling. This arises from the fact that $\Im$ is non-diagonal in αSL. Fortunately $\Re$ dominates the interaction, typically representing around 98% of its magnitude. From a knowledge of $\Im$, $\Re$ and A_J for the ground state a_l can be obtained and is the same for all the multiplets of a given electronic configuration. Hence, once a_l is known A_J can be calculated for all other multiplets. For the calculations presented the 'F-Shell Empirical' programs of Dr Mike Reid were used to determine $\Im$ and the free-ion wavefunctions. Tables A.1, A.2 and A.3 give the appropriate free ion wavefunctions, listed to components down to 1% of the total wavefunction. Table A.4 gives the values of the magnetic hyperfine constants A_J for the analyses of Chapter 4.

Table A.2: Intermediate-coupled free-ion wavefunctions and Lande g factors for LaF_3:Pr^{3+}

Multiplet	Wavefunction	Lande g Factor
$^3H_4$	$0.1578\|\ ^3H_4\ \rangle+0.1578\|\ ^1G_4\rangle$	0.80
$^3H_5$	$1.0000\|^3H_5\rangle$	1.03
$^3H_6$	$0.9986\|^3H_6\rangle$	1.17
$^3F_2$	$0.9886\|^3F_2\rangle+0.1498\|^1D_2\rangle$	0.67
$^3F_3$	$1.0000\|^3F_3\rangle$	1.08
$^3F_4$	$0.8422\|^3F_4\rangle+0.1094\|^3H_4\rangle-0.5280\|^1G_4\rangle$	1.17
$^1G_4$	$0.5384\|^3F_4\rangle-0.1175\|^3H_4\rangle+0.8345\|^1G_4\rangle$	1.07
$^1D_2$	$0.2829\|^3P_2\rangle+0.1475\|^3F_2\rangle-0.9477\|^1D_2\rangle$	1.03
$^3P_0$	$0.9957\|^3P_0\rangle$	-
$^3P_1$	$1.0000\|^3P_1\rangle$	1.17
$^1I_6$	$0.9986\|^1I_6\rangle$	1.00
$^3P_2$	$-0.9591\|^3P_2\rangle-0.2817\|^1D_2\rangle$	1.46
$^1S_0$	$0.9957\|^1S_0\rangle$	-

Table A.3: Intermediate-coupled free-ion wavefunctions and Lande g factors for LaF_3:Tb^{3+}

Multiplet	Wavefunction	Lande g Factor
$^7F_6$	$-0.9792\|^7F_6\rangle+0.1399\|^5G_6^1\rangle-0.1311\|^5G_6^3\rangle$	1.49
$^7F_5$	$-0.9852\|^7F_5\rangle$	1.50
$^7F_4$	$0.9781\|^7F_4\rangle-0.1031\|^5D_4^1\rangle+0.1003\|^5D_4^3\rangle$	1.47
$^7F_3$	$0.9763\|^7F_3\rangle+0.1175\|^5D_3^3\rangle-0.1345\|^5D_3^1\rangle$	1.49
$^7F_2$	$-0.9745\|^7F_2\rangle+0.1267\|^5D_2^3\rangle-0.1574\|^5D_2^1\rangle$	1.49
$^7F_1$	$0.9739\|^7F_1\rangle-0.1301\|^5D_1^3\rangle+0.1712\|^5D_1^1\rangle$	1.49
$^7F_0$	$1.0000\|^7F_0\rangle$	-
$^5D_4^3$	$-0.1584\|^7F_4\rangle-0.1281\|^3F_4^8\rangle-0.1022\|^5F_4^2\rangle$	
	$+0.5622\|^5D_4^1\rangle\ +0.2206\|^5D_4^2\rangle-0.7416\|^5D_4^3\rangle$	1.46

Table A.4: Derived magnetic hyperfine structure constants (in MHz) for low-lying multiplets of Pr^{3+}, Tb^{3+} and Ho^{3+}, calculated from those for the ground multiplets identified by t.

R.E.$^{3+}$ Ion	Multiplet	A Value
Ho^{3+}	$^5I_8$	812^t
	$^5I_7$	883
	$^5I_6$	969
	$^5I_5$	1176
	$^5I_4$	1408
	$^5F_5$	684
	$^5S_2$	285
Pr^{3+}	$^3H_4$	1093^t
	$^3H_5$	802
	$^3H_6$	633
	$^3F_2$	1053
	$^3F_3$	716
	$^3F_4$	665
	$^1G_4$	662
	$^1D_2$	758
	$^3P_1$	102
	$^1I_6$	802
	$^3P_2$	482
Tb^{3+}	$^7F_6$	530^t
	$^7F_5$	468
	$^7F_4$	556
	$^7F_3$	410
	$^7F_2$	395
	$^7F_1$	386
	$^5D_4$	527

Appendix B

Laser Spectroscopy of the L Centre in BaF_2:Sm^{3+}

Preliminary studies of Sm^{3+} doped into BaF_2 crystals were undertaken. Due to the more promising progress in other areas, this work did not develop past its infancy. Unlike CaF_2:RE^{3+} and SrF_2:RE^{3+}, BaF_2 crystals doped with RE^{3+} have been largely neglected optically with the notable exceptions of BaF_2:Eu^{3+} [106], [112] and BaF_2:Er^{3+} [157],[131]. Some minor spectroscopic results pertaining to the dominant centre for BaF_2:0.1%Sm^{3+} crystals is presented here.

Excitation to the $^4G_{\frac{5}{2}}$ multiplet in the 17300-18200 region yields four fluorescence peaks which can all be correlated with the same centre. Fluorescence observed to the $^6H_{\frac{5}{2}}$ multiplet (shown in Figure B.2) is weakly polarised for ⟨111⟩ oriented crystals but shows no polarisation dependence for ⟨100⟩ oriented samples. This is in agreement with that expected for a C_{3v} symmetry centre as expected for the BaF_2 host. The excitation peaks at 17736, 17979 and 18087 cm^{-1} are consistent with transitions from the Z_1 ground state to the A_1, A_2 and A_3 levels of the $^4G_{\frac{5}{2}}$ multiplet. It is noted that the A_2-A_3 spearation of 108 cm^{-1} is a considerably smaller splitting of the cubic Γ_8 level, than that observed for the A centres in CaF_2:Sm^{3+} and SrF_2:Sm^{3+}. This is indicative of a weaker axial distortion. The fourth peak observed in excitation at 17719 cm^{-1} is the $Z_2 \rightarrow A_1$ transition. This places the Z_2 state 17 cm^{-1} above the ground state and thus having a Boltzmann population roughly 25% of that of the ground state accounting for the intensity of this transition in excitation. The $Z_2 \rightarrow A_2$ and A_3 transitions at 17962 and 18070 cm^{-1} respectively can also be observed for amplification of this spectrum. Transitions to the $^4F_{\frac{3}{2}}$ multiplet in the 18850-18950 region can be observed in Figure B.3, This shows two sets of two transitions, each separated by 7 cm^{-1}, the splitting of the $^4F_{\frac{3}{2}}$ cubic Γ_8. The observed transition energies are 18883, 18890, 18901 and 18907 cm^{-1} which are assigned as the $Z_2 \rightarrow B_1$ and B_2, $Z_1 \rightarrow B_1$ and B_2 transitions respectively.

Fluorescence to the $^6H_{\frac{5}{2}}$ multiplet is observed in the 17750-17600 cm^{-1} region. The $A_1 \rightarrow Z_1$ and Z_2 transitions can be observed at 17736 and 17719 cm^{-1}. this, the cubic ground state splitting of 17 cm^{-1} is confirmed. An additional transition at 17622 cm^{-1} is assigned as the $A_1 \rightarrow Z_3$ transition. This places the Z_3 state at 114

cm^{-1} above the ground state.

In addition to the CW dye experiments performed above, both the $^4G_{\frac{5}{2}}$ and $^4F_{\frac{3}{2}}$ multiplets were excited using the Photochemical Research Associates Model LN107 dye laser pumped by the PRA LN1000 pulsed nitrogen laser to obtain the $^4G_{\frac{5}{2}}$ fluorescent lifetime which was recorded on the Hitachi Model VC 6275 digital storage oscilloscope. Coumarin 540A can be used to excite the $^4G_{\frac{5}{2}}$ multiplet, whilst either that dye or the more efficient Coumarin 500 dye can be used to excite $^4F_{\frac{3}{2}}$ multiplet. As with the CaF_2 and SrF_2 cases, the excitation of the $Z_1 \rightarrow B_1$ transition yields no rise time for the fluorescent transient obtained monitoring the $A_1 \rightarrow Z_1$ transition. This indicates that the $^4F_{\frac{3}{2}}$ state has no measureable and thus do not fluorescence. A result expected from the lack of emission observed for this multiplet under CW excitation. The resulting decay was therefore fitted to a single exponential expression. The fit is shown in Figure B.1 and yielded the $^4G_{\frac{5}{2}}A_1$ state lifetime of 23.6 milliseconds

Table B.1: $^6H_{\frac{5}{2}}$, $^4G_{\frac{5}{2}}$ and $^4F_{\frac{3}{2}}$ multiplet energy levels of the C_{3v} symmetry centre in BaF_2:Sm^{3+} as measured in air cm^{-1} (± 1 cm^{-1} unless otherwise stated)

Multiplet	State	Energy
$^6H_{\frac{5}{2}}$	Z_1	0
	Z_2	17
	Z_3	114
$^4G_{\frac{5}{2}}$	A_1	17736
	A_2	17979
	A_3	18087
$^4F_{\frac{3}{2}}$	B_1	18901
	B_2	18907

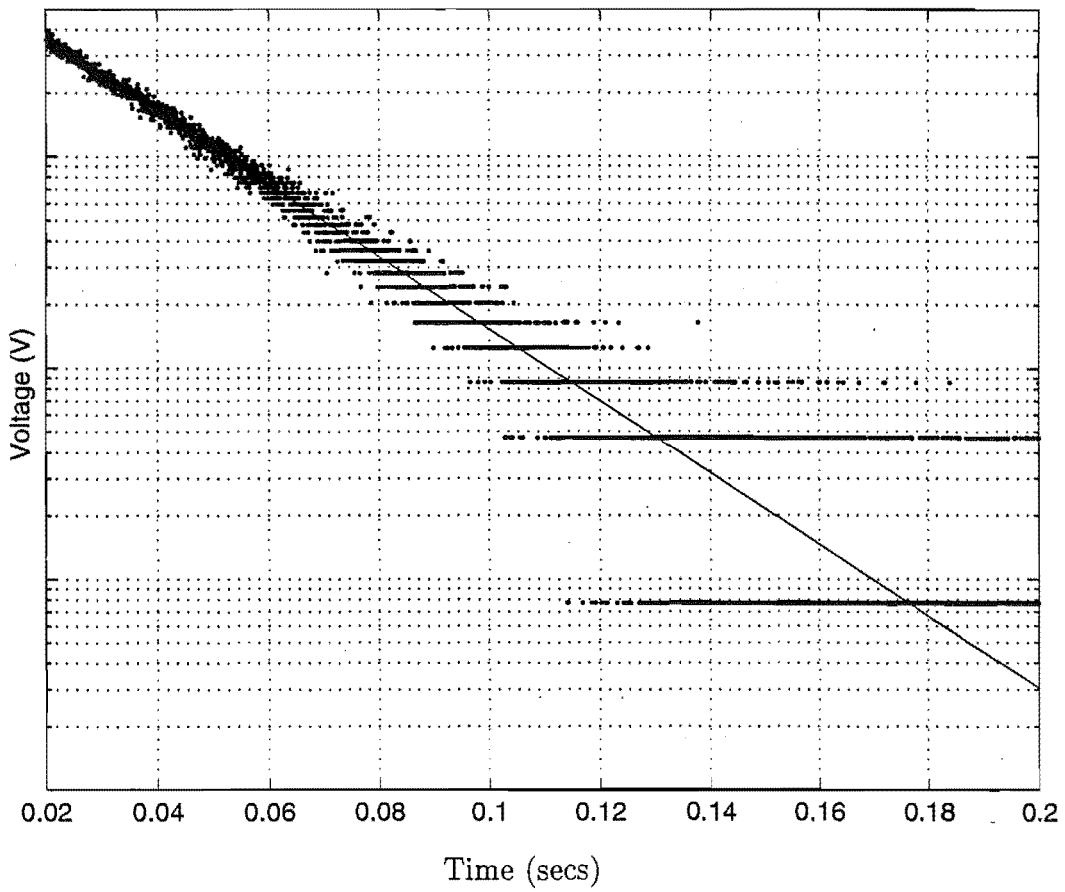

Figure B.1: 16K fluorescence transient for the C_{3v} symmetry centre in BaF_2:0.1%Sm^{3+}. The $^4G_{\frac{5}{2}}A_1 \rightarrow {}^6H_{\frac{5}{2}}Z_1$ transition at 17736 cm^{-1} cm^{-1} has been monitored.

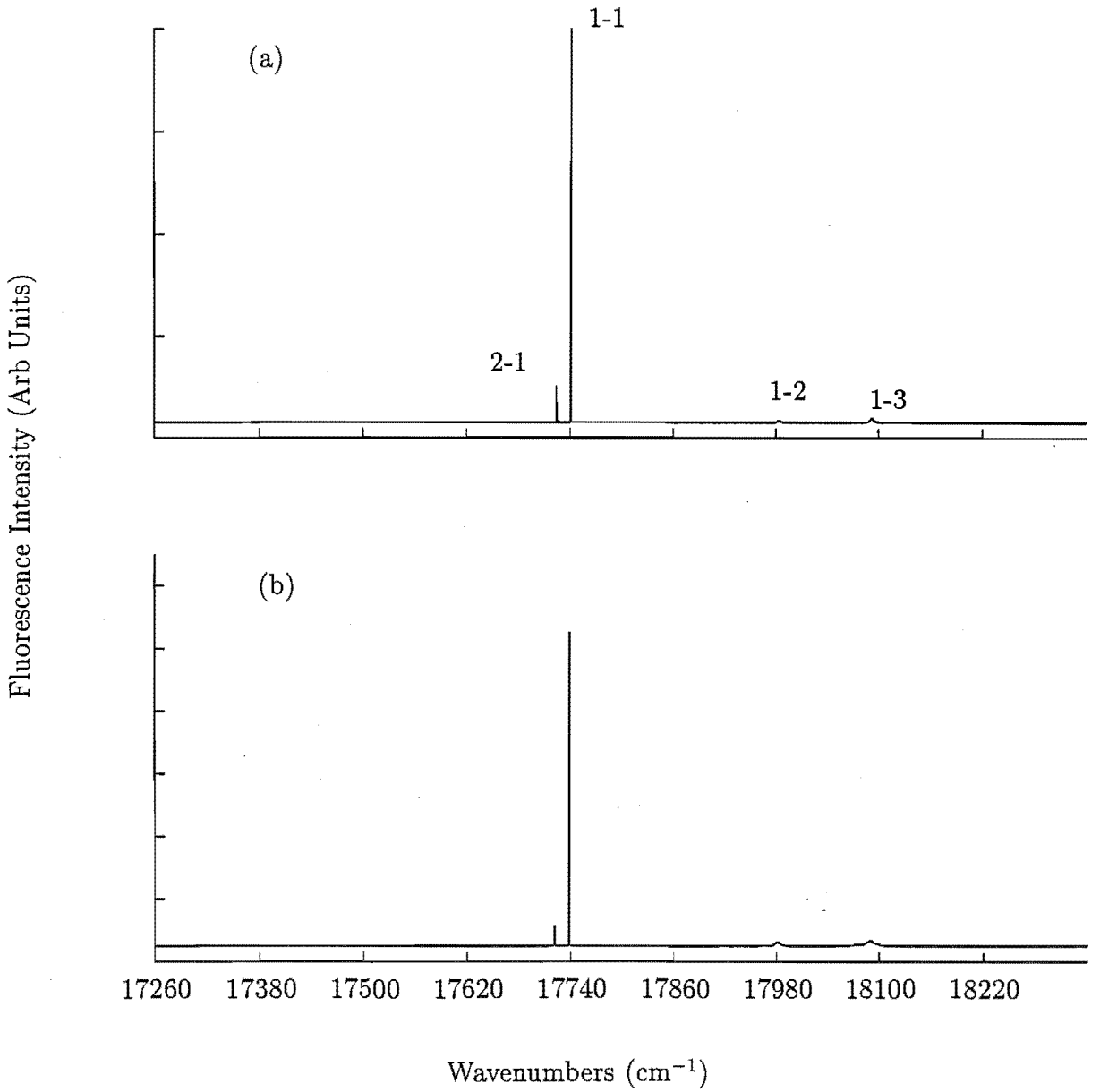

Figure B.2: Excitation spectrum of the $^4G_{\frac{5}{2}}$ multiplet for the L centre in BaF_2:0.1Sm^{3+} (a) monitoring all fluorescence in zero order on the SPEX 1700 spectrometer and (b) monitoring the 16767 cm^{-1} transition. The spectra were recorded at 16K.

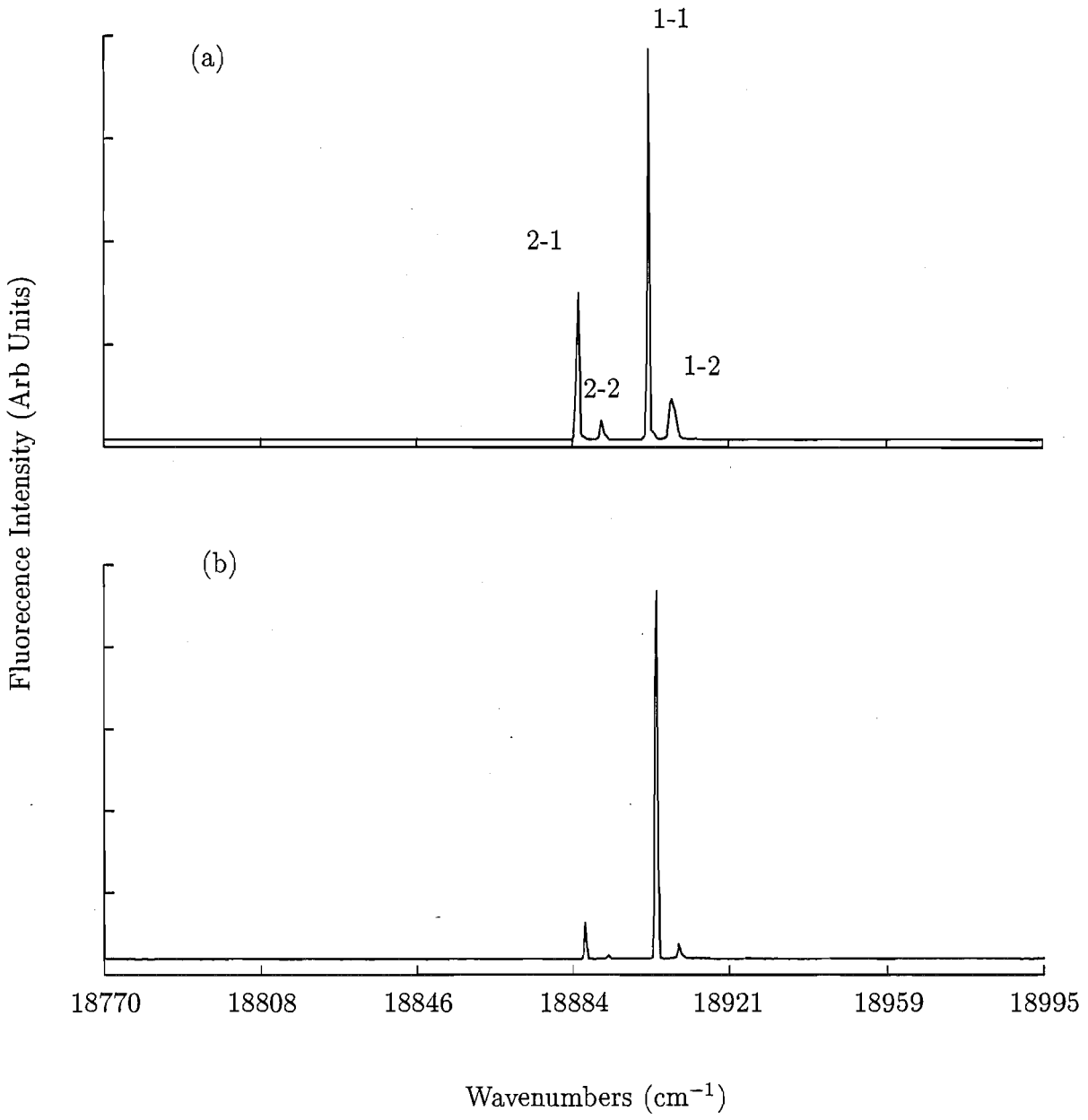

Figure B.3: Excitation spectrum of the $^4F_{\frac{3}{2}}$ multiplet for the L centre in BaF_2:0.1Sm^{3+} (a) monitoring all fluorescence in zero order on the SPEX 1700 spectrometer and (b) monitoring the 17736 cm^{-1} transition. The spectra were recorded at 16K.

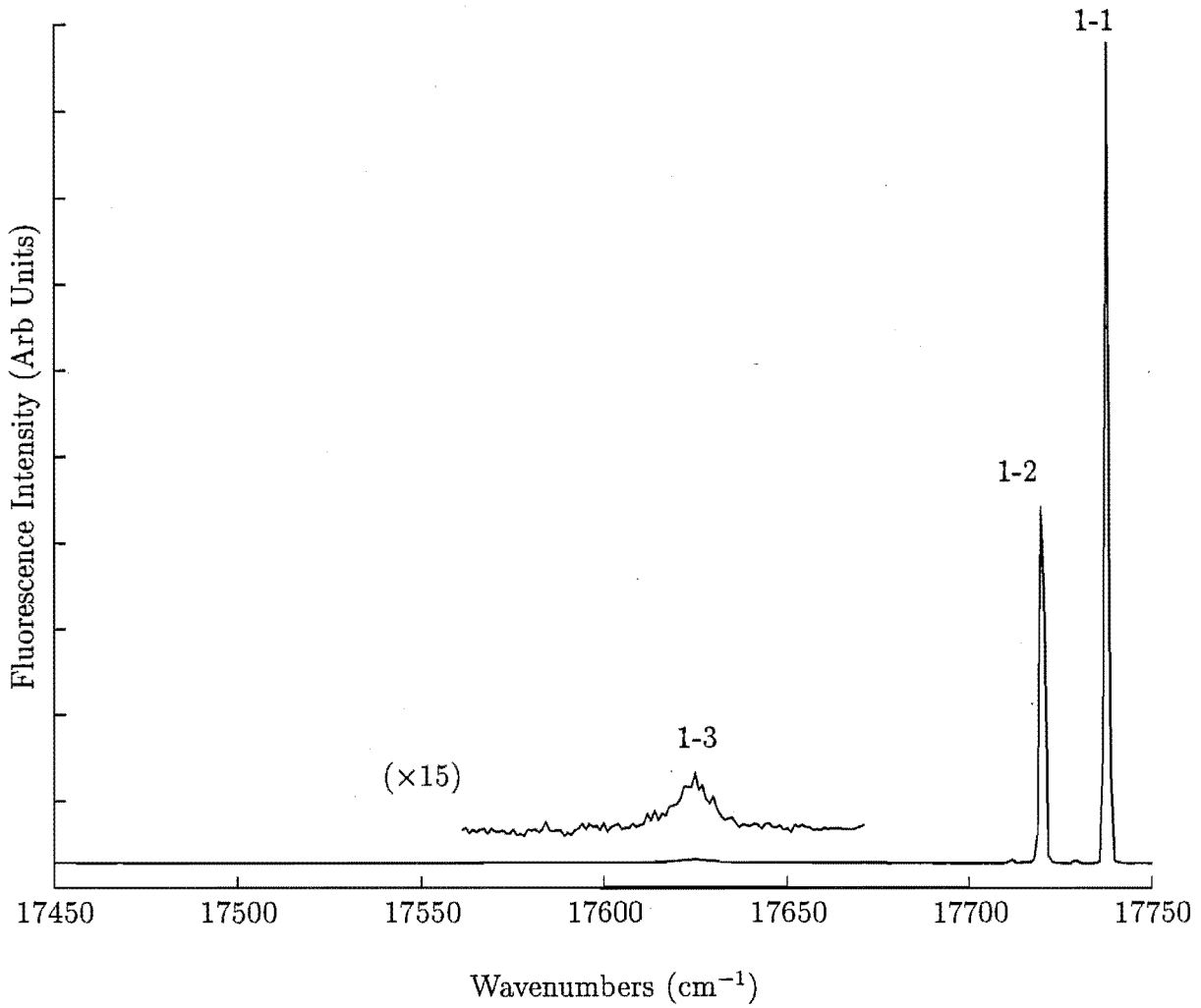

Figure B.4: Fluorescence spectrum of the C_{3v} symmetry centre in BaF_2:0.1%Sm^{3+} for transitions $^4G_{\frac{5}{2}} \rightarrow {}^6H_{\frac{5}{2}}$. Excitation is at the 18907 cm^{-1} $Z_1 \rightarrow B_1$ transition. The spectrum was recorded at 16K.

References

[1] Schawlow A L and Townes C H, 1958. *Infrared and Optical Masers* Phys. Rev. Lett. **7**, 118.

[2] Mamian T H, 1960. *Stimulated Optical Radiation in Ruby Masers* Nature **187**, 493.

[3] Smith W V and Sorokin P P, 1966. *The Laser* McGraw-Hill Inc (New York).

[4] Luthy W and Weber H P, 1995. *Diode Pumped IR Solid State Lasers* Infrared Phys. Technol. **36** (1), 267.

[5] Visser R, Andriessen J, Dorenbos P and Eijk C W E, 1993. *Ce^{n+} Energy Levels in Alkaline Earth Fluorides and Cerium-Electron, Cerium-Hole Interactions* J. Phys.: Condens. Matter **5**, 5887.

[6] Digonnet M J F, 1993. *Rare Earth Doped Fiber Lasers and Amplifiers* Marcel Dekker Inc (New York).

[7] Kaminskii A A, 1987. *Laser Crystals: Their Physics and Properties.* Springer Verlag (Heidlberg).

[8] Weber M J and Bierig R W, 1964. *Paramagnetic Resonance and Relaxation of Trivalent Rare Earth Ions in Calcium Fluoride I. Resonance Spectra and Crystal Fields.* Phys. Rev. **134** (6A), A1492.

[9] Kittel C, 1986. *Introduction to Solid State Physics* John Wiley & Sons Inc (New York).

[10] Cirillo-Penn K M and Wright J C, 1991. *Identification of Defect Structures in Eu^{3+}:CaF_2 by Site Selective Spectroscopy of Relaxation Dynamics.* J. Lum. **48&49**, 505.

[11] Freeth C A, 1980. *Solid State Spectroscopy: The Transverse Zeeman Effect in CaF_2:Er^{3+} Crystals* Ph.D. Thesis (University of Canterbury).

[12] Reeves R J, 1987. *Laser Selective Excitation of Praseodymium Ions in Hydrogenated Fluorite Crystals* Ph.D. Thesis (University of Canterbury).

[13] Han T P J, 1988. *Solid State Spectroscopy: Laser Selective Excitation Studies of Neodymium* Ph.D. Thesis (University of Canterbury).

[14] Cockcroft N J, 1987. *Solid State Spectroscopy: Laser Selective Excitation of Erbium Ions in Crystalline Solids.* Ph.D. Thesis (University of Canterbury).

[15] Mujaji M, 1992. *Solid State Spectroscopy: Laser Selective Excitation of Holmium Ions in Crystalline Solids.* Ph.D. Thesis (University of Canterbury).

[16] Murdoch K M, 1993. *Laser Spectroscopy, Energy Transfer and Bleaching Processes in Crystalline Rare Earth Centres.* Ph.D. Thesis (University of Canterbury).

[17] Mujaji M, Jones G D and Syme R W G, 1992. *Polarisation Study and Crystal Field Analysis of the Laser Selective Excitation Spectra of Ho^{3+} Ions in CaF_2 and SrF_2 Crystals.* Phys. Rev. B **46** (22), 14398.

[18] Heron R J, 1994. *Infrared Spectroscopy of Hyperfine Structure of the Principal Ho^{3+} Centre in CaF_2.* 4th Year Report (University of Canterbury).

[19] Ranon U and Lee K, 1969. *Paramagnetic Resonance in a Trigonal Site in SrF_2* Phys. Rev. **188** (2), 539.

[20] Brown M R, Thomas H, Whiting J S S and Shand W A, 1969. *Experiments on Er^{3+} in SrF_2 II, Concentration Dependence of Site Symmetry* J. Chem. Phys. **50** (2), 891.

[21] Corish J, Catlow C R A, Jacobs P W M and Ong S H, 1982. *Defect Aggregation in Anion Excess Fluorites. Dopant Monomers and Dimers.* Phys. Rev. B. **25**(10), 6425.

[22] Tallant D R and Wright J C, 1975. *Selective Laser Excitation of Charge Compensated Sites in CaF_2:Er^{3+}* J. Chem. Phys. **65** (5), 2074.

[23] Freeth C A, Jones G D and Syme R W G, 1982. *The Transverse Zeeman Effect in Calcium Fluoride Crystals Containing Erbium* J. Phys. C: Solid State Phys. **15**, 5667.

[24] Weissbluth M, 1978. *Atoms and Molecules* Academic Press (London).

[25] Wybourne B G, 1965. *Spectroscopic Properties of Rare Earths* Interscience (New York).

[26] Nielson C W and Koster G F, 1963. *Spectroscopic Coefficients for the p^N, d^N and f^N Configurations.* M.I.T. Press (Massachuetts).

[27] Rotenburg M, Bivens R, Metropolis N and Wooten J K, 1959. *The 3j and 6j Symbols* M.I.T. Press (Massachusetts).

[28] Edmonds A R, 1957. *Angular Momentum in Quantum Mechanics* Princeton University Press (New Jersey).

[29] Wybourne B G, 1962. *Nuclear Moments and Intermediate Coupling.* J. Chem. Phys. **37** (8), 1807.

[30] Slichter C P, 1978. *Principles of Magnetic Resonance.* Springer Verlag (Heidelberg).

[31] Judd B R, 1962. *Optical Absorption Intensities of Rare Earth Ions.* Phys. Rev. **127**(3), 750

[32] Ofelt G S, 1962. *Intensities of Crystal Spectra of Rare Earth Ions.* J. Chem. Phys. **37**(3), 511.

[33] Lowther J E, 1974. *Spectroscopic Transition Probabilities of Rare Earth Ions.* J. Phys. C: Solid State Phys. **7**, 4393.

[34] Koster G F, Dimmock J O, Wheeler R G and Statz H, 1963. *Properties of the Thirty Two Point Groups* M.I.T. Press (Massachusetts).

[35] Feofilov P P, 1959. *Polarized Luminescence of Atoms, Molecules and Crystals*

[36] Voron'ko Yu K, Osiko A V, Osiko V V, Sobol' A A, Ushakov S N and Tsymbal L I, 1994. *Mobility of Interstitial Fluorine Bound Activator Centres of TR^{3+} Ions in the Fluorite Structure.* Phys. Solid State **36**(3), 410.

[37] Jamison S P and Reeves R J, 1995. *Optical Depolarisation in CaF_2:RE^{3+} and SrF_2:RE^{3+} C_{4v} Centres Due to Dipole Reorientation.* J. Lum. **66&67**, 169.

[38] Hall J L and Schumacher R T, 1962. Phys. Rev. B, **127** (6), 1892.

[39] Dieke G H, 1967. *Hyperfine Structure and Magnetic Behavior of Trivalent Holmium in Hexagonal $LaCl_3$.* Physica **33**, 212.

[40] Agladze N I, Popova M N and Zhizhin G N, 1993. *Study of Isotope Composition in Crystals by High Resolution Spectroscopy of Monoisotope Impurity.* JETP **76** (6), 1110.

[41] Boonyarith T, Martin J P D and Manson N B, 1993. *Hyperfine Structure of* $^5I_8 \rightarrow {}^5F_5$ *Optical Transitions Within the Trigonal Center of* CaF_2*:*Ho^{3+}. Phys. Rev. B **47** (22), 14696.

[42] Martin J P D, Boonyarith T, Manson N B, Mujaji and Jones G D, 1993. *Hyperfine Coupling Between Crystal Field Levels in the Tetragonal Centre of* CaF_2*:*Ho^{3+}. J. Phys.: Condensed Matter **5**, 1333.

[43] Boonyarith T, Martin J P D and Manson N B, 1994. *Hyperfine Resonances in the Tetragonal Centre of* Ho^{3+} *in* CaF_2. J. Lum. **59**, 361.

[44] Macfarlane R M, Burum D P, Shelby R M, 1984. *Hyperfine Structure and Nuclear and Electronic Zeeman Effect of the* $^1D_2 \rightarrow {}^3H_4$ *Transition of* Pr^{3+}*:*CaF_2. Phys. Rev. B **29** (5), 2390.

[45] Reeves R J, Jones G D, Syme R W G, 1992. *Site Selective Laser Spectrosocpy of* Pr^{3+} C_{4v} *Symmetry Centres in Hydrogenated* CaF_2*:*Pr^{3+} *and* SrF_2*:*Pr^{3+} *Crystals.* Phys. Rev. B **46** (10), 5939.

[46] Jones G D and Murdoch K M, 1993. *Laser Site Selective Spectroscopy of* Tb^{3+} *Ions in* CaF_2 *and* SrF_2. J. Lum. **60&61**, 131.

[47] Falin M L, Konkin A L and Zaripov M M, 1986. *The Electron Nuclear Interaction of the Non-Kramers Ion* Tb^{3+} *in* CaF_2. J. Phys. C: Solid State Phys. **19**, 3013.

[48] Kornienko L S and Rybaltovskii AA O, 1972. *EPR of Tetragonal* Ho^{3+} *Centers in* CaF_2 *Crystals.* Sov. Phys. - Sol. Stat. **13** (7), 1785.

[49] Boonyarith T, 1994. *High Resolution Laser Spectroscopy of Trivalent Holmium Ions in Calcium Fluoride Crystals.* Ph.D. Thesis (Australian National University).

[50] Macfarlane R M and Shelby R M, 1987. *Coherent Transient and Holeburning Spectroscopy of Rare Earth Ions in Crystals* in Spectroscopy of Solids Containing Rare Earth Ions. Editors A A Kaplyanskii and R M Macfarlane. Elsevier Science Publishers (Amsterdam).

[51] Loudon R, 1990. *The Quantum Theory of Light.* Clarendon Press (Oxford).

[52] Macfarlane R M, 1990. *Inhomogeneous Broadening of Spectral Lines in Doped Insulators.* J. Lum. **45**, 1.

[53] Macfarlane R M, 1987. *Optical Spectral Linewidths in Solids* in Lasers, Spectroscopy and New Ideas: A Tribute to Arthur L Schawlow. Editors W M Yen and M D Levenson. Springer Verlag (Heidelberg).

[54] Schiff , 1968. *Quantum Mechanics* 3rd Ed. McGraw-Hill Book Company (New York).

[55] Sakurai J J, 1985. *Modern Quantum Mechanics* Addison-Wesley Publishing Company Inc. California.

[56] Macfarlane R M, Burum D P and Shelby D P, 1982. *New Determination of the Nuclear Magnetic Moment of* $^{141}Pr^{3+}$ Phys. Rev. Lett. **49**(9), 636.

[57] Reeves R J and Macfarlane R M, 1992. *Persistent Spectral Hole Burning Induced by Ion Motion in* $CaF_2{:}Pr^{3+}{:}D^-$ *and* $SrF_2{:}Pr^{3+}{:}D^-$ *Crystals.* J. Opt. Soc. Am. B **9** (9), 764.

[58] Reeves R J and Macfarlane R M, 1993. *Spectral Hole Burning Study of Magnetic and Hyperfine Interactions in* $SrF_2{:}Pr^{3+}{:}D^-$ *and* $CaF_2{:}Pr^{3+}{:}D^-$ Phys. Rev. B **47** (1), 158.

[59] Manson N B, Hasan Z, Fisk P T H, Reeves R J, Jones G D and Macfarlane R M, 1992. *Superhyperfine Structure of* F^-, H^-, D^- *and* T^- *Charge Compensated* Pr^{3+} *Centres in* CaF_2 *and* SrF_2 *Crystals.* J. Phys.: Condens. Matter **4**, 5591.

[60] Burum D P, Shelby R M and Macfarlane R M, 1982. *Hole Burning and Optically Detected Fluorine NMR in* $Pr^{3+}{:}CaF_2$ Phys. Rev. B **25** (5), 3009.

[61] Martin J P D, Boonyarith T, Manson N B, Khong Y L and Jones G D, 1994. *Strain Broadening of Optical Transitions with Hyperfine Structure* Phys. Rev. B **49** (22), 1994.

[62] Tissue B M and Wright J C, 1987. *Site-Selective Laser Spectroscopy of* $CaF_2{:}Pr^{3+}$ *and* $CaF_2{:}Pr^{3+}$, R^{3+} $(R^{3+}{=}Y^{3+}, Gd^{3+}, Nd^{3+})$. Phys. Rev. B. **36**(18), 9781.

[63] Cleven C D, Lee S H and Wright J C, 1991. *Clustering and Perclation of Defects in* $Pr^{3+}{:}SrF_2$ *Using Site-Selective Spectroscopy.* Phys. Rev. B. **44**(1), 23.

[64] Wells J R, 1993. *Solid State Spectroscopy: Zeeman Studies of Rare Earth Doped Alkaline Earth Fluorides.* M.Sc Thesis (University of Canterbury).

[65] Wells J P R and Jones G D. Unpublished work.

[66] Chaminade J P, Macfarlane R M, Ramaz F and Vial J C, 1991. *High Resolution Laser Spectroscopy of Rare Earth Doped* $CsCdBr_3$. J. Lum. **48&49**, 531.

[67] Abragham A and Bleaney B, 1970. *Electron Paramagnetic Resonance of Transition Ions* Oxford University Press (New York).

[68] Carnall W T, Crosswhite H and Crosswhite H M, 1977. *Energy Level Structure and Transition Probabilities of the Trivalent Lanthanides in LaF_3.* Argonne National Laboratory Report.

[69] Forrester P A and Hempstead C F, 1962. *Paramagnetic Resonance of Tb^{3+} Ions in $CaWO_4$ and CaF_2.* Phys. Rev. **126** (3), 923.

[70] Antipin A A, Livanova L D and Shekun L Ya, 1968. *Paramagnetic Resonance and Spin Lattice Relaxation in SrF_2:Tb^{3+} Single Crystals.* Sov. Phys. - Sol. Stat. **10** (5), 1025.

[71] Kaiser W, Garrett C G B and Wood D L, 1961. *Fluorescence and Optical Maser Effects in CaF_2:Sm^{2+}.* Phys. Rev. **123** (3), 766.

[72] Wood D L and Kaiser W, 1962. *Absorption and Fluorescence of Sm^{2+} in CaF_2, SrF_2 and BaF_2.* Phys. Rev. **126** (6), 2079.

[73] Rabbiner N, 1963. *Fluorescence of Sm^{3+} in CaF_2.* Phys. Rev. **130** (2), 502.

[74] Ewanizky T F, Caplan P J and Pastore J R, 1965. *Polarisation of CaF_2:Sm^{3+} Fluorescence.* J. Chem. Phys. **43** (12), 4351.

[75] Rabbiner N, 1967. *Tetragonal Crystal Field Energy Levels - CaF_2:Sm^{3+} and CdF_2:Sm^{3+}.* J. Opt. Soc. Am. **57** (11), 1376.

[76] Nara H and Schlesinger M, 1971. *Experimental and Theoretical Study of the Low Lying Energy Level Structure of Sm^{3+} in CaF_2.* Phys. Rev. B **3** (1), 58.

[77] Low W, 1964. *Electron Spin Resonance Studies with Superconducting Magnets: The Spectrum of Dy^{3+} and Sm^{3+} in CaF_2.* Phys. Rev. **134** (6A), A1479.

[78] Antipin A A, Kurkin L N, Livanova L D, Potvoroa L Z and Shekun L Ya, 1965. *Paramagnetic Resonance of Trivalent Samarium in Single Crystals of CaF_2.* Sov. Phys. - Sol. Stat. **7** (5), 1271.

[79] Evans H W and McLaughlan S D, 1966. *Electron Paramagnetic Resonance of Sm^{3+} Ions on Trigonal Sites in CaF_2.* Phys. Lett. **23** (11), 638.

[80] Newman R C and Woodward R J, 1974. *An EPR Analysis of Yb^{3+}, Er^{3+} and Sm^{3+} Centres in Strontium Fluoride.* J. Phys. C: Sol. Stat. **7**, L432.

[81] Dieke G H, 1968. *Spectra and Energy Levels of Rare Earth Ions in Crystals.* Interscience (New York).

[82] Yaney P P, Schaeffer D M and Wolf J L, 1975. *Fluorescence and Absorption Studies of* $Sr_{0.999-x}Gd_{0.001}Ce_xF_{2.001+x}$ Phys. Rev. B. **11**(7), 2460.

[83] Loh E, 1968. $4f^N \rightarrow 4f^{N-1}5d$ *Spectra of Rare Earth Ions in Crystals.* Phys. Rev. **175** (2), 175.

[84] Elcombe M M and Pryor A W, 1970. *The Lattice Dynamics of Calcium Fluoride.* J. Phys. C: Solid State Phys. **3**, 492.

[85] Bilz H and Kress W, 1979. *Phonon Dispersion Relations in Insulators.* Springer Series in Solid State Sciences Vol 10, Springer Verlag (Heidelberg).

[86] Krishnamurthy N and Soots V, 1972. *Second Order Raman Spectra of Fluorites.I. Critical Point Analysis.* Can. J. Phys. **50**, 849.

[87] Kaiser W, Spitzer W G, Kaiser R H and Howarth L E, 1962. *Infrared Properties of* CaF_2, SrF_2 *and* BaF_2. Phys. Rev. **127**(6), 1950.

[88] Bosomworth D R, 1967, *Far-Infrared Optical Properties of* CaF_2, SrF_2, BaF_2 *and* CdF_2. Phys. Rev. **157**(3), 709.

[89] Ward R W and Whippy P W, 1974. *Vibronic Sideband of* Er^{3+} *in* CaF_2. Can. J. Phys. **52**, 1185.

[90] Aizenburg I B, Malkin B Z and Stolov A L, 1972. *Cubic Centers of the* Er^{3+} *Ion in Crystals of the Fluorite Type.* Sov. Phys. - Solid State **13** (9), 2155.

[91] Reid M F and Butler P H, 1982. *The Point Group Crystal Field and the Superposition Model for* Re^{3+} *ions in* CaF_2 *and* SrF_2. J. Phys. C: Solid State Phys. **15**, 4103.

[92] Jouart J P, Bouffard M, Klein G and Mary G, 1991. *Cubic* Eu^{3+} *Centres in Fluorite Type Crystals.* J. Lum. **50**, 273.

[93] Moore D S and Wright J C, 1981. *Laser Spectroscopy of Defect Chemistry in* CaF_2:Er^{3+}. J. Chem. Phys. **74** (3), 1626.

[94] Tallant D R, Moore D S and Wright J C, 1977. *Defect Equilibria an Fluorite Structure Crystals.* J. Chem. Phys. **67** (6), 2897.

[95] Cockcroft N J, Jones G D and Syme R W G, 1990. *Site-Selective Laser Spectroscopy of Deuterated* SrF_2:Er^{3+} J. Chem. Phys. **92** (4), 2166.

[96] Katsutoshi M and Awazu K, 1968. *Oxygen Penetration into CaF_2:Sm^{3+} Crystals.* J. Chem. Solids **29**, 1269.

[97] Krotova L V, Osiko V V and Udovenchik V T, 1965. *The Effect of Oxygen Impurity Ions on the Optical Properties of CaF_2:Sm^{3+} Crystals.* Sov. Phys. - Solid State **7** (1), pg 181.

[98] Khong Y L, 1991. *Solid State Spectroscopy: Laser Spectroscopy of Praseodymium Doped Mixed Alkaline Earth Fluorides* Ph.D Thesis (University of Canterbury).

[99] Richman I, 1964. *Vibronic Spectra of SrF_2:Sm^{3+} and BaF_2:Sm^{3+}.* Phys. Rev. **133**(5A), A1364.

[100] Han T P J, Jones G D and Syme R W G, 1993. *Site-Selective Spectroscopy of Nd^{3+} Centres in CaF_2:Nd^{3+} and SrF_2:Nd^{3+}.* Phys. Rev. B. **47**(22), 14706.

[101] Flinn G P, Jang K W, Ganem J, Jones M L, Meltzer R S and Macfarlane R M, 1994. *Sample Dependent Optical Dephasing in Bulk Crystalline Samples of Y_2O_3:Eu^{3+}* Phys. Rev. B **49** (9), 5821.

[102] Voronko Yu K, Kaminskii A A and Osiko V V, 1966. *Analysis of the Optical Spectra of Pr^{3+}, Nd^{3+}, Eu^{3+} and Er^{3+} in Fluorite Crystals (Type 1) by the Concentration Series Method* Sov. Phys. JETP **22** (3), 501.

[103] Zakharchenya B P and Rusanov I B, 1966. *Experimental Proof of the Existence of Strictly Cubic Centres in a CaF_2:Eu^{3+} Crystal.* Sov. Phys. - Sol. Stat. **8** (1), 31.

[104] Hamers R J, Wietfeldt and Wright J C, 1982. *Defect Chemistry in CaF_2:Eu^{3+}.* J. Chem. Phys. **77** (2), 683.

[105] Jouart J P, Bissieux C, Mary G and Egee M, 1985. *A Spectroscopic Study of Eu^{3+} Centres in SrF_2 using a Site-Selective Excitation Technique.* J. Phys. C: Solid State Phys. **18**, 1539.

[106] Jouart J P, Bissieux C and Mary G, 1987. *Site-Selective Laser Spectroscopy of BaF_2:Eu^{3+}.* J. Lum. **37**, 159.

[107] Gorller-Walrand C, Behets M, Porcher P, Moune-Minn O K and Laursen I, 1985. *Analysis of the Fluorescence Spectrum of $LiYF_4$:Eu^{3+}.* Inorg. Chim. Acta **109**, 83.

[108] Fluyt L, Binnemans K and Görller-Walrand C, 1995. *Intensity Parametrisation of $LiYF_4$:Eu^{3+}.* J. Alloys. Comp. **225**, 71.

[109] Pellé F, Gardant N, Genotelle M, Goldner Ph and Porcher P, 1995. *Optical Properties of Eu^{2+} and Laser Site Selective Spectroscopy of Eu^{3+} in $CsCdBr_3$*. J. Phys. Chem. Solids **56**(7), 1003.

[110] Cirillo-Penn K M and Wright J C, 1990. *Laser Spectroscopic Measurement of Point-Defect Dynamics in Eu^{3+}:CaF_2*. Phys. Rev. B **41**(15), 10799.

[111] den Hartog H W and Nakata R, 1983. *EPR and Ionic Thermocurrents Experiments on Cubic Solid Solutions $Sr_{1-x}Eu_xF_{2+x}$*. J. Phys. Soc. (Japan) **52**(9), 3110.

[112] Silversmith A J and Macfarlane R M, 1992. *Spectral-Hole-Burning Study of the Hyperfine Interaction in Axial Eu^{3+} Centres in CaF_2, SrF_2 and BaF_2*. Phys. Rev. B **45**(11), 5811.

[113] Wright J C, 1976. *Upconversion and Excited State Energy Transfer in Rare Earth Doped Materials*. In Radiationless Processes in Molecules and Condensed Phases, Vol 5 of Topics in Applied Physics. Springer-Verlag (Heidelberg).

[114] Tissue B M and Wright J C, 1989. *Phonon-Assisted Energy Transfer Within Dimers in Pr^{3+}:CaF_2*. J. Lum. **44**, 33.

[115] Capobianco J A, Raspa N, Monteil A and Malinowski M, 1993. *Energy Transfer Upconversion in $Gd_3Ga_5O_{12}$:Pr^{3+}*. J. Phys.: Condens. Matter **5**, 6083.

[116] Case W E, Koch M E and Kueny A W, 1990. *The photon avalanche in Rare Earth Crystals*. J. Lum. **45**, 351.

[117] Chivian J S, Case W E and Eden D D, 1979. *The Photon Avalanche: A New Phenomenon in Pr^{3+} -Based Infrared Quantum Counters*. Appl. Phys. Lett. **35**(2), 124.

[118] Wietfeldt J R, Moore D S, Tissue B M and Wright J C, 1986. *Mechanism of Non-resonant Energy Transfer Between Ions in SrF_2:Er^{3+}*. Phys. Rev. B. **33**(8), 5788.

[119] Tissue B M and Wright J C, 1989. *Magnetic Field Induced Enhancements in Energy Transfer Within Dimers in SrF_2:Er^{3+}*. **44**, 121.

[120] Strickland N M and Jones G D, 1996. *Room-Temperature Upconversion Fluorescence of Rare Earth Centres in CaF_2*. J. Lum. **66&67**(1-6), 198.

[121] Wells J P R and Reeves R J, 1996. *Upconversion Flourescence of Eu^{3+} Doped Alkaline Earth Fluorides*. J. Lum. **66&67**(1-6), 219.

[122] Zhang Xiao, Jouart J P, Bouffard M and Mary G, 1994. *Site-Selective Upconversion Luminescence of Ho^{3+} Doped Crystals.* Phys. Stat. Sol. (b) **184**, 559.

[123] Moine B, Dujardin and Pedrini C, 1994. *Excited State Absorption of Eu^{2+} Ions in Pure Fluoride Crystals.* J. Lum. **58**, 339.

[124] Dejneka M, Snitzer E and Riman R E, 1995. *Blue, Green and Red Fluorescence and Energy Transfer of Eu^{3+} in Fluoride Glasses.* J. Lum. **65**, 225.

[125] Lenth W and Macfarlane R M, 1990. *Excitation Mechanisms for Upconversion Lasers.* J. Lum. **45**, 346.

[126] Cockcroft N J, 1994. *Application of Energy Upconversion Spectroscopy to Novel Laser and Phosphor Design.* J. Alloys and Comp. **207&208**, 33.

[127] Silversmith A J and Radlinski A J, 1985. *Zeeman Spectroscopy of the G1 Centre in CaF_2:Eu^{3+}* J. Phys. C: Solid State Phys. **18**, 4385.

[128] Porcher P and Caro P, 1976. *Crystal Field Parameters for Eu^{3+} in KY_3F_{10}.* J. Chem. Phys. **65**(1), 89.

[129] Porcher P and Caro P, 1978. *Crystal Field Parameters for Eu^{3+} in KY_3F_{10}.II. Intensity Parameters.* J. Chem. Phys. **68**(9), 4176.

[130] Porcher P and Caro P, 1978. *Crystal Field Parameters for Eu^{3+} in KY_3F_{10}.III. Radiative and Nonradiative Transition Probabilities.* J. Chem. Phys. **68**(9), 4183.

[131] Dean T, 1996. *Infrared Spectroscopy of the Principal Er^{3+} Centre in BaF_2 and SrF_2 Crystals.*

[132] Kask N E, Kornienko L S and Fakir M, 1964. *Electron Paramagnetic Resonance and Spin Lattice Relaxation of the Nd^{3+} Ion in CaF_2 Single Crystals.* Sov. Phys. - Solid State **6**, 430.

[133] Voronko Yu K, Kaminskii A A and Osiko V V, 1966. *Analysis of the Optical Spectra of CaF_2:Nd^{3+}.* Sov. Phys. JETP **22**(2), 295.

[134] Voronko Yu K, Kaminskii A A and Osiko V V, 1966. *Analysis of the Optical Spectra of Pr^{3+}, Nd^{3+}, Eu^{3+} and Er^{3+} in Fluorite Crystals (Type I) by the Concentration Series Method.* Sov. Phys. JETP **22**(3), 501.

[135] Miller M P and Wright J C, 1978. *Importance of Defect Clustering in the Analysis of BaF_2:Er^{3+} Optical Spectra.* Phys. Rev. B. **18**(7), 3753.

[136] Moore D S and Wright J C, 1979. *Evidence for Cluster Control of the Defect Equilibria in Fluorite Structure Crystals.* Chem. Phys. Lett. **66**(1), 173.

[137] Seelbinder M B and Wright J C, 1981. *Identification of Higher Order Clusters in Charge Compensated Materials Using Three-Body Energy Transfer.* J. Chem. Phys. **75**(10), 5070.

[138] Kazanskii S A, 1984. *Superstructure Regions in the Lattice of the Solid Solution* $(CaF_2)_{1-x}(ErF_3)_x$ *with* $x \geq 0.001$. JETP Lett. **38**(9), 521.

[139] Luxbacher T, Fritzer H P, Sabry-Grant R and Flint C D, 1995. *Fast Cross Relaxation in Lanthanide Hexachloroelpasolites: Application of the Shell Model.* Chem. Phys. Letters **241**, 103.

[140] Luxbacher T, Fritzer H P and Flint C D, 1995. *Cross Relaxation From the* $^4G_{\frac{5}{2}}$ *State of* Sm^{3+} *in* $Cs_2NaSm_xY_{1-x}Cl_6$ *and* $Cs_2NaSm_xGd_{1-x}Cl_6$*: A Comparison of Multipole-Multipole and Anisotropic Dielectric Shell Models.* J. Phys. Condens. Matter **7**, 9683.

[141] Foster D R, Richardson F S and Schwartz R W, 1985. *Optical Spectra and Crystal Field Analysis of* Sm^{3+} *in the Cubic* Cs_2NaYCl_6 *Host.* J. Chem. Phys. **82**(2), 618.

[142] Vasquez S O and Flint C D, 1995. *A Shell Model for Cross Relaxation in Elpasolite Crystals: Application to the* $^3P_0$ *and* $^1G_4$ *States of* $Cs_2NaY_{1-x}Pr_xCl_6$. Chem. Phys. Letters **238**, 378.

[143] Dexter D L, 1953. *A Theory of Sensitized Luminescence in Solids.* J. Chem. Phys. **21**(5), 836.

[144] Heber J, Dornauf H and Siebold H, 1981. *New Aspects in Energy Tranfer in Inhomogeneous Systems.* J. Lum. **24&25**, 735.

[145] Ward R W and Clyman B P, 1975. *Far-Infrared Resonant Mode Absorption By Erbium Impurities in* CaF_2. J. Phys. C: Solid State Phys. **8**, 872.

[146] Hayes W, Wiltshire M C K, Manthey W J and McClure D S, 1973. *Localised Vibrational Modes Induced in* CaF_2 *by Rare Earth Impurities.* J. Phys. C: Solid State Phys. **6**, L273.

[147] Ellens A, Andres H, ter Heerdt M L H, Wegh R T, Meijerink A and Blasse G, 1995. *The Variation of the Electron-Phonon Coupling Strength Through the Trivalent Lanthanide Ion Series.* J. Lum. **66&67**, 240.

[148] Ellens A, 1996. *Electron-Phonon Coupling of Lanthanide Ions in Solids (Elekron-Fonon Koppeling van Lanthanide Ionen in Vaste Stoffen).* Ph.D. Thesis, Deybe Institute (University of Utrecht).

[149] Reisfeld R and Boehm L, 1972. *Energy Transfer Between Samarium and Europium in Phosphate Glasses.* J. Solid State Chem. **4**, pg 417.

[150] Riseberg L A and Weber M J, 1976. *Relaxation Phenomena in Rare Earth Luminescence.* in 'Progress in Optics XIV'. Editor E Wolf. North Holland.

[151] Miller M P and Wright J C, 1979. *Multiphonon and Energy Transfer Relaxation in Charge Compensated Crystals.* J. Chem. Phys. **71**(1), 324.

[152] Weber M J, 1973. *Multiphonon Relaxation of Rare-Earth Ions in Yttrium Orthoaluminate.* Phys. Rev. B. **8**(1), 54.

[153] Cockcroft N J, Jones G D and Syme R W G, 1989. *Upconversion Fluorescence Spectroscopy of Er^{3+} Pairs in $CsCdBr_3$.* J. Lum. **43**, 275.

[154] Mujaji M, Jones G D and Syme R W G, 1992. *Upconversion Fluorescence Spectroscopy of Ho^{3+} Dimer Pairs in $CsCdBr_3$.* J. Lum. **53**, 473.

[155] Mujaji M, Jones G D and Syme R W G, 1993. *Site-Selective Spectroscopy of Ho^{3+} Ions in $CsCdBr_3$ Crystals.* Phys. Rev. B **48**(2), 710.

[156] Antipin A A, Kurkin I I, L D Livanova, Potvoroa L D and Shekun L Ya, 1966. *Electron Paramagnetic Resonance in CaF_2:Sm^{3+}, SrF_2:Sm^{3+} and BaF_2:Sm^{3+} Crystals.* Sov. Phys. - Tech. Phys. **11**(6), 821.

[157] Miller M P and Wright J C, 1978. *Single Site Multiphonon and Energy Transfer Relaxation Phenomena in BaF_2:Er^{3+}.* J. Chem. Phys. **68**(4), 1548.

[158] Strickland N M, 1996. *Laser Excitation and Infrared Absorption Spectroscopy of Rare-Earth Ions Centres in Fluorite Crystals.* Ph.D. Thesis (University of Canterbury).